Dynamics of coherent structures over wind turbine blade

Majd Armaly

▶ **To cite this version:**

Majd Armaly. Dynamics of coherent structures over wind turbine blade. Fluid mechanics [physics.class-ph]. Normandie Université, 2024. English. ⟨NNT : 2024NORMR005⟩. ⟨tel-04546242⟩

HAL Id: tel-04546242

https://theses.hal.science/tel-04546242v1

Submitted on 15 Apr 2024

HAL is a multi-disciplinary open access archive for the deposit and dissemination of scientific research documents, whether they are published or not. The documents may come from teaching and research institutions in France or abroad, or from public or private research centers.

L'archive ouverte pluridisciplinaire **HAL**, est destinée au dépôt et à la diffusion de documents scientifiques de niveau recherche, publiés ou non, émanant des établissements d'enseignement et de recherche français ou étrangers, des laboratoires publics ou privés.

HAL Authorization

Normandie Université

UNIVERSITÉ DE ROUEN NORMANDIE

THÈSE

Pour obtenir le diplôme de doctorat

Spécialité **MECANIQUE DES FLUIDES, ENERGETIQUE, THERMIQUE, COMBUSTION, ACOUSTIQUE**

Préparée au sein de l'**Université de Rouen Normandie**

Dynamics of coherent structures over wind turbine blade

Présentée et soutenue par

MAJD ARMALY

Thèse soutenue le 21/02/2024

devant le jury composé de :

MME ARMELLE CESSOU	Directeur de recherche - Université de Rouen Normandie	Directeur de thèse
M. JEAN-MARC FOUCAUT	Professeur des Universités - ECOLE CENTRALE LILLE	Président du jury
M. BERTRAND LECORDIER	- Université de Rouen Normandie	Co-encadrant Co-encadrant
MME LUMINITA DANAILA	Professeur des Universités - Université de Rouen Normandie	Membre du jury
MME GAELE PERRET	Maître de Conférences - Université Le Havre Normandie	Membre du jury
M. LUDOVIC CHATELLIER	Maître de Conférences HDR - UNIVERSITE POITIERS	Rapporteur du jury
M. NICOLAS MAZELLIER	Professeur des Universités - Université d'Orléans	Rapporteur du jury

Thèse dirigée par **ARMELLE CESSOU** (COMPLEXE DE RECHERCHE INTERPROFESSIONNEL EN AEROTHERMOCHIMIE)

ED 591 PSIME

CORIA UMR 6614

Dynamics of coherent structures over wind turbine blade

Submitted for the degree of
Doctor of Philosophy

by

Majd Armaly

Director: **Armelle Cessou**

Supervisor: **Bertrand Lecordier**

21 February 2024

Abstract

Abstract

The primary objective of the thesis is to quantitatively assess the dynamic behavior of turbulent airflow around a NACA airfoil as a function of the upstream flow. The upstream flow consists of a family of coherent structures, each with its own distinct temporal and spatial scales. Additionally, this upstream flow may include a mean shear due to a large-scale boundary layer. These situations are commonly encountered in wind and marine turbine farms, where the wake generated by one turbine becomes the upstream flow for the next one, and where the atmospheric boundary layer can influence the dynamics of the airfoil's airflow. Aerodynamic research on wind turbines has primarily focused on the general response of airfoils, and the flow downstream. However, airfoils are not considered yet in an upstream flow with the presence of a family of coherent structures. This study takes into account the spatial and temporal aspects, which is crucial for understanding how efficiently the kinetic energy carried by these coherent motions is captured within the wake. The novelty of the project is to provide a complementary and more detailed analysis of the airfoil-upstream flow interactions based on the analysis of the intermittency of the upstream conditions. This helps to gain insights into the dynamic response of the downstream airfoil and the distribution of kinetic energy over the airfoil. To achieve this goal, pressure distributions (coherent structures) must be phase-averaged with a conditioning based on the dynamics of the upstream flow. This type of analysis represents a novel approach and requires the development of specialized methods to be applied to such complex cases. One of the key areas of investigation within the project is the study of the total turbulent kinetic energy (TKE) when the upstream coherent structure packets interact with the downstream airfoil. Additionally, further research can be involved into turbulent kinetic energy, considering the interactions between different components of fluctuations, such as the interactions between coherent and random motion. This thesis work is integrated in the framework of DYNEOL (ANR-17-CE06-0020) project that is funded by the French National Agency of Research (ANR). The project is a collaborative research involving four French laboratories, including the CORIA laboratory.

Resumé

L'objectif principal de cette thèse est d'évaluer quantitativement le comportement dynamique de l'écoulement d'air turbulent autour d'un profil aérodynamique NACA en fonction de l'écoulement en amont. L'écoulement en amont est constitué d'une famille de structures cohérentes, chacune ayant ses propres échelles temporelles et spatiales. En outre, cet écoulement en amont peut inclure un cisaillement moyen dû à une couche limite à grande échelle. Ces situations se rencontrent couramment dans les parcs d'éoliennes et de turbines marines, où le sillage généré par une turbine devient l'écoulement en amont de la suivante, et où la couche limite atmosphérique peut influencer la dynamique de l'écoulement de l'air du profil aérodynamique. La recherche aérodynamique sur les éoliennes s'est principalement concentrée sur la réponse générale des profils aérodynamiques et sur l'écoulement en aval. Cependant, les profils aérodynamiques ne sont pas encore pris en compte dans un écoulement en amont avec la présence d'une famille de structures cohérentes. Cette étude prend en compte les aspects spatiaux et temporels, ce qui est crucial pour comprendre comment l'énergie cinétique transportée par ces mouvements cohérents est capturée dans le sillage. La nouveauté du projet est de fournir une analyse complémentaire et plus détaillée des interactions entre le profil aérodynamique et l'écoulement en amont, basée sur l'analyse de l'intermittence des conditions en amont. Cela permet de mieux comprendre la réponse dynamique de l'aile en aval et la distribution de l'énergie cinétique sur l'aile. Pour atteindre cet objectif, les distributions de pression (structures cohérentes) doivent être moyennées en phase avec un conditionnement basé sur la dynamique du flux en amont. Ce type d'analyse représente une nouvelle approche et nécessite le développement de méthodes spécialisées à appliquer à des cas complexes. L'un des principaux domaines d'investigation du projet est l'étude de l'énergie cinétique turbulente totale (TKE) lorsque les paquets de structures cohérentes en amont interagissent avec le profil aérodynamique en aval. En outre, d'autres recherches peuvent être menées sur l'énergie cinétique turbulente, en considérant les interactions entre les différentes composantes des fluctuations, telles que les interactions entre le mouvement cohérent et le mouvement aléatoire. Ce travail de thèse est intégré dans le cadre du projet DYNEOL (ANR-17-CE06-0020) qui est financé par l'Agence Nationale de la Recherche (ANR). Le projet est une recherche collaborative associant quatre laboratoires français.

Acknowledgements

I would like to thank all those who have played a role in shaping my journey and offering their unwavering support along the way.

First and foremost, I extend my gratitude to the director of CORIA laboratory and this PhD project, Armelle Cessou.

I also wish to convey my sincere appreciation to the esteemed members of the jury for dedicating their valuable time, providing insightful feedback, and offering constructive criticism during the evaluation process of this manuscript. Special acknowledgment goes to Jean Marc Foucaut for serving as the president of my jury, Ludovic Chatelier and Nicolas Mazelier for their roles as reporters, and Gaelle Perret for being a jury member.

Furthermore, I am deeply grateful to my supervisor and leader, Bertrand Lecordier, who essentially carried all the responsibility for my research work. His support, guidance, and expertise in experimentation have been vitally important throughout my doctoral journey. Despite facing numerous challenges, particularly in a domain outside his specialization, his encouragement and patience helped me navigate through difficulties and achieve the objectives of my study under his supervision. Working with him was truly a pleasure, and the opportunities he provided for me to present at international and national conferences, including those in the USA, Australia, France, and Belgium, will greatly benefit my future career. Participating in international conferences provided a wonderful opportunity to engage with fellow researchers, exchange ideas, create new connections within the field, and explore various research centers.

I extend my thanks to Luminita Danaila for her invaluable contributions as a collaborator in turbulence research, despite facing challenges due to illness. This situation required me to fulfill critical and sensitive tasks alone, which also can be considerably difficult. For instance, difficulties in analyzing, verifying and understanding my results.

Additionally, I express my gratitude to Emilien Varea and Corine Lacour for their contributions throughout the project, particularly in its initial stages and the first year.

I want to acknowledge the contributions of all individuals, colleagues, metrology team and friends who have supported me in various capacities during my doctoral studies, with special mention to Gilles Godard and Guillaume Lesage. Where, they consistently providing motivation and positive energy, especially during the final stages of manuscript writing.

Lastly, i wish to express my heartfelt appreciation to my family for their endless love, encouragement, and unwavering belief in my abilities. Their support and sacrifices have

been the foundation of my academic pursuits. I am profoundly grateful to my father, Hussein Armaly, and my mother, Hassiba Armaly, whose encouragement, patience, and sacrifices have supported me through the challenges of my whole academic journey, since my childhood. I extend my sincere thanks to my brothers and my sister for their care and being beside me since i got born, as the younger among them.

Contents

1 Preface **1**
- 1.1 Marine renewable energy . . . 2
  - 1.1.1 Offshore wind energy . . . 5
- 1.2 Context . . . 9
  - 1.2.1 Scope . . . 9
  - 1.2.2 Objectives . . . 9
- 1.3 Thesis outline . . . 10

2 Bibliography **13**
- 2.1 Aerodynamic failures and defeats . . . 14
- 2.2 Turbulent flows . . . 15
  - 2.2.1 Main components of turbulent flows . . . 15
  - 2.2.2 Plane and axisymmetric wakes . . . 16
  - 2.2.3 Vortices formation in turbulent wakes . . . 18
  - 2.2.4 Periodic and non-periodic wake structures . . . 21
- 2.3 Mechanism of energy transfer . . . 23
  - 2.3.1 Richardson energy cascade . . . 23
  - 2.3.2 Kolmogorov similarity laws in energy cascade . . . 24
  - 2.3.3 Kinetic energy of the mean flow . . . 27
  - 2.3.4 Kinetic energy of the turbulence . . . 29
  - 2.3.5 Kinetic energy of the coherent and random structures . . . 32
- 2.4 Wakes interactions . . . 35
- 2.5 Conclusions and research focus . . . 38

3 Experimental setup **39**
- 3.1 Wind tunnel . . . 40
  - 3.1.1 Test section . . . 41
- 3.2 Experiment installation . . . 43
  - 3.2.1 Measurement technique (HS-PIV) . . . 43
  - 3.2.2 Experimental obstacles and configurations. . . . 44
  - 3.2.3 Laser sheet and seeding particles . . . 46
  - 3.2.4 Cameras and spatial calibration . . . 47
  - 3.2.5 Alignement . . . 48
  - 3.2.6 Recordings and synchronization . . . 49
- 3.3 PIV post processing . . . 51
- 3.4 Overview of experimental parameters . . . 52

4 Wake phase decomposition: Methodologies **55**
- 4.1 Introduction . . . 56
- 4.2 Phase decomposition by “pressure sensor” . . . 56

4.2.1 Implementation of methodology and setup . . . 57
4.2.2 Synchronization of microphone . . . 58
4.2.3 Evaluation of phase decomposition by statistics . . . 60
4.3 Phase decomposition by "a posteriori" . . . 64
4.3.1 Implementation of methodology . . . 64
4.3.2 Evaluation of phase decomposition by statistics . . . 67
4.4 Detection of coherent motion (CM) . . . 71
4.4.1 Detection using "pressure sensor" method . . . 72
4.4.2 Detection using "a posteriori" method . . . 73
4.5 Conclusion . . . 76

5 Temporal and spatial periods analysis 79
5.1 Temporal auto-correlation (Temporal period) . . . 80
5.1.1 Cylinder configurations . . . 81
5.1.2 Airfoil configurations . . . 83
5.2 Power spectrum and temporal cross correlation analysis . . . 86
5.2.1 Cylinder configurations . . . 87
5.2.2 Airfoils configurations . . . 89
5.3 Spatial autocorrelation (Spatial period) . . . 92
5.3.1 Spatial periods as a function of samples . . . 93
5.3.2 Spatial autocorrelation average . . . 97
5.3.3 Observations review and conclusions . . . 100

6 Mechanism of energy exchange with no turbulence effect 103
6.1 First order statistics . . . 104
6.2 Total fluctuation energy exchanges . . . 107
6.2.1 2D - planes for total turbulent kinetic energy budget . . . 107
6.2.2 Summary of total turbulent kinetic energy budget . . . 112
6.2.3 Cross section profiles for total turbulent kinetic energy budget . . . 114
6.2.4 Decomposed total kinetic energy in phases . . . 118
6.3 CM and RM interaction TKE . . . 120
6.3.1 2D - planes of coherent motion (CM) energy budget . . . 120
6.3.2 Summary of coherent motion (CM) energy budget . . . 126
6.3.3 Cross section profiles of coherent motion (CM) energy budget . . . 128
6.3.4 2D - planes of Random motion (RM) energy budget . . . 133
6.3.5 Summary of random motion (RM) energy budget . . . 139
6.3.6 Cross section profiles of random motion (RM) energy budget . . . 141
6.4 Observations, reviews, and conclusions . . . 146

7 Two-point energy exchange with no turbulence effect 149
7.1 Two-point turbulent kinetic energy balance . . . 149
7.1.1 Second-order structure functions $\overline{(\Delta u)^2}$ . . . 150
7.1.2 Third-order structure functions $\overline{(\Delta u)^3}$ . . . 153
7.1.3 Fourth order structure functions $\overline{(\Delta u)^4}$ . . . 156
7.2 Observations, reviews and conclusions . . . 159

8 Mechanism of energy exchange with turbulence effect 161
8.1 Introduction to turbulence near wall . . . 162
8.1.1 Turbulent Boundary Layer regions . . . 162
8.1.2 Theory of Turbulent Boundary Layer . . . 164

8.2 Experimental Setup . . . 166
8.2.1 Test section . . . 166
8.2.2 Obstacles installation . . . 166
8.2.3 Turbulent boundary layer characteristics . . . 167
8.2.4 PIV measurement technique . . . 169
8.2.5 PIV processing . . . 170
8.3 First order statistics . . . 171
8.4 Total fluctuation energy exchanges . . . 174
8.4.1 2D - planes for total turbulent kinetic energy budget . . . 175
8.4.2 Cross section profiles for total turbulent kinetic energy budget . . . 178
8.5 Non organized coherent motion in airfoil wake . . . 181
8.6 CM and RM interaction TKE . . . 182
8.6.1 Cross section profiles of coherent motion (CM) energy budget . . . 182
8.6.2 Cross section profiles of random motion (RM) energy budget . . . 184
8.7 Observations, reviews and conclusions . . . 186

9 General conclusions and perspectives 189
9.1 General conclusions . . . 189
9.2 Perspectives . . . 192

Appendices 201

Appendix A Extensions on energy exchange with no turbulence effect 203
A.1 Single cylinder configuration . . . 203
A.1.1 First order statistics . . . 203
A.1.2 Total fluctuations energy exchange . . . 205
A.1.3 Decomposed first order statistics . . . 207
A.1.4 Decomposed total kinetic energy in phases . . . 209
A.1.5 CM energy exchange and interaction with RM . . . 211
A.1.6 RM energy exchange and interaction with CM . . . 216
B.2 Double cylinder configuration . . . 219
B.2.1 First order statistics . . . 220
B.2.2 Total fluctuations energy exchange . . . 221
B.2.3 Decomposed first order statistics . . . 224
B.2.4 Decomposed total kinetic energy in phases . . . 226
B.2.5 CM energy exchange and interaction with RM (based on upstream wake phase decomposition) . . . 228
B.2.6 RM energy exchange and interaction with CM (based on upstream wake phase decomposition) . . . 233
B.2.7 CM energy exchange and interaction with RM (based on downstream wake phase decomposition) . . . 236
B.2.8 RM energy exchange and interaction with CM (based on downstream wake phase decomposition) . . . 241
C.3 Cylinder-airfoil configuration . . . 242
C.3.1 First order statistics . . . 242
C.3.2 Total fluctuations energy exchange . . . 243
C.3.3 Decomposed first order statistics . . . 246
C.3.4 Decomposed total kinetic energy in phases . . . 248
C.3.5 CM energy exchange and interaction with RM . . . 250
C.3.6 RM energy exchange and interaction with CM . . . 255

D.4 Single airfoil configuration . . . 259
D.4.1 First order statistics . . . 259
D.4.2 Total fluctuations energy exchange . . . 259
D.4.3 Decomposed first order statistics . . . 260
D.4.4 Decomposed total kinetic energy in phases . . . 261
D.4.5 CM energy exchange and interaction with RM . . . 263
D.4.6 RM energy exchange and interaction with CM . . . 266
E.5 Double airfoil configuration . . . 267
E.5.1 First order statistics . . . 267
E.5.2 Total fluctuations energy exchange . . . 268
E.5.3 Decomposed first order statistics . . . 269
E.5.4 Decomposed total fluctuations . . . 270
E.5.5 CM energy exchange and interaction with RM . . . 272
E.5.6 RM energy exchange and interaction with CM . . . 275

Appendix B Extensions on energy exchange with turbulence effect 277
A.1 Single cylinder configuration . . . 277
A.1.1 First order statistics . . . 277
A.1.2 Total fluctuations energy exchange . . . 279
A.1.3 Decomposed total kinetic energy in phases . . . 281
A.1.4 CM energy exchange and interaction with RM . . . 283
A.1.5 RM energy exchange and interaction with CM . . . 288
B.2 Double cylinder configuration . . . 291
B.2.1 First order statistics . . . 291
B.2.2 Total fluctuations energy exchange . . . 292
B.2.3 Decomposed total kinetic energy in phases . . . 295
B.2.4 CM energy exchange and interaction with RM . . . 297
B.2.5 RM energy exchange and interaction with CM . . . 301
C.3 Cylinder-airfoil configuration . . . 304
C.3.1 First order statistics . . . 304
C.3.2 Total fluctuations energy exchange . . . 305
C.3.3 Decomposed total kinetic energy in phases . . . 308
C.3.4 CM energy exchange and interaction with RM . . . 310
C.3.5 RM energy exchange and interaction with CM . . . 314
D.4 Airfoil configuration . . . 317
D.4.1 First order statistics . . . 317
D.4.2 Total fluctuations energy exchange . . . 317
E.5 Double airfoil configuration . . . 318
E.5.1 First order statistics . . . 318
E.5.2 Total fluctuations energy exchange . . . 319

List of Figures

1.1 Examples of renewable energies . . . 2
1.2 Tidal barrage schematic. Figure is referred to [1]. . . . 3
1.5 Osmotic power process. Figure referred to [**osmotic**]. . . . 5
1.6 The first wind turbine built in 1888. Figure is referred to [5]. . . . 6
1.9 Wind farm. . . . 9

2.2 Reynolds decomposition. . . . 15
2.3 Axisymmetric wake. Figure is referred to Davidson [10]. . . . 17
2.5 Von Kàrmàn vortex street in the wake of airfoil. Figure is referred to Yarusevych [16]. . . . 20
2.6 Richardson cascade. Figure is referred to Davidson [10]. . . . 23
2.7 Kolmogrov length scales in subranges, Figure is referred to Pope [6] . . . 24
2.8 Kolmogrov energy transfer between scales. Figure is referred to Pope [6]. 26
2.10 Flow visualization of two cylinders interactions in the function of gap distance (Figure from Igrashi [44]). . . . 36
2.11 Flow patterns for two cylinders configuration arranged in tandem (figure from Igrashi [46]). . . . 36
2.12 Strouhal number data for two cylinders configuration arranged in tandem (figure from Sumner [50]). . . . 37
2.13 Relevant configurations. . . . 38

3.1 Closed loop wind tunnel. . . . 40
3.2 (a) Installed test section. (b) Drilled plate for obstacles insertion. . . . 41
3.3 (a) Laser doppler anemometer probe. (b) Streamwise mean velocity in function of motor frequency. . . . 42
3.4 (a) Flow characteristics at low and high motor frequencies . . . 42
3.5 Particle Image Velocimetry (PIV) process. . . . 43
3.6 Experimental set-up. . . . 44
3.7 (a) Employed obstacles. (b) Cylinder-Airfoil configuration (Top). Double airfoil configuration (Bottom). . . . 45
3.8 Configurations and dimensions. . . . 46
3.9 Periscope fixation. . . . 47
3.10 Experimental set-up. . . . 47
3.11 cameras images before calibration. . . . 48
3.12 Alignement of laser sheet and calibration grid. . . . 49
3.13 Particle images for the three cameras. . . . 49
3.14 Recordings and triggers. . . . 50
3.15 Velocity fluctuations comparison in different Δt. . . . 50
3.16 Reconstruction of a complete image from the three camera views of the calibration grid - Final image size: 4256×934 $pixels^2$ - Imposed image resolution: 12 $pixels/mm$. . . . 51

3.17 Instantaneous velocity fields in both directions. 52

4.1 Schematic of experimental setup. 57
4.2 Microphone sensor probe position. (a) Schematic view. (b) Realistic view. 57
4.3 Microphone sensor probe position in real dimensions. 58
4.4 (a) Programmed pulse generator and authorization. (b) Filtering signal and conversion. 59
4.5 Synchronization. 60
4.6 Phase shift between raw and filtered signal at $Re = 8000$. 60
4.7 Profiles of streamwise velocity (X-direction) at two Reynolds numbers ($Re = 2000$ and $Re = 8000$). 61
4.8 Profiles of spanwise velocity (Y-direction) at two Reynolds numbers ($Re = 2000$ and $Re = 8000$). 61
4.9 (a) and (d) are the non synchronized mean velocity and RMS along x direction, respectively. (b) and (e) are the synchronized mean velocity and RMS along X direction at $\Phi = 0°$, respectively. (c) and (f) are the synchronized mean velocity and RMS along X direction at $\Phi = 180°$, respectively. 62
4.10 (a), (d) are the synchronized mean velocity and RMS along X direction, respectively ($Re = 2000$). (b), (e) are the synchronized mean velocity and RMS along X direction, respectively ($Re = 4000$). (c) and (f) are the synchronized mean velocity and RMS along X direction, respectively ($Re = 8000$). All the statistics in this Figure are for $\Phi = 0°$. 63
4.11 Cross-correlation zone (red frame) between the instantaneous velocity field in a cylinder wake (top) and the reference phase average velocity field in a cylinder wake (bottom) at $Re = 2000$ 65
4.12 Cross-correlation zone (red frame) between the instantaneous velocity field in an airfoil wake (top) and the reference phase average velocity field in an airfoil wake (bottom) at $Re = 2000$ 66
4.13 (a) phase shift in cross correlation signal (1D). (b) Spatial phase shift (2D). 67
4.14 Data output (phases) after applying the approach for 190,000 velocity fields (38 second record) 67
4.15 Profiles of streamwise velocity (X-direction) at two Reynolds numbers ($Re = 2000$ and $Re = 8000$). 68
4.16 Profiles of spanwise velocity (Y-direction) at two Reynolds numbers ($Re = 2000$ and $Re = 8000$). 68
4.17 Root Mean Square (RMS) of streamwise velocity in cylinder wake at $Re = 2000$. 69
4.18 Profiles of streamwise velocity (X-direction) at two Reynolds numbers ($Re = 2000$ and $Re = 8000$). 70
4.19 Profiles of spanwise velocity (Y-direction) at two Reynolds numbers ($Re = 2000$ and $Re = 8000$). 70
4.20 Root Mean Square (RMS) of streamwise velocity in airfoil wake at $Re = 2000$. 71
4.21 Triple decomposition for $Re = 2000$ and $\Phi = 0°$. (a) Time average $\overline{f(x,t,\phi=0)}$. (b) coherent structures (CM), $f_c(x,t,\phi=0)$. (c) The random fluctuations in an instantaneous field (RM), $f_r(x,t,\phi=0)$. 72
4.22 Coherent structures evolution (sinusoidal motion) at $Re = 8000$. 73

4.23 Coherent structures (CM) detection in cylinder wake at Re = 2000, representing coherent component of velocity fluctuations $\widetilde{u}$ in streamwise direction. . . . 74
4.24 Coherent structures (CM) detection in cylinder wake at Re = 8000, representing coherent component of velocity fluctuations $\widetilde{u}$ in streamwise direction. . . . 75
4.25 Coherent structures (CM) detection in airfoil wake at Re = 2000, representing coherent component of velocity fluctuations $\widetilde{u}$ in streamwise direction. . . . 75
4.26 Coherent structures (CM) detection in airfoil wake at Re = 8000, representing coherent component of velocity fluctuations $\widetilde{u}$ in streamwise direction. . . . 76

5.1 (a) Temporal signals, (b) autocorrelation of streamwise (u) and spanwise (v) velocity fluctuations at $Re = 2000$. The positions of signals measurement are at $X/D = 3.5$, $Y/D = 1$ and $X/D = 3.5$, $Y/D = 0$ for streamwise and spanwise velocity fluctuations, respectively. . . . 81
5.2 Temporal auto-correlations of streamwise (u) and spanwise (v) velocity fluctuations at different positions in single cylinder wake, at $Re = 2000$ and $Re = 8000$. . . . 82
5.3 Temporal auto-correlations of streamwise (u) and spanwise (v) velocity fluctuations at different positions in double cylinder wake, at $Re = 2000$ and $Re = 8000$ . . . 83
5.4 Temporal auto-correlations of streamwise (u) and spanwise (v) velocity fluctuations at different positions in single airfoil wake, at $Re = 2000$ and $Re = 8000$. . . . 84
5.5 Temporal autocorrelations of streamwise (u) and spanwise (v) velocity fluctuations at different positions in cylinde-airfoil wake. . . . 85
5.6 Temporal autocorrelations of streamwise (u) and spanwise (v) components at different positions in single and double airfoil wakes, at $Re = 8000$. . . 86
5.7 (a) Power spectrum (spanwise velocity component) at different locations downstream of the cylinder wake. (b) Time correlations (spanwise velocity component) at the center of the cylinder wake, between a reference point ($X/D = 3.5$) and 4 different points downstream. . . . 87
5.8 (a) Power spectrum (spanwise velocity component) at different locations downstream of the cylinder wake. (b) Time correlations (spanwise velocity component) at the center of the double cylinder wake, between a reference point in upstream cylinder wake ($X/D = 3.5$) and 4 different points downstream the second cylinder (double cylinder wake). . . . 88
5.9 Time correlations (spanwise velocity component) at the center of the double cylinder wake, between a reference point behind downstream cylinder ($X/D = 13.5$) and 3 different points downstream (double cylinder wake). 89
5.10 (a) Power spectrum (spanwise velocity component) at different locations downstream of the airfoil wake. (b) Time correlations (spanwise velocity component) at the center of the airfoil wake, between a reference point located at $X/C = 3.5$ and 3 different points downstream. . . . 90

5.11 (a) Power spectrum (spanwise velocity component) at different locations (6 points) downstream of the composed wake (cylinder + airfoil). (b) Time correlations(spanwise velocity component) between a reference point located at $X/D = 3.5$ and 4 different points downstream the airfoil. . . . 91
5.12 (a) Power spectrum (spanwise velocity component) at different locations downstream of the cylinder wake. (b) Time correlations (spanwise velocity component) at the center of double airfoil wake, between a reference point in upstream airfoil wake ($X/C = 3.5$) and 4 different points downstream second airfoil. . . . 92
5.13 (a) Spatial profiles (signals) at an instant, (b) autocorrelation of streamwise (u) and spanwise (v) velocity fluctuations at $Re = 2000$. The profiles positions are at: $Y/D = 1$ and $Y/D = 0$ for streamwise and spanwise velocity fluctuations, respectively. . . . 93
5.14 Spatial period distribution over samples (histogram) of streamwise (u) and spanwise (v) fluctuations in single and double cylinder wakes, at $Re = 2000$ and $Re = 8000$. Each class (group) in the histogram is normalised by the total number of samples. . . . 94
5.15 Spatial period distribution fitted to probability density function (PDF) in single and double cylinder wakes, at $Re = 2000$ and $Re = 8000$ . . . 95
5.16 Spatial period distribution over samples of streamwise (u) and spanwise (v) fluctuations in single and double airfoil wakes, at $Re = 2000$ and $Re = 8000$. Each class (group) in the histogram is normalised by the total number of samples . . . 96
5.17 Spatial period distribution fitted to probability density function (PDF) in single and double airfoil wakes, at $Re = 2000$ and $Re = 8000$ . . . 96
5.18 Spatial period distribution over samples of streamwise (u) and spanwise (v) fluctuations in cylinder-airfoil wake, at $Re = 2000$ and $Re = 8000$. Each class (group) in the histogram is normalised by the total number of samples. 97
5.19 Spatial autocorrelation of streamwise (u) and spanwise (v) fluctuations in single and double cylinder wakes, at $Re = 2000$ and $Re = 8000$ . . . 98
5.20 Spatial autocorrelation of streamwise (u) and spanwise (v) fluctuations in single and double airfoil wakes, at $Re = 2000$ and $Re = 8000$. . . . 99
5.21 Spatial autocorrelation of streamwise (u) and spanwise (v) fluctuations in cylinder-airfoil wake, at $Re = 2000$ and $Re = 8000$. . . . 100
5.22 Temporal and spatial periods of coherent motion (CM) within wakes of five configurations and for both Reynolds numbers ($Re = 2000$ and $Re = 8000$). 101

6.1 Streamwise (X direction) mean velocity in single and double airfoil wake configurations. . . . 104
6.2 Spanwise (Y direction) mean velocity in single and double airfoil wake configurations, at $Re = 2000$. . . . 105
6.3 RMS of streamwise velocity (X direction) in single and double airfoil wake configurations, at $Re = 2000$. . . . 105
6.4 RMS of spanwise velocity (Y direction) in single and double airfoil wake configurations, at $Re = 2000$. . . . 106
6.5 Streamwise and spanwise (X and Y direction) mean velocity in single and double cylinder, cylinder-airfoil wake configurations. . . . 106
6.6 Production $\overline{u_i u_j}\frac{\partial \overline{U_i}}{\partial x_j}$ of total turbulent kinetic energy by mean velocity in single and double airfoil wake at $Re = 2000$. Terms are normalised by U_0^3/D. 108

6.7 Advection $\overline{U_j}\frac{\partial(\overline{0.5q^2})}{\partial x_j}$ of total kinetic energy by mean flow in single and double airfoil wakes at $Re = 2000$. Terms are normalised by U_0^3/D. . . . 109
6.8 Dissipation $\bar{\epsilon}$ of total turbulent kinetic energy in single and double airfoil wake at $Re = 2000$. Terms are normalised by U_0^3/D. 110
6.9 Diffusion $\frac{\partial(0.5q^2u_j)}{\partial x_j}$ of total kinetic energy by turbulence in single and double airfoil wakes at $Re = 2000$. Terms are normalised by U_0^3/D. . . . 111
6.10 Diffusion $\frac{\partial\overline{pu_j}}{\partial x_j}$ of total kinetic energy by pressure in single and double airfoil wakes at $Re = 2000$ (estimated). Terms are normalised by U_0^3/D. . 112
6.11 Zones in the wakes of single and double cylinder, single and double airfoil, and cylinder-airfoil configurations. 113
6.12 Total turbulent kinetic energy terms in single and double airfoil wake for two Reynolds number ($Re = 2000$ and $Re = 8000$). Terms are normalised by U_0^3/D. 115
6.13 Total turbulent kinetic energy terms in single and double airfoil wake for two Reynolds number ($Re = 2000$ and $Re = 8000$. Terms are normalised by U_0^3/D. 116
6.14 Total turbulent kinetic energy terms in single and double cylinder wake for two Reynolds number ($Re = 2000$ and $Re = 8000$). Terms are normalised by U_0^3/D. 117
6.15 Total turbulent kinetic energy terms in single and double cylinder wake for two Reynolds number ($Re = 2000$ and $Re = 8000$). Terms are normalised by U_0^3/D. 117
6.16 Total turbulent kinetic energy terms in cylinder-airfoil wake for two Reynolds number ($Re = 2000$ and $Re = 8000$). Terms are normalised by U_0^3/D. 118
6.17 Decomposed terms in 18 phases at $Re = 2000$ in double airfoil wake (videos). Terms are normalised by U_0^3/D 119
6.18 Temporal variation $\frac{1}{2}\overline{\frac{\partial\tilde{q}^2}{\partial t}}$ of coherent motion (CM) in single and double airfoil wakes at Reynolds number $Re = 2000$. Terms are normalised by U_0^3/D. 121
6.19 Production $\overline{\tilde{u}_i\tilde{u}_j}\frac{\partial\overline{U_i}}{\partial x_j}$ of coherent motion (CM) in single and double airfoil wakes at Reynolds number $Re = 2000$, phase decomposition based on upstream airfoil. Terms are normalised by U_0^3/D. 121
6.20 Production $-\overline{\langle u_i'u_j'\rangle\frac{\partial\tilde{u}_i}{\partial x_j}}$ of random motion (RM) by coherent motion at $Re = 2000$, phase decomposition based on upstream airfoil. Terms are normalised by U_0^3/D. 122
6.21 Advection $\frac{1}{2}\overline{U_j}\frac{\partial\overline{\tilde{q}^2}}{\partial x_j}$ of coherent motion (CM) in single and double airfoil wakes at Reynolds number $Re = 2000$, phase decomposition based on upstream airfoil. Terms are normalised by U_0^3/D. 123
6.22 Dissipation $\bar{\tilde{\epsilon}}$ of coherent motion (CM) in single and double airfoil wakes at Reynolds number $Re = 2000$, phase decomposition based on upstream airfoil. Terms are normalised by U_0^3/D. 124
6.23 Pure diffusion $\frac{1}{2}\frac{\partial\overline{\tilde{q}^2\tilde{u}_j}}{\partial x_j}$ of coherent motion (CM) in single and double airfoil wakes at Reynolds number $Re = 2000$, phase decomposition based on upstream airfoil. Terms are normalised by U_0^3/D. 125

6.24 Diffusion $\frac{\partial \overline{\tilde{u}_i \langle u_i' u_j' \rangle}}{\partial x_j}$ of Reynolds stresses by coherent motion (CM) in single and double airfoil wakes at Reynolds number $Re = 2000$, phase decomposition based on upstream airfoil. Terms are normalised by U_0^3/D. 125
6.25 Diffusion $\frac{\partial \overline{\tilde{p}\tilde{u}_j}}{\partial x_j}$ of coherent motion (CM) by pressure in single and double airfoil wakes at Reynolds number $Re = 2000$ (estimated), phase decomposition based on upstream airfoil. Terms are normalised by U_0^3/D. 126
6.26 Zones in the wakes of single and double cylinder, single and double airfoil, and cylinder-airfoil configurations. 127
6.27 Coherent motion (CM) energy budget terms in single and double airfoil wake for two Reynolds number ($Re = 2000$ and $Re = 8000$), phase decomposition based on upstream airfoil. Terms are normalised by U_0^3/D. 129
6.28 Coherent motion (CM) energy budget terms in single and double airfoil wake for two Reynolds number ($Re = 2000$ and $Re = 8000$), phase decomposition based on upstream airfoil. Terms are normalised by U_0^3/D. 130
6.29 Coherent motion (CM) energy budget terms in single and double cylinder wake for two Reynolds number ($Re = 2000$ and $Re = 8000$), phase decomposition based on upstream cylinder. Terms are normalised by U_0^3/D. 131
6.30 Coherent motion (CM) energy budget terms in single and double cylinder wake for two Reynolds number ($Re = 2000$ and $Re = 8000$), phase decomposition based on upstream cylinder. Terms are normalised by U_0^3/D. 131
6.31 Coherent motion (CM) energy budget terms in double cylinder wake for two Reynolds number ($Re = 2000$ and $Re = 8000$), phase decomposition based on downstream cylinder. Terms are normalised by U_0^3/D. 132
6.32 Coherent motion (CM) energy budget terms in cylinder-airfoil wake for two Reynolds number ($Re = 2000$ and $Re = 8000$), phase decomposition based on upstream cylinder. Terms are normalised by U_0^3/D. 133
6.33 Temporal variation $\frac{1}{2}\overline{\frac{\partial q'^2}{\partial t}}$ of random motion (RM) in single and double airfoil wakes at Reynolds number $Re = 2000$, normalised by U_0^3/D. 134
6.34 Production $\overline{u_i' u_j'} \frac{\partial \overline{U_i}}{\partial x_j}$ of random motion (RM) by mean flow at $Re = 2000$, normalised by U_0^3/D. 135
6.35 Production $\overline{\langle u_i' u_j' \rangle \frac{\partial \tilde{u}_i}{\partial x_j}}$ of random motion (RM) by coherent motion at $Re = 2000$, phase decomposition based on upstream airfoil. Terms are normalised by U_0^3/D. 135
6.36 Advection $\frac{1}{2}\overline{U}_j \frac{\partial \overline{q'^2}}{\partial x_j}$ of random motion (RM) in single and double airfoil wakes at Reynolds number $Re = 2000$, normalised by U_0^3/D. 136
6.37 Dissipation $\overline{\epsilon'}$ of random motion (RM) by viscous stress at $Re = 2000$, normalised by U_0^3/D. 137
6.38 Pure diffusion $\frac{1}{2}\frac{\partial \overline{q'^2 u_j'}}{\partial x_j}$ of random motion (RM) in single and double airfoil wakes at Reynolds number $Re = 2000$, normalised by U_0^3/D. 138
6.39 Diffusion $\frac{1}{2}\frac{\partial \overline{\tilde{u}_j \langle q'^2 \rangle}}{\partial x_j}$ of random motion (RM) by coherent motion (CM) interaction in single and double airfoil wakes at Reynolds number $Re = 2000$, phase decomposition based on upstream airfoil. Terms are normalised by U_0^3/D. 138

6.40 Diffusion $\frac{\partial \overline{p' u_j'}}{\partial x_j}$ of random motion (RM) by pressure in single and double airfoil wakes at Reynolds number $Re = 2000$ (estimated), normalised by U_0^3/D. 139
6.41 Zones in the wakes of single and double cylinder, single and double airfoil, and cylinder-airfoil configurations. 140
6.42 Random motion (RM) energy budget terms in single and double airfoil wake for two Reynolds number ($Re = 2000$ and $Re = 8000$), phase decomposition based on upstream airfoil. Terms are normalised by U_0^3/D. 142
6.43 Random motion (RM) energy budget terms over upstream (single airfoil wake) and downstream (double airfoil wake) airfoil for two Reynolds number ($Re = 2000$ and $Re = 8000$), phase decomposition based on upstream airfoil. Terms are normalised by U_0^3/D. 143
6.44 Random motion (RM) energy budget terms in single and double cylinder wake for two Reynolds number ($Re = 2000$ and $Re = 8000$), phase decomposition based on upstream cylinder. Terms are normalised by U_0^3/D. 144
6.45 Random motion (RM) energy budget terms in single and double cylinder wake for two Reynolds number ($Re = 2000$ and $Re = 8000$), phase decomposition based on upstream cylinder. Terms are normalised by U_0^3/D. 145
6.46 Random motion (RM) energy budget terms in single and double cylinder wake for two Reynolds number ($Re = 2000$ and $Re = 8000$), phase decomposition based on downstream cylinder. Terms are normalised by U_0^3/D. 145
6.47 Random motion (RM) energy budget terms in cylinder-airfoil wake for two Reynolds number ($Re = 2000$ and $Re = 8000$), phase decomposition based on upstream cylinder. Terms are normalised by U_0^3/D. 146

7.1 2nd order moment structure functions $\overline{(\Delta u)^2}$ at Re = 2000 and 8000, decomposed at 0°, 100°, 180°, 280° phase shifts and without phase decomposition. Second-order structure functions $\overline{(\Delta u)^2}$ are normalized with respect to the variances at the two points. Phase decomposition is based on the upstream cylinder in both wakes. 151
7.2 2nd order moment structure functions $\overline{(\Delta u)^2}$ at Re = 2000 and 8000, decomposed at 0°, 100°, 180°, 280° phase shifts and without phase decomposition. 2nd order functions $\overline{(\Delta u)^2}$ are normalized with respect to the variances at the two points. Phase decomposition is based on the downstream cylinder in double cylinder wake and the upstream cylinder in cylinder-airfoil wake. 152
7.3 Second-order structure functions $\overline{(\Delta u)^2}$ at Re = 2000 and 8000, decomposed at 0°,100°, 180°, 280° phase shifts and without phase decomposition. Second-order structure functions $\overline{(\Delta u)^2}$ are normalized with respect to the variances at the two points. Phase decomposition is based on the upstream airfoil in both wakes. 153
7.4 Third-order structure functions $\overline{(\Delta u)^3}$ at $Re = 2000$ and 8000, decomposed at 0°,100°,180°,280° phase shifts and without phase decomposition. Third order structure functions $\overline{(\Delta u)^3}$ are normalised by $\overline{(\Delta u)^2}^{3/2}$. Phase decomposition is based on the upstream cylinder in both wakes. 154

7.5 Third order structure functions $\overline{(\Delta u)^3}$ at Re = 2000 and 8000, decomposed at 0°,100°,180°,280° phase shifts and without phase decomposition. 3rd order functions $\overline{(\Delta u)^3}$ are normalised by $(\overline{(\Delta u)^2})^{3/2}$. Phase decomposition is based on the downstream cylinder in the two-cylinder wake and the upstream cylinder in the cylinder-airfoil wake. 155
7.6 Third order structure functions $\overline{(\Delta u)^3}$ at Re = 2000 and 8000, decomposed at 0°,100°,180°,280° phase shifts and without phase decomposition. Third order structure functions $\overline{(\Delta u)^3}$ are normalised by $(\overline{(\Delta u)^2})^{3/2}$. Phase decomposition is based on the upstream airfoil in both wakes. 156
7.7 Fourth order structure functions$\overline{(\Delta u)^4}$ at $Re = 2000$ and 8000, decomposed at 0°,100°,180°,280° phase shifts and without phase decomposition. Fourth order structure functions $\overline{(\Delta u)^4}$ are normalised by $(\overline{(\Delta u)^2})^2$. Phase decomposition is based on the upstream cylinder in both wakes. 157
7.8 Fourth order structure functions $\overline{(\Delta u)^4}$ at $Re = 2000$ and 8000, decomposed at 0°,100°,180°,280° phase shifts and without phase decomposition. Fourth order structure functions $(\Delta u)^4$ are normalised by $(\overline{(\Delta u)^2})^2$. Phase decomposition is based on the downstream cylinder in double cylinder wake and the upstream cylinder in cylinder-airfoil wake. 158
7.9 Fourth order structure functions $\overline{(\Delta u)^4}$ at Re = 2000 and 8000, decomposed at 0°,100°,180°,280° phase shifts and without phase decomposition. Fourth order structure functions $\overline{(\Delta u)^4}$ are normalised by $(\overline{(\Delta u)^2})^2$. Phase decomposition is based on an upstream airfoil in both wakes. 159

8.2 Turbulent Boundary Layer profile. Graph is obtained from [100]. 164
8.3 LML wind tunnel. 166
8.4 (a) Measurement position in wind tunnel. (b) Installed obstacles in test section. (c) Laser sheet in test section. 167
8.5 Profiles of streamwise mean velocity obtained by Hot Wire Anemometry: ♦, $R_\theta = 8100$; □, $R_\theta = 11500$; ▲, $R_\theta = 14800$; ∘, $R_\theta = 20600$; −, Van Driest profile. Data is referred to Carlier study [103]. 168
8.6 Profiles of RMS obtained by Hot Wire Anemometry: ♦, $R_\theta = 8100$; □, $R_\theta = 11500$; ▲, $R_\theta = 14800$; ∘, $R_\theta = 20600$. Data are referred to Carlier study [103]. 169
8.7 Laser sheet path. 170
8.8 Instantaneous velocity fields in both directions. 171
8.9 Streamwise (X direction) mean velocity in single and double airfoil wakes at $z^+ = 3125$. 172
8.10 Spanwise (Y direction) mean velocities in single and double airfoil wakes at $z^+ = 3125$. 172
8.11 RMS of streamwise velocity (X direction) in single and double airfoil wake configurations, at $z^+ = 3125$. 173
8.12 RMS of spanwise velocity (Y direction) in single and double airfoil wake configurations, at $z^+ = 3125$. 173
8.13 Streamwise and spanwise (X and Y directions) mean velocity in single and double cylinder, cylinder-airfoil wake configurations. 174
8.14 Production $\overline{u_i u_j}\frac{\partial \overline{U_i}}{\partial x_j}$ of total turbulent kinetic energy by mean velocity in single and double airfoil wake at $z^+ = 3125$. Terms are normalised by U_0^3/D. 175
8.15 Advection $\overline{U_j}\frac{\partial(\overline{0.5q^2})}{\partial x_j}$ of total kinetic energy by mean velocity in single and double airfoil wakes at $z^+ = 3125$. Terms are normalized by U_0^3/D. . . . 176

8.16 Dissipation $\bar{\epsilon}$ of total turbulent kinetic energy in single and double airfoil wake at $z^+ = 3125$. Terms are normalized by U_0^3/D. 177
8.17 Diffusion $\frac{\partial(\overline{0.5q^2u_j})}{\partial x_j}$ of total turbulent kinetic energy by Reynolds stresses in single and double airfoil wake at $z^+ = 3125$. Terms are normalized by U_0^3/D.177
8.18 Diffusion $\frac{\partial\overline{pu_j}}{\partial x_j}$ of total turbulent kinetic energy by pressure stresses in single and double airfoil wake at $z^+ = 3125$ (estimated). Terms are normalized by U_0^3/D. 178
8.19 Total TKE terms in single and double airfoil wake at two heights from the wall ($z^+ = 500$ and $z^+ = 3125$). Terms are normalized by U_0^3/D. 179
8.20 Total TKE terms in single and double airfoil wake at two heights from the wall ($z^+ = 500$ and $z^+ = 3125$). Terms are normalised by U_0^3/D. 179
8.21 Total TKE terms in single and double cylinder wake at two heights from the wall ($z^+ = 500$ and $z^+ = 3125$). Terms are normalized by U_0^3/D. . . . 180
8.22 Total TKE terms in cylinder-airfoil wake at two heights from the wall ($z^+ = 500$ and $z^+ = 3125$). Terms are normalised by U_0^3/D. 181
8.23 Comparison in spanwise (Y) instantaneous velocity fields. 182
8.24 Coherent motion (CM) energy budget terms in single and double cylinder wake at two heights from the wall ($z^+ = 500$ and $z^+ = 3125$), phase decomposition based on upstream cylinder. Terms are normalized by U_0^3/D183
8.25 Coherent motion (CM) energy budget terms in cylinder-airfoil wake at two heights from the wall ($z^+ = 500$ and $z^+ = 3125$), phase decomposition based on upstream cylinder. Terms are normalized by U_0^3/D 184
8.26 Random motion (RM) energy budget terms in single and double cylinder wake configurations at two heights from the wall ($z^+ = 500$ and $z^+ = 3125$). Phase decomposition is based on upstream cylinder. Terms are normalized by U_0^3/D. 185
8.27 Random motion (RM) energy budget terms in cylinder-airfoil wake at two heights from the wall ($z^+ = 500$ and $z^+ = 3125$), phase decomposition based on upstream cylinder. Terms are normalized by U_0^3/D 186

A.1 Streamwise (X direction) mean velocities in cylinder wake 203
A.2 Spanwise (Y direction) mean velocities in cylinder wake 204
A.3 RMS of streamwise velocities (X direction) in cylinder wake 204
A.4 RMS of spanwise velocities (Y direction) in cylinder wake 205
A.5 Production of total turbulent kinetic energy by mean velocity in cylinder wake 205
A.6 Advection of total kinetic energy by mean velocity in cylinder wake . . . 206
A.7 Diffusion of total turbulent kinetic energy by turbulence in cylinder wake 206
A.8 Diffusion of total turbulent kinetic energy by pressure in cylinder wake . 207
A.9 Dissipation of total turbulent kinetic energy in cylinder wake 207
A.10 Mean of streamwise direction (X) for one particular phase (phases decomposed) in cylinder wake 208
A.11 Mean of spanwise direction (Y) for one particular phase (phases decomposed) in cylinder wake 208
A.12 RMS of streamwise direction (X) for one particular phase (phases decomposed) in cylinder wake 209
A.13 RMS of spanwise direction (Y) for one particular phase (phase decomposed) in cylinder wake 209
A.14 Decomposed production by mean at $Re = 2000$ in cylinder wake 210

A.15 Decomposed advection term at $Re = 2000$ in cylinder wake 210
A.16 Decomposed diffusion by turbulence at $Re = 2000$ in cylinder wake 210
A.17 Decomposed diffusion by pressure at $Re = 2000$ in cylinder wake 211
A.18 Decomposed dissipation at $Re = 2000$ in cylinder wake 211
A.19 Coherent motion (CM) production and dissipation $Re = 2000$ 212
A.20 Coherent motion (CM) transport and RM-interaction terms at $Re = 2000$ 213
A.21 Coherent motion (CM) production and dissipation at $Re = 8000$ 214
A.22 Coherent motion (CM) transport and RM-interaction terms at $Re = 8000$ 215
A.23 Random motion (RM) production and dissipation $Re = 2000$ 216
A.24 Random motion (RM) transport terms in cylinder wake at $Re = 2000$ . . 217
A.25 Random motion (RM) production and dissipation $Re = 8000$ 218
A.26 Random motion (RM) transport terms in cylinder wake at $Re = 8000$ . . 219
A.27 Streamwise (X direction) mean velocities in double cylinder wake 220
A.28 Spanwise (Y direction) mean velocities in double cylinder wake 220
A.29 RMS of streamwise velocities (X direction) in double cylinder wake . . . 221
A.30 RMS of spanwise velocities (Y direction) in double cylinder wake 221
A.31 Production of total turbulent kinetic energy by mean velocity in double cylinder wake 222
A.32 Advection of total kinetic energy by mean velocity in double cylinder wake 222
A.33 Diffusion of total turbulent kinetic energy by turbulence in double cylinder wake 223
A.34 Diffusion of total turbulent kinetic energy by pressure in double cylinder wake 223
A.35 Dissipation of total turbulent kinetic energy in double cylinder wake . . . 224
A.36 RMS of streamwise direction (X) for one particular phase (phases decomposed) in double cylinder wake 224
A.37 Mean velocity of spanwise direction (Y) for one particular phase (phases decomposed) in double cylinder wake 225
A.38 RMS of streamwise direction (X) for one particular phase (phases decomposed) in double cylinder wake 225
A.39 RMS of spanwise direction (Y) for one particular phase (phase decomposed) in double cylinder wake 226
A.40 Decomposed production by mean at $Re = 2000$ in double cylinder wake . 226
A.41 Decomposed advection at $Re = 2000$ in double cylinder wake 227
A.42 Decomposed diffusion by turbulence at $Re = 2000$ in double cylinder wake 227
A.43 Decomposed diffusion by pressure at $Re = 2000$ in double cylinder wake . 227
A.44 Decomposed dissipation at $Re = 2000$ in double cylinder wake 228
A.45 Coherent motion (CM) production and dissipation $Re = 2000$ in double cylinder wake 229
A.46 Coherent motion (CM) transport and RM-interaction terms at $Re = 2000$ in double cylinder wake 230
A.47 Coherent motion (CM) production and dissipation at $Re = 8000$ in double cylinder wake 231
A.48 Coherent motion (CM) transport and RM-interaction terms at $Re = 8000$ in double cylinder wake 232
A.49 Random motion (RM) production and dissipation terms in double cylinder wake at $Re = 2000$ 233
A.50 Random motion (RM) transport terms in double cylinder wake at $Re = 2000$ 234

A.51 Random motion (RM) production and dissipation in double cylinder wake at $Re = 8000$ . . . 235
A.52 Random motion (RM) transport terms in double cylinder wake at $Re = 8000$ 236
A.53 Coherent motion (CM) production and dissipation at $Re = 2000$ in double cylinder wake based on second obstacle phase decomposition . . . 237
A.54 Coherent motion (CM) transport and RM-interaction terms at $Re = 2000$ in double cylinder wake on second obstacle phase decomposition . . . 238
A.55 Coherent motion (CM) production and dissipation at $Re = 8000$ in 2 cylinders wake based on second obstacle phase decomposition . . . 239
A.56 Coherent motion (CM) transport and RM-interaction terms at $Re = 8000$ in double cylinder wake . . . 240
A.57 Production of RM by CM interaction (created by downstream cylinder) . 241
A.58 Diffusion of RM by CM interaction (created by downstream cylinder) . . 241
A.59 Streamwise (X direction) mean velocities in cylinder wake . . . 242
A.60 Spanwise (Y direction) mean velocities in cylinder-airfoil wake . . . 242
A.61 RMS of streamwise velocities (x direction) in cylinder-airfoil wake . . . 243
A.62 RMS of spanwise velocities (y direction) in cylinder-airfoil wake . . . 243
A.63 Production of total turbulent kinetic energy by mean velocity in cylinder-airfoil wake . . . 244
A.64 Advection of total kinetic energy by mean velocity . . . 244
A.65 Diffusion of total turbulent kinetic energy by turbulence in cylinder-airfoil wake . . . 245
A.66 Diffusion of total turbulent kinetic energy by pressure in cylinder-airfoil wake 245
A.67 Dissipation of total turbulent kinetic energy in cylinder-airfoil wake . . . 246
A.68 Mean velocity of streamwise direction (X) for one particular phase (phases decomposed) in cylinder-airfoil wake . . . 246
A.69 Mean velocity of spanwise direction (Y) for one particular phase (phases decomposed) in cylinder-airfoil wake . . . 247
A.70 RMS of streamwise direction (X) for one particular phase (phases decomposed) in cylinder-airfoil wake . . . 247
A.71 RMS of spanwise direction (Y) for one particular phase (phase decomposed) in cylinder-airfoil wake . . . 248
A.72 Decomposed production by mean at $Re = 2000$ in cylinder wake . . . 248
A.73 Decomposed advection at $Re = 2000$ in cylinder-airfoil wake . . . 249
A.74 Decomposed diffusion by turbulence at $Re = 2000$ in cylinder-airfoil wake 249
A.75 Decomposed diffusion by pressure at $Re = 2000$ in cylinder-airfoil wake . 249
A.76 Decomposed dissipation at $Re = 2000$ in cylinder-airfoil wake . . . 250
A.77 Coherent motion (CM) production and dissipation $Re = 2000$ in cylinder-airfoil wake . . . 250
A.78 Coherent motion (CM) transport and RM-interaction terms at $Re = 2000$ in cylindre-airfoil wake . . . 252
A.79 Coherent motion (CM) production and dissipation at $Re = 8000$ in cylinder-airfoil wake . . . 253
A.80 Coherent motion (CM) transport and RM-interaction terms at $Re = 8000$ in cylinder-airfoil wake . . . 254
A.81 Random motion (RM) production and dissipation at $Re = 2000$ in cylinder-airfoil wake . . . 255
A.82 Random motion (RM) transport terms in cylinder wake at $Re = 2000$ in cylinder-airfoil wake . . . 256

A.83 Random motion (RM) production and dissipation terms in cylinder-airfoil wake at $Re = 8000$ . . . 257
A.84 Random motion (RM) transport terms in cylinder-airfoil wake at $Re = 8000$ 258
A.85 Mean velocities in airfoil wake at high Reynolds number $Re = 8000$ . . . 259
A.86 RMS of velocities (Y direction) in airfoil wake at high Reynolds number $Re = 8000$ . . . 259
A.87 Total kinetic energy of turbulence in airfoil wake at $Re = 8000$. Terms are normalised by D/U_0^3 . . . 260
A.88 RMS of streamwise direction (X) for one particular phase (phases decomposed) in single airfoil wake . . . 261
A.89 RMS of spanwise direction (Y) for one particular phase (phase decomposed) in airfoil wake . . . 261
A.90 Decomposed production by mean at $Re = 2000$ in airfoil wake . . . 262
A.91 Decomposed advection at $Re = 2000$ in airfoil wake . . . 262
A.92 Decomposed diffusion by turbulence at $Re = 2000$ in airfoil wake . . . 262
A.93 Decomposed diffusion by pressure at $Re = 2000$ in airfoil wake . . . 263
A.94 Decomposed dissipation at $Re = 2000$ in airfoil wake . . . 263
A.95 Coherent motion (CM) production and dissipation at $Re = 8000$ in airfoil wake . . . 264
A.96 Coherent motion (CM) transports at $Re = 8000$ in airfoil wake . . . 265
A.97 Random motion (RM) production and dissipation terms in airfoil wake at $Re = 8000$ . . . 266
A.98 Random motion (RM) transport terms in airfoil wake at $Re = 8000$ . . . 267
A.99 Mean velocities in double airfoil wake at high Reynolds number $Re = 8000$ 268
A.100 RMS of velocities (y direction) in double airfoil wake at high Reynolds number $Re = 8000$ . . . 268
A.101 Total kinetic energy of turbulence in double airfoil wake at $Re = 8000$. Terms are normalised by D/U_0^3 . . . 269
A.102 RMS of streamwise direction (X) for one particular phase (phases decomposed) in double airfoil wake . . . 270
A.103 RMS of spanwise direction (Y) for one particular phase (phase decomposed) in double airfoil wake . . . 270
A.104 Decomposed production by mean at $Re = 2000$ in double airfoil wake . . . 271
A.105 Decomposed advection at $Re = 2000$ in double airfoil wake . . . 271
A.106 Decomposed diffusion by turbulence at $Re = 2000$ in double airfoil wake . 271
A.107 Decomposed diffusion by pressure at $Re = 2000$ in double airfoil wake . . 272
A.108 Decomposed dissipation at $Re = 2000$ in double airfoil wake . . . 272
A.109 Coherent motion (CM) production and dissipation at $Re = 8000$ in 2 airfoils wake . . . 273
A.110 Coherent motion (CM) transport and RM-interaction at $Re = 8000$ in double airfoil wake . . . 274
A.111 Random motion (RM) production and dissipation terms in double airfoil wake at $Re = 8000$ . . . 275
A.112 Random motion (RM) energy budget in double airfoil wake at $Re = 8000$ 276

B.1 Streamwise (X direction) mean velocities in cylinder wake . . . 277
B.2 Spanwise (Y direction) mean velocities in cylinder wake . . . 278
B.3 RMS of streamwise velocities (X direction) in cylinder wake . . . 278
B.4 RMS of spanwise velocities (Y direction) in cylinder wake . . . 279

B.5 Production of total turbulent kinetic energy by mean velocity in cylinder wake. Term is normalized by U_0^3/D. 279
B.6 Advection of total kinetic energy by mean velocity in cylinder wake. Terms is normalized by U_0^3/D. 280
B.7 Diffusion of total turbulent kinetic energy by Reynolds stresses in cylinder wake. Term is normalized by U_0^3/D. 280
B.8 Diffusion of total turbulent kinetic energy by pressure stresses in cylinder wake. Term is normalized by U_0^3/D. 281
B.9 Dissipation of total turbulent kinetic energy in cylinder wake. Term is normalized by U_0^3/D. 281
B.10 Decomposed production by mean at $z^+ = 500$ in cylinder wake.Term is normalized by U_0^3/D. 282
B.11 Decomposed advection at $z^+ = 500$ in cylinder wake. Term is normalized by U_0^3/D. 282
B.12 Decomposed diffusion by turbulence at $z^+ = 500$ in cylinder wake.Term is normalized by U_0^3/D. 282
B.13 Decomposed diffusion by pressure at $z^+ = 500$ in cylinder wake.Term is normalized by U_0^3/D. 283
B.14 Decomposed dissipation at $z^+ = 500$ in cylinder wake. Term is normalized by U_0^3/D. 283
B.15 Coherent motion (CM) production and dissipation $z^+ = 500$. Terms are normalized by U_0^3/D. 284
B.16 Coherent motion (CM) transports at $z^+ = 500$. Terms are normalized by U_0^3/D. 285
B.17 Coherent motion (CM) production and dissipation at $z^+ = 3125$. Terms are normalised by U_0^3/D. 286
B.18 Coherent motion (CM) transports at $z^+ = 3125$. Terms are normalised by U_0^3/D. 287
B.19 Random motion (RM) energy budget in cylinder wake at $z^+ = 500$. Terms are normalised by U_0^3/D. 289
B.20 Random motion (RM) energy budget in cylinder wake at $z^+ = 3125$. Terms are normalised by U_0^3/D. 290
B.21 Streamwise (X direction) mean velocities in double cylinder wake 291
B.22 Spanwise (Y direction) mean velocities in double cylinder wake 291
B.23 RMS of streamwise velocities (X direction) in double cylinder wake. . . . 292
B.24 RMS of spanwise velocities (Y direction) in double cylinder wake. 292
B.25 Production of total turbulent kinetic energy by mean velocity in double cylinder wake. Term is normalized by U_0^3/D. 293
B.26 Advection of total kinetic energy by mean velocity in double cylinder wake. Term is normalized by U_0^3/D. 293
B.27 Diffusion of total turbulent kinetic energy by turbulence in double cylinder wake. Term is normalized by U_0^3/D. 294
B.28 Diffusion of total turbulent kinetic energy by turbulence in double cylinder wake. Term is normalized by U_0^3/D. 294
B.29 Dissipation of total turbulent kinetic energy in double cylinder wake. Term is normalised by U_0^3/D. 295
B.30 Decomposed production by mean at $Re = 4667$ in double cylinder wake. Term is normalized by U_0^3/D. 295

B.31 Decomposed advection at $z^+ = 500$ in double cylinder wake. Term is normalized by U_0^3/D. . . . 295
B.32 Decomposed diffusion by pressure at $z^+ = 500$ in double cylinder wake. Term is normalised by U_0^3/D. . . . 296
B.33 Decomposed diffusion by pressure at $z^+ = 500$ in double cylinder wake. Term is normalised by U_0^3/D. . . . 296
B.34 Decomposed dissipation at $z^+ = 500$ in double cylinder wake. Term is normalised by U_0^3/D. . . . 296
B.35 Coherent motion (CM) production and dissipation at $z^+ = 500$. Terms are normalised by U_0^3/D. . . . 297
B.36 Coherent motion (CM) transports at $z^+ = 500$. Terms are normalised by U_0^3/D. . . . 298
B.37 Coherent motion (CM) production and dissipation at $z^+ = 3125$. Terms are normalised by U_0^3/D. . . . 299
B.38 Coherent motion (CM) transports at $z^+ = 3125$. Terms are normalised by U_0^3/D. . . . 300
B.39 Random motion (RM) energy budget in double cylinder wake at $z^+ = 500$. Terms are normalised by U_0^3/D. . . . 302
B.40 Random motion (RM) energy budget in double cylinder wake at $z^+ = 3125$. Terms are normalised by U_0^3/D. . . . 303
B.41 Streamwise (X direction) mean velocities in cylinder-airfoil wake 304
B.42 Spanwise (Y direction) mean velocities in cylinder-airfoil wake 304
B.43 RMS of streamwise velocities (X direction) in cylinder-airfoil wake 305
B.44 RMS of spanwise velocities (Y direction) in cylinder-airfoil wake 305
B.45 Production of total turbulent kinetic energy by mean velocity in cylinder-airfoil wake. Term is normalized by U_0^3/D. . . . 306
B.46 Advection of total kinetic energy by mean velocity in cylinder-airfoil wake. Term is normalized by U_0^3/D. . . . 306
B.47 Diffusion of total turbulent kinetic energy by turbulence in cylinder-airfoil wake. Term is normalized by U_0^3/D. . . . 307
B.48 Diffusion of total turbulent kinetic energy by pressure in cylinder-airfoil wake. Term is normalized by U_0^3/D. . . . 307
B.49 Dissipation of total turbulent kinetic energy in cylinder-airfoil wake. Term is normalized by U_0^3/D. . . . 308
B.50 Decomposed production by mean at $z^+ = 500$ in cylinder-airfoil wake. Term is normalized by U_0^3/D. . . . 308
B.51 Decomposed advection at $z^+ = 500$ in cylinder-airfoil wake. Term is normalized by U_0^3/D. . . . 308
B.52 Decomposed diffusion by turbulence at $z^+ = 500$ in cylinder-airfoil wake. Term is normalized by U_0^3/D. . . . 309
B.53 Decomposed diffusion by pressure at $z^+ = 500$ in cylinder-airfoil wake. Term is normalized by U_0^3/D. . . . 309
B.54 Decomposed dissipation at $z^+ = 500$ in cylinder-airfoil wake. Term is normalized by U_0^3/D. . . . 309
B.55 Coherent motion (CM) production and dissipation $z^+ = 500$. Terms are normalized by U_0^3/D. . . . 310
B.56 Coherent motion (CM) transports at $z^+ = 500$. Terms are normalized by U_0^3/D. . . . 311

B.57 Coherent motion (CM) production and dissipation $z^+ = 3125$. Terms are normalised by U_0^3/D. 312
B.58 Coherent motion (CM) transports at $z^+ = 3125$. Terms are normalized by U_0^3/D. 313
B.59 Random motion (RM) energy budget in cylinder-airfoil wake at $z^+ = 500$.Terms are normalized by U_0^3/D. 315
B.60 Random motion (RM) energy budget in cylinder-airfoil wake at $z^+ = 3125$. Terms are normalized by U_0^3/D. 316
B.61 Mean velocities in single airfoil wake at $z^+ = 500$ 317
B.62 RMS of velocities in single airfoil wake at $z^+ = 500$ 317
B.63 Total kinetic energy of turbulence in single airfoil wake at $z^+ = 500$. Terms are normalized by U_0^3/D 318
B.64 Mean velocities in double airfoil wake at $z^+ = 500$ 319
B.65 RMS of velocities in double airfoil wake at $z^+ = 500$ 319
B.66 Total kinetic energy of turbulence in double airfoil wake at $z^+ = 500$. Terms are normalized by U_0^3/D 320

List of Tables

3.1 Camera views parameters. 48
3.2 Experiment setup parameters. 53

4.1 Parameters of non-synchronized data. 58
4.2 Parameters of synchronized data. 58

6.1 Coefficients α_{PIV} as a function of Reynolds numbers. 110
6.2 Gain and lost in wakes for total turbulent kinetic energy. 114
6.3 Gain and lost in wakes for coherent motion (CM) kinetic energy budget. . 128
6.4 Gain and loss in wakes for random motion (RM) kinetic energy budget. . 141

8.1 Characteristics of the turbulent boundary layer (TBL) - first part. 167
8.2 Characteristics of the turbulent boundary layer (TBL) - second part. . . . 167
8.3 Experiment setup parameters. 170
8.4 Coefficients α_{PIV} as a function of heights from wall. 176
8.5 Number of samples per phase 183

Nomenclature

Acronym

PV Photo-voltaic

DC Direct current

OTEC Ocean thermal energy conversion

KW, MW, GW Kilowatts, Megawatts and Gigawatts, respectively

VAWT Vertical axis wind turbines

HAWT Horizontal axis wind turbines

DYNEOL Dynamique d'éolien

CORIA Complexe de Recherche Interprofessionnel en Aerothermochimie

LML Laboratoire de mécanique de Lille

LEGI Laboratoire des Ecoulements Géophysiques et Industriels

PPRIME Pole Poitevin de Recherche pour l'ingénieur en Matériaux, Mécanique et Energétique

Nd-YAG neodymium-doped yttrium aluminium garnet

fps Frame per second

PIV Particle Image Velocimetry

2D-2C Two dimentions - two components

FFT Fast Fourir Transform

CM Coherent motion

RM Random motion

POD Proper orthogonal decomposition

RMS Root Mean Squared

HS-PIV High speed Particle Images Velocimetry

LDA Laser Doppler Anemometer

TBL Turbulent Boundary Layer

NACA National Advisory Committee for Aeronautics

SNR Signal-Noise Ratio

PTU Programmable Timing Unit

PDF Probability Density Function

TKE Turbulent Kinetic Energy

General Fluid Mechanics

U_i	Instantaneous velocity vector	$\mathrm{m\,s^{-1}}$
$\overline{U_i}$	Temporal average of velocity vectors	$\mathrm{m\,s^{-1}}$
u_i	Velocity fluctuations	$\mathrm{m\,s^{-1}}$
P	Instantaneous pressure	$\mathrm{kg\,m^{-1}\,s^{-2}}$
$\overline{P}$	Temporal average of pressure	$\mathrm{kg\,m^{-1}\,s^{-2}}$
p	Pressure fluctuations	$\mathrm{kg\,m^{-1}\,s^{-2}}$
ρ	Fluid density	$\mathrm{kg\,m^{-3}}$
ν	Fluid Kinematic Viscosity	$\mathrm{m^2\,s^{-1}}$
τ_{ij}	Reynolds stress tensor	$\mathrm{kg\,m^{-1}\,s^{-2}}$
Re	Reynolds number	–
∇	Divergence	–
D	Cylinder diameter	m
St	Strouhal number	–
f_s	Shedding frequency	Hz
ϕ	Phase	$^\circ$
T, t	Time	s

Turbulence

η	Kolmogorov length scale	m
ℓ	length scale	m
u_η	Kolmogorov velocity scale	$\mathrm{m\,s^{-1}}$

τ_η	Kolmogorov time scale	s
Re_η	Kolmogorov Reynolds number	1
ℓ	Inertial scale	m
ℓ_{DI}	Dissipation scale	m
ℓ_{EI}	Energy containing-inertial scale	m
τ_{EI}	Transfer rate	$\mathrm{m^2\,s^{-3}}$
ϵ	Dissipation rate	$\mathrm{m^2\,s^{-3}}$
$\widetilde{\epsilon}$	Dissipation rate of coherent motion	$\mathrm{m^2\,s^{-3}}$
E	Energy rate	$\mathrm{m^2\,s^{-3}}$
E	Wave number	$\mathrm{m^{-1}}$
q^2	Total kinetic energy of turbulence	$\mathrm{m^2\,s^{-3}}$
q'^2	Kinetic energy of random motion	$\mathrm{m^2\,s^{-3}}$
$\widetilde{q}^2$	Kinetic energy of coherent motion	$\mathrm{m^2\,s^{-3}}$
$\langle u_i \rangle$	Phase average of velocity vectors	$\mathrm{m\,s^{-1}}$
$\widetilde{u_i}$	Coherent fluctuation of velocity vector	$\mathrm{m\,s^{-1}}$
$\widetilde{p}$	Coherent fluctuation of pressure	$\mathrm{kg\,m^{-1}\,s^{-2}}$
u_i'	Random fluctuation of velocity vector	$\mathrm{m\,s^{-1}}$
p'	Random fluctuation of pressure	$\mathrm{kg\,m^{-1}\,s^{-2}}$
α	pitch angle	$^\circ$
C	Chord length	m
$C(\Delta t, \Delta X)$	Autocorrelation	–
$C(\Delta t)$	Cross correlation	–
λ_u	Spatial period of streamwise fluctuations	m
λ_v	Spatial period of spanwise fluctuations	m
U_{conv}	Convective velocity	$\mathrm{m\,s^{-1}}$
α_{PIV}	Dissipation coefficient	–
ϵ_{PIV}	PIV dissipation	$\mathrm{m^2\,s^{-3}}$
$S_2, \overline{(\Delta u)^2}$	2nd order structure function	$(\mathrm{m/s})^2$
$S_3, \overline{(\Delta u)^3}$	3rd order structure function	$(\mathrm{m/s})^3$
$S_4, \overline{(\Delta u)^4}$	2nd order structure function	$(\mathrm{m/s})^4$

Re_c	Reynolds number based on chord length	–
z^+	Normalized height from the wall	–
U_e, U_∞	Freestream velocity	$\mathrm{m\,s^{-1}}$
U^+	Normalized velocity in TBL	–
TI	Turbulence intensity	%
τ_w	shear stress at the wall	$\mathrm{kg\,m^{-1}\,s^{-2}}$
u_τ	characteristic velocity in TBL	$\mathrm{m\,s^{-1}}$
δ	TBL thickness	m
δ^*	Displacement thickness	m
θ	momentum thickness	m
H	Shape factor	–
cf	Skin-friction coefficient	–
Re_τ	Reynolds number based friction velocity	–
Re_θ	Reynolds number based on momentum thickness	–
U, V, W	Mean velocities in X,Y and Z directions	$\mathrm{m\,s^{-1}}$
u, v, w	Instantaneous velocity fluctuations in X,Y and Z directions	$\mathrm{m\,s^{-1}}$
κ	Von Karman constant	0.41

CHAPTER 1

Preface

Contents

1.1 Marine renewable energy **2**
1.1.1 Offshore wind energy 5
1.2 Context **9**
1.2.1 Scope 9
1.2.2 Objectives 9
1.3 Thesis outline **10**

Introduction to Renewable energy

The environment is highly influenced, global warming is increasing, and running out of oil, coal, and other fossil fuels lets us think about another energy source. What about renewable energy ? Renewable energy comes from sources or processes that are constantly replenished (recyclable). These energy sources include solar energy, hydroelectric energy, geothermal energy, biomass energy, hydrogen energy, and marine energy.

Figure 1.1a shows the solar energy; the power is collected using photo-voltaic (PV) cells made from silicon or other materials. These cells transform sunlight into electricity and power anything from the smallest garden light to entire neighborhoods. Hydraulic energy is extracted from a specific amount of falling water (reserved behind a dam) due to its velocity or position. This is used to spin a generator's turbine blades to create electricity, as shown in Figure 1.1b. Geothermal energy uses the heat trapped in the Earth's core created by the slow decay of radioactive particles in rocks at the planet's center. By drilling wells, we can bring highly heated water to the surface, which can be used as a hydro-thermal resource to turn turbines and create electricity, as explained in Figure 1.1c. Biomass energy uses organic material from plants and animals, including crops, trees, and waste wood. Waste is burned to create heat, which powers a steam turbine and generates electricity, shown in Figure 1.1d. Figure 1.1e shows the hydrogen energy, non-toxic fuel, and new and ascending types of renewable energies. The raw material for hydrogen

production is abundant water, which leads to a completely renewable power. Hydrogen is combined with oxygen without combustion in an electrochemical reaction. (fuel cell) to produce electricity (DC). The product of hydrogen utilization is pure water or water vapor. Marine energy uses the power of the wind or water to turn a blade over or in the seas, where the motion of these blades in today's turbines power a generator, which produces electricity. Figure 1.1f shows some types of marine energy. Not all renewable energy types are fully clean (do not release pollutants) or green (come from natural sources). For example, biomass energy is green but needs to be cleaner as it realizes greenhouse gasses when burning biofuel.

(a) Solar energy[1].

(b) Hydraulic energy[2].

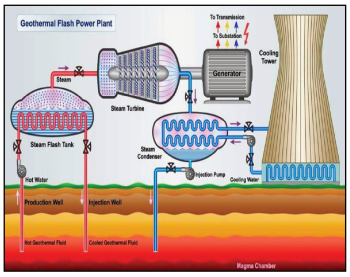

(c) Geothermal energy[3].

(d) Biomass energy[4].

(e) Hydrogen energy[5].

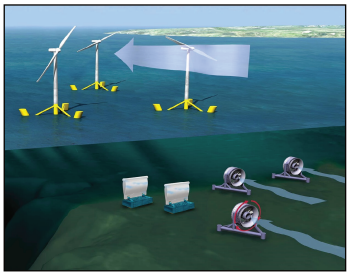

(f) Marine energy[6].

Figure 1.1: Examples of renewable energies

Renewable energy is essential as it has the potential to provide a ready supply of power without using finite natural resources. There is also a lower risk of environmental problems like fuel spills and minimal emissions issues while reducing the need for imported fuels. Renewable energy could meet our power needs for years with reliable supplies and fuel diversification.

1.1 Marine renewable energy

Seas and oceans are gifted with vast reserves of renewable energy. The waters can offer one of the most extensive clean energy resources through waves and currents. Still, these can only be applied if the technology can be successfully developed to exploit such resources reliably and cost-effectively. Over the past decade, marine energies have been on the rise, even if it came late; the first industrial application aiming at exploiting ocean energy, irrespective of the technology, was the tidal power station of Rance (240

[1] https://energy.mit.edu/research/future-solar-energy/
[2] http://hydraulicenergyianiara.blogspot.com/2017/10/how-water-can-do-energy.html
[3] https://dizz.com/geothermal-energy/
[4] https://www.bfmtv.com/economie/entreprises/energie/
[5] https://www.azom.com/article.aspx?ArticleID=21121
[6] https://www.ensta-bretagne.fr/en/marine-renewable-energies-mre

MW), which celebrates its fiftieth year of operation in 2017. For countries and territories with extensive maritime areas, renewable marine energy can significantly contribute to low-carbon electricity production in the energy mix. This is particularly the case with islands that are separate from continental networks and conventional production. Marine renewable energy takes different forms of energy, such as kinetic energy from winds and currents, mechanical energy from ocean waves, potential energy from tidal amplitude, vertical temperature gradients in oceans, and osmotic pressure from horizontal salinity gradients.

Tidal energy

The gravitational attraction and subsequent relative motion of the earth, moon, and sun induce tidal movements in the oceans and seas of the world [1]. The extracted energy is related to the change in sea level (potential energy) and associated currents (kinetic energy). This change is minimal compared to the motions of the planets. However, it is still a significant resource of energy. Most tidal barrage schemes have been built in or considered for estuary locations. They involve constructing a barrage across an estuary, allowing tidal waters to fill the estuary through sluice gates and then emptying the water back into the sea via turbines, shown in 1.2.

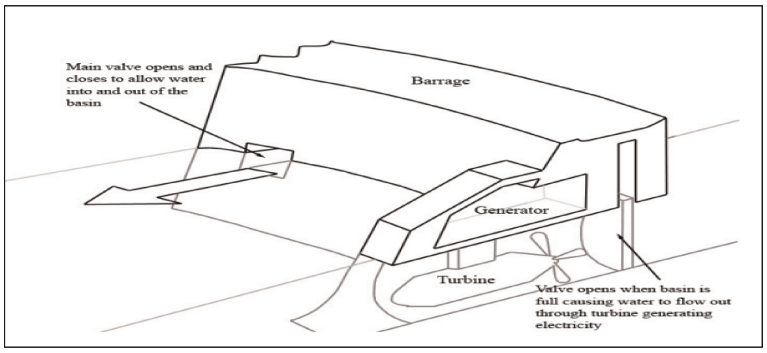

Figure 1.2: Tidal barrage schematic. Figure is referred to [1].

Waves energy

The wind blows across the ocean, creating waves at the ocean's top. Ocean waves are converted to electricity with wave energy converter [2]. Ocean waves will move the wind energy converter, and that motion drives a generator that creates electricity, as shown in Figure 1.3. These converters are anchored miles offshore in deep water, where wave energy is vital. There is a wide variety of wave energy technologies, resulting from the different ways energy can be absorbed from the waves, and also depending on the water depth and location (shoreline, near-shore, offshore). The situation in Europe was dramatically changed by the decision made in 1991 by the European Commission to include wave energy in their Research and development program on renewable energies. The first projects started in 1992. Since then, about thirty projects on wave energy have been funded by the European Commission, involving many teams active in Europe.

Figure 1.3: Wave energy[7].

Ocean thermal energy conversion (OTEC)

Ocean thermal energy conversion (OTEC) uses the difference in temperature between cool ocean depths (around five °C) and warmer shallow or surface seawater (around 25°C) to run a heat engine and produce, for example, electricity. The operation starts when water flows through a large pipe and heat exchanger, which heats a liquid with a low boiling point, such as ammonia. As the boiling ammonia creates steam, it turns a turbine generator to produce electricity—a second pipe extracts cool, deep water from the ocean, condensing the steam to liquid form. As the ammonia is recycled, the process repeats as shown in Figure 1.4.

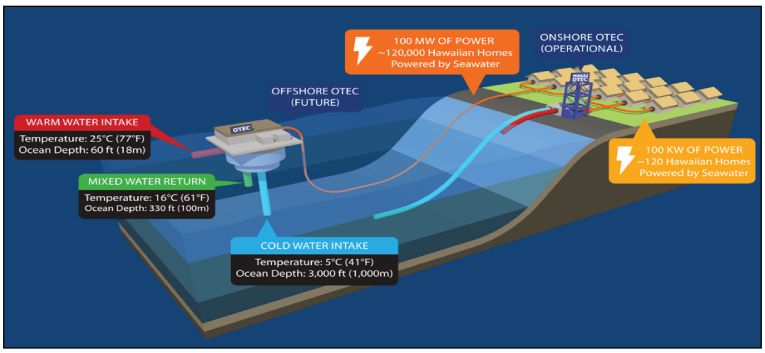

Figure 1.4: Ocean thermal energy conversion[8].

Osmotic energy

The salinity gradient energy is achievable in places where a solution flow with a specific salinity concentration runs into other solutions with different salinity concentrations [3]. The best application of this energy source is when the low salinity flows of water (river water) mix with saline water (sea water). The main factor in salinity gradient energy is the "difference of chemical potential" between the diluted and concentrated solutions. This natural process is operated if the mixing is done (partly) reversibly when freshwater moves towards high-concentration water through the semipermeable membrane, which will create high pressure in the high concentration side as shown in Figure 1.5. A turbine will

[7] https://www.ecosources.org/82-le-pelamis-des-articulations-pour-capter
[8] https://techxplore.com/news/2015-08-celebrating-hawaii-ocean-thermal-energy.html

be exploited to generate electricity through a generator to benefit from the high pressure obtained.

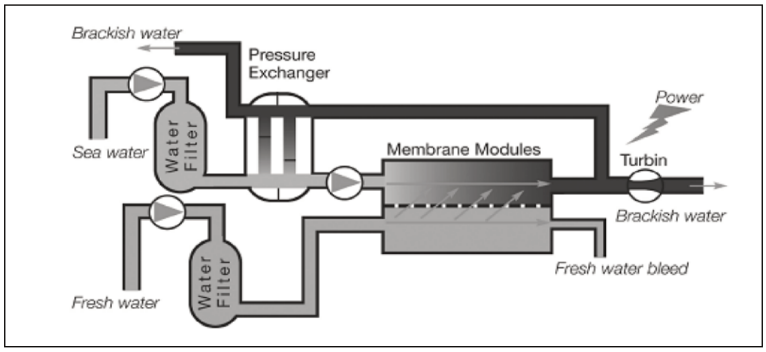

Figure 1.5: Osmotic power process. Figure referred to [**osmotic**].

Offshore wind energy

Wind energy has been the fastest in its development among all the renewable energies [4]. Offshore wind energy is a clean and renewable energy obtained by taking advantage of the force of the wind produced on the high seas. The wind forces lead to the rotation of the wind turbines by rotating their blades. Wind turbines are attached to generators to convert wind power to electrical power. At seas, it reaches a higher and more constant speed than on land due to the absence of barriers and thicker boundary layer.

1.1.1 Offshore wind energy

Among the most promising innovations, floating offshore wind energy is the future solution for expanding the scope of offshore operations. The growth of this technology is happening depending on the country and some factors like limited space on land and general environmental impact (bird death and noise). Floating wind turbines overseas confront higher wind speeds and increase with the distance to the coast. Overseas, the wind is more uniform (softer), leading to fewer turbulence effects; therefore, the fatigue is less critical and leads to an increase in the lifetime of the offshore wind turbine generator.

Time history of wind energy and turbines

A wind turbine is a machine used to convert kinetic energy from the wind into mechanical energy converted into electricity. Wind turbines operate when the wind moves over the rotor blades. Blades will rotate the turbine rotor, and the rotor drives the generator to produce electric energy. The development of sailboats led directly to the development of the first recorded wind-powered device in Persia. In around 500 B.C. Persians were using sails to drive a millstone for grain grinding, and China used it to pump drinking water and agricultural land irrigation. Windmills became familiar in Europe between 1300 and 1850 A.D. for grinding grains. The first wind turbine to produce electricity was built in Scotland in 1887. The wind turbine was created by Prof James Blyth of Anderson's College and installed in the garden of his holiday cottage. It was used to charge accumulators to power the lighting in the place, thus making it the first house in the world to have its electricity supplied by wind power. Then, in 1888, Charles Brush built the first US wind turbine (12 kW) to charge 408 batteries stored in the cellar of his mansion, shown in Figure 1.6. The

turbine, which ran for 20 years, had a rotor diameter of 50m and 144 rotor blades. The history of wind turbines are shown in details by Gipe [5].

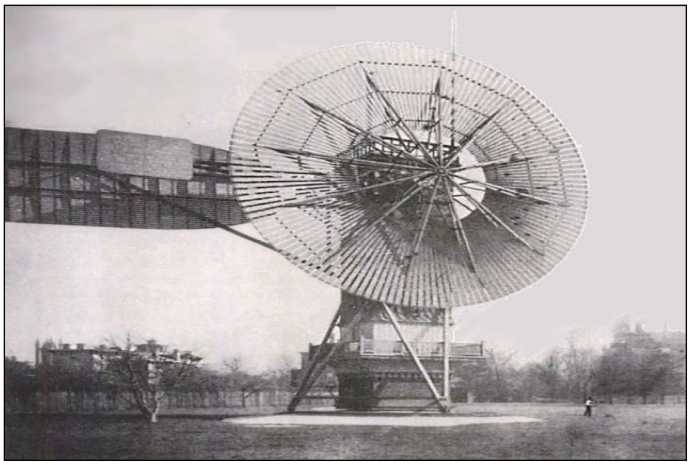

Figure 1.6: The first wind turbine built in 1888. Figure is referred to [5].

Denmark owed much of the development of wind turbines for electricity production to Poul la Cour, a scientist who showed more vision than his American and English counterparts by transforming his initial invention into the prototype of a power station driven by wind power. Poul la Cour began his wind turbine tests to bring electricity to the rural population of Denmark between 1890 and 1900. In 1903, Poul la Cour founded the Society of Wind Electricians. La Cour was the first to discover that fast-rotating wind turbines with fewer rotor blades were most efficient in generating—electricity production. In 1931, a vertical-axis wind turbine design called the Darrieus wind turbine was patented by a French aeronautical engineer, Georges Jean Marie Darrieus. After the Second War, Johannes Juul, a student of Poul la Cour, built a 200 Kw "Gedser wind turbine," which was an innovative design of a breakthrough in the development of wind turbines; it operated until the 1960s. However, electricity generation through wind power was sluggish at that period as fossil fuels were relatively cheap. In the 1970s and 1980s, a fast rise in oil prices occurred, and global warming increased, leading to the accelerated development of wind generators.
In 1975 NASA wind turbine program to develop utility-scale wind turbines started. “This research and development program pioneered many of the multi-megawatt turbine technologies in use today, including steel tube towers, variable-speed generators, composite blade materials, partial-span pitch control, and aerodynamic, structural, and acoustic engineering design capabilities. Danish wind turbine manufacturer ’Vestas’ produced its first modern wind turbine in 1978. To satisfy the gross electricity demand and to minimize the dependency on fossil fuels, large-scale wind power is planned to be executed. The first offshore wind farm in the world was constructed in southern Denmark in 1991, shown in Figure 1.7. It includes 11 wind turbines manufactured by Bonus Energy, each with a capacity of 450 kW.

Figure 1.7: 1st offshore wind farm-Denmark[9].

Offshore wind energy projects

European countries have paved the way to deliver 111 GW of wind capacity by 2030 in their National Energy and Climate Plans, but this requires almost a constant trifold in delivery rates. Hornsea Wind Farm is a Round 3 wind farm in the UK that began construction in 2018. Phase one was completed in January 2021, with a capacity of 1218 MW, making it the largest in the world on its completion, and it cost around 4.2 billion £. The eventual wind farm group will have a total capacity of up to 6 gigawatts[10](GW). In France, EDF Renewables currently has four offshore wind projects: Dunkirk, Fécamp, Courseulles, and Saint-Nazaire. These future wind farms will provide the equivalent of the electricity consumption of more than 2 million people. These projects are going to cost more than 2 billion euros. Saint-Nazaire will consist of 80 offshore wind turbines with a unit capacity of 6 megawatts (MW) for a total capacity of 480 MW[10]. The two Norman projects of Courseulles and Fécamp will produce enough electricity to cover the equivalent of the electricity consumption of nearly 630,000 people[10], or more than 90% of the inhabitants of Calvados, and more than 770,000 people, or more than 60 % of the inhabitants of Seine-Maritime, respectively. The future Dunkerque wind farm will have an installed capacity of nearly 600 MW. It will provide the equivalent of about 40% of the electricity needs of the Nord department.

Wind turbine types

Wind turbines are divided into two main types concerning their axis of rotation.

Vertical axis wind turbines (VAWT): In 1931, a vertical-axis wind turbine design called the Darrieus wind turbine, shown in Figure 1.8a is patented by Georges Jean Marie Darrieus, a French aeronautical engineer. A Darrieus machine is a low-torque, high-speed device that generates AC (alternating current). Generally, Darrieus requires a physical push, so some exterior power source is used to start rotating because the initial torque is extremely low. This machine consists of two or three blades(helical) that are

[9] https://www.cleanenergywire.org/news/oil-majors-pay-eu13-bln-entry-fee-quantum-leap-\offshore-wind-energy

[10] https://www.edf-renouvelables.com/en/project-development/offshore-wind/

vertically oriented and rotate around a perpendicular shaft. This type of wind turbine is still used today but not widely as a horizontal-axis wind turbine.

Horizontal axis wind turbines (HAWT): The rotor generally has 2 or 3 blades rotating around a horizontal axis. The sweep diameter of these blades ranges from 80 to almost 200 meters. The longer the blades, the greater the electricity production capacity. This type of wind turbines is shown in Figure 1.8b. When several wind turbines are installed on the same site, this is called a "wind park" or "wind farm".

(a) Darrieus wind turbine[11].

(b) Horizontal wind turbine[12].

Figure 1.8: Wind turbine types.

Wind turbines regulations and developements

The amount of power the generator can handle is limited. When the wind speed is very high, there is more power available than the generator can handle, so to avoid overloading it, the amount of energy is reduced by stall regulation. However, high-intensity turbulence appears when a stall occurs, which decreases the lifetime of the downstream wind turbines; the amount of turbulence intensity is reduced by pitch regulation.

Stall regulation Stall regulation was the first common way on early turbines until the 1990s. In stall regulation, blades are rigidly attached as they don't need to twist and change their angle of attack (resultant vector of wind speed vector and wind turbine rotation vector) since that happens automatically while the wind speed increases. However, when the blade stalls, it causes turbulent swirling airflow, which is quite unpredictable and causes a lot of vibrations and extreme forces that can shorten the lifetime of the blades and other wind turbine components.

Pitch regulation The blade pitch control is activated in the high wind speed region to limit the stresses imposed on the mechanical components to limit the output power generated. Limiting the aerodynamic torque that driving the generator is critical to ensure that the mechanical parts of the turbine will not be stressed due to overloads caused by

[11] https://www.universal-sci.com/headlines/2017/1/4/how-do-wind-turbines-work?utm_content=cmp-true

[12] https://www.wired.com/story/offshore-wind-farms-are-spinning-up-in-the-us-at-last/

wind fluctuations and turbulence. When the wind speed increases, the blades will twist to decrease the angle of attack and then decrease the lift force. In this regulation, as the flow remains attached, we have fewer vibrations and lower extreme energies than a stall regulated.

1.2 Context

As wind energy draws attention from many countries, researchers are concerned with developing and evolving. The developments of turbine regulations to limit the power (avoid generator failures) and decrease the turbulence stresses (avoid fatigue and aerodynamic losses) show the deep concern for wind energy worldwide. For instance, in wind farms, turbines are impacted by wakes (turbulence stresses) generated by upwind turbines, experiencing significant reductions in the mean available wind power and fatigue of materials that reduces the turbines' lifetime. In this context, fundamental research studies also help better understand the physics of turbulence behind obstacles of wind farms.

Figure 1.9: Wind farm.

1.2.1 Scope

French National Agency of Research (ANR) funded a project named 'DYNEOL', which aims to quantify the dynamical behavior of the turbulent flow around a blade as a function of the upstream flow. This upstream flow may consists of a family of coherent structures with their own time and spatial scales. This project is supported by a collaboration of 4 French laboratories: CORIA, LML, LEGI, and PPRIME.

1.2.2 Objectives

Coherent motion is characterized by its periodic nature, consisting of large structures that significantly contribute to the turbulent kinetic energy. The study's objectives can be summarized as follows:

- Analyzing coherent motion scales in the upstream wake and their evolution as they crossing an obstruction downstream. This provide insights on the periodic nature and the characteristics of these coherent motions, both prior to and following their interaction with the downstream obstacle (Chapter 5).

- Coherent motion is involved in the mechanism of the exchange of kinetic energy with turbulence (random fluctuations). Therefore, studying the dynamics of flow around wind turbine blade in function of upstream flow (i.e. coherent motion) provide better understand for the mechanism of energy exchange over the blade. This objective helps to reveal the fundamental role of coherent motion on wind turbine blade and the downstream wake. The study of kinetic energy exchange can be conducted under two conditions: one in the absence of turbulence effects (Chapter 6) and the other in the presence of turbulence effects, associated with the turbulent boundary layer (TBL) (Chapter 8). Furthermore, the investigation extends to gain a more comprehensive understanding of the energy mechanisms within scale-by-scale energy turbulence (Chapter 7).

1.3 Thesis outline

The thesis comprises the following chapters:

- The preface (Introduction) chapter provided background information regarding the research application, problem statement and hypotheses related to renewable energy and wind turbines.
- Chapter 2 is the literature review, showing comprehensive analyses, references and sources focused on wake studies.
- Chapter 3 shows the experimental setup, include information about the wind tunnel's dimensions, airflow velocity range, turbulence intensity, test section characteristics and the used measurement tool (technique). Post processing of experimental data are also shown in this chapter.
- Chapter 4 shows two methodologies to decompose the phases of coherent structures within upstream wake. These methodologies of phase decomposition including an experimental approach and extending to an a posteriori perspective.
- Chapter 5 marks the first part of the experimental results obtained within a laminar wind tunnel. Consequently, the effects of three-dimensional turbulence or turbulent boundary layers are not considered. This chapter focuses on the investigation of time periods, power spectra (frequencies), and spatial periods of coherent motion (CM) in obstacle wakes. These studies are primarily conducted using temporal and spatial autocorrelation.
- Chapter 6 marks the second part of the experimental results obtained within a laminar wind tunnel. The focus is on evaluating the exchange of total turbulent kinetic energy (TKE) as a function of upstream flow. Moreover, studying the kinetic energy associated with various structures within the wakes, such as coherent motion (CM) and random motion (RM).
- Chapter 7 marks the third part of the experimental results obtained within a laminar wind tunnel. The focus is on evaluating the exchange of turbulent kinetic energy (TKE) at two points in space as a function of upstream flow. This is done by investigating high order moments (Second, third, and fourth-orders) structure functions.

- Chapter 8 marks the experimental results obtained within a turbulent boundary layer (TBL) wind tunnel. Consequently, the effects of three-dimensional turbulence or turbulent boundary layers are considered. The aim of this chapter is to reveal the role exerted by an upstream wake placed in a Turbulent Boundary Layer (TBL), on the downstream flow.
- Finally is the general conclusions and the perspectives

CHAPTER 2

Bibliography

Summary

This chapter presents a comprehensive bibliographical study that includes references and sources related to turbulent and shear flows. In the context of shear flows, the chapter provides detailed insights into the process of vortices detachment from the boundary layer over an obstacle surface. Furthermore, it investigates both periodic (CM) and non-periodic (RM) structures within wake flows. The chapter also provides an overview of the Richardson and Kolmogorov viewpoints on energy transfer. An extensive derivation of equations concerning the total turbulent kinetic energy and the kinetic energy associated with various structures (CM and RM) within the wakes are shown. Additionally, the chapter discusses wake interactions in the context of flow behind two cylinders in a tandem configuration.

Contents

2.1 Aerodynamic failures and defeats **14**
2.2 Turbulent flows **15**
2.2.1 Main components of turbulent flows 15
2.2.2 Plane and axisymmetric wakes 16
2.2.3 Vortices formation in turbulent wakes 18
2.2.4 Periodic and non-periodic wake structures 21
2.3 Mechanism of energy transfer **23**
2.3.1 Richardson energy cascade 23
2.3.2 Kolmogorov similarity laws in energy cascade 24
2.3.3 Kinetic energy of the mean flow 27
2.3.4 Kinetic energy of the turbulence 29
2.3.5 Kinetic energy of the coherent and random structures 32
2.4 Wakes interactions **35**
2.5 Conclusions and research focus **38**

2.1 Aerodynamic failures and defeats

In 1940, America was shocked by the spread news "TACOMA NARROWS BRIDGE COLLAPSES." This bridge was one of the most modern engineering designs in the world, which was suspended by cables, see Figure 2.1. The news concerned a prominent engineering professor when he read the whole story. The professor intuitively realized that a specific aerodynamic phenomenon must have led to the collapse. He was correct and became publicly famous for what is now known as the von Kármán vortex street[2].

The failure was explained due to the resonance phenomenon, where the periodic forces of the flow synchronize with the system's natural frequency. In resonance, small periodic driving forces can add up to large oscillations over time because the energy is stored. In this case, the periodic driving force comes from an effect called vortex shedding. This is where fluid flowing past a blunt object oscillates as coherent structures are formed on the backside. When these alternating zones of low pressure occur near the structure's natural frequency, even very low speed of wind can lead to major oscillations and then collapse. Von Kàrmàn was known for many interpretations, especially in structural mechanics and aerodynamics, e.g., Aircraft flutter and fatigue phenomenon of structures facing oscillated flows (alternative forces).

Figure 2.1: Tacoma Narrows bridge collapse[1]

In wind farms, turbines create a complicated turbulent flow that is composed of large (alternating forces) and small scales. These turbulent flows exert a significant influence on downstream wind turbines. One of the major blockages to better wing design and fatigue reduction is our lack of understanding the complex nature of turbulence and their interaction with structures. Wind farms are composed of multiple obstacle wakes in addition to the rotation effect. Each obstacle can shed vortices frequently and in an organized way. The shedded vortices are embedded in the composed wake leading to a reduce in energy production of downstream wind turbines. Engineers and researchers of every sort (i.e. wake interactions) are actively seeking solutions to optimize the positioning of wind turbines within farms to mitigate these effects.

[1] https://www.britannica.com/topic/Tacoma-Narrows-Bridge
[2] https://aerospaceengineeringblog.com/boundary-layer-separation-and-pressure-drag/

2.2 Turbulent flows

Turbulence is a complex phenomenon that arises due to the interaction of fluid flow with various forces, gradients, and instabilities. Turbulent flows fluctuate randomly in time and are highly disordered in space, exhibiting a wide range of length scales (eddie size). The velocity fields are unpredictable due to their sensitivity to even minor variations in initial conditions, leading to substantial changes in subsequent flow behavior. Although the flow appears to be random and unpredictable, however, its statistical properties can be analysed as in Pope [6] for instance. On the other hand, large scales that are generated at the backside of obstacles are more organized and predicted by their regular frequency. The study of turbulence primarily revolves around deriving statistical predictions from the chaotic solutions of a nonlinear partial differential Equation (Navier-Stokes Equation). This Equation encapsulates the complex dynamics of turbulent flows. By understanding the statistical behaviors emerging from tumultuous chaos, researchers can reveal patterns within apparent randomness, leading to a deeper understanding of turbulence and its influence on various natural and engineered processes.

2.2.1 Main components of turbulent flows

In the late 19th century, Reynolds significantly contributed to fluid mechanics and turbulence. Reynolds decomposition is a fundamental concept in fluid dynamics used to analyze the behavior of turbulent flows. It allows us to separate the flow variables into mean and fluctuating components, enabling a clearer understanding of how a fluid behaves on average and deviates from that average, as shown by Osborne Reynolds [7]. Figure 2.2 shows the variation characteristic of streamwise velocity in turbulent flows concerning time, which does not happen in laminar flow. In several research studies, Reynolds decomposition was mentioned later as Lumley [8], Pope [6] and Townsend [9].

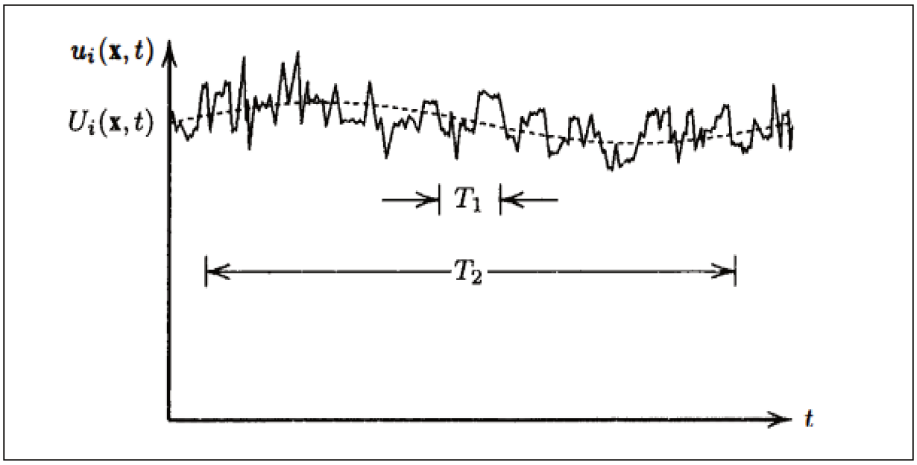

Figure 2.2: Reynolds decomposition.

In a flowing fluid, quantities like velocity and pressure continuously change in space and time. Reynolds decomposition is a technique that breaks down these quantities into two main components:

- Mean Component (Time-Averaged Component):

  The mean component represents the average behavior of the flow over a certain period. It is obtained by averaging the instantaneous value of a variable over time.

It can be calculated as follows:

$$\overline{f(x,t)} = \frac{1}{T}\int_0^T f(x,t)\,dt. \tag{2.1}$$

- Fluctuating Component (Reynolds-Stress Component):

  The fluctuating component represents the deviations from the mean behavior at any given point in space and time. It characterizes the turbulent or unsteady nature of the flow.

  $$f(x,t)' = f(x,t) - \overline{f(x,t)}. \tag{2.2}$$

  For velocity "U_i" the fluctuating component is denoted as "u_i"

  $$u_i = U_i - \overline{U_i} \tag{2.3}$$

  For pressure "P" the fluctuating component is denoted as "p"

  $$p = P - \overline{P}. \tag{2.4}$$

We obtain a clearer picture of the flow behavior by decomposing the flow variables into mean and fluctuating components. The mean component provides insight into the dominant flow patterns, while the fluctuating component helps to understand the turbulence or unsteadiness in the flow. This decomposition is a powerful tool in various areas, such as aerodynamics, meteorology, and engineering, where understanding the behavior of complex fluid flows is crucial for design, analysis, and optimization.

2.2.2 Plane and axisymmetric wakes

Wakes are narrow, elongated regions aligned with the flow direction and filled with large and small eddies. The wake eddies can be seen in nature as the flow behind a bridge pier immersed in a river stream or of a ship propelled through the water are often visible on the surface. Wakes, in general, are extremely complex, poorly understood flows. Therefore, a simplified geometry has to be investigated to understand the physics. One can begin by considering a plane wake produced by a body infinite in one direction and whose cross-section does not vary concerning that direction, i.e cylinder, sphere, or disk (3D objects). In an axisymmetric wake, the flow patterns exhibit rotational symmetry around the object's axis. The wake is typically more complex than a plane wake and can include features such as vortex rings, helical structures, and a recirculation region behind the object. The specific characteristics of the axisymmetric wake depend on the shape of the object and the Reynolds number of the flow. Figure 2.3 shows an example of the axisymmetric wake for a cylinder. The Figure shows a velocity deficit in the center of the wake due to the flow separation and the formation of vortices around the object. At the center line of the axisymmetric wakes, the streamwise fluctuation (u) is not correlated by spanwise fluctuation (v), which leads to $\overline{uv} = 0$.

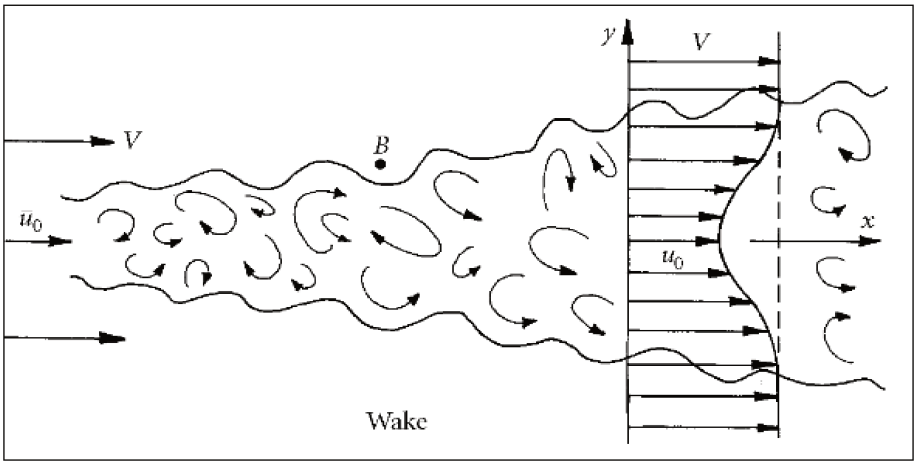

Figure 2.3: Axisymmetric wake. Figure is referred to Davidson [10].

To explain further the basic dynamics of the cylinder wake, Navier-Stokes-Equations for incompressible fluids will be considered as an initial point:

$$\frac{\partial U_j}{\partial t} + U_i \frac{\partial U_j}{\partial x_i} = \frac{-1}{\rho} \frac{\partial P}{\partial x_j} + \nu \frac{\partial^2 U_j}{\partial x_i \partial x_i}. \tag{2.5}$$

,where ν is the kinematic viscosity. This equation is considered as a starting point in many fluids studies and turbulence researches, for instance Hinze [11] and Mathieu [12]. By taking the convective term and decomposing the velocity components U_i and U_j into the mean and the total fluctuating parts as shown in Equation 2.3 (Reynolds decomposition).

$$U_i \frac{\partial U_j}{\partial x_i} = \frac{\partial}{\partial x_i}(U_i U_j) = \frac{\partial}{\partial x_i}[(\overline{U_i} + u_i)(\overline{U_j} + u_j)]. \tag{2.6}$$

$$U_i \frac{\partial U_j}{\partial x_i} = \frac{\partial}{\partial x_i}(\overline{U_i U_j} + \overline{U_i} u_j + u_i \overline{U_j} + u_i u_j). \tag{2.7}$$

Applying time averaging to the previous Equation will rub out some terms that owned one fluctuating part since the mean of the fluctuating term is equal to zero ($\overline{u_i} = 0$). The equation is :

$$\overline{U_i \frac{\partial U_j}{\partial x_i}} = \overline{U_i} \frac{\partial \overline{U_j}}{\partial x_i} + \frac{\partial}{\partial x_i} \overline{(u_i u_j)}. \tag{2.8}$$

By substituting the convective term in the Navier-Stokes Equation and averaging the rest of the terms, we obtain the following equation:

$$\frac{\partial \overline{U_j}}{\partial t} + \overline{U_i} \frac{\partial \overline{U_j}}{\partial x_i} = \frac{-1}{\rho} \frac{\partial \overline{P}}{\partial x_j} + \frac{\partial}{\partial x_i}[\nu \frac{\partial \overline{U_j}}{\partial x_i} - \overline{u_i u_j}]. \tag{2.9}$$

The previous Equation revealed an additional term from the convective part added to the laminar stresses (viscous term), see Hinze [11] and Pope [6]. The other term is related to the turbulent stresses or Reynolds tensor stresses $\tau_{ij} = -\rho \overline{u_i u_j}$.

By achieving the Equation above, we can apply it to the wake dynamics. However, this requires certain assumptions highlighted by Davidson [10]:

- Steady flow consideration

- Axial gradients in the Reynolds stresses $\frac{\partial}{\partial x}\tau_{ij}$ are considerably smaller in magnitude compared to the transverse gradients.
- Laminar stresses contribution is neglected.
- The transverse component of the mean inertia term $(\overline{U_i}.\nabla)\overline{U_y}$ is very small.
- Pressure term is neglected

Considering these assumptions significantly helps to facilitate the physics of understanding wake dynamics. As a result of these considerations, the Navier-Stokes Equation simplifies to the following form:

$$\rho\overline{U_j}\frac{\partial\overline{U_i}}{\partial x_i} = \rho\overline{U_j}(\nabla.\overline{U_i}) = \rho\overline{U_x}(\frac{\partial\overline{U_x}}{\partial x} + \frac{\partial\overline{U_y}}{\partial y}) = \frac{\partial\tau_{ij}}{\partial y}. \tag{2.10}$$

Using the continuity Equation ($\nabla.\overline{U_i} = 0$), a simplified momentum deficit (drag on the obstacle) Equation is obtained. The continuity Equation of velocity is multiplied by a constant V to convert it to the Equation of momentum Equation 2.11.

$$\frac{\partial}{\partial x}(\rho\overline{U_x})V + \frac{\partial}{\partial y}(\rho\overline{U_y})V = 0. \tag{2.11}$$

By substracting Equation 2.10 from Equation 2.11, Equation of momentum deficit appears Equation 2.12.

Equation 2.12 shows the momentum deficit equation, where V is the external velocity and the quantity $V - U_x$ is the velocity deficit. To find the behavior of the length and velocity scales in self-preserving wakes, we focused on using the momentum integral.

$$\frac{\partial}{\partial x}[\rho\overline{U_x}(V - \overline{U_x})] + \frac{\partial}{\partial y}[\rho\overline{U_y}(V - \overline{U_x})] = -\frac{\partial\tau_{ij}}{\partial y}. \tag{2.12}$$

The momentum deficit in a wake is constant ($D = \int_{-\infty}^{\infty}\rho\overline{U_i}(V - \overline{U_i})\,dy = constant$), shown by Davidson [10]. This is unlike many other free shear flows for which the local Reynolds number remains constant or increases down-stream, in the axisymmetric wake it drops slowly. Thus, viscous effects continuously become more important until. Eventually, they may dominate (if the flow extends far enough downstream). These varying viscous effects, together with the many very different possibilities for the structure of the near wake from other generators, considerably complicate the interpretation of the data.

2.2.3 Vortices formation in turbulent wakes

Vortices are created in places where high shear forces exist in the flow. Obstacles or rigid bodies in the flow exert frictional drag forces on the fluid, which leads to the surface boundary layer. On the other hand, fluid exerts pressure drag on the obstacles, associated with creating eddies behind the body (boundary layer separation). Any immersed round body with a diameter D will force the surrounding fluid to flow in curved streamlines just after it, see Figure 2.4. This curvature of the streamlines causes the flow to speed up or accelerate to balance the centripetal forces created by the curved streamlines. When the flow speeds up or accelerates, a region of dropping fluid pressure is created; this region is called favorable pressure gradient $\frac{\partial P}{\partial x} < 0$ (extend between 0 and 90 degrees in laminar boundary layer). Further along the body, where the streamline is directed, the inverse happens, and the fluid flows into a region of higher pressure; this region is called adverse

pressure gradient $\frac{\partial P}{\partial x} > 0$ (extend between 90 to 180 degree in laminar boundary layer). The separation happens where the $\frac{\partial U}{\partial y} = 0$. In turbulent boundary layers, the turbulent transport of momentum (needed to recover retarded flow by viscosity) is very effective, and this helps to persist for longer distances without separation. The adverse pressure gradient strengthens the viscous forces close to the wall. As a result, the separation point (between the flow velocity close to the surface and the free stream velocity) becomes very strong to push back these separated layers. It leads to the quick growth of the boundary layer or recirculation zone (see diagram below). The separated layers developed into two pulsating vortices in the downstream wake behind the cylinder by that push from the free stream.

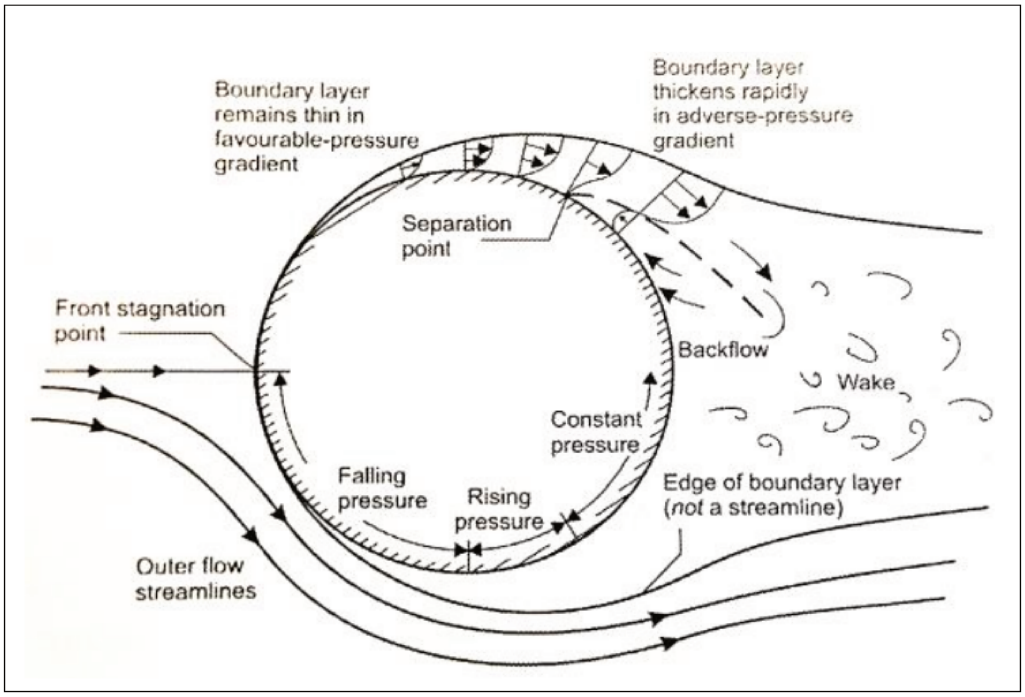

Figure 2.4: Separation layer on cylinder surface[3].

Flow around a circular cylinder remains a good example in fluid mechanics, where intensive investigations are continued even today to understand the complex unsteady dynamics of the cylinder wake flow. The non-dimensional quantities describing the flow around a smooth circular cylinder depend on the cylinder Reynolds number Re (ratio of inertial to viscous forces in a fluid), expressed by Equation 2.13.

$$Re = \frac{DU}{\nu}. \tag{2.13}$$

Where D is the diameter of the cylinder, U is the upstream flow velocity, and ν is the kinematic viscosity. The flow undergoes tremendous changes as the Reynolds number is increased from zero. The flow regimes experienced with increasing Re are summarized in Sumer and Fredsoe [13] table. The mean flow in a wake behind a cylinder is characterized by $U_x >> U_y$ and $\frac{\partial}{\partial x} << \frac{\partial}{\partial y}$. The flow regimes increase their complexity as ν is reduced. At high values of ν we have a steady, symmetric flow pattern. As Re approaches unity, the upstream-downstream symmetry is lost. In the range $Re = 5 - 40$, steady vortices

[3] https://aerospaceengineeringblog.com/boundary-layer-separation-and-pressure-drag/

attached to the rear of the cylinder are formed. When Re reaches a value of around 40, instability is observed in the form of an oscillation of the wake, and by reaching $Re = 100$, the vortices start to peel off from the rear of the cylinder in a regular, periodic manner. The flow is still laminar, but we have lost the top-bottom symmetry. The laminar Karman street persists up to $Re \approx 200$, at which point three-dimensional instabilities develop. By $Re = 400$, low turbulence levels appear within the vortices. Nevertheless, the periodicity of the vortex shedding remains quite robust. An example of coherent vortex shedding accompanied with turbulence within an airfoil wake is shown in Figure 2.5. The turbulence is characterized by the sudden transition from a turbulent vorticity field to an irrotational external motion. There is still relatively little fine-scale turbulence below $Re = 10^3$, and the interface between the turbulent and irrotational fluid undulates on a large scale only. Eventually, Above $Re = 10^5$, the turbulence appears to be more fully developed, with a pronounced fine-scale structure, as shown by Davidson [10]. As ν is reduced, the flow becomes more and more complex until, eventually, turbulence sets in. This example is important since it illustrates the key role played by Re in determining the state of a flow. Thus, when Re is large, the viscous forces, and hence viscous dissipation, are small.
Roshko in 1954 [14] begins with investigating the wake development behind circular cylinders at Reynolds numbers from $Re = 40 - 40000$, using standard hot-wire anemometer technique to study velocity fluctuations. Bloor and Gerrard, in 1966 [15], show high agreement with Roshko [14] observations by analyzing the vortex strength and its variation with distance downstream in the function of Reynolds numbers.

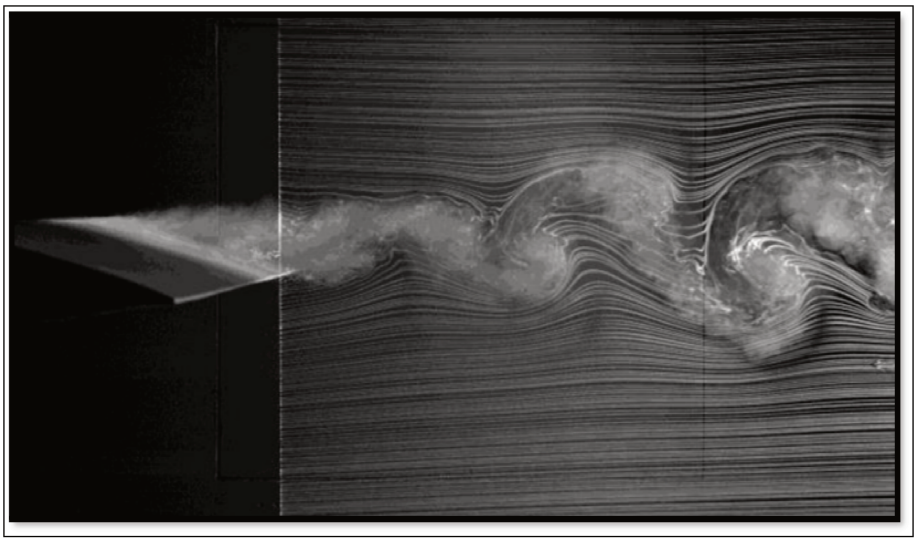

Figure 2.5: Von Kàrmàn vortex street in the wake of airfoil. Figure is referred to Yarusevych [16].

Abernathy and Kronauer, in 1961 [17], studied the time history of the van Karman vortex formation; they provided that the formation of the vortex streets from the vortex layers (emanated from bluff bodies) is explained by the growth of disturbances in two infinite, initially parallel vortex rows. The interaction of these two vortex rows leads to the formation of concentrated clouds of vorticity with a net strength diminished by the vorticity swept into the cloud from the opposite vortex row. Zdravkovich [18] in 1968 showed the formation of the Von Karman vortex by smoke observation by changing the Reynolds number slowly from 30 to 90. He concluded that the instability of the shear layers in a certain Reynolds number leads to the initial staggered vorticity concentration.

Later, in 1986 Triantafyllou and Chryssostomidis [19] emphasized the main cause of vortices creation at both low ($Re = 56$) and high ($Re = 140000$) Reynolds numbers is the absolute instability. His contribution shows that the rolling-up process reinforces both the concentration of vorticity and the circulation of the future vortex cores. It also shows that the sinuous oscillations begin nearer to the cylinder, increasing their amplitude. It is evident that the staggered arrangement of the vortex rows is closely related to the sinuous oscillations that represent the vortex street in the classical sense. The twin vortices are no longer seen behind the cylinder at very high Reynolds. This was explained due to strong sinuous oscillations, which now appear immediately behind the cylinder, have detached them, and have been carried downstream. Based on Prandtl film [20], shows the streamlines of the flow after an obstacle (cylinder) using aluminum particles. Using properties of critical points to find out the process of vortex shedding, Perry and Chong in 1980 [21] concluded that the cavity (recirculation zone) which is formed during the starting-up process is closed and all the saddles are joined together. However, during the vortex-shedding process, the cavity is open, the separatrices do not necessarily join the saddles, and instant 'alleyways ' of fluid penetrate the cavity. To simplify the shedding vortices, a vortex is forming near the top of the cylinder surface. Below and to the right of the first vortex is another vortex which was formed and shed a short period before. Thus, the flow process in the wake of a cylinder involves the formation and shedding of vortices alternately from one side and then the other. This phenomenon is of major importance in engineering design because the alternate formation and shedding of vortices also create alternating forces, which occur more frequently as the velocity of the flow increases.

2.2.4 Periodic and non-periodic wake structures

It is discussed in the previous section that according to Osborne Reynolds, turbulent flows are decomposed into two main components: The mean component and the fluctuating component. The fluctuating component is due to wake structures or wake eddies with their different sizes. It is known in the turbulence field that by increasing the structure size, the eddies become slower in speed, as shown in the Kolmogorov energy spectrum [22]. Regarding flows behind obstacles, it is shown in previous studies that until a certain Reynolds number, two large, stable, and attached vortices are created at the rear side of the cylinder. By increasing the Reynolds number, an instability of the shear layer (attached vortices) occurs, which causes a steepening of the waves. A combination of the annular tiny vortices formed longer waves, resulting in bigger eddies. The effect is that boundary layer separation at the two sides of the cylinder occurs in an alternating fashion, with a frequency expressed by the Strouhal number St,

$$St = \frac{f_s D}{U}. \tag{2.14}$$

where f_s is the frequency of the shed vortices, D is the diameter of the obstacles, and U is the velocity of the flow. It is a dimensionless number commonly used as a measure of the predominant shedding frequency f_s. The shedded vortices with a specific frequency f_s, are also called periodic structures or coherent structures.

In particular, Von Kármán demonstrated theoretically, via a stability analysis of two vortex rows, that the Strouhal number is nearly constant. It is known, however, that the Strouhal number varies with Reynolds number, surface roughness, turbulence intensity, etc. In the other hand, during the growth of the large structures (periodic), there is a rapid entrainment due to the folding of the interface and engulfing of irrotational fluid, as shown by Townsend [23, 24]. This interaction and deformation of the large structures cause the

production of small or random structures (non-periodic) with increasing intensity. The bounding surface, overturning by the main eddies of the turbulence, or a 'nibbling' by the smallest eddies, the resultant initial motion is likely to be quasi-isotropic in the sense that it is not highly organized. Hinze [11] also shows that the irrotational/turbulent flow interface will advance into the irrotational fluid at a rate that depends on the local mean strain rate and the local degree of anisotropy of the turbulence near the interface. The previous studies emphasize that large structures always accompany small structures all-around. In this context, Reynolds and Hussein [25, 26, 27] proposed the first mathematical method of turbulent fields, which accounts for instantaneous field decomposition. They were able to extract the organized wave motion (periodic) from a background field of finite turbulent fluctuations by introducing an artificial periodic wave in the upstream side of a turbulent shear layer. The first term in Equation 2.15 represents the mean motion $\overline{f(x,t,\phi_i)}$ or the time average of the whole instantaneous field, as shown in Equation 2.16. The second term in Equation 2.15 accounts for the coherent motion $f_c(x,t,\phi_i)$ and is quasi-periodic. The third term in Equation (2.15) delineates the random motion $f_r(x,t,\phi_i)$. The three terms in Equation (2.15) construct the whole field at an instant t, $f(x,t,\phi_i)$,

$$\underbrace{f(x,t,\phi_i)}_{\textbf{Instantaneous}} = \underbrace{\overline{f(x,t)}}_{\textbf{Mean motion}} + \underbrace{\widetilde{f}_c(x,t,\phi_i)}_{\textbf{Coherent motion}} + \underbrace{f'_r(x,t,\phi_i)}_{\textbf{Random motion}} . \tag{2.15}$$

$$\underbrace{\overline{f(x,t)}}_{\textbf{Mean motion}} = \underbrace{\overline{f(x,t)}}_{\textbf{Time average}} = \frac{1}{T}\int_0^T f(x,t)\,dt. \tag{2.16}$$

$\overline{f(x,t,\phi_i)}$ represents the temporal average of the fluctuations in the flow.

$$\underbrace{\widetilde{f}_c(x,t,\phi_i)}_{\textbf{Coherent motion}} = \underbrace{\langle (f(x,t,\phi_i)\rangle}_{\textbf{Phase average}} - \underbrace{\overline{f(x,t)}}_{\textbf{Time average}} . \tag{2.17}$$

Coherent motion (periodic fluctuations) is obtained by the difference between the phase average $\langle f(x,t,\phi_i)\rangle$ and the time average $\overline{f(x,t,\phi_i)}$, as shown in Equation (2.17). The phase average $\langle f(x,t,\phi_i)\rangle$ is then the average, at any point in space, of the values of f that are realized at a particular phase ϕ, Equation 2.18,

$$\underbrace{\langle f(x,t,\phi_i)\rangle}_{\textbf{Phase average}} = \frac{1}{N}\sum_{n=0}^{N} f(x,t,\phi_i). \tag{2.18}$$

The random motion (turbulent or non-periodic fluctuations) is found by the difference between the instantaneous velocity field and the phase average (Equation 2.19),

$$\underbrace{f'_r(x,t,\phi_i)}_{\textbf{Random motion}} = \underbrace{f(x,t,\phi_i)}_{\textbf{Instantaneous}} - \underbrace{\langle f(x,t,\phi_i)\rangle}_{\textbf{Phase average}} . \tag{2.19}$$

On average, the background turbulence (non-periodic) and the organized motion (periodic) are uncorrelated. Some useful properties that follow from the basic definitions are given below.

$$\begin{aligned} &\langle f'\rangle = 0, \qquad \overline{\widetilde{f}} = 0, \qquad \overline{f'} = 0, \\ &\overline{\overline{f}g} = \overline{f}\,\overline{g}, \quad \langle\widetilde{f}g\rangle = \widetilde{f}\langle g\rangle, \quad \langle\overline{f}g\rangle = \overline{f}\langle g\rangle, \\ &\overline{\langle f\rangle} = \overline{f}, \qquad \langle\overline{f}\rangle = \overline{f}, \qquad \overline{\widetilde{f}g'} = \langle\widetilde{f}g'\rangle = 0. \end{aligned} \tag{2.20}$$

One can proceed by suitable manipulation with Navier-Stockes equations to obtain governing Equations related to velocity $(u'_i, \widetilde{u}_i)$ or pressure $(p'_i, \widetilde{p}_i)$, as shown by Philips study

in 1967 [28]. Involving periodic or non-periodic oscillations in Navier-Stokes equations helps fully describe a field of turbulent flow.

2.3 Mechanism of energy transfer

The mechanism of energy transfer in turbulence is a fundamental concept that explains how energy is transferred between different scales of motion within a turbulent flow. It is the driving force behind the turbulent cascade, where energy from large-scale eddies is transferred to smaller scales until it is eventually dissipated into heat at the smallest scales. Turbulent flows also involve complex interactions between different scales of motion. The energy transfer is not limited to a one-way process but involves interactions between various scales, contributing to turbulence's intricate and chaotic nature.

2.3.1 Richardson energy cascade

Turbulent wakes with high Reynolds numbers ($Re = UL/\nu$) are rich in different sizes of eddies. The lifespan of a typical eddy is rather short, of the order of its so-called turn-over time, ℓ/u_ℓ. Eddies are conceived to be a turbulent motion localized over a region of size ℓ that is at least moderately coherent over this region. The region occupied by a larger eddy can also contain smaller eddies. The largest of these eddies have a size comparable with the characteristic geometric length scale of the mean flow (diameter of cylinder). The smaller eddies are themselves unstable, and they, in turn, pass their energy onto even smaller structures, and so on. Thus, there is a continual cascade of energy from the large scale down to the small at each instant. Crucially, viscosity plays no part in this cascade. That is, since Re is large, and the viscous stresses acting on the large eddies are negligible. Inertial forces essentially drive the whole process. However, the cascade comes to a halt when the eddy size becomes so small, and Re based on the size of the smallest eddies, is of order unity. At this point, the viscous forces become significant, and dissipation starts to become important.

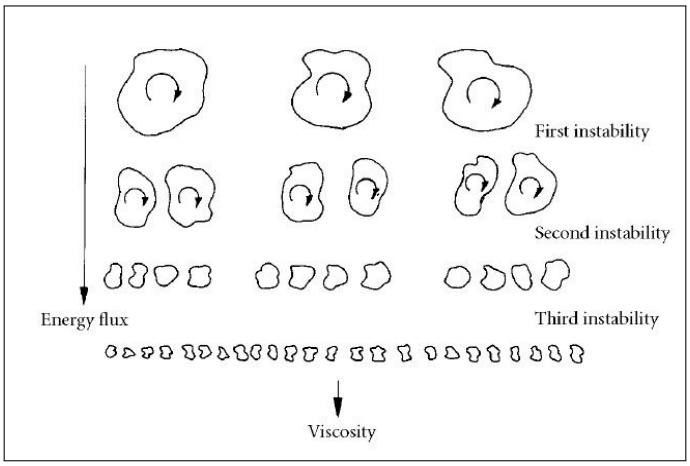

Figure 2.6: Richardson cascade. Figure is referred to Davidson [10].

Dissipation exists in regions with a large instantaneous velocity gradient (shear stress). This suggests that the dissipation of mechanical energy within a turbulent flow is concentrated in the smallest eddies, which is true. The dissipation rate of the kinetic energy in a fluid is $\epsilon = 2\nu S_{ij} S_{ij}$, where S_{ij} is the strain rate tensor.

The observation that a broad spectrum of eddy sizes exist at an instant, and that dissipation is associated predominantly with the smallest eddies, led Richardson to introduce the concept of the energy cascade for high-Re turbulence in 1922. Richardson summarized his notion by:

> "Big whorls have little whorls, Which feed on their velocity; And little whorls have lesser whorls, And so on to viscosity"

Thus we have a picture of large-scale eddies being continually created by the mean flow, and these eddies then break up through a sequence of inviscid instabilities into finer and finer structures. Energy is destroyed only in the final stages of this process when the structures are very small. In this sense, viscosity plays a rather passive role, mopping up whatever energy cascades down from above. In brief, the idea of the energy cascade (introduced by Richardson (1922)) is that kinetic energy enters the turbulence (through the production mechanism) at the largest scales of motion. This energy is then transferred (by inviscid processes) to smaller and smaller scales until, at the smallest scales, the energy is dissipated by viscous action.

In general, large eddies are characterized by anisotropy and are affected by the boundary conditions of the flow. The largest eddies have energy of order u_0^2 and timescale $\tau_0 = \ell_0/u_0$, so the energy transfer rate can be supposed to scale as,

$$\beta \sim \frac{u_o^2}{t_o} \sim \frac{u_o^3}{\ell_0}. \tag{2.21}$$

This characteristic time of a vortex structure of size ℓ_0 corresponds to the time of this structure undergoing significant distortion, as explained in Frisch [29] study. The cascade at high Reynolds numbers indicates also the dissipation ϵ is independent of the viscosity ν, where it scales as $\epsilon = u_0^3/\ell_0$

2.3.2 Kolmogorov similarity laws in energy cascade

In 1941, Kolmogorov made a significant contribution to getting a better understanding of the energy cascade of turbulent scales. Turbulent scales are divided into an energy-containing range and a universal-containing range, which is divided into inertial and dissipation subranges, as shown in Figure 2.7.

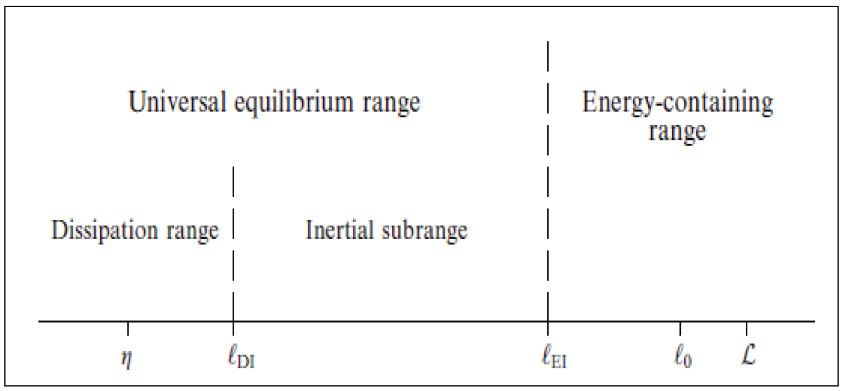

Figure 2.7: Kolmogrov length scales in subranges, Figure is referred to Pope [6]

The contribution of Kolmogrov [30] is stated in the form of different hypotheses. The hypothesis of local isotropy states that within the scales smaller than the energy-containing

range and at sufficiently high Reynolds number, the small-scale turbulent motions ($\ell \ll \ell_0$) are statistically isotropic. Kolmogorov introduced a length scale ℓ_{EI} as the demarcation between anisotropic and isotropic eddies. The first similarity hypothesis of Kolmogorov shows that small-scale eddies depend on the rate of energy transfer T_{EI}, at which they receive energy from the larger scales (which is approximately equal to the dissipation rate ϵ). On the other hand, it also depends on the viscous dissipation, which is related to the kinematic viscosity ν. The small-scale motions' statistics are universal and similar in every high Reynolds number turbulent flow. This scale represents the scale of which the energy is dissipated in the form of heat. The smallest scales are crucial in understanding the statistical behavior of turbulence and are derived from Kolmogorov's theory of turbulence [31], that's why they are named as Kolmogorov scales (length, velocity, and time scales):

$$\eta = \left(\nu^3/\epsilon\right)^{1/4}. \tag{2.22a}$$

$$u_\eta = (\epsilon\nu)^{1/4}. \tag{2.22b}$$

$$\tau_\eta = (\nu/\epsilon)^{1/2}. \tag{2.22c}$$

η is the Kolmogorov length scale that represents the smallest spatial scale, ν is the kinematic viscosity, and ϵ is the mean dissipation rate of turbulent kinetic energy. Two definitions that arise from Kolmogorov definitions are clearly explained in Frisch [29] and Pope [6] textbooks. First, the Reynolds number based on the Kolmogorov scales is unity (the notion of the cascade that large eddy proceeds to smaller and smaller scales until the Reynolds number is small enough for dissipation to be effective). It is shown in Equation 2.23. The second definition that arose is the dissipation rate ϵ, which is shown in Equation 2.24.

$$Re_\eta = \frac{u_\eta \eta}{\nu} = 1. \tag{2.23}$$

$$\epsilon = \nu \left(\frac{u_\eta}{\eta}\right)^2 = \frac{\nu}{\tau_\eta^2}. \tag{2.24}$$

Then, Kolmogorov proposed a mathematical model for the energy spectrum in the inertial subrange of turbulence (intermediate range of scales between the large and small scales). The scale ℓ is considered to be between the dissipation scale and the integral length scale ℓ_0, where the energy is injected. In well-developed turbulence, an energy cascade takes place in the inertial subrange. In the inertial subrange ($\ell < \ell_{EI}$) referring to the universal equilibrium range, the timescales $\ell/u(\ell)$ are small compared to ℓ_0/u_0, this permits small eddies to adapt quickly for maintaining the dynamic equilibrium with the energy-transfer rate T_{EI} imposed by the large eddies. In the mentioned subrange, eddies are much bigger than the dissipative eddies (Kolmogorov scales), and this supposed their Reynolds number $u\ell/\nu$ is large. Consequently, their motion is less affected by viscosity. This is the second similarity hypothesis of Kolmogorov. In this subrange of energy cascade (for $\ell_\eta \ll \ell \ll \ell_0$), the dominant process is the transfer of energy to successively smaller scales.

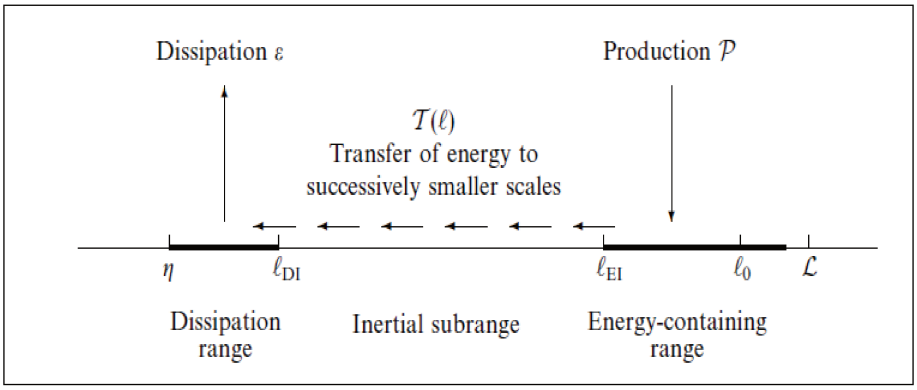

Figure 2.8: Kolmogrov energy transfer between scales. Figure is referred to Pope [6].

Figure 2.8 shows the schema of the rate of energy transfer from large to smaller scales. T_{EI} is the rate of energy transfer from large scales to intermediate scales. This rate determines the constant rate of energy transfer through the inertial subrange, the rate at which energy leaves the inertial subrange and enters the dissipation range T_{DI}; and hence the dissipation rate ϵ.

The distribution of turbulent kinetic energy among eddies of different sizes is still an open question and requires further investigation. Kolmogorov also answered this question by his energy spectrum that is derived from his theory in 1941, referring to studies [31, 30]. It describes the distribution of turbulent kinetic energy among different length scales (or equivalently, wavenumbers k) within the inertial subrange of fully developed turbulence. Motions of lengthscale ℓ correspond to wavenumber $k = 2\pi/\ell$ and that the energy in the wavenumber range (k_a, k_b) is :

$$K = \int_{k_a}^{k_b} E(k)\, dk, \tag{2.25}$$

where $E(k)$ represents the energy of eddies at a specific wavenumber k, which is the inverse of eddy size (larger k corresponds to smaller eddies and vice versa), experiments and numerical simulations in many turbulent flows have verified the Kolmogorov energy spectrum. It provides important insights into the statistical behavior of turbulence and the distribution of energy among different scales in a turbulent flow field.

In the inertial subrange, turbulence is characterized by a balance between the energy injection at large scales and the energy dissipation at small scales. Kolmogorov's energy spectrum provides a quantitative expression for this distribution of energy in the inertial subrange. In the inertial subrange, the energy of eddies is proportional to their size raised to a power of -5/3. This is known as the "Kolmogorov energy spectrum" represented as:

$$E(k) \propto k^{-5/3}. \tag{2.26}$$

Figure 2.9 shows the Kolmogorov energy spectrum. It provides insights into the distribution of turbulent kinetic energy among different scales in a developed turbulent flow.

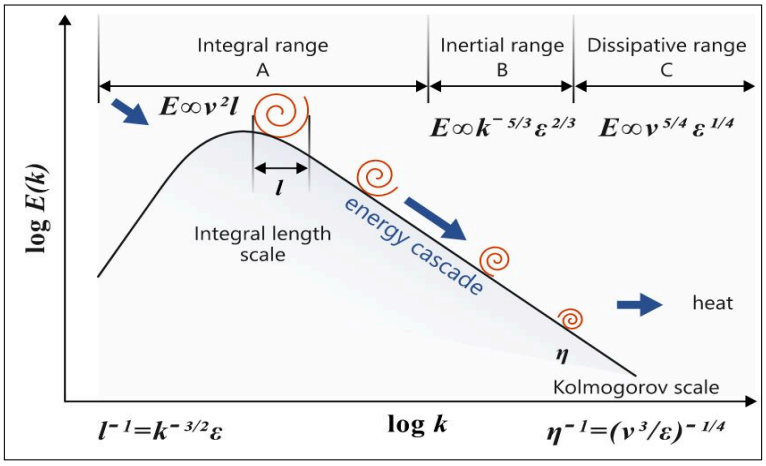

Figure 2.9: Energy spectrum cascade[4].

2.3.3 Kinetic energy of the mean flow

The premier studies of turbulent flows were credited to Osborne Reynolds. Reynolds [7] determined the leading understanding of turbulence in 1885, characterized by the dimensionless number that carries his name. Reynolds decomposed the quantities of velocity and pressure into an average quantity and fluctuating components (shown in previous sections) and included them in the equation of flow motion. The equations of motion of an incompressible fluid are:

$$\frac{\partial U_i}{\partial t} + U_j \frac{\partial U_i}{\partial x_j} = -\frac{1}{\rho}\frac{\partial P}{\partial x_i} + \nu \frac{\partial^2 U_i}{\partial x_j \partial x_j}. \tag{2.27}$$

Turbulent motion plays an important role in stress production in the mean flow, where it has a high contribution to the redistribution of the kinetic energy. Turbulence consists of random velocity fluctuations, so it must be treated with statistical methods. All quantities are decomposed into mean values and fluctuations with zero mean. Turbulent velocity fluctuations can generate large momentum fluxes between different parts of the flow. These fluxes are considered as stresses, i.e. turbulent momentum fluxes are commonly called Reynolds stresses. Reynolds stresses are derived from the momentum equation using Reynolds decomposition of velocity and pressure quantities, as shown in Equation 2.2. The decomposed quantities are shown in Equations 2.28a and 2.28b.

$$U_i = \overline{U_i} + u_i. \tag{2.28a}$$

$$P = \overline{P} + p. \tag{2.28b}$$

By integrating the previous equations of decomposition quantities into the momentum Equation 2.27, the equation becomes :

$$\frac{\partial U_i}{\partial t} + \frac{\partial}{\partial x_j}(\overline{U_i} + u_i)(\overline{U_j} + u_j) = -\frac{1}{\rho}\frac{\partial}{\partial x_i}(\overline{P} + p) + \nu \frac{\partial^2}{\partial x_j \partial x_j}(\overline{U_i} + u_i). \tag{2.29}$$

[4] https://2021.help.altair.com/2021/hwsolvers/acusolve/topics/acusolve/training_manual/turb_scales_energy_cascasde_r.htm

By taking the time average of all terms in Equation 2.29. The Equation of motion for a steady flow becomes:

$$\overline{U_j}\frac{\partial \overline{U_i}}{\partial x_j} + \overline{u_j\frac{\partial u_i}{\partial x_j}} = -\frac{1}{\rho}\frac{\partial \overline{P}}{\partial x_i} + \nu\frac{\partial^2 \overline{U_i}}{\partial x_j \partial x_j}. \tag{2.30}$$

Equation 2.30 shows that the mean transport of fluctuating momentum may change the momentum of the mean. The mean fluctuating momentum term may be written as:

$$\overline{u_j\frac{\partial u_i}{\partial x_j}} = \frac{\partial}{\partial x_j}\overline{u_i u_j} - \overline{u_i\frac{\partial u_j}{\partial x_j}}. \tag{2.31}$$

If we apply the decomposition rule (Equation 2.28a) to the continuity Equation , we obtain:

$$\frac{\partial U_i}{\partial x_i} = \frac{\partial}{\partial x_i}(\overline{U_i} + u_i) = \frac{\partial \overline{U_i}}{\partial x_i} + \frac{\partial u_i}{\partial x_i} = 0. \tag{2.32}$$

If the averaging of all the terms in this equation is taken, the last term vanishes (mean of all fluctuation quantities are zero).

$$\frac{\partial \overline{U_i}}{\partial x_i} = \frac{\partial \overline{U_j}}{\partial x_j} = 0. \tag{2.33a}$$

$$\frac{\partial u_i}{\partial x_i} = \frac{\partial u_j}{\partial x_j} = 0. \tag{2.33b}$$

Therefore, the mean fluctuating term (Equation 2.31) is reduced to:

$$\overline{u_j\frac{\partial u_i}{\partial x_j}} = \frac{\partial}{\partial x_j}\overline{u_i u_j}. \tag{2.34}$$

Due to the concept of Reynolds decomposition, turbulent motion can be considered as a phenomenon that generates additional stresses within the mean flow. As a result, all stresses in the flow, including those from the turbulent fluctuations, can be combined into one Equation known as the Reynolds momentum Equation:

$$\overline{U_j}\frac{\partial \overline{U_i}}{\partial x_j} = \frac{\partial}{\partial x_j}(\frac{\overline{P}}{\rho}\delta_{ij} + \nu\frac{\partial \overline{U_i}}{\partial x_j} - \overline{u_i u_j}). \tag{2.35}$$

The symbol δ_{ij} is the Kronecker-delta defined by: $\delta_{ij} = \begin{cases} 1, & \text{if i = j,} \\ 0, & \text{if i} \neq \text{j.} \end{cases}$

Stresses are combined in one variable τ_{ij}:

$$\tau_{ij} = -\frac{\overline{P}}{\rho}\delta_{ij} + \nu\frac{\partial \overline{U_i}}{\partial x_j} - \overline{u_i u_j}. \tag{2.36}$$

So, Reynolds momentum Equation becomes:

$$\overline{U_j}\frac{\partial \overline{U_i}}{\partial x_j} = \frac{\partial \tau_{ij}}{\partial x_j}. \tag{2.37}$$

The Equation governing the dynamics of the mean flow energy $\frac{1}{2}\overline{U_i U_i}$ is obtained by multiplying the Equation 2.37 by $\overline{U_i}$.

$$\overline{U_j}\frac{\partial}{\partial x_j}(\frac{1}{2}\overline{U_i U_i}) = \frac{\partial}{\partial x_j}(\tau_{ij}U_i) - \tau_{ij}\frac{\partial \overline{U_i}}{\partial x_j}. \tag{2.38}$$

The involvement of the pressure to the deformation work in an incompressible fluid is zero, $-\overline{p}\,(\partial\overline{u_i}/\partial x_i) = 0$. The final aspect of the Equation governing the dynamics of the mean flow energy becomes:

$$\overline{U_j}\frac{\partial}{\partial x_j}(\frac{1}{2}\overline{U_iU_i}) = \frac{\partial}{\partial x_j}(-\frac{1}{\rho}\overline{PU_i}\delta_{ij} + \nu\overline{U_i}\frac{\partial\overline{U_i}}{\partial x_j} - \overline{u_iu_jU_i}) - \nu\frac{\partial\overline{U_i}}{\partial x_j}\frac{\partial\overline{U_i}}{\partial x_j} + \overline{u_iu_j}\frac{\partial\overline{U_i}}{\partial x_j}. \quad (2.39)$$

The previous Equation helps understand turbulence's impact through Reynolds stresses on the mean flow. The terms of the Equation are defined as the following:

- $\overline{U_j}\frac{\partial}{\partial x_j}(\frac{1}{2}\overline{U_iU_i})$ is the transport term of the kinetic energy of the base mean flow.
- $-\frac{\partial}{\partial x_j}\left(\frac{1}{\rho}\overline{PU_i}\delta_{ij}\right)$ is the pressure work on the mean flow.
- $\frac{\partial}{\partial x_j}\left(\nu\overline{U_i}\frac{\partial\overline{U_i}}{\partial x_j}\right)$ is the transport of mean energy flow by viscous stresses (mechanical work contribution).
- $\frac{\partial}{\partial x_j}\left(\overline{u_iu_jU_i}\right)$ is the transport of mean energy flow by Reynolds stresses (mechanical work contribution).
- $\nu\frac{\partial\overline{U_i}}{\partial x_j}\frac{\partial\overline{U_i}}{\partial x_j}$ is the viscous dissipation of the mean flow.
  The contribution of viscous stresses to the deformation work is always negative. Thus, viscous dissipation is considered as a loss term to the kinetic energy budget.
- $\overline{u_iu_j}\frac{\partial\overline{U_i}}{\partial x_j}$ is the turbulent energy production.
  The contribution of Reynolds stresses to the deformation work is also dissipative in most flows. Negative values of $\overline{u_iu_j}$ tend to occur in situations with positive $\left(\partial\overline{U_i}/\partial x_j\right)$. The negative correlation between both sides shows the loss of the kinetic energy from the mean flow. Since turbulent stresses perform the deformation work and the kinetic energy of the turbulence benefits from this work (turbulence drains energy from the base flow), it is known as turbulent energy production.

It is noted that viscous dissipation and turbulence production will have the same sign, as the energy transferred to heat and turbulence by the base flow (loss from mean flow). In most flows, the two viscous terms in Equation 2.39 are negligible, as explained in the textbook of Tennekes and Lumley [8]. Lumley [8] also shows that turbulence terms (turbulence production and energy transport by turbulence) are ul/ν times as large as the viscous terms. This Reynolds number tends to be very large, and consequently, viscous terms become more negligible. This again illustrates that the gross structures of turbulent flows tend to be virtually independent of viscosity. Although the equation for the energy of the mean flow is helpful in obtaining additional insight into the dynamics of turbulent motion, it does not contain any more information than the momentum equation for the mean flow.

2.3.4 Kinetic energy of the turbulence

The kinetic energy of turbulence refers specifically to the kinetic energy associated with the fluctuating turbulent motion in a flow. It represents the energy stored in the turbulent eddies and fluctuations that continuously vary in time. The kinetic energy of turbulence is the main parameter in characterizing and quantifying the intensity and strength of turbulent motion within the flow. The equation governing the mean kinetic energy $\frac{1}{2}\overline{u_iu_i}$

of the turbulent velocity fluctuations is obtained by multiplying the steady Navier-Stockes Equation 2.27 by u_i and applying Reynolds decomposition, taking the time average of all the terms and subtracting the kinetic energy of the mean flow (Equation 2.39) :

$$U_j \frac{\partial U_i}{\partial x_j} = -\frac{1}{\rho}\frac{\partial P}{\partial x_i} + \nu \frac{\partial^2 U_i}{\partial x_j \partial x_j}. \tag{2.40}$$

$$U_i \frac{\partial U_i U_j}{\partial x_j} - U_i U_i \frac{\partial U_j}{\partial x_j} = -U_i \frac{1}{\rho}\frac{\partial p}{\partial x_i} + U_i \frac{\partial}{\partial x_j}\left(\nu \frac{\partial U_i}{\partial x_j}\right). \tag{2.41}$$

$$U_i \frac{\partial U_i U_j}{\partial x_j} - U_i U_i \frac{\partial U_j}{\partial x_j} = -\frac{1}{\rho}\frac{\partial U_i P}{\partial x_i} + \frac{P}{\rho}\frac{\partial U_i}{\partial x_i} + \frac{\partial}{\partial x_j}\left(\nu U_i \frac{\partial U_i}{\partial x_j}\right) - \nu \frac{\partial U_i}{\partial x_j}\frac{\partial U_i}{\partial x_j}. \tag{2.42}$$

According to the continuity equation of the incompressible flow, pressure terms $P/\rho(\partial U_i/\partial x_i)$ and $U_i U_i(\partial U_j/\partial x_j)$ are eliminated. Using Reynolds decomposition, U_i is decomposed into mean and fluctuating components, and Equation 2.42 becomes as follows:

$$(\overline{U_i}+u_i)\frac{\partial}{\partial x_j}(\overline{U_i}+u_i)(\overline{U_j}+u_j) = -\frac{1}{\rho}\frac{\partial}{\partial x_i}(\overline{U_i}+u_i)(\overline{P}+p) + (\overline{U_i}+u_i)\frac{\partial}{\partial x_j}\left(\nu \frac{\partial}{\partial x_j}(\overline{U_i}+u_i)\right). \tag{2.43}$$

By simplifying and detailing all the terms of Equation 2.43, it becomes as follow:

$$\begin{aligned}
&\overline{U_i}\frac{\partial}{\partial x_j}\overline{U_i U_j} + \overline{U_i}\frac{\partial}{\partial x_j}\overline{U_i}u_j + \overline{U_i}\frac{\partial}{\partial x_j}u_i\overline{U_j} + \overline{U_i}\frac{\partial}{\partial x_j}u_i u_j \\
&+u_i\frac{\partial}{\partial x_j}\overline{U_i U_j} + u_i\frac{\partial}{\partial x_j}\overline{U_i}u_j + u_i\frac{\partial}{\partial x_j}u_i\overline{U_j} + u_i\frac{\partial}{\partial x_j}u_i u_j \\
&= -\frac{1}{\rho}\frac{\partial}{\partial x_i}\overline{U_i P} - \frac{1}{\rho}\frac{\partial}{\partial x_i}\overline{U_i}p - \frac{1}{\rho}\frac{\partial}{\partial x_i}u_i\overline{P} - \frac{1}{\rho}\frac{\partial}{\partial x_i}u_i p \\
&+\frac{\partial}{\partial x_j}\left(\nu\overline{U_i}\frac{\partial\overline{U_i}}{\partial x_j}\right) + \frac{\partial}{\partial x_j}\left(\nu\overline{U_i}\frac{\partial u_i}{\partial x_j}\right) + \frac{\partial}{\partial x_j}\left(\nu u_i\frac{\partial\overline{U_i}}{\partial x_j}\right) + \frac{\partial}{\partial x_j}\left(\nu u_i\frac{\partial u_i}{\partial x_j}\right) \\
&-\nu\frac{\partial\overline{U_i}}{\partial x_j}\frac{\partial\overline{U_i}}{\partial x_j} - \cancel{\nu\frac{\partial\overline{U_i}}{\partial x_j}\frac{\partial u_i}{\partial x_j}}^{zero} - \cancel{\nu\frac{\partial u_i}{\partial x_j}\frac{\partial\overline{U_i}}{\partial x_j}}^{zero} - \nu\frac{\partial u_i}{\partial x_j}\frac{\partial u_i}{\partial x_j}.
\end{aligned} \tag{2.44}$$

By taking the time average of all the terms in Equation 2.44, the Equation is reduced into:

$$\begin{aligned}
&\overline{\overline{U_i}\frac{\partial}{\partial x_j}(\overline{U_i U_j})} + \overline{\overline{U_i}\frac{\partial}{\partial x_j}(u_i u_j)} + \overline{u_i\frac{\partial}{\partial x_j}(\overline{U_i}u_j)} + \overline{u_i\frac{\partial}{\partial x_j}(u_i\overline{U_j})} + \overline{u_i\frac{\partial}{\partial x_j}(u_i u_j)} = \\
&-\frac{1}{\rho}\overline{\frac{\partial}{\partial x_i}\overline{U_i P}} - \frac{1}{\rho}\overline{\frac{\partial}{\partial x_i}u_i p} + \overline{\frac{\partial}{\partial x_j}\left(\nu\overline{U_i}\frac{\partial\overline{U_i}}{\partial x_j}\right)} + \overline{\frac{\partial}{\partial x_j}\left(\nu u_i\frac{\partial u_i}{\partial x_j}\right)} - \nu\overline{\frac{\partial\overline{U_i}}{\partial x_j}\frac{\partial\overline{U_i}}{\partial x_j}} - \nu\overline{\frac{\partial u_i}{\partial x_j}\frac{\partial u_i}{\partial x_j}}.
\end{aligned} \tag{2.45}$$

By considering each term on the left-hand side of the Equation separately and resolving them, we arrive at a set of five following sub-Equations:

$$\overline{\overline{U_i}\frac{\partial}{\partial x_j}(\overline{U_i U_j})} = \overline{\overline{U_i U_j}\frac{\partial\overline{U_i}}{\partial x_j}} + \overline{\overline{U_i U_i}\frac{\partial\overline{U_j}}{\partial x_j}} = \overline{\overline{U_j}\frac{\partial}{\partial x_j}(\frac{1}{2}\overline{U_i U_i})}. \tag{2.46a}$$

$$\overline{\overline{U_i}\frac{\partial}{\partial x_j}(u_i u_j)} = \overline{\frac{\partial}{\partial x_j}(\overline{U_i}u_i u_j)} - \overline{u_i u_j\frac{\partial\overline{U_i}}{\partial x_j}}. \tag{2.46b}$$

$$\overline{u_i \frac{\partial}{\partial x_j}(\overline{U_i} u_j)} = \overline{u_i u_j \frac{\partial \overline{U_i}}{\partial x_j}} + \overline{u_i \overline{U_i} \frac{\partial u_j}{\partial x_j}} = \overline{u_i u_j \frac{\partial \overline{U_i}}{\partial x_j}}. \tag{2.46c}$$

$$\overline{u_i \frac{\partial}{\partial x_j}(u_i \overline{U_j})} = \overline{u_i \overline{U_j} \frac{\partial u_i}{\partial x_j}} + \overline{u_i u_i \frac{\partial \overline{U_j}}{\partial x_j}} = \overline{u_i \overline{U_j} \frac{\partial u_i}{\partial x_j}} = \overline{\overline{U_j} \frac{\partial}{\partial x_j}(\frac{1}{2} u_i u_i)}. \tag{2.46d}$$

$$\overline{u_i \frac{\partial}{\partial x_j}(u_i u_j)} = \overline{u_i u_j \frac{\partial u_i}{\partial x_j}} + \overline{u_i u_i \frac{\partial u_j}{\partial x_j}} = \overline{u_j \frac{\partial}{\partial x_j}(\frac{1}{2} u_i u_i)} = \overline{\frac{\partial}{\partial x_j}(\frac{1}{2} u_i u_i u_j)}. \tag{2.46e}$$

The term $\overline{u_i u_j \partial \overline{U_i} / \partial x_j}$ in Equations 2.46b and 2.46c cancelled each other from the general Equation 2.45. In addition to continuity rule, the five terms in Equation 2.45 reduced to 2 terms in the following Equation:

$$\begin{aligned} &\overline{\overline{U_i} \frac{\partial}{\partial x_j}(\overline{U_i U_j})} + \overline{\overline{U_j} \frac{\partial}{\partial x_j}(\frac{1}{2} u_i u_i)} = -\frac{1}{\rho} \overline{\frac{\partial}{\partial x_j} \overline{U_i P}} - \frac{1}{\rho} \overline{\frac{\partial}{\partial x_i} u_i p} + \frac{\partial}{\partial x_i} \left(\nu \overline{U_i} \frac{\partial \overline{U_i}}{\partial x_j} \right) \\ &+ \frac{\partial}{\partial x_j} \left(\nu u_i \frac{\partial u_i}{\partial x_j} \right) - \overline{\frac{\partial}{\partial x_j}(\overline{U_i} u_i u_j)} - \overline{\frac{\partial}{\partial x_j}(\frac{1}{2} u_i u_i u_j)} - \nu \frac{\partial \overline{U_i}}{\partial x_j} \frac{\partial \overline{U_i}}{\partial x_j} - \nu \frac{\partial u_i}{\partial x_j} \frac{\partial u_i}{\partial x_j}. \end{aligned} \tag{2.47}$$

Subtracting Equation 2.47 from Equation 2.39, which governs the kinetic energy of the mean flow, we obtain the mean kinetic energy of the total turbulence.

$$\overline{\overline{U_j} \frac{\partial}{\partial x_j}(\frac{1}{2} u_i u_i)} = -\frac{\partial}{\partial x_j} \left(\frac{1}{\rho} \overline{u_j p} - \overline{\nu u_i \frac{\partial u_i}{\partial x_j}} + \frac{1}{2} \overline{u_i u_i u_j} \right) - \overline{\nu \frac{\partial u_i}{\partial x_j} \frac{\partial u_i}{\partial x_j}} - \overline{u_i u_j} \frac{\partial \overline{U_i}}{\partial x_j}. \tag{2.48}$$

The rate of change of turbulent kinetic energy $\frac{1}{2}\overline{u_i u_i}$ is thus due to pressure-gradient work, transport by turbulent velocity fluctuations, transport by viscous stresses, and two kinds of deformation work. The transport terms (divergences of energy flux) are like those in Equation 2.39. According to Gauss-Ostrogradsky theorem in Erwen's book [32], Frank notes [33], and many other fluid mechanics studies, the energy flux out of or into a closed control volume V is zero. The mentioned theorem is shown in Equation 2.49, where n_j is a unit vector normal to the surface element ds. Equation 2.49 shows the transport terms by stresses $\frac{\partial}{\partial x_j}(\overline{\tau_{ij} u_i})$ integrates to zero if the integration refers to a control volume V on whose surface S, τ_{ij} or u_i vanishes. For further simplification, Lumley [8] shows that the work performed by stresses on a surface of a volume is zero due to the redistribution of energy from one point to another in the flow.

$$\int_v \frac{\partial}{\partial x_j}(\overline{\tau_{ij} u_i})\, dv = \int_s n_j \overline{\tau_{ij} u_i}\, ds = 0. \tag{2.49}$$

The deformation work terms are more important. The turbulence production $-\overline{u_i u_j} \frac{\partial \overline{U_i}}{\partial x_j}$ occurs in 2.39 and in 2.48 with opposite signs. As expected, the term represents the transfer of momentum between the mean flow and turbulent fluctuations, reflecting the dynamic interactions between them. In this process, the turbulent fluctuations draw energy from the mean flow, decreasing the mean flow's kinetic energy. Conversely, the turbulence is energized as it receives kinetic energy from the mean flow. The last term in Equation 2.48 is the rate at which viscous stresses perform deformation work against the fluctuating strain rate. This is always a drain of energy since the term is quadratic in $\partial u_i / \partial x_j$. This term is called viscous dissipation. Unlike the dissipation term in 2.39, it is essential to the dynamics of turbulence and cannot be ordinarily neglected. In most shear flows, production and dissipation do not balance, though they are nearly always of the same order of magnitude.

2.3.5 Kinetic energy of the coherent and random structures

When coherent motion coexists with random or turbulent flow, an interesting interaction takes place. The coherent motion interacts with the random turbulent flow, leading to a locally enhanced turbulent cascade. In other words, the presence of coherent structures can influence the behavior of turbulent fluctuations, resulting in increased energy transfer and dissipation at certain locations. As discussed before in Section 2.2.4, Reynolds and Hussain [25] decomposed the velocity and the pressure into 3 main components: Mean velocity, coherent fluctuations, and Random fluctuations:

$$U_i = \overline{U_i} + \widetilde{u_i} + u_i'. \tag{2.50}$$

$$P = \overline{P} + \widetilde{p} + p'. \tag{2.51}$$

Indeed, to fully describe a field of turbulent flow, one can employ suitable manipulations of the Navier-Stokes equations that involve periodic or non-periodic oscillations (coherent and random structures). These manipulations lead to additional governing equations related to velocity, which are essential for capturing the complexities and dynamics of turbulent flow. The Equations of the kinetic energy involving the interaction between periodic and non-periodic structures can be derived through the Navier Stokes Equation,

$$\frac{\partial U_i}{\partial t} + U_j \frac{\partial U_i}{\partial x_j} = -\frac{1}{\rho}\frac{\partial P}{\partial x_i} + \nu \frac{\partial^2 U_i}{\partial x_j \partial x_j} \tag{2.52}$$

By involving the three components (Triple decomposition) of the flow, the Equation becomes:

$$\begin{aligned} \frac{\partial(\overline{U_i} + \widetilde{u_i} + u_i')}{\partial t} + (\overline{U_i} + \widetilde{u_i} + u_i')\frac{\partial(\overline{U_i} + \widetilde{u_i} + u'i)}{\partial x_j} = -\frac{1}{\rho}\frac{\partial(\overline{P} + \widetilde{p} + p')}{\partial x_i} + \\ \nu \frac{\partial^2(\overline{U_i} + \widetilde{u_i} + u_i')}{\partial x_j \partial x_j} \end{aligned} \tag{2.53}$$

Taking the phase average of the terms in an Equation involving periodic or non-periodic oscillations is a common approach to eliminate the random component and obtain a simplified description of the system, as shown in Equation 2.54.

$$\begin{aligned} &\langle \cancel{\frac{\partial \overline{U_i}}{\partial t}}^{zero} \rangle + \langle \frac{\partial \widetilde{u_i}}{\partial t} \rangle + \langle \cancel{\frac{\partial u_i'}{\partial t}}^{zero} \rangle + \langle \overline{U_j}\frac{\partial \overline{U_i}}{\partial x_j} \rangle + \langle \overline{U_j}\cancel{\frac{\partial u_i'}{\partial x_j}}^{zero} \rangle + \langle \overline{U_j}\frac{\partial \widetilde{u_i}}{\partial x_j} \rangle + \langle u_j'\cancel{\frac{\partial \overline{U_i}}{\partial x_j}}^{zero} \rangle \\ &+ \langle u_j'\frac{\partial u_i'}{\partial x_j} \rangle + \langle u_j'\cancel{\frac{\partial \widetilde{u_i}}{\partial x_j}}^{zero} \rangle + \langle \widetilde{u_j}\frac{\partial \overline{U_i}}{\partial x_j} \rangle + \langle \widetilde{u_j}\cancel{\frac{\partial u_i'}{\partial x_j}}^{zero} \rangle + \langle \widetilde{u_j}\frac{\partial \widetilde{u_i}}{\partial x_j} \rangle \\ &= -\frac{1}{\rho}\left[\langle \frac{\partial \overline{P}}{\partial x_i} \rangle - \langle \frac{\partial \widetilde{p}}{\partial x_i} \rangle - \langle \cancel{\frac{\partial p'}{\partial x_i}}^{zero} \rangle \right] + \langle \nu \frac{\partial^2 \overline{U_i}}{\partial x_j \partial x_j} \rangle + \langle \nu \frac{\partial^2 \widetilde{u_i}}{\partial x_j \partial x_j} \rangle + \langle \nu \cancel{\frac{\partial^2 u_i'}{\partial x_j \partial x_j}}^{zero} \rangle \end{aligned} \tag{2.54}$$

The following Equation 2.55 consists of the mean flow and the coherent fluctuations (periodic structures):

$$\begin{aligned} \langle \frac{\partial \widetilde{u_i}}{\partial t} \rangle + \langle \overline{U_j}\frac{\partial \overline{U_i}}{\partial x_j} \rangle + \langle \overline{U_j}\frac{\partial \widetilde{u_i}}{\partial x_j} \rangle + \langle \frac{\partial u_i' u_j'}{\partial x_j} \rangle + \langle \widetilde{u_j}\frac{\partial \overline{U_i}}{\partial x_j} \rangle + \langle \frac{\partial \widetilde{u_i}\widetilde{u_j}}{\partial x_j} \rangle = \\ -\frac{1}{\rho}\langle \frac{\partial \overline{P}}{\partial x_i} \rangle - \frac{1}{\rho}\langle \frac{\partial \widetilde{p}}{\partial x_i} \rangle + \langle \nu \frac{\partial^2 \overline{U_i}}{\partial x_j \partial x_j} \rangle + \langle \nu \frac{\partial^2 \widetilde{u_i}}{\partial x_j \partial x_j} \rangle \end{aligned} \tag{2.55}$$

A temporal average is applied to remove high-frequency fluctuations associated with coherent structures, as shown in Equation 2.56 to eliminate the coherent fluctuations in a flow field.

$$\begin{aligned}\overline{\langle\cancel{\frac{\partial\widetilde{u_i}}{\partial t}}\rangle}^{zero} + \overline{\langle\overline{U_j}\frac{\partial\overline{U_i}}{\partial x_j}\rangle} + \overline{\langle\cancel{\overline{U_j}\frac{\partial\widetilde{u_i}}{\partial x_j}}\rangle}^{zero} + \overline{\langle\frac{\partial u_i'u_j'}{\partial x_j}\rangle} + \overline{\langle\cancel{\widetilde{u_j}\frac{\partial\overline{U_i}}{\partial x_j}}\rangle}^{zero} + \overline{\langle\frac{\partial\widetilde{u_i}\widetilde{u_j}}{\partial x_j}\rangle} = \\ -\frac{1}{\rho}\overline{\langle\frac{\partial\overline{P}}{\partial x_i}\rangle} - \frac{1}{\rho}\overline{\langle\cancel{\frac{\partial\widetilde{p}}{\partial x_i}}\rangle}^{zero} + \overline{\langle\nu\frac{\partial^2\overline{U_i}}{\partial x_j\partial x_j}\rangle} + \overline{\langle\cancel{\nu\frac{\partial^2\widetilde{u_i}}{\partial x_j\partial x_j}}\rangle}^{zero}\end{aligned} \tag{2.56}$$

By applying both phase averaging and time averaging to the Equation 2.54, we obtain an equation for the mean velocity. This is shown in the following Equation 2.57:

$$\overline{\overline{U_j}\frac{\partial\overline{U_i}}{\partial x_j}} + \overline{\frac{\partial u_i'u_j'}{\partial x_j}} + \overline{\frac{\partial\widetilde{u_i}\widetilde{u_j}}{\partial x_j}} = -\frac{1}{\rho}\frac{\partial\overline{P}}{\partial x_i} + \nu\frac{\partial^2\overline{U_i}}{\partial x_j\partial x_j} \tag{2.57}$$

This Equation shows the equilibrium of the mean velocity, it highlights Reynolds stresses $\overline{\widetilde{u_i}\widetilde{u_j}}$ $\overline{u_i'u_j'}$ that correspond to coherent motion and random motion, respectively. These motions perturb the mean velocity or inversely. The gradient of mean velocity induces velocity fluctuations.

Then, by subtracting Equation 2.57 (mean flow Equation) from Equation 2.55 (mean flow and coherent fluctuation) we obtain an Equation governing the dynamics of the coherent motion:

$$\begin{aligned}\frac{\partial\widetilde{u_i}}{\partial t} + \overline{U_j}\frac{\partial\widetilde{u_i}}{\partial x_j} + \widetilde{u_j}\frac{\partial\overline{U_i}}{\partial x_j} + \frac{\partial}{\partial x_j}(< u_i'u_j' > - \overline{u_i'u_j'}) + \frac{\partial}{\partial x_j}(\widetilde{u_i}\widetilde{u_j} - \overline{\widetilde{u_i}\widetilde{u_j}}) = \\ -\frac{1}{\rho}\frac{\partial\widetilde{p}}{\partial x_i} + \nu\frac{\partial^2\widetilde{u_i}}{\partial x_j\partial x_j}\end{aligned} \tag{2.58}$$

Then by subtracting Equation 2.55 (mean flow and coherent fluctuation) from Equation 2.53 (total flow components) we obtain we obtain an Equation governing the dynamics of the random motion:

$$\begin{aligned}\frac{\partial u_i'}{\partial t} + \overline{U_j}\frac{\partial\ u_i'}{\partial x_j} + \widetilde{u_j}\frac{\partial u_i'}{\partial x_j} + u_j'\frac{\partial\overline{U_i}}{\partial x_j} + u_j'\frac{\partial\widetilde{u_i}}{\partial x_j} + \frac{\partial}{\partial x_j}\left(u_i'u_j' - \langle u_i'u_j'\rangle\right) = \\ -\frac{1}{\rho}\frac{\partial p'}{\partial x_i} + \nu\frac{\partial^2 u_i'}{\partial x_j\partial x_j}\end{aligned} \tag{2.59}$$

To derive the Equation governing the kinetic energy of coherent motion, the Equation 2.58 is first multiplied by $\widetilde{u_i}$, followed by the application of phase and temporal averaging. This is shown below:

$$\begin{aligned}\overline{\langle\widetilde{u_i}\frac{\partial\widetilde{u_i}}{\partial t}\rangle} + \overline{\langle\widetilde{u_i}\overline{U_j}\frac{\partial\widetilde{u_i}}{\partial x_j}\rangle} + \overline{\langle\widetilde{u_i}\widetilde{u_j}\frac{\partial\overline{U_i}}{\partial x_j}\rangle} + \overline{\langle\widetilde{u_i}\frac{\partial}{\partial x_j}\langle u_i'u_j'\rangle\rangle} - \overline{\langle\widetilde{u_i}\cancel{\frac{\partial}{\partial x_j}\overline{u_i'u_j'}}\rangle}^{zero} \\ +\overline{\langle\widetilde{u_i}\frac{\partial}{\partial x_j}\widetilde{u_i}\widetilde{u_j}\rangle} - \overline{\langle\widetilde{u_i}\cancel{\frac{\partial}{\partial x_j}\overline{\widetilde{u_i}\widetilde{u_j}}}\rangle}^{zero} = -\overline{\langle\widetilde{u_i}\frac{\partial\widetilde{p}}{\partial x_i}\rangle} + \overline{\langle\widetilde{u_i}\nu\frac{\partial^2\widetilde{u_i}}{\partial x_j\partial x_j}\rangle}\end{aligned} \tag{2.60}$$

$$\begin{aligned}\overline{\frac{1}{2}\frac{\partial\widetilde{q}^2}{\partial t}} + \overline{\frac{1}{2}\overline{U_j}\frac{\partial\widetilde{q}^2}{\partial x_j}} + \overline{\widetilde{u_i}\widetilde{u_j}\frac{\partial\overline{U_i}}{\partial x_j}} + \overline{\frac{\partial}{\partial x_j}(\widetilde{u_i}\langle u_i'u_j'\rangle)} - \overline{\langle u_i'u_j'\rangle\frac{\partial\widetilde{u_i}}{\partial x_j}} \\ +\overline{\frac{1}{2}\frac{\partial}{\partial x_j}(\widetilde{q}^2\widetilde{u_j})} = -\overline{\frac{\partial}{\partial x_i}(\widetilde{p}\widetilde{u_i})} + \overline{\widetilde{\epsilon}}\end{aligned} \tag{2.61}$$

The concluding component of the Equation governing the kinetic energy of coherent motion can be expressed as follows:

$$\frac{1}{2}\overline{\frac{\partial \tilde{q}^2}{\partial t}} + \frac{1}{2}\overline{U_j}\frac{\partial \overline{\tilde{q}^2}}{\partial x_j} + \overline{\tilde{u}_i\tilde{u}_j}\frac{\partial \overline{U_i}}{\partial x_j} + \frac{\partial}{\partial x_j}\left(\overline{\tilde{p}\tilde{u}_j} + \overline{\tilde{u}_i\langle u_i' u_j'\rangle} + \frac{1}{2}\overline{\tilde{q}^2\tilde{u}_j}\right) - \overline{\langle u_i' u_j'\rangle\frac{\partial \tilde{u}_i}{\partial x_j}} + \bar{\tilde{\epsilon}} = 0. \tag{2.62}$$

- $\frac{1}{2}\overline{\frac{\partial \tilde{q}^2}{\partial t}}$ is the temporal evolution of the coherent motion kinetic energy.
- $\frac{1}{2}\overline{U_j}\frac{\partial \overline{\tilde{q}^2}}{\partial x_j}$ is the transport of coherent motion kinetic energy by the mean flow (advection of cohrent motion).
- $\overline{\tilde{u}_i\tilde{u}_j}\frac{\partial \overline{U_i}}{\partial x_j}$ is the production of coherent motion kinetic energy by the mean flow.
- $\frac{\partial}{\partial x_j}\left(\overline{\tilde{p}\tilde{u}_j}\right)$ is the transport of coherent motion kinetic energy by the pressure work (diffusion by pressure stresses).
- $\frac{\partial}{\partial x_j}\left(\overline{\tilde{u}_i\langle u_i' u_j'\rangle}\right)$ is the transport of kinetic energy by Reynolds stresses-coherent motion interaction (diffusion of Reynolds stresses by coherent motion velocity).
- $\frac{1}{2}\frac{\partial}{\partial x_j}\left(\overline{\tilde{q}^2\tilde{u}_j}\right)$ is the pure transport of coherent motion kinetic energy (diffusion of coherent motion by its movement).
- $\overline{\langle u_i' u_j'\rangle\frac{\partial \tilde{u}_i}{\partial x_j}}$ is the production of random motion kinetic energy by coherent motion.
- $\bar{\tilde{\epsilon}}$ is the dissipation of the coherent motion kinetic energy.

The distinction between Equation 2.62 and the kinetic energy of total fluctuations Equation 2.48 arises from the addition of two terms, both of which pertain to the interaction between random and coherent structures. These terms are associated with the production of random structures by coherent structures and the diffusion of coherent structures due to their mutual interaction. Due to the large size of coherent structures, they possess more significant inertia and are less affected by the dissipative effects of viscosity. As a result, the dissipation of energy within these structures is minimal, and they tend to retain their energy content over relatively longer time scales.

To derive the equation governing the kinetic energy of random motion, Equation 2.59 is first multiplied by u_i', followed by the application of phase and temporal averaging. This is shown below:

$$\begin{aligned}&\overline{\langle u_i'\frac{\partial u_i'}{\partial t}\rangle} + \overline{\langle u_i'\overline{U_j}\frac{\partial u_i'}{\partial x_j}\rangle} + \overline{\langle u_i'\widetilde{u_j}\frac{\partial u_i'}{\partial x_j}\rangle} + \overline{\langle u_i' u_j'\frac{\partial \overline{U_i}}{\partial x_j}\rangle} + \overline{\langle u_i' u_j'\frac{\partial \widetilde{u_i}}{\partial x_j}\rangle} + \\ &\overline{\langle u_i'\frac{\partial}{\partial x_j}u_i' u_j'\rangle} - \cancelto{zero}{\overline{\langle u_i'\frac{\partial}{\partial x_j}\langle u_i' u_j'\rangle\rangle}} = -\overline{\langle u_i'\frac{\partial p'}{\partial x_i}\rangle} + \overline{\langle u_i'\nu\frac{\partial^2 u_i'}{\partial x_j\partial x_j}\rangle}\end{aligned} \tag{2.63}$$

$$\overline{\frac{1}{2}\frac{\partial q'^2}{\partial t}} + \overline{\frac{1}{2}\overline{U_j}\frac{\partial q'^2}{\partial x_j}} + \overline{\frac{1}{2}\widetilde{u_j}\langle\frac{\partial q'^2}{\partial x_j}\rangle} + \overline{u_i' u_j'\frac{\partial \overline{U_i}}{\partial x_j}} + \overline{\langle u_i' u_j'\rangle\frac{\partial \widetilde{u_i}}{\partial x_j}} + \overline{\frac{\partial}{\partial x_j}q'^2 u_j'} = -\overline{\frac{\partial p' u_i'}{\partial x_i}} + \bar{\epsilon} \tag{2.64}$$

The concluding component of the Equation governing the kinetic energy of random motion can be expressed as follows:

$$\frac{1}{2}\frac{\overline{\partial q'^2}}{\partial t} + \frac{1}{2}\overline{U_j}\frac{\partial \overline{q'^2}}{\partial x_j} + \overline{u_i'u_j'}\frac{\partial \overline{U_i}}{\partial x_j} + \frac{\partial}{\partial x_j}\left(\overline{p'u_j'} + \frac{1}{2}\overline{\widetilde{u_j}\langle q'^2\rangle} + \frac{1}{2}\overline{q'^2u_j'}\right) + \overline{\langle u_i'u_j'\rangle\frac{\partial \widetilde{u_i}}{\partial x_j}} + \overline{\epsilon'} = 0. \tag{2.65}$$

- $\frac{1}{2}\frac{\overline{\partial q'^2}}{\partial t}$ is the temporal evolution of the random motion kinetic energy.
- $\frac{1}{2}\overline{U_j}\frac{\partial \overline{q'^2}}{\partial x_j}$ is the transport of random motion kinetic energy by the mean flow (advection of random motion).
- $\overline{u_i'u_j'}\frac{\partial \overline{U_i}}{\partial x_j}$ is the production of random motion kinetic energy by the mean flow.
- $\frac{\partial}{\partial x_j}\left(\overline{p'u_j'}\right)$ is the transport of random motion kinetic energy by the pressure work (diffusion by pressure stresses).
- $\frac{1}{2}\frac{\partial}{\partial x_j}\left(\overline{\widetilde{u_j}\langle q'^2\rangle}\right)$ is the transport of kinetic energy by random-coherent motion interaction (diffusion of random motion by coherent motion velocity).
- $\frac{1}{2}\frac{\partial}{\partial x_j}\left(\overline{q'^2u_j'}\right)$ is the pure transport of random motion kinetic energy (diffusion of random motion by its movement).
- $\overline{\langle u_i'u_j'\rangle\frac{\partial \widetilde{u_i}}{\partial x_j}}$ is the production of random motion kinetic energy by coherent motion.
- $\overline{\epsilon}$ is the dissipation of the random motion kinetic energy.

A notable observation is that the sign of the production term representing the generation of random structures by coherent motion $\overline{\langle u_i'u_j'\rangle\frac{\partial \widetilde{u_i}}{\partial x_j}}$ is reversed between the two Equations 2.62 and 2.65. This inversion suggests a transfer of energy from coherent motion to random structures, resulting in a loss of energy from the coherent motion and a gain of energy in the random fluctuations. This term is connected to the phenomenon of entrainment, as explained in section 2.2.4, and has been extensively discussed by Townsend in his works [23, 24].

2.4 Wakes interactions

In various engineering applications such as high-rise buildings, marine structures, and heat exchange tubes, the flow over multiple bluff bodies in close proximity is common. These interactions between multiple wakes result in complex flow patterns that often lead to significant flow-induced forces. Zdravkovich has conducted extensive research on bluff bodies and wake interactions, as illustrated by a substantial number of studies [34, 35, 36, 37, 38]. The dynamics of wake interaction between a pair of side-by-side identical cylinders are notably influenced by the distance between the bodies, as shown by Kang [39] and Peshard [40]. Williamson [41] studied two parallel side-by-side cylinder wake interactions. The study shows that when the gap distance between cylinders is large (typically exceeding 5 cylinder diameters), the mutual interference between the wakes is minimal, resulting in two separate single-cylinder wakes. The two vortex streets synchronize as the gap distance decreases (typically less than 5 cylinder diameters). If the gap is relatively large, the wake is characterized by two parallel vortex streets undergoing "anti-phase shedding." While, with a relatively smaller gap, the wake transitions to "in-phase shedding", and

the two vortex streets merge into a “binary vortex”, as named by Williamson. Sumner [42, 43] studies show the wake and its proximity interference effects by modifying the longitudinal and transverse spacing between the cylinders. Igarashi [44, 45, 46] investigate experimentally the characteristics of the flow around two circular cylinders in subcritical range ($87000 < Re < 520000$). In these three contributions, the cylinders were set in tandem configuration to study the interaction of both cylinders' wakes. The studies were carried out on two cylinders with equal diameters [44, 46] and different diameters [45]. For instance, Figure 2.10 in Igarashi study [44] shows the flow visualization between two cylinders (equal diameters) for different gap distances.

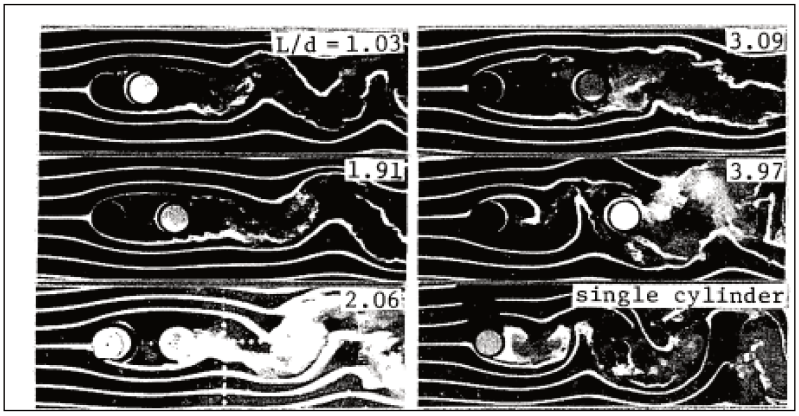

Figure 2.10: Flow visualization of two cylinders interactions in the function of gap distance (Figure from Igrashi [44]).

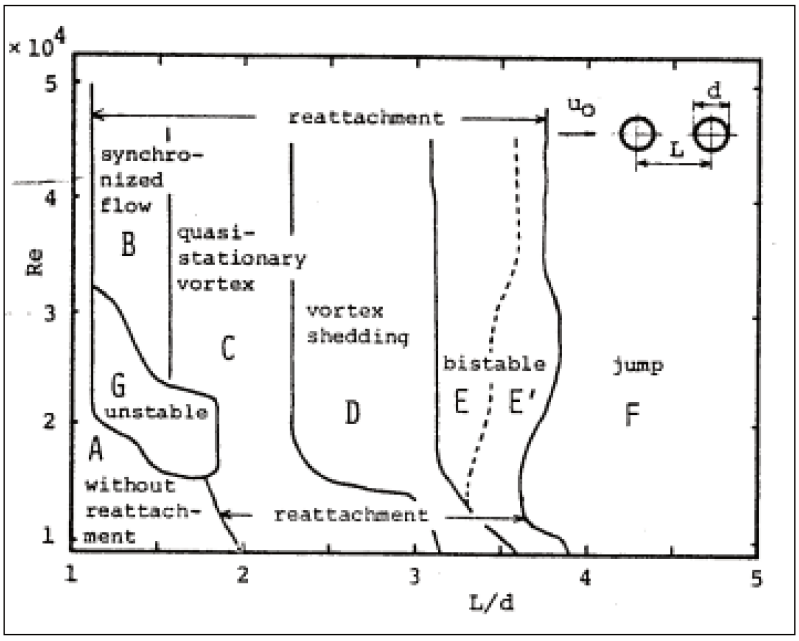

Figure 2.11: Flow patterns for two cylinders configuration arranged in tandem (figure from Igrashi [46]).

In the wake interaction between two cylinders (arranged in tandem), distinct flow patterns appeared depending on the gap distance between the cylinders. Igrashi shows these patterns [44, 45] in Figure 2.11 and labeled from A to G. These patterns can provide

more information on the complex dynamics of cylinder wake interactions. Pattern A involves a situation where the separated shear layer from the upstream cylinder remains detached from the downstream cylinder. In Pattern B, a synchronized phenomenon was revealed: vortex formation of the shear layer and subsequent shedding in the near wake of the downstream cylinder. It is accompanied by the reattachment of the other shear layer onto the downstream cylinder. One remark is that vortex shedding frequency remains consistent regardless of the free stream velocity. Pattern C exhibits the formation of quasi-stationary vortices between the cylinders, showing a different flow configuration. Transitioning to Pattern D, the previously quasi-stationary vortices become unstable, resulting in intermittent vortex shedding. In pattern E, the separated shear layer from the upstream cylinder rolls up intermittently for a moment in front of the downstream cylinder. This pattern is a bistable flow in the transition region between patterns d and f. A variation of this bistable behavior is presented in Pattern E', where one particular pattern dominates for an extended duration within this transitional region. In the largest gap pattern F, the separated shear layer from the upstream cylinder consistently rolls up in front of the downstream cylinder. Lastly, Pattern G signifies an unstable flow within the transition region connecting Patterns A, B, and C. These patterns collectively provide a comprehensive view of the evolving wake interactions between two cylinders arranged in tandem. This is also shown in new numerical studies, as illustrated by Hu [47]. Igarashi also presents his significant investigations involving configurations with more than two cylinders (tandem arrangements), as highlighted in studies such as [48, 49]. Sumner [50] verified in his contribution Strouhal number in the function of Reynolds number and gap distance, as shown in Figure 2.12.

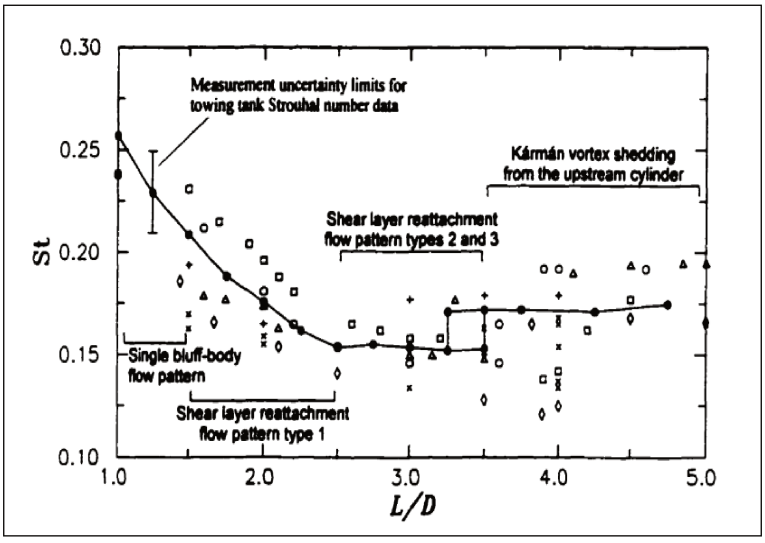

Figure 2.12: Strouhal number data for two cylinders configuration arranged in tandem (figure from Sumner [50]).

Figure 2.12 clearly illustrates that at a particular gap distance, the flow behavior is predominantly influenced by the Von Kármán vortices originating upstream (St = 0.2).

2.5 Conclusions and research focus

This chapter has provided a comprehensive review of wake studies and their interactions, offering an extensive analysis of the existing literature in the domain of turbulent and shear flows. Additionally, the chapter includes demonstrations related to the total turbulent kinetic energy and the kinetic energy associated with different structures (CM and RM) within the wake. In this context, detailed insights are offered into both periodic (CM) and non-periodic (RM) structures found within wake flows.
Medici and Alfredsson [51] demonstrated in their research that wind turbines act as bluff bodies in vortices shedding. This study revealed the presence of both periodic and non-periodic events in the wake of a turbine. Consequently, to create a simplified academic flow characterized by low Reynolds numbers, bluff bodies were selected for wake generation. Thus, our research is focus on investigating the energy exchange within single and double bluff body wakes configurations, as represented in Figure 2.13. The configurations involve simple obstacles geometry that are related to wind farms, such as cylinders and airfoils. Further details on these configurations are provided in Chapter 3, which outlines the experimental setup in a wind tunnel.
Studies related to single cylinder wakes with various background investigations are also highlighted in this chapter. The ongoing interest of scientists in the exploration of double wake interactions are shown by the research work of Igrashi [44, 45, 46, 48, 49]. Some of these studies have configurations closely related to our research, including both single and double-cylinder configurations as shown in Figure 2.13. However, a specific investigation into the mechanisms of energy exchange associated with various structures (CM and RM) within double wakes configurations remains not studied yet.

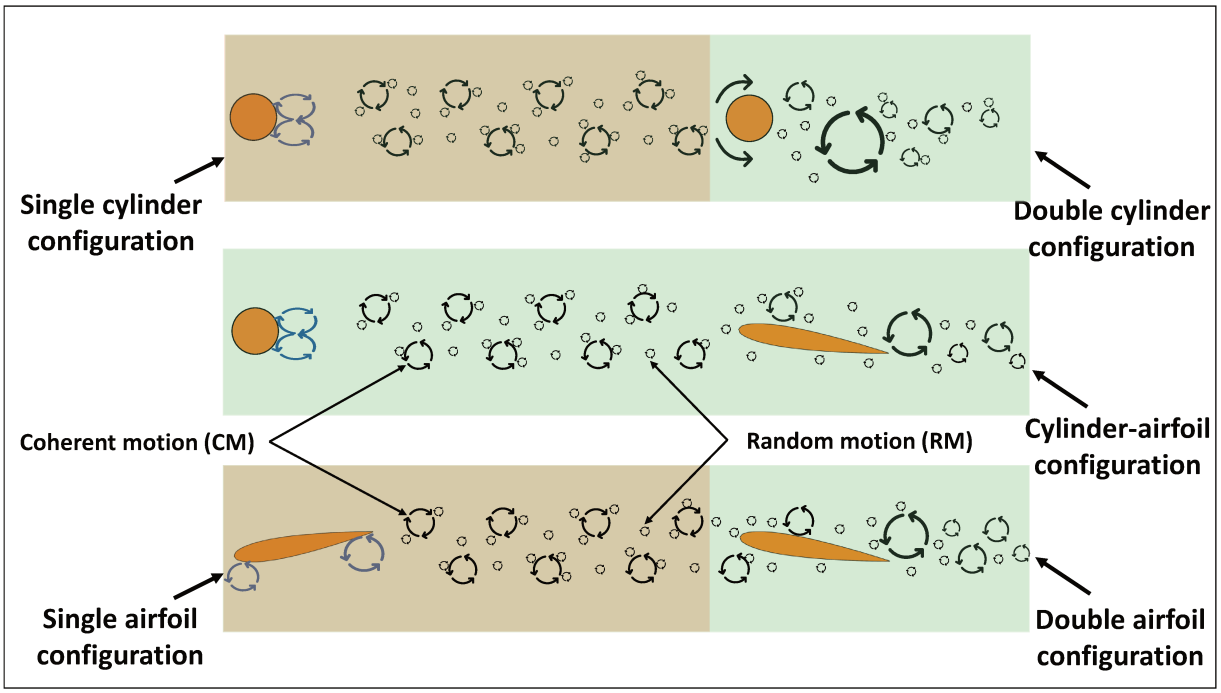

Figure 2.13: Relevant configurations.

CHAPTER 3

Experimental setup

Summary

Coherent structures embedded in wakes are the focus of study. The study helps to uncover the consequence of upstream wake (behind first obstacle) on another obstacle placed downstream in function of the upstream wake. This issue pertains to wind turbine parks and obstacles considered alike are cylinders and airfoils. To investigate this phenomenon, experiments are conducted in a low subsonic wind tunnel, specifications are detailed in this chapter. These specifications include information about the wind tunnel's dimensions, airflow velocity range, turbulence intensity and test section characteristics. In this investigation, high-speed particle image velocimetry (HS-PIV) is used as a measurement tool at multiple Reynolds numbers. Furthermore, improvements in the anemometry acquisitions to increase fluctuations range are illustrated within this chapter. This technique ensures that the temporal aspects of the fluid dynamics are adequately resolved. Moreover, by increasing largely datasets reaching 190,000 images, this also ensures robust statistical analysis. The section also demonstrates the post-processing of images acquired through HS-PIV.

Contents

3.1 Wind tunnel **40**
3.1.1 Test section 41
3.2 Experiment installation **43**
3.2.1 Measurement technique (HS-PIV) 43
3.2.2 Experimental obstacles and configurations. 44
3.2.3 Laser sheet and seeding particles 46
3.2.4 Cameras and spatial calibration 47
3.2.5 Alignement 48
3.2.6 Recordings and synchronization 49
3.3 PIV post processing **51**
3.4 Overview of experimental parameters **52**

3.1 Wind tunnel

The experiments are conducted within a subsonic wind tunnel located at Coria laboratory. This wind tunnel is designed as a closed-circuit system and is characterized by having a square-shaped test section. A top view of the wind tunnel components is shown in Figure 3.1a. The wind tunnel is equipped with a three-phase electric motor (fan), where the rotational speed of the fan is directly proportional to the frequency of the sinusoidal voltage applied to its terminals. The primary function of the fan is to generate airflow within the test section by both blowing and suction. The fan has a maximum power output of 2 HP and operates at a maximum frequency of 60 Hz. It is positioned downstream, following the divergence section of the wind tunnel. To prevent any air leakage, the low-speed subsonic wind tunnel has been equipped with plastic bristles. These bristles serve as a seal to maintain the integrity of the airflow within the tunnel. The quality of a wind tunnel is determined by its ability to generate a flow stable in time, and homogeneous in space. This is achieved through the installation of a convergent (ratio 9:1), which facilitates flow convergence before the air enters the test section, as shown in Figure 3.1b.

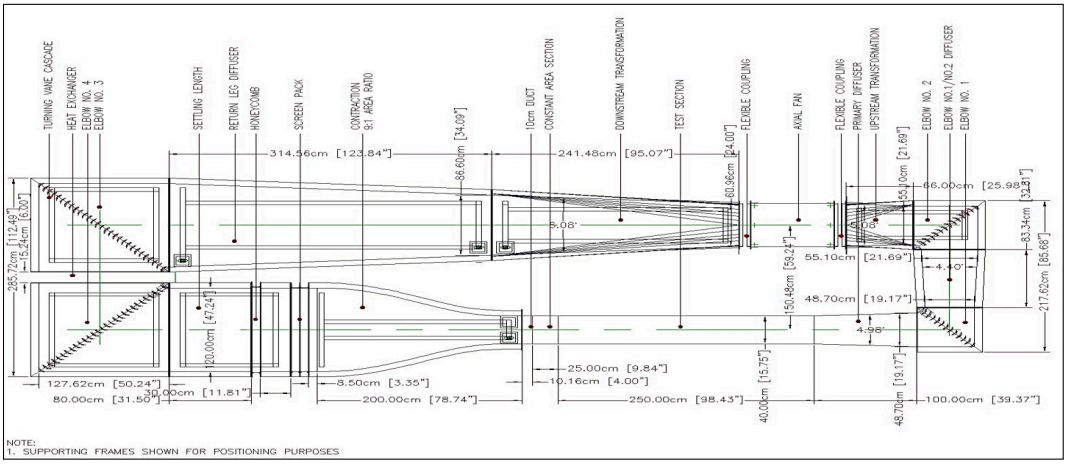

(a) Wind tunnel top view.

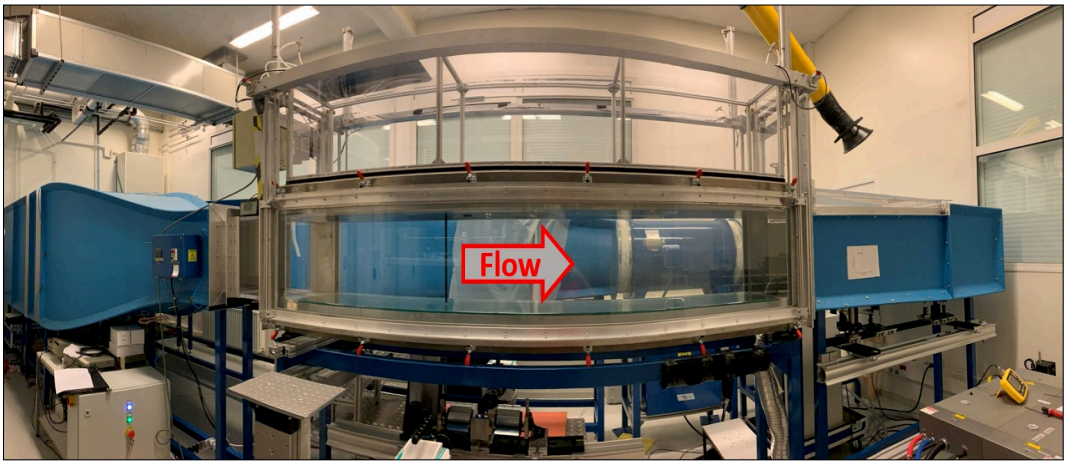

(b) Wind tunnel front view.

Figure 3.1: Closed loop wind tunnel.

3.1.1 Test section

The test section, designed and manufactured in 2021 at CORIA, serves as a replacement for the original one. This replacement is done after a displacement of the wind tunnel to a new experimental room in 2021. Unlike the initial install with plexiglass windows, the new test section is equipped with glass windows for hazards prevention during high-energy laser experiments. Additionally, a pneumatic system has been integrated into the test section to facilitate the vertical opening of its windows without causing disturbances to the experimental equipment.

The test section of the wind tunnel is a square section with dimensions of $40 \times 40\ cm^2$ and 2.5 m long as shown in Figure 3.2a. The cross section is drilled at its end with an 80 mm hole to insert the smoking machine tube for particles injection, Figure 3.2a. The section features a flexible and smooth ceiling that is adjustable (slope of the ceiling) to compensate the influence of boundary layer development. Boundary layers tend to "shrink" the effective flow section and to increase the velocity at the center of the airflow. This point becomes particularly important when conducting studies over extended distances downstream of the obstacle or when investigating the progression of the boundary layer itself. The ceiling of the test section is constructed with interchangeable plates, which can be customized based on the specific experiments being conducted. These plates are drilled with holes at precise intervals to facilitate the insertion of obstacles at designated positions as required for the experiments, as shown in Figure 3.2b. The wind tunnel has a transparent test section, characterised by glass windows on all four sides to allow extensive use of optical techniques.

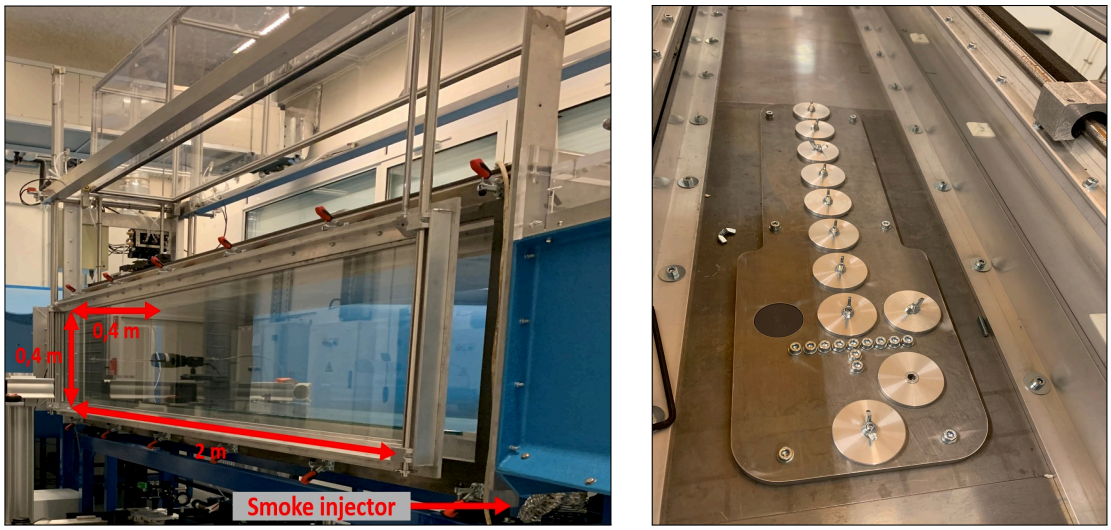

(a) (b)

Figure 3.2: (a) Installed test section. (b) Drilled plate for obstacles insertion.

Flow velocity and the rotational speed of the axial fan should be verified before starting measurements campaign. Verifying this relation is done by Laser Doppler Anemometry (LDA) for higher precision. The LDA principle is based on the Doppler effect, where the frequency shift of laser light scattered by particles in a flowing fluid is used to determine the velocity of those particles, see Tropea [52]. LDA offers advantages like, high spatial resolution, and the ability to measure velocity at specific points in a fluid. Therefore, fixed position in downstream direction is considered to be 9 cm from the inlet of the test section (after fluid convergence). The acquisition of LDA is done in function of section

height. Figure 3.3b shows mean velocity of flow direction as a function of motor frequency. The flow velocity of the tunnel ranges from 0.23 m/s to 16.6 m/s and is set by motor frequency adjustment through frequency controller.

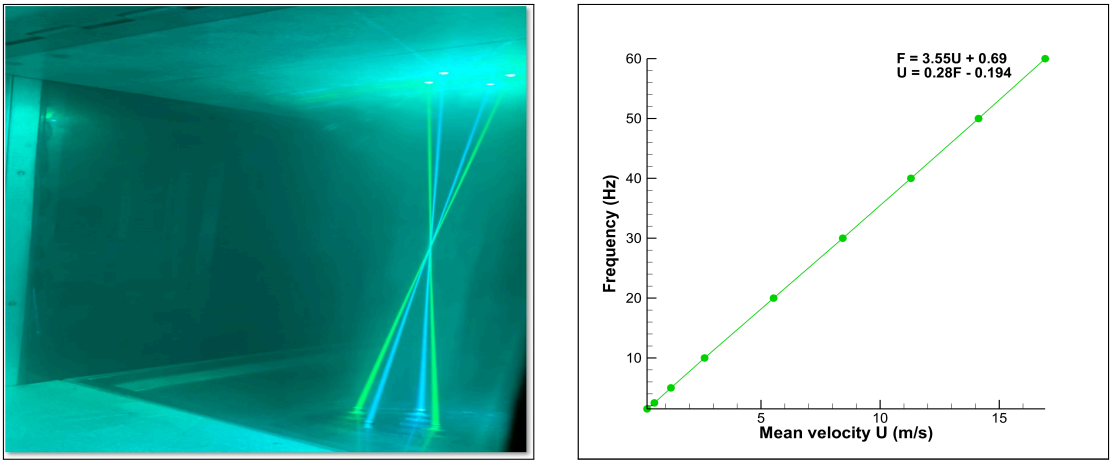

(a) (b)

Figure 3.3: (a) Laser doppler anemometer probe. (b) Streamwise mean velocity in function of motor frequency.

The second verification step before initiating measurements within the new test section (after displacement of wind tunnel) pertains to the assessment of residual turbulence intensity. In this context, the upstream flow exhibits a very low residual turbulent intensity level, less than 0.5%, regardless of whether low or high motor frequencies are employed. This is represented in Figures 3.4a and 3.4b.

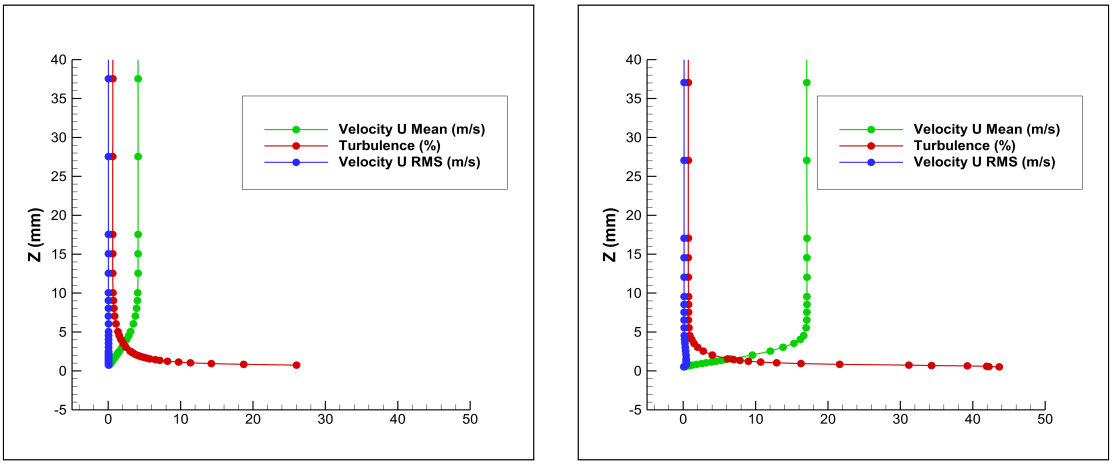

(a) 15 Hz motor frequency. (b) 60 Hz motor frequency.

Figure 3.4: (a) Flow characteristics at low and high motor frequencies

Figures 3.4a and 3.4b show variations in mean velocity, turbulence intensity, and the root mean square (RMS) of mean velocity fluctuations as a function of height. The measurements extend from the bottom of the test section until the middle of the test section (200 mm). These measurements are provided for two different motor frequencies (flow speed). Figures 3.4a and 3.4b show that the mean velocity, turbulence intensity and RMS become uniform after 6 mm and 4 mm heights for both motor frequencies,

respectively. These figures present also the turbulent boundary layer (TBL) thickness that is developed at the surface of the test section. The thickness of TBL is around 8 mm for 4 m/s flow speed (15 Hz) and 4 mm for 16.6 m/s (60 Hz).

3.2 Experiment installation

3.2.1 Measurement technique (HS-PIV)

High-Speed Particle Image Velocimetry (HS-PIV) is an advanced variant of Particle Image Velocimetry (PIV) that allows capturing high-speed flow with high temporal resolution. It involves the rapid acquisition of image pairs at very short time intervals and high repetition rate to precisely track the movement of particles within a fluid. This enables the measurement of fluid velocity vectors and dynamics flow pattern. HS-PIV is particularly valuable in studying fast-flowing or rapidly changing fluid dynamics in fields such as aerodynamics, combustion, and fluid mechanics research. Small particles (seeding), often reflective or neutrally buoyant are seeded into the fluid. These particles follow the flow, allowing their motion to represent the motion of the surrounding fluid. A laser sheet is directed into the flow, illuminating a thin cross-section of the fluid containing the particles. The particles scatter the laser light, creating a pattern of illuminated particles. High-speed cameras capture images of the illuminated particles. These images are typically taken in pairs, with a short time delay between them. This time delay is known as the time interval Δt. Image Processing Software is then used to analyze the images and get the vector fields.

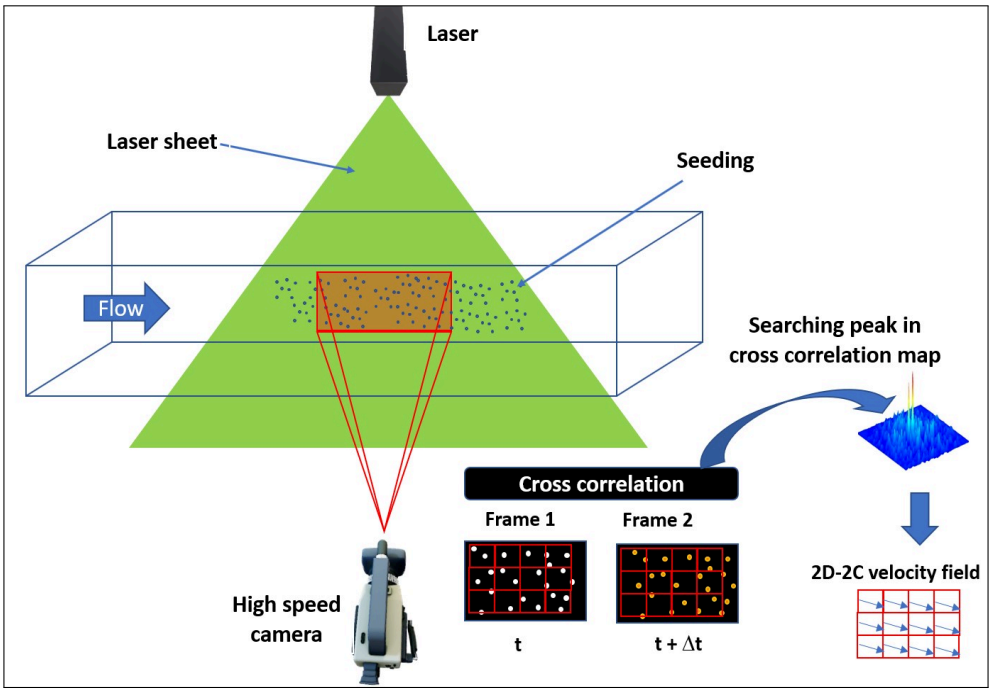

Figure 3.5: Particle Image Velocimetry (PIV) process.

The software identifies particle patterns contained in interrogation windows of each image and tracks their displacement between the two images. This is done by the cross correlation, as shown in Equation 3.1. In this equation, $f(x,t)$ and $g(x+\Delta x, t+\Delta t)$ represent two 2D signals (frames) separated spatially by Δx and temporally by Δt. Cross-

correlation measures the similarity between two signals or images as a function of a relative displacement. The result is a 2D map where each point represents the degree of similarity (correlation) at a specific displacement. Peaks in a cross-correlation map indicate areas where the two signals match, thus indicating the particles displacement. The precise displacement is finally computed by subpixel algorithm, see [53]. From this displacement, calculation of the velocity vectors of the fluid at each point in the illuminated plane is able to be done. This process is shown in the Figure 3.5.

$$C_{fg}(x, \Delta t) = \int_{-\infty}^{+\infty} f(x, t) \times g(x + \Delta x, t + \Delta t)\, dx \tag{3.1}$$

The calculated velocity vectors can be used to create instantaneous velocity field visualizations, which represent how fluid moves through the illuminated plane. This can include streamlines, velocity contour plots, and other visualizations.

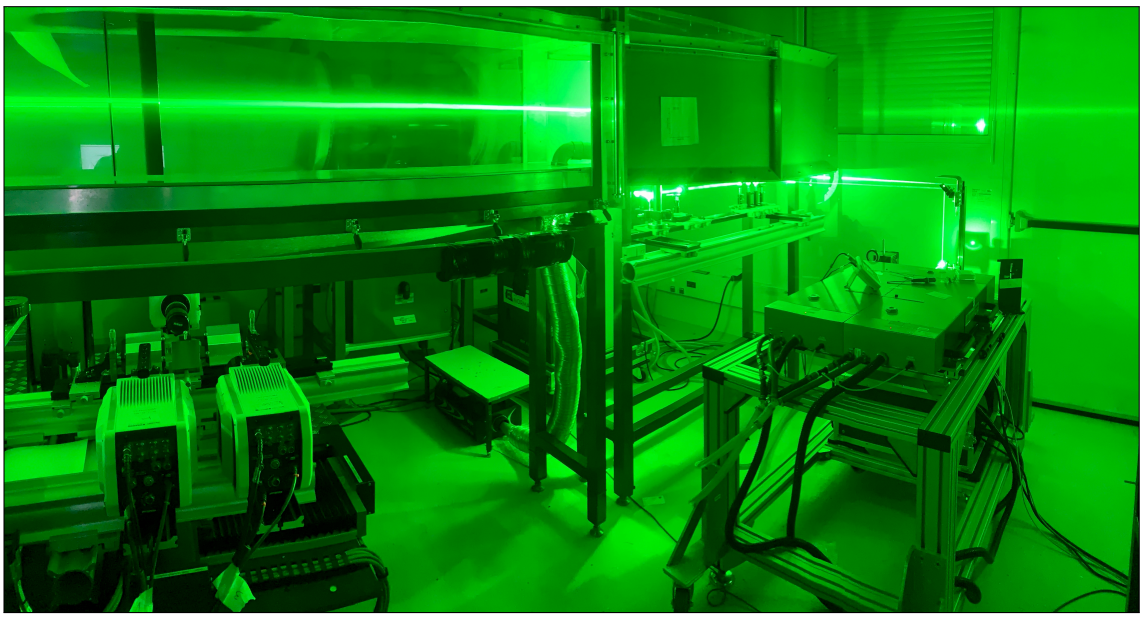

Figure 3.6: Experimental set-up.

3.2.2 Experimental obstacles and configurations.

This study considers several obstacles placed within the wind tunnel to visualize airflow patterns over and around these obstacles. Specifically, the selected obstacles closely resemble those encountered in wind farms, including cylindrical shapes and airfoils of wind turbines which are alike to wind turbine towers, respectively. The employed cylinder has a 10 *mm* diameter with 40 *cm* long (width of test section). The used airfoils are NACA 0015 profile with 40 *cm* long and 5 *cm* chord length. Figure 3.7a shows the obstacles, which include both the cylinder and the airfoil. Obstacles been accurately drilled at one end, allowing them to be firmly fixed to the customized plate located on the roof of the test section. At the opposite end of these obstacles, a small rubber piece is pasted to provide a smooth surface, allowing the obstacles to rest gently on the glass surface within the wind tunnel. This arrangement ensures that the obstacles remain securely in place without experiencing any vibrations caused by their interaction with the flowing fluid. Additionally, a protective measure has been taken by applying a matte black coating to the obstacles. This precautionary step serves to prevent any reflections of light originating

from the obstacle material. Such reflections can be dangerous to both humans and sensitive equipment.

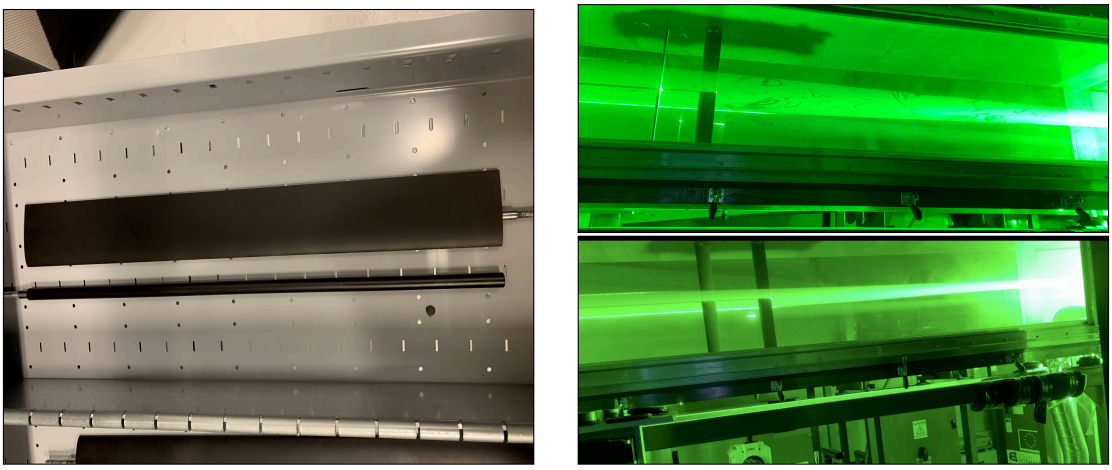

(a) (b)

Figure 3.7: (a) Employed obstacles. (b) Cylinder-Airfoil configuration (Top). Double airfoil configuration (Bottom).

Both of the obstacles are used to create five distinct configurations. These configurations are as follows:

- **Single Cylinder Configuration.**
- **Double Cylinder Configuration:** In this setup, two cylinders are positioned with a separation of 10 D (10 cm), measured from the center of one cylinder to the center of the other as shown in Figure 3.8.
- **Single Airfoil Configuration:** The airfoil is positioned with a pitch angle of 10° at the center of rotation (COR) to avoid the aerodynamic stall, see [54]. The location of the COR for the airfoil is illustrated in Figure 3.8.
- **Cylinder-Airfoil Configuration:** This configuration involves placing a cylinder and an airfoil with a 13 D separation distance (13 cm), measured from the center of the cylinder to the center of rotation (COR) of the airfoil, see Figure 3.8. The airfoil is inclined with a pitch angle of 10°.
- **Double Airfoil Configuration:** In this arrangement, two airfoils are spaced with a center-to-center separation distance of 20 cm, resulting in 15 cm between the trailing edge of upstream airfoil and the leading edge of the downstream one. The upstream airfoil is inclined with a pitch angle of $-10°$, while the downstream airfoil is set to angle 10°, see Figure 3.8. This configuration is selected to permit the leading edge of the downstream airfoil to receives the vortices created by the upstream airfoil.

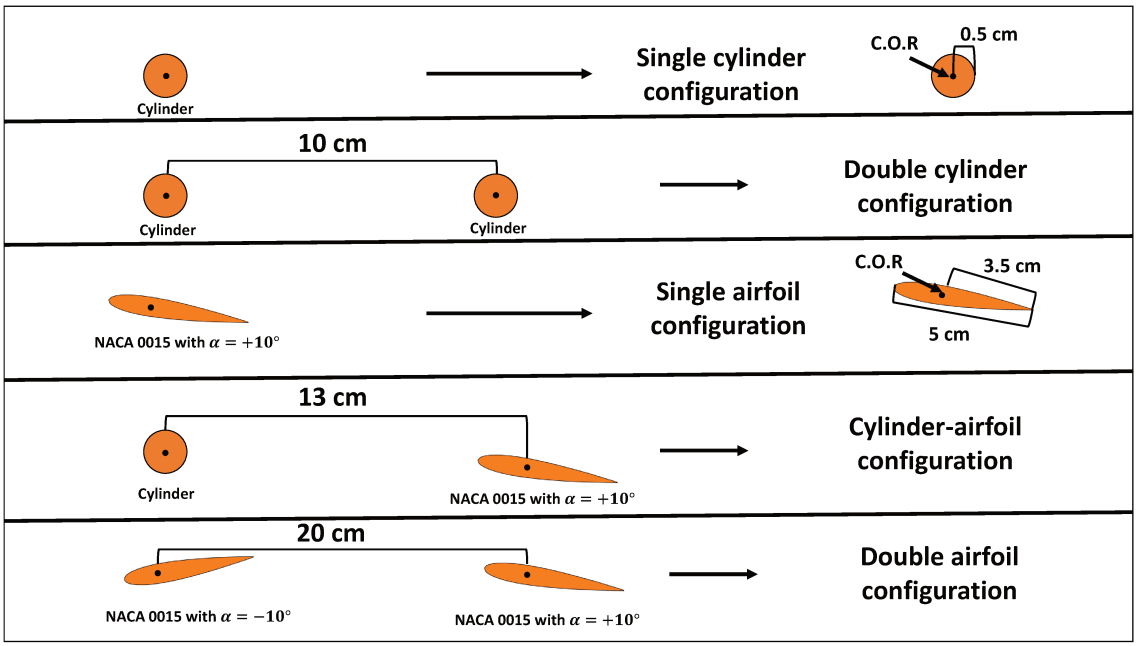

Figure 3.8: Configurations and dimensions.

3.2.3 Laser sheet and seeding particles

In this study, two components of in-plane velocity fields (2C-2D) are measured by high speed Particle Image Velocimetry (HS-PIV). The process involves the injection of particles into the fluid, which are then visualized using high-speed cameras to calculate their displacement subsequently. The particles are generated by FOGBURST 1500 smoking machine using normal smoke fluid (SMOKE5L-N). These particles are small (order of micrometers), allowing them to effectively trace the fluid's motion. A comparison of different tracers in PIV is shown by Hamdi [55]. The scattering ensures excellent visibility in the high-speed camera images, by raising the signal to noise ration (SNR). A double cavity high-speed Nd-YAG laser (532 nm) of 50 kHz maximum frequency with a power of 15 $mJ/pulse/cavity$ is used to illuminate the vast field of view. Both cavities are linked to the same trigger cable leading to the discharge of the cavities simultaneously (single frame mode). Laser sheets superposition avoid zones with different intensities at an instant image. To create the light sheet, the laser beam passes through a cylindrical lens ($f = -75$ mm), spherical lens ($f = 150$ mm), cylindrical lens (f= -50 mm), and reflective mirrors. The set of diverging and converging lenses is to enlarge the diameter of the laser beam (beam expander) for a thinner and focused laser sheet. The cylindrical lens diverges the light to illuminate the test section. Optical lenses are positioned at the downstream end, under the divergence section of the wind tunnel. This placement ensures that the area of interest for the study remains undisturbed by the optical lenses. The laser sheet is directed into the middle region of the test section using a periscope from the downstream side of the wind tunnel, see Figure 3.9. This setup provides a wide field of view for visualizing the flow behind the two obstacles. The periscope is also protected from high smoke injection (smoke particles stuck on mirror) by deviating the particles after the mirror in the tunnel, Figure 3.9b. Setting the laser sheet path from the downstream side minimizes disturbances within the interested area of the current study.

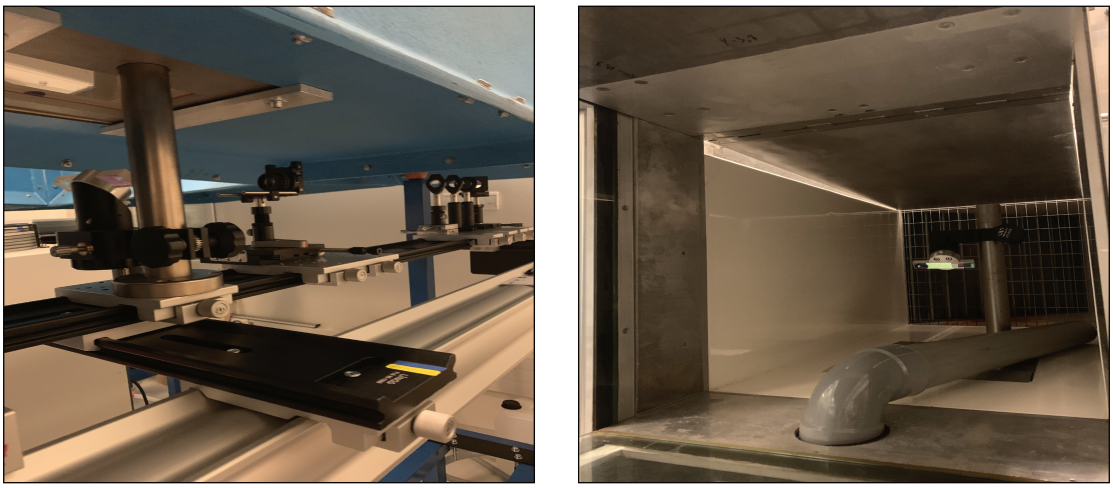

(a) (b)

Figure 3.9: Periscope fixation.

Figure 3.10 is the detailed scheme of all the equipments of the experiment setup and the light path since its departure from the cavities. This setup configuration is designed to achieve a wide field of view behind the second obstacle (region of interest).

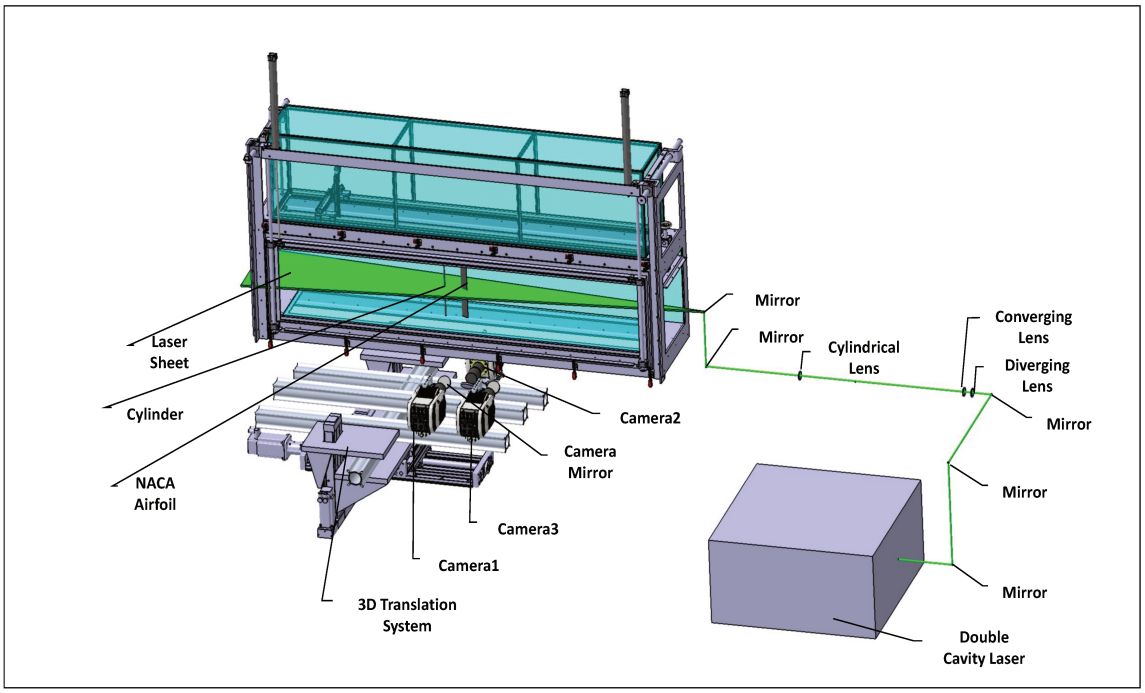

Figure 3.10: Experimental set-up.

3.2.4 Cameras and spatial calibration

Capturing the temporal development of long velocity fields downstream the obstacles leads to setting up an optical arrangement of three high-speed cameras ($f_{max} = 20\ kHz$) in a side-by-side configuration. The three cameras have a spatial resolution of 1280×800 $pixels^2$, with 12 bits depth for each pixel. The cameras are fitted with NIKKOR-ED objective lenses with a focal length of 180 mm, and each objective was equipped with

a 20 mm macro extension ring from Nikon. This combination of lenses and extensions leads to a magnification factor of 10 $pixels/mm$. Cameras and the corresponding imaging reflecting mirrors are installed under the test section to visualize the field of view from the bottom side, as shown in Figures 3.6 and 3.10. In these Figures, one can also observe the installation of cameras mounted on a 3D displacement system positioned under the test section. This displacement system have three translation axes, providing access to all positions within a volumetric region of the fluid contained in the test section. This displacement system interfaces with computer software, facilitating easy adjustments to both the translation distance and the translation velocity. This translation system exhibits high accuracy, operating with a precision level less than a millimeter.

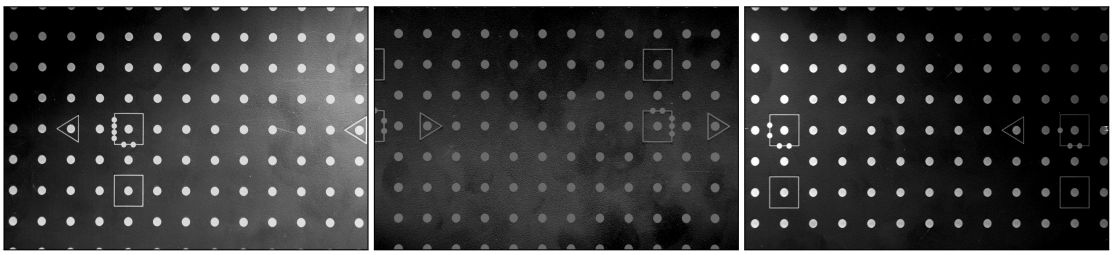

(a) camera 1. (b) camera 2. (c) camera 3.

Figure 3.11: cameras images before calibration.

The cameras are precisely calibrated using a large size grid measuring 40×20 cm^2. The calibration grid has a spacing between mesh points 1 cm. The three successive camera views before the calibration are shown in Figure 3.11. These views exhibit slight variations in their magnification factors and viewing angles. Table 3.1 provides information of the parameters associated with these camera views. Calibration allows canceling optical distortions, enabling the precise alignment and combination of the captured images. However, the side-by-side camera setup requires a view overlap between camera images to conserve continuity in the field of view. The camera views are then subjected to a merging process facilitated by the large size of the calibration grid, see Section 3.3.

Camera views parameters			
	Camera 1	Camera 2	Camera 3
Dimension x (mm)	126.2	126.4	125.2
Dimension Y (mm)	78.8	79.1	78.3
Angle (degree)	0.265	0.06	0.023

Table 3.1: Camera views parameters.

3.2.5 Alignement

The alignment of the laser is a critical and effective step of the Particle Image Velocimetry (PIV) setup. The validation of laser alignment is one of the requirements before any measurements. A visual representation of the laser alignment process is illustrated in Figure 3.12.

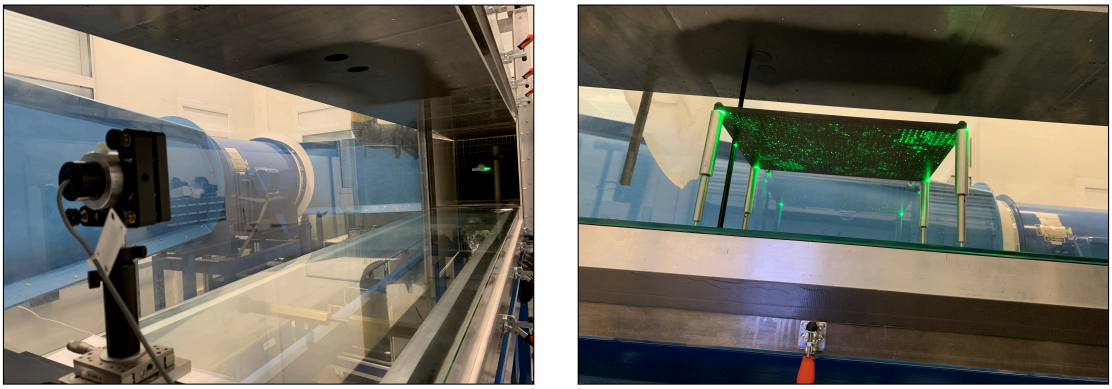

(a) Laser sheet alignement. (b) Calibration grid alignement.

Figure 3.12: Alignement of laser sheet and calibration grid.

During this step, it becomes necessary to precisely adjust the height of the laser sheet so that it aligns perfectly with the center of the test section, maintaining a fixed distance of 20 *cm* from the surface of the test section, Figure 3.12a. This alignment not only guarantees that the laser sheet is exactly at the center of the test section but also ensures that it matches in height with the calibration grid (Figure 3.12b). This alignment is of particular significance since it corresponds to the focal plane of the cameras focus (particles in focus). The three camera views of particles are shown in Figure 3.13. The laser sheet is prevented from lighting the zone between the two obstacles due to the existence of the airfoil (2nd obstacle). However, this limitation does not impede our study since our research focus is primarily on the region over and behind the second obstacle. To conclude, this alignment plays a crucial role in achieving high-quality images, leading to improved accuracy and performance in the Particle Image Velocimetry (PIV) computation.

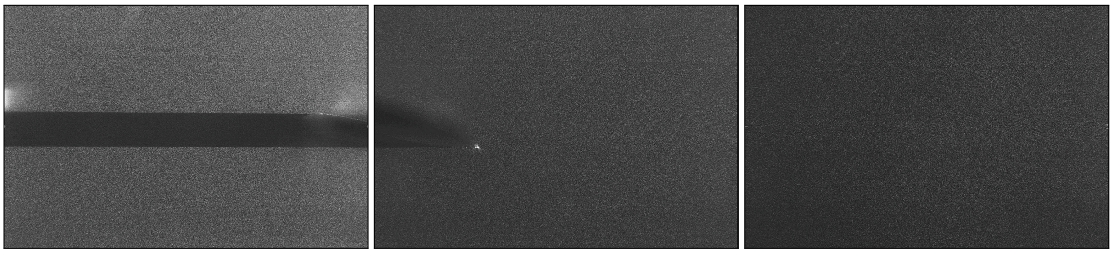

(a) camera 1. (b) camera 2. (c) camera 3.

Figure 3.13: Particle images for the three cameras.

3.2.6 Recordings and synchronization

The laser cavities are synchronized in a single-frame mode to enhance the signal-to-noise ratio (SNR) on images. Similarly, the cameras are linked through a shared trigger cable to enable simultaneous recording, as shown in Figure 3.14a. The acquisition cycles are managed using a commercial Programmable Timing Unit (PTU) from LAVISION, which is illustrated in Figure 3.14b. Images are acquired in time series mode by commercial LAVISION (Davis) software ($\Delta t = \frac{1}{f_{acq}}$).

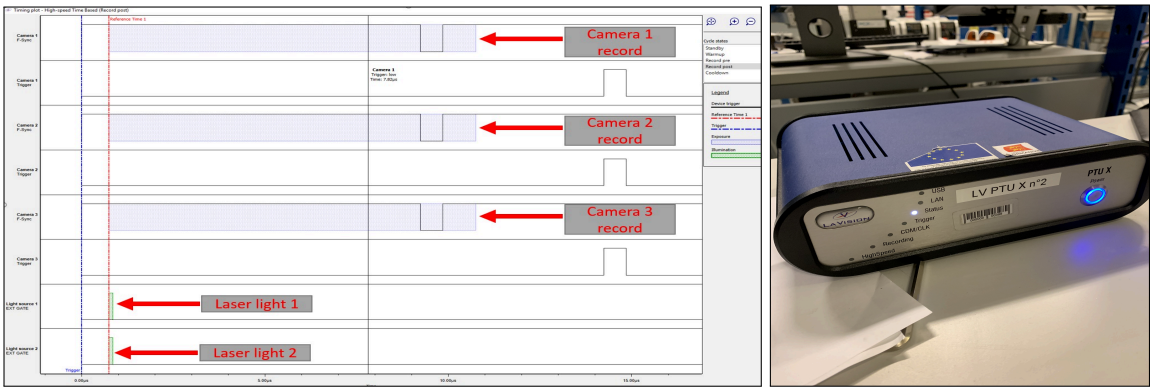

(a) Synchronization signals. (b) Programmable Timing Unit.

Figure 3.14: Recordings and triggers.

Before setting up a measurement campaign, optimisation of acquisition parameters of PIV system range is done. This optimisation maximize the velocity fluctuations range. For example, adjustments applied to the time intervals (recording frequency) between successive images to increase the velocity range of measurements. Figure 3.15 shows an instantaneous transverse fluctuation $(v - \overline{v})$ measurement at two different Δt. PIV computation for these two vectors fields are calculated by Lavision post processing tool for verification purpose. It is observed that large fluctuations are occurred at $\Delta t = 100$ for a Reynolds number (Re) of 4000. This is also demonstrated in the study of Jeon and Chatellier [56].

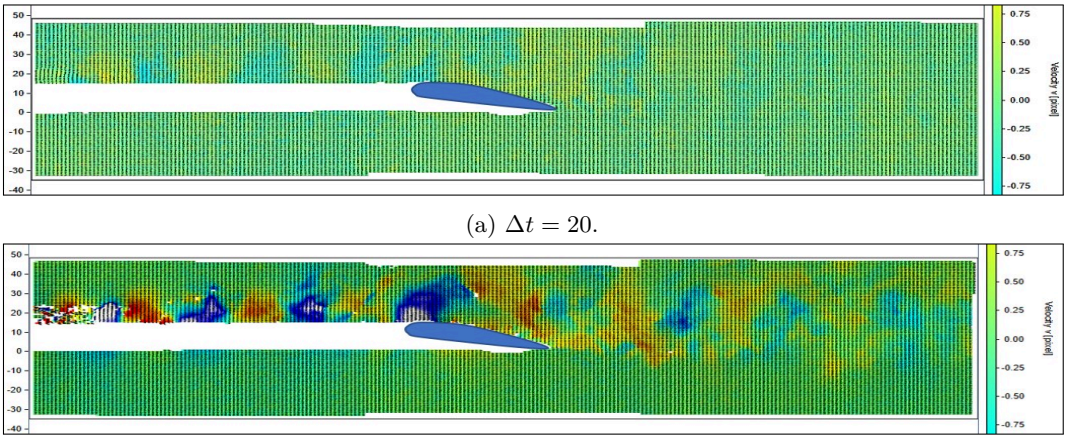

(a) $\Delta t = 20$.

(b) $\Delta t = 100$.

Figure 3.15: Velocity fluctuations comparison in different Δt.

The acquisition rate is highly dependent and influenced by the vortices mean flow velocity and the shedding frequency. For instance, Reynolds numbers based on cylinder diameter of 2000 (3 m/s), 4000 (6 m/s), and 8000 (12 m/s) are optimized to acquisition rates of 5, 10 and 20 kHz in single frame mode, (equivalent to $\Delta t = 200$ μs, 100 μs and 50 μs in double frame mode, respectively). As a result, the acquisition times for these settings are 38 s, 19 s, and 9.5 s, respectively. This adjustment leads to the capture of 190000 images, see Table 3.2. The adjustment helps also in preserving excellent image quality and high dynamical behavior of wakes far away from obstacles.

3.3 PIV post processing

This combination of the three images leads to a substantial field of view with a size of $360 \times 75\ mm^2$. Images are processed by adaptative PIV algorithm. This algorithm dynamically adjusts the size of the interrogation window based on the local flow conditions. Smaller windows are used in areas with high velocity gradients or turbulence, while larger windows are used in more uniform regions. The PIV calculation on the acquired images is entirely based on processing codes developed in CORIA laboratory [57], which are continuously improved and adapted to specific situations.
Before the PIV computation, the first step consists in recombining the view of the three cameras into a single image. Spatial calibration of each camera is performed from the recording of a point pattern grid covering the entire field of view. The camera models are based on third-order 2D polynomial functions to compensate any view tilt and image distortion. Concerning the image reconstruction, PIV interpolation scheme with image deformation are used, proven to be compatible with sub-pixel techniques for the velocity measurements [58].

An illustration of the image reconstruction processing of the calibration grid is shown in Figure 3.16. The three camera field of views are marked with rectangles of different colors. The rectangles show the image overlaps of the common areas (around 1 cm) to ensure the continuity of the velocity field measurement. During the image reconstruction, constant offset of 120 $pixel/cm$ is imposed in both directions, which leads to a slight magnification of the initial image resolution. The PIV processing starts with a background correction of images using an averaged image computed over each time sequence. In the present work, the PIV algorithm with image deformation has been retained to improve spatial resolution and maintaining a reasonable computing time.

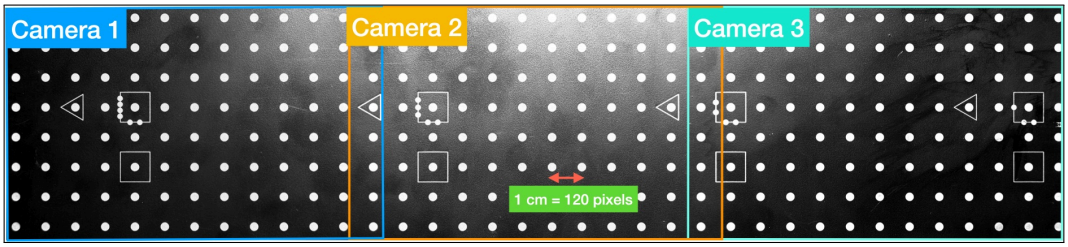

Figure 3.16: Reconstruction of a complete image from the three camera views of the calibration grid - Final image size: $4256 \times 934\ pixels^2$ - Imposed image resolution: 12 $pixels/mm$.

The initial interrogation window size is fixed to $32 \times 32\ pixels^2$ ($2.66 \times 2.66\ mm^2$) and is progressively reduced to $16 \times 16\ pixels^2$ ($1.33 \times 1.33\ mm^2$) with 50% of overlap during the deformation process. The final size of the vector grid is 529×113 nodes. Intermediate velocity fields during the process are calculated using a continuous window shift approach, see [57]. It offers high accuracy with a low addition computational cost compared to the classical PIV algorithm. This enables rapid convergence of the deformation process. The number of iterative steps for the deformation is dynamically adapted from the flow properties of intermediate predictors. On average, it is equal to 3. The PIV algorithm uses a masking technique for areas not to be calculated, avoiding some issues on image edges and the boundaries of areas without particles (e.g., obstacle, shadow zone upstream of the second obstacle). All the velocity fields are scaled and validated with a final validation rate higher than 98%. The computation time for a whole time sequence of 190,000 images ($38s$ at 5 KHz) is around four days on a recent bi-processor Linux cluster with 96 cores.

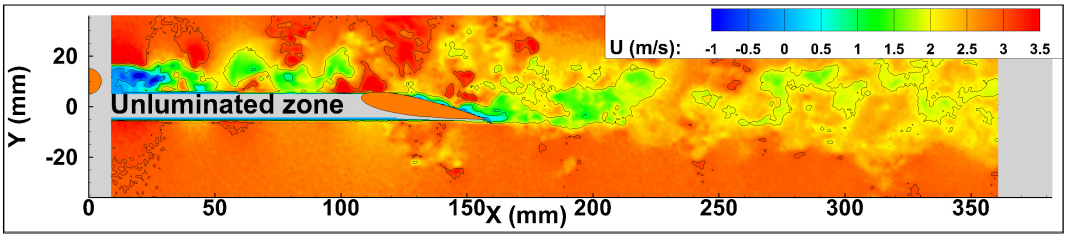

(a) Velocity field in streamwise direction (X direction).

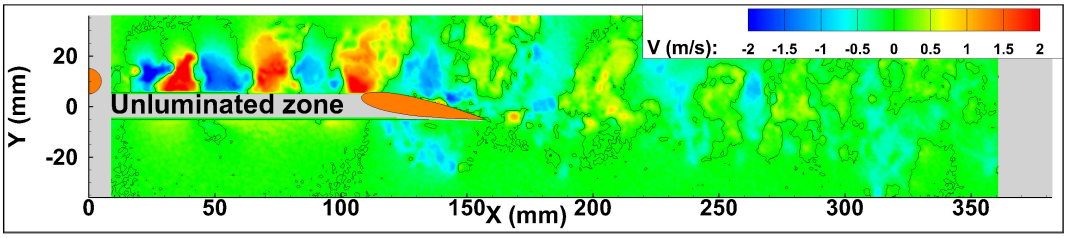

(b) Velocity field in spanwise direction (Y direction).

Figure 3.17: Instantaneous velocity fields in both directions.

3.4 Overview of experimental parameters

Within the context of our study, Table 3.2 provides a comprehensive overview of the experimental parameters. Table 3.2 offers insights into the configurations of both the cylinder and the airfoil. The table includes the calculation of shedding vortex frequencies based on Equation 3.2, see Chang's work on symmetric airfoils [59]. In Equation 3.2, (St) is the Strouhal number, (u) is the inlet velocity, (f) is the shedding frequency, (c) is the chord length of the airfoil , and α is the pitch angle. The pitch angle (α) is set at 10 degrees to ensure a sinusoidal motion pattern behind the airfoil. It is worth showing that $csin(\alpha)$ can be interpreted as the vertical distance blocked by the airfoil, which is equivalent to the cylinder's diameter in the previous case. Furthermore, Ausoni's comprehensive numerical and experimental analysis [60] underscores the constancy of the Strouhal number and the linear increase in vortex shedding frequency with respect to Reynolds numbers. These findings are further agreed by Jian's research [61]. Therefore, one can reliably estimate the phenomenon of vortex shedding in the wake of an airfoil, Table. 3.2. The Strouhal number of the airfoil case is calculated as follows,

$$St = \frac{fcsin\alpha}{u} \tag{3.2}$$

Experiment parameters								
x	Re_d	St	Shedding freq.(Hz)	No. periods	Acquisition freq.(Hz)	$\Delta t(\mu s)$	Acquisition time(s)	No. images
Single cylinder	2000	0.2	60	2280	5000	200	38	190K
	4000	0.2	120	2280	10000	100	19	
	8000	0.2	240	2280	20000	50	9.5	
x	Re_c	St	Shedding freq.(Hz)	No. periods	Acquisition freq.(Hz)	$\Delta t(\mu s)$	Acquisition time(s)	No. images
Single airfoil	10000	0.21	72.5	2755	5000	200	38	190K
	20000	0.21	145	2755	10000	100	19	
	40000	0.21	290	2755	20000	50	9.5	

Table 3.2: Experiment setup parameters.

Finally, each acquisition run of 190,000 images has a size of 825 gigabytes (GB) stored in CORIA server. This cumulates to a substantial 12.5 terabytes (TB) of stored data for all five configurations and three Reynolds numbers. These data are duplicated in second series of data leading to 25 terabytes (TB) for further statistical studies (future research). However, in this research study only one serie of data is taken into consideration to minimize computation time.

CHAPTER 4

Wake phase decomposition: Methodologies

Summary

The far aim of the project is to experimentally assess the dynamical behavior of the flow around a downstream obstacle (cylinder or blade), as a function of the upstream flow. The wake behind the upstream obstacle is composed of coherent structures and random structures. Coherent structures are known with their periodicity and repetitive events. Therefore, they can be broken down into multiple phases using various techniques such as Proper Orthogonal Decomposition (POD) or vortex identification. Phases decompositions will help to better understand the downstream flow (over and behind the second obstacle) in function of upstream flow (behind first obstacle). In this chapter, two methodologies to decompose the phases of coherent structures within upstream wake are presented. This decomposition of phases is a necessary step for far aim study, as it helps in separating coherent and random structures in wake flows. These methodologies of phase decomposition including an experimental approach and extending to an a posteriori perspective. Evaluations of decomposition methods are presented by statistics and coherent structures detection. The method with better reliability and precision will be further employed for the study analyses.

Contents

4.1 Introduction **56**
4.2 Phase decomposition by "pressure sensor" **56**
4.2.1 Implementation of methodology and setup 57
4.2.2 Synchronization of microphone 58
4.2.3 Evaluation of phase decomposition by statistics 60
4.3 Phase decomposition by "a posteriori" **64**
4.3.1 Implementation of methodology 64
4.3.2 Evaluation of phase decomposition by statistics 67
4.4 Detection of coherent motion (CM) **71**

4.4.1 Detection using “pressure sensor” method 72
4.4.2 Detection using “a posteriori” method 73
4.5 Conclusion **76**

4.1 Introduction

Wake flows have been widely studied over the past decades in various fields of research, i.e. flow behind a vertical structure, behind an airplane blade or behind a boat. Whenever the fluid flow faced an obstacle, the resulting disturbed flow downstream is referred to as a shear flow as shown in studies of Drazin [62], Cantwell [63], or Landahl [64]. The term ” shear flows ” is used to describe the alternating flow pattern that arises due to the interaction between the fluid and the obstacle. Numerous studies, including Batchelor [65], Herman [66], or Tritton [67], have analyzed shear flows, contributing to a deeper understanding of fluid dynamics in the presence of obstacles. As discussed previously, wakes exhibit a coherent structure family (large vortices) as in the single cylinder wake referred to as Williamson [68] study, or several families as in the rotor wake (wind), as shown Valery [69] or Medici [51]. Coherent structures behind a cylinder exhibits a sinusoidal motion. These structures are in function with Reynolds number, high Reynolds increase the frequency of detaching these large structures. The presence of almost periodic flow patterns, attributed to the Von Kármán vortices, provides an opportunity to establish the concept of phases. The periodic movement reminds us of the street of Bénard-Von Kármán. The latter is very substantial for the obstacle dynamics and the fluid, or the interaction between the two. In this context, Bénard-Von Kármán street can increase fatigue, reduce life time for structures and reduce energy production for wind turbines located behind each other (i.e wind farms). This is why the study of Von Kàrmàn’s street (coherent structures) behind an obstacle are currently taken into account in aerodynamic structure designs. Coherent structures have a frequency which is related to the Strouhal Equation ($St = fD/U$), where f is the frequency of large vortices, D the characteristic length and U is the velocity in the direction of the flow. This chapter is based on the sinusoidal flow (coherent motion) decomposition behind an obstacle into different phases. Therefore, two approaches for decomposing the phases of an upstream wake are presented: the "a priori" (pressure sensor) perspective and the "a posteriori" perspective.

4.2 Phase decomposition by “pressure sensor”

Phase decomposition of experimental flow by pressure sensor allows to reduce the quantity of measurement data. This is achieved by enabling a direct focus on the specific phase of coherent structures that require measurement. To simplify, the recorded data without pressure sensor are usually filtered by different mathematical methods (POD, vortex identification. . .), and this required huge data recordings to ensure statistic convergence. Thus, this approach decomposes the experimental flow phases without resorting to these mathematical methods. Therefore, an approach for better statistical description of the vortex shedding produced by a cylinder is proposed. However, carrying out direct phase decomposition in the experiment presents a challenging task. It is very sensitive and demands extensive efforts and validations, given that all measurements will be based on the accuracy of this step. In this section, execution and validation of the technique are presented.

4.2.1 Implementation of methodology and setup

The measurements are carried out in the wind tunnel described in Chapter 3 before the displacement to the new experimental room. In these measurements, the technique used for data acquisition is a 2D-2C low speed Particle Image Velocimetry (PIV). JAI camera (RM/TM-4200CL) with a resolution of 2048×2048 $pixels^2$ (12 bits), running at 8 fps (fps: frame per second) is used for data acquisition. An Nd:YAG laser (532 nm) illuminates a 10.4×10.4 $cm2$ field of view. Its maximum frequency is 10 Hz. The laser beam passes through an expander beam, spherical lens ($f = 1000$ mm), cylindrical lens ($f = -100$ mm) and a mirror, see Figure 4.1. The focus laser sheet is 0.5 mm thick. The time between pulses is set to 20 μs. The PIV post-processing is performed using an in house code. The interrogation window size is 32×32 $pixels^2$ (1.6×1.6 $mm2$). The overlap is set to 50%, producing a vector field of 127×127.

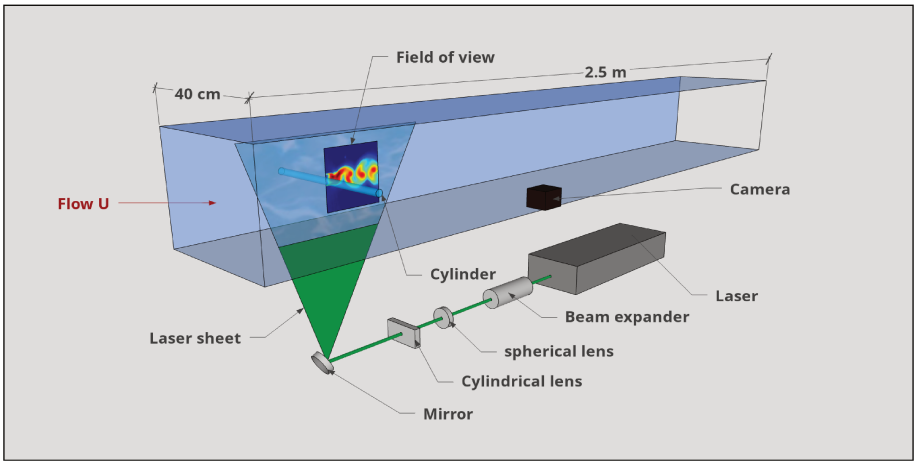

Figure 4.1: Schematic of experimental setup.

Vortices detection is performed by placing a microphone sensor (Mark: Brüel & Kjaer, Type: 4182, Sensitivity: $3,65$ mv/Pa and Sampling rate : 20 kHz), after the cylinder to estimate the dynamical pressure of the flow. The microphone sensor is shown in Figure 4.2a is connected to a flexible tube (1 mm) inserted in a 3 mm steel tube (probe in the flow), as illustrated in Figure 4.2b.

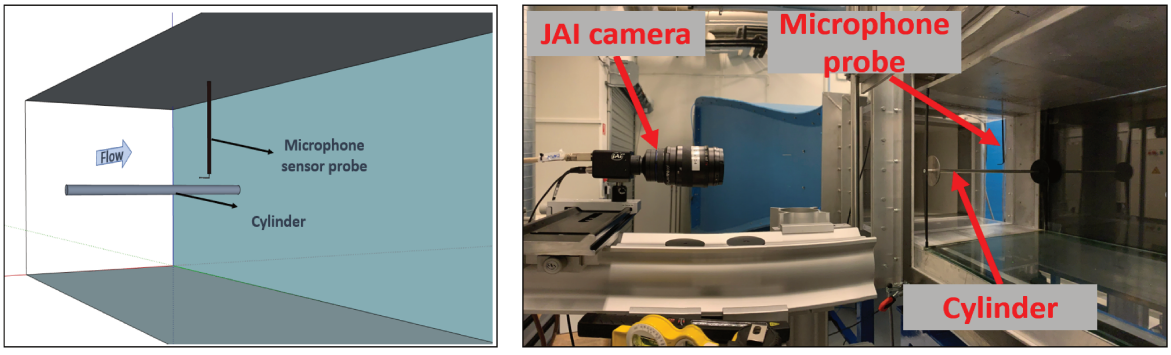

(a) (b)

Figure 4.2: Microphone sensor probe position. (a) Schematic view. (b) Realistic view.

Figure 4.4a shows the positioning and orientation of the microphone probe relative to the main flow. The microphone's position is precisely fixed after the cylinder recirculation zone ($X/D = 3.5, Y/D = 2$), see Figure 4.4b. This precise placement of the microphone probe is optimized to enhance the dynamic of the recorded signals. The microphone is set far from the measurements plane (along a direction normal to that plane) to minimize possible influence on the flow.

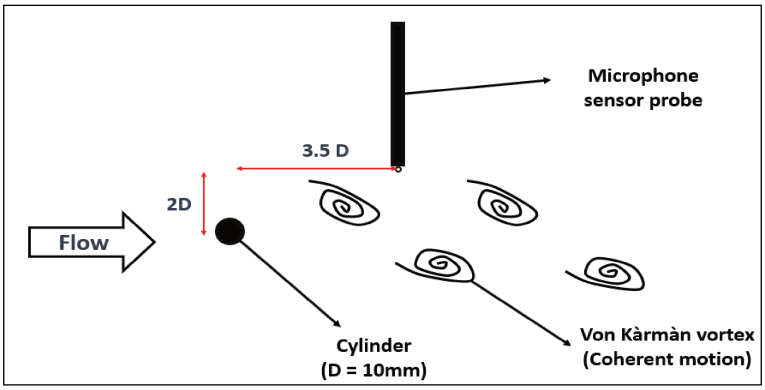

Figure 4.3: Microphone sensor probe position in real dimensions.

Images acquisition is done using Dantec software to verify the phase decomposition effectiveness. Data acquisition is synchronized with vortex generation (detected by the microphone sensor behind the cylinder). Non-synchronized data are also recorded, as a reference case. Three different Reynolds numbers are set. Table 4.1 gives the experimental characteristics of the recorded data. Nine phase shifts are set for synchronized data acquisition, see Table 4.2.

Non-synchronized Data					
Re_d	St	Shedding freq. (Hz)	No. phases	Time shift (ms)	Couple of images
2000	0.2	60	no phases	no time shift	10000
4000	0.2	120	no phases	no time shift	10000
8000	0.2	240	no phases	no time shift	10000

Table 4.1: Parameters of non-synchronized data.

Synchronized Data					
Re_d	St	Shedding freq. (Hz)	No. phases	Time shift (ms)	Couple of images
2000	0.2	60	9 phase shifts	each 4 ms	5000
4000	0.2	120	9 phase shifts	each 2 ms	5000
8000	0.2	240	9 phase shifts	each 1ms	5000

Table 4.2: Parameters of synchronized data.

4.2.2 Synchronization of microphone

Synchronizing data acquisition with vortex generation first requires a clear detection of the vortices, and their dynamics, just behind the cylinder. The microphone signal only

triggers the data acquisition at the maximum pressure level. The pressure level in the flow is weak while in the frame of the acceptable range of the microphone sensibility. The pressure signal obtained from the microphone is quasi-periodic, thus indicating all phases of vortex generation. The signal obtained is very sensitive to the position and orientation of the microphone relative to the cylinder. The position should be closer to the cylinder and after the recirculation zone. Many tests had performed to find the right position of the microphone in the wake. The position is chosen after performing Fast Fourier Transform (FFT) in a matrix of positions. Then the position with higher peak for the corresponding frequency and lower noise is chosen. The orientation must be perpendicular to the main flow direction. Where the transverse fluctuations are important, inducing the rolling process of large vortices, referred to as Thiesset [70] study. Data acquisitions were performed for particular phases of coherent motion (CM), using trigger systems as shown in Figure 4.4. In detail, the analog quasi-periodic signal that comes from the microphone enters several electronic devices. The first signal is filtered in two stages, high pass filter and low pass filter at the frequency corresponds to Von-Kármán's street. This frequency is calculated by the Strouhal Equation ($St = fD/U$) for corresponding speed in the wind tunnel. The filtered signal is turned into digital signal by an analog-digital converter box. The converted signal enters authorization zone to manage the data acquisition: If the signal overlaps with the synchronization signal, an acquisition signal of PIV at one particular phase of shedding vortices is created (camera recording). In the other hand, if the signal does not overlap, it loops the laser without an acquisition signal (without camera recording). The overlap between the pressure signal of the microphone and a synchronization signal defines the reference phase (phase = 0). Knowing the inlet velocity U, Strouhal number St, and the cylinder diameter D, the period is calculated using the Strouhal relation ($T = D/StU$). The period is verified and measured using experimental data. Finally, owing to the reference phase and the period, other phases can be acquired by delaying the acquisition time (time shifts), which variates with the frequency of the shedding vortices. The procedure of synchronizing data with microphone sensor using trigger systems is illustrated in Figure 4.5.

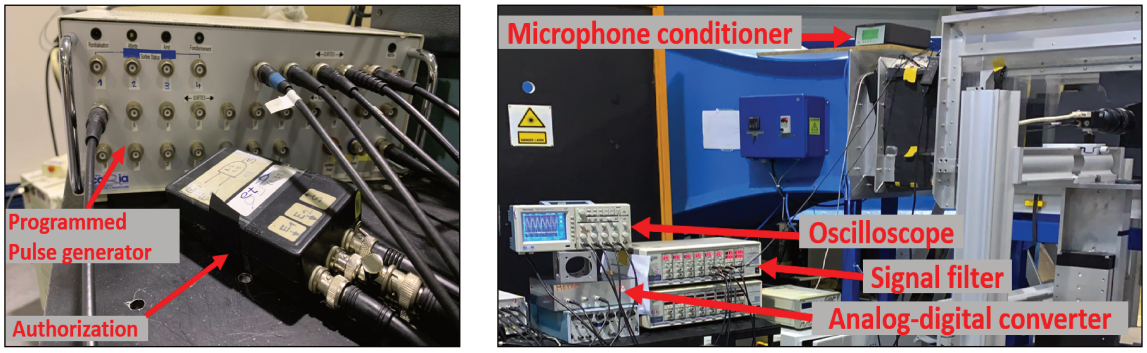

(a) (b)

Figure 4.4: (a) Programmed pulse generator and authorization. (b) Filtering signal and conversion.

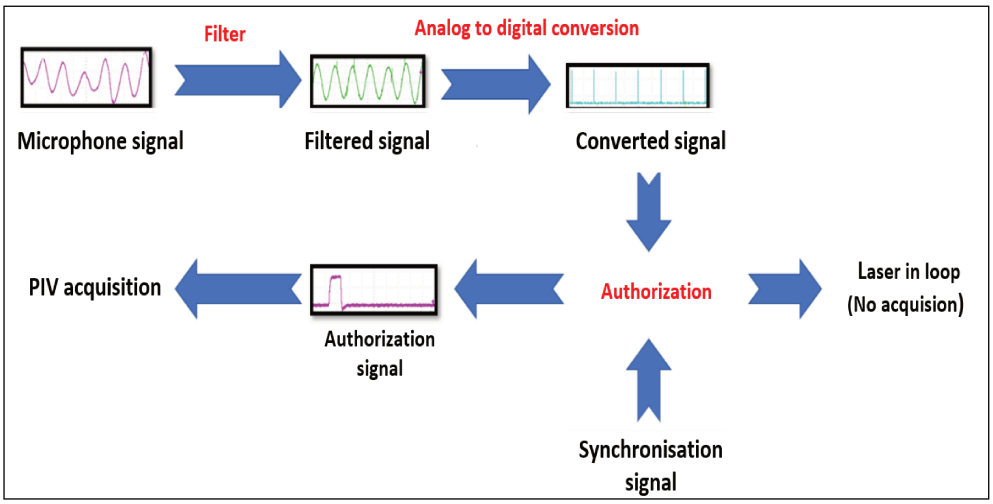

Figure 4.5: Synchronization.

A small phase shift (1 ms) is remarked between raw (Non filtered microphone signal) and filtered microphone signal, as shown in Figure 4.6. The phase shift is due to the electronics within the filter box. However, this phase shift remains constant for a given Reynolds number.

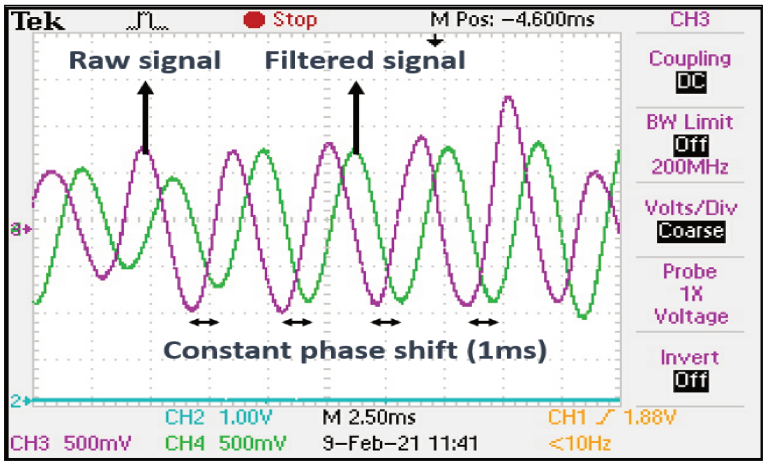

Figure 4.6: Phase shift between raw and filtered signal at $Re = 8000$.

4.2.3 Evaluation of phase decomposition by statistics

The first validation of our phase lock PIV recording approach is based on the streamwise profile analysis. The profiles are studied at the center of the cylinder, i.e. at the center of the wake. Figure 4.7 shows the profile of the average velocity U (velocity in the direction of the flow) for two different Reynolds numbers, and for four different phases. One can obviously see the oscillation of the phased (synchronized) data, which does not exist in the non-phased (non-synchronized) data. These oscillations appeared due to the constancy of the spatial position of the vortices (each acquisition set up when the vortices are at the same spatial position, for one phase). The amplitudes of the fluctuation increase with increasing speed. Figures 4.7 and 4.8 show the profile of the average velocity U (velocity in flow direction) and V (velocity in the transverse direction). These figures are shown for two Reynolds numbers and for four different phases. In Figure 4.8, one can clearly

see the precision of the sensor (microphone) at each phase. For example, at $\Phi = 0°$ and at $\Phi = 180°$, the data are opposed (also $\Phi = 90°$ with $\Phi = 270°$). This observation is supported by the data shown in Figure 4.8, where the mean velocity in the transverse direction (based on non-synchronized data) are found to be zero. In contrast, Figure 4.7 indicates that the speed averages (based on non-synchronized data) are relatively large.

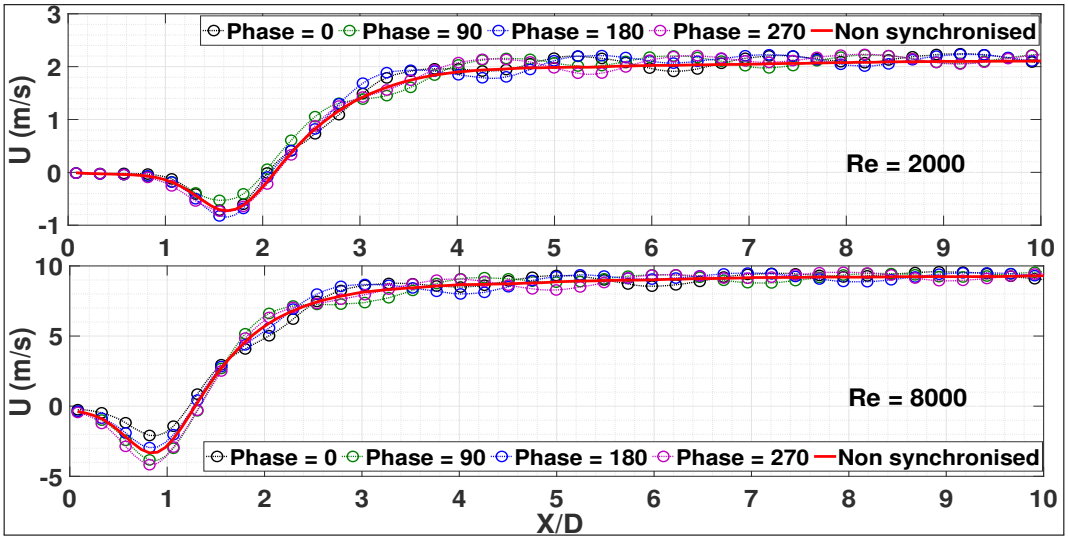

Figure 4.7: Profiles of streamwise velocity (X-direction) at two Reynolds numbers ($Re = 2000$ and $Re = 8000$).

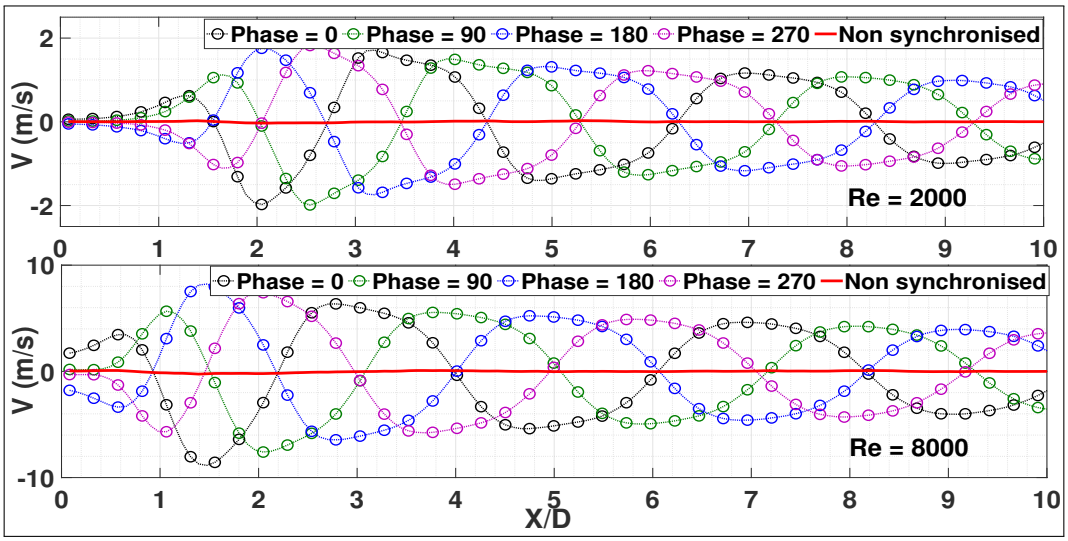

Figure 4.8: Profiles of spanwise velocity (Y-direction) at two Reynolds numbers ($Re = 2000$ and $Re = 8000$).

The nearly periodic nature of the flow, due to the Von Kármán vortices, allows for the concept of phase to be defined. Von Kàrmàn vortices are well structured and organized. The basis of our technique, correctly evaluated from the organization of the vortices. Phase-averaged statistics (i.e., computed for each phase of the CM) may thus be appraised. The quality of phase decomposition must also be checked on lower-order statistics, such as the mean of the velocity field and Root Mean Squared. Figures 4.9 (a) and 4.9 (d)

show the mean velocity and the RMS (Root-Mean-Squared) of the streamwise velocity component ($Re = 2000$) over 10000 images, with no distinction among phases (without microphone synchronization). In that case, the coherent structures of the wake disappears completely following the random positioning in the acquisition cycle. Figures 4.9 (b), 4.9 (e) and Figures 4.9 (c) and 4.9 (f) represent the mean velocity ($Re = 2000$) and the RMS at $\Phi = 0°$ and $\Phi = 180°$ over 5000 images, respectively. Figures 4.9 (e) and 4.9 (f) reveal the vortex street in the wake, by figuring out the fluctuations at a particular phase of acquisitions. RMS is maximum in regions where shear is most important and gradually decreases downstream behind the obstacle. The spatial distribution of the Vortex-street patterns at $\Phi = 0°$, is typically opposed to that at $\Phi = 180°$. This emphasizes the precision of the microphone synchronization in the Particles Image Velocimetry (PIV) measurements system.

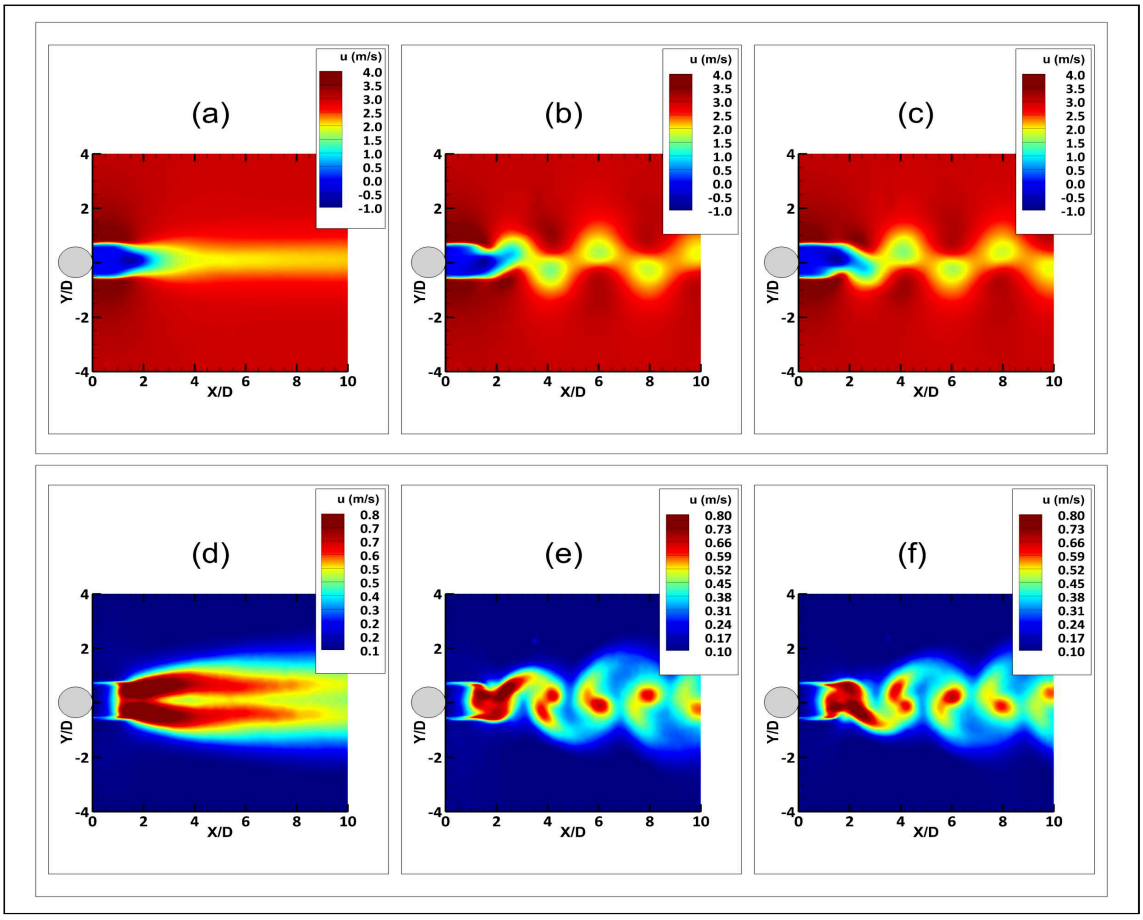

Figure 4.9: (a) and (d) are the non synchronized mean velocity and RMS along x direction, respectively. (b) and (e) are the synchronized mean velocity and RMS along X direction at $\Phi = 0°$, respectively. (c) and (f) are the synchronized mean velocity and RMS along X direction at $\Phi = 180°$, respectively.

Phase decomposition by pressure sensor is effective not only for low velocities but also for high velocities. Figures 4.10 (b), (e)) and Figures 4.10 (c), (f) represent the average velocity and RMS for Reynolds, $Re = 4000$ and $Re = 8000$ respectively. The increase in velocity keeps the same position and numbers of the vortices (temporal changes). More speed reveals more small vortices (more blurry region) on the large vortex (Von Kàrmàn vortex). Increasing of small vortices is explained by the increase in transport by diffusion,

as shown by Armaly [71].

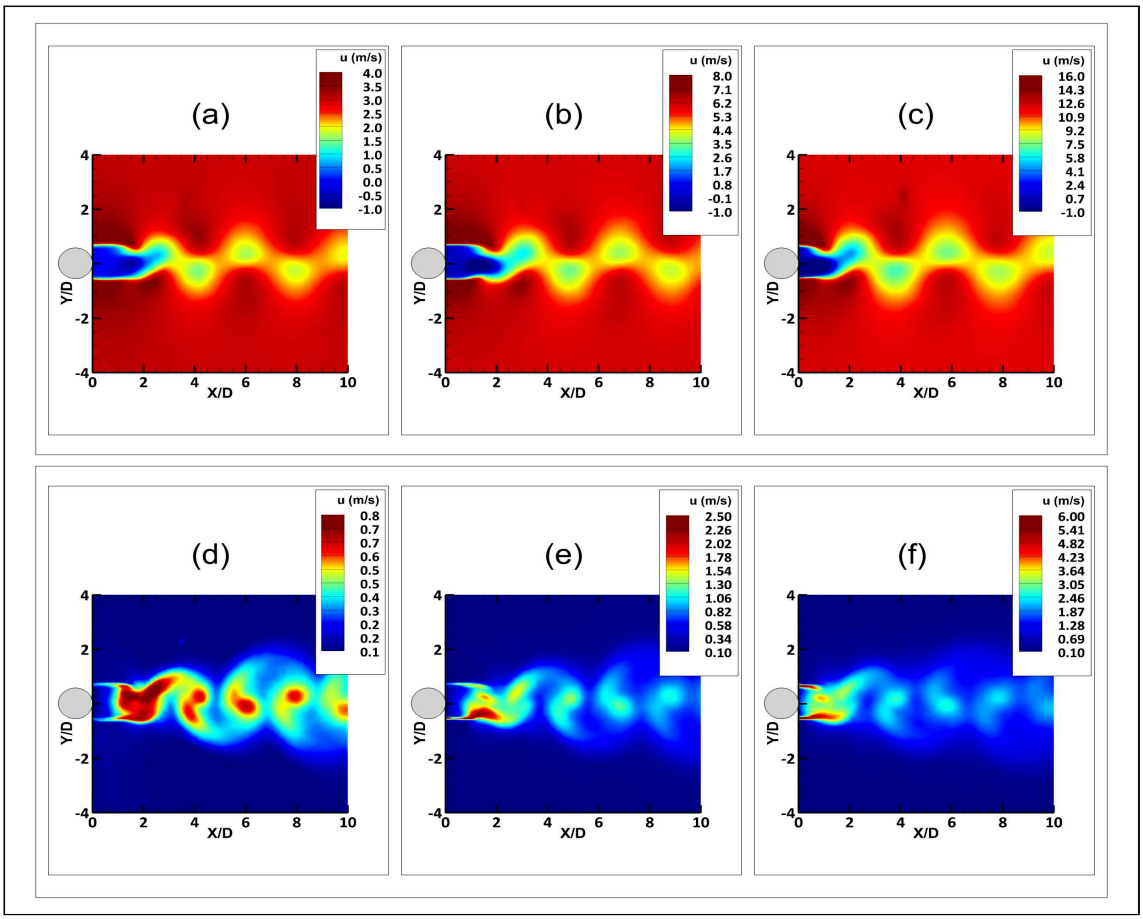

Figure 4.10: (a), (d) are the synchronized mean velocity and RMS along X direction, respectively ($Re = 2000$). (b), (e) are the synchronized mean velocity and RMS along X direction, respectively ($Re = 4000$). (c) and (f) are the synchronized mean velocity and RMS along X direction, respectively ($Re = 8000$). All the statistics in this Figure are for $\Phi = 0°$.

The first validation of first order statistics provides us with significant insight into an experimental phase averaging technique. This provides a complementary and detailed analysis of the upstream flow based on the analysis of its periodicity. This makes it possible to visualize the distribution of kinetic energy at each phase of the evolution of coherent motion and thus obtain the spectral distributions of kinetic energy and pressure, as in Thiesset [72], Danaila [73] and Djeridi [74]. This conditioning of the upstream flow helps us to evaluate the behavior of the structure on the downstream obstacle with respect to each phase. This type of analysis requires experimental developments (aforementioned previously) in order to be applied to such complex cases. To conclude this section, the approach with pressure sensor works for cylinder wake and not for airfoil wake. This limitation can be attributed to the presence of low-pressure oscillations in the wake of an airfoil.

4.3 Phase decomposition by "a posteriori"

Concerning the phase decomposition, the first solution tested was to place a high-sensitivity microphone fitted with a capillary tube in the wake of the first obstacle as shown previously and by Armaly [71]. By analog processing of the pressure signal, the value of phase analysis was possible, and all the advantages over a simple statistical approach have been demonstrated. However, the microphone approach has several drawbacks:

- Despite the microphone probe being very small and shifted some millimeters from the measurement plane, it is still affecting the wake.
- The microphone position is fixed until the PIV images are recorded. As further simplification, phase-lock analysis can be exclusively based on the structures generated by the first obstacle, otherwise microphone position should be changed
- The use of microphone is critical in the airfoil case, as the pressure variations were smaller than the cylinder, so phase detection presented a significant uncertainty.

4.3.1 Implementation of methodology

Following the previous remarks, a phase detection approach directly from the velocity fields has been developed, see Armaly [75]. The approach is used for low and high speed Particle Images Velocimetry (PIV). The comprehensive details of this experimental setup is outlined in chapter 3.

In this processing approach, to determine the phase of instantaneous velocity fields required two main elements: the first is the reference phase-average velocity field and the second is the spatial period of coherent structures.
The processes involving how to acquire these two principal elements are shown below:

- Firstly, a reference phase average velocity field (1st principal element) is determined. An instantaneous velocity field is selected from the data set (see Figures 4.11a and 4.12a for cylinder and airfoil cases, respectively). This instantaneous velocity field is considered to be representative of an arbitrary reference phase velocity field. Therefore, each iterated instantaneous field in the data set is correlated with the base velocity field (chosen instantaneous field), limiting the calculation to the area where the CM are most intense, as shown in Figures 4.11 and 4.12 (red frame). When the normalized correlation coefficient between the two fields reaches a maximum, the two velocity fields are considered to have sufficient similarities leading to one identical phase. The average velocity field involves then all instantaneous vector fields with one identical phase. Note that, only transverse velocity component v is used in the correlation calculation.
  Over 190,000 velocity fields of one-time series, nearly 9,000 to 11,000, are identified to be related to the same phase. The average of all the velocity fields provides the reference velocity field for the case of the cylinder and the airfoil (Figures 4.11b and 4.12b, respectively). The two reference fields also show that the coherent structures, far downstream of the obstacle are observable. Remarking that the velocity fluctuations are minimal, indicating good coherent structure detection. An alternative method for calculating the reference phase-averaged velocity involves employing Proper Orthogonal Decomposition (POD) to filter an instantaneous velocity field, as demonstrated by Foucaut et al. [76].

- Secondly, the spatial period (2nd principal element) of coherent structures within the reference phase average field is obtained. This is done by 1D auto-correlation of the spanwise velocity component v. The correlation lag is in streamwise direction or in the plane of symmetry of the obstacle ($y = 0\ mm$). The oscillation period of the auto-correlation signal allows us to determine the average spatial distance between vortices with high precision. For instance, values of spatial period are obtained: 40.75 mm and 34.86 mm for cylinder and airfoil wakes, respectively. This is illustrated in Figures 4.11 and 4.12 for both wakes, respectively. Note that the spatial periods are corresponding to phase 360° of coherent motion. Once these steps are completed, the reference field can be used to determine the phase of the coherent structure of the instantaneous velocity fields.

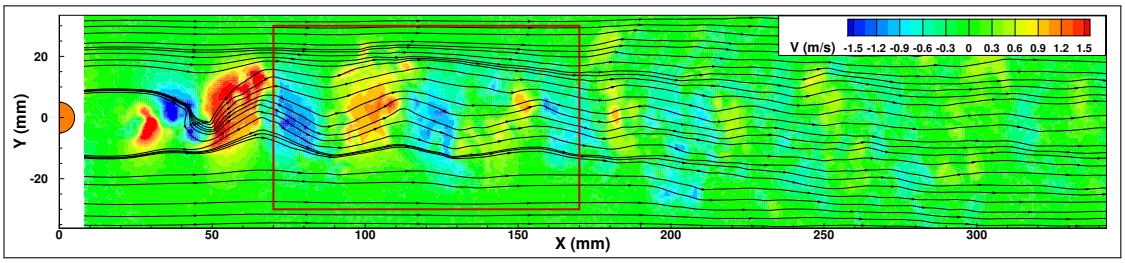

(a) Instantaneous velocity field in a cylinder wake.

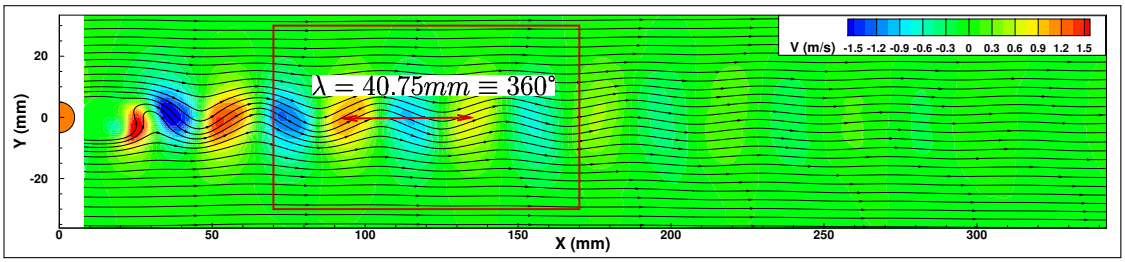

(b) Reference phase average velocity field of cylinder wake.

Figure 4.11: Cross-correlation zone (red frame) between the instantaneous velocity field in a cylinder wake (top) and the reference phase average velocity field in a cylinder wake (bottom) at $Re = 2000$

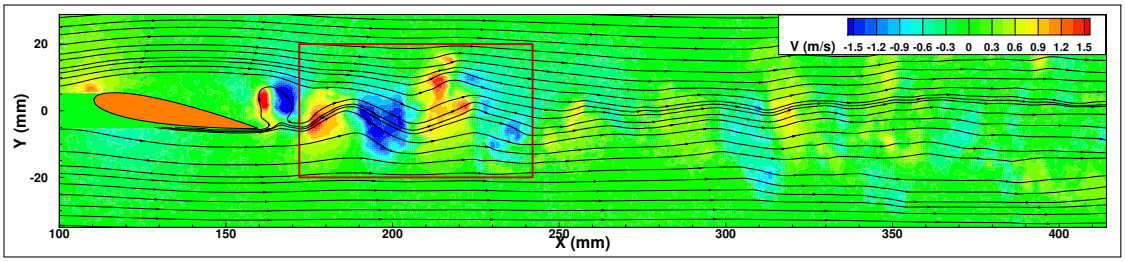

(a) Instantaneous velocity field in a an airfoil wake.

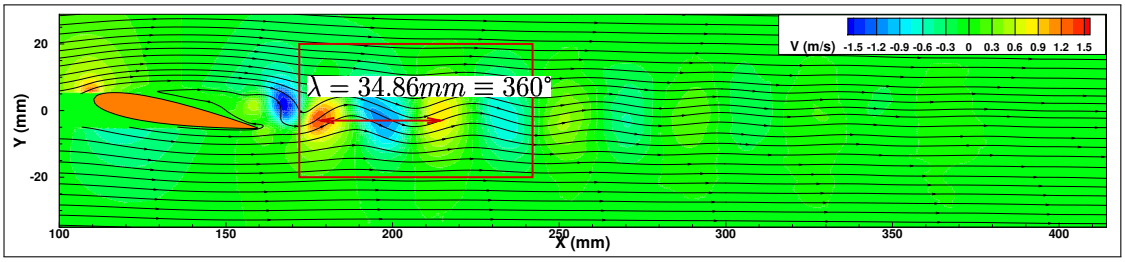

(b) Reference phase average velocity field of airfoil wake.

Figure 4.12: Cross-correlation zone (red frame) between the instantaneous velocity field in an airfoil wake (top) and the reference phase average velocity field in an airfoil wake (bottom) at $Re = 2000$

Finally, to detect the phase of structures on an instantaneous velocity field, a normalized cross correlation with the reference phase average velocity field is performed. The correlation is performed in a restrictive area behind the obstacle (red frame in Figures 4.11 and 4.12 for the cylinder and the airfoil, respectively). The transverse velocity component (v) is chosen in cross-correlation to ensure higher amplitudes of fluctuations. Cross-correlation coefficient is calculated for different relative positive and negative field offsets τ_x along the X direction. It can be seen as a 2D cross-correlation performed only along one main direction (direction of the main component of the flow). The result is a sinusoidal signal whose position of maxima relative to zero ($\tau_x = 0$) provide the spatial shift (Δ_ϕ) between the mean coherent structures of the reference phase average field and the coherent structures of the instantaneous field, as shown in Figure 4.13a. Instead of using the maximum position of the correlation signal, shift values Δ_ϕ are computed. The most accurate approach to determining the offset value is to use the zero crossings of the obtained sinusoidal function. An interpolating of the envelope at each crossing is used to improve the measurement of the spatial offset, as it is done in PIV with sub-pixel approach. The spatial phase shift between coherent structures in both fields (reference and instantaneous) can also be seen directly in 2D perspective as shown in Figure 4.13b. Knowing the distance between the vortices on the reference field and the spatial offset as described previously, a phase varying in a range of 0° to 360° fields is then assigned to each instantaneous velocity field of the time sequence. The phase of the instantaneous velocity field can be calculated by the following Equation (4.1) :

$$\phi_{inst} = \frac{\Delta_\phi}{\lambda_{ref}} \times 360° \tag{4.1}$$

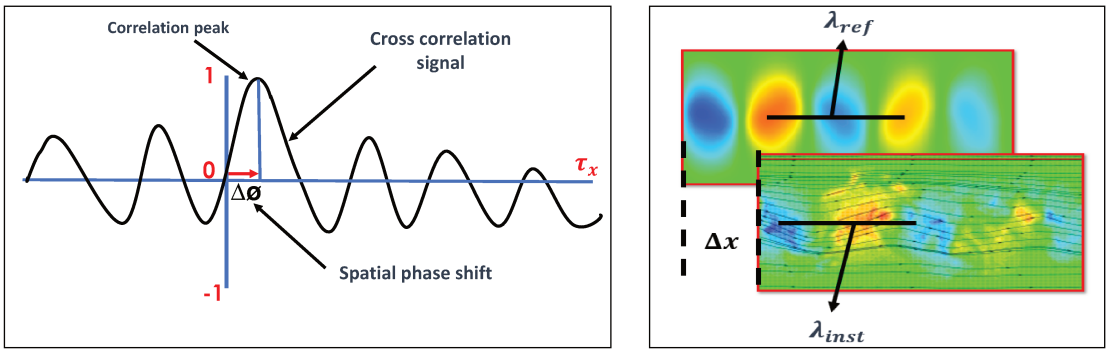

(a) (b)

Figure 4.13: (a) phase shift in cross correlation signal (1D). (b) Spatial phase shift (2D).

It is very valuable to illustrate the consistency and reliability of the proposed approach as shown in Figure 4.14. Figure 4.14a shows the phase evolution as a function of sample number in the case of the cylinder. A sawtooth signal, characterizing the periodic ejection of coherent structures downstream of the cylinder is measured with a very good regularity. This is due to the fundamental frequency given by the Strouhal's frequency of the cylinder. Figure 4.14b shows the distribution over 18 phases for the whole time sequence of 38 seconds. A satisfactory statistical distribution of the instantaneous fields classification is obtained. An average of 10,000 instantaneous velocity fields in each phase class is reported.

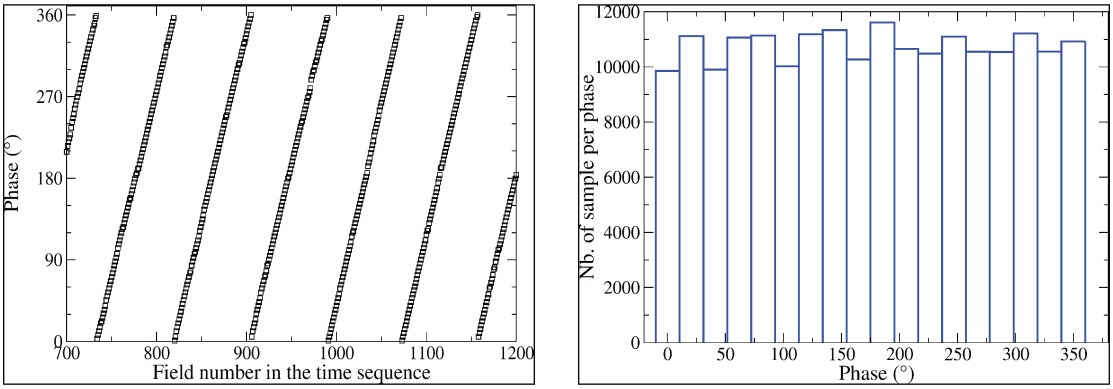

(a) Coherent motion phases in function of samples (images) indices.

(b) Number of samples (images) in each phase over a full time record.

Figure 4.14: Data output (phases) after applying the approach for 190,000 velocity fields (38 second record)

4.3.2 Evaluation of phase decomposition by statistics

The quality of phase decomposition must be first checked on low-order statistics, such as the mean of the velocity field and Root Mean Squared (RMS). Therefore, an effective initial step involves examining the mean velocity profiles at the center of the wakes, precisely where the fluctuations reach their peak amplitudes.

Cylinder case

Figures 4.15 and 4.16 show the mean velocity profiles U (streamwise (X) direction) and V (spanwise (Y) directions) within a cylinder center wake ($Y/D = 0$), respectively. The

profiles are presented for two Reynolds numbers and four different phases ($\Phi = 0°$, $90°$, $180°$, $270°$). Phased average profiles exhibit a sinusoidal shape carried by the averaged velocity profiles. Note that spanwise velocity average is null.

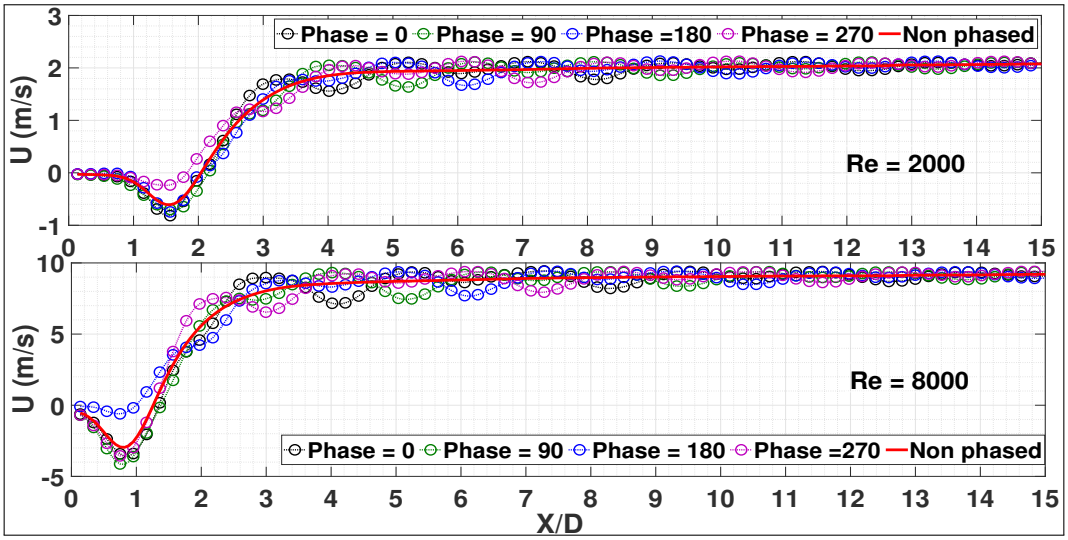

Figure 4.15: Profiles of streamwise velocity (X-direction) at two Reynolds numbers ($Re = 2000$ and $Re = 8000$).

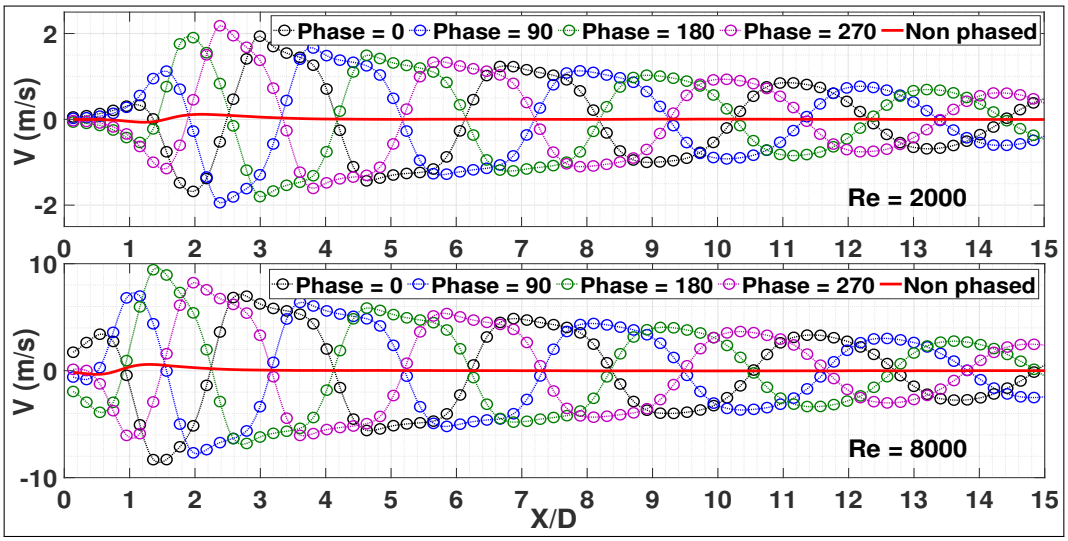

Figure 4.16: Profiles of spanwise velocity (Y-direction) at two Reynolds numbers ($Re = 2000$ and $Re = 8000$).

Figure 4.17 shows the Root Mean Square (RMS) of stream wise velocity (X direction) in the cylinder wake at $Re = 2000$. In Figure 4.17a, the RMS related to non decomposed data is shown. This Figure shows the total fluctuations (CM and RM) on X direction, with no distinction between phases. It shows very high magnitude just behind cylinder and decrease by moving downstream. In Figure 4.17b, the RMS for a given phase is shown. The fluctuations of random motion (RM) and (CM) fluctuation are revealed. Random structures over coherent structures at one particular phase are observed.

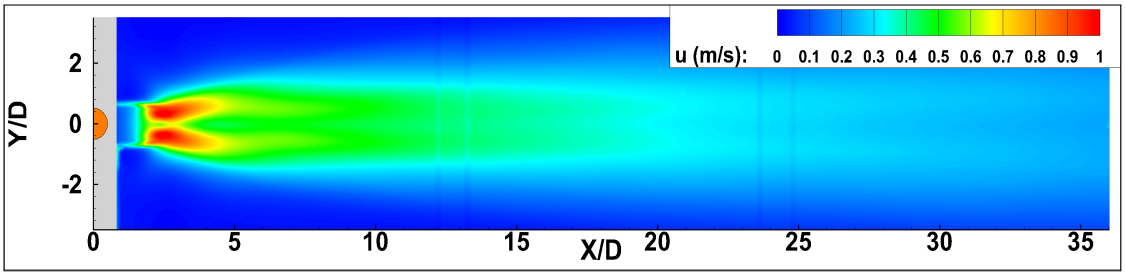

(a) Root mean square (RMS) without phase decomposition.

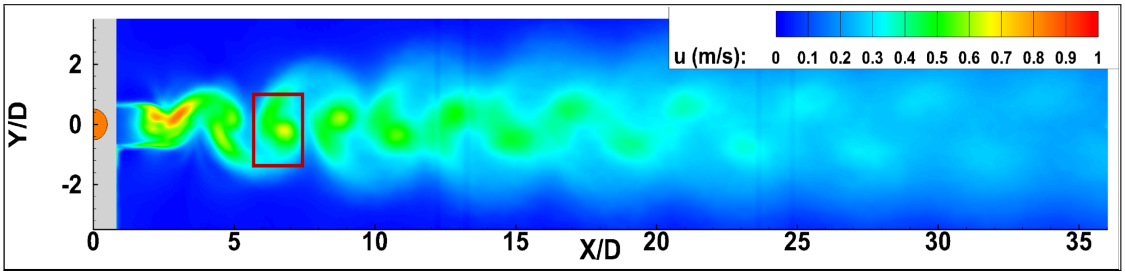

(b) Root mean square (RMS) with phase decomposition ($\phi = 0$).

Figure 4.17: Root Mean Square (RMS) of streamwise velocity in cylinder wake at $Re = 2000$.

CM fluctuations appeared due to variations in their characteristics close to their spatial positioning for a given phase. These characteristics include: time period, intensity and size of large vortices (CM). For instance, the zone indicated by red rectangle in Figure 4.17b shows the high variability of CM characteristics (period, intensity and size).

Airfoil case

Figures 4.18 and 4.19 show the mean velocity profiles U (streamwise (X) direction) and V (spanwise (Y) directions) within an airfoil center wake ($Y/C = 0$), respectively. The profiles are presented for two Reynolds numbers and four different phases ($\Phi = 0°$, $90°$, $180°$, $270°$). Phased average profiles exhibit a sinusoidal shape carried by the averaged velocity profiles.

In comparison Figure 4.19 with Figure 4.16, and as expected, the fluctuations in an airfoil wake is much smaller than the fluctuations of a cylinder wake. The fluctuations tends to $2m/s$ in an airfoil wake and to $10m/s$ in a cylinder wake for the same Reynolds number ($Re = 8000$).

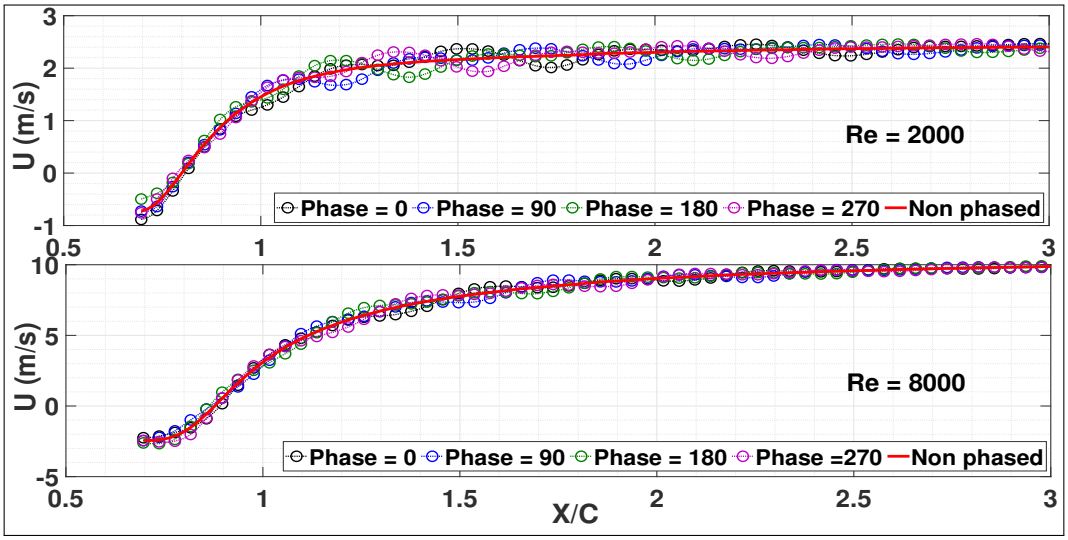

Figure 4.18: Profiles of streamwise velocity (X-direction) at two Reynolds numbers ($Re = 2000$ and $Re = 8000$).

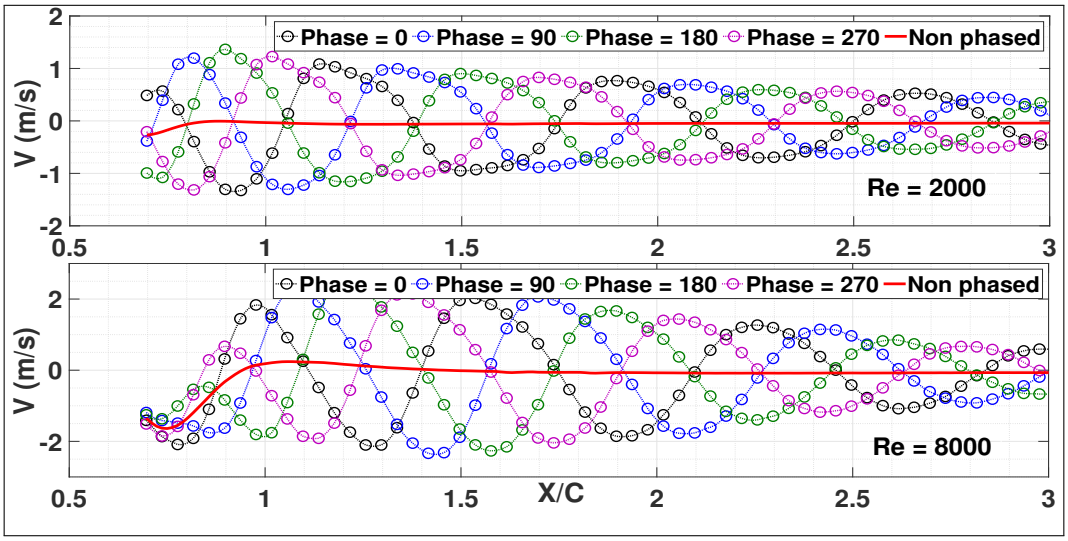

Figure 4.19: Profiles of spanwise velocity (Y-direction) at two Reynolds numbers ($Re = 2000$ and $Re = 8000$).

Figure 4.20 illustrates the Root Mean Square (RMS) of the streamwise velocity (in the X direction) within the wake of the airfoil at $Re = 2000$. Figures 4.20a and 4.20b present the RMS of the streamwise velocity for both non-decomposed and decomposed-by-phases datasets.

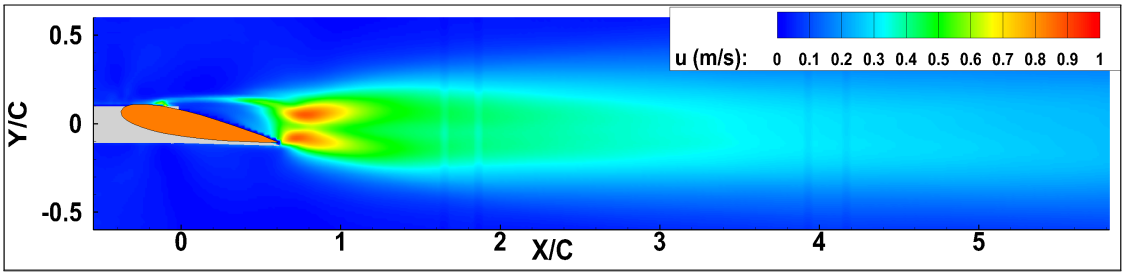

(a) Root mean square (RMS) without phase decomposition.

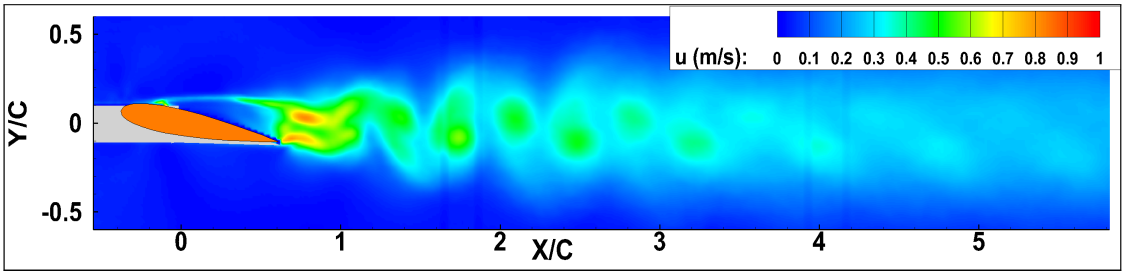

(b) Root mean square (RMS) with phase decomposition ($\phi = 0$).

Figure 4.20: Root Mean Square (RMS) of streamwise velocity in airfoil wake at $Re = 2000$.

The evaluation of both methods show significantly the reliability of "aposteriori" method in both wakes. In case of cylinder wake, both of the methods (pressure sensor and a posteriori) show high agreement in mean velocity profiles (i.e Figures 4.8 and 4.16). However, the pressure sensor method is limited in cylinder wake and not able to proceed further.
To conclude, a comparison is done between both of the methods concerning first order statistics and limitations. It is important to note that coherent motion (CM) remains undetected in the flow with either method. Consequently, a study focused on the detection of coherent motion (CM) has been conducted for both of these approaches.

4.4 Detection of coherent motion (CM)

Tracking coherent motion (CM) and associated dynamics, provides insight into the nature of the flow. For quantitative analysis of coherent structures, proper orthogonal decomposition (POD) has been widely applied to axisymmetric flows, including jets, mixing layers, and wakes of axisymmetric bodies as shown in Vitkovicova [77]. POD is a mathematical modal decomposition technique that extracts the most energetic structures from the flow of a turbulent field. By applying the POD, it is possible to determine flow patterns that correspond to structures with a large energetic contribution to the flow. These structures do not necessarily correspond to coherent structures, but rather correspond to the events which statistically contribute the most to the energy of the flow, referring to as Kostas study [78]. It is possible to obtain both the dominant frequency producing in the wakes of the cylinder and structures that have the greatest influence on wake formation. To overcome this shortcoming, our approach can be applied to categorize the phases that represents the dynamic motion of the coherent structures. For this academic configuration, the triple decomposition is applied. Triple decomposition allows to see how the coherent structures play their role in a wake, see Hussein and Reynolds [25, 26, 27]. Therefore, this method can be considered to as a second check on the quality of phase decomposition.

Triple decomposition is a mathematical tool of turbulent fields (Equation 4.2) which accounts for the quasi-periodicity of the coherent motion (CM), for each phase.

$$\underbrace{f(x,t,\phi_i)}_{\textbf{Instantaneous}} = \underbrace{\overline{f(x,t,\phi_i)}}_{\textbf{Mean motion}} + \underbrace{\widetilde{f}_c(x,t,\phi_i)}_{\textbf{Coherent motion}} + \underbrace{f'_r(x,t,\phi_i)}_{\textbf{Random motion}} \quad . \tag{4.2}$$

This Equation corresponds to the decomposition initially proposed by Hussein and Reynolds [25, 26, 27] for an organized wave. They decomposed the instantaneous turbulent field $f(x,t)$ into three main components: time average $\overline{f(x,t,\phi_i)}$ (average of unsynchronized data), the random fluctuations in an instantaneous field $f_r(x,t,\phi_i)$ and the coherent structures $f_c(x,t,\phi_i)$, as shown in Equation 4.2. Coherent motion $f_c(x,t,\phi_i)$ is obtained by difference between the phase average $\langle f(x,t)\rangle$ (average of the synchronized data) and the time average $\overline{f(x,t)}$, see Equation 4.3.

$$\underbrace{\widetilde{f}_c(x,t,\phi_i)}_{\textbf{Coherent motion}} = \underbrace{\langle (f(x,t,\phi_i)\rangle}_{\textbf{Phase average}} - \underbrace{\overline{f(x,t,\phi_i)}}_{\textbf{Time average}} \quad . \tag{4.3}$$

Random motion (RM) can be found, either by the difference between the instantaneous velocity field $f(x,t,\phi_i)$ and the phase average $\langle f(x,t)\rangle$ (random structures over coherent motion) or with time average $\overline{f(x,t,\phi_i)}$ (random structures in random spatial position if there is no coherent motion), shown in Equation 4.4.

$$\underbrace{f'_r(x,t,\phi_i)}_{\textbf{Random motion}} = \underbrace{f(x,t,\phi_i)}_{\textbf{Instantaneous}} - \underbrace{\langle f(x,t,\phi_i)\rangle}_{\textbf{Phase average}} \quad . \tag{4.4}$$

4.4.1 Detection using "pressure sensor" method

The detection of coherent motion (CM) is done by Triple decomposition method, explained above. Figure 4.21 shows the triple instantaneous decomposition of the wake, at $Re = 2000$ for $\Phi = 0°$. The function $f(x,t,\phi_i)$ is the sum of the three components equal to the instantaneous velocity field, shown in Equation 4.2. Checking the validity of this decomposition by adding up all components is shown in contributions such as [79, 80]. Coherent motion is dominant near the cylinder, but gradually weakens before disappearing as the distance to the cylinder increases, see Figure 4.21. Coherent motion makes the flow more complex, as it induces additional shear and interactions with other scales of motion. Coherent motion enhances the exchange of energy between different flow components.

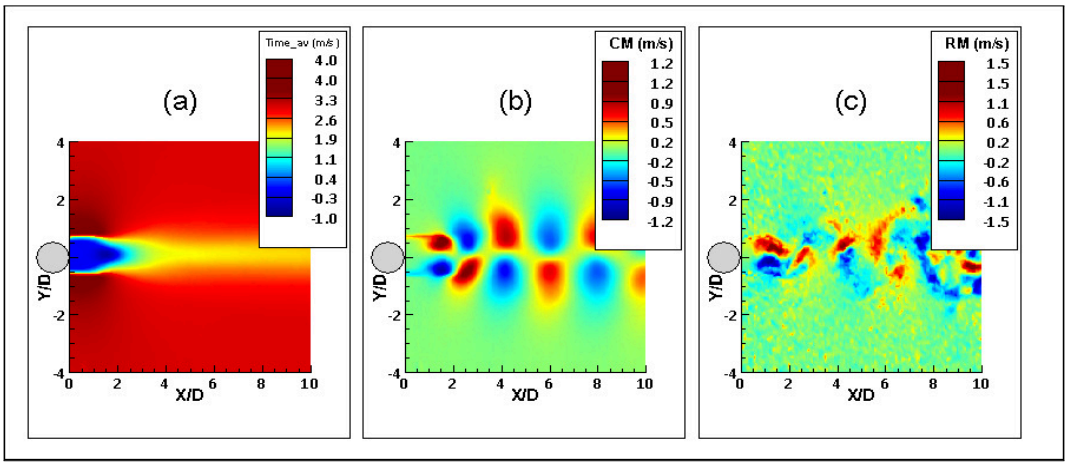

Figure 4.21: Triple decomposition for $Re = 2000$ and $\Phi = 0°$. (a) Time average $\overline{f(x,t,\phi=0)}$. (b) coherent structures (CM), $f_c(x,t,\phi = 0)$. (c) The random fluctuations in an instantaneous field (RM), $f_r(x,t,\phi = 0)$.

The evolution of coherent structures is very much essential for the verification of our technique, and for further detailed analysis of turbulence, such as turbulent kinetic energy balance in function of (CM) phases. Figure 4.22 shows the evolution of coherent structures every 45° (every 9 phases) for $Re = 8000$. One can clearly see the development of structures with the inversion of negative vortices and positive vortices at $\Phi = 180°$ and $\Phi = 360°$. The technique has been validated for different Reynolds numbers. This shows that our acquisition device is well synchronized with the flow. The technique makes it possible to analyze the dynamics of flows with a double vision for coherent structures and random flow. The activity of coherent structures is analyzed for each particular phase or different temporal period, as shown in Figure 4.22.

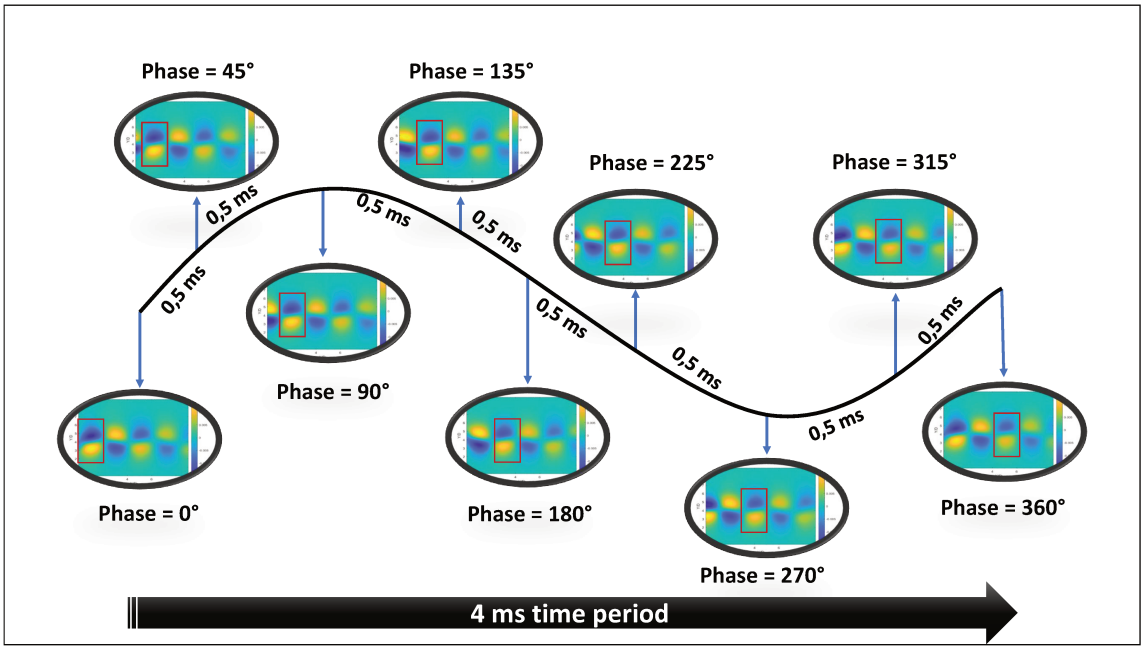

Figure 4.22: Coherent structures evolution (sinusoidal motion) at $Re = 8000$.

This illustration highlights that this approach (pressure sensor) is able to detect coherent motion (CM) within cylinder wake and not airfoil wake. This limitation is attributed to low fluctuations in airfoil wake as shown previously.

4.4.2 Detection using "a posteriori" method

Coherent structures exhibit dynamic variations based on different phases. The detection method of coherent structures is done by triple decomposition as presented in the previous section (Microphone approach).

Cylinder case

Figure 4.23 shows the coherent structures in a cylinder wake at $Re = 2000$. Coherent structures are well identified for $\phi = 0°$ (top) and $\phi = 180°$ (bottom). Figure 4.23 also shows the total inversion in phase (sign opposition) of the structures: between $\phi = 0°$ and $\phi = 180°$. Each two vertical spots, represent one vortex in Von Kàrmàn vortices street. In this Figure, the vortex center is observed through the presence of a zero-velocity zone positioned between two distinct vertical spots. This is demonstrated in other research works, as discussed by Acheson [81] and Decher [82].

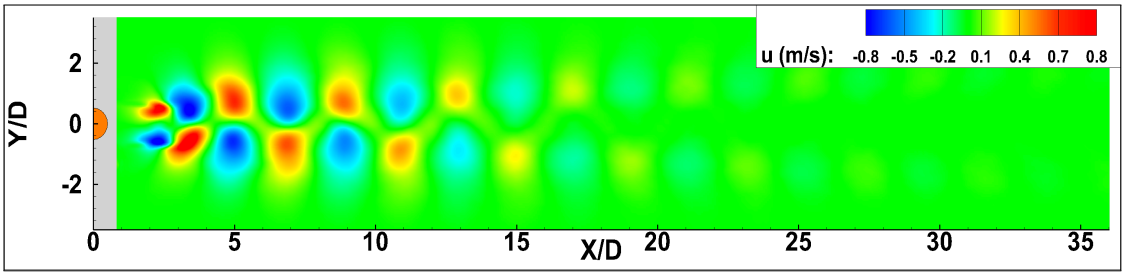

(a) Coherent structures at $\phi = 0$.

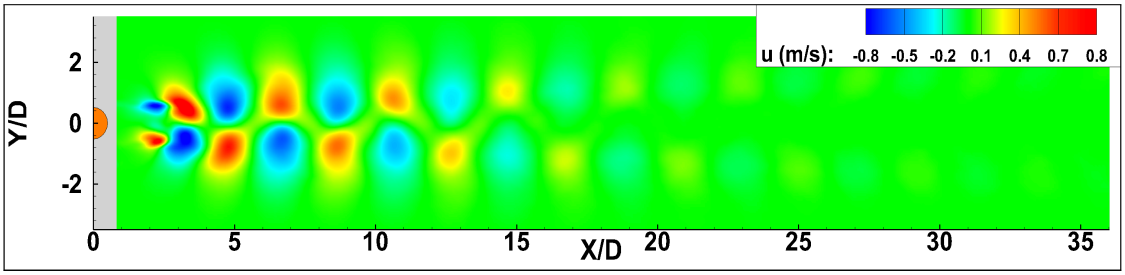

(b) Coherent structures at $\phi = 180$.

Figure 4.23: Coherent structures (CM) detection in cylinder wake at Re = 2000, representing coherent component of velocity fluctuations $\widetilde{u}$ in streamwise direction.

Figure 4.24 shows the coherent structures in a cylinder wake at $Re = 8000$. In Figure 4.24, the velocity magnitude intensity of the coherent structures is increased compared to that in Figure 4.23 ($Re = 2000$). For further clarification, vortices can resist more in downstream direction to keep alive. It also shows that coherent structures begin their detachment closer to the cylinder comparing to Figure 4.23 (Re = 2000). This is due to the recirculation zone length that becomes smaller in higher Reynolds number, as shown in many studies like Ouro [83] and Thiesset [70]. Figure 4.24 also shows the total inversion in phase (sign opposition) of the structures: between $\phi = 0°$ (top) and $\phi = 180°$ (bottom).

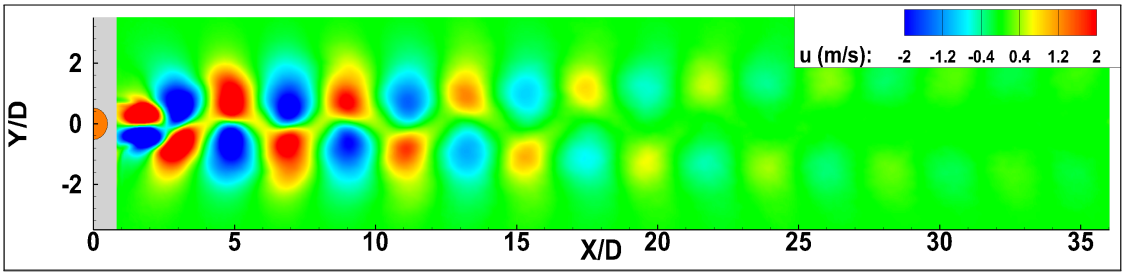

(a) Coherent structures at $\phi = 0$.

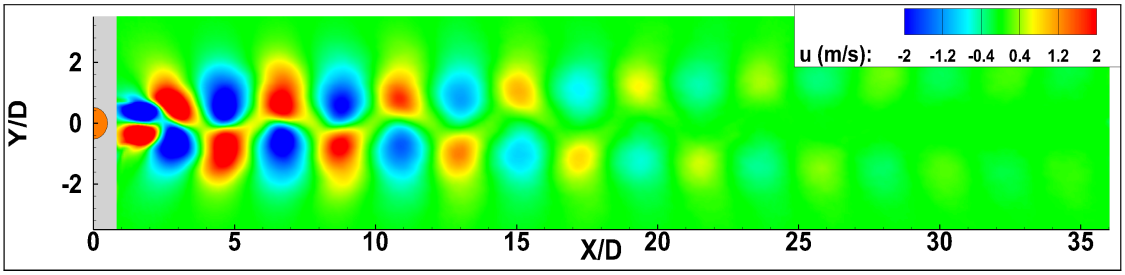

(b) Coherent structures at $\phi = 180$.

Figure 4.24: Coherent structures (CM) detection in cylinder wake at Re = 8000, representing coherent component of velocity fluctuations $\widetilde{u}$ in streamwise direction.

Airfoil case

Figures 4.25 and 4.26 show the coherent structures velocity in an airfoil wake at $Re = 2000$ and $Re = 8000$, respectively. In both figures, complete phase inversion (opposite sign) of the structures also shown between $\phi = 0°$ (top) and $\phi = 180°$ (bottom).

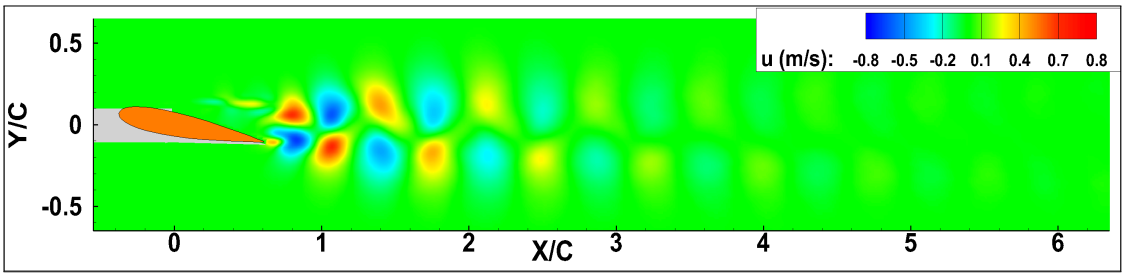

(a) Coherent structures at $\phi = 0$.

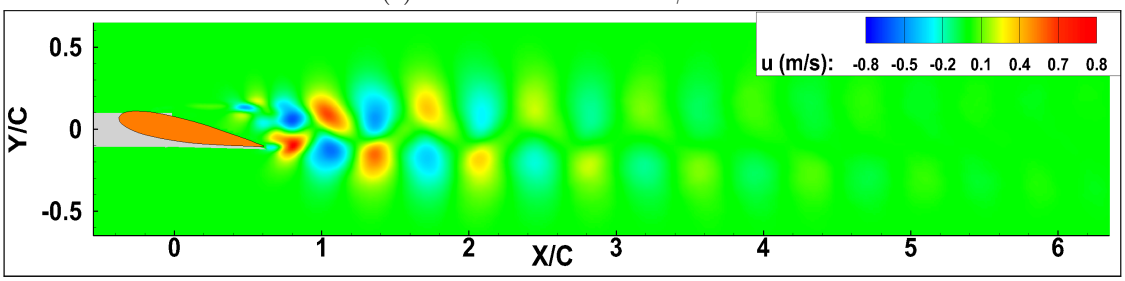

(b) Coherent structures at $\phi = 180$.

Figure 4.25: Coherent structures (CM) detection in airfoil wake at Re = 2000, representing coherent component of velocity fluctuations $\widetilde{u}$ in streamwise direction.

These figures clearly demonstrate decreased fluctuations (coherent motion intensity) in comparison to the wake behind the cylinder for the same Reynolds numbers. For

instance, at $Re = 8000$, coherent structures (CM) within the airfoil wake completely dissipate after traveling 100 mm downstream from the trailing edge, corresponding to a distance of (2 X/C). In contrast, these structures continue to be persistent in the wake behind the cylinder for a notably longer distance, remaining visible until 300 mm downstream, equivalent to (30 X/D). The naturally unstable separated shear layer of airfoil undergoes the transition from laminar to turbulent flow depending on Reynolds number. The separated shear layer has the potential to reattach to the surface of the airfoil. This is shown in different contributions referring to as airfoil wakes, Tani [84] and Yarusevych [85]. For example, at low Reynolds numbers, this separated shear layer is unable to reattach, leading to the formation of a wider wake (close to the airfoil). This can be shown in Figure 4.25, where the separation point along the trailing edges is still pertinent (no reattachment). On the other hand, at higher Reynolds numbers, a turbulent separated shear layer has the capability to reattach, leading to the creation of a laminar separation bubble and a more confined wake (close to the airfoil). This phenomenon is illustrated in Figure 4.26, where the separation point along the trailing edge is disappeared, and wake becomes narrower close to the airfoil.

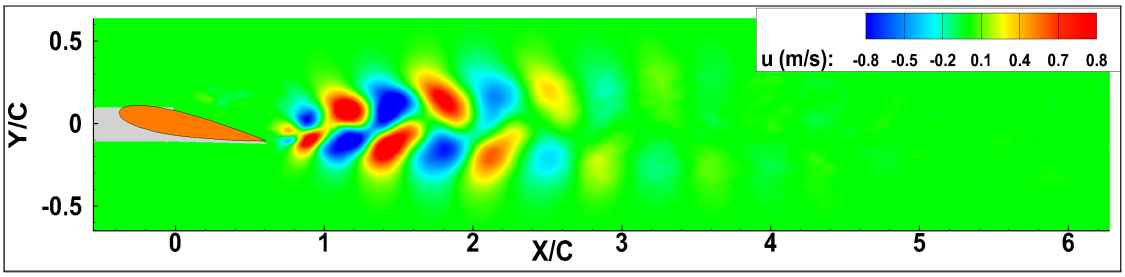

(a) Coherent structures at $\phi = 0$.

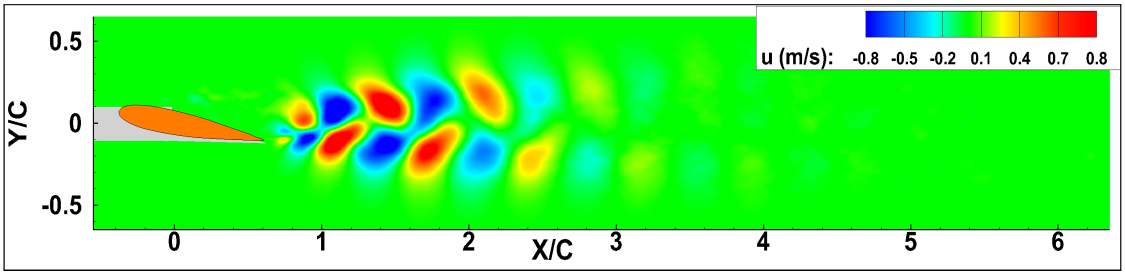

(b) Coherent structures at $\phi = 180$.

Figure 4.26: Coherent structures (CM) detection in airfoil wake at $Re = 8000$, representing coherent component of velocity fluctuations $\widetilde{u}$ in streamwise direction.

This illustration highlights the capability of this approach to determine the phase and detect the coherent motion (CM) behind both the cylinder and the airfoil.

4.5 Conclusion

The comparison of both methods highlights the considerable reliability of the "aposteriori" approach in both wake studies. For instance, in the case of the cylinder wake, both methods (pressure sensor and "aposteriori") exhibit an agreement in the mean velocity profiles. While, the pressure sensor method faces limitations when applied to the cylinder wake, preventing its further progress (airfoil wake). Moreover, detecting coherent structures in the airfoil wake using a microphone sensor is challenging, which can result in reduced confidence

in the measurements. This approach is also very sensitive to noise such as: aerodynamic, wind tunnel motor or experiment instruments noises. However, decomposition by “a posteriori” method is able to decompose the phases of cylinder and airfoil (low fluctuations magnitude) wakes. It can also be applied in any position of the flow without interrupting the measurements or re-change the position of microphone. By relying on this method, one can ensure that the flow remains undisturbed by any probe. This adaptability provides significant flexibility when analyzing interactions within the wake. This approach can be applied to low and high speed Particle Image Velocimetry (PIV) data. Based on the information presented in this chapter, the methodology of "a posteriori" phase decomposition will be employed in the subsequent stages of our study. It shows a great reliability and precision of decomposing the phases of wakes.

CHAPTER 5

Temporal and spatial periods analysis

Summary

As shown in Chapter 4, the wakes formed behind obstacles exhibit periodic motion which are known as coherent motion (CM). This raises the question of whether the time period and frequency of coherent motion can be influenced by the upstream flow. The advantages of time-resolved Particle Image Velocimetry (PIV) that is detailed in Chapter 3 make it possible to analyze temporal periods and frequency of coherent motion within the wakes of obstacles. Thus, this chapter focuses on the investigation of time periods, power spectra (frequencies), and spatial periods of coherent motion in obstacle wakes. These studies are primarily conducted using temporal and spatial autocorrelation. The research presented in this chapter investigate also the development and transmission of coherent motion between two positions in a field. This analysis helps in determining whether coherent motion remains alive or undergoes deformation as it moves between these positions. The study utilizes temporal cross-correlation between the two positions within the field to assess this phenomenon. These analyses are discussed by the presentation of various configurations that involve the combination of two primary obstacles: a 1 *cm* cylinder and a NACA 0015 airfoil.

Contents

5.1 Temporal auto-correlation (Temporal period) **80**
5.1.1 Cylinder configurations 81
5.1.2 Airfoil configurations 83
5.2 Power spectrum and temporal cross correlation analysis **86**
5.2.1 Cylinder configurations 87
5.2.2 Airfoils configurations 89
5.3 Spatial autocorrelation (Spatial period) **92**
5.3.1 Spatial periods as a function of samples 93
5.3.2 Spatial autocorrelation average 97
5.3.3 Observations review and conclusions 100

5.1 Temporal auto-correlation (Temporal period)

One of the primary advantages of time-resolved Particle Image Velocimetry (PIV) is its capability to analyze temporal periods within the wakes of obstacles. These analyses are presented for five different configurations and compared. These configurations are as follows:

- Cylinder configurations: including; single and double cylinder configurations.
- Airfoil configurations: including; single airfoil, double airfoil and cylinder-airfoil configurations.

Temporal periods are determined by analyzing time auto-correlations at specific locations. This assessment evaluates how closely a signal resembles itself at various time lags. By computing time auto-correlations for a given time lag (Δt), it becomes possible to understand the relationship between a signal's values at that lag and its values at different time points. The calculation of the autocorrelation with respect to lag time (Δt) can be achieved using Equation 5.1,

$$C(\Delta t) = \frac{\frac{1}{T}\int_{t=0}^{T} X(t) \times X(t+\Delta t)\, dt}{\frac{1}{T}\int_{t=0}^{T} X(t)^2\, dt} = \frac{1}{T}\frac{\int_{t=0}^{T} X(t) \times X(t+\Delta t)\, dt}{\sigma_X^2}. \tag{5.1}$$

$C(\Delta t)$ is the normalized auto-correlation by variance, and it indicates the degree of similarity of a signal at different time lags (Δt). $C(\Delta t)$ can range from -1 to 1, where 1 indicates a perfect positive correlation, -1 indicates a perfect negative correlation, and 0 indicates no correlation.

For further simplification, velocity fluctuation values are measured over time at a specific location. This temporal signal of velocity fluctuations is then examined by autocorrelation analyses through Equation 5.1. In Figure 5.1, an example of temporal signals and the autocorrelation within a cylinder wake is presented for both streamwise and spanwise velocity fluctuations at $Re = 2000$. The positions of signals measurement are at $X/D = 3.5$, $Y/D = 1$ and $X/D = 3.5$, $Y/D = 0$ for streamwise and spanwise velocity fluctuations, respectively. It is observed that the autocorrelation of the temporal signal for spanwise (v) velocity fluctuation is higher than that for streamwise velocity fluctuation (u). This is due to organized fluctuations on spanwise direction compared to streamwise direction.

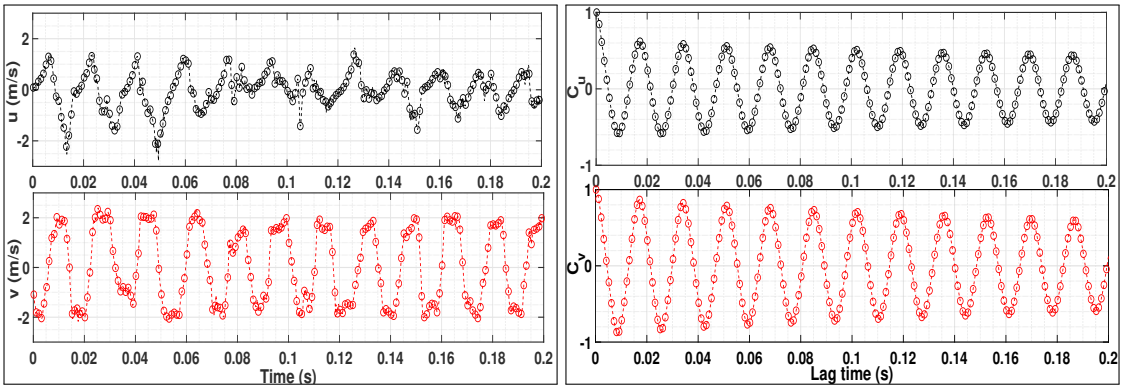

(a) Temporal signals of streamwise (top) and spanwise velocity fluctuations (bottom).

(b) Autocorrelation of streamwise (top) and spanwise velocity fluctuations (bottom).

Figure 5.1: (a) Temporal signals, (b) autocorrelation of streamwise (u) and spanwise (v) velocity fluctuations at $Re = 2000$. The positions of signals measurement are at $X/D = 3.5$, $Y/D = 1$ and $X/D = 3.5$, $Y/D = 0$ for streamwise and spanwise velocity fluctuations, respectively.

5.1.1 Cylinder configurations

Single cylinder wake

Temporal autocorrelation for single cylinder wake is reported in this section. Figure 5.2 (bottom) shows autocorrelations at various positions within a cylinder wake at $Re = 2000$ and $Re = 8000$. Figure 5.2 includes the corresponding spatial positions clearly at the top. Each black cross ($Y/D = 1$) in Figure 5.2 (top) corresponds to a specific location of autocorrelation for streamwise (u) velocity fluctuations. These positions are shifted $1D$ in spanwise direction to ensure higher streamwise velocity fluctuations. Red squares ($Y/D = 0$) represent autocorrelations for spanwise (v) velocity fluctuations at different positions within the wake. In Figure 5.2a, it is shown that time differences between signals peaks at all locations are equal. This ensures the stability of time period within the cylinder wake. For example, the time difference between each peak in Figure 5.2a ($Re = 2000$) is close to 0.017 s equivalent to a frequency of 59 Hz. Note that the peak magnitudes of streamwise fluctuations are significantly lower compared to those of spanwise fluctuations. In Figure 5.2b ($Re = 8000$), time differences between peaks becomes close to 0.00415 s equivalent to a frequency of 241 Hz. These observations agreed with theoretical values that are shown in Table 3.2.

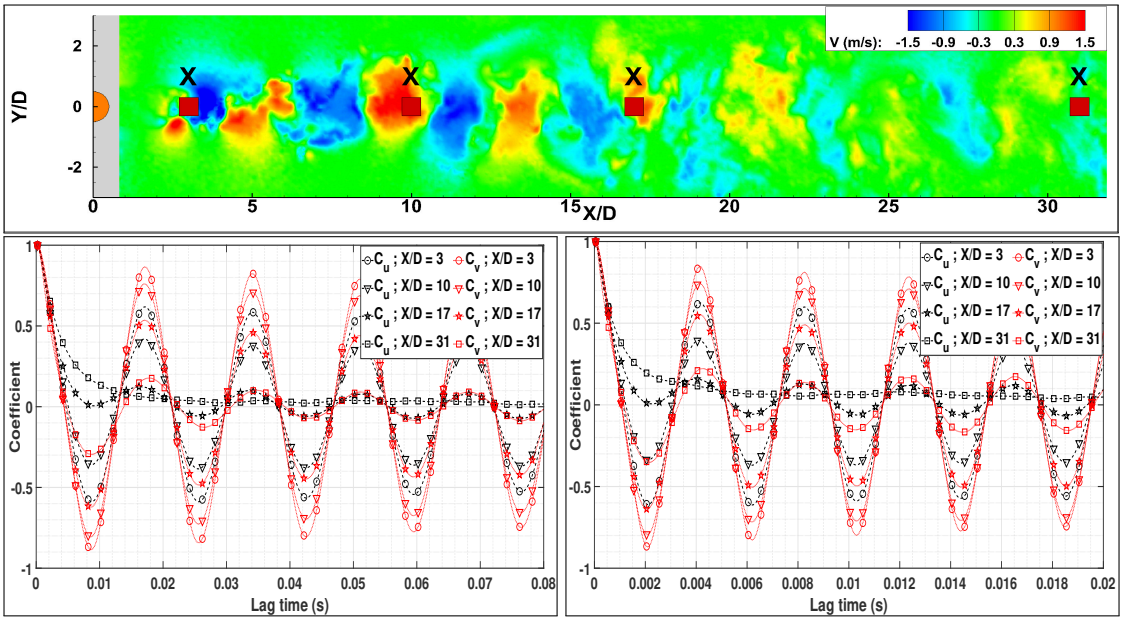

(a) $Re = 2000$ (b) $Re = 8000$

Figure 5.2: Temporal auto-correlations of streamwise (u) and spanwise (v) velocity fluctuations at different positions in single cylinder wake, at $Re = 2000$ and $Re = 8000$.

Double cylinder wake

Temporal autocorrelation for double cylinder wake is reported in this section. Figure 5.3 (bottom) shows autocorrelations at various positions within double cylinder wake at $Re = 2000$ and $Re = 8000$. Figure 5.3 includes the corresponding spatial positions clearly at the top. Each black cross ($Y/D = 1$) in Figure 5.2 (top) corresponds to a specific location of autocorrelation for streamwise (u) velocity fluctuations. These positions are shifted 1 D in spanwise direction to ensure higher streamwise velocity fluctuations. Red squares ($Y/D = 0$) represent autocorrelations for spanwise (v) velocity fluctuations at different positions within the wake. Figure 5.3 shows that the peak magnitudes of streamwise fluctuations significantly lower (null in further distances) compared to those of spanwise fluctuations. In Figure 5.3a, one can observe that signals peaks are not equally distanced. This shows the non stable time period within double cylinder wake, particularly at closer distances. For example, the time difference between first two peaks at $X/D = 13$ in Figure 5.2a ($Re = 2000$) is close to 0.028 s equivalent to a frequency of 36 Hz. While, the time difference between the second two peaks is 0.023 s equivalent to a frequency of 44 Hz. This is proved theoretically ($f_s = \frac{StU}{D}$) by the mean velocity U at ($X/D = 10$, $Y/D = 0$) that measures 2.01 m/s for $Re = 2000$ leading to a shedding frequency $f_s = 40.2$ Hz. The theoretical frequency falls between the two measured frequency. Moving downstream within double cylinder wake stabilizes the time period and reduce slightly first and second time differences to 0.026 and 0.025, respectively. The same phenomenon is observed for higher Reynolds number in Figure 5.3b. The first and second peak time differences are increased to 0.0065 s ($f_s = 154$ Hz) and 0.0053 s ($f_s = 189$ Hz). This is proved theoretically by the mean velocity U at ($X/D = 10$, $Y/D = 0$) that measures 9.03 m/s for $Re = 8000$ leading to a shedding frequency $f_s = 180.6$ Hz. The theoretical frequency also falls between two measured frequency. These observations can be explained due to the influence of the upstream cylinder wake. The upstream cylinder wake reduces the upstream mean velocity effecting consequently the frequency of coherent motion (CM)

behind second cylinder.

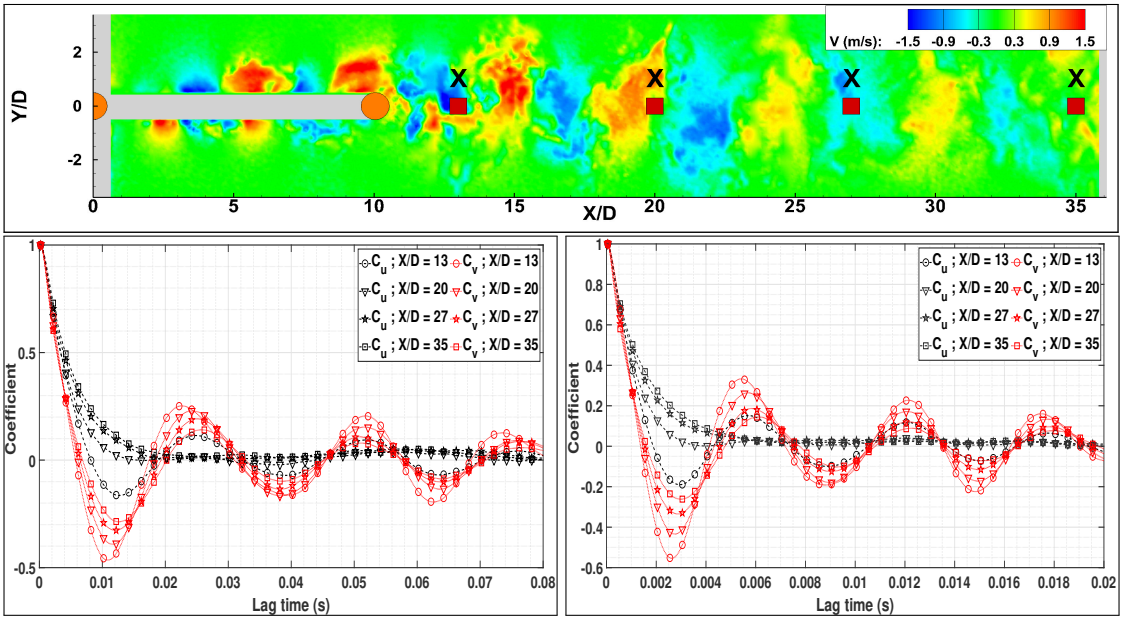

(a) $Re = 2000$ (b) $R = 8000$

Figure 5.3: Temporal auto-correlations of streamwise (u) and spanwise (v) velocity fluctuations at different positions in double cylinder wake, at $Re = 2000$ and $Re = 8000$

5.1.2 Airfoil configurations

Single airfoil wake

Temporal autocorrelation for single airfoil wake is reported in this section. Figure 5.4 (bottom) shows autocorrelations at various positions within airfoil wake at $Re = 2000$ and $Re = 8000$. Figure 5.4 includes the corresponding spatial positions clearly at the top. Each black cross ($Y/C = 0.2$) in Figure 5.4 (top) corresponds to a specific location of autocorrelation for streamwise (u) velocity fluctuations. These positions are shifted $0.2C$ in spanwise direction to ensure higher streamwise velocity fluctuations. Red squares ($Y/C = 0$) represent autocorrelations for spanwise (v) velocity fluctuations at different positions within the wake. In Figure 5.4a, it is shown that time differences between signals peaks at all locations is equal. This ensures the stability of time period within the airfoil wake. For example, the time difference between each peak in Figure 5.4a ($Re = 2000$) is close to $0.014s$ equivalent to a frequency of $71Hz$, see Table 3.2. Note that the peak magnitudes of streamwise fluctuations are significantly lower compared to those of spanwise fluctuations. In Figure 5.2b ($Re = 8000$), time differences between peaks are close to $0.0034s$ equivalent to a frequency of $294Hz$. These observations are close to theoretical values that is presented in Table 3.2. Figure 5.2b shows that the temporal correlations decorrelated rapidly due to the lower coherent motion (CM) energy at high Reynolds numbers in the airfoil wake.

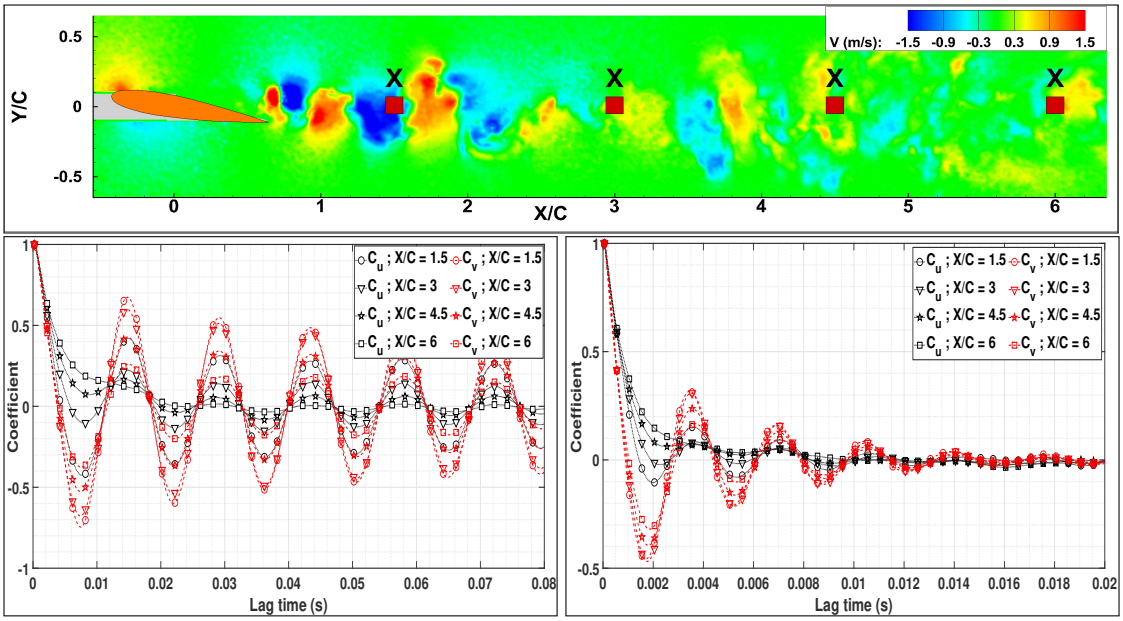

(a) $Re = 2000$ (b) $Re = 8000$

Figure 5.4: Temporal auto-correlations of streamwise (u) and spanwise (v) velocity fluctuations at different positions in single airfoil wake, at $Re = 2000$ and $Re = 8000$.

Cylinder-airfoil wake

Temporal autocorrelation for cylinder-airfoil wake is reported in this section. Figure 5.5 (bottom) shows autocorrelations at various positions within cylinder-airfoil wake at $Re = 2000$ and $Re = 8000$. Figure 5.5 includes the corresponding spatial positions clearly at the top. Each black cross ($Y/D = 1$) in Figure 5.2 (top) corresponds to a specific location of autocorrelation for streamwise (u) velocity fluctuations. These positions are shifted $1D$ in spanwise direction to ensure higher streamwise velocity fluctuations. Red squares ($Y/D = 0$) represent autocorrelations for spanwise (v) velocity fluctuations at different positions within the wake. In Figures 5.5a and 5.5b, one can observe that autocorrelation signals have a time periods ($T = 0.017$ and $0.00415s$, respectively) similar to what is shown in cylinder wake (Figure 5.2). However, peaks in Figures 5.5a and 5.5b show lower magnitudes compared to cylinder wakes due to further distances and the presence of the airfoil. This similarity in time periods underscores the strong influence of the cylinder wake on the airfoil wake. Coherent structures generated by the cylinders dominate behind the airfoil due to their higher energy content. The persistence of cylinder coherent motion (CM) downstream can also be attributed to the airfoil's geometry, which allows CM to cross over the airfoil leading edge with minimal energy loss.

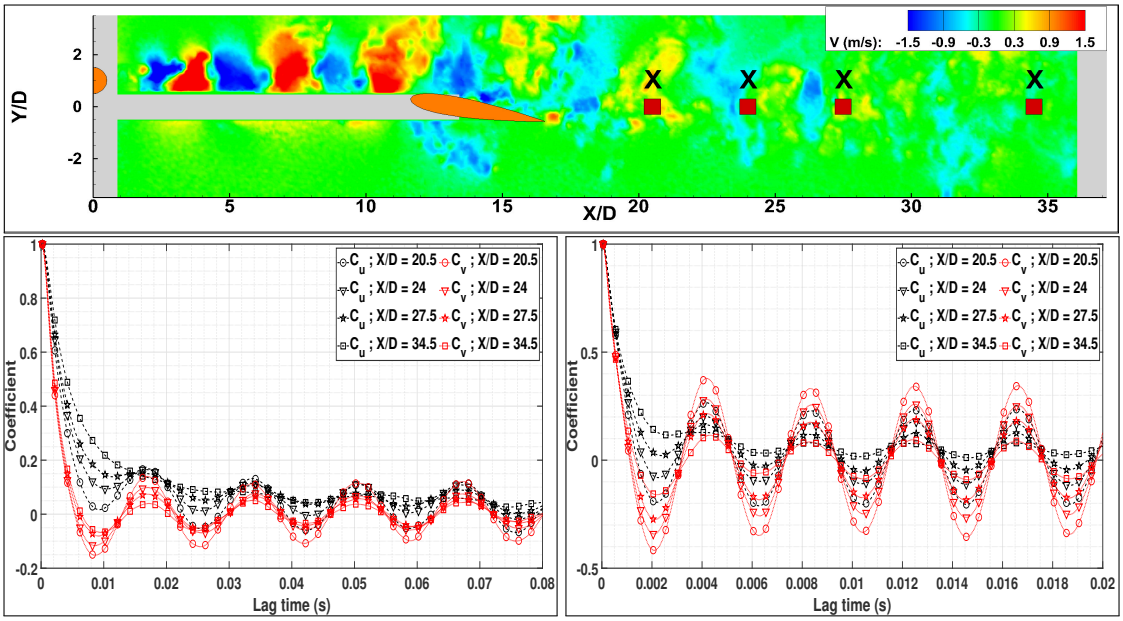

(a) $Re = 2000$ (b) $Re = 8000$

Figure 5.5: Temporal autocorrelations of streamwise (u) and spanwise (v) velocity fluctuations at different positions in cylinde-airfoil wake.

Double airfoil wake

Temporal autocorrelation for double airfoil wake is reported in this section. Figure 5.6 (bottom) shows autocorrelations at various positions within double airfoil wake at $Re = 2000$ and $Re = 8000$. Figure 5.4 includes the corresponding spatial positions clearly at the top. Each black cross ($Y/C = 0.2$) in Figure 5.4 (top) corresponds to a specific location of autocorrelation for streamwise (u) velocity fluctuations. These positions are shifted $0.2C$ in spanwise direction to ensure higher streamwise velocity fluctuations. Red squares ($Y/C = 0$) represent autocorrelations for spanwise (v) velocity fluctuations at different positions within the wake. Figures 5.6a and 5.6b show similar time periods for both Reynolds number seen in single airfoil wake (Figures 5.4a and 5.4b). However, peak magnitudes are lower compared to single airfoil wake due to further distances. The persistence of first airfoil coherent motion (CM) downstream is attributed to the airfoil's geometry, which allows CM to cross over with minimal energy loss.

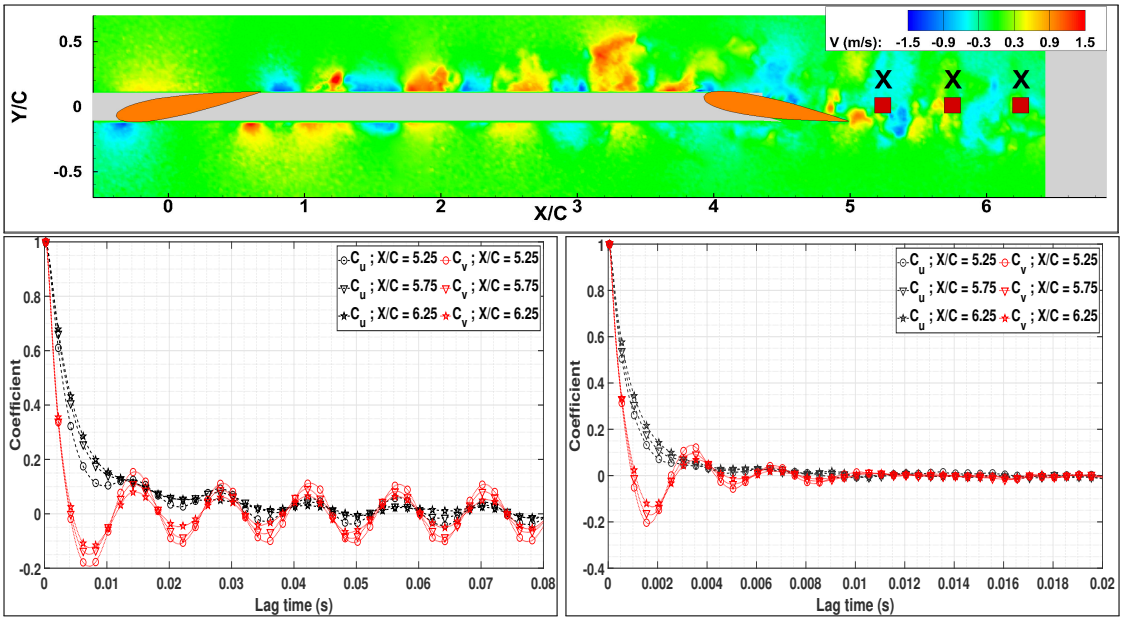

(a) $Re = 2000$ (b) $Re = 8000$

Figure 5.6: Temporal autocorrelations of streamwise (u) and spanwise (v) components at different positions in single and double airfoil wakes, at $Re = 8000$.

5.2 Power spectrum and temporal cross correlation analysis

The second advantage of time-resolved Particle Image Velocimetry (PIV) is its capability to analyze the power spectrum and spatial-time correlations within the wakes of obstacles. These analyses are presented for the five different configurations as aforementioned above. Power spectrum provides a signal in terms of its frequency components. This shows how the power or energy in a signal is distributed across different frequencies. Mathematically, the power spectrum is computed through the Fast Fourier Transform (FFT) of the signal, denoted as FFT(X(t)), followed by squaring the magnitude to obtain the power spectrum. The sampling rate for the Fourier transform is set at 5000 samples per second, corresponding to the acquisition frequency achievable with high-speed PIV. This analyses are studied only for $Re = 2000$. This process allows for a detailed examination of the frequency content and energy distribution within the signal. In other hand, temporal correlation measures the similarity or relationship between two signals, which are sequences of measurements taken at different points in time. This analysis can offer insights into the behaviors of vortices as they cross between two specific locations in the flow field. The cross correlation between two signals X and Y with a lag time (Δt) is calculated using Equation 5.2,

$$CC(\Delta t) = \frac{\frac{1}{T}\int_{t=0}^{T} X(t) \times Y(t+\Delta t)\, dt}{\frac{1}{T}\int_{t=0}^{T} X(t) \times Y(t)\, dt} = \frac{1}{T}\frac{\int_{t=0}^{T} X(t) \times Y(t+\Delta t)\, dt}{\sigma_{XY}^2}. \tag{5.2}$$

$CC(\Delta t)$ is the normalized cross-correlation by standard deviations, and it indicates the degree of similarity between the two signals at different time lags (Δt). $CC(\Delta t)$ can range from -1 to 1, where 1 indicates a perfect positive correlation, -1 indicates a perfect negative correlation, and 0 indicates no correlation.

5.2.1 Cylinder configurations

Single cylinder wake

The analyses are firstly applied to a simple and fundamental configuration, presented in this section. Figure 5.7 shows power spectrum and cross correlations for different position in cylinder wake (bottom of Figure 5.7). Figure 5.7 includes the corresponding spatial positions clearly at the top. Each square's color in Figure 5.7 corresponds to its specific analysis (bottom of Figure 5.7). The green square with a red cross, as indicated in Figure 5.7, is used in both analyses. Specifically, the green square corresponds to the power spectrum analysis, while the red cross corresponds to the cross-correlation analysis. Figure 5.7a shows the power spectrum at different locations downstream the cylinder wake. One observe that in the near field, the value of power spectrum is very high, in addition to the harmonics which diminish by moving downstream. The fundamental frequency is close to 60 Hz as shown in the Table 3.2. The harmonics were also shown by a POD study of [86], where the fundamental frequency and the third harmonic frequency have higher amplitudes than the second and the fourth harmonics. In the far field, the power of the vortices frequency (less vortices energy) begins to detract.
Figure 5.7b shows the time correlations for the spanwise velocity component in a cylinder wake. To compute the correlations, a reference position is fixed at the center of the cylinder wake near-field ($X/D = 3.5$) represented by the red cross in positions field (top of Figure 5.7). The positions to be tested in correlation with the reference position are located downstream from the reference point. In Figure 5.7b, one observe that the correlation coefficient is reduced 50% after 0.4 seconds for the closest position $X/D = 10$. In far fields, generated vortices are still alive, while lower in energy, as shown in Figure 5.7b.

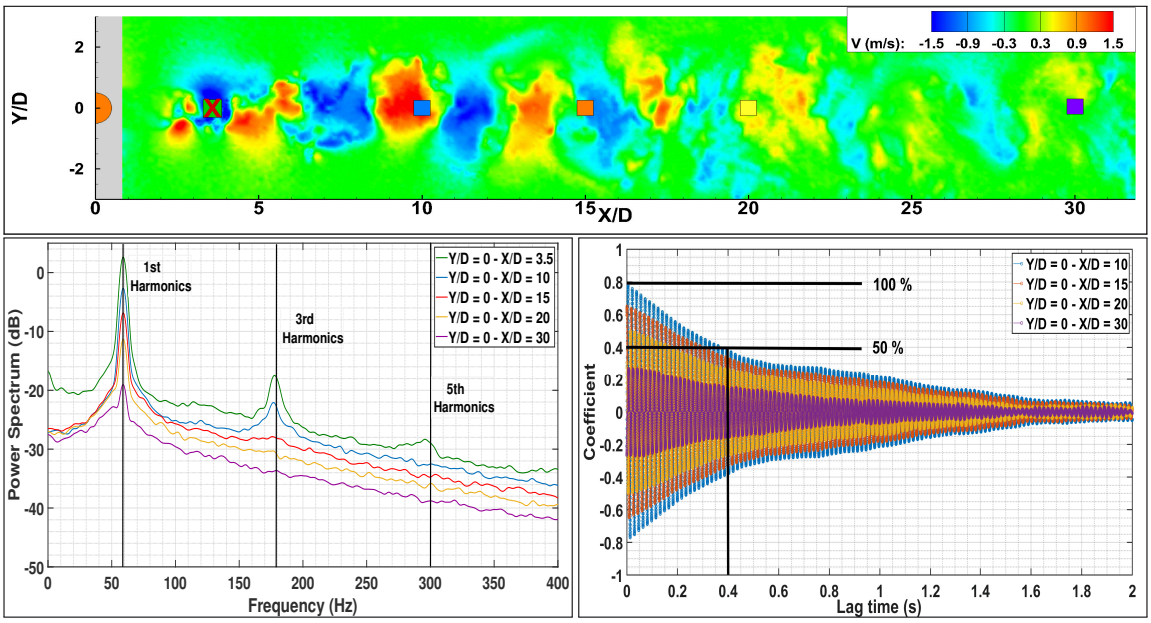

(a) (b)

Figure 5.7: (a) Power spectrum (spanwise velocity component) at different locations downstream of the cylinder wake. (b) Time correlations (spanwise velocity component) at the center of the cylinder wake, between a reference point ($X/D = 3.5$) and 4 different points downstream.

Double cylinder wake

Double cylinder configuration is presented in this section. Figure 5.8 shows power spectrum and cross correlations for different position in double cylinder wake (bottom of Figure 5.8). The analogue probe positions are placed at similar positions as single cylinder wake. Figure 5.8 includes the corresponding spatial positions clearly at the top. Each square's color in the Figure corresponds to its specific analysis (bottom of Figure 5.8). The white square with a red cross, as indicated in Figure 5.8, is used in correlation analyses. Figure 5.8a shows the power spectrum at different locations downstream the second cylinder exist in an upstream cylinder (double cylinder wake). This figure shows lower magnitude of frequency energies and a disappearance of harmonics frequencies. Moreover, the fundamental frequency of vortices shedded from cylinders are shifted from 60 Hz to 40 Hz. This shift is due to the existence of downstream cylinder.

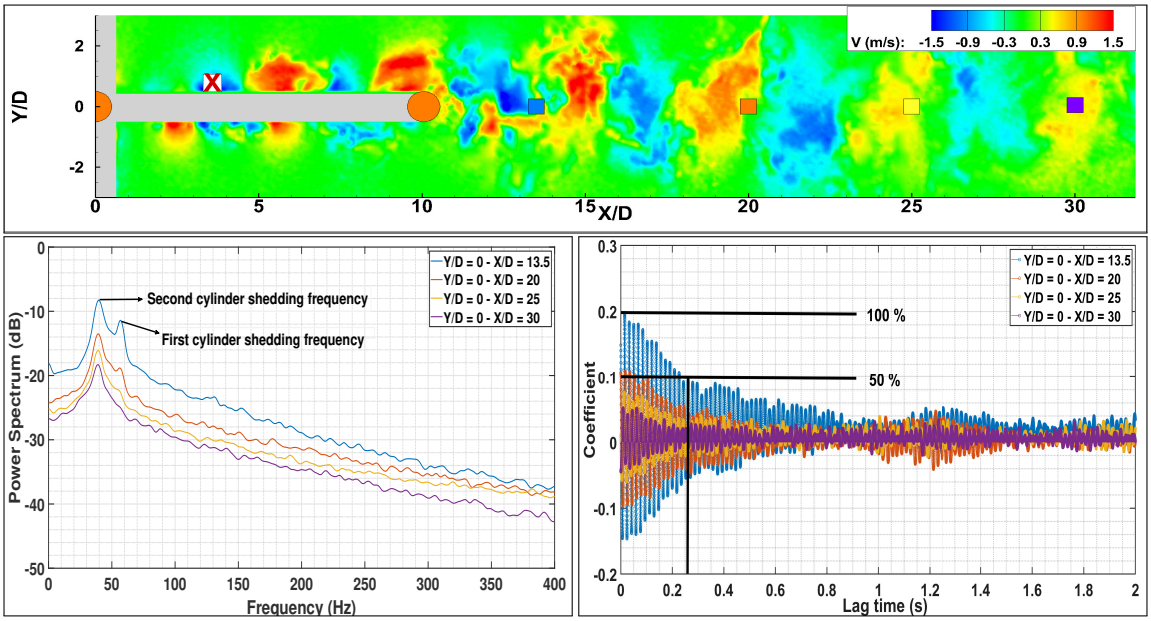

(a) (b)

Figure 5.8: (a) Power spectrum (spanwise velocity component) at different locations downstream of the cylinder wake. (b) Time correlations (spanwise velocity component) at the center of the double cylinder wake, between a reference point in upstream cylinder wake ($X/D = 3.5$) and 4 different points downstream the second cylinder (double cylinder wake).

Figure 5.8b presents the temporal correlations for the spanwise velocity component within the double cylinder wake. These temporal correlations are calculated by fixing the reference position in the near-field of the wake created by the upstream cylinder ($X/D = 3.5$). Various positions downstream of the second cylinder are then examined for their correlation with this reference position. This analysis provides insights into the behavior of vortices generated by the upstream cylinder as they imping the second cylinder, reaching the downstream wake (double cylinder wake). The results shown in Figure 5.8b reveals a significant low level of correlation between the vortices generated by the upstream cylinder and those present downstream of the second cylinder. In Figure 5.8b, one observe that an attenuation of 50% is occured to the correlation coefficient over 0.25 s. This attenuation is faster than the case of the cylinder wake, see Figure 5.7b. These observations suggest that the vortices produced by the upstream cylinder undergo significant deformation as

they pass through the downstream cylinder. Consequently, lack of similarity is observed between large shedded vortices at these two positions.
Figure 5.9 presents the temporal correlations for the spanwise velocity component within the double cylinder wake, while by fixing the reference position behind the downstream cylinder ($X/D = 13.5$). Three positions downstream of the second cylinder are then examined for their correlation with this reference position. This figure shows, a reduction of 50 % within the correlation is occured after less than 0.1 s. This reduction is significantly faster compared to what was observed in the previous case (Figure 5.8b). This can be attributed to the mix of vortices frequencies behind the second cylinder and the lower magnitudes in power spectrum (dB). For instance, behind the second cylinder, dominant frequencies are: $f_s = 40$ and 60 Hz with close magnitudes in power spectrum (dB). This can increase the decorrelation time with another position that is also mixed in frequencies.

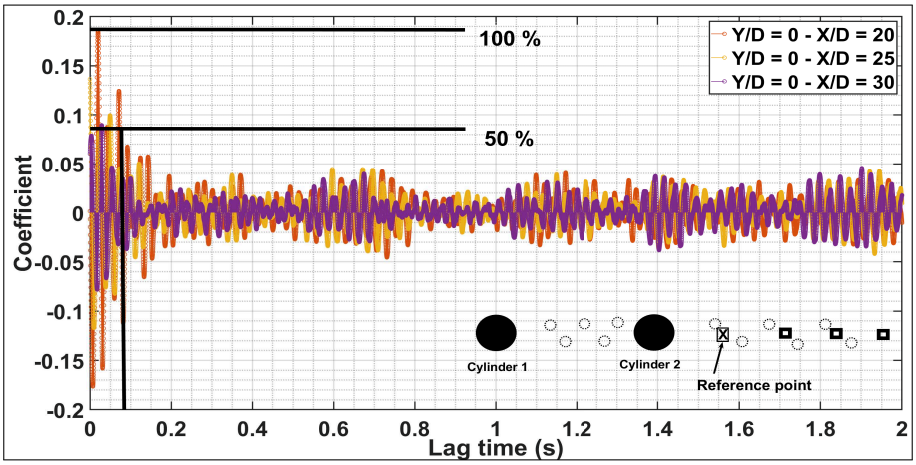

Figure 5.9: Time correlations (spanwise velocity component) at the center of the double cylinder wake, between a reference point behind downstream cylinder ($X/D = 13.5$) and 3 different points downstream (double cylinder wake).

5.2.2 Airfoils configurations

The analysis are applied then on wakes of complex obstacle shape, represented by NACA airfoils. These analyses are reported further in this section.

Single airfoil wake

The initial configuration corresponds to the simple airfoil wake. Figure 5.10 shows power spectrum and cross correlations for different positions in the airfoil wake (bottom of Figure 5.10). Figure 5.10 includes the corresponding spatial positions clearly at the top. Each square's color in the Figure corresponds to its specific analysis (bottom of Figure 5.10). The green square with a red cross, as indicated in the figure, is used in both analyses. Specifically, the green square corresponds to the power spectrum analysis, while the red cross corresponds to the cross-correlation analysis. Therefore, Figure 5.10a shows the power spectrum at different locations downstream the airfoil wake. The fundamental frequency is close to 70 Hz with an existence of 2nd and 3rd harmonic frequencies, however with amplitudes much smaller than that those in the cylinder wake (Figure 5.7a). Figure 5.10b shows the time correlations for the spanwise velocity component in an airfoil wake. The reference position is fixed at the center of the airfoil wake at $X/C = 1$ (equivalent to 2 cm from airfoil trailing edge), and the positions to be tested have an offset of 1 X/C (5

cm) downstream. In Figure 5.7b, one observes that the correlation coefficient is reduced by 50% after ≈ 0.2 seconds for the closest position $X/C = 2$. This shows that vortices generated by an airfoil have half of the life time of the vortices generated by a cylinder (Figure 5.7b).

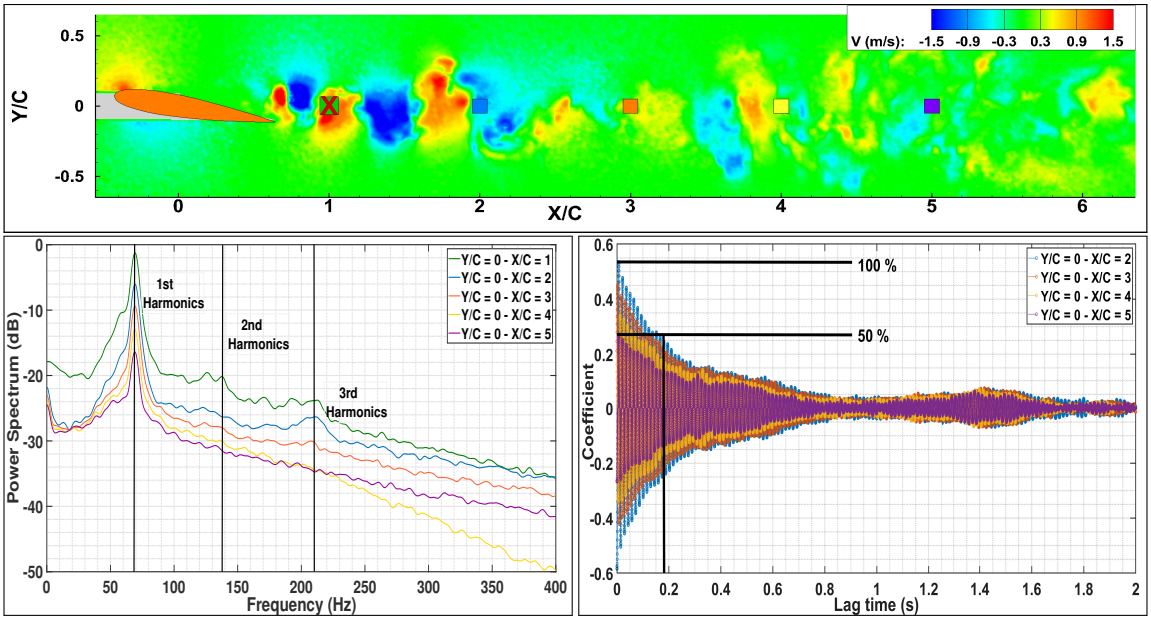

(a) (b)

Figure 5.10: (a) Power spectrum (spanwise velocity component) at different locations downstream of the airfoil wake. (b) Time correlations (spanwise velocity component) at the center of the airfoil wake, between a reference point located at $X/C = 3.5$ and 3 different points downstream.

Cylinder-airfoil wake

It is worth studying power spectrum and time correlation in a wake of different obstacles shape. Figure 5.11 shows power spectrum and cross correlations for different position in cylinder-airfoil wake (bottom of Figure 5.11). The figure includes the corresponding spatial positions clearly at the top. Each square's color in the figure corresponds to its specific analysis (bottom of Figure 5.11). The white square with a red cross, as indicated in the Figure, is used in correlation analyses. In Figure 5.11a, one observes that all positions have the frequency of the cylinder and no vortices frequency from the airfoil is observed. This shows the dominating process of cylinder wake over airfoil wake. Figure 5.11b shows the time correlations for the spanwise velocity component in cylinder-airfoil wake. The reference position is fixed in upstream center wake (cylinder) at $X/D = 3.5$. The first position in the spanwise direction to be tested is aligned with the leading edge ($Y/D = 0.5$), while the second is aligned close to the trailing edge (Y/D = -0.5). In Figure 5.11b, position aligned with leading edge shows a reduction of 50% in correlation after ≈ 0.4 *s*. This time of correlation reduction is close to what was observed in cylinder wake, see Figure 5.7b. This shows that this position is still highly dominated by the cylinder wake. By comparing two spanwise positions at the same downstream position ($X/D = 17.5$), near the leading edge, the correlations with the cylinder wake are much higher than those of the leading edge. This effect might be due to the high generation of vortices from the airfoil's trailing edge. In the far-field region ($X/C = 27.5$), both positions have exhibit a good

correlation due to the recombination between cylinder and airfoil vortices. This behavior is also shown by the power spectrum in Figure 5.11a, where all points downstream of an airfoil tend to synchronize with cylinder wake. In other words, the downstream points are highly affected by the upstream wake (cylinder) by taking the frequency of the vortices generated in the cylinder wake.

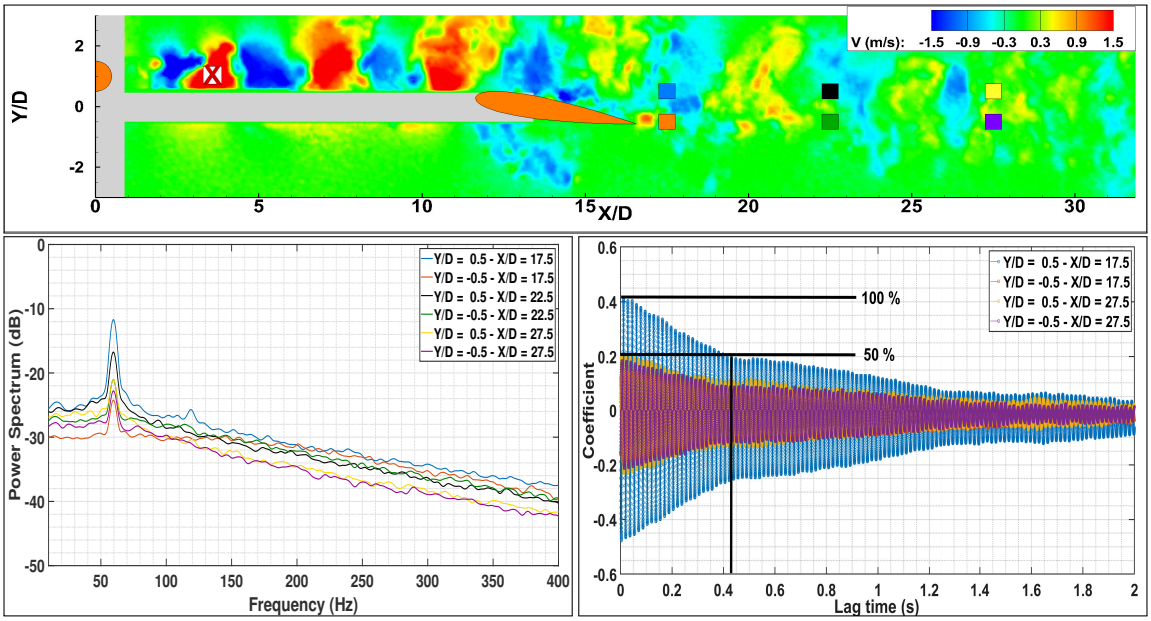

(a) (b)

Figure 5.11: (a) Power spectrum (spanwise velocity component) at different locations (6 points) downstream of the composed wake (cylinder + airfoil). (b) Time correlations(spanwise velocity component) between a reference point located at $X/D = 3.5$ and 4 different points downstream the airfoil.

Double airfoil wake

The second configuration involves a double airfoil wake with an inverted pitch angle ($\pm 10°$). This inversion is done to direct the vortices generated from upstream airfoil toward the downstream airfoil. Figure 5.12 shows power spectrum and cross correlations for different position in double airfoil wake (bottom of Figure 5.12). The Figure displays the corresponding spatial positions at the top. Each square's color in the Figure corresponds to its specific analysis (bottom of Figure 5.12). The white square with a red cross indicated in the Figure, is used in correlation analyses as a reference point. Figure 5.12a shows the power spectrum at various positions downstream the second airfoil (double airfoil wake). Significantly, the fundamental frequency, which is close to 70 Hz, remains in this configuration close to vortex frequencies of the upstream airfoil. However, the amplitudes of these frequencies are considerably smaller than those observed in the wake of a single airfoil (Figure 5.10a). This might be due to the existence of the second airfoil and also further distances between the reference point and the positions downstream the second airfoil. Despite the reduced magnitudes, the frequencies of the vortices remain consistent, with no observable shift in their frequencies compared to the case of the double cylinder wake. Figure 5.12b illustrates the temporal correlations for the spanwise velocity component within the double airfoil wake. The reference position is fixed in the center of the upstream airfoil wake at $X/C = 1$. Two positions are tested for correlation with the reference

position: one aligned with the leading edge (Y/C = 0.1) and other aligned with the trailing edge (Y/D = -0.1) in the spanwise direction. In Figure 5.12b, position aligned with leading edge shows a reduction of 50% in correlation after ≈ 0.66 s. This long time can be explained as the areas where the impact of coherent motion is minimal, causing the correlation to diminish at a slower rate in comparison to regions with more energetic coherent motion (CM). The low correlation can be attributed to the substantial distance between these positions. Additionally, there is an asymmetry in the correlation due to the persistence of one vortex sense relative to the inverted sense.

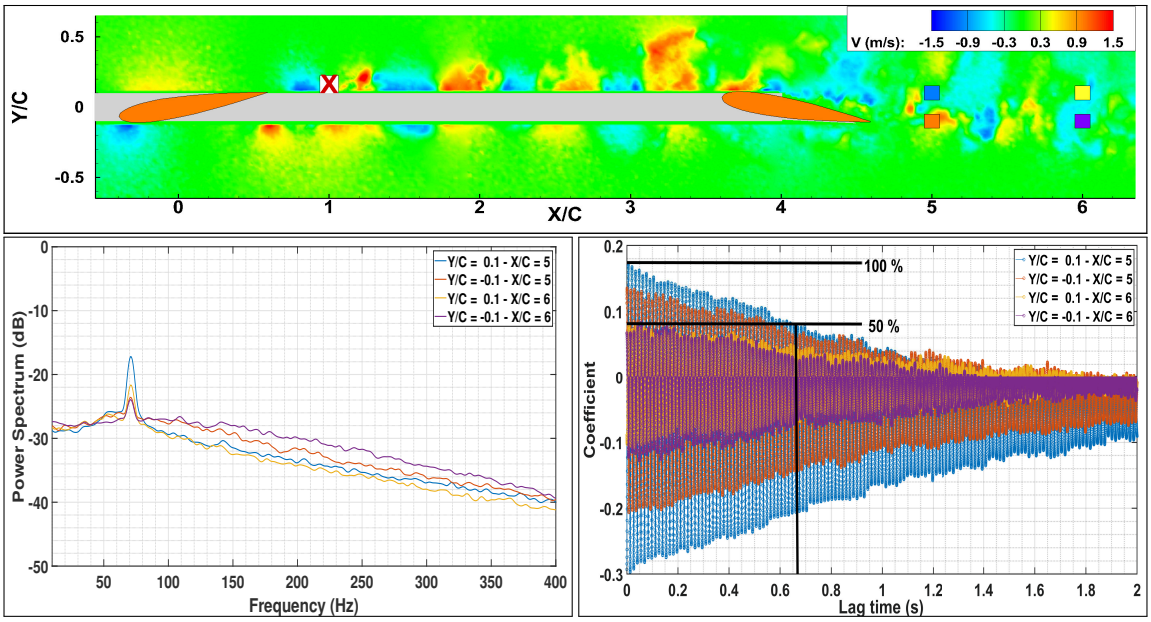

(a) (b)

Figure 5.12: (a) Power spectrum (spanwise velocity component) at different locations downstream of the cylinder wake. (b) Time correlations (spanwise velocity component) at the center of double airfoil wake, between a reference point in upstream airfoil wake (X/C = 3.5) and 4 different points downstream second airfoil.

5.3 Spatial autocorrelation (Spatial period)

Spatial periods are determined by analyzing auto-correlations in a profile of different locations at an instant. This assessment evaluates how closely a signal resembles itself at various distance lags. When autocorrelations are calculated for a particular lag distance (Δx), it enables the identification of high signal values at that lag distance, indicating a high degree of similarity. This similarity often corresponds to the presence of large turbulent structures, which are referred to as coherent motion. The calculation of the autocorrelation with respect to lag distance (Δx) are calculated using Equation 5.3,

$$C(\Delta x) = \frac{\frac{1}{L}\int_{x=0}^{L} f(x) \times f(x+\Delta x)\, dx}{\frac{1}{L}\int_{x=0}^{L} f(x)^2\, dx} = \frac{1}{L}\frac{\int_{x=0}^{L} f(x) \times f(x+\Delta x)\, dx}{\sigma_X^2}. \tag{5.3}$$

$C(\Delta x)$ is the auto-correlation function normalized by variance, and it indicates the degree of similarity of a signal at different distance lags (Δx). $C(\Delta x)$ can range from -1 to 1, where 1 indicates a perfect positive correlation, -1 indicates a perfect negative correlation, and 0 indicates no correlation.

In Figure 5.13, an example of spatial profiles (signals) and the autocorrelation within a cylinder wake is presented for both streamwise and spanwise velocity fluctuations at $Re = 2000$. These spatial profiles are measured at an instant of time and at positions: $Y/D = 1$ and $Y/D = 0$ for streamwise and spanwise velocity fluctuations, respectively. This shift in position for streamwise fluctuations is to detect higher amplitudes compared to center wake position. However, Figure 5.13 shows that the autocorrelation of spatial signal for spanwise (v) velocity fluctuation is higher than that for streamwise velocity fluctuation (u).

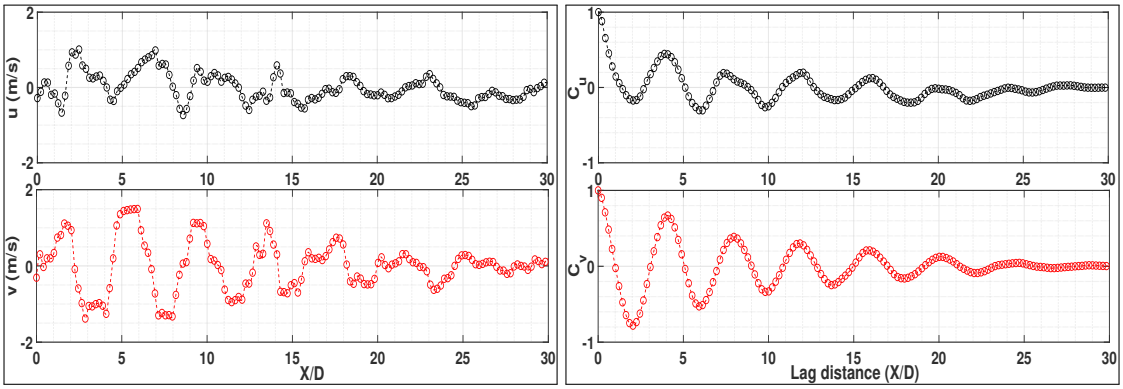

(a) Spatial profiles (signals) of streamwise (top) and spanwise velocity fluctuations (bottom).

(b) Autocorrelation of streamwise (top) and spanwise velocity fluctuations (bottom).

Figure 5.13: (a) Spatial profiles (signals) at an instant, (b) autocorrelation of streamwise (u) and spanwise (v) velocity fluctuations at $Re = 2000$. The profiles positions are at: $Y/D = 1$ and $Y/D = 0$ for streamwise and spanwise velocity fluctuations, respectively.

The spatial autocorrelation signal exhibits a sinusoidal behavior, which indicates the presence of coherent structures within the wake. This characteristic can be used to determine the spatial period of these coherent structures within the wake.
The process for computing the instantaneous spatial period is as follows,

- Obtain profile values at a specific spanwise position in the wake that represents instantaneous fluctuations.
- Calculate the deviation of each data point on the profile from the average value. Note that a group of points (3×3 grid) averaged is considered as one point.
- Apply a median filter and increase the number of data points through interpolation to obtain a better autocorrelation signal.
- Search for peaks in the instantaneous autocorrelation signal and compute the differences in peak positions, which represent the instantaneous spatial period.

The average of instantaneous autocorrelation signals is then applied to find the spatial period of coherent motion (CM) in wakes.

5.3.1 Spatial periods as a function of samples

In this section, the analysis pertains to samples or instantaneous data. Histograms of spatial periods are computed for each configuration to illustrate their distribution. Instantaneous spatial periods (λ) distribution are then fitted to probability density function

(PDF) as normal distribution. Histograms and PDF include spatial periods computed by streamwise (λ_u) and spanwise (λ_v) fluctuations autocorrelation (spatial), for comparison purposes. However, λ_u is less accurate due to lower autocorrelation coefficient of streamwise fluctuations. These analyses are reported for configurations mentioned previously.

Single and double cylinder wakes

Histogram and probability density functions for single and double cylinder wakes are reported. Figures 5.14a and 5.14b show histograms of spatial periods (λ) at $Re = 2000$ and $Re = 8000$ within single and double cylinder wakes, respectively. In Figures 5.14a and 5.14b, the corresponding profile positions used for autocorrelation computation are presented at the top. The red profile at center wake position ($Y/D = 0$) corresponds to spanwise fluctuations. The black profile position ($Y/D = 1$) is representing the streamwise fluctuations, shifted $1D$ in spanwise direction for higher fluctuations values. In these figures, numerical data are grouped in classes (bins) with a width of $0.5\lambda/D$ and normalised by the total number of samples. In Figure 5.14a, one observe that the spatial period (λ) in most of the samples falls within the range of $4D$ and $4.5D$ for both Reynolds numbers ($Re = 2000$ and $Re = 8000$). In double cylinder wake (Figure 5.14b), it is shown that the range of most samples is shifted to a range between $5.5D$ and $6.5D$.

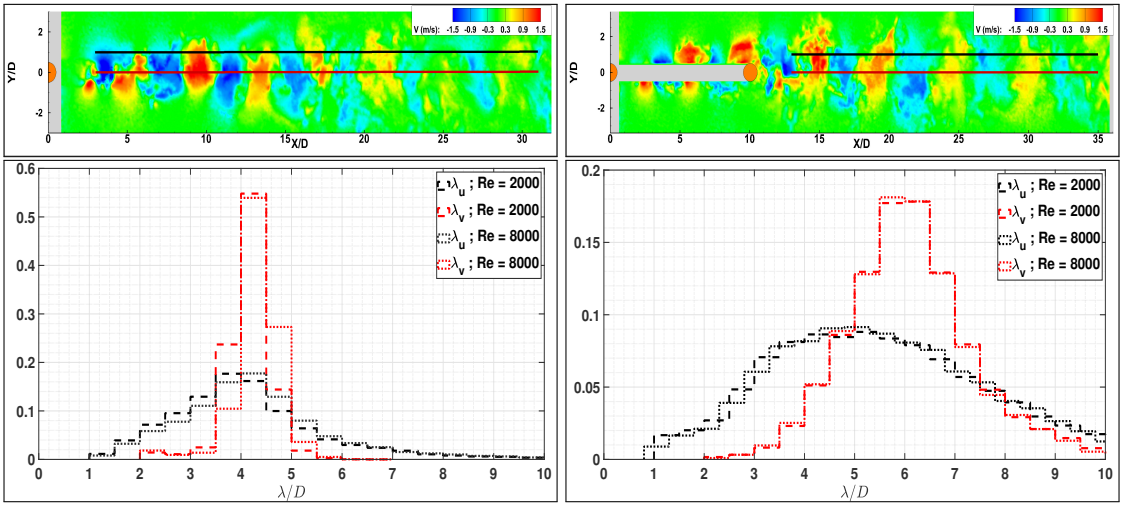

(a) Single cylinder wake

(b) Double cylinder wake

Figure 5.14: Spatial period distribution over samples (histogram) of streamwise (u) and spanwise (v) fluctuations in single and double cylinder wakes, at $Re = 2000$ and $Re = 8000$. Each class (group) in the histogram is normalised by the total number of samples.

Figures 5.15a and 5.15b show probability density function (PDF) of spatial periods (λ) at $Re = 2000$ and $Re = 8000$ within single and double cylinder wakes, respectively. In single cylinder wake (Figure 5.15a), PDF show that 90% of samples indicate that λ measures $4.2D$ at $Re = 2000$ and 83% measures $4.5D$ at $Re = 8000$. In double cylinder wake (Figure 5.15b), PDF show that 30% of samples measuring a value of $6.1D$ for both Reynolds numbers ($Re = 2000$ and $Re = 8000$). The low percentage is attributed to the presence of the upstream wake that increase the variation of λ between the samples.

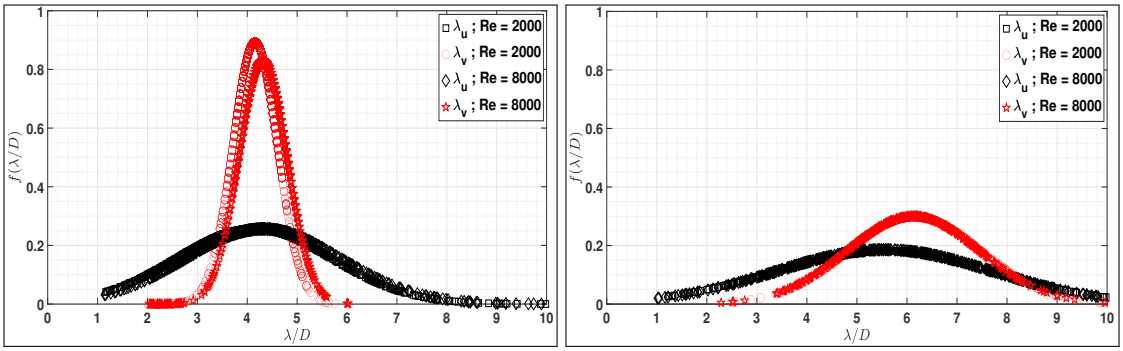

(a) Single cylinder wake

(b) Double cylinder wake

Figure 5.15: Spatial period distribution fitted to probability density function (PDF) in single and double cylinder wakes, at $Re = 2000$ and $Re = 8000$

Single and double airfoil wakes

Histogram and probability density functions for single and double airfoil wakes are reported. Figures 5.16a and 5.16b show histograms of spatial periods (λ) at $Re = 2000$ and $Re = 8000$ within single and double airfoil. In Figures 5.16a and 5.16b, the corresponding profile positions used for autocorrelation computation are presented at the top. The red profile at center wake position ($Y/C = 0$) is corresponds to spanwise fluctuations. The black profile position ($Y/C = 0.2$) is representing the streamwise fluctuations, shifted $0.2C$ in spanwise direction for higher fluctuations values. wakes, respectively. In these Figures, numerical data are grouped in classes (bins) with a width of $0.1\lambda/C$ ($0.5\lambda/D$) and normalised by the total number of samples. In Figure 5.16a, one observe that the spatial period (λ) in most of the samples falls within the range of $0.7C$ and $0.8C$ for both Reynolds numbers ($Re = 2000$ and $Re = 8000$). In double airfoil wake (Figure 5.16b), it is shown that most of the samples remain in a similar range as in single airfoil wake (between $0.7C$ and $0.8C$). However, fewer samples fall within the range of $0.7C$ and $0.8C$, and more samples appear at other spatial period ranges compared to the single airfoil wake (Figure 5.16a).

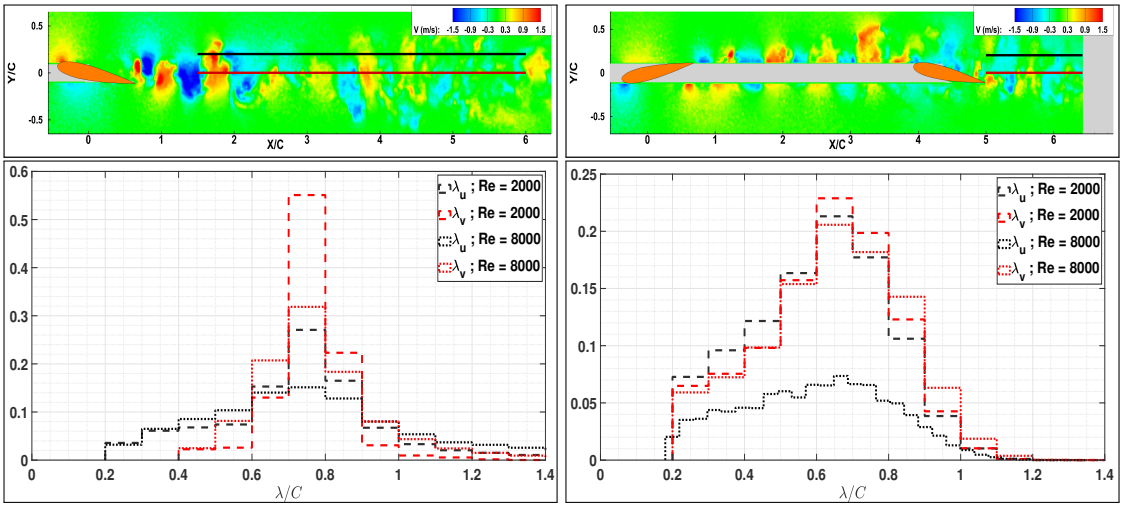

(a) Single airfoil wake (b) Double airfoil wake

Figure 5.16: Spatial period distribution over samples of streamwise (u) and spanwise (v) fluctuations in single and double airfoil wakes, at $Re = 2000$ and $Re = 8000$. Each class (group) in the histogram is normalised by the total number of samples

Figures 5.17a and 5.17b show probability density function (PDF) of spatial periods (λ) at $Re = 2000$ and $Re = 8000$ within single and double cylinder wakes, respectively. In single cylinder wake (Figure 5.17a), PDF show that 84% of samples indicate that λ measures $0.76C$ at $Re = 2000$ and 45% of samples measures $0.78C$ at $Re = 8000$. The decrease of λ at higher Reynolds number ($Re = 8000$) is attributed to the reduced persistence of coherent motion (CM) in the airfoil wake. In double airfoil wake (Figure 5.17b), PDF show that 45% of samples measuring a value of $0.65C$ for both Reynolds numbers ($Re = 2000$ and $Re = 8000$). The low percentage is attributed to the presence of the upstream wake and further distances, increasing the variation of λ between the samples.

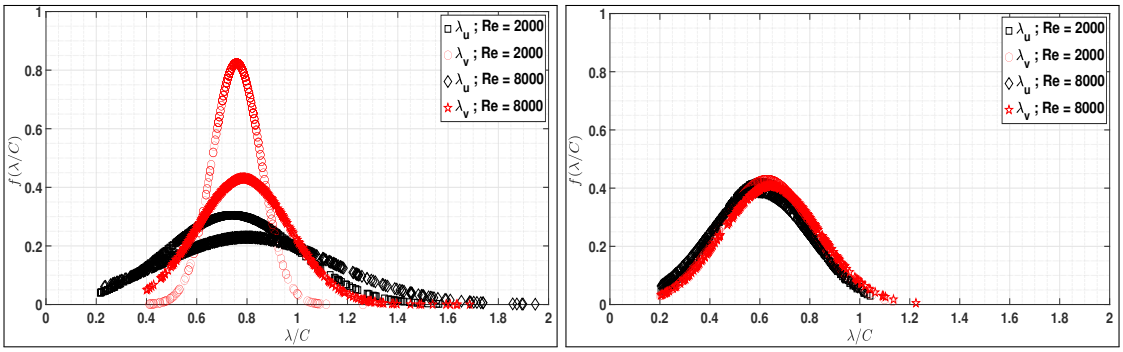

(a) Single airfoil wake (b) Double airfoil wake

Figure 5.17: Spatial period distribution fitted to probability density function (PDF) in single and double airfoil wakes, at $Re = 2000$ and $Re = 8000$

Cylinder-airfoil wake

Histogram and probability density functions for cylinder-airfoil wake are reported. Figure 5.18a shows the histograms of spatial periods (λ) at $Re = 2000$ and $Re = 8000$ within cylinder-airfoil wake. In Figure 5.18a, the corresponding profile positions used for autocor-

relation computation are presented at the top. The red profile at center wake position ($Y/D = 0$) corresponds to spanwise fluctuations. The black profile position ($Y/D = 1$) is representing the streamwise fluctuations, shifted $0.2C$ in spanwise direction for higher fluctuations values. In this Figure, numerical data are grouped in classes (bins) with a width of $0.5\lambda/D$ and normalized by the total number of samples. In Figure 5.18a, one observe that the spatial period (λ) in most of the samples falls within the range of $4D$ and $4.2D$ for both Reynolds numbers ($Re = 2000$ and $Re = 8000$). This observation is similar to what is shown in single cylinder wake, see Figure 5.14a. However, peak position contains fewer samples (≈ 0.3) compared to single cylinder wake (≈ 0.55).

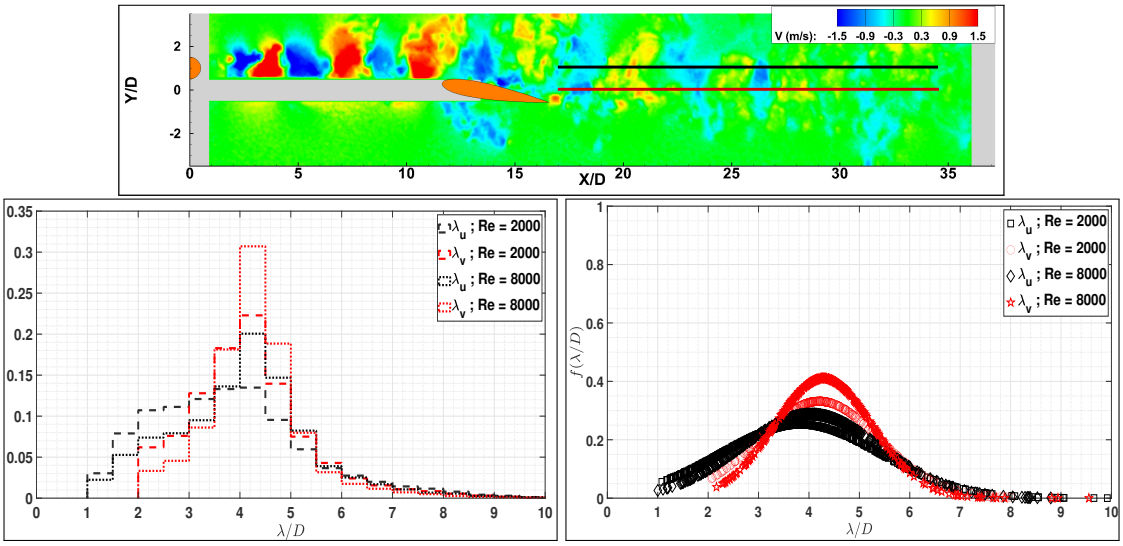

(a) Spatial period distribution (histogram)

(b) Spatial period distribution fitted to PDF

Figure 5.18: Spatial period distribution over samples of streamwise (u) and spanwise (v) fluctuations in cylinder-airfoil wake, at $Re = 2000$ and $Re = 8000$. Each class (group) in the histogram is normalised by the total number of samples.

Then, Figure 5.18b shows probability density function (PDF) of spatial periods (λ) at $Re = 2000$ and $Re = 8000$ within cylinder-airfoil wake. In Figure 5.18b, PDF show that 35% and 43% of samples indicate that λ measures $4.2D$ at $Re = 2000$ and $Re = 8000$, respectively. The decrease shown in histogram and PDF compared to cylinder wake, is due to the presence of the airfoil, and further position of autocorrelation profile from upstream cylinder.

5.3.2 Spatial autocorrelation average

In this section, average of spatial autocorrelation is computed over all samples. This helps to find the average spatial period (λ) in the wake of previous configurations.

Single and double cylinder wake

The average of spatial correlation within single and double cylinder wakes are reported in this section. Figures 5.19a and 5.19b present the average spatial autocorrelation within single and double cylinder wakes at two different Reynolds numbers ($Re = 2000$ and $Re = 8000$), respectively. Figure 5.19a reveals sinusoidal signals that represent the positions of coherent structures in the wake. Significantly, the autocorrelation coefficients

for spanwise fluctuations are higher than those for streamwise fluctuations, making spanwise fluctuations more suitable for computing the spatial period. The spatial periods are determined by measuring the distance between two peaks in the autocorrelation signal. The results in Figure 5.19a show that the spatial periods are approximately $4.2D$ for $Re = 2000$ and $4.5D$ for $Re = 8000$. This suggests that the Reynolds number has minimal influence on the spatial period in the cylinder wake.

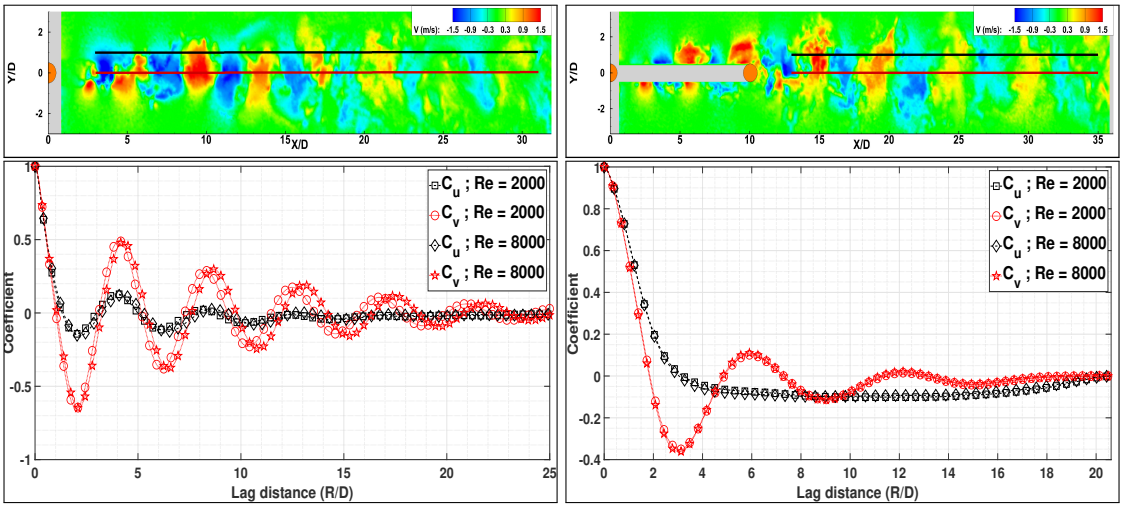

(a) Single cylinder wake

(b) Double cylinder wake

Figure 5.19: Spatial autocorrelation of streamwise (u) and spanwise (v) fluctuations in single and double cylinder wakes, at $Re = 2000$ and $Re = 8000$

On the other hand, Figure 5.19b shows a significant lower coefficient of autocorrelation on spanwise fluctuation compared to single cylinder, with no streamwise autocorrelation. Figure 5.19b shows that the mean spatial period (distance between peaks) increased to approximately $6.1D$ compared to single cylinder wake. This is referred to the decrease in coherent motion (CM) frequency behind second cylinder, see Equation 5.4. Where, U_{conv} is the convective velocity, λ is the spatial period and f_s is the shedding frequency of the vortices. The observations in single and double cylinder wake agreed with what is seen in Section 5.3.1.

$$U_{conv} = \lambda \times f_s \tag{5.4}$$

Single and double airfoil wake

This section discusses spatial correlation analyses conducted on single and double airfoil wakes. Figures 5.20a and 5.20b present the average spatial autocorrelations within single and double airfoil wakes at two different Reynolds numbers ($Re = 2000$ and $Re = 8000$), respectively. In Figure 5.20a, it is observed that the correlation coefficients at $Re = 2000$ are higher than those at $Re = 8000$, while the distances between the two correlation peaks for both spanwise and streamwise fluctuations remain approximately constant at around $0.76C$ (or $3.8D$). This consistency suggests that the spatial period remains unchanged with increased velocity, as the effect of the upstream wake is not considered.

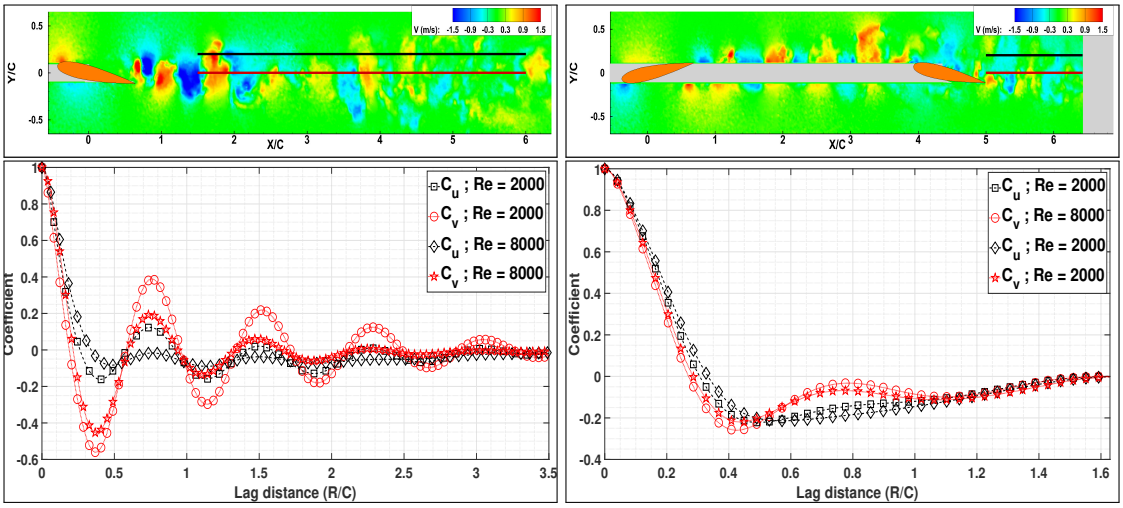

(a) Single airfoil wake

(b) Double airfoil wake

Figure 5.20: Spatial autocorrelation of streamwise (u) and spanwise (v) fluctuations in single and double airfoil wakes, at $Re = 2000$ and $Re = 8000$.

In contrast, Figure 5.20b shows significantly lower spatial correlation with only one peak compared to the single airfoil wake. This difference can be attributed to the shorter lag distance associated with the autocorrelation profile length. Consequently, the spatial period can be calculated as the distance between the first negative peak and the first positive peak, which corresponds to approximately $\lambda/2$. Thus, the spatial period is slightly decreased compared to the single airfoil wake, measuring approximately $0.7C$. The observations in single and double airfoil wake agreed with what is seen in Section 5.3.1.

Cylinder-airfoil wake

Spatial period of coherent motion in cylinder-airfoil wake is reported in this section. Figure 5.21 (left) presents the average spatial autocorrelations within cylinder-airfoil wakes at two different Reynolds numbers ($Re = 2000$ and $Re = 8000$). Figure 5.21 shows a spatial period measuring $4.2D$ which is similar to cylinder wake. This finding underscores that when the downstream obstacle is an airfoil, the wake characteristics downstream closely resemble those of the upstream wake. The observation in cylinder-airfoil wake agreed with what is seen in Section 5.3.1.

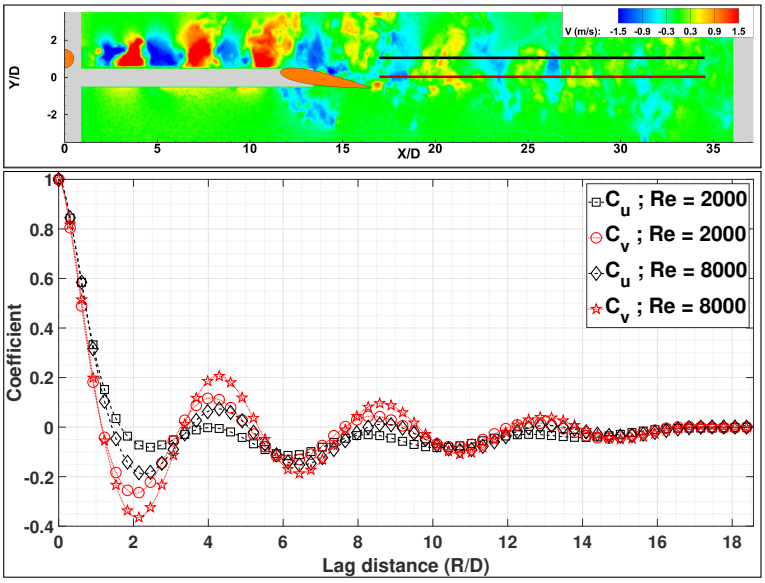

Figure 5.21: Spatial autocorrelation of streamwise (u) and spanwise (v) fluctuations in cylinder-airfoil wake, at $Re = 2000$ and $Re = 8000$.

5.3.3 Observations review and conclusions

In this chapter, temporal and spatial periods of coherent motion (CM) are investigated for five configurations. Figure 5.22 summarizes the spatial and temporal periods of coherent motion (CM) within aforementioned configurations. In Figure 5.22, temporal periods at $Re = 8000$ are lower compared to those at $Re = 2000$. Shedding frequencies of the coherent motions can be deduced by the inverse of these temporal periods ($f_s = 1/T$). The shedding frequencies of single cylinder and airfoil wake are compared to theoretical values of Table 3.2 and show good agreement. In Figure 5.22, one observes that spatial periods remains approximately constant in function of Reynolds number for the shown configurations. However, a small shift of spatial period occurred in cylinder wake between two Reynolds numbers. This shift can be attributed to the small changes in Strouhal number (St) at higher Reynolds number ($Re = 8000$). For example, a small changes in St leads to slight changes in spatial spacing between coherent structures. Figure 5.22 shows that, single and double airfoil wakes have a close and a smallest spatial periods compared to other wakes configurations. The small difference in spatial period is due to further distances downstream and lower energy in airfoil vortices. In double cylinder wake, the spatial period increased approximately to $6.1D$ compared to other wake configurations. This is referred to the decrease in coherent motion (CM) frequency behind second cylinder as discussed previously.

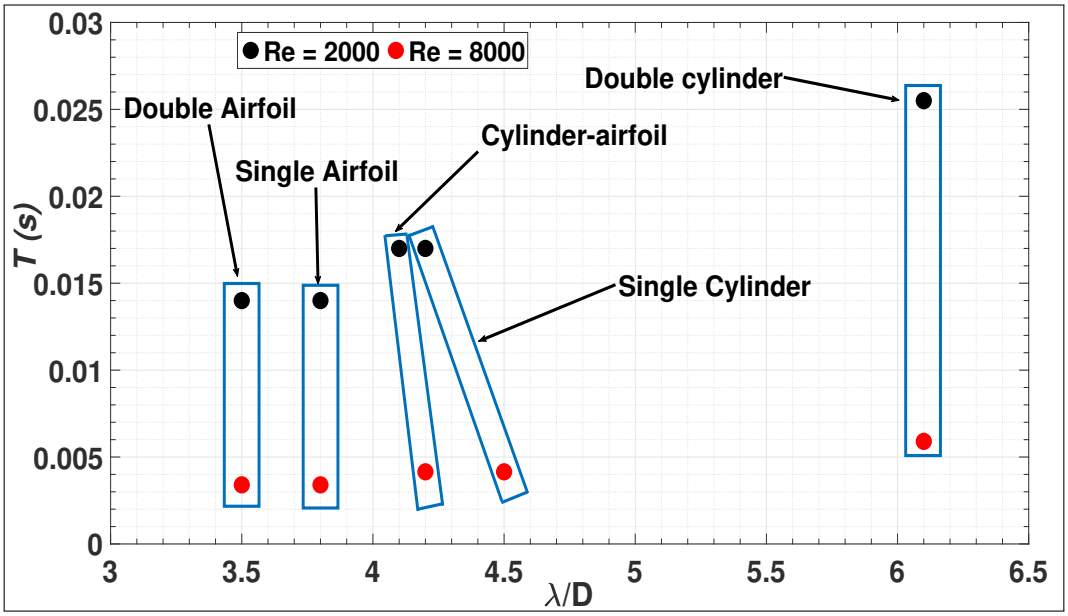

Figure 5.22: Temporal and spatial periods of coherent motion (CM) within wakes of five configurations and for both Reynolds numbers ($Re = 2000$ and $Re = 8000$).

Cross correlations between two positions in wakes are also studied in this chapter. They showed that lower correlation is occurred by moving downstream in wakes. This study showed also that coherent motion in airfoil wake deformed faster and have a lower life time compared to coherent motion in cylinder wake.

CHAPTER 6

Mechanism of energy exchange with no turbulence effect

Summary

As shown in Chapter 4, the wakes formed behind obstacles are characterized by a combination of coherent motion (CM) and random motion (RM). Coherent motion, reminiscent of the Von Kármán street, interacts with random motion, resulting in locally enhanced turbulent cascade. This energy exchange extends beyond just the mean flow and turbulent flow interaction; it also involves the interaction between coherent motion (CM) and random motion (RM) within the turbulent flow. This energy exchange between coherent motion (CM) and random motion (RM) is highlighted by the kinetic energy budget at one point in space. This chapter marks the first part of the experimental results obtained within the laminar wind tunnel. Consequently, the effects of three-dimensional turbulence or turbulent boundary layers are not considered. The focus is on evaluating the exchange of turbulent kinetic energy (TKE) as a function of the upstream flow. As a further simplification, the turbulent kinetic energy exchange is studied within single and double wakes to visualize the influence of the first obstacle on the downstream one. This is discussed by the presentation of various configurations that involve the combination of two primary obstacles, i.e. a 1 *cm* cylinder and a NACA 0015 airfoil.

Contents

6.1 First order statistics **104**
6.2 Total fluctuation energy exchanges **107**
6.2.1 2D - planes for total turbulent kinetic energy budget 107
6.2.2 Summary of total turbulent kinetic energy budget 112
6.2.3 Cross section profiles for total turbulent kinetic energy budget . 114
6.2.4 Decomposed total kinetic energy in phases 118
6.3 CM and RM interaction TKE **120**
6.3.1 2D - planes of coherent motion (CM) energy budget 120
6.3.2 Summary of coherent motion (CM) energy budget 126

6.3.3 Cross section profiles of coherent motion (CM) energy budget . 128
6.3.4 2D - planes of Random motion (RM) energy budget 133
6.3.5 Summary of random motion (RM) energy budget 139
6.3.6 Cross section profiles of random motion (RM) energy budget . 141
6.4 Observations, reviews, and conclusions **146**

6.1 First order statistics

First order statistics offer insights into the flow's overall behavior. They help in characterizing the flow's fundamental properties, such as its direction, magnitude, and distribution. This information is crucial for the mechanism of energy exchange. For instance, mean velocity profiles contribute to the calculation of turbulent kinetic energy, which quantifies the energy associated with turbulent fluctuations. Moreover, to ensure the quality of images acquired by Particle Image Velocimetry (PIV), it is essential to first examine lower-order statistics, such as the mean velocity field or the RMS. Figure 6.1 shows the mean velocity in the streamwise direction for both single and double airfoil wake configurations at a Reynolds number of 2000. It is observed that L2 (length of downstream wake) in Figure 6.1b is larger than L1 (length of upstream wake) in Figure 6.1b (L2 > L1). This is due to the lower upstream mean velocity of the second airfoil compared to the first airfoil.
Behind the upstream airfoil (Figure 6.1a), a recirculation zone with negative velocity is observed. This phenomenon is alike to what is typically observed in the wake of a cylinder, as reported in studies such as [87] and [70]. In contrast, when considering the downstream airfoil within an upstream wake, the recirculation zone disappears (Figure 6.1b). This suggests that the interaction between the downstream airfoil and the upstream wake create changes to the flow over the airfoil compared to the case of a single airfoil wake, i.e higher mean velocity over the downstream airfoil.

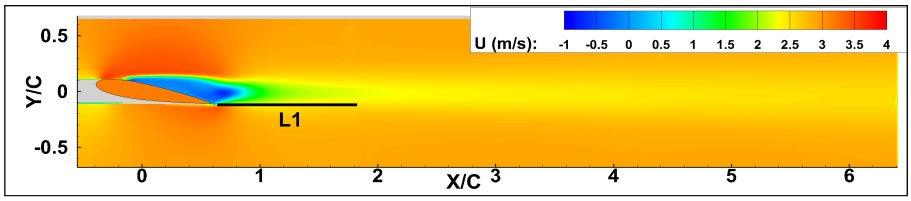

(a) Single airfoil wake.

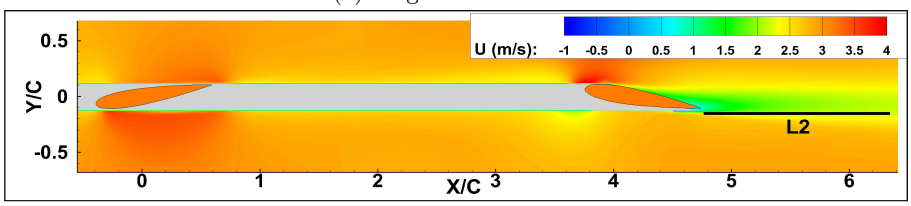

(b) Double airfoil wake.

Figure 6.1: Streamwise (X direction) mean velocity in single and double airfoil wake configurations.

Figure 6.2 shows the mean velocity in spanwise direction for both single and double airfoil wake configurations at $Re = 2000$. Between the two configurations, there is a slight difference in the distribution of spanwise velocity. The negative and positive spots observed behind the upstream airfoil (Figure 6.2a) disappear behind the downstream airfoil (Figure

6.2b). In other hand, a negative spanwise velocity is observed (Figure 6.2b) over the airfoil, which is not observed in the upstream airfoil. This suggests that the presence of the upstream airfoil modifies the spanwise velocity distribution compared to the single airfoil case.

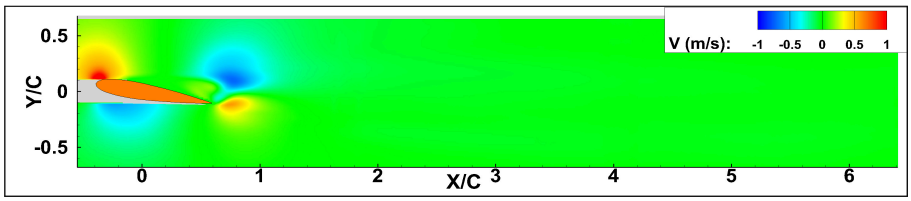

(a) Single airfoil wake.

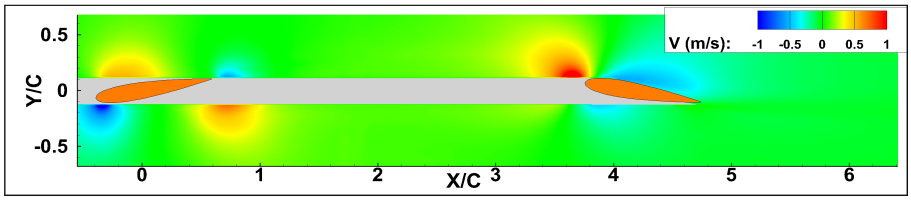

(b) Double airfoil wake.

Figure 6.2: Spanwise (Y direction) mean velocity in single and double airfoil wake configurations, at $Re = 2000$.

In the context of first-order statistics, the Root Mean Square (RMS) is computed to analyze maps of total fluctuations. Figure 6.3 shows the Root Mean Square (RMS) in the streamwise direction (X direction) for both single and double airfoil wake configurations at $Re = 2000$. In the case of the single airfoil wake (Figure 6.3a), the RMS exhibits significant values with peak magnitudes behind the airfoil. As one moves downstream, the RMS gradually decreases. However, the RMS values experience a re-increase over the downstream airfoil, as shown in double airfoil wake configuration (Figure 6.3b).

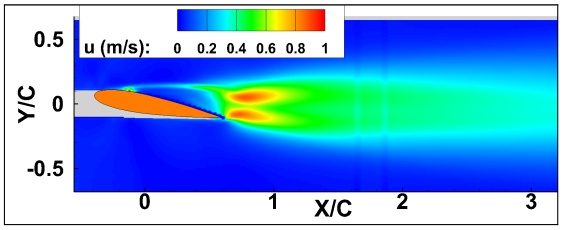

(a) Single airfoil wake.

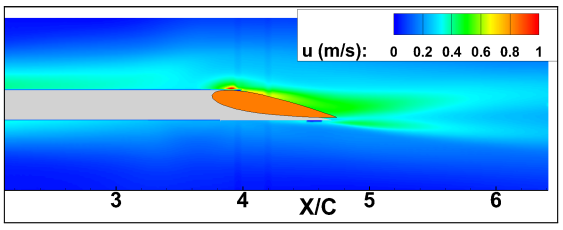

(b) Double airfoil wake.

Figure 6.3: RMS of streamwise velocity (X direction) in single and double airfoil wake configurations, at $Re = 2000$.

Figure 6.4 shows the RMS in the spanwise direction (Y direction) for both single and double airfoil wake configurations at $Re = 2000$. In single airfoil wake configuration (Figure 6.4a), one observes that the RMS in the spanwise direction shows higher values compared to Figure 6.3a. This is attributed to higher total fluctuations in spanwise direction behind the airfoil. However, In the case of double airfoil wake configuration (Figure 6.4b), the RMS shows lower magnitudes than that observed in Figure 6.3b over the airfoil.

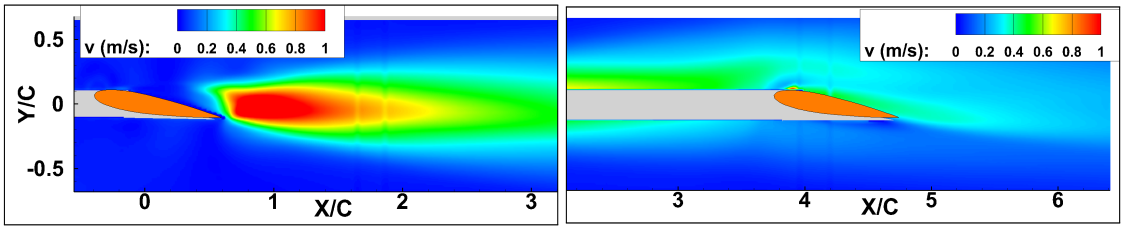

(a) Single airfoil wake.

(b) Double airfoil wake.

Figure 6.4: RMS of spanwise velocity (Y direction) in single and double airfoil wake configurations, at $Re = 2000$.

This chapter is focused on the previous configurations, single and double airfoil configurations. However, other configurations such single, double cylinder and cylinder-airfoil wake configurations are briefly reported for later illustrations in this chapter. Figures 6.5a and 6.5b show the mean velocity in streamwise (X) and spanwise (Y) directions within single cylinder wake configuration at $Re = 2000$, respectively. Figures 6.5c and 6.5d show the mean velocity in streamwise (X) and spanwise (Y) directions within double cylinder wake configuration at $Re = 2000$, respectively. Figure 6.5c shows that the wake behind the downstream cylinder becomes wider compared to single cylinder wake (Figure 6.5a). This is attributed to the existence of the downstream cylinder that increase the velocity deficit downstream.

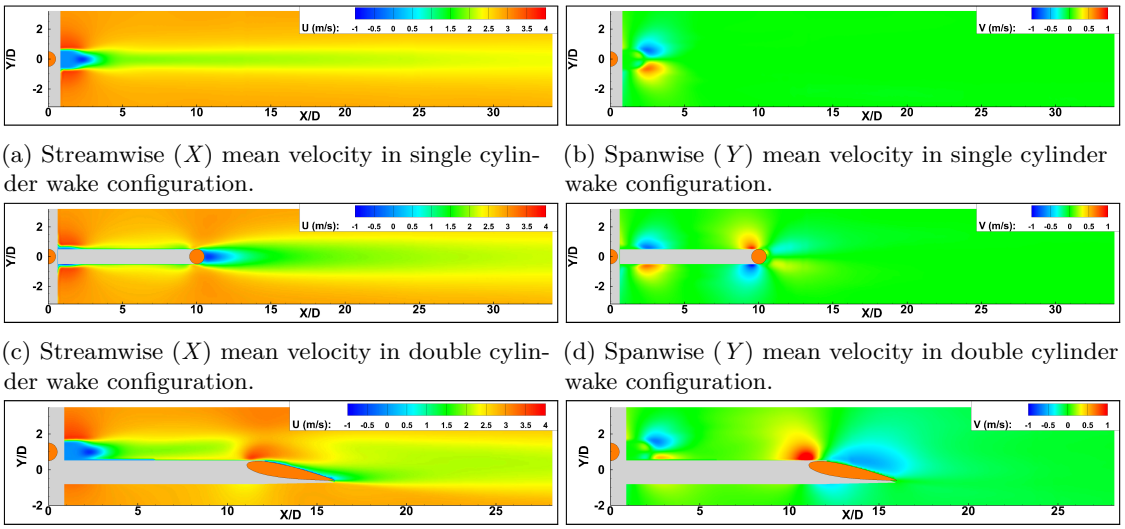

(a) Streamwise (X) mean velocity in single cylinder wake configuration.

(b) Spanwise (Y) mean velocity in single cylinder wake configuration.

(c) Streamwise (X) mean velocity in double cylinder wake configuration.

(d) Spanwise (Y) mean velocity in double cylinder wake configuration.

(e) Streamwise (X) mean velocity in cylinder-airfoil wake configuration.

(f) Spanwise (Y) mean velocity in cylinder-airfoil wake configuration.

Figure 6.5: Streamwise and spanwise (X and Y direction) mean velocity in single and double cylinder, cylinder-airfoil wake configurations.

Figures 6.5e and 6.5f show the mean velocity in streamwise (X) and spanwise (Y) directions within cylinder-airfoil wake configuration at $Re = 2000$, respectively. In Figure 6.5e, one observes that the streamwise velocity is significantly low inside the wake except at the leading edge. This is due to the acceleration of the flow over the leading edge of the airfoil.

6.2 Total fluctuation energy exchanges

The leading studies on turbulent kinetic energy equations can be attributed to the work of Osborne Reynolds [7]. Reynolds investigated the exchange of energy related to total fluctuations, including both fluctuations: Coherent fluctuations or motion (CM) and Random fluctuations or motion (RM). The transport equation illustrates the dynamics and characteristics of turbulence in the flow at a specific location (i.e one point equation). This is reported in Equation 6.1, which provides insights into the nature and mechanisms of turbulence. However, Equation 6.1 is different from Reynolds stress transport equation which permits identifying the mechanism of transport of individual Reynolds stress terms [88]. Equation 6.1 is essential to understand the behavior of turbulence at a given point in the flow. In Equation (6.1), U_i is the mean velocity along the i_{th} direction. Term u_i represent the fluctuations of the instantaneous velocity field along the i_{th} direction. q^2 represents the kinetic energy, computed with the axisymmetry hypothesis $(2u^2 + v^2)$, consequent from higher magnitude of v component compared to other components, see Thiesset [70]. Finally, ϵ is the turbulent kinetic energy dissipation rate.

$$\underbrace{\left(\overline{u_i u_j}\frac{\partial \overline{U_i}}{\partial x_j}\right)}_{\textbf{Production}} + \underbrace{\left(\overline{U_j}\frac{\partial(\overline{0.5q^2})}{\partial x_j}\right)}_{\textbf{Advection}} + \underbrace{\left(\underbrace{\frac{\partial \overline{pu_j}}{\partial x_j}}_{\textbf{by pressure}} + \underbrace{\frac{\partial(\overline{0.5q^2u_j})}{\partial x_j}}_{\textbf{by turbulence}}\right)}_{\textbf{Diffusion}} + \underbrace{\bar{\epsilon}}_{\textbf{Dissipation}} = 0. \quad (6.1)$$

The TKE transport equation contains four main terms (Production, Advection, Diffusion and Dissipation). Production of turbulent energy is the initial term at left hand side, and will be greatest near the positions of maximum shear and significant degree of anisotropy ($\overline{v^2}/\overline{u^2} > 1$ or $\overline{u^2}/\overline{v^2} > 1$). The second term of the equation is the advection, or the transport of the fluctuations due to mean velocity. It represents the exchange of turbulent kinetic energy between distinct zones within the wake. In general, the energy exchange involves either a loss or a gain at a specific point in the flow field. The third term is the diffusion, which is divided into diffusion due to pressure and diffusion due to turbulence. Turbulent diffusion term explains how the turbulent kinetic energy is diffused from locations where turbulence is produced, to other places where production is smaller, or absent. The last term is the dissipation (occurring at smallest scales, or Kolmogorov scales), and reflects the work done by smallest eddies against viscous stresses. Dissipation is conventionally considered positive (loss > 0), thus production term becomes negative (gain < 0). In this framework, each term of the equation was assessed to perceive the mechanism of turbulent kinetic energy (Production - Transport - Dissipation).

6.2.1 2D - planes for total turbulent kinetic energy budget

This section shows total turbulent kinetic energy budget terms in single and double airfoil wake configurations. Errors in velocity gradient computations that originate from the absence of data in obstacles zones and their shadow zone are not treated. These errors are particularly at the borders of these zones.

Production

Production signifies the transfer of kinetic energy between the mean flow and turbulent fluctuations within the fluid. This energy exchange typically results in a reduction of

kinetic energy in the mean flow and an increase in the kinetic energy associated with turbulence. Figures 6.6a and 6.6b show the production term maps in single and double airfoil wake configurations at $Re = 2000$, respectively (see Sections D.4.2 and E.5.2 for higher Reynolds number). The production is observed in regions where maximum shear of the mean velocity takes place, represented by $\overline{uv}(\frac{\partial \overline{U}}{\partial Y} + \frac{\partial \overline{V}}{\partial X})$. Additionally, production is observed where the maximum level of anisotropy occurs, expressed as $(\overline{u^2} - \overline{v^2})\frac{\partial \overline{U}}{\partial X}$. In the wake of a single airfoil, the production of vortices initiates slightly over the airfoil and extends downstream for a distance equivalent to one chord length ($1X/C$). The negative sign associated with this phenomenon signifies that there is an energy gain to turbulence. In contrast, in the wake of a double airfoil configuration, the process of vortex production of downstream airfoil starts earlier, closer to the leading edge, and continues until it approaches the vicinity of the airfoil's trailing edge. This observation suggests that the wake generated by the upstream airfoil influence the separation point of vortex shedding from the downstream airfoil, and enhances the aerodynamic stall. The small positive line over the leading edge is due to an error in velocity gradient computations, originate from the absence of data in the airfoil zone and the shadow between both airfoils.

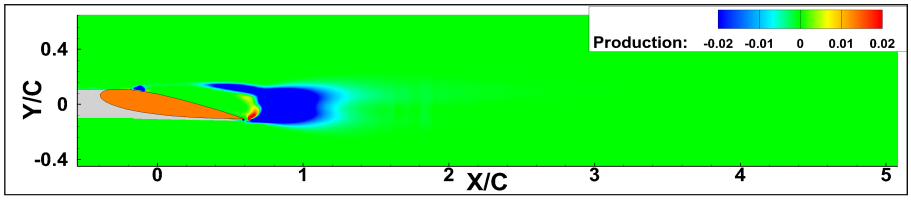

(a) Single airfoil wake.

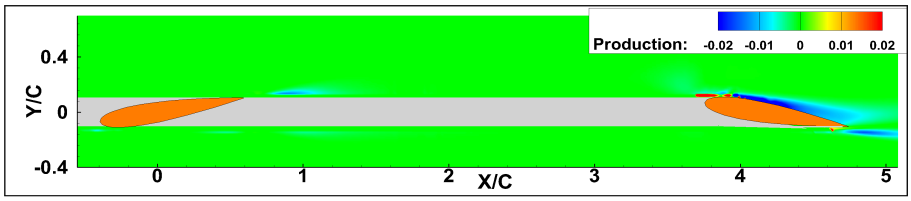

(b) Double airfoil wake.

Figure 6.6: Production $\overline{u_i u_j}\frac{\partial \overline{U_i}}{\partial x_j}$ of total turbulent kinetic energy by mean velocity in single and double airfoil wake at $Re = 2000$. Terms are normalised by U_0^3/D.

Advection

Advection refers to as the phenomenon where fluctuations are transported along by the mean flow of the fluid. This phenomenon captures how the mean velocity field transports turbulent kinetic energy from one location to another within the fluid. Figures 6.7a and 6.7b show the advection term in single and double airfoil wakes at $Re = 2000$, respectively (see Sections D.4.2 and E.5.2 for higher Reynolds number). These figures illustrate that advection is a bidirectional term, exhibiting both positive (indicative of loss) and negative (indicative of gain) advection. The positive advection signifies a loss of fluctuations from this location, while the negative advection represents a gain of the transported fluctuations as influenced by the mean flow of the fluid. In the case of the single airfoil wake, the advection reaches its maximum values at the wake's onset and along its periphery (shear zones), primarily influenced by the prevailing mean velocity. However, within the central region of the airfoil wake, the advection is negative, indicating a zone where the influence of the mean velocity is relatively low and reversed.

In the case of the double airfoil wake, particularly when concentrating on the downstream airfoil, advection achieves high values primarily around the leading edge and in close zone to the trailing edge of the airfoil. Conversely, at the central zone over the the airfoil itself, the influence of the mean velocity appears to be relatively low. This results in an airfoil's boundary layer with a weak reversal flow over the downstream airfoil.

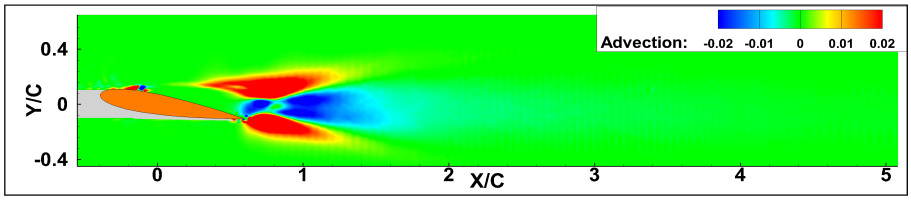

(a) Single airfoil wake.

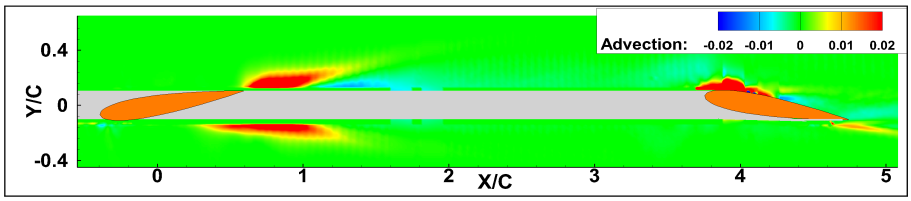

(b) Double airfoil wake.

Figure 6.7: Advection $\overline{U_j}\frac{\partial(\overline{0.5q^2})}{\partial x_j}$ of total kinetic energy by mean flow in single and double airfoil wakes at $Re = 2000$. Terms are normalised by U_0^3/D.

Dissipation

Dissipation describes the process of converting kinetic energy into heat within a fluid due to viscosity. It particularly exists in regions where high shear and strain rate occur. As our analysis is based upon 2D-2C PIV, terms involving derivatives in the third direction are not available. For instance, it is well known that the energy dissipation rate is underestimated. Other methods are to be used to assess a corrected value of this quantity. The dissipation rate is first computed by Equation (6.2), and then corrected using Chen & Zhou [89] data to get access to the non-resolved data, as in the cylinder wake configuration, see Armaly [71].

$$\epsilon_{PIV} = \gamma \left[8\overline{\left(\frac{\partial u}{\partial x}\right)^2} + 2\overline{\left(\frac{\partial u}{\partial y}\right)^2} + 2\overline{\left(\frac{\partial v}{\partial x}\right)^2} - \overline{\left(\frac{\partial v}{\partial y}\right)^2} \right]. \tag{6.2}$$

The dissipation rate ϵ_{PIV} (computed from PIV data) is much smaller than the values of ϵ estimated with hot wire anemometry (Chen & Zhou [89]). Therefore, a correction is applied to ϵ_{PIV} to reach the values reported by Chen & Zhou [89] for the same flow, and for the same Reynolds number. However, it's important to note that this method is effective only within the wake of a cylinder and under specific Reynolds number conditions. To address this shortcoming, an alternative approach involving coefficient correction is employed. This can be illustrated by considering that the diffusion terms tend to approach zero as the entire flow field is integrated. As the PIV field becomes larger, this integration progressively reaches zero, as demonstrated in Equation 2.49. In agreement with this hypothesis, Equation 6.3 is derived, as in Thiesset [70]. Then coefficients α_{PIV} are computed for different Reynolds numbers, Table 6.1.

$$\int_{(x,y)} \left(\overline{U_j} \frac{\partial(\overline{0.5q^2})}{\partial x_j} + \overline{u_i u_j} \frac{\partial \overline{U_i}}{\partial x_j} \right) dxdy = - \int_{(x,y)} \bar{\epsilon}\, dxdy \tag{6.3}$$

$$\alpha_{PIV} = - \frac{\int_{(x,y)} \left(\overline{U_j} \frac{\partial(\overline{0.5q^2})}{\partial x_j} + \overline{u_i u_j} \frac{\partial \overline{U_i}}{\partial x_j} \right) dxdy}{\int_{(x,y)} \bar{\epsilon}\, dxdy} \tag{6.4}$$

Used coefficients for dissipation correction		
Re	2000	8000
α_{PIV}	2.24	7.60

Table 6.1: Coefficients α_{PIV} as a function of Reynolds numbers.

Figures 6.8a and 6.8b show the dissipation term in single and double airfoil wake, respectively (see Sections D.4.2 and E.5.2 for higher Reynolds number). It is observed in Figure 6.8a that the dissipation reaches maximum value at the center line of the wake. The dissipation is maximum where higher strain and shear occur, reflecting the conversion of turbulent kinetic energy into thermal energy at smaller scales. This term is consistently positive and is interpreted as a loss of energy within the turbulent flow.

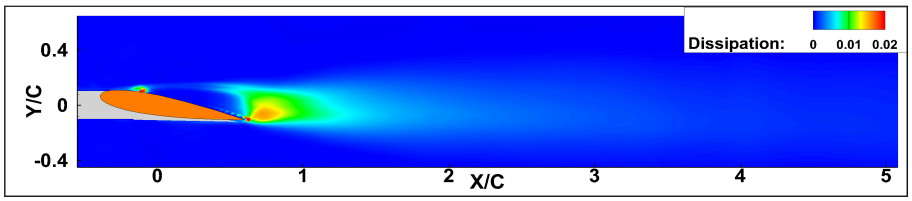

(a) Single airfoil wake.

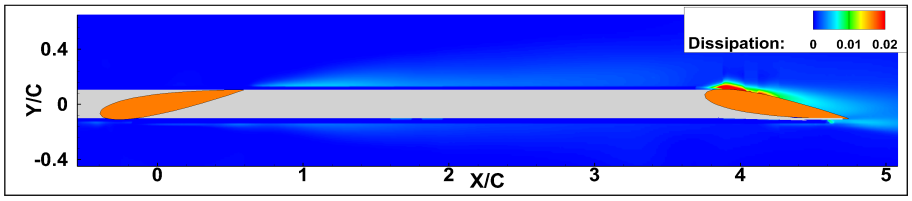

(b) Double airfoil wake.

Figure 6.8: Dissipation $\bar{\epsilon}$ of total turbulent kinetic energy in single and double airfoil wake at $Re = 2000$. Terms are normalised by U_0^3/D.

In the wake of a single airfoil, the highest levels of dissipation occur at the trailing edge of the airfoil and up to one chord length ($X/C < 1$) downstream. In the case of a double airfoil wake, the peak of dissipation shifts to the area above the leading edge of the airfoil due to the presence of the upstream wake. The upstream wake has the effect of reducing dissipation downstream of the second airfoil, while simultaneously strengthening dissipation over the airfoil itself. This change in dissipation patterns is a result of the complex interactions between the wakes of the two airfoils in close proximity.

Diffusion

Diffusion is defined where fluctuations are transported due to stresses (fluctuations). Diffusion is decomposed into two different components: diffusion done by Reynolds stresses (turbulence) and diffusion driven by the pressure stresses (pressure fluctuations). Figures 6.9a and 6.9b show the diffusion through turbulence in single and double airfoil wake configurations at $Re = 2000$, respectively, (see Sections D.4.2 and E.5.2 for higher Reynolds number).

In the wake of a single airfoil, turbulent diffusion is more pronounced at the center of the wake, where turbulent stresses are at their maximum, leading to a substantial loss (positive) of turbulent energy from the center wake zone. Conversely, at the periphery of the wake, turbulent diffusion is negative due to gain of turbulent fluctuations at this zone arriving from the center wake for instance. In the case of a double airfoil wake, turbulent diffusion exhibits distinct characteristics. Above the airfoil, the boundary layer is marked by a positive diffusion pattern due to the concentration of turbulent stresses in this region. However, immediately above this turbulent layer, there is a thinner negative diffusion layer, primarily attributed to the influence of mean velocity.

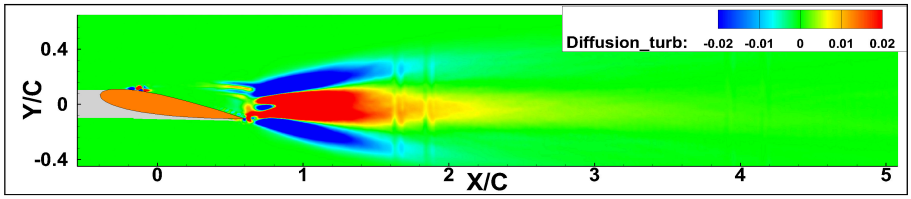

(a) Single airfoil wake.

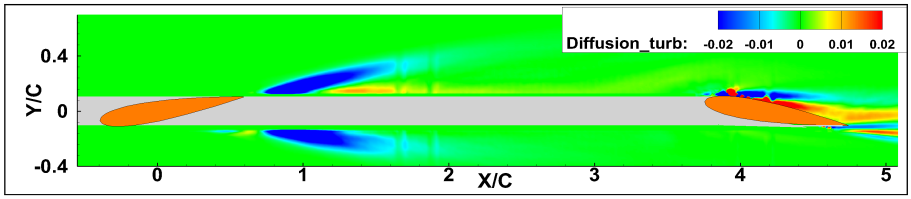

(b) Double airfoil wake.

Figure 6.9: Diffusion $\frac{\partial(\overline{0.5q^2u_j})}{\partial x_j}$ of total kinetic energy by turbulence in single and double airfoil wakes at $Re = 2000$. Terms are normalised by U_0^3/D.

In other hand, pressure field is not available from experimental data, therefore the pressure-diffusion term cannot be calculated. This term is estimated by balancing the TKE equation. Diffusion through pressure is thus determined from the budget equation, by considering that all the other terms are correctly evaluated. Figures 6.10a and 6.10b depict the diffusion through pressure in single and double airfoils wake at $Re = 2000$, respectively, (see Sections D.4.2 and E.5.2 for higher Reynolds number). This term in turn indicate the transport of the fluctuations through pressure stresses.

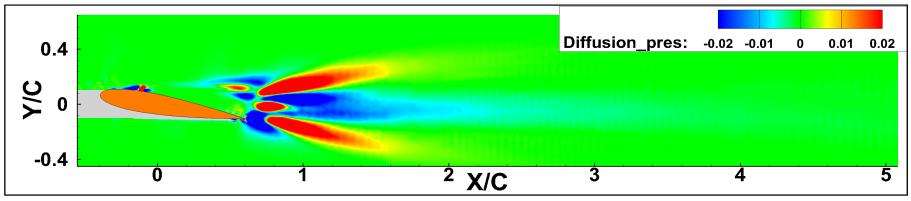

(a) Single airfoil wake.

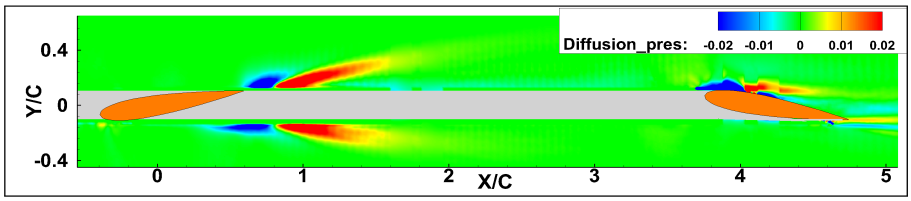

(b) Double airfoil wake.

Figure 6.10: Diffusion $\frac{\partial \overline{pu_j}}{\partial x_j}$ of total kinetic energy by pressure in single and double airfoil wakes at $Re = 2000$ (estimated). Terms are normalised by U_0^3/D.

In single airfoil wake, particularly closer to the airfoil body (near-wake region), there is often an out of phase correlation between velocity and pressure fluctuations. When the flow velocity is higher (positive fluctuations), the pressure tends to be lower (negative fluctuations), and vice versa. This out of phase correlation is associated and reinforced with vortex shedding (periodic alternation of low and high-pressure regions) behind the bluff body as shown by Obi [90]. Combining both turbulent and pressure diffusion terms, one obtain a pattern resembling the advection term but with an inverted sign. This phenomenon can be explained by pressure diffusion significant role near the airfoil, resulting in negative contributions (opposite to advection). Tsai's work [91] supports this observation by showing very high correlation coefficients (negative) between pressure and velocity fluctuations near bluff bodies. Turbulent diffusion, on the other hand, makes positive contributions closer to the center of the wake opposite to pressure contribution far from the airfoil. This observation is supported by Lumley [92], where turbulent diffusion is opposed by pressure diffusion in homogeneous turbulence.

In the case of a double airfoil wake, energy transport through pressure diffusion occurs over the blade. This term is considered as a loss (positive) of energy at the middle zone over the airfoil and a gain (negative) at the leading edge (opposite to advection).
To conclude, all terms appear to be important for the first chord length downstream first airfoil, and are closely symmetric with respect to the center line of the wake. The terms exhibit zero values in a region over the airfoil (single airfoil wake), that represents the recirculation zone. The two main terms, advection and diffusion appear to be complementary. The positive regions in advection terms, become negative in diffusion terms and *vice versa*. This shows the conversion from the transport of the kinetic energy of the mean velocity to the transport of the kinetic energy by the fluctuation quantities.

6.2.2 Summary of total turbulent kinetic energy budget

To summarize, gain and loss of energy fluctuations between the terms of total turbulent kinetic energy budget are reported. These are shown in different zones for different wake configurations at $R = 2000$. **Gain** and **loss** of energy fluctuations for each term are explained as follows:

- Production by the mean flow is recognized as a continuous **gain** of energy for

turbulent structures.

- Advection by the mean flow is seen as a **loss** when it involves the transfer of energy fluctuations by the mean flow form a particular zone in the direction of the flow (positive effect). Conversely, it is considered a **gain** when it results a transfer of energy fluctuations to particular zone (negative values).
- Diffusion terms transfer energy fluctuations via Reynolds stresses and pressure stresses from particular zone, resulting in **loss** (positive values). However, diffusion terms are considered **gain** when the energy is transferred to particular zone (resulting in negative values.
- Dissipation represents a continuous **loss** of energy fluctuations, which dissipate into heat.

Detailed explanations and descriptions of these terms can be found in Table 6.2, where the correspondent zones are illustrated in Figure 6.11. The abbreviations C, CC, CA, A, and AA stand for cylinder, double cylinders, cylinder-airfoil, airfoil, and double airfoils configurations, respectively. The number following these abbreviations indicates the zone number.

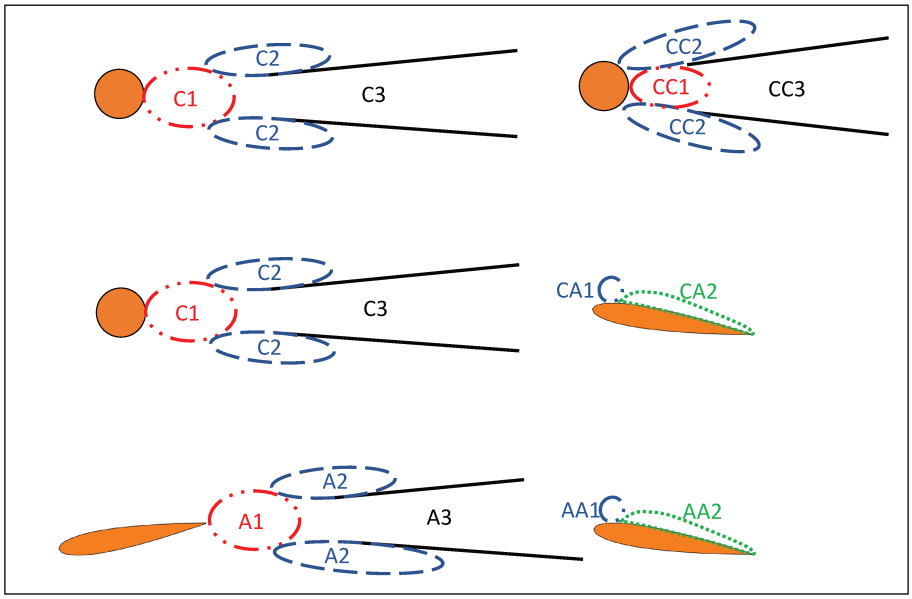

Figure 6.11: Zones in the wakes of single and double cylinder, single and double airfoil, and cylinder-airfoil configurations.

Gain and lost zones in wakes					
Zone	Production	Advection	Turbulence diffusion	Pressure diffusion	Dissipation
C1	gain	gain & loss	gain & loss	gain & loss	loss
C2	-	loss	gain	loss	loss
C3	-	gain	loss	gain	loss
CC1	-	gain	gain & loss	gain & loss	loss
CC2	gain	loss	gain	loss	loss
CC3	-	gain	loss	gain	loss
A1	gain	gain & loss	gain & loss	gain & loss	loss
A2	-	loss	gain	loss	loss
A3	-	gain	loss	gain	loss
CA1	-	loss	gain	loss	loss
CA2	gain	gain	loss	gain	loss
AA1	-	loss	gain & loss	gain	loss
AA2	gain	gain	gain & loss	loss	loss

Table 6.2: Gain and lost in wakes for total turbulent kinetic energy.

6.2.3 Cross section profiles for total turbulent kinetic energy budget

Cross section profiles of total turbulent kinetic energy are studied for the given wake configurations.

Single and double airfoil wake

Figures 6.12a and 6.12b provide profiles along the Y direction at positions $X/C = 1.6$ and $X/C = 5.6$ for both single and double airfoil wakes, respectively. The profiles are reported at locations 5 cm behind the upstream airfoil ($X/C = 1.6$) and 5 cm behind the downstream airfoil ($X/C = 5.6$). Two Reynolds numbers based on a 1 cm cylinder diameter are studied. In the wake of a single airfoil, Figure 6.12a shows that advection and turbulent diffusion exhibit nearly similar traces but with opposite signs (previously discussed). Pressure diffusion exhibits the same sign as advection and is considered a gain downstream the airfoil wake. This contrasts with turbulent diffusion, where the sign is opposite, implying a loss of energy. The dissipation is maximum at the center line of the airfoil wake and gradually decreases. The production is zero at the center line and maximum within high shear regions in downstream wake. This is in agreement with the previous studies of Townsend [9] performed at higher Reynolds number (8400) in cylinder wake using hot wire anemometry. It is important to highlight that with increasing Reynolds numbers, certain terms may experience unexpected reductions. This can be attributed to the changes in aerodynamic characteristics and flow patterns around the airfoil modifying the magnitudes of certain terms.

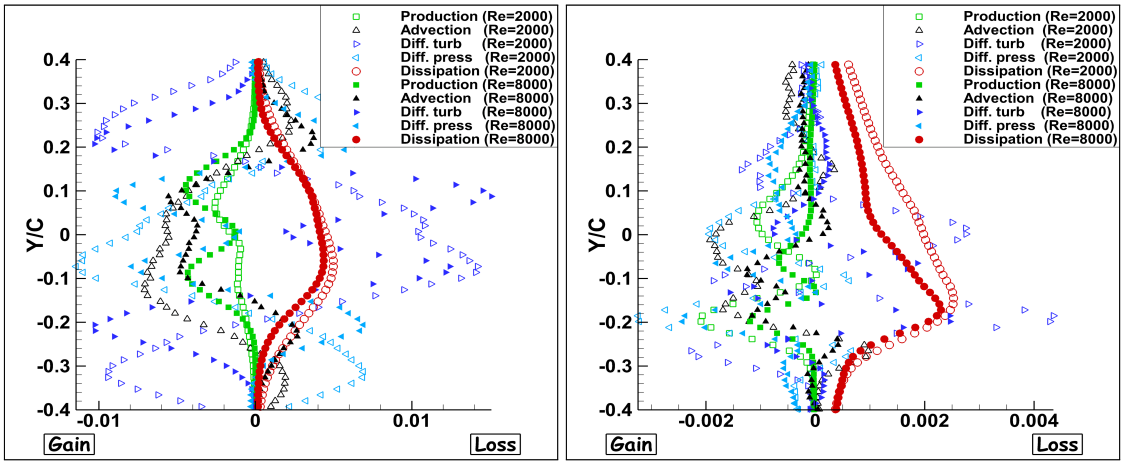

(a) Profiles 5 *cm* behind the airfoil ($X/C = 1.6$), in single airfoil configuration.

(b) Profiles 5 *cm* behind downstream airfoil ($X/C = 5.6$), in double airfoil configuration.

Figure 6.12: Total turbulent kinetic energy terms in single and double airfoil wake for two Reynolds number ($Re = 2000$ and $Re = 8000$). Terms are normalised by U_0^3/D.

In the double airfoil wake (Figure 6.12b), all terms, both at low and high Reynolds numbers, are lower compared to the single airfoil wake case. This reduction can be attributed to the lower energy production in the double airfoil configuration. In this configuration, the exchange of energy terms exhibits higher amplitudes, or peaks, at the trailing edge of the downstream airfoil (located at $Y/C = -0.2$), while lower magnitudes are observed at the leading edge. This difference between the energy exchange at both edges results in different profiles behavior (loss of symmetry between edges) compared to the wake of a single airfoil.
Figures 6.13a and 6.13b show profiles along the Y direction at two specific positions: $X/C = 0.3$ and $X/C = 4.3$, respectively, for both single and double airfoil wake configurations. The profiles initiate at the surface of the airfoil and extend out of the wake, where the positions over the airfoils are $0.6C$ (60% of chord length) referring to the leading edge in X direction. In the absence of an upstream wake and at high Reynolds number, production and turbulent diffusion terms above the airfoil exhibit higher values compared to other terms, where most of the energy is transported by turbulent stresses from this zone (loss). In this context, energy production is compensate by the turbulent diffusion term, resulting in a situation where production and diffusion are approximately equal. The contributions from other terms over the airfoil are minimal. With the presence of an upstream wake, the maxima of all the terms are shifted towards the surface of the airfoil, as shown in Figure (6.13b). This observation indicates that the layer above the airfoil (energy transfer occurs) is amplified, and the energy transfer mechanism becomes more pronounced. Production and diffusion experience significant reductions, and all terms converge to zero values at a position of $0.15Y/C$. It also shows that terms at low Reynolds number have slightly higher values than those at higher Reynolds due to lower effect of upstream mean velocity, opposed to what happened in single airfoil wake. In summary, the presence of an upstream airfoil wake leads to essential changes in the energy distribution and transfer mechanisms above the airfoil, resulting in decreased energy production, reduced diffusion, and a more balanced distribution of terms in the energy equation.

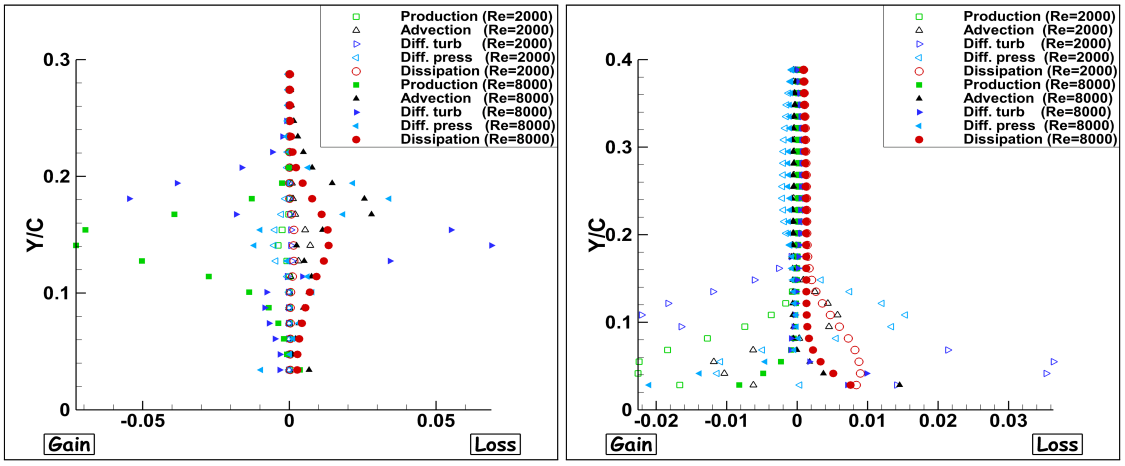

(a) Profiles at $X/C = 0.3$ over the airfoil, in single airfoil configuration.

(b) Profiles at $X/C = 4.3$ over downstream airfoil, in double airfoil configuration.

Figure 6.13: Total turbulent kinetic energy terms in single and double airfoil wake for two Reynolds number ($Re = 2000$ and $Re = 8000$. Terms are normalised by U_0^3/D.

Single and double cylinder wake

Cylinders wakes are also studied to allow a comparative analysis. Figures 6.14a and 6.14b provide profiles along the Y direction at positions $X/D = 5$ and $X/D = 15$ for both single and double cylinder wakes, respectively. These profiles are extracted at a location 5 cm behind both the upstream and downstream cylinders. The profiles correspond to two different Reynolds numbers based on a 1 cm cylinder diameter.

In the wake of a single cylinder (Figures 6.14a), the terms related to advection and diffusion (turbulence and pressure) are completely opposite in sign, while exhibit only slight differences in magnitude. When comparing low and high Reynolds numbers, all terms tend to be slightly higher at low Reynolds number except dissipation (higher at $Re = 8000$). This slight difference is due to smaller recirculation zone at $Re = 8000$ resulting in more contracted wake (shifted upstream). However, when the wake of an upstream cylinder is added (Figures 6.14b), some changes are remarked. Energy transport by advection decreases due to the reduction of mean velocity at the center of the wake. All terms tend to converge to similar magnitudes. This uniformity arises because, behind the second cylinder, the recirculation zone becomes negligible for both Reynolds number cases and the wake geometry pattern remains the same. The upstream wake contributes to the decreased production of vortices downstream of the second cylinder. Furthermore, the presence of the upstream cylinder wake significantly reduces the dissipation of energy at both Reynolds number, as shown in Figure 6.14b, (see Section B.2.2).

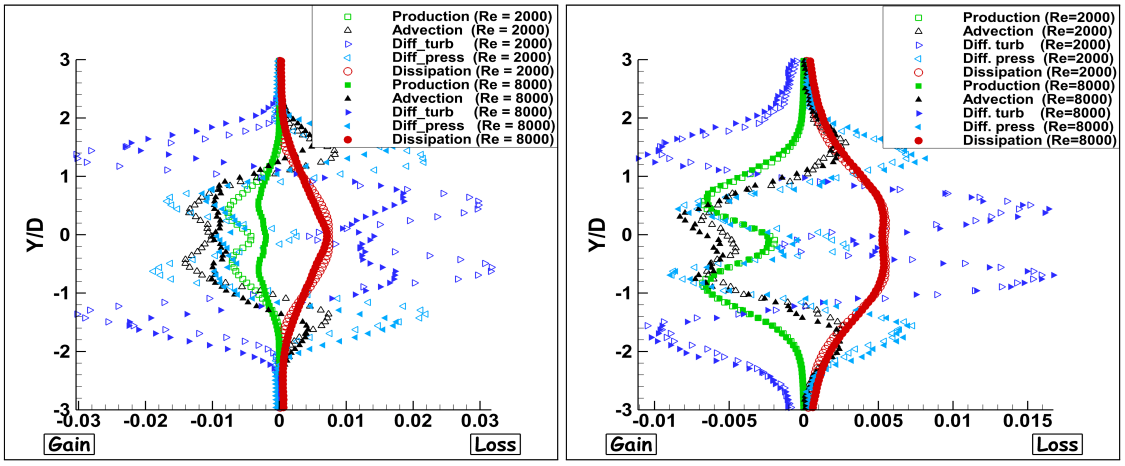

(a) Profiles 5 cm behind the cylinder ($X/D = 5$), in single cylinder configuration.

(b) Profiles 5 cm behind downstream cylinder ($X/D = 15$), in double cylinder configuration.

Figure 6.14: Total turbulent kinetic energy terms in single and double cylinder wake for two Reynolds number ($Re = 2000$ and $Re = 8000$). Terms are normalised by U_0^3/D.

Energy term comparisons can also be extended to positions further downstream in the wake. For instance, Figures 6.15a and 6.15b present profiles along the Y direction at locations $X/D = 15$ and $X/D = 25$ for both single and double cylinder wakes, respectively. By moving 10 cm downstream, single cylinder wake maintains the general shape of energy transfer profiles between the terms, however with reduced magnitudes (i.e dissipation reductions: $\approx 5.5 \times 10^{-3}$ for $Re = 2000$; $\approx 4.5 \times 10^{-3}$ for $Re = 8000$). In contrast, the double cylinder wake displays different shape of the energy profiles, which become wider and gradually approaches zero outside the wake region. This transformation indicates a widening in energy exchange within the downstream wake (double cylinder configuration) instead of being concentrated at the center of wake (single cylinder configuration). Magnitude reductions of all terms are observed by moving downstream in double cylinder wake configuration is also accompanied with (i.e dissipation reductions: $\approx 4 \times 10^{-3}$ for $Re = 2000$; $\approx 3.5 \times 10^{-3}$ for $Re = 8000$).

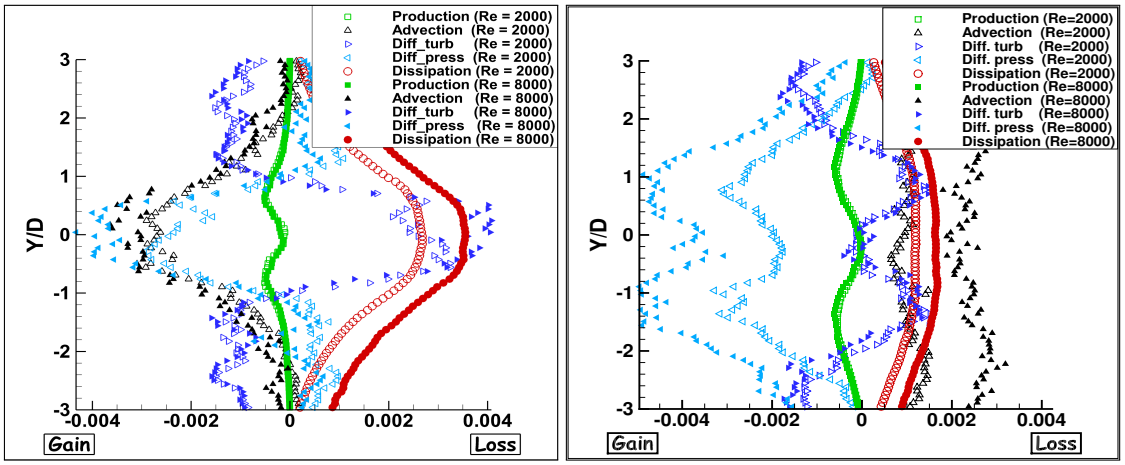

(a) Profiles 15 cm behind first cylinder ($X/D = 15$), in single cylinder configuration.

(b) Profiles 15 cm behind downstream cylinder ($X/D = 25$), in double cylinder configuration.

Figure 6.15: Total turbulent kinetic energy terms in single and double cylinder wake for two Reynolds number ($Re = 2000$ and $Re = 8000$). Terms are normalised by U_0^3/D.

Cross section profiles in cylinder-airfoil configuration

The turbulent kinetic energy terms for the cylinder-airfoil configuration are also reported. These data are valuable for conducting further comparative analyses among various flow configurations. Figure 6.16a shows profiles along Y direction at position 5 cm downstream an airfoil placed in cylinder wake. In this setup (particularly where the airfoil is the downstream obstacle), all energy terms exhibit significant reductions (i.e dissipation reductions: $\approx 2 \times 10^{-3}$ for $Re = 2000$; $\approx 2 \times 10^{-3}$ for $Re = 8000$) when compared to the double cylinder wake. In Figure 6.16a, one observes a sudden increase in advection and diffusion (pressure) terms at $Y/D = 1$ that corresponds to the energy arising from the upstream wake (cylinder). Figure 6.16b shows profiles along Y direction over the airfoil surface, specifically at a distance $0.6C$ ($X/D = 14$) from the leading edge in cylinder-airfoil configuration. A small bump is observed in the profiles of Figure 6.16b. This bump is attributed to the presence of a thick layer of high advection over the blade, which extends downstream the airfoil. In the bump region, the highest values are associated with advection and turbulent diffusion, as highlighted in Figure 6.16b. (see Section C.3.2)

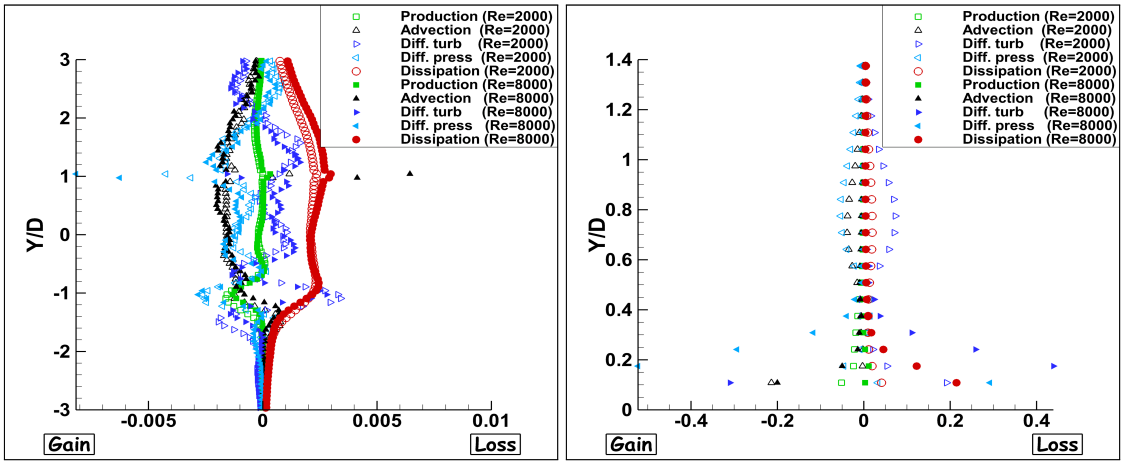

(a) Profiles 5 cm downstream the airfoil ($X/D = 21$), in cylinder-airfoil configuration.

(b) Profiles at $X/D = 14$ over downstream airfoil, in cylinder-airfoil configuration.

Figure 6.16: Total turbulent kinetic energy terms in cylinder-airfoil wake for two Reynolds number ($Re = 2000$ and $Re = 8000$). Terms are normalised by U_0^3/D.

6.2.4 Decomposed total kinetic energy in phases

An unanswered question remains and concerns, the evolution of energy balance terms dominating at a particular phase. Gaining insights into the behavior of each term within the total turbulent kinetic energy at specific phases has a significant importance. This analysis provides insights into the contribution of random motion during a specific phase, contributing to the formation of one phase of coherent motion. This collective behavior is referred to as total energy exchange, as the fluctuations involve both random motion and coherent motion (represented as one phase)

To address this, each term of the total turbulent kinetic energy is decomposed into 18 phases, allowing for a more comprehensive visualization of flow dynamics. Figure 6.17 shows all the terms of total turbulent kinetic energy, decomposed in 18 phases. These terms are presented in function of upstream wake (phases) in a video integrated in Figure 6.17.

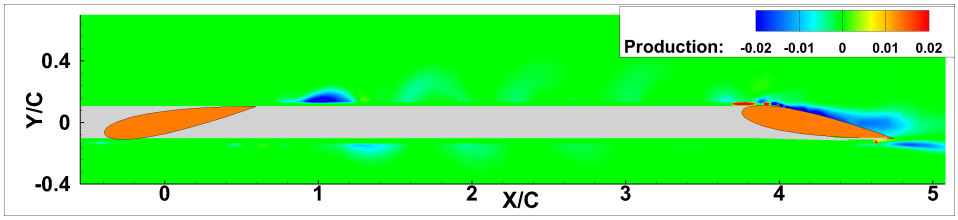

(a) Production.

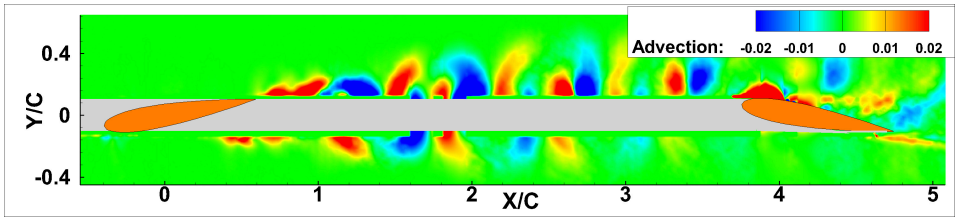

(b) Streamwise advection (X direction).

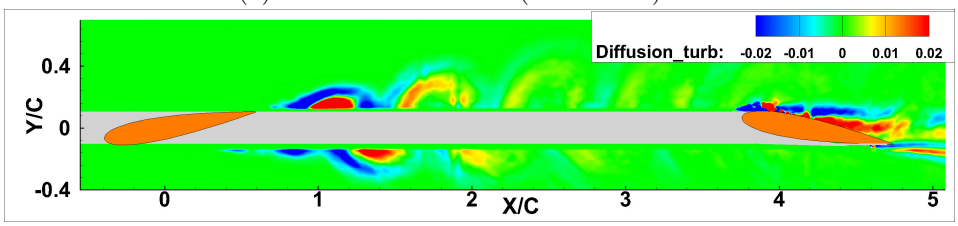

(c) Diffusion by turbulence stresses.

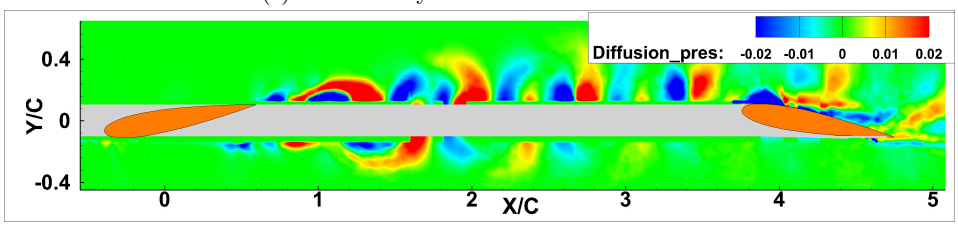

(d) Diffusion by pressure stresses.

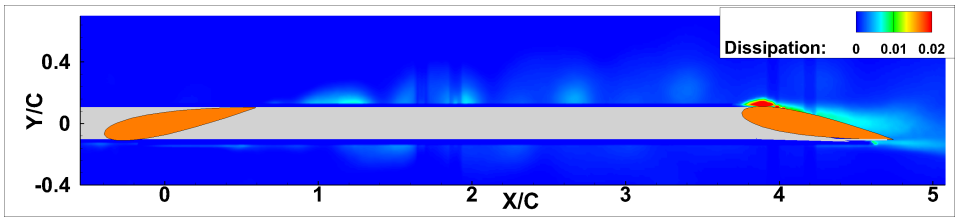

(e) Dissipation.

Figure 6.17: Decomposed terms in 18 phases at $Re = 2000$ in double airfoil wake (videos). Terms are normalised by U_0^3/D

All the terms demonstrate asymmetry concerning the upstream wake at a particular phase. The transport and dissipation terms persist in the further region of the wake and gradually decrease as one moves downstream. These observations provide a detailed view

of the mechanism of random motion over one phase of coherent motion In the other hand, over the downstream airfoil, observations reveal that at each phase of motion, a distinct response occurs over the blade, especially when a vortex interacts with it.

6.3 CM and RM interaction TKE

In situations where coherent motion coexists with random or turbulent flow, an important interaction is revealed. Coherent motion interacts with the random turbulent flow, resulting in localized enhancements in the turbulent cascade. In other words, the presence of coherent structures has the potential to impact the behavior of turbulent fluctuations, ultimately causing enhanced energy transfer and dissipation at specific locations. The importance of phase averaging methods that is previously shown in chapter 4 is employed in this section.

6.3.1 2D - planes of coherent motion (CM) energy budget

The turbulent kinetic energy associated with coherent motion refers to as the largest portion of kinetic energy within a turbulent flow. That is attributed to organized and structured motion which is detached from boundary layers of obstacles. The difference between Equation 6.5 and the equation for the kinetic energy of total fluctuations, as described in Equation 6.1, can be attributed to the inclusion of two additional terms. These terms specifically address the interaction between random and coherent structures within the flow.

$$\frac{1}{2}\overline{\frac{\partial \tilde{q}^2}{\partial t}} + \frac{1}{2}\overline{U_j}\frac{\partial \overline{\tilde{q}^2}}{\partial x_j} + \overline{\tilde{u}_i\tilde{u}_j}\frac{\partial \overline{U_i}}{\partial x_j} + \frac{\partial}{\partial x_j}\left(\overline{\tilde{p}\tilde{u}_j} + \overline{\tilde{u}_i\langle u_i' u_j'\rangle} + \frac{1}{2}\overline{\tilde{q}^2\tilde{u}_j}\right) + \left(-\overline{\langle u_i' u_j'\rangle\frac{\partial \tilde{u}_i}{\partial x_j}}\right) + \overline{\tilde{\epsilon}} = 0. \tag{6.5}$$

The first term due to interaction is the production of random structures by coherent structures accounts for the generation of random turbulent structures as a result of the presence and actions of coherent structures $-\overline{\langle u_i' u_j'\rangle\frac{\partial \tilde{u}_i}{\partial x_j}}$. In essence, coherent structures can induce or trigger the formation of turbulent fluctuations in the flow. The second term due to interaction is the diffusion of Reynolds stress by coherent motion work $\frac{\partial \overline{\tilde{u}_i\langle u_i' u_j'\rangle}}{\partial x_j}$. On the other hand, diffusion of coherent structures involves the dispersion or spreading of coherent structures within the flow due to their periodic movement and their interaction with pressure stresses. These additional terms provide more comprehensive understanding of how coherent and random structures interact and contribute to the overall kinetic energy of the turbulent flow.

Temporal variation

Phases decomposition enables to investigate the phase variation (temporal derivative) of coherent fluid motion. In Figure 6.18, the temporal variation term is showed in the wake for both single and double airfoils at $Re = 2000$, respectively. The phases are decomposed based on the upstream airfoil in the flow configuration. Note that this term becomes null when the motion of coherent fluid motion (CM) is averaged over a full period. However, as shown in Figure 6.18, residual values that is negligible compared to other terms are observed. These values are primarily due to computation errors arising from an insufficient number of convergent phases considered in the analysis.

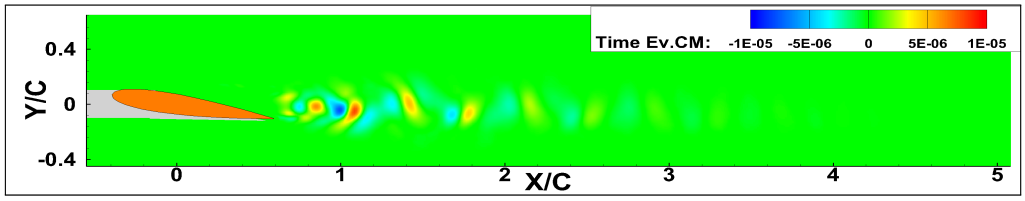

(a) Single airfoil wake.

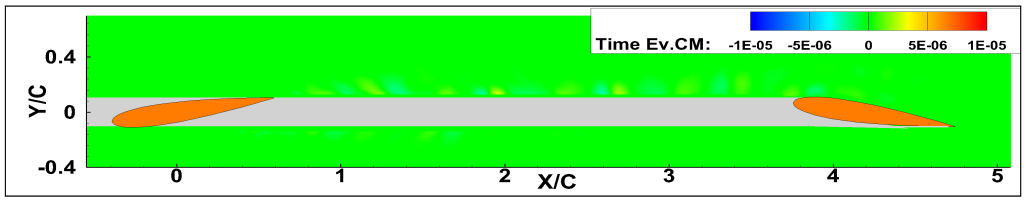

(b) Double airfoil wake.

Figure 6.18: Temporal variation $\frac{1}{2}\overline{\frac{\partial \tilde{q}^2}{\partial t}}$ of coherent motion (CM) in single and double airfoil wakes at Reynolds number $Re = 2000$. Terms are normalised by U_0^3/D.

Production

Production of coherent motion marks the beginning of the cascade process, where the energy of coherent motion feed smaller scales energy. As previously discussed, the production of turbulent kinetic energy (TKE) reaches its maxima in regions characterized by the maximum gradients in mean velocity and the highest levels of anisotropy. Coherent motion is characterized by its anisotropic nature, significantly contributing to the generation of TKE. Figure 6.19 shows the production of coherent motion by the mean velocity for the wake of both single and double airfoils at $Re = 2000$. In single airfoil wake (Figure 6.19a), production of coherent motion (CM) gradually starts at the separation point over the airfoil and extend one chord length $1X/C$ downstream the airfoil. In the case of a double airfoil wake (Figure 6.19b), the production of coherent motion (CM) originating from the downstream airfoil is reduced and begins earlier, closer to the leading edge. This can be explained by the upstream shift in the position of the boundary layer separation point, (see Sections D.4.5 and E.5.5 for higher Reynolds number).

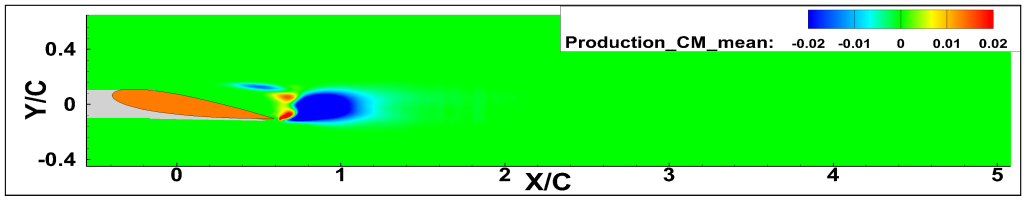

(a) Single airfoil wake.

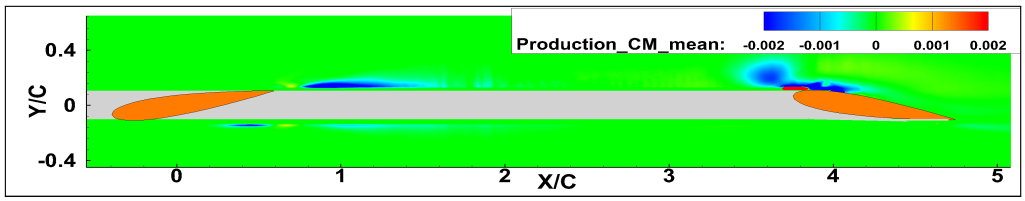

(b) Double airfoil wake.

Figure 6.19: Production $\overline{\tilde{u}_i\tilde{u}_j}\frac{\partial \overline{U_i}}{\partial x_j}$ of coherent motion (CM) in single and double airfoil wakes at Reynolds number $Re = 2000$, phase decomposition based on upstream airfoil. Terms are normalised by U_0^3/D.

In Equation 6.5, a new term, $-\overline{\langle u_i' u_j' \rangle \frac{\partial \widetilde{u_i}}{\partial x_j}}$ appears, characterizing the production of random motion due to coherent motion. The presence of a negative sign in front of this term signifies that coherent motion (CM) is losing this amount of energy to random motion (RM). Thus, this term is considered as a loss (positive) for coherent motion, in contrast to the previous production term, which represented a gain for coherent motion.

Figure 6.20 shows the production of random motion by the coherent motion for the wake of both single and double airfoils at $Re = 2000$. In single airfoil wake (Figure 6.20a), one observes that the energy lost from coherent motion are very high at the wake border (high shear). This term shows important values and comparable to other terms.

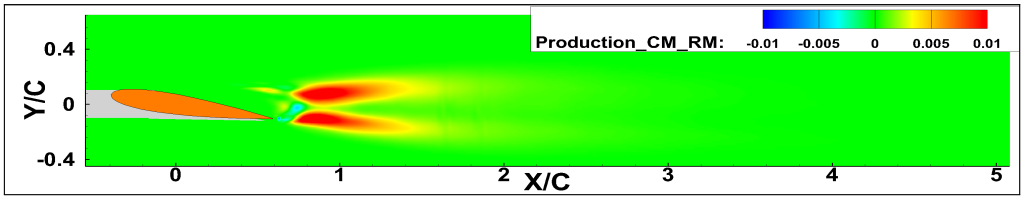

(a) Single airfoil wake.

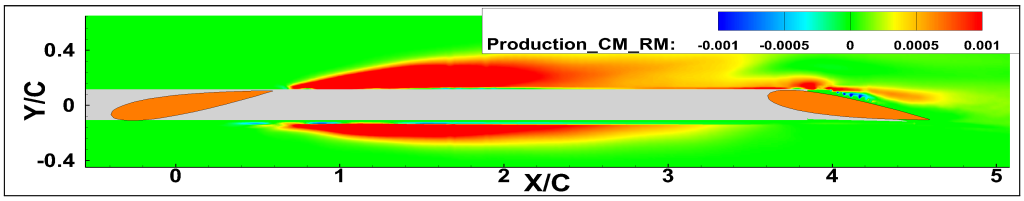

(b) Double airfoil wake.

Figure 6.20: Production $-\overline{\langle u_i' u_j' \rangle \frac{\partial \widetilde{u_i}}{\partial x_j}}$ of random motion (RM) by coherent motion at $Re = 2000$, phase decomposition based on upstream airfoil. Terms are normalised by U_0^3/D.

In the case of a double airfoil wake (Figure 6.20b), the loss of coherent motion (CM) persists over the downstream airfoil, however with a lower magnitude. This phenomenon can be attributed to the reduced energy of coherent motion arriving at the second airfoil downstream.

Advection

This term illustrates the transport of coherent motion by the mean velocity. Figure 6.21 shows the advection term for the wakes of both single and double airfoil at $Re = 2000$. In the wake of a single airfoil (Figure 6.21a), positive advection is observed in areas where the mean flow is dominant, such as at the borders of the wake onset or where coherent motion detaches (production peaks). Figure 6.21a shows a negative advection at the center of the wake, where the energy of coherent motion is transported in the opposite direction to the flow. For further simplification, in regions with high turbulence, energy is transported by the mean velocity in a negative direction. In the double airfoil wake (Figure 6.21b), a negative advection of coherent motion is observed over the downstream airfoil. This is linked to airfoil boundary layer which is enhanced in an upstream wake. In contrast, a positive zone is appeared at the point where it collides with upstream vortices, particularly near the leading edge. At this position of the downstream airfoil, turbulent kinetic energy is highly influenced by the mean flow, (see Sections D.4.5 and E.5.5 for higher Reynolds number).

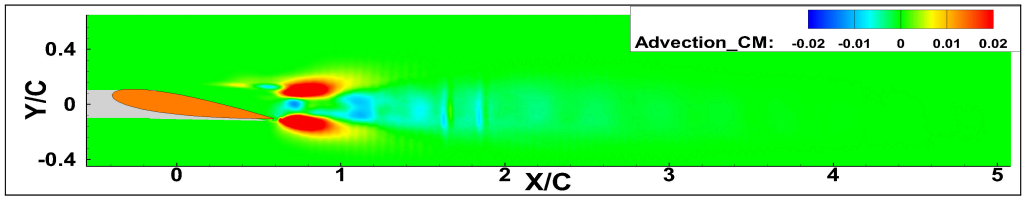

(a) Single airfoil wake.

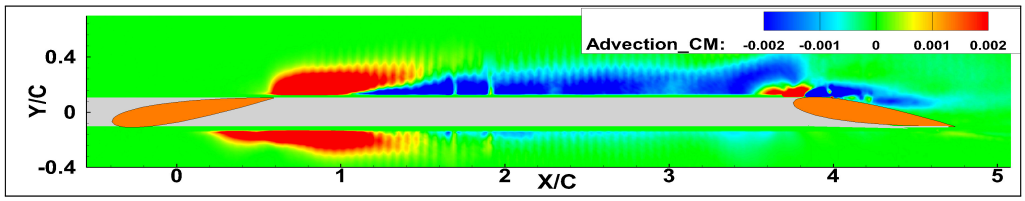

(b) Double airfoil wake.

Figure 6.21: Advection $\frac{1}{2}\overline{U_j}\frac{\partial\overline{\tilde{q}^2}}{\partial x_j}$ of coherent motion (CM) in single and double airfoil wakes at Reynolds number $Re = 2000$, phase decomposition based on upstream airfoil. Terms are normalised by U_0^3/D.

Dissipation

Coherent motion is also characterized as non-viscous fluctuations or structures. These coherent structures (CM) are relatively unaffected by viscosity. It is known that regions marked by high shear and strain rates are indicated by viscous dissipation. The dissipation of coherent structures is calculated by the Equation 6.6.

$$\widetilde{\epsilon} = \overline{\left(\frac{\partial \tilde{u}_i}{\partial x_j} + \frac{\partial \tilde{u}_j}{\partial x_i}\right)^2}. \tag{6.6}$$

Figure 6.22 shows the dissipation of coherent motion in the wake of both single and double airfoils at $Re = 2000$. In both wakes (Figures 6.22a and 6.22b), the dissipation of coherent structures are negligible (i.e. order 10^{-3} in single airfoil case) compared to other terms. This is explained as the presence of viscosity has a minimal impact on the large scale energy containing structures such as coherent motion, (see Sections D.4.5 and E.5.5 for higher Reynolds number).

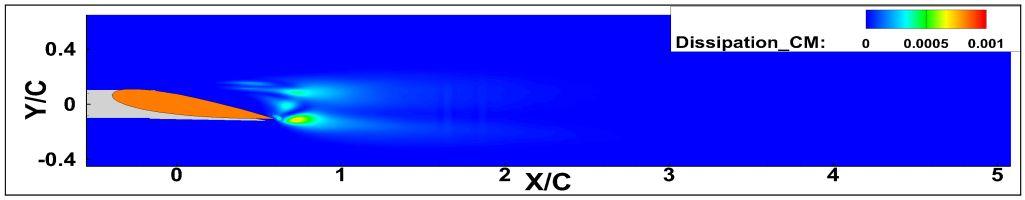

(a) Single airfoil wake.

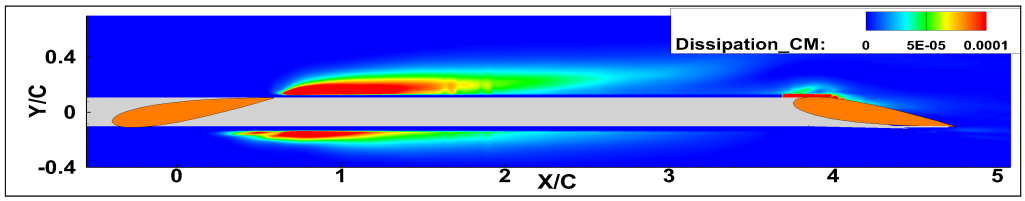

(b) Double airfoil wake.

Figure 6.22: Dissipation $\overline{\tilde{\epsilon}}$ of coherent motion (CM) in single and double airfoil wakes at Reynolds number $Re = 2000$, phase decomposition based on upstream airfoil. Terms are normalised by U_0^3/D.

Diffusion

The diffusion of coherent motion can be categorized into three different types: pure diffusion, diffusion through interaction with random structures, and diffusion driven by pressure. Figure 6.23 shows the pure diffusion of coherent motion (CM) for both single and double airfoil wakes at $Re = 2000$, (see Sections D.4.5 and E.5.5 for higher Reynolds number). In Figure 6.23a, one observes that this type of diffusion is significantly lower compared to previously discussed terms such as production and advection. This figure illustrates the dispersion of kinetic energy associated with coherent motion during its evolution within the wake. The term exhibits a positive value in regions where coherent motion (CM) passes through. For instance, Figure 6.23a shows two parallel positive diffusion zones within the airfoil wake, signifying the passage of coherent motion (CM). These parallel positive diffusion areas are more organized and pronounced in cylinder wake due to more energetic coherent motion (CM), see Section A.1.5. Conversely, negative zones at the center wake indicate the receive amount of coherent motion from the exterior and considered as a gain. In double airfoil wake configuration (Figure 6.23b), limited energy of coherent motion is arriving at the leading edge of the downstream airfoil. Thus, the pure diffusion of coherent motion becomes less significant.

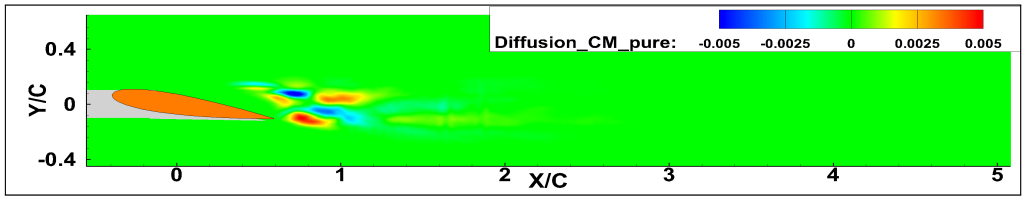

(a) Single airfoil wake.

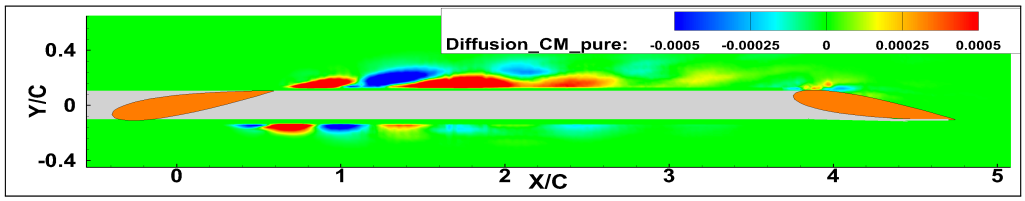

(b) Double airfoil wake.

Figure 6.23: Pure diffusion $\frac{1}{2}\frac{\partial \overline{\tilde{q}^2 \tilde{u}_j}}{\partial x_j}$ of coherent motion (CM) in single and double airfoil wakes at Reynolds number $Re = 2000$, phase decomposition based on upstream airfoil. Terms are normalised by U_0^3/D.

Figure 6.24 represents the diffusion of Reynolds stresses by coherent motion (CM) for both single and double airfoil wakes at $Re = 2000$. In single airfoil wake (Figure 6.24a), diffusion reaches its positive peak at the center of the wake and negative peak at the wake periphery. This is due to the high concentration of coherent structures and turbulence, at the wake's center, which contrasts with the conditions at the wake's periphery where the influence of the mean velocity dominates. Within the double airfoil wake configuration (Figure 6.24b), the presence of coherent structures persists over the downstream airfoil, leading to the diffusion of random motion across the airfoil surface, (see Sections D.4.5 and E.5.5 for higher Reynolds number).

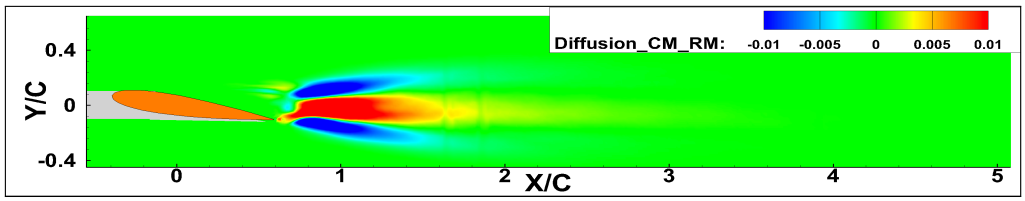

(a) Single airfoil wake.

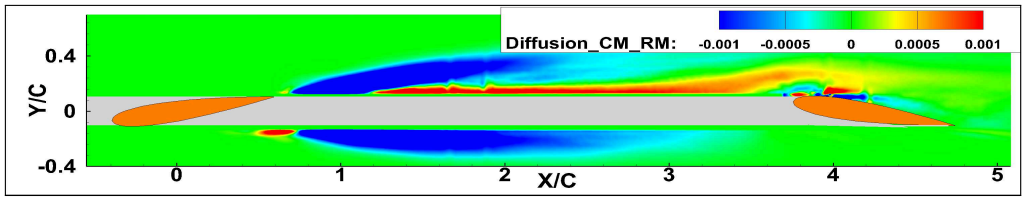

(b) Double airfoil wake.

Figure 6.24: Diffusion $\frac{\partial \overline{\tilde{u}_i \langle u_i' u_j' \rangle}}{\partial x_j}$ of Reynolds stresses by coherent motion (CM) in single and double airfoil wakes at Reynolds number $Re = 2000$, phase decomposition based on upstream airfoil. Terms are normalised by U_0^3/D.

Figure 6.25 represents the diffusion of coherent motion (CM) by pressure for both single and double airfoil wakes at $Re = 2000$ (estimated). In single airfoil wake (Figure 6.25a), one observes that positive values are also concentrated at the wake's center, while

negative values are in the regions of high shear, situated immediately behind the airfoil. This observation provides an explanation for the energy transport dynamics within the wake.

To simplify, the presence of positive values at the center of the wake indicates the dominance of high-pressure fluctuations in this region. This suggests that the energy of coherent structures is diffused from this zone driven by the existence of pressure fluctuations. In contrast, the negative values observed in the high shear regions directly behind the airfoil signify that energy is gained in these zones.

In the double airfoil wake, represented in Figure 6.25b, the influence of pressure stresses persists, particularly over the downstream airfoil. This presence of pressure stresses leads to the diffusion of coherent motion across the airfoil, (see Sections D.4.5 and E.5.5 for higher Reynolds number).

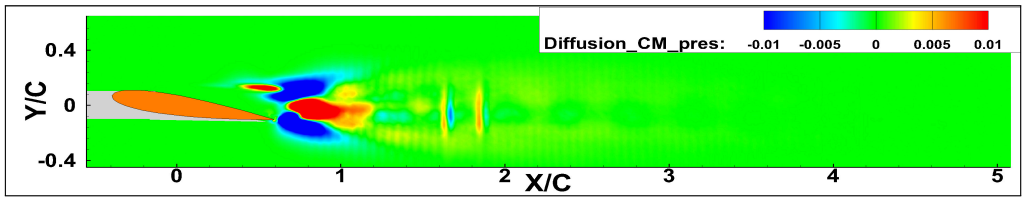

(a) Single airfoil wake.

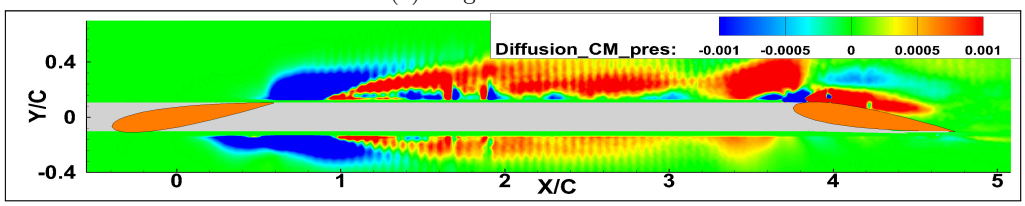

(b) Double airfoil wake.

Figure 6.25: Diffusion $\frac{\partial \overline{\tilde{p}\tilde{u}_j}}{\partial x_j}$ of coherent motion (CM) by pressure in single and double airfoil wakes at Reynolds number $Re = 2000$ (estimated), phase decomposition based on upstream airfoil. Terms are normalised by U_0^3/D.

6.3.2 Summary of coherent motion (CM) energy budget

To summarize, gain and loss of energy fluctuations between the terms of random motion energy budget are reported. These are shown in different zones of different wake configurations at $R = 2000$. **Gain** and **loss** of energy fluctuations for each term are explained as follows:

- Production by the mean flow is recognized as a continuous **gain** of energy for coherent structures (CM).
- Advection by the mean flow is seen as a **loss** when it involves the transfer of energy fluctuations by the mean flow form a particular zone in the direction of the flow (positive values). Conversely, it is considered a **gain** when it results a transfer of energy fluctuations to particular zone (negative values).
- Diffusion terms transfer energy via coherent motion movement, CM-RM interactions, and pressure stresses from particular zone, resulting in **loss** (positive values). However, diffusion terms are considered **gain** when the energy is transferred to particular zone (resulting in negative values).

- Dissipation represents a continuous **loss** of energy fluctuations, which dissipate into heat.

Detailed explanations and descriptions of these terms can be found in Table 6.3, where the correspondent zones are illustrated in Figure 6.26. The abbreviations C, CC, CA, A, and AA stand for cylinder, double cylinders, cylinder-airfoil, airfoil, and double airfoils configurations, respectively. The number following these abbreviations indicates the zone number.

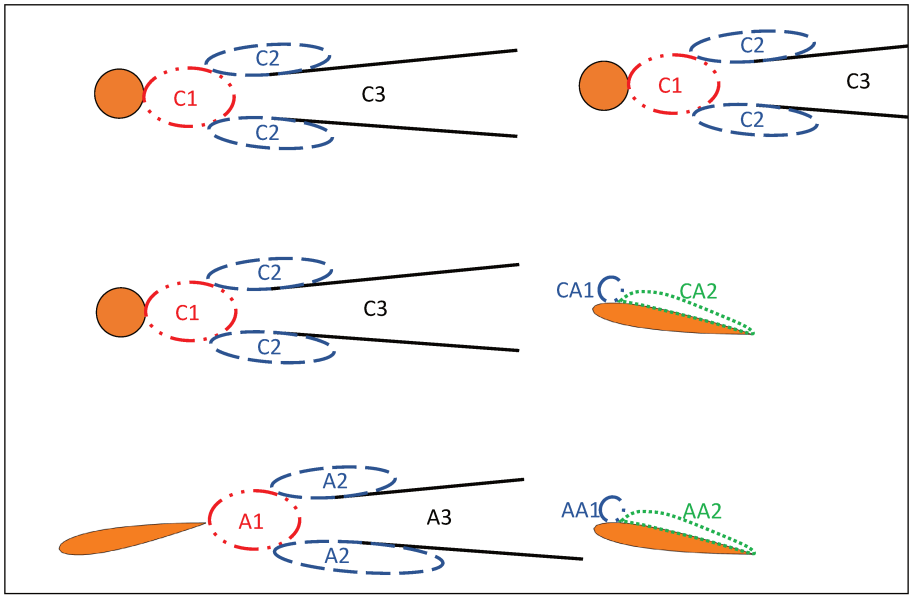

Figure 6.26: Zones in the wakes of single and double cylinder, single and double airfoil, and cylinder-airfoil configurations.

Gain and lost zones in wakes						
Zone	Production	Advection by mean	Pure diffusion	Interaction diffusion	Pressure diffusion	Dissipation
C1	gain	gain & loss	gain & loss	gain & loss	gain & loss	loss
C2	-	loss	gain & loss	gain	gain	loss
C3	-	gain	gain & loss	loss	loss	-
CC1	-	loss	gain & loss	loss	gain	loss
CC2	gain	loss	gain & loss	gain	loss	loss
CC3	-	gain	gain & loss	loss	loss	-
A1	gain	gain & loss	gain & loss	gain & loss	gain & loss	loss
A2	-	loss	gain & loss	gain	gain	loss
A3	-	gain	gain & loss	loss	loss	-
CA1	-	gain & loss	gain & loss	gain	gain & loss	loss
CA2	-	gain & loss	gain & loss	loss	gain & loss	loss
AA1	-	loss	gain & loss	gain & loss	gain	loss
AA2	-	gain	gain & loss	gain & loss	loss	loss

Table 6.3: Gain and lost in wakes for coherent motion (CM) kinetic energy budget.

6.3.3 Cross section profiles of coherent motion (CM) energy budget

Single and double airfoil wake

As previously discussed, coherent motion phases are decomposed based on the first (obstacle) airfoil. In the context of this study, cross-section profiles have been examined at different locations to demonstrate the energy exchange associated with coherent motion. Figures 6.27a and 6.27b present profiles along the Y direction at two specific positions $X/C = 1.6$ and $X/C = 5.6$ for both single and double airfoil wakes, respectively. These profiles are generated at a distance of 5 cm $(1X/C)$ behind both the upstream and downstream airfoils. Note that two different Reynolds numbers, based on a 1 cm cylinder diameter, have been considered for comparison purposes. In the case of the single airfoil wake, it is observed that coherent structures (CM) exhibit higher advection and interaction diffusion effects at the lower Reynolds number ($Re = 2000$), while production is comparatively lower, as shown in Figure 6.27a. The opposing profiles of advection and diffusion imply an exchange of energy between these two processes. On the other hand, within the double airfoil wake, all the terms are reduced to smaller magnitudes. Moreover, at high Reynolds numbers, all terms are significantly smaller compared to low Reynolds numbers. This is attributed to lower energetic coherent structures detached from upstream airfoil at higher Reynolds numbers, which results in a reduced persistence of these structures behind the downstream airfoil.

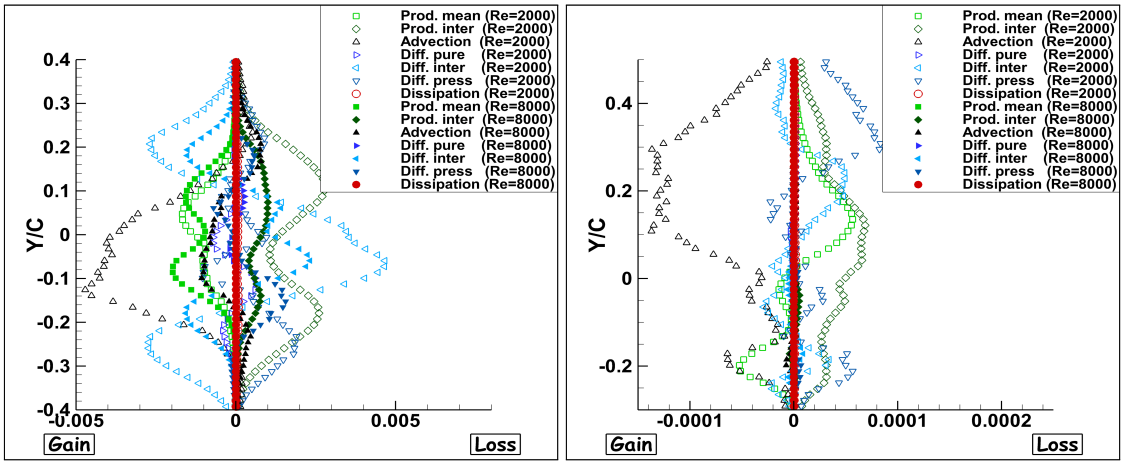

(a) Profiles 5 cm behind the airfoil ($X/C = 1.6$), in single airfoil configuration.

(b) Profiles 5 cm behind downstream airfoil ($X/C = 5.6$), in double airfoil configuration.

Figure 6.27: Coherent motion (CM) energy budget terms in single and double airfoil wake for two Reynolds number ($Re = 2000$ and $Re = 8000$), phase decomposition based on upstream airfoil. Terms are normalised by U_0^3/D.

In the context of investigating the airflow over airfoils, Figures 6.27a and 6.27b present profiles along the Y direction at two specific positions: $X/C = 0.3$ and $X/C = 4.3$, respectively, for both single and double airfoil wake configurations. The profiles initiate at the surface of the airfoil and extend out of the wake, where the positions over the airfoils are $0.6C$ (60% of chord length) referring to the leading edge in X direction.

In the single airfoil wake configuration, it is seen that production, advection and pressure diffusion play an important role at low Reynolds numbers when compared to other terms and to higher Reynolds number, as shown in Figure 6.28a. This observation can be explained by the disappearance of the separation point over the airfoil at high Reynolds numbers.

When an upstream airfoil wake is introduced in the case of the double airfoil wake, the maxima peaks of advection, diffusion, and production terms are shifted to the airfoil surface, as shown in Figure 6.28b. Moreover, significant shift occurs in the advection and diffusion terms, transitioning from positive to negative values. This shift can be attributed to the generation of high stresses (Reynolds and pressure) by the upstream airfoil wake, which persist over the downstream airfoil. These pressure effects are responsible for altering the direction of advection and diffusion in the downstream airfoil wake.

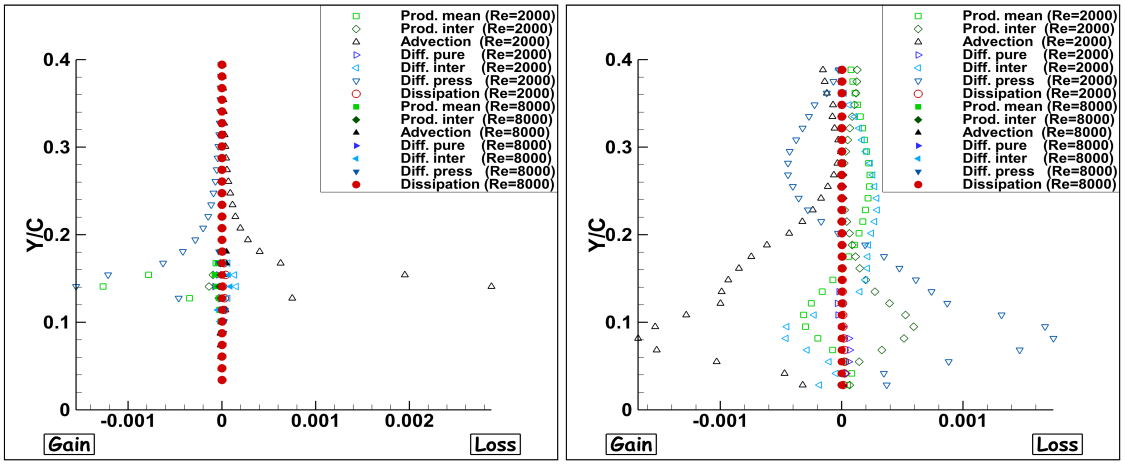

(a) Profiles at $X/C = 0.3$ over the airfoil, in single airfoil configuration.

(b) Profiles at $X/C = 4.3$ over downstream airfoil, in double airfoil configuration.

Figure 6.28: Coherent motion (CM) energy budget terms in single and double airfoil wake for two Reynolds number ($Re = 2000$ and $Re = 8000$), phase decomposition based on upstream airfoil. Terms are normalised by U_0^3/D.

When comparing the energy exchange associated with coherent motion to the total energy exchange, it is significant that all terms exhibit lower magnitudes in the case of coherent motion.

Single and double cylinder wake

Cross-section profiles have been examined at different positions within single and double cylinder wakes to illustrate the energy exchange associated with coherent motion as a function of downstream location. Figures 6.29a and 6.29b present profiles along the Y direction, specifically at a position 5 cm downstream the first ($X/D = 5$) and second cylinder ($X/D = 15$) for both single and double cylinder wakes, respectively. These figures clearly show that the magnitude of coherent motion energy terms in the single cylinder wake is significantly higher when compared to the double cylinder wake. It seems that coherent motion generated by the first obstacle (cylinder) loses a substantial amount of energy as it travels behind the second cylinder in the double cylinder wake. Furthermore, the profiles of Figures 6.29a and 6.29b indicate that the dominant terms contributing to coherent motion energy are advection and diffusion. These terms exhibit opposing behaviors with a slight difference in magnitude. This opposition can be attributed to the exchange of coherent motion energy between advection and diffusion as it varies with downstream position within the wake, (see Sections A.1.5 and B.2.5 for more details).

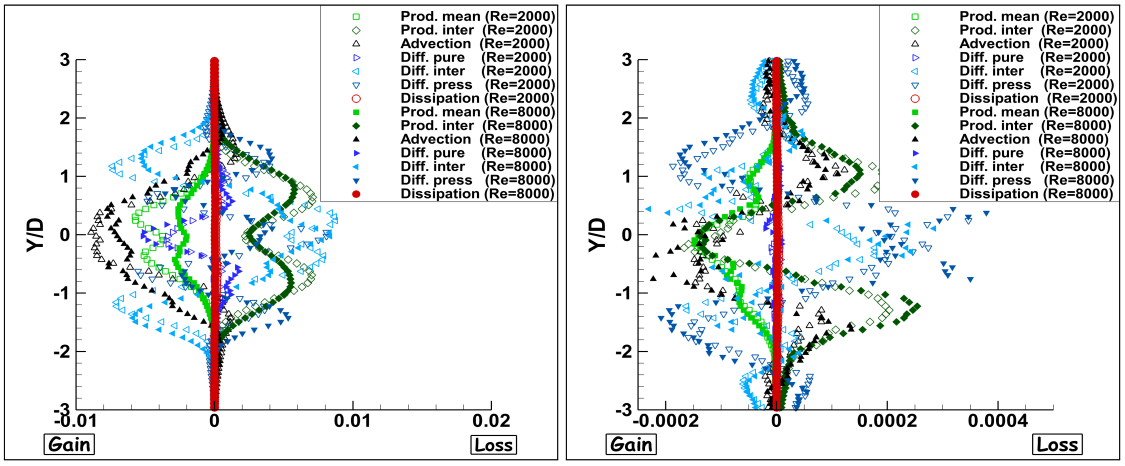

(a) Profiles 5 *cm* behind the cylinder ($X/D = 5$), in single cylinder configuration.

(b) Profiles 5 *cm* behind downstream cylinder ($X/D = 15$), in double cylinder configuration.

Figure 6.29: Coherent motion (CM) energy budget terms in single and double cylinder wake for two Reynolds number ($Re = 2000$ and $Re = 8000$), phase decomposition based on upstream cylinder. Terms are normalised by U_0^3/D.

Figures 6.30a and 6.30b present profiles along the Y direction, at a distance of 15 *cm* downstream from the first ($X/D = 15$) and second cylinder ($X/D = 25$) for both single and double cylinder wakes, respectively. These figures clearly show a significant reduction in the magnitude of coherent motion energy terms by moving downstream from the cylinders in both single and double cylinder configurations. This observation shows that the energy exchange associated with coherent motion decreases with increasing downstream distance, due to the cascade process of coherent motion. Furthermore, by moving downstream, the range of energy exchange in the transverse direction widens. For example, when comparing Figures 6.29a and 6.30a, the profiles exhibit smoother peaks in the far wake zone ($X/D = 15$) and sharper peaks in the near wake zone ($X/D = 5$).

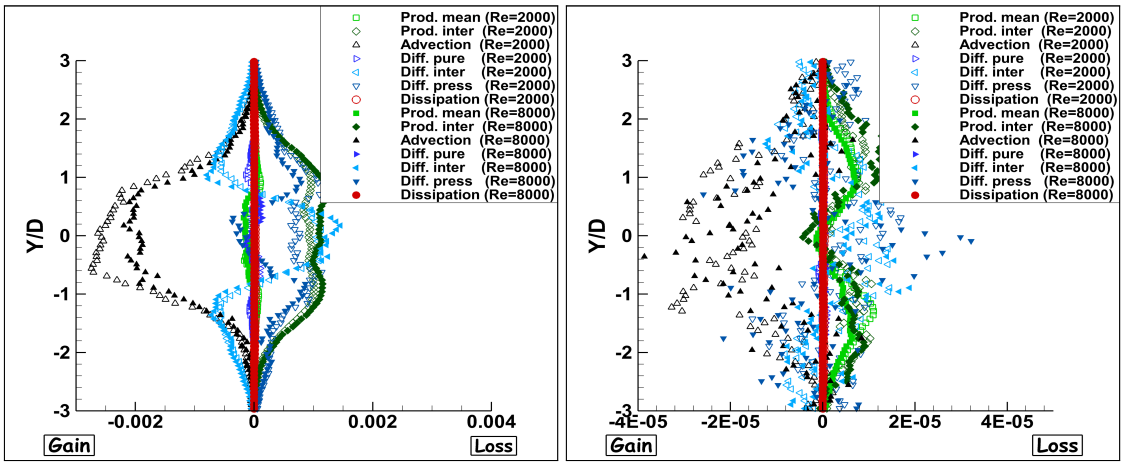

(a) Profiles 15 *cm* behind the cylinder ($X/D = 15$), in single cylinder configuration.

(b) Profiles 15 *cm* behind downstream cylinder ($X/D = 25$), in double cylinder configuration.

Figure 6.30: Coherent motion (CM) energy budget terms in single and double cylinder wake for two Reynolds number ($Re = 2000$ and $Re = 8000$), phase decomposition based on upstream cylinder. Terms are normalised by U_0^3/D.

The previous observations was based on first cylinder phases decomposition. The question still remaining to be answered is that what could change if phases are decomposed with respect to second cylinder. Figures 6.31a and 6.31b present profiles along the Y direction, at distances of 5 cm ($X/D = 15$) and 15 cm ($X/D = 25$) downstream the second cylinder in double cylinder wakes, respectively. The phase decomposition in these figures are decomposed based on second cylinder, see Section B.2.7.
In Figure 6.31a, one observes that the advection shifts to the positive side at the center of the wake, which is opposite to what is previously observed in Figure 6.29a. An explanation is that the zone of advection for coherent motion (CM) behind the second obstacle (cylinder) extends downstream compared to coherent motion (CM) of upstream cylinder. This extension of advection is explained due to higher velocity zones immediately behind the second cylinder compared to upstream cylinder. Conversely, in the far wake (Figure 6.31b), the advection is returned to negative side where the effect of the shear by the mean flow becomes lower compared to the border of the wake. Then the diffusion carried the energy from the advection to be transported to lower scales. These observations demonstrate the dynamic interplay between coherent motion (CM) generation, diffusion, and advection as we move along the wake of the double cylinder configuration. In conclusion, the energy exchange profiles of coherent motion, whether based on the upstream or downstream obstacle, show lower magnitudes in the wake of a double cylinder configuration when compared to the wake of a single cylinder. This observation indicates that the presence of the second cylinder results in a reduction in the magnitude of energy exchange associated with coherent motion.

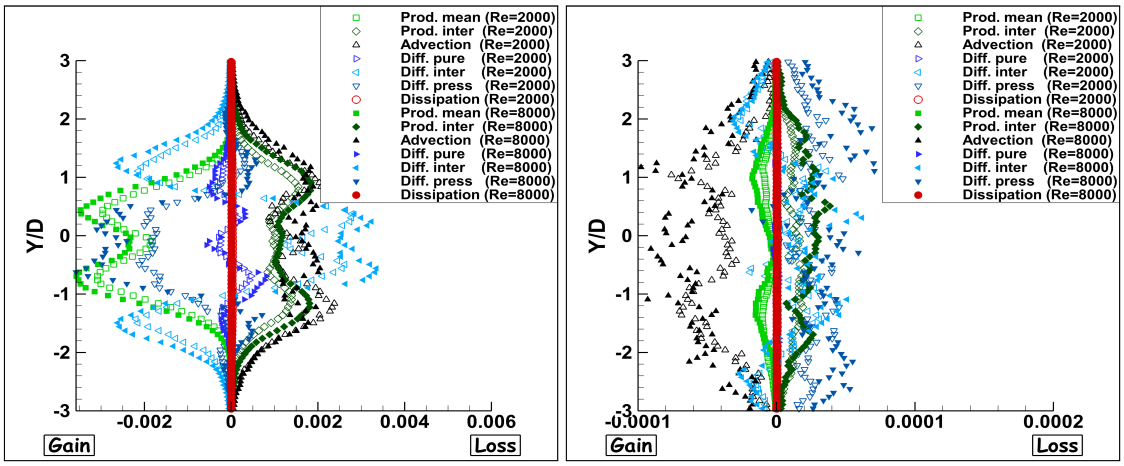

(a) Profiles 5 cm behind downstream cylinder ($X/D = 15$), in double cylinder configuration.

(b) Profiles 15 cm behind downstream cylinder ($X/D = 25$), in double cylinder configuration.

Figure 6.31: Coherent motion (CM) energy budget terms in double cylinder wake for two Reynolds number ($Re = 2000$ and $Re = 8000$), phase decomposition based on downstream cylinder. Terms are normalised by U_0^3/D.

Cylinder-airfoil wake

The profiles of coherent motion energy exchange in a cylinder-airfoil configuration are discussed. Figure 6.32a shows profiles at a distance of 5 cm ($X/D = 21$) downstream from the second obstacle (airfoil) in a cylinder-airfoil wake. Significantly, the magnitude of coherent motion energy exchange in this configuration is higher than that observed in Figure 6.29b, which is the double cylinder wake configuration. This suggests that coherent motion generated by a cylinder can resist more effectively to the presence of an airfoil

compared to a second cylinder. The coherent motion is able to climb the leading edge of the airfoil without an intense cascade of its energy. This climbing behavior also leads to a deviation in the cylinder wake, shown in the second peak of advection and diffusion at $Y/D = 2$ downstream of the airfoil, (see Section C.3.5 for more details). In Figure 6.32b, the profiles are obtained over the airfoil, at a distance of $0.6C$ (from leading edge) over the airfoil in the cylinder-airfoil wake. The advection of coherent motion is positive at low Reynolds number, while negative at high Reynolds number. This behavior is explained by the presence of positive and negative spots in the advection over the airfoil. The energetic coherent motion detached from the cylinder has the ability to increase the shear over the airfoil when compared to the double airfoil wake (Figure 6.28b). This phenomenon highlights the complex physics over the airfoil within the cylinder-airfoil configuration.

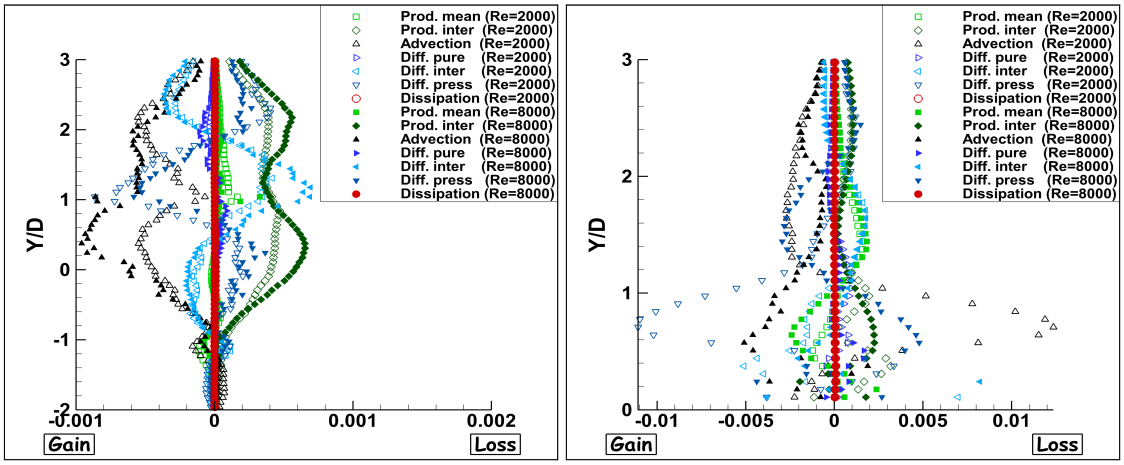

(a) Profiles 5 *cm* behind the airfoil ($X/D = 21$), in cylinder-airfoil wake.

(b) Profiles at $X/D = 14$ over downstream airfoil, in cylinder-airfoil configuration.

Figure 6.32: Coherent motion (CM) energy budget terms in cylinder-airfoil wake for two Reynolds number ($Re = 2000$ and $Re = 8000$), phase decomposition based on upstream cylinder. Terms are normalised by U_0^3/D.

6.3.4 2D - planes of Random motion (RM) energy budget

The turbulent kinetic energy associated with random motion refers to smaller portion of kinetic energy within a turbulent flow compared to coherent motion. That results in non organized and non structured motion which is produced by coherent motion and boundary layers. The difference between Equation 6.7 and the Equation for the kinetic energy of total fluctuations, as described in Equation 6.1, can be attributed to the inclusion of two additional terms. These terms specifically address the interaction of coherent motion and random motion.

$$\frac{1}{2}\overline{\frac{\partial q'^2}{\partial t}} + \frac{1}{2}\overline{U_j}\frac{\partial \overline{q'^2}}{\partial x_j} + \overline{u_i'u_j'}\frac{\partial \overline{U_i}}{\partial x_j} + \frac{\partial}{\partial x_j}\left(\overline{p'u_j'} + \frac{1}{2}\overline{\widetilde{u_j}\langle q'^2\rangle} + \frac{1}{2}\overline{q'^2u_j'}\right) + \overline{\langle u_i'u_j'\rangle\frac{\partial \widetilde{u_i}}{\partial x_j}} + \overline{\epsilon'} = 0. \tag{6.7}$$

Temporal variation

High-speed Particle Image Velocimetry provide the temporal evolution (temporal derivative) of random motion (RM). In Figure 6.33, the temporal variation term is showed for the

wakes of both single and double airfoil configurations at $Re = 2000$. It is shown that this term is null and converges to zero with higher number of data.

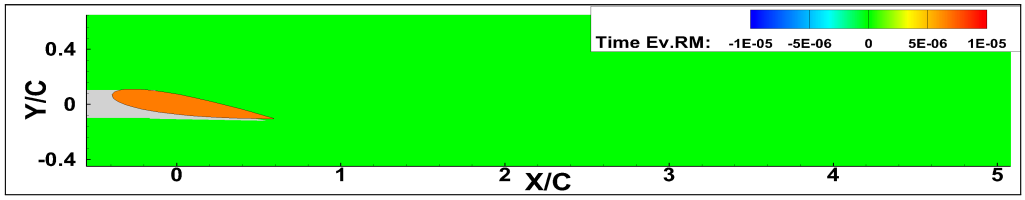

(a) Single airfoil wake.

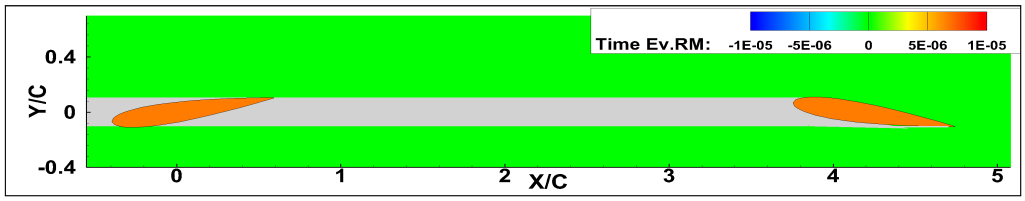

(b) Double airfoil wake.

Figure 6.33: Temporal variation $\frac{1}{2}\frac{\overline{\partial q'^2}}{\partial t}$ of random motion (RM) in single and double airfoil wakes at Reynolds number $Re = 2000$, normalised by U_0^3/D.

Production

The production of random motion can be divided into two main components: production of random motion by mean flow and production of random motion by coherent motion. Figure 6.34 illustrates the production of random motion by mean flow for both single and double airfoil wake configurations at $Re = 2000$, (see Sections D.4.6 and E.5.6 for higher Reynolds number). In the case of the single airfoil wake (Figure 6.34a), the production of random motion is different to what was previously observed in the coherent motion budget. The observed difference is attributed to the more isotropic behavior of random motion, which leads to $(\overline{u'^2} - \overline{v'^2})\frac{\partial \overline{U}}{\partial X} \approx 0$. As a consequence, this condition results in zero production of random motion at the center of the wake.

Within the double airfoil wake (Figure 6.34b), the production of random motion from downstream airfoil is significantly lower than the production from the upstream airfoil. However, the production of random motion from downstream airfoil is higher when compared to the production of coherent motion ($\approx \times 10$). Moreover, this figure indicates that the separation point of vortices has shifted upstream, moving closer to the leading edge of the airfoil.

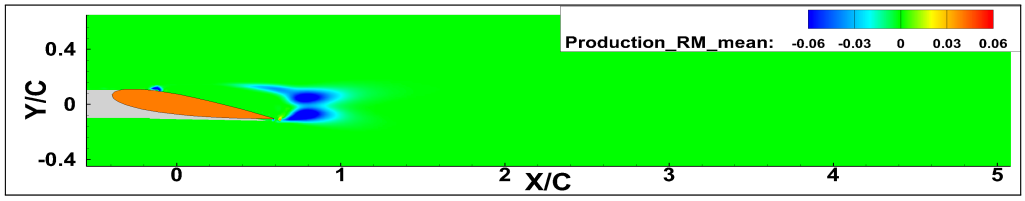

(a) Single airfoil wake.

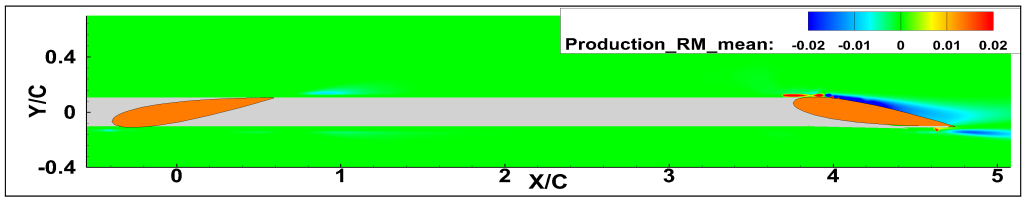

(b) Double airfoil wake.

Figure 6.34: Production $\overline{u_i' u_j'} \frac{\partial \overline{U_i}}{\partial x_j}$ of random motion (RM) by mean flow at $Re = 2000$, normalised by U_0^3/D.

Figure 6.35 provides an overview of the production of random motion by coherent motion for both single and double airfoil wake configurations at $Re = 2000$, (see Sections D.4.6 and E.5.6 for higher Reynolds number). In the single airfoil wake (Figure 6.35a), production of random motion through coherent motion is relatively smaller ($\leq \times 5$) when compared to the production by mean flow, as seen in Figure 6.34a. The production of random motion is mainly occurred in two distinct zones: first, in the high-shear zone near the obstacle (airfoil), and second, at the periphery of the wake (intermittence surface). These observations are in agreement with findings by Townsend [23, 24]. In the case of the double airfoil wake, Figure 6.35b, the production of random motion (RM) from coherent motion (CM) occurs at the separation point downstream the airfoil, close to the leading edge. This position represents a significant source of entrainment.

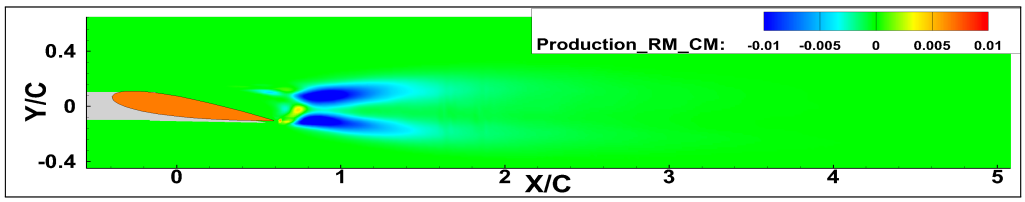

(a) Single airfoil wake.

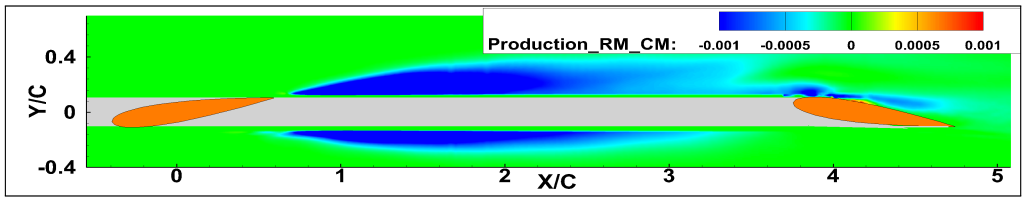

(b) Double airfoil wake.

Figure 6.35: Production $\overline{\langle u_i' u_j' \rangle \frac{\partial \widetilde{u_i}}{\partial x_j}}$ of random motion (RM) by coherent motion at $Re = 2000$, phase decomposition based on upstream airfoil. Terms are normalised by U_0^3/D.

Advection

Advection is recognized as the transport of large-scale quantities by the mean flow, but it can also refer as the transport of smaller scales by the mean flow. In Figure 6.36, advection by mean flow is illustrated for both single and double airfoil wake configurations at $Re = 2000$, (see Sections D.4.6 and E.5.6 for higher Reynolds number). In the case of the single airfoil wake, Figure 6.36a, the advection of random motion is similar to what was previously observed in the context of coherent motion advection. In double airfoil wake, Figure 6.36b, the advection of random motion over the downstream airfoil demonstrates higher values ($\approx \times 10$) when compared to the advection of coherent motion. This significant difference can be attributed to higher production of random motion (RM) from the downstream airfoil compared to coherent motion (CM).

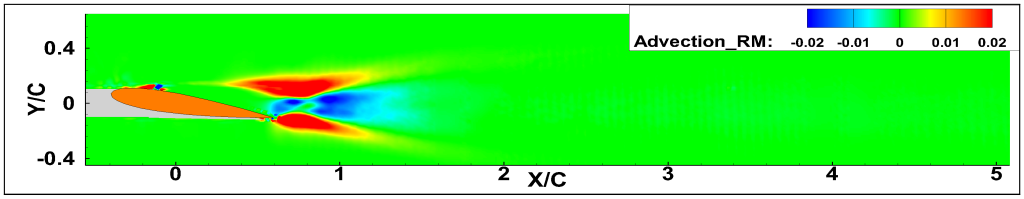

(a) Single airfoil wake.

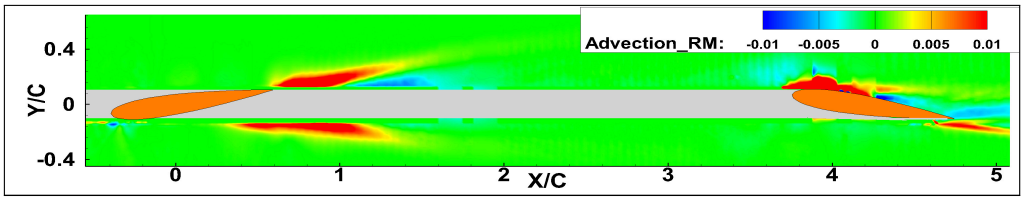

(b) Double airfoil wake.

Figure 6.36: Advection $\frac{1}{2}\overline{U_j}\frac{\partial \overline{q'^2}}{\partial x_j}$ of random motion (RM) in single and double airfoil wakes at Reynolds number $Re = 2000$, normalised by U_0^3/D.

Dissipation

Dissipation of random motion consider the sink of the turbulent kinetic energy. In other words, dissipation accounts for the process by which turbulent kinetic energy is transferred to mean flow by viscous stresses in form of heat. Figure 6.37 illustrates the dissipation of random motion due to viscous stresses for both single and double airfoil wake configurations at $Re = 2000$, (see Sections D.4.6 and E.5.6 for higher Reynolds number). In the single airfoil wake, Figure 6.37a, the dissipation occurs immediately behind the airfoil (obstacle). In double airfoil wake, Figure 6.37b, the dissipation region is shifted upstream over the downstream airfoil compared to single airfoil wake. These observations are in agreement with what was previously discussed in Figures 6.8a and 6.8b, for the total fluctuations (CM and RM).

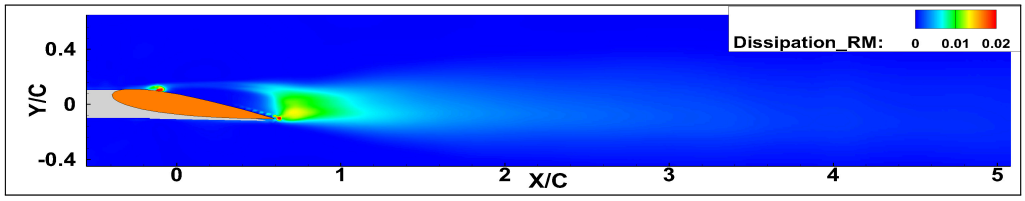

(a) Single airfoil wake.

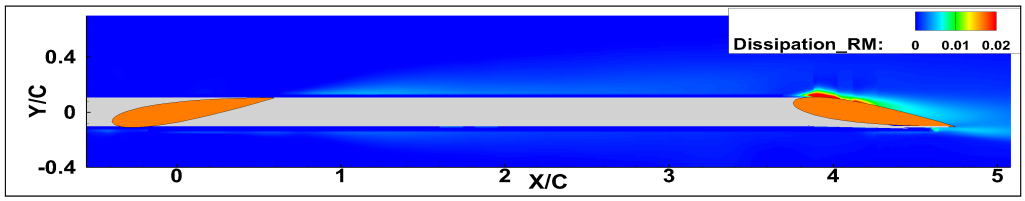

(b) Double airfoil wake.

Figure 6.37: Dissipation $\overline{\epsilon'}$ of random motion (RM) by viscous stress at $Re = 2000$, normalised by U_0^3/D.

Diffusion

Diffusion of Random motion is also categorized into three main types: pure diffusion, diffusion through interaction with coherent structures, and diffusion driven by pressure work. Figure 6.38 shows the pure diffusion of random motion for both single and double airfoil wake configurations at $Re = 2000$, (see Sections D.4.6 and E.5.6 for higher Reynolds number). This term illustrates the transfer of random motion energy through the influence of random stresses (RM pure movement). As shown in Figure 6.38a, this transfer is observed to be important behind the airfoil. The transport of random motion energy is transferred from the wake (loss) to the wake's periphery (gain), possibly transitioning into the advection process. Consequently, this highlights the idea that diffusion driven by Reynolds stresses complements the advection process. In the case of the double airfoil wake, Figure 6.38b, both positive and negative diffusion layers are observed over the downstream airfoil with significant values. This positive layer essentially represents the airfoil boundary layer, which is overlaid by negative layer where the influence of the mean flow starts to dominate. Thus, the energy of random motion undergoes a transfer from the positive zone (loss) to the negative zone (gain) within these diffusion layers.

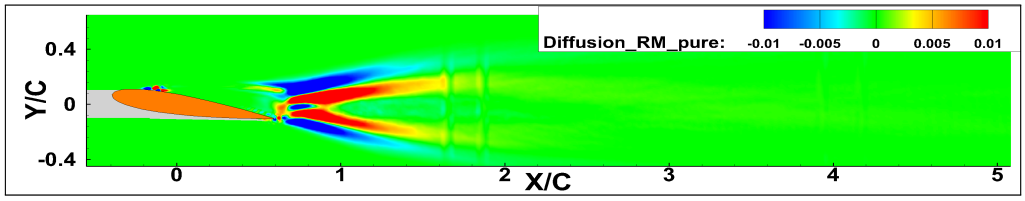

(a) Single airfoil wake.

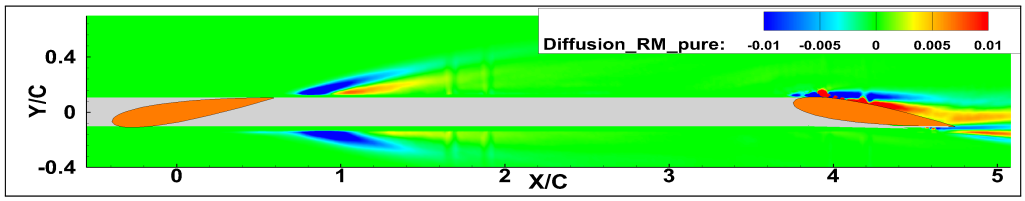

(b) Double airfoil wake.

Figure 6.38: Pure diffusion $\frac{1}{2}\frac{\partial \overline{q'^2 u'_j}}{\partial x_j}$ of random motion (RM) in single and double airfoil wakes at Reynolds number $Re = 2000$, normalised by U_0^3/D.

Figure 6.39 shows the diffusion of random motion by its interaction with coherent motion for both single and double airfoil wake configurations at $Re = 2000$. (see Sections D.4.6 and E.5.6 for higher Reynolds number). This term holds significant importance in the transport of random motion through the influence (interaction) of coherent motion. To simplify, random motion is carried along by coherent motion, and this term represents the diffusion process that occurs when random motion is transported at coherent motion (CM) velocity. In single airfoil wake, Figure 6.39a, the transported random motion (RM) by coherent motion (CM) is concentrated at the center of airfoil wake, where positive peaks occurred (loss). The transport of random motion also occurred over the downstream airfoil in double airfoil wake, as illustrated in Figure 6.39b. This is attributed to the persistence of coherent motion (generated by upstream obstacle) over the downstream airfoil. The persistence of coherent motion over the downstream airfoil leads to significant random motion diffusion.

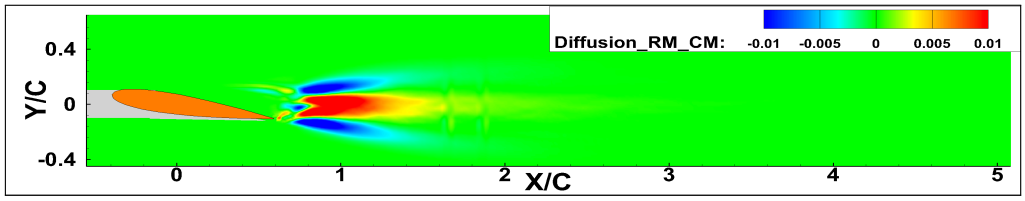

(a) Single airfoil wake.

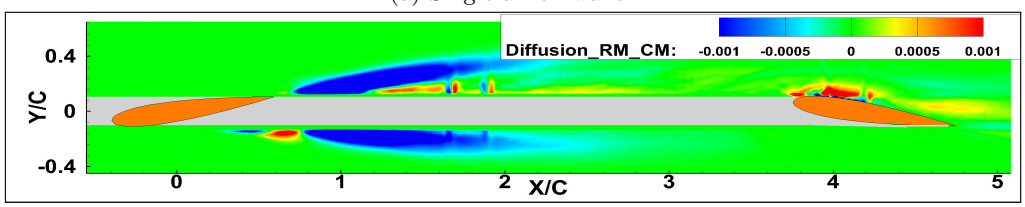

(b) Double airfoil wake.

Figure 6.39: Diffusion $\frac{1}{2}\frac{\partial \widetilde{u_j}\langle q'^2\rangle}{\partial x_j}$ of random motion (RM) by coherent motion (CM) interaction in single and double airfoil wakes at Reynolds number $Re = 2000$, phase decomposition based on upstream airfoil. Terms are normalised by U_0^3/D.

Figure 6.40 shows the diffusion of random motion by pressure stresses (estimated) for both single and double airfoil wake configurations at $Re = 2000$. (see Sections D.4.6 and E.5.6 for higher Reynolds number). In the single airfoil wake (Figure 6.40a), the diffusion process driven by pressure is similar to other diffusion terms close to the airfoil, where loss of energy observed at the center wake and gain of energy at the periphery of the wake.

In double airfoil wake, Figure 6.40b, pressure diffusion is observed to transfer energy from the central body of the airfoil to regions characterized by high velocity dominance or shear, such as the edges of the airfoil. This is in contrast to what is observed in the advection term, where the direction of energy transfer is inverted. This complex interaction characterizes the energy transfer within the wake of single and double airfoil configuration.

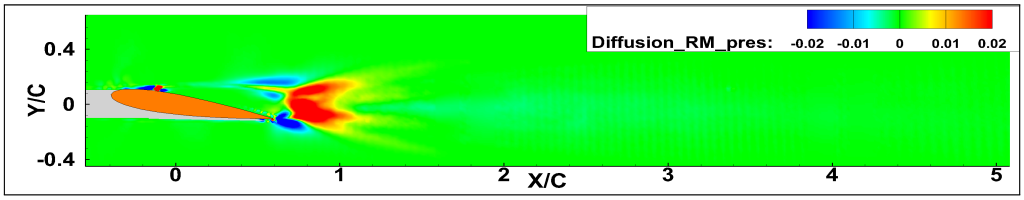

(a) Single airfoil wake.

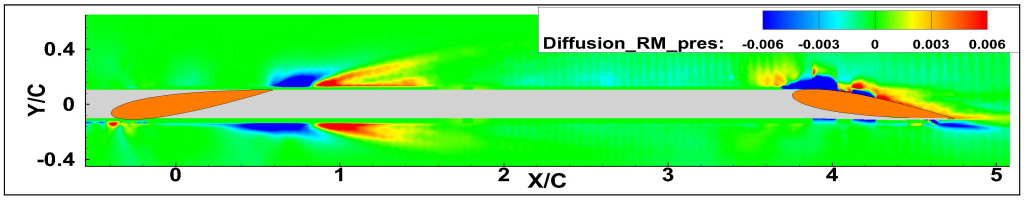

(b) Double airfoil wake.

Figure 6.40: Diffusion $\frac{\partial \overline{p' u'_j}}{\partial x_j}$ of random motion (RM) by pressure in single and double airfoil wakes at Reynolds number $Re = 2000$ (estimated), normalised by U_0^3/D.

6.3.5 Summary of random motion (RM) energy budget

To summarize, gain and loss of energy fluctuations between the terms of random motion energy budget are reported. These are shown in different zones of different wake configurations at $R = 2000$. **Gain** and **loss** of energy fluctuations for each term are explained as follows:

- Production by the mean flow is recognized as a continuous **gain** of energy for turbulent structures (RM).
- Production by CM is seen as a **gain** (negative) when it results in RM energy, and considered as a **loss** (positive) of energy from coherent motion (CM).
- Advection by the mean flow is seen as a **loss** when it involves the transfer of random motion by the mean flow form a particular zone in the direction of the flow (positive effect). Conversely, it is considered a **gain** when it results a transfer of energy fluctuations to particular zone (negative effect).
- Diffusion terms transfer energy via random motion or Reynolds stresses, CM-RM interactions, and pressure stresses from particular zone, resulting in **loss** (positive effect). However, diffusion terms are considered **gain** when the energy is transferred to particular zone (resulting in negative effect).

- Dissipation represents a continuous **loss** of energy fluctuations, which dissipate into heat.

Detailed explanations and descriptions of these terms can be found in Table 6.4, where the correspondent zones are illustrated in Figure 6.41. The abbreviations C, CC, CA, A, and AA stand for cylinder, double cylinders, cylinder-airfoil, airfoil, and double airfoils configurations, respectively. The number following these abbreviations indicates the zone number.

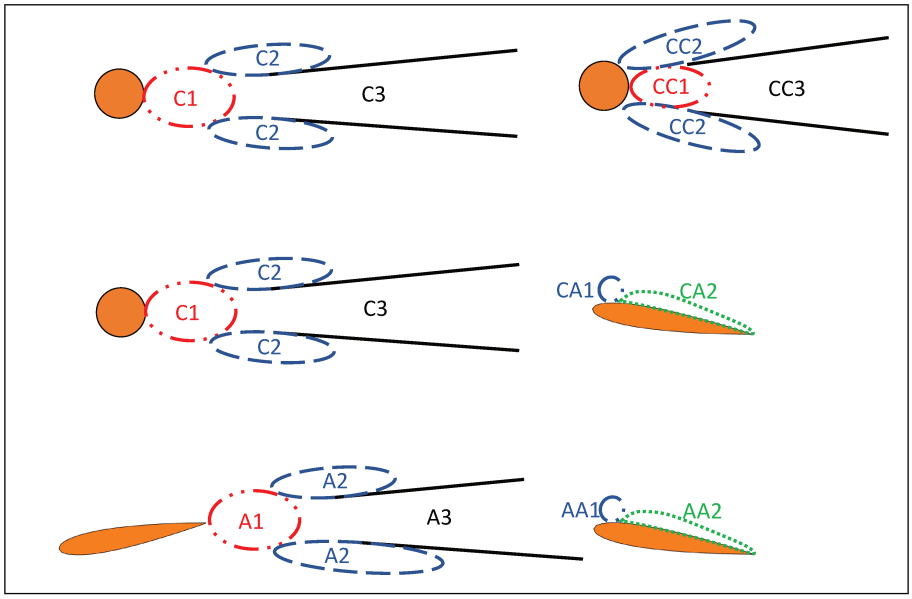

Figure 6.41: Zones in the wakes of single and double cylinder, single and double airfoil, and cylinder-airfoil configurations.

Gain and loss zones in wakes							
Zone	Production by mean	Production by CM	Advection by mean	Pure diffusion	Interaction diffusion	Pressure diffusion	Dissipation
C1	-	-	gain & loss	gain & loss	gain & loss	gain & loss	loss
C2	gain	gain	loss	gain	gain	gain	loss
C3	-	-	gain	loss	loss	loss	loss
CC1	-	-	gain	gain & loss	gain & loss	gain & loss	loss
CC2	gain	gain	loss	gain	gain	gain	loss
CC3	-	-	gain	loss	loss	loss	loss
A1	-	-	gain & loss	gain & loss	gain & loss	gain & loss	loss
A2	gain	gain	loss	gain	gain	gain	loss
A3	-	-	gain	loss	loss	loss	loss
CA1	gain	gain	loss	gain & loss	gain	gain	loss
CA2	gain	-	gain	loss	loss	loss	loss
AA1	-	gain	loss	gain & loss	loss	gain	loss
AA2	gain	gain	gain	gain & loss	loss	loss	loss

Table 6.4: Gain and loss in wakes for random motion (RM) kinetic energy budget.

6.3.6 Cross section profiles of random motion (RM) energy budget

Single and double airfoil wake

The examination of random motion energy exchange at different positions using cross-section profiles provides also valuable understanding into the energy transfer of the flow. Figures 6.42a and 6.42b present profiles along the Y direction for both single and double airfoil wakes, respectively. The profiles were positioned at a distance 5 cm downstream from the first ($X/C = 1.6$) and second airfoil ($X/C = 4.6$). Close to the airfoil in the single airfoil wake (Figure 6.42a), one observes that the energy exchange of random motion have similar order of magnitude with coherent motion energy exchange, however with some changes within the terms. The production of random motion by coherent motion is shifted to the negative side (indicating gain), and the diffusion by interaction becomes lower (≈ 0.002). These changes may be balanced by the dissipation terms, which become significant within random motion. Moreover, the advection term increases with Reynolds number, in contrast to what has been observed in coherent motion energy due to aerodynamic stall. In comparison with single airfoil wake (Figure 6.42a), Figure 6.42b shows lower magnitudes of the energy exchange behind the second airfoil, except for the production term at low Reynolds numbers, where an increase is observed. This increase in the production term is attributed to an extended zone of important shear downstream towards the measurement point. A loss of symmetry is also observed at the center wake compared to the single airfoil wake profiles (Figure 6.42a). This symmetry loss can be explained by the shifting of the separation point upstream over the second airfoil. This highlights the effect of upstream obstacle on the distribution of random motion energy within the wake.

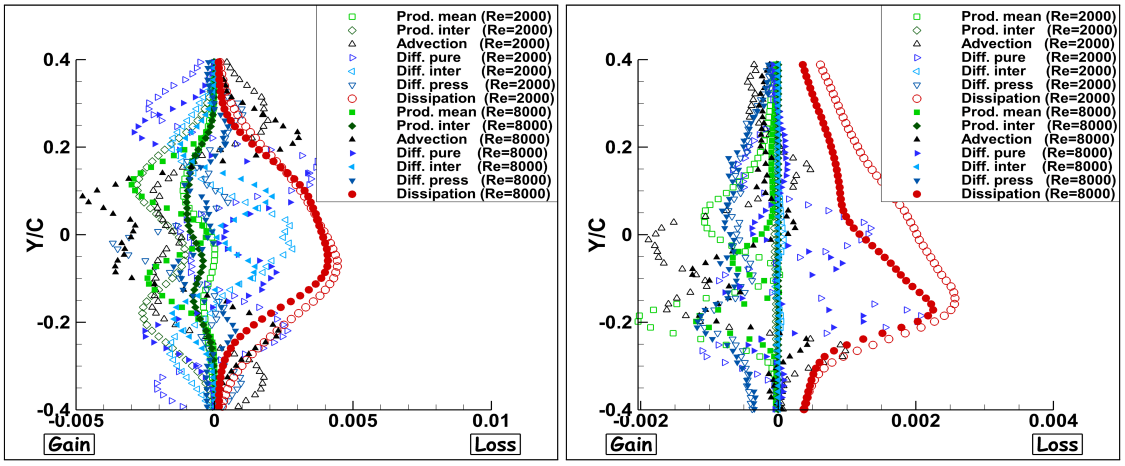

(a) Profiles 5 *cm* behind the airfoil ($X/C = 1.6$), in single airfoil configuration.

(b) Profiles 5 *cm* behind downstream airfoil ($X/C = 5.6$), in single airfoil configuration.

Figure 6.42: Random motion (RM) energy budget terms in single and double airfoil wake for two Reynolds number ($Re = 2000$ and $Re = 8000$), phase decomposition based on upstream airfoil. Terms are normalised by U_0^3/D.

Figures 6.43a and 6.43b present profiles along the Y direction at two specific positions: $X/C = 0.3$ and $X/C = 4.3$, respectively, for both single and double airfoil wake configurations. The profiles initiate at the surface of the airfoil and extend out of the wake, where the positions over the airfoils are $0.6C$ (60% of chord length) referring to the leading edge in X direction. In single airfoil wake, all terms increase strictly reaching a peak at $Y/C = 0.15$. At this position and at high Reynolds number, the production of random motion is relatively high compared to other terms. This is explained that at high Reynolds number, the airfoil edges experience high shear, and the production of structures shifts upstream. Thus, the production of random motion starts from a point closer to the leading edge and extends $1X/C$ downstream the airfoil, see Section D.4.6. In double airfoil wake configuration, all terms initiate their maximum peaks at the surface of the airfoil and converge to zero values at a position of $0.15Y/C$, Figure 6.43b. This observation refer to the disappearance of recirculation zone over the second airfoil which consider as zero values in case of upstream airfoil (Figure 6.43a).

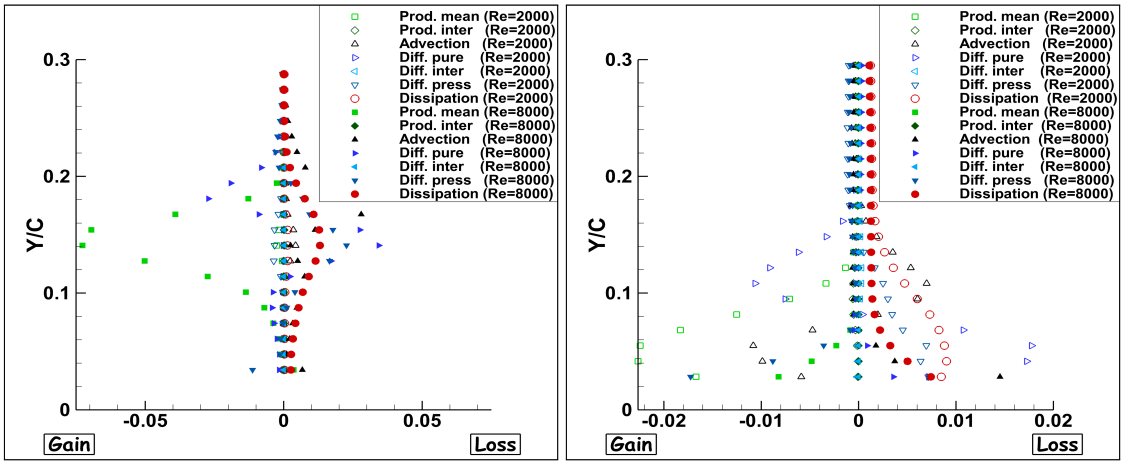

(a) Profiles at $X/C = 0.3$ over the airfoil, in single airfoil configuration.

(b) Profiles at $X/C = 4.3$ over downstream airfoil, in double airfoil configuration.

Figure 6.43: Random motion (RM) energy budget terms over upstream (single airfoil wake) and downstream (double airfoil wake) airfoil for two Reynolds number ($Re = 2000$ and $Re = 8000$), phase decomposition based on upstream airfoil. Terms are normalised by U_0^3/D.

Single and double cylinder wake

The energy exchange of random motion in single and double cylinder wake configurations is also reported using cross sectional profiles. Figures 6.44a and 6.44b present cross-sectional profiles along the Y direction at a distance of 5 cm downstream the first ($X/D = 5$) and second cylinder ($X/D = 15$) for both single and double cylinder wake configurations, respectively.

In the single cylinder wake (Figure 6.44a), a balance of energy exchange among various transport terms is observed. For instance, at $Re = 2000$ and within the center of the wake, it is observed that advection balances both diffusion through interaction and through pressure. This high level of energy exchange between transport terms is shown by equal magnitudes for the same Reynolds number for example. The balance between these terms confirms the equation for random motion energy exchange. Figure 6.44a also highlights a small shift in the magnitudes of these terms at higher Reynolds numbers. This shift is attributed to the presence of a smaller recirculation zone behind the cylinder at higher Reynolds numbers, resulting in the observed differences in term magnitudes. In contrast, in the double cylinder wake (Figure 6.44b), it is observed that all terms associated with low and high Reynolds numbers become similar when compared to the single cylinder wake. Production and advection are equal in magnitude, while pure diffusion is slightly higher than these terms. The increased production by mean flow and pure diffusion, compared to the single cylinder wake, can be explained by extended zones of significant Reynolds stresses and shear downstream in this configuration, (see Sections A.1.6 and B.2.6 for more details).

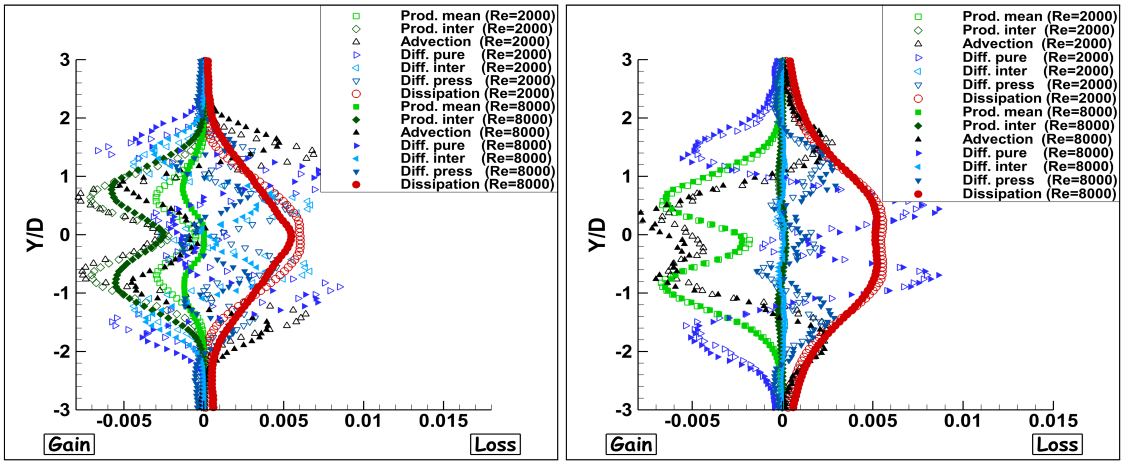

(a) Profiles 5 cm behind the cylinder ($X/D = 5$), in single cylinder configuration.

(b) Profiles 5 cm behind downstream cylinder ($X/D = 15$), in double cylinder configuration.

Figure 6.44: Random motion (RM) energy budget terms in single and double cylinder wake for two Reynolds number ($Re = 2000$ and $Re = 8000$), phase decomposition based on upstream cylinder. Terms are normalised by U_0^3/D.

Figures 6.45a and 6.45b show cross-section profiles along the Y direction at a distance of 15 cm downstream from the first ($X/D = 15$) and second cylinder ($X/D = 25$) for both single and double cylinder wake configurations, respectively. In these profiles, both figures show a significant reduction in magnitude when compared to the profiles at a closer distance (5 cm) to the cylinders. This reduction is expected as the flow evolves downstream and the energy exchange processes becomes lower. In the single cylinder wake (Figure 6.45a), the same behavior is observed as in Figure 6.44a but with lower magnitudes. Each term still maintains its characteristic sign (positive or negative), indicating that the profiles shape persist even at greater distances from the cylinder. In the double cylinder wake (Figure 6.45b), it is remarked that advection has shifted to the positive side, and pressure diffusion is shifted to the negative side when compared to the profiles closer to the cylinders. This suggests that in the far wake of the double cylinder configuration, wake developed more rapidly compared to the single cylinder wake.

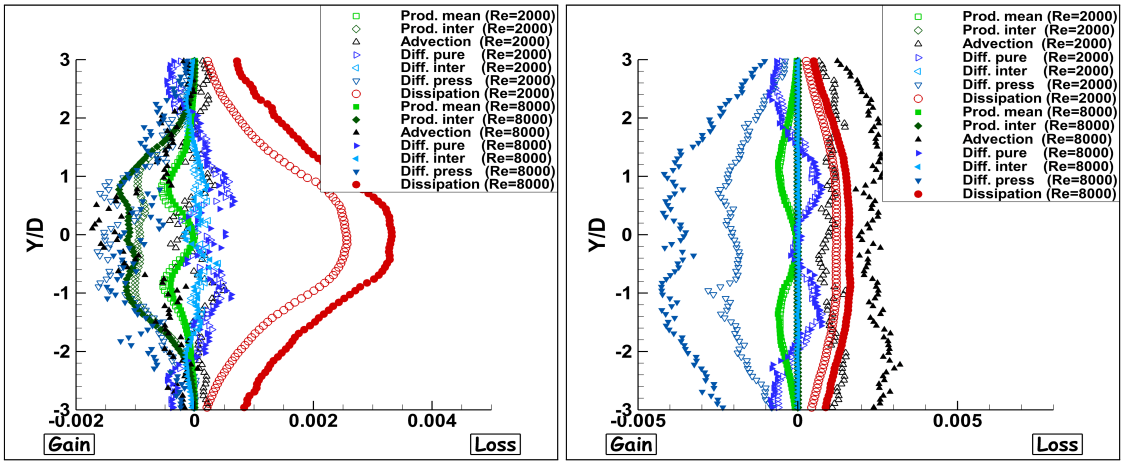

(a) Profiles 15 cm behind the cylinder ($X/D = 15$), in single cylinder configuration.

(b) Profiles 15 cm behind downstream cylinder ($X/D = 25$), in double cylinder configuration.

Figure 6.45: Random motion (RM) energy budget terms in single and double cylinder wake for two Reynolds number ($Re = 2000$ and $Re = 8000$), phase decomposition based on upstream cylinder. Terms are normalised by U_0^3/D.

Profiles with phase decomposition based on downstream cylinder are presented. Figures 6.46a and 6.46b present profiles along Y direction at distances of 5 cm ($X/D = 15$) and 15 cm ($X/D = 25$) downstream the second cylinder, respectively. These profiles are computed based on downstream cylinder phase decomposition. Figure 6.46a shows closely the same observations as in double cylinder wake (Figure 6.44b), however with significant reduction of pure diffusion. This can be explained due to other diffusion terms that took the difference in the budget. Figure 6.46b shows the same observation as those mentioned in Figure 6.45b.

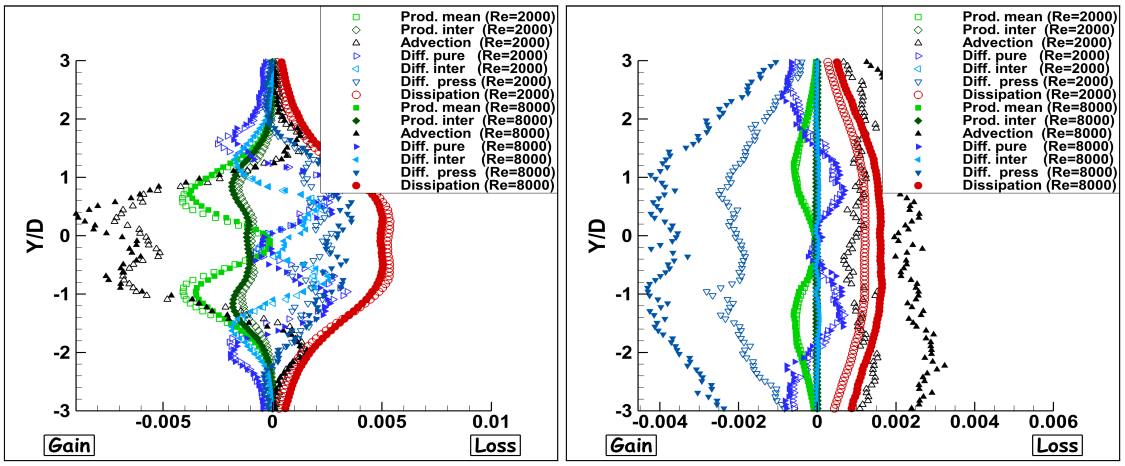

(a) Profiles 5cm behind downstream cylinder ($X/D = 15$), in double cylinder configuration.

(b) Profiles 15cm behind downstream cylinder ($X/D = 25$), in double cylinder configuration.

Figure 6.46: Random motion (RM) energy budget terms in single and double cylinder wake for two Reynolds number ($Re = 2000$ and $Re = 8000$), phase decomposition based on downstream cylinder. Terms are normalised by U_0^3/D.

Cylinder-airfoil wake

In the context of cylinder-airfoil wake analysis, profiles illustrating differences in random motion energy exchange are presented.

Figure 6.47a shows profiles at a distance of 5 cm ($X/D = 21$) downstream from the second obstacle (airfoil) in a cylinder-airfoil wake configuration. The magnitudes of random motion energy exchange in this figure is higher compared to the energy exchange of coherent motion shown in Figure 6.32a. In the case of random motion, the energy is redistributed among all terms, revealing a significant increase in dissipation at high Reynolds numbers. In Figure 6.47b, the profiles are obtained over the airfoil, specifically at a distance of $0.6C$ from the leading edge ($X/D = 14$), in cylinder-airfoil configuration. In this figure, all terms reach their maximum peaks at the surface of the airfoil and converge to zero as one moves in the transverse direction, except advection at low Reynolds number where the airfoil boundary layer is thicker compare to higher Reynolds number, (see Section C.3.6 for more details).

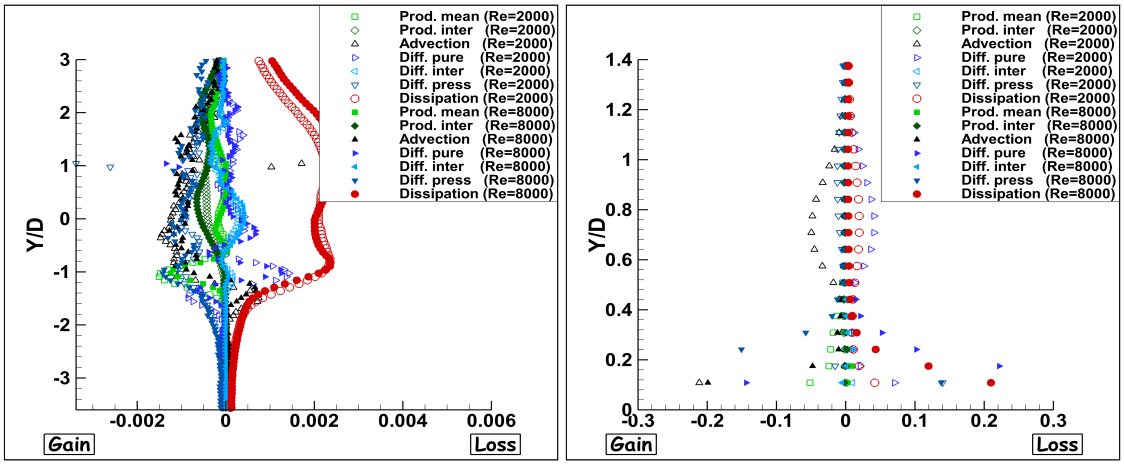

(a) Profiles $5cm$ behind the airfoil ($X/D = 21$), in cylinder-airfoil wake.

(b) Profiles at $X/D = 14$ over downstream airfoil, in cylinder-airfoil configuration.

Figure 6.47: Random motion (RM) energy budget terms in cylinder-airfoil wake for two Reynolds number ($Re = 2000$ and $Re = 8000$), phase decomposition based on upstream cylinder. Terms are normalised by U_0^3/D.

6.4 Observations, reviews, and conclusions

This chapter showed in details the mechanisms of energy exchange without the influence of turbulence (TBL). It offers a comprehensive exploration of the energy exchange of each fluctuation component, namely Coherent Motion (CM) and Random Motion (RM) within the wake affected by an upstream wake. The study of energy exchange mechanisms through total turbulence, coherent motion (CM), and random motion (RM) equations for various configurations reveals several important observations:

- **Enhanced energy exchange over downstream airfoil:**
  - Upstream wakes, whether from a cylinder or an airfoil, enhance the energy exchange (all terms) of CM and RM over the surface of a downstream airfoil.
  - Upstream wakes, whether from a cylinder or an airfoil, leads to a shift in the separation point over the downstream airfoil in the upstream direction.

  - The energy exchange is more pronounced when the upstream wake is generated by a cylinder compared to an airfoil.

- **Reduced energy exchange behind downstream obstacle:**
  - Upstream wakes, whether from a cylinder or an airfoil, reduce the energy exchange of CM behind a downstream obstacle.
  - The energy exchange of RM is generally slightly reduced behind a downstream obstacle. However, in some cases, such as the production term, there may be a slight increase at the measurement point. This increase can be attributed to the extension of the shear zone downstream.

- **Persistence of coherent motion energy:**
  - Coherent motion generated by a cylinder or an airfoil has the ability to persist over a downstream airfoil, whereas it loses most of its energy behind a downstream cylinder.
  - The generation of coherent motion is observed from a downstream cylinder placed in an upstream wake, however this phenomenon is not observed for an airfoil.
  - The generation of coherent motion from a downstream obstacle is lower than the generation of random motion, reaching lower magnitudes

- **Reduction of energy exchange by moving downstream:**
  - The energy exchange of CM and RM decreases as a function of downstream distance due to the cascade process.

CHAPTER 7

Two-point energy exchange with no turbulence effect

Summary

This chapter pertains to the third part of the experimental results obtained within the laminar wind tunnel. The focus is assessing the exchange of turbulent kinetic energy (TKE) at two space points as a function of the upstream flow. Second, third, and fourth-order structure functions provide essential insight into the physics of the turbulent cascade; they offer detailed information compared to one-point turbulent kinetic energy (see Chapter 6). These structure functions provide valuable details on scale-by-scale energy distribution (second-order), the direction along which this energy flows across scales (third-order), and aspects such as intermittency at each scale within the turbulent flow (fourth-order). Two-point structure functions are studied based on streamwise fluctuations (u). All these aspects are tackled for various configurations built upon two primary obstacles: a 1 cm cylinder and a NACA 0015 airfoil.

Contents

7.1 Two-point turbulent kinetic energy balance **149**
7.1.1 Second-order structure functions $\overline{(\Delta u)^2}$ 150
7.1.2 Third-order structure functions $\overline{(\Delta u)^3}$ 153
7.1.3 Fourth order structure functions $\overline{(\Delta u)^4}$ 156
7.2 Observations, reviews and conclusions **159**

7.1 Two-point turbulent kinetic energy balance

Higher-order moments are of great importance in the fundamental understanding of the dynamics of turbulent flows referred to Warhaft [93]. The second, third, and fourth-order structure functions indicate the scale-by-scale energy, the direction towards which this energy flows across scales, and an insight (even partial) into internal intermittency, see

Gauding [94]. The approach developed in this chapter represents a first step, as we only focus on increments of u, along separations parallel to the streamwise direction X. A much more insightful methodology is to be developed for this flow by accounting for the directionality of the flow, i.e. increments of all velocity components along all spatial directions. It is interesting, for instance, to assess the exact way the coherent motions would affect the direction of the cascade (through the sign and value per se of the third-order structure functions), as well as the values of the flatness at each scale (pertaining to the internal intermittency of the flow). These issues are currently investigated and will be reported elsewhere. As a first step of this approach, we focus on the exact way the energy is transferred between coherent motion and random motion. Coherent motion retains information on the initial conditions of the flow, here upstream conditions (say, another blade, another obstacle in a general way). Therefore, studying the dependence of turbulent statistics upon the coherent motions, which are directly linked to the upstream conditions of the flow

7.1.1 Second-order structure functions $\overline{(\Delta u)^2}$

Second-order structure functions represent the quantity of energy transferred at each scale, similar to spectral analysis. Equation 7.1 defines the second-order structure function, S_2, where the velocity (fluctuations) difference (also called increment) is measured over a spatial distance R, and the average is done over X direction (which is interpreted as an ensemble average). Results are presented at the center-line of wakes ($Y/D = 0$) and around 5 cm downstream obstacles. Second-order structure functions at a scale R indicate the energy contained at all scales smaller or equal to R.

$$S_2(R) = \overline{(\Delta u)^2} = \overline{(u(X+R) - u(X))^2}. \tag{7.1}$$

Upstream cylinder's wake

Figures 7.1a and 7.1a show the second-order structure functions at the centerline of single and double cylinder wakes for two Reynolds numbers, respectively. The figures show the structure functions (S_2) for four phases, compared to the baseline case (the latter is defined as no phase decomposition), as Armaly [95]. The second-order structure function S_2 is normalized through the variances of u at the two points. Therefore, the large-scale limit of these normalized structure functions should be equal to 2. Differences with respect to this limit are due to inhomogeneity of the flow. The phased data in Figure 7.1a highlight the energy distribution for different phases for a single cylinder wake. The centerline is at $Y/D = 0$, with a reference position 5 cm ($X/D = 5$) behind the upstream cylinder. At $R/D = 1$, the maximum energy is contained for the phase 0°, and 180°, while the minimum for other opposite phases 100° and 280°, in agreement with the passage of the coherent motions. For example, the energy of large scales at phases 0° and 180° are slightly higher than for the phases 100° and 280° before higher variations of the phases (at $R/D > 1$). This can be linked to a more significant energy generation at these phases in one point TKE (see Section A.1.4). It is observed at phases 0° and 180°, the vortices are ready to be detached with their higher quantity of energy. In contrast, at phases 100° and 280°, the vortices are already detached and, therefore, lower energy is contained in large-scale vortices. It is also remarked that small scales are affected in energy distribution at different phases, as shown in Figure 7.1a. This ensures the interaction between large (coherent motion CM) and small (random motion RM) scales. Concerning baseline data,

values of S_2 for non-phased data are between results for different phases, with the same energy for large scales. For larger scales, oscillations of S_2 are visible, with a periodicity proportional to the distance between two successive vortices in Von Kármán street. This is referred to as coherent motion (CM).

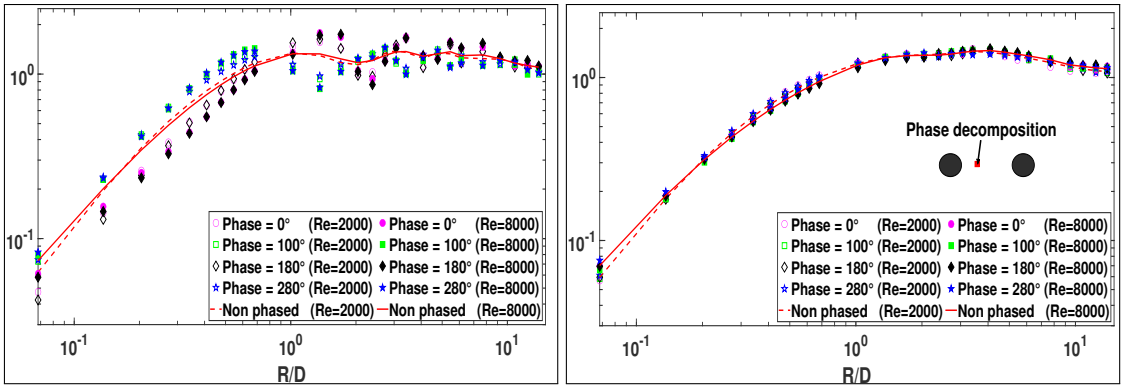

(a) Central line at $Y/D = 0$ with a reference position at $X/D = 5$ in single cylinder wake.

(b) Central line at $Y/D = 0$ with a reference position at $X/D = 15$ in double cylinder wake.

Figure 7.1: 2nd order moment structure functions $\overline{(\Delta u)^2}$ at Re = 2000 and 8000, decomposed at 0°, 100°, 180°, 280° phase shifts and without phase decomposition. Second-order structure functions $\overline{(\Delta u)^2}$ are normalized with respect to the variances at the two points. Phase decomposition is based on the upstream cylinder in both wakes.

In Figure 7.1b, the phased data show the energy distribution across various phases within the wake of a double-cylinder configuration. The phases are decomposed based on the upstream cylinder. The central reference line is positioned precisely at the wake's center ($Y/D = 0$), with a reference point at 5 cm ($X/D = 15$) behind the downstream cylinder. In this figure, by energy examination at decomposed and non-decomposed phases, one observes that the energy levels converge, making it difficult to distinguish between phases or identify the oscillations typically present in a cylinder wake (Figure 7.1a). It is also observed that small scales have slightly lower energy in double cylinder wake compared to single cylinder wake (i.e., baseline case). Figure 7.2a shows the energy distribution across various phases within the wake of a double cylinder through phase decomposition based on the downstream cylinder. The second-order structure functions in this figure are similar to Figure 7.1b and not to Figure 7.1a, as expected. This shows a lower energy generation from the downstream cylinder than the upstream cylinder or in single cylinder wake (Figure 7.1a).

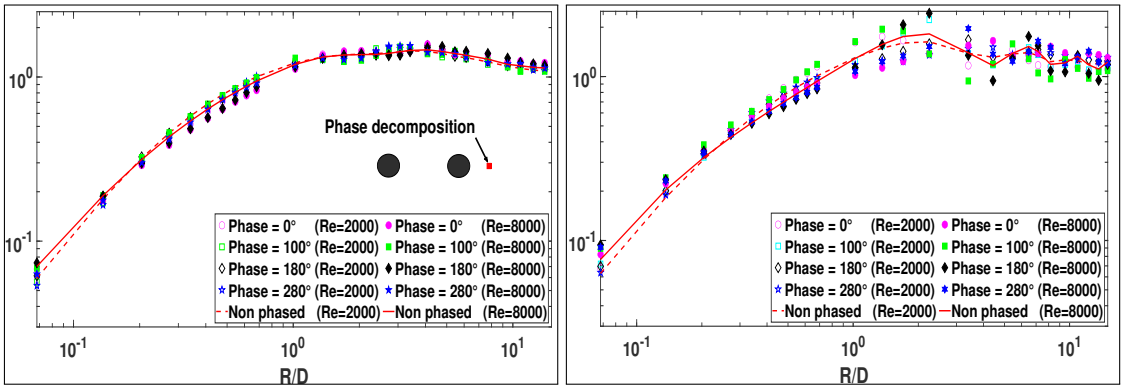

(a) Central line at $Y/D = 0$ with a reference position at $X/D = 15$ in double cylinder wake.

(b) Central line at $Y/D = 0$ with a reference position at $X/D = 21$ in cylinder-airfoil wake.

Figure 7.2: 2nd order moment structure functions $\overline{(\Delta u)^2}$ at Re = 2000 and 8000, decomposed at 0°, 100°, 180°, 280° phase shifts and without phase decomposition. 2nd order functions $\overline{(\Delta u)^2}$ are normalized with respect to the variances at the two points. Phase decomposition is based on the downstream cylinder in double cylinder wake and the upstream cylinder in cylinder-airfoil wake.

Figure 7.2b shows the second-order structure functions at the center of cylinder-airfoil wake (interaction of cylinder wake with airfoil wake). These results are presented for two different Reynolds numbers. The central reference line is precisely positioned at $Y/D = 0$, corresponding to the center of the downstream airfoil. The reference point is $X/D = 21$, related to a location 5 cm behind the downstream airfoil. This figure reveals an essential phenomenon of great interest: the large-scale vortices in this configuration exhibit significantly higher energy levels when compared to the previous configuration for all phases and both Reynolds numbers (i.e., $S_2(2.5) > 2$). This phenomenon can be explained by the interaction of vortices generated by the upstream wake with the structures created by the airfoil. This combination results in a substantial increase in energy when compared to the wake generated by a single cylinder, as shown in Figure 7.1a.

Upstream airfoil's wake

Figures 7.3a and 7.3b show the second-order structure functions at the center of a single and double airfoil wakes for two Reynolds numbers, respectively. The figures indicate the structure function (S_2) for four phases and the baseline case (without phases decomposition). The second-order structure function S_2 is normalized with respect to the variances at the two points. In Figure 7.3a, one can observe that the energy distribution among phases at large scales is relatively lower compared to what is observed in Figure 7.1a (which represents the wake generated by a single cylinder). In other words, the oscillation effect on energy distribution within the wake of a single airfoil is lower. This indicates that the energy of vortices in the wake of an airfoil is generally lower than that of a cylinder. Conversely, in the case of the double airfoil wake, Figure 7.3b, it is shown that smaller scales exhibit significantly higher energy levels when compared to all previous cases. This observation highlights a distinct difference in energy distribution within the wake when two airfoils are present, and it may be indicative of unique flow patterns and interactions between the airfoils.

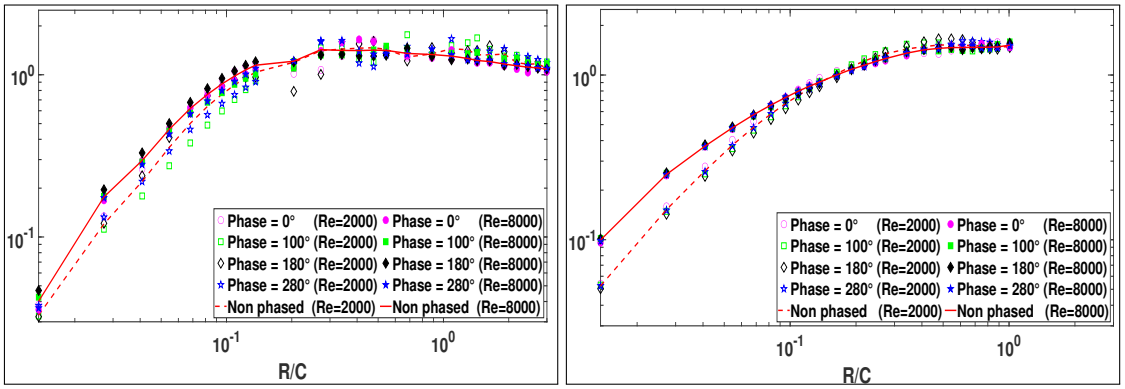

(a) Central line at $Y/C = 0$ with a reference position at $X/C = 1.6$ in single airfoil wake.

(b) Central line at $Y/C = 0$ with a reference position at $X/C = 5.6$ in double airfoil wake.

Figure 7.3: Second-order structure functions $\overline{(\Delta u)^2}$ at Re = 2000 and 8000, decomposed at 0°,100°, 180°, 280° phase shifts and without phase decomposition. Second-order structure functions $\overline{(\Delta u)^2}$ are normalized with respect to the variances at the two points. Phase decomposition is based on the upstream airfoil in both wakes.

7.1.2 Third-order structure functions $\overline{(\Delta u)^3}$

Equation (7.2) defines the third-order structure function, denoted as S_3. The velocity (fluctuations) difference is measured over a spatial distance R, and the ensemble average is done over X direction. The third-order structure function reflects the statistical behavior of velocity fluctuations at a specific spatial separation distance R. The sign of S_3 is a crucial indicator in turbulence studies, helping to characterize the direction of energy transfer and the organization of turbulent eddies in a fluid flow. When S_3 is negative, it signifies a direct cascade process. In a direct cascade, the largest scales of turbulence break down and lead to the generation of progressively smaller eddies. This phenomenon is a fundamental turbulence characteristic, where energy flows from larger to smaller scales. Inversely, positive S_3 signifies an inverse cascade, where small-scale structures combine and interact to form larger-scale structures.

$$S_3(R) = \overline{(\Delta u)^3} = \overline{(u(X+R) - u(X))^3}. \tag{7.2}$$

Upstream cylinder's wake

Figures 7.4a and 7.4b show the third-order structure functions at the center of single and double cylinder wakes for two Reynolds numbers, respectively. The figures show the structure function (S_3) for four phases and the baseline case, where phase decomposition is based on upstream cylinder wake. Third-order function S_3 is normalized using second-order structure functions $\overline{(\Delta u)^2}^{3/2}$. The cascade behavior is very different for all phases. Phases 0° and 180° exhibit a more enhanced cascade effect compared to phases 100° and 280°. This distinction is clear in the rapid decrease of the third-order structure function (S_3) from $R/D = 10^0$ to lower values in a negative direction for phases 0° and 180°, whereas the transition is smoother for phases 100° and 280°. The third-order structure function highlights a direct cascade (negative S_3) at smaller scales and an inverse cascade (positive S_3) at large scales for phases 0° and 180° in single cylinder wake, see Figure 7.4a. This behavior indicates the breakdown of large-scale turbulent structures into smaller-scale

eddies, which is a characteristic of a direct cascade. Furthermore, it suggests a tendency for larger-scale structures to exhibit oscillations (positive and negative S_3), due to their inhomogeneous behavior. On the other hand, the third-order structure functions reveal an inverse cascade pattern for most scales at phases 100° and 280°. This observation underscores that the energy transfer within the turbulence is not uniform for different phases. Concerning double cylinder wake, the third-order structure function, Figure 7.4b, exhibits no distinction between phases. In this Figure, all phases show a smooth convergence from approximately $R/D = 10^0$ close to zero. This behavior indicates a consistent and direct cascade process for all phases within the double-cylinder wake.

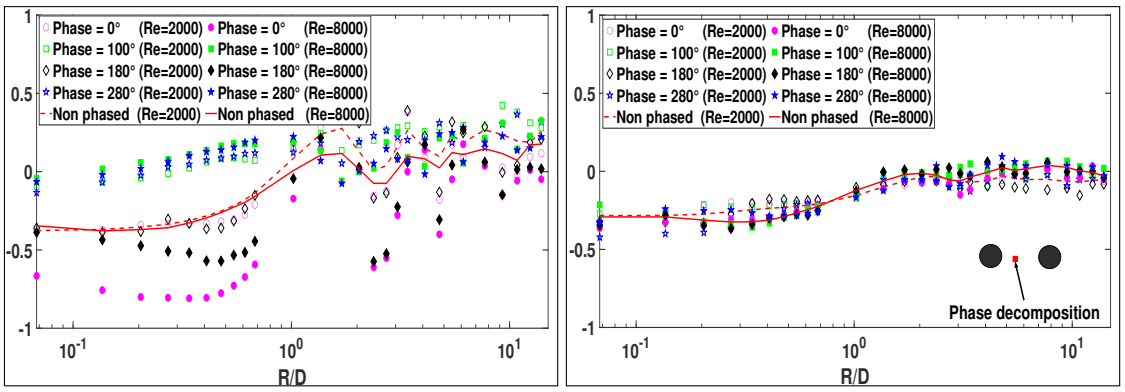

(a) Central line at $Y/D = 0$ with a reference position at $X/D = 5$ in single cylinder wake.

(b) Central line at $Y/D = 0$ with a reference positionat $X/D = 15$ in double cylinder wake.

Figure 7.4: Third-order structure functions $\overline{(\Delta u)^3}$ at $Re = 2000$ and 8000, decomposed at 0°,100°,180°,280° phase shifts and without phase decomposition. Third order structure functions $\overline{(\Delta u)^3}$ are normalised by $\overline{(\Delta u)^2}^{3/2}$. Phase decomposition is based on the upstream cylinder in both wakes.

Figure 7.5a shows the third-order structure functions at the centerline of the wake behind two cylinders for two Reynolds numbers (2000 and 8000). The figure shows the structure-function (S_3) for four phases and the baseline case, where phase decomposition is based on the downstream cylinder. In Figure 7.5a, the difference between phases becomes more significant and pronounced than those in Figure 7.4b, particularly when observing the cascade behavior at phases 0° and 180°, where values decrease rapidly. This pattern of behavior in Figure 7.5a is approaching the observations in Figure 7.4a, which represents a single cylinder wake. However, the differences between phases are less pronounced in Figure 7.5a, due to the coherent motion with lower energy in this case. To conclude, the absence of distinct phase differences or coherent motions in the third-order structure function within the wake of the double cylinders suggests a higher degree of symmetry and coherence in the turbulent flow. This implies an influence from coherent motions that typically play a role in the energy cascade process. The behavior in this configuration is similar to a single-cylinder wake but with fewer phase-dependent variations.

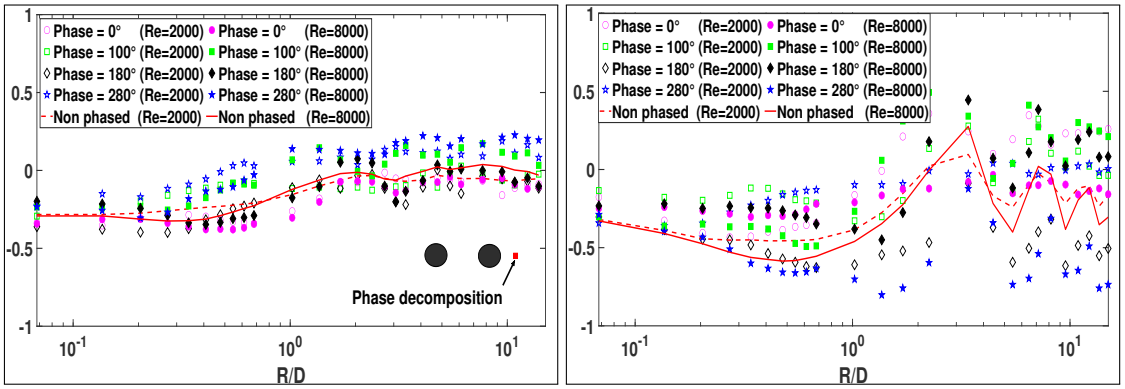

(a) Central line at $Y/D = 0$ with a reference position at $X/D = 15$ in double cylinder wake.

(b) Central line at $Y/D = 0$ with a reference position at $X/D = 21$ in cylinder-airfoil wake.

Figure 7.5: Third order structure functions $\overline{(\Delta u)^3}$ at Re = 2000 and 8000, decomposed at 0°,100°,180°,280° phase shifts and without phase decomposition. 3rd order functions $\overline{(\Delta u)^3}$ are normalised by $(\overline{(\Delta u)^2})^{3/2}$. Phase decomposition is based on the downstream cylinder in the two-cylinder wake and the upstream cylinder in the cylinder-airfoil wake.

Figure 7.5b shows the third-order structure functions at the center of cylinder-airfoil wake (interaction of cylinder wake with airfoil wake). These results are presented for two different Reynolds numbers. The central reference line is positioned in the same location as the second-order structure function. In this figure, a complex behavior is observed in which both direct and inverse cascade processes exist. At small scales, the structure-function exhibits characteristics of a direct cascade, where energy is transferred from larger to smaller scales. Conversely, at larger scales, an inverse cascade occurs sometimes, and the direct cascade persists in others. For instance, at high Reynolds numbers and phases 100° and 180°, the cascade transitions to an inverse cascade at larger scales. Similarly, this transition to an inverse cascade occurs at low Reynolds numbers and phases 0° and 100°. It should be noted, however, that for large scales, our approach reaches some limits because of the combined effect of possible lack of convergence in statistics and the presence of inhomogeneity. Thus, the inverse cascade is one possible scenario. Further investigations are required in this direction.

In this configuration (cylinder-airfoil), intensified oscillations (direct and inverse cascade process) are observed at larger scales. This phenomenon is attributed to the inhomogeneous dynamics exhibited by large scales arising from the interaction between coherent motion originating from the cylinder and turbulence generated by the airfoil. The general trend in the third structure function shows that a direct cascade occurs at small scales and then evolves to an inverse cascade at a certain scale (i.e., $R/D = 1$), only to return to a direct cascade eventually. This behavior is particularly evident in the non-decomposed data, Figure 7.5b, illustrating the dynamic nature of energy transfer within the wake of the cylinder-airfoil interaction.

Upstream airfoil's wake

Figures 7.6a and 7.6b show the third-order structure functions at the center of single and double airfoil wakes for two Reynolds numbers, respectively. The Figures show the structure-function (S_3) for four phases and the baseline case, where phase decomposition is based on upstream airfoil wake. In the case of the single airfoil wake (Figure 7.6a), differences between phases at small scales within the cascade process are observed. For instance, at phases 100° and 280°, there is a higher presence of direct cascade compared

to phases 0° and 180°. Note that at low Reynolds numbers, small scales at phase 0° are involved in an inverse cascade, which differs significantly from what is observed in a single cylinder wake (Figure 7.4a). The cascade for all phases converges smoothly to zero regarding the large scales. In contrast, Figure 7.6b shows the double airfoil wake. The inverse cascade is more prominent at large scales, especially for phases 100° and 280°. Moreover, unlike the single airfoil wake, the direct cascade for all phases does not exhibit significant differences at small scales.

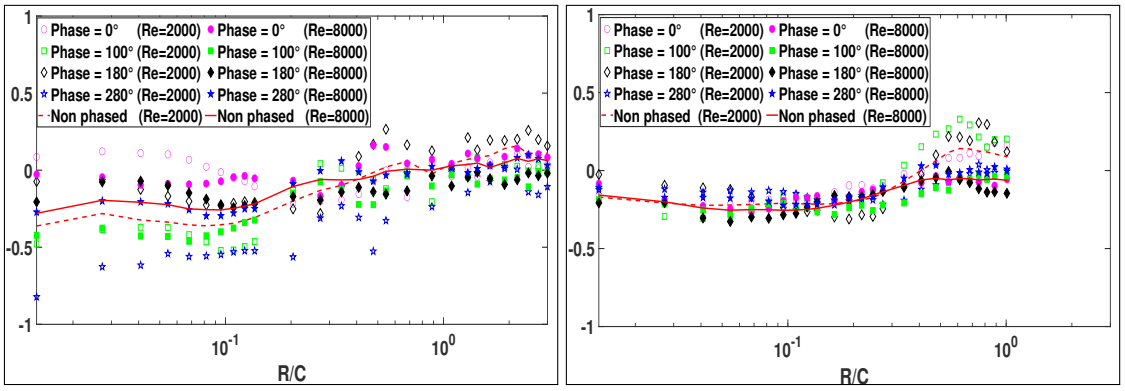

(a) Central line at $Y/C = 0$ with a reference position at $X/C = 1.6$ in single airfoil wake.

(b) Central line at $Y/C = 0$ with a reference position at $X/C = 5.6$ in double airfoil wake.

Figure 7.6: Third order structure functions $\overline{(\Delta u)^3}$ at Re = 2000 and 8000, decomposed at 0°,100°,180°,280° phase shifts and without phase decomposition. Third order structure functions $\overline{(\Delta u)^3}$ are normalised by $(\overline{(\Delta u)^2})^{3/2}$. Phase decomposition is based on the upstream airfoil in both wakes.

7.1.3 Fourth order structure functions $\overline{(\Delta u)^4}$

The fourth-order structure function is beneficial for studying intermittency in turbulence. Intermittency refers to the irregular and sporadic occurrence of extreme events within turbulent flows. Intermittency can arise from various factors, including the complex interactions of turbulent eddies and the nonlinear dynamics of turbulence. It can also be influenced by the presence of coherent structures, the geometry of the flow, or specific flow conditions. Equation 7.3 defines the fourth-order structure-function, denoted as S_4. The fourth-order structure function reflects the statistical behavior of velocity fluctuations at a specific spatial separation distance R.

$$S_4(R) = \overline{(\Delta u)^4} = \overline{(u(X+R) - u(X))^4} \tag{7.3}$$

Upstream cylinder's wake

Figures 7.7a and 7.7b show the fourth order structure functions at the center of single and double cylinder wakes for two Reynolds numbers, respectively. The figures show the structure-function (S_4) for four phases and the baseline case, where phase decomposition is based on upstream cylinder wake. The fourth-order structure function S_4 is normalized using the second-order structure functions $(\overline{(\Delta u)^2})^2$. In the single-cylinder wake, distinctions between phases are evident, and the intermittency is significantly high at smaller scales for certain phases. For example, at phases 0° and 180°, the intermittency is very

high relative to phases 100° and 280°. This observation highlights the presence of higher dissipation at these phases, which can be attributed to the high shear in regions where turbulence production is significant (as explained earlier in Figure 7.1a). Additionally, at these phases (0° and 180°), there is evidence of interaction intermittency at large scales, indicating interactions between large-scale turbulent structures and other scales within the flow. On the other hand, Figure 7.7b illustrates that the dissipation behind the second cylinder is lower, and the interaction of large scales is also reduced for all phases within the double cylinder wake (phases decomposition based on the upstream cylinder). This observation suggests that, compared to the first cylinder, the second cylinder dampens the dissipation of turbulent energy and the interactions between large-scale turbulent structures.

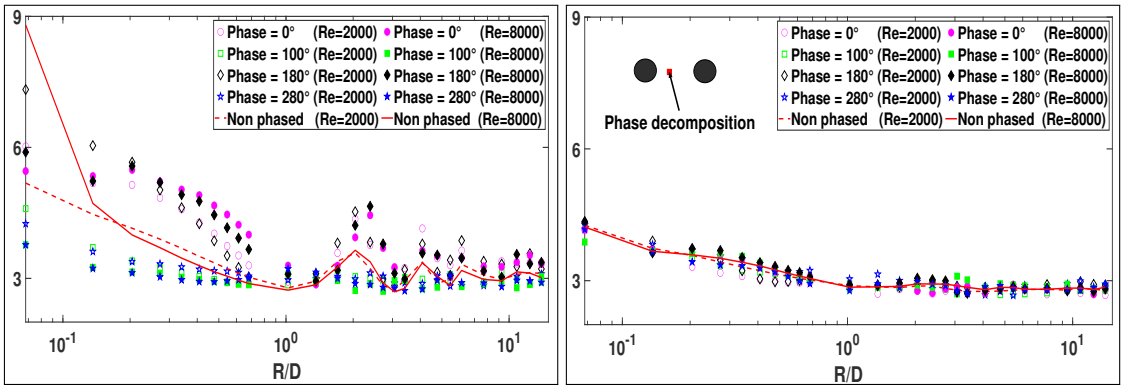

(a) Central line at $Y/D = 0$ with a reference position at $X/D = 5$ in single cylinder wake.

(b) Central line at $Y/D = 0$ with a reference position at $X/D = 15$ in double cylinder wake.

Figure 7.7: Fourth order structure functions$\overline{(\Delta u)^4}$ at $Re = 2000$ and 8000, decomposed at 0°,100°,180°,280° phase shifts and without phase decomposition. Fourth order structure functions $\overline{(\Delta u)^4}$ are normalised by $(\overline{(\Delta u)^2})^2$. Phase decomposition is based on the upstream cylinder in both wakes.

Concerning the wake within the double cylinder configuration with phases decomposition based on downstream cylinder (Figure 7.8a), the fourth-order structure functions exhibit similar characteristics to those seen in Figure 7.7b, with a very slight difference. The remarkable difference observed is that, for high Reynolds numbers and phases 0° and 180°, the intermittency becomes slightly higher for intermediate and large scales in Figure 7.8a.

Figure 7.8b shows the fourth-order structure functions at the center of cylinder-airfoil wake (interaction of cylinder wake with airfoil wake). These results are presented for two different Reynolds numbers. The central reference line is positioned in the same location as the second-order structure function. In the cylinder-airfoil wake, distinctions between phases are observed at intermediate and large scales. Specifically, at both high and low Reynolds numbers, phases exhibit higher intermittency at phase 280° and phase 180°, respectively. This observation emphasizes the upstream cylinder wake's significant influence on the airfoil wake's behavior, particularly at large scales. This behavior is consistent with the previous analysis of third-order structure functions, where it was observed that large scales interact with other scales downstream of the airfoil and increase their energy. It can also be explained as an interaction of large scales with other scales, leading to the observed intermittency patterns at different phases.

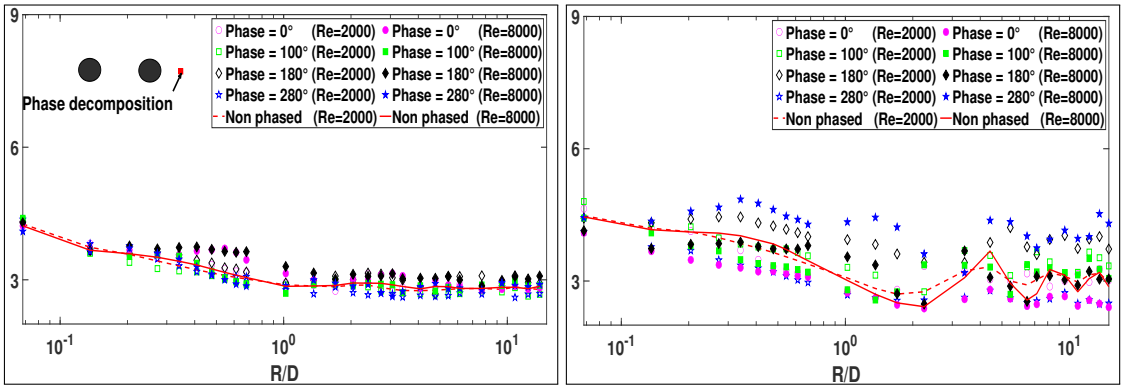

(a) Central line at $Y/D = 0$ with a reference position at $X/D = 15$ in double cylinder wake.

(b) Central line at $Y/D = 0$ with a reference position at $X/D = 21$ in cylinder-airfoil wake.

Figure 7.8: Fourth order structure functions $\overline{(\Delta u)^4}$ at $Re = 2000$ and 8000, decomposed at 0°,100°,180°,280° phase shifts and without phase decomposition. Fourth order structure functions $(\Delta u)^4$ are normalised by $(\overline{(\Delta u)^2})^2$. Phase decomposition is based on the downstream cylinder in double cylinder wake and the upstream cylinder in cylinder-airfoil wake.

Upstream airfoil's wake

Figures 7.9a and 7.9b show the fourth-order structure functions at the center of single and double airfoil wakes for two Reynolds numbers, respectively. The figures show the structure-function (S_4) for four phases and the baseline case, where phase decomposition is based on upstream airfoil wake. Fourth order function S_4 is normalized using the second-order structure functions $(\overline{(\Delta u)^2})^2$. In the single airfoil wake (Figure 7.9a), higher intermittency is observed at phases 100° and 280° within small scales due to relatively higher dissipation. This aligns with third-order structure function observations, where the cascade was more enhanced and pronounced at these phases. In the double airfoil wake (Figure 7.9b), dissipation is increased at smaller scales relative to the single airfoil wake. Moreover, slight changes at large scales are evident in the double airfoil wake. These changes can be attributed to interactions between large-scale turbulence generated by the upstream airfoil and the downstream airfoil. These interactions may involve energy exchange between large and small scales or interactions among various scales of turbulence.

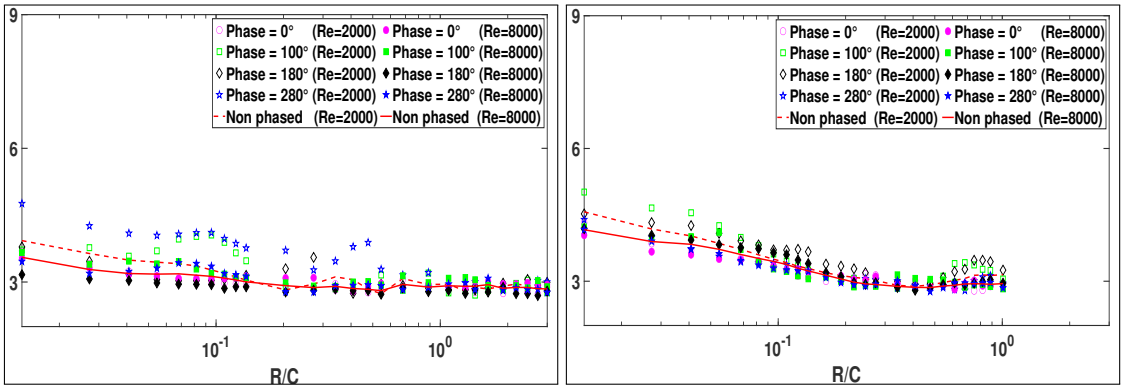

(a) Central line at $Y/C = 0$ with a reference position at $X/C = 1.6$ in single airfoil wake.

(b) Central line at $Y/C = 0$ with a reference position at $X/C = 5.6$ in double airfoil wake.

Figure 7.9: Fourth order structure functions $\overline{(\Delta u)^4}$ at Re = 2000 and 8000, decomposed at 0°,100°,180°,280° phase shifts and without phase decomposition. Fourth order structure functions $\overline{(\Delta u)^4}$ are normalised by $(\overline{(\Delta u)^2})^2$. Phase decomposition is based on an upstream airfoil in both wakes.

In summary, the fourth-order structure functions highlight the intermittency, interactions, and dissipation within the wake resulting from the interaction of a cylinder wake with an airfoil wake.

7.2 Observations, reviews and conclusions

In this chapter, second, third, and fourth-order structure functions are studied in details for various configurations. These structure functions, provide essential insight into the physics of the turbulent cascade. They provide valuable details about scale-by-scale energy distribution (second-order), the direction along which this energy flows across scales (third-order), and aspects such as intermittency at each scale within the turbulent flow (fourth-order). The analyses extend across different phases of coherent structures, revealing a pronounced influence of coherent motion phases on smaller structures. This underscores the significant impact of coherent motion on the characteristics of smaller-scale structures within the studied context. A review on the observations shown in this chapter can be as follow,

- **In single cylinder wake**, it is shown that large scale vortices contain maximum energy at phases 0° and 180°. Enhanced direct cascade (negative S_3) at smaller scales and inverse cascade (positive S_3) at large scales for phases 0° and 180° are observed. The intermittency is significantly high at smaller scales at phases 0° and 180° relative to phases 100° and 280°.

- **In double cylinder wake**, smaller scales have slightly lower energy than single cylinder wake. No significant differences are shown between phases' decomposition based on the upstream or downstream cylinders in the energy distribution study (S_2). With phase decomposition based on the upstream cylinder, the direct cascade process is consistent for all phases. Dissipation and large-scale interaction behind the second cylinder are lower than the single-cylinder wake. With phase decomposition based on the downstream cylinder, the cascade direction (S_3) is close to what is shown in cylinder wake, however, with lower magnitudes between phases. The intermittency

becomes slightly higher for intermediate and large scales at certain phases compared to phase decomposition based on the upstream cylinder.

- **In cylinder-airfoil wake**, large-scale vortices exhibit significantly higher energy levels when compared to other configurations for all phases and both Reynolds numbers. In this configuration, the third structure function shows a more enhanced direct cascade for smaller scales than other configurations. The interactions between the large-scale vortices generated by the upstream cylinder and the turbulence from the downstream airfoil result in alterations at large scales. These interactions contribute to the inhomogeneity of large structures. Phases 280° and 180° exhibit higher intermittency than other phases. This emphasizes the upstream cylinder wake's significant influence on the airfoil wake's behavior.
- **In single airfoil wake**, the oscillation effect on energy distribution within the wake of a single airfoil is lower compared to cylinder wake. This indicates that the energy of vortices in the wake of an airfoil is generally lower than that of a cylinder. Phases 100° and 280°, have higher presence of direct cascade at smaller scales compared to phases 0° and 180°. Higher intermittency is observed at phases 100° and 280° within small scales due to relatively higher dissipation.
- **In double airfoil wake**, smaller scales exhibit significantly higher energy levels when compared to all previous cases. Dissipation is increased at smaller scales relative to the single airfoil wake. Slight changes at large scales are observed due to the interactions between large-scale vortices generated by the upstream airfoil and the downstream airfoil turbulence leading to more inhomogeneous large structures.

CHAPTER 8

Mechanism of energy exchange with turbulence effect

Summary

This chapter marks the second part of the experimental results obtained within a turbulent boundary layer (TBL) wind tunnel. Consequently, the effects of three-dimensional turbulence or turbulent boundary layers are considered. The aim of this chapter is to reveal the role exerted by an upstream wake placed in a Turbulent Boundary Layer (TBL), on the downstream flow. The methodology is based upon assessing transport equations for the total kinetic energy (TKE) with the inclusion of both Coherent (CM) and Random (RM) Motions. 2C-2D in-plane velocity fields (couples of 30000 images) are measured behind the obstacles (Cylinders and airfoils) by Particle Image Velocimetry (PIV). Consequently, varoius configurations are presented and discussed that involve the combination of two primary obstacles: a 1cm cylinder and a NACA 0015 airfoil. The measurements planes are at three different heights ($z^+ = z/\frac{\nu}{u_\tau}$) from the wall: $z^+ = 500$, $z^+ = 1500$ and $z^+ = 3125$. Different heights lead to different local Reynolds numbers based on the cylinder diameter, i.e. Re = 4666, 5333 and 6000.

Contents

8.1 Introduction to turbulence near wall **162**
8.1.1 Turbulent Boundary Layer regions 162
8.1.2 Theory of Turbulent Boundary Layer 164
8.2 Experimental Setup **166**
8.2.1 Test section 166
8.2.2 Obstacles installation 166
8.2.3 Turbulent boundary layer characteristics 167
8.2.4 PIV measurement technique 169
8.2.5 PIV processing 170
8.3 First order statistics **171**
8.4 Total fluctuation energy exchanges **174**

8.4.1 2D - planes for total turbulent kinetic energy budget 175
8.4.2 Cross section profiles for total turbulent kinetic energy budget . 178
8.5 Non organized coherent motion in airfoil wake **181**
8.6 CM and RM interaction TKE **182**
8.6.1 Cross section profiles of coherent motion (CM) energy budget . 182
8.6.2 Cross section profiles of random motion (RM) energy budget . 184
8.7 Observations, reviews and conclusions **186**

8.1 Introduction to turbulence near wall

Wall-bounded flows involve fluids moving near solid surfaces, like walls. These fluids were earlier studied by Hanger [96] and Reynolds [97]. The "no-slip condition" is crucial here, meaning that the fluid sticks to the wall's speed. This leads to the generation of vorticity, or swirling motion, at the wall due to the abrupt change in velocity. This vorticity can undergo various changes within the fluid, such as diffusion or amplification. The Reynolds number (Re) is a way to describe the nature of fluid flow. It helps us to determine whether inertia or viscosity dominates in a particular flow. High Reynolds numbers suggest that inertia is the dominant force in the flow, which often leads to turbulence. D'Alembert's paradox highlights a seeming contradiction when we consider flows without viscosity. In such inviscid flows, theory suggests there should be no drag (resistance) on objects immersed in the flow. However, in real-world scenarios, we observe drag forces due to factors like flow separation and the creation of wakes. Prandtl's contribution was to recognize the importance of viscosity, even in high Reynolds number flows. He argued that some level of viscosity always plays a role, helping to explain why drag and other flow phenomena exist even when inertia seems dominant. This insight helped bridge the gap between theoretical predictions and real-world observations of fluid flow.

8.1.1 Turbulent Boundary Layer regions

In a boundary layer, the velocity profile is influenced by different physical mechanisms depending on the specific region being examined. As a result, the boundary layer can be mainly divided into two distinct regions: the inner region, characterized by high viscosity and proximity to the wall, and the outer region, often referred to as the wake region, where turbulence prevails. This differentiation can be illustrated by considering the behavior of shear stress, denoted as τ_{uw}, defined as follows: $\tau_{uw} = -\rho\overline{uw} + \mu\frac{\partial U}{\partial z}$, see Tiomajou [98]. Where ρ represents density, $\overline{uw}$ signifies the Reynolds stress, and μ denotes dynamic viscosity. In most parts of the boundary layer, the dominant factor influencing τ_{uw}, is the Reynolds stress term $-\rho\overline{uw}$. However, this predominance changed near the wall, where the viscous term becomes essential due to the high velocity gradients in that region. Figure 8.1 shows the visual representation of the turbulent boundary layer in three evolution phases (laminar boundary layer - transition zone - turbulent boundary layer) . This figure likely illustrates how the boundary layer evolves through different phases, showing also the inner (viscous, buffer and overlap sublayers) and outer regions (developed turbulence) in turbulent boundary layer.

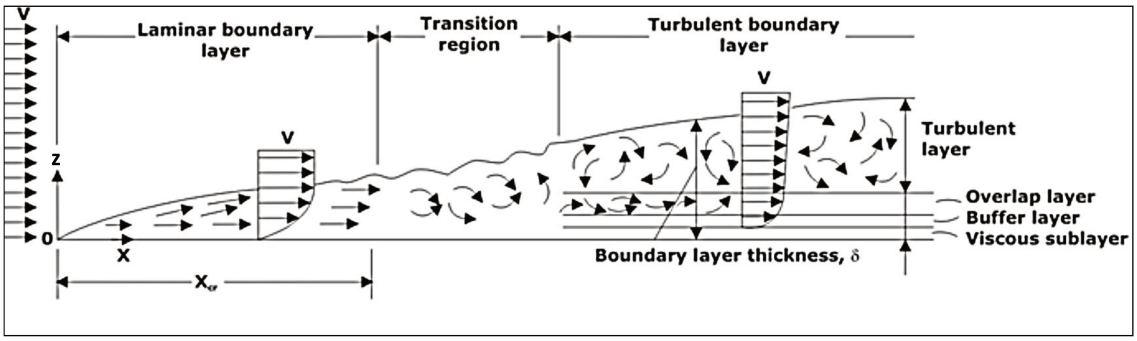

Figure 8.1: Turbulent Boundary Layer zones[1].

Inner region

This region encompasses approximately 10% of the boundary layer and extends up to $z = 0.1\delta$, where δ represents the boundary layer thickness. Close to the wall, the influence of convective terms becomes insignificant when compared to the effects of viscosity and turbulence. In case of a zero pressure gradient, the streamwise momentum equation can be expressed as:

$$\frac{\partial \tau_{uw}}{\partial z} = 0, \tag{8.1}$$

where, $\tau_{uw} = -\rho\overline{uw} + \mu\frac{\partial U}{\partial z}$, and by integrating this equation, we obtain $\tau_{uw} = \tau_w$, where τ_w represents the wall shear stress. u_τ and $\frac{\nu}{u_\tau}$ are the characteristic velocity and length scales, respectively. Through dimensional analysis, one can derive the universal form of the velocity profile as

$$U^+ = f(z^+). \tag{8.2}$$

Here, U^+ is defined as $\frac{U}{u_\tau}$, and z^+ is expressed as $\frac{zu_\tau}{\nu}$. In the near-wall section of the inner region, where $z^+ < 5$, which is often referred to as the viscous sublayer, the influence of viscosity is predominant. In this region, the wall shear stress τ_w can be expressed as:

$$\tau_w = \mu\frac{\partial U}{\partial z}. \tag{8.3}$$

This equation signifies that the wall shear stress is determined primarily by the viscous effects, and it provides an essential characterization of the flow behavior in the very close vicinity of the boundary wall.

Outer region

The outer region of the boundary layer covers approximately 90% of its thickness, extending from $z = 0.1\delta$ to the outer boundary of the boundary layer. In this region, turbulence effects dominate, and the characteristic velocity and length scales are denoted as u_τ ($u_\tau = \sqrt{\frac{\tau_w}{\rho}}$) and δ, respectively. Through dimensional analysis, we can express the velocity profile as

$$\frac{U}{u_\tau} = f'\left(\frac{z}{\delta}\right). \tag{8.4}$$

[1] https://exomechanicals.blogspot.com/2021/03/boundary-layer-in-fluids.html?utm_source=feedburner&utm_medium=feed&utm_campaign=Feed:+ExoMechanicals+(EXO+MECHANICALS)&m=1

This equation illustrates that the velocity profile in the outer region is primarily influenced by turbulence characteristics.

Logarithmic region

At high Reynolds numbers, there is a shared region that link the inner and outer regions of the boundary layer, where the influence of viscous terms becomes negligible. In this common region, asymptotic methods can be employed to derive the velocity profile. When considering the inner region close to the wall with $z/\delta \to 0$ and the outer region with $z^+ \to \infty$, we obtain a logarithmic velocity profile

$$U^+ = \frac{1}{\kappa} \ln(z^+) + C. \tag{8.5}$$

κ represents the Von Karman constant, and C is a constant that is experimentally determined, as in Zanoun [99]. Commonly accepted values for these constants are $\kappa = 0.41$ and C = 5.0, although they may slightly vary depending on specific flow conditions. Figure 8.2 shows the main velocity profile in Turbulent Boundary Layer. This figure likely provides a visual representation of how the velocity changes across the boundary layer, illustrating the behavior in the inner, logarithmic, and outer regions. It's worth to note that within this transitional region, there is also a buffer layer where the velocity profile transitions between the logarithmic region and the viscous sublayer. This buffer layer typically spans $5 < z^+ < 50$. Buffer region features that Reynolds stresses are very close to viscous stresses $\rho\overline{uw} \simeq \mu\frac{\partial U}{\partial z}$,

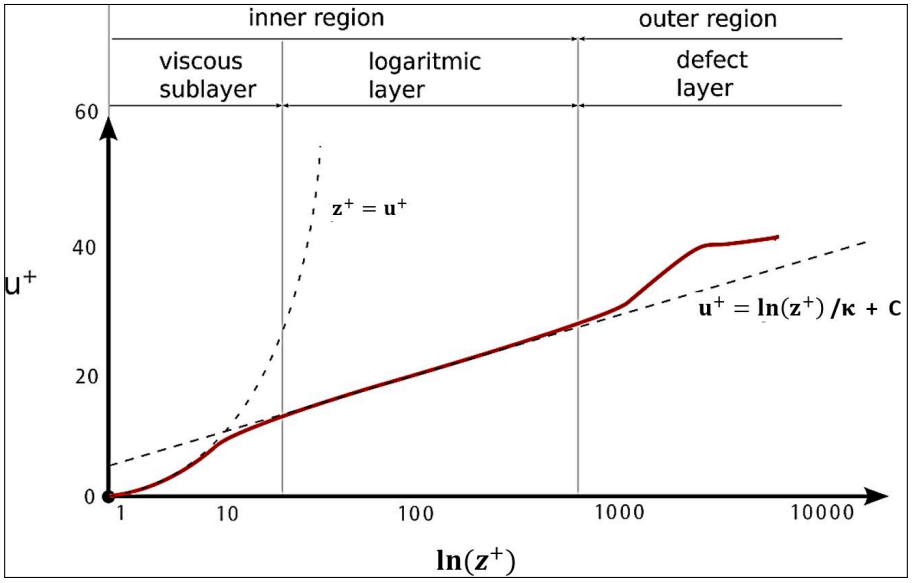

Figure 8.2: Turbulent Boundary Layer profile. Graph is obtained from [100].

8.1.2 Theory of Turbulent Boundary Layer

In wall-bounded flows, a boundary layer is formed at the region close to the wall where the effect of viscosity is dominant and influences the dynamics of the flow. This boundary layer initially starts as laminar, but with increasing Reynolds number, it transitions to a fully turbulent state. In an idealized fluid, the flow consists of a viscous boundary layer near the wall and an inviscid outer flow with no velocity fluctuations. However, in

real-world scenarios, the outer flow also exhibits turbulence, which can be quantified using the turbulence intensity (TI) equation

$$TI = \frac{\sqrt{\frac{1}{3}(\overline{u^2} + \overline{v^2} + \overline{w^2})}}{U_\infty}. \tag{8.6}$$

The laminar-to-turbulent transition in a flow is influenced by the turbulence intensity, and other aspects of the flow, such as the development of the turbulent boundary layer, separation point, and heat transfer, are all affected by the turbulence intensity of the outer flow.

The edge of the turbulent boundary layer is characterized by the transition from irrotational outer flow to the rotational turbulent boundary-layer flow. The thickness of the turbulent boundary layer (δ) is defined as the point where the velocity of the flow (u) reaches 0.99 times the freestream velocity of the flow (U_e). While δ spatially and temporally varies due to strong fluctuations in the boundary layer, its characteristics can be explained by two important quantities: the displacement thickness (δ^*) and the momentum thickness (θ), given by

$$\delta^* = \int_0^\infty \left[1 - \frac{\overline{U}(z)}{U_e}\right] dz. \tag{8.7}$$

$$\theta = \frac{\overline{U}(z)}{U_e} \int_0^\infty \left[1 - \frac{\overline{U}(z)}{U_e}\right] dz. \tag{8.8}$$

The displacement thickness (δ^*) represents the distance by which the flow must be displaced outward to account for the velocity loss in the boundary layer due to friction, while the momentum thickness (θ) represents the thickness of an imaginary layer within the flow with momentum equal to the loss of momentum in the real fluid within the turbulent boundary layer. The ratio of displacement thickness to momentum thickness is called the shape factor (H), given by

$$H = \frac{\delta^*}{\theta}. \tag{8.9}$$

In wall-bounded turbulent flows, the wall shear stress plays a crucial role and is defined as

$$\tau_w = \nu \frac{\partial \overline{u}}{\partial z}. \tag{8.10}$$

where the subscript 'w' denotes the value at the wall. The skin-friction coefficient (cf) is a dimensionless quantity that characterizes the wall shear stress and is defined as

$$cf = \frac{\tau_w(x)}{\frac{1}{2}\rho U_e^2}. \tag{8.11}$$

The normalization is based on the wall viscous length scale ($\delta_\nu = \frac{\nu}{u_\tau}$) and the friction velocity scale ($u_\tau = \sqrt{\frac{\tau_w}{\rho}}$). The Reynolds number based on this friction velocity is defined as $Re_\tau = \frac{u_\tau \delta}{\nu}$, and another frequently used Reynolds number is based on the momentum thickness, given by $Re_\theta = \frac{U_e \theta}{\nu}$.

In near-wall turbulent flows at high Reynolds numbers, the flow consists of a thin boundary layer near the wall where strong velocity gradients occur and a region outside the boundary layer where the flow behaves nearly inviscid. This means that gradients of

mean values in the flow direction parallel to the wall (X direction) are much smaller than those in the transverse direction (Y direction).

8.2 Experimental Setup

8.2.1 Test section

The experimentation phase was conducted within the limits of the boundary layer wind tunnel at the Lille Fluid Mechanics Laboratory (LMFL) in the framework of ANR program "DYNEOL", previously discussed in Section 1.2.1. Within this framework, the collaborative experiments are considered as part of the CORIA-LMFL experimental partnership. This wind tunnel is equipped with a test section that measures 2 m in width, 1 m in height, and spans a great length of 20 m, see Figure 8.3. The advantage of this particular wind tunnel configuration lies in its essential length coupled with a relatively modest free-stream velocity, denoted as U_∞ and peaking at 10 m/s. This design feature (20 m long) provides a crucial purpose of generation a substantially thick boundary layer, which reaches a thickness of approximately 24 centimeters at the terminal end of the test section. This leads most of the studies to be carried out at the terminal end of the wind tunnel section where the turbulent boundary layer is well developed. The free-stream turbulence intensity in the wind-tunnel is relatively low, of the order of 0.3% of U_∞. The wind tunnel itself operates as a closed-loop system, and the test section possesses transparent viewing windows on all four sides. This integrated feature is to facilitate the extensive utilization of optical techniques throughout the experimentation process. To gain more on the wind tunnel's specifications and underlying design principles, further valuable insights can be found in the comprehensive study conducted by Stanislas [101]. Additionally, WALLTURB program held in Lille describes also the wall turbulence of the wind tunnel, this is shown by Stanislas [102].

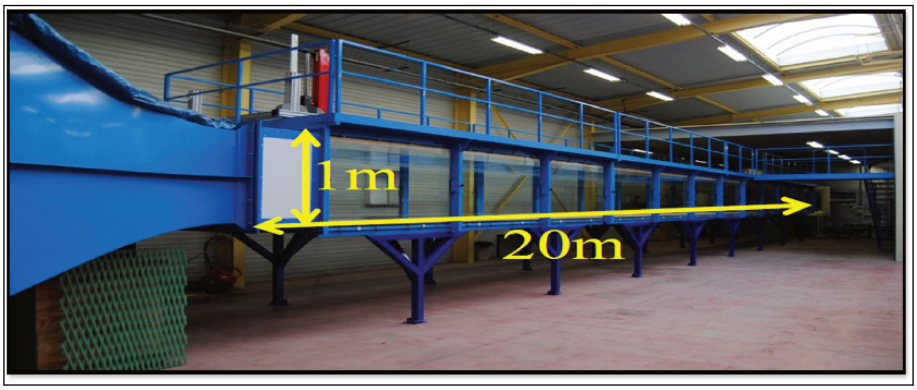

Figure 8.3: LML wind tunnel.

8.2.2 Obstacles installation

Within the context of this research study, obstacles are installed at a distance of 17 m downstream (X direction), highlighted by a red rectangle in Figure 8.4a. The installed obstacles are shown in Figure 8.4b. These obstacles interact with the developed turbulent boundary layer contributing to the comprehensive study of turbulence and its impact. Obstacles (cylinders and airfoils) used for the experiments are similar to those used in the laminar wind tunnel of CORIA laboratory, seen in Chapter 6. The obstacles are painted black to avoid any reflections during the experiment.

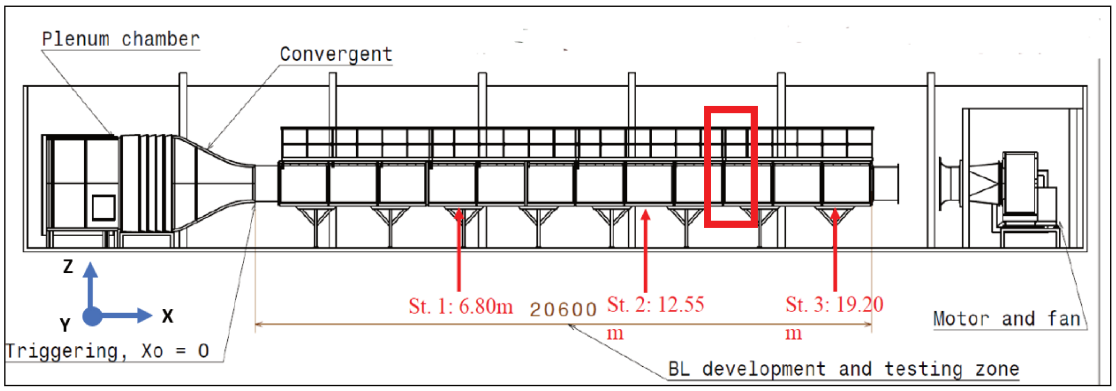

(a)

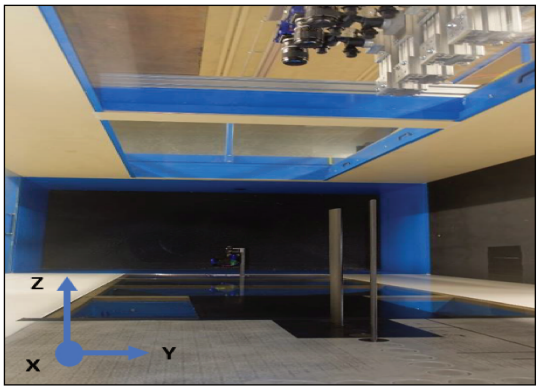

(b)

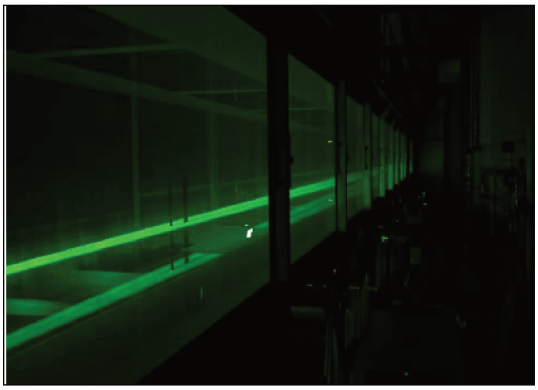

(c)

Figure 8.4: (a) Measurement position in wind tunnel. (b) Installed obstacles in test section. (c) Laser sheet in test section.

8.2.3 Turbulent boundary layer characteristics

The necessary parameters characterizing the studied turbulent boundary layer (TBL) are precisely detailed in Tables 8.1 and 8.2. These tables present a comprehensive set of parameters, including the TBL thickness (δ), displacement thickness (δ_*), momentum thickness (θ), shape factor (H), represented as δ/θ, wall friction velocity (U_τ), Reynolds number based on momentum thickness (Re_θ) represented as $U_e\theta/\nu$, Reynolds number based on friction velocity (Re_τ) calculated as $\delta U_\tau/\nu$, normalized pressure gradient ($\partial p/\partial x^+$), and the normalization factor (ν/U_τ). The importance of these parameters leads to characterizing and understanding the complex flow dynamics within the boundary layer.

X (m)	U_e **(m/s)**	δ **(cm)**	δ_* **(cm)**	θ **(cm)**	**H**
17	10	22	3.20	2.5	1.3

Table 8.1: Characteristics of the turbulent boundary layer (TBL) - first part.

X (m)	U_τ **(m/s)**	Re_θ	Re_τ	$\frac{\partial p}{\partial x}^+$	$\frac{\nu}{U_\tau}$ **(mm)**
17	0.34	16800	5095	-1.4×10^-4	0.04

Table 8.2: Characteristics of the turbulent boundary layer (TBL) - second part.

Figure 8.5 shows the mean velocity profiles of four Reynolds numbers using classical

semi-logarithmic representation. The profiles shown in Figure 8.5 are referred to Carlier and Stanislas study [103] using Hot Wire Anemometer. These profiles exhibit clear universality close to the wall and are in line with the well-known Van Driest Equation 8.12. Von Kàrmàn constant κ in Equation 8.12 is 0.41. The Reynolds-number range covered in the data reveals a significant logarithmic region, extending over at least one decade. These profiles are also shown in studies, such as in Foucaut [104, 105].

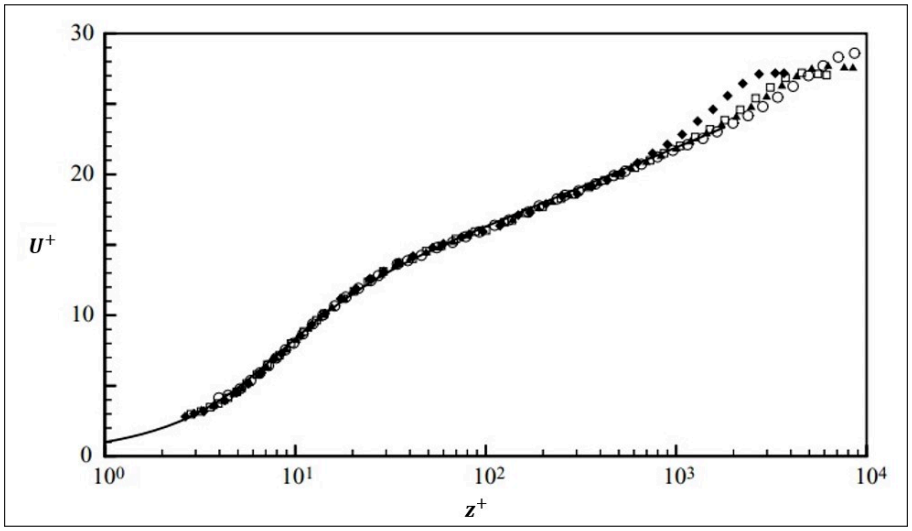

Figure 8.5: Profiles of streamwise mean velocity obtained by Hot Wire Anemometry: ♦, $R_\theta = 8100$; □, $R_\theta = 11500$; ▲, $R_\theta = 14800$; ∘, $R_\theta = 20600$; −, Van Driest profile. Data is referred to Carlier study [103].

$$U^+(z^+) = \int_0^{z^+} \frac{2dz^+}{b + \sqrt{b^2 + 4a(z^+)}} \quad \text{with} \begin{cases} a(z^+) = [\kappa y^+(1 - exp(z^+/c^+))]^2 \\ b = 1, \\ c^+ = 2 \end{cases} \tag{8.12}$$

Figure 8.6 shows the profiles of turbulence intensities for four Reynolds numbers, scaled in wall units and as a function of both z/δ away from the wall and z^+ near the wall. A good universality is remarked in both representations. Specifically, the peak amplitude of all three fluctuations seems to exhibit independence with respect to Reynolds numbers when expressed in terms of wall units.

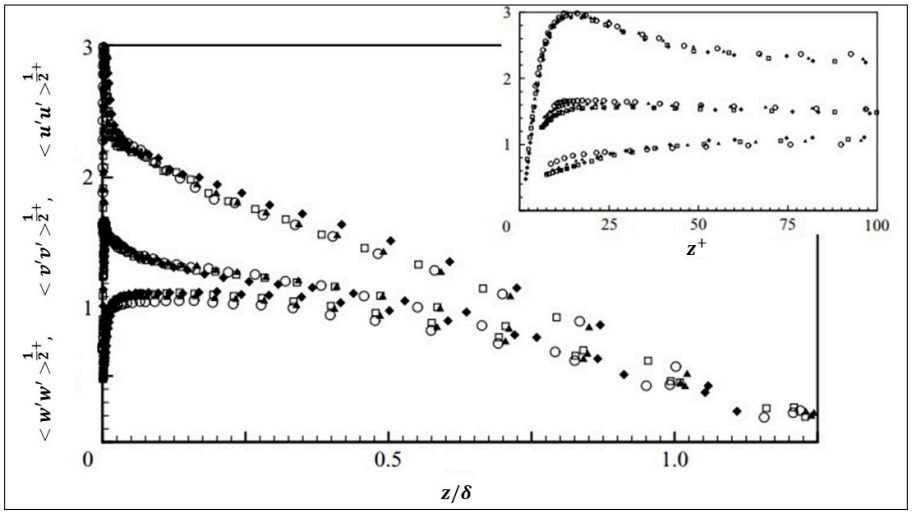

Figure 8.6: Profiles of RMS obtained by Hot Wire Anemometry: ⧫, $R_\theta = 8100$; □, $R_\theta = 11500$; ▲, $R_\theta = 14800$; ○, $R_\theta = 20600$. Data are referred to Carlier study [103].

8.2.4 PIV measurement technique

The experimental measurements, were conducted using low speed 2C-2D Particle Image Velocimetry (PIV) technique, precisely in the longitudinal direction, aligning with the Von Kármán street generation, as illustrated in Figure 8.4c. The data acquisitions are performed in the streamwise/spanwise (X-Y) planes of the turbulent boundary to characterize the cross-section of the vortices produced by obstacles. This measurement technique provides detailed insights of velocity fields and turbulence characteristics within the boundary layer. Four Lavision sCMOS cameras with spatial resolution 2560×2160 $pixels^2$ are installed in row at the top of the wind tunnel (at $z = 1.2$ m from the field of view) to enlarge the field of view. The cameras are equipped with micro Nikkor 105 mm lens to obtain a magnification of 15 $pixel/mm$. The cameras are working at 4 frames per second (fps) and $f\#$ number is set to 8. A Nd-YAG (BMI) laser (532 nm) is used to illuminate 59×15 cm^2 field of view. The laser produces pulses of 130 mJ with a maximal frequency 12 Hz. The laser beam passed through a spherical lens ($f = 5000$ mm), cylindrical lens ($f = 80$ mm) and reflection mirrors, see Figure 8.7. The laser sheet at the focus line is 0.7 mm thick in the field of view and was introduced in the wind tunnel through the bottom glass with two 4" mirrors. The last mirror was placed 1.5 m downstream the end of the field of view to minimize the perturbation.

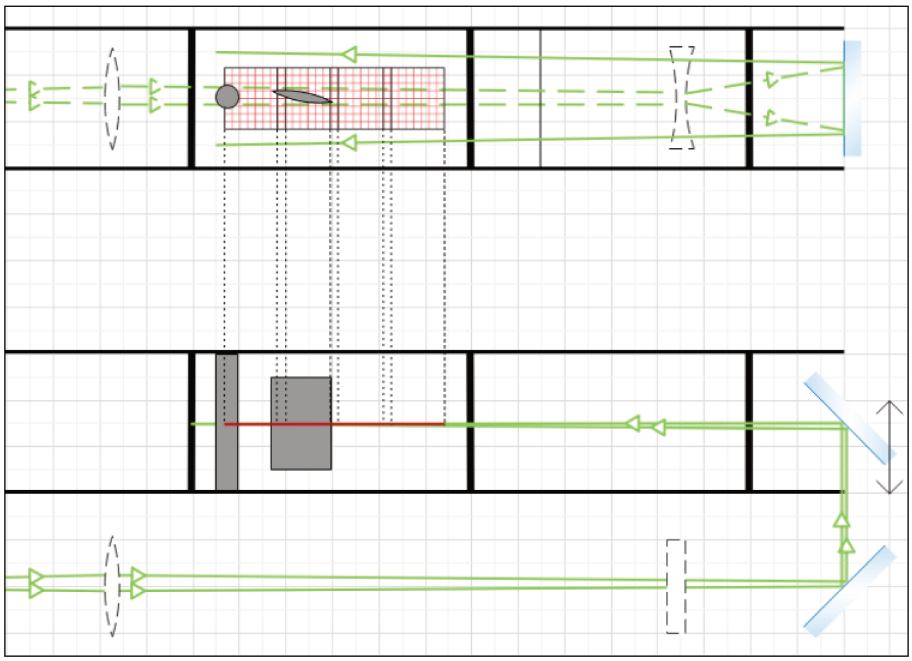

Figure 8.7: Laser sheet path.

The measurements planes is in the logarithmic region and at three different heights from the wall: $z = 20\ mm$ ($z^+ = 500$ where $z^+ = U_\tau z/\nu$), $z = 60\ mm$ ($z^+ = 1500$) and $z = 125\ mm$ ($z^+ = 3125$). These heights correspond to three different Reynolds numbers ($Re = UD/\nu$) based on the cylinder diameter, $Re = 4666$, 5333 and 6000, respectively. These Reynolds numbers are equivalent to three Reynolds number based on airfoil chord $Re_c = 23333$, 26666 and 30000 respectively, as detailed in Table 8.3.

X	z^+	Re_d	St	Shedding freq.(Hz)	Couple images
Single cylinder	500	4666	0.21	140	10000
	1500	5333	0.21	160	
	3125	6000	0.21	180	
X	z^+	Re_c	St	Shedding freq.(Hz)	Couple images
Single airfoil	500	23333	0.21	170	10000
	1500	26666	0.21	193.5	
	3125	30000	0.21	218	
Double obstacle	**x**	**x**	**x**	**x**	30000

Table 8.3: Experiment setup parameters.

8.2.5 PIV processing

Time between pulses is 120 μs for all studied cases. The PIV post processing is performed using the in-house code developed in LMFL laboratory. The processing is done by use of an in-house modification from the MatPIV toolbox for Matlab, written by Sveen (2004). A 2 times 3 points Gaussian fit for the cross-correlation peak is used. The analysis is done with a multipass/multigrid approach, developed and illustrated by Scarano [106]. The four interrogation windows begin with $64 \times 64\ pixels^2$ and ending with $24 \times 24\ pixels^2$ (corresponding to $1.6 \times 1.6\ mm^2$). Overlap is set to 50%, yielding 937×211 vector field.

To eliminate the spurious vectors, the universal outlier detection shown by Westerweel and Scarano [107] is applied. Before the last pass, an image deformation is also applied to improve results quality as shown by Lecordier [57]. Data are validated and saved as Network Common Data Form (NetCDF).

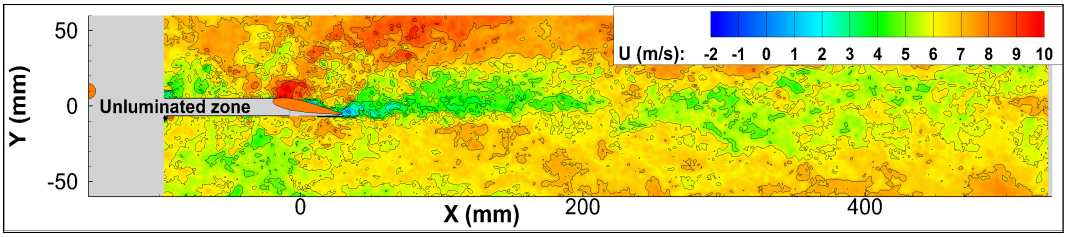

(a) Velocity field in streamwise direction (X direction).

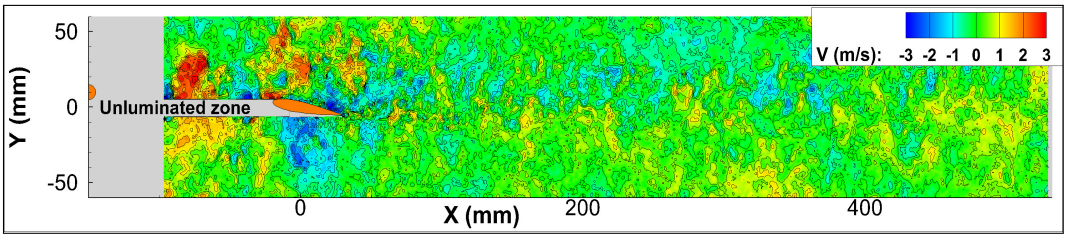

(b) Velocity field in spanwise direction (Y direction).

Figure 8.8: Instantaneous velocity fields in both directions.

8.3 First order statistics

First order statistics play a fundamental role in understanding flow dynamics. They provide essential insights into the overall behavior of the flow, helping to characterize its fundamental properties, including direction, magnitude, and distribution. This information is important for understanding the mechanisms of energy exchange within the flow. Figure 8.9 shows the mean velocity in the streamwise direction for both single and double airfoil wakes at $z^+ = 3125$. Behind the upstream airfoil (Figure 8.9a), the recirculation zone (demonstrated in Figure 6.1a) is disappeared. This observation can be attributed to the impact of the Turbulent Boundary Layer, which prevent the evolution of the wake and vortices detachment from the airfoil. The confined and narrow width of the wake provides further evidence for this interpretation. Moreover, it is observed that the airfoil wake goes down by moving downstream. This can be explained by the presence of significant spanwise fluctuations (v), see Figure 8.6.

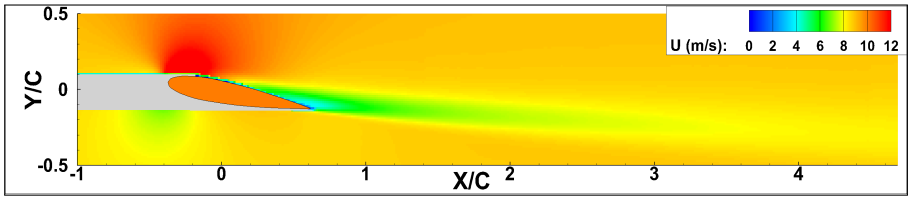

(a) Single airfoil wake.

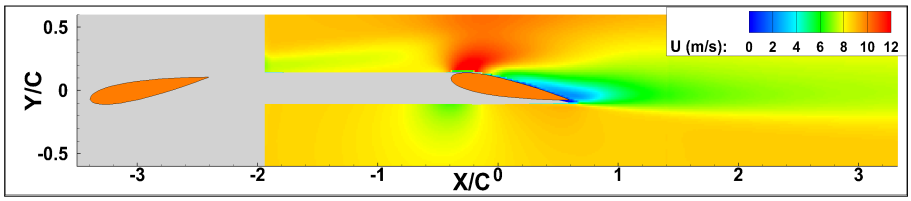

(b) Double airfoil wake.

Figure 8.9: Streamwise (X direction) mean velocity in single and double airfoil wakes at $z^+ = 3125$.

In contrast, when considering the downstream airfoil, a weak recirculation zone appears (Figure 8.9b). The downstream airfoil wake becomes more horizontal and no longer moving down. This suggests a decrease in the dominance of the turbulent boundary layer. Figure 8.10 shows the mean velocity in spanwise direction for both single and double airfoil wakes at $z^+ = 3125$. Between the two configurations, there is a slight difference in the distribution of spanwise velocity. The negative spot observed over the upstream airfoil (Figure 8.10a) is significantly decreased over the downstream airfoil (Figure 8.10b).

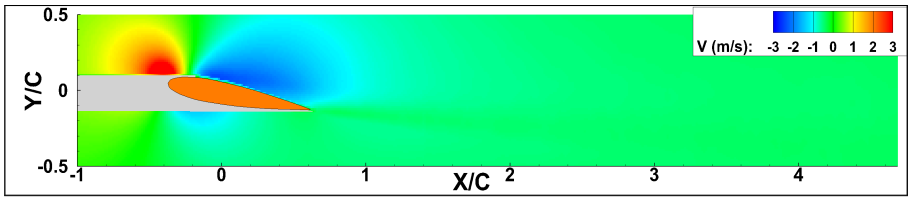

(a) Single airfoil wake.

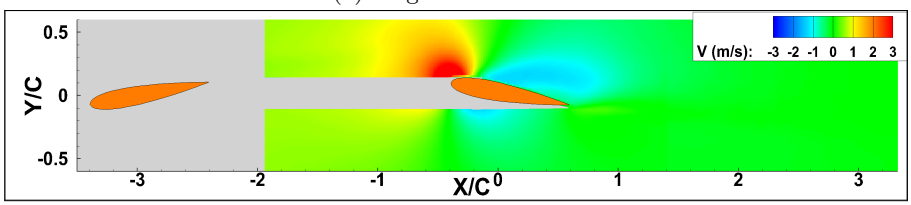

(b) Double airfoil wake.

Figure 8.10: Spanwise (Y direction) mean velocities in single and double airfoil wakes at $z^+ = 3125$.

Figure 8.11 shows the Root Mean Square (RMS) in the streamwise direction (X direction) for both single and double airfoil wake configurations at $z^+ = 3125$. In the case of the single airfoil wake (Figure 8.11a), the RMS exhibits significant values with peak magnitudes behind the airfoil. As one moves downstream, the RMS gradually decreases. However, the RMS values experience a re-increase over the downstream airfoil exceeding RMS values observed upstream, see Figure 8.11b for double airfoil wake configuration.

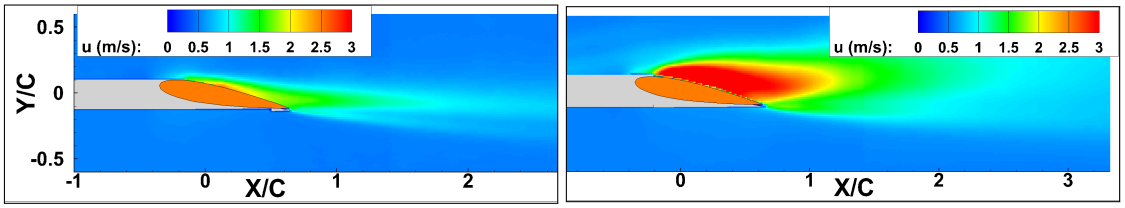

(a) Single airfoil wake. (b) Double airfoil wake.

Figure 8.11: RMS of streamwise velocity (X direction) in single and double airfoil wake configurations, at $z^+ = 3125$.

Figure 8.12 shows the RMS in the spanwise direction (Y direction) for both single and double airfoil wake configurations at $z^+ = 3125$. These observations align with those illustrated for the RMS in the streamwise direction within both single and double airfoil wake configurations.

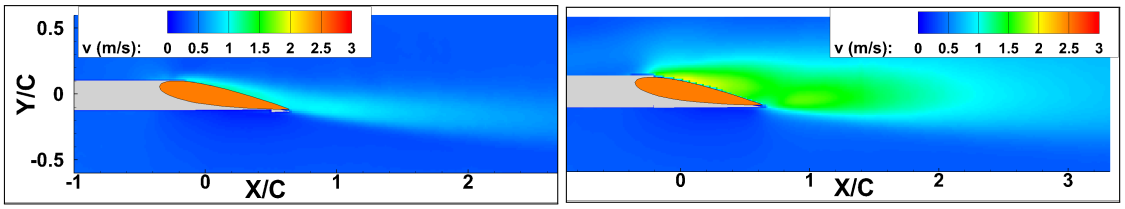

(a) Single airfoil wake. (b) Double airfoil wake.

Figure 8.12: RMS of spanwise velocity (Y direction) in single and double airfoil wake configurations, at $z^+ = 3125$.

This chapter provides a detailed examination of the single and double airfoil configurations. However, it briefly discusses other configurations, such as single, double cylinder wake and cylinder-airfoil wake configurations. For the single cylinder wake configuration at $z^+ = 3125$, Figures 8.13a and 8.13b show the mean velocity profiles in the streamwise (X) and spanwise (Y) directions, respectively. Figures 8.13c and 8.13d show the mean velocity in streamwise (X) and spanwise (Y) directions within double cylinder wake configuration at $z^+ = 3125$, respectively. Figure 8.13c shows that the wake behind the downstream cylinder widens in comparison with the single cylinder wake (shown in Figure 8.13a). This expansion is attributed to the presence of the downstream cylinder, which increases the velocity deficit downstream.

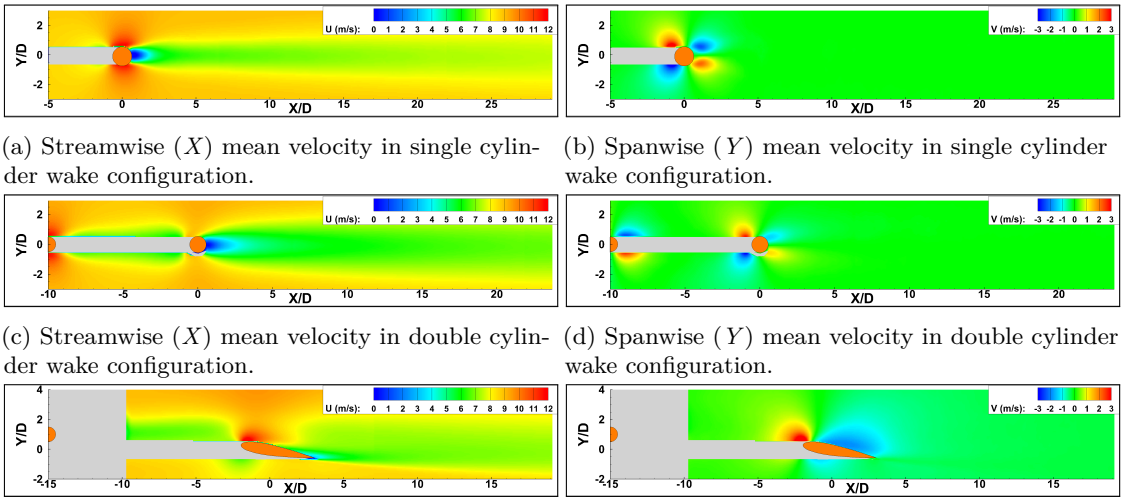

(a) Streamwise (X) mean velocity in single cylinder wake configuration.

(b) Spanwise (Y) mean velocity in single cylinder wake configuration.

(c) Streamwise (X) mean velocity in double cylinder wake configuration.

(d) Spanwise (Y) mean velocity in double cylinder wake configuration.

(e) Streamwise (X) mean velocity in cylinder-airfoil wake configuration.

(f) Spanwise (Y) mean velocity in cylinder-airfoil wake configuration.

Figure 8.13: Streamwise and spanwise (X and Y directions) mean velocity in single and double cylinder, cylinder-airfoil wake configurations.

Figures 8.13e and 8.13f show the mean velocity in streamwise (X) and spanwise (Y) directions within cylinder-airfoil wake configuration at $z^+ = 3125$, respectively. In Figure 8.13e, it is observed that the velocity within the wake is reduced, except at the leading edge. This reduction in velocity is primarily attributed to the flow acceleration over the leading edge of the airfoil.

8.4 Total fluctuation energy exchanges

The transport equation illustrates the dynamics and characteristics of turbulence in the flow at a specific location (one point). Equation 8.13 is studied for obstacles wakes within the Turbulent Boundary Layer (TBL). In Equation (8.13), U_i is the mean velocity along i_{th} direction. Term u_i represent the fluctuations of the instantaneous velocity field along i_{th} direction. q^2 is the kinetic energy, computed by adding the square of the three velocity fluctuations ($u^2 + v^2 + w^2$). Statistics along Z direction (w) are not measured and are then estimated by combining the axisymmetric hypothesis in the near wake as in [70], and the profiles of turbulence intensity, see Carlier [103]. Computations is carried out by superposing the two flows through the continuity between the dominance of the near-wake (axisymmetric hypothesis) and the dominance of TBL (turbulence intensity profiles). For further simplification, it's assumed that w^2 is close to u^2 in the near wake region (see Thiesset [70]). In Turbulent Boundary Layer (TBL) dominance, the ratio u^2/w^2 tends to 3.7, 2.86 and 2.3 for $z^+ = 500$, $z^+ = 1500$ and $z^+ = 3125$, respectively (see Foucaut [104, 105] and Carlier's [103] studies). The statistics of velocity fluctuations are required to assess the turbulent kinetic energy budget. Finally, ϵ is the kinetic energy dissipation rate.

$$\underbrace{\left(\overline{u_i u_j}\frac{\partial \overline{U_i}}{\partial x_j}\right)}_{\textbf{Production}} + \underbrace{\left(\overline{U_j}\frac{\partial(\overline{0.5q^2})}{\partial x_j}\right)}_{\textbf{Advection}} + \underbrace{\left(\underbrace{\frac{\partial \overline{pu_j}}{\partial x_j}}_{\textbf{by pressure}} + \underbrace{\frac{\partial(\overline{0.5q^2u_j})}{\partial x_j}}_{\textbf{by turbulence}}\right)}_{\textbf{Diffusion}} + \underbrace{\overline{\epsilon}}_{\textbf{Dissipation}} = 0. \quad (8.13)$$

8.4.1 2D - planes for total turbulent kinetic energy budget

This section shows total turbulent kinetic energy budget terms in single and double airfoil wake configurations.

Production

Figure 8.14 shows the production term maps in single and double airfoils wake at $z^+ = 3125$ (see Sections D.4.2 and E.5.2 for closer to wall case). In the wake of a single airfoil, it is observed that the production term within the Turbulent Boundary Layer (TBL) is significantly lower than that of the case with no TBL. Same results are given for both Reynolds numbers (see Sections 6.2.1 and D.4.2). The production of vortices initiates over the airfoil and extends downstream for a small distance equivalent to $0.2X/C$. This reduction is attributed to the enhancement of u^2 by the TBL leading to lower v^2/u^2 ratio.

In the double airfoil configuration, the production of vortices is more pronounced. This production persists for a short distance, approximately $0.4X/C$ downstream. This observation suggests that the presence of the wake generated by the upstream airfoil in TBL, enhances the production of turbulence. This can be explained due to higher v^2/u^2 ratio, in addition to higher Reynolds stresses $\overline{uv}$ over the airfoil. This is in contrast with situations with no TBL effect, where the upstream wake reduces the production of turbulence by the downstream airfoil, see Section 6.2.1.

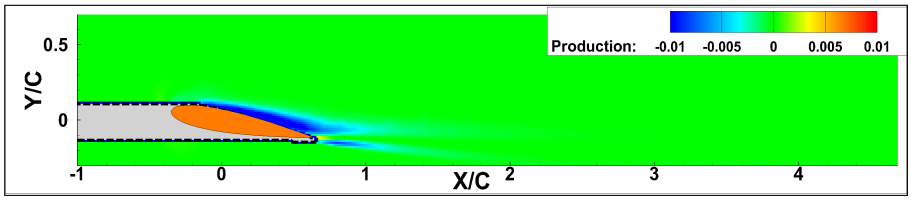

(a) Single airfoil wake.

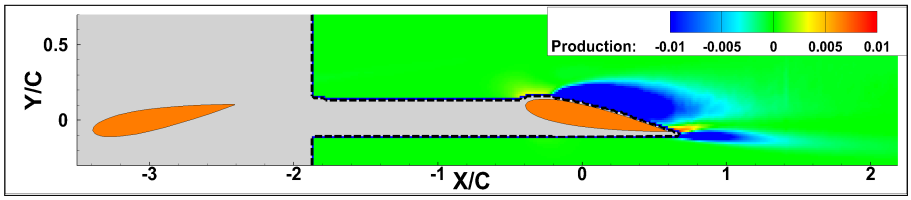

(b) Double airfoil wake.

Figure 8.14: Production $\overline{u_i u_j}\frac{\partial \overline{U_i}}{\partial x_j}$ of total turbulent kinetic energy by mean velocity in single and double airfoil wake at $z^+ = 3125$. Terms are normalised by U_0^3/D.

Advection

Figures 8.15a and 8.15b show the advection term in single and double airfoil wakes at $z^+ = 3125$, respectively (see Sections D.4.2 and E.5.2 for closer to wall case). In the case of the single airfoil wake, advection reaches its maximum values at leading and trailing edges of the airfoil influenced by the prevailing mean velocity. However, within the central region of the airfoil wake, the advection is negative indicating the airfoil boundary layer or a zone where the flow is reversed. In the case of the double airfoil wake (Figure 8.15b), advection map over the downstream airfoil is significantly higher compared to single airfoil wake configuration. This is attributed to higher production of turbulence from the downstream airfoil within TBL.

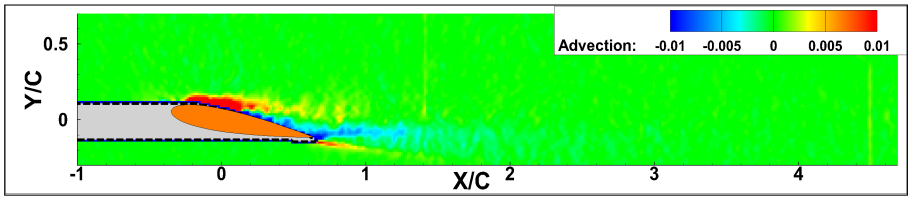

(a) Single airfoil wake.

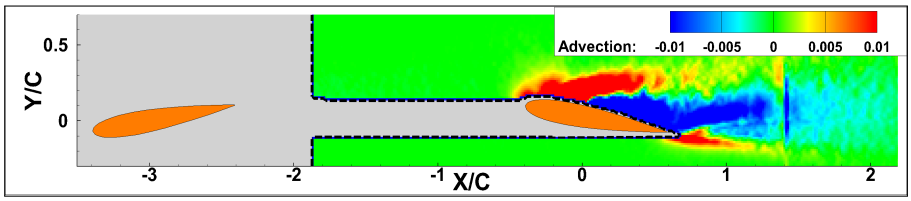

(b) Double airfoil wake.

Figure 8.15: Advection $\overline{U_j}\frac{\partial(\overline{0.5q^2})}{\partial x_j}$ of total kinetic energy by mean velocity in single and double airfoil wakes at $z^+ = 3125$. Terms are normalized by U_0^3/D.

Dissipation

Dissipation is first computed by Equation 8.14 and then corrected by coefficients shown in Table 8.4. Computation method is illustrated in Section 6.2.1.

$$\epsilon_{PIV} = \nu\left[8\overline{\left(\frac{\partial u}{\partial x}\right)^2} + 2\overline{\left(\frac{\partial u}{\partial y}\right)^2} + 2\overline{\left(\frac{\partial v}{\partial x}\right)^2} - \overline{\left(\frac{\partial v}{\partial y}\right)^2}\right]. \tag{8.14}$$

Used coefficients for dissipation correction		
z^+	500	3125
α_{PIV}	2.44	4.5

Table 8.4: Coefficients α_{PIV} as a function of heights from wall.

Figures 8.16a and 8.16b show the dissipation term in single and double airfoil wake, respectively (see Sections D.4.2 and E.5.2 for closer to wall case). The maximum values of dissipation are observed to be over the airfoil. Dissipation is highest in areas where there is greater strain and shear, which enhances the energy of the small scales. When comparing Figure 8.16a with Figure 8.16b, one can observe that the addition of the upstream wake increases the dissipation on the downstream airfoil. This increase is attributed to the greater Reynolds stresses resulting from the upstream wake with TBL, in contrast to what occurs in the case with no TBL (see Sections 6.2.1 and D.4.2).

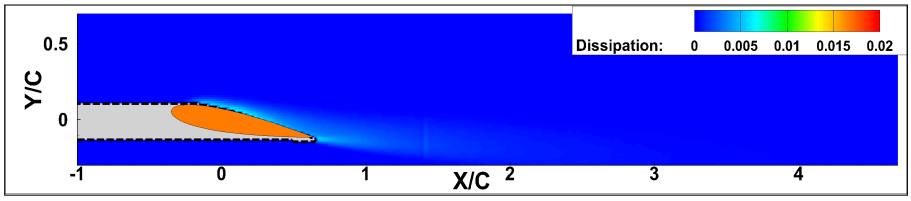

(a) Single airfoil wake.

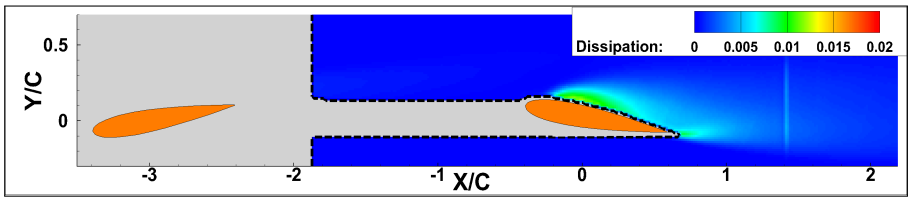

(b) Double airfoil wake.

Figure 8.16: Dissipation $\bar{\epsilon}$ of total turbulent kinetic energy in single and double airfoil wake at $z^+ = 3125$. Terms are normalized by U_0^3/D.

Diffusion

Figures 8.17a and 8.17b show the diffusion through Reynolds stresses in single and double airfoil wakes at $z^+ = 3125$, respectively (see Sections D.4.2 and E.5.2 for closer to wall case). In single airfoil wake, diffusion reaches positive peaks over the airfoil center, where stresses are at their maximum. Negative peaks are observed where mean velocity dominates, especially at the leading and trailing edges. In the case of a double airfoil wake, one can observe that the diffusion through Reynolds stresses is enhanced over the downstream airfoil. This phenomenon can be attributed to higher production of turbulence.

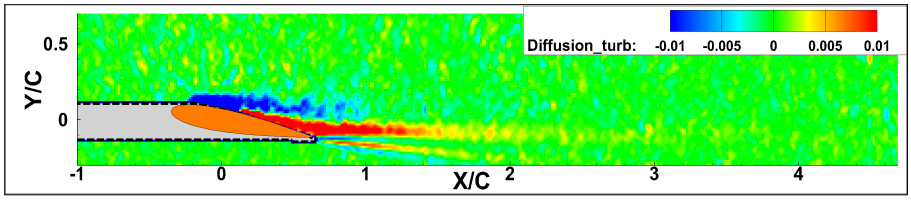

(a) Single airfoil wake.

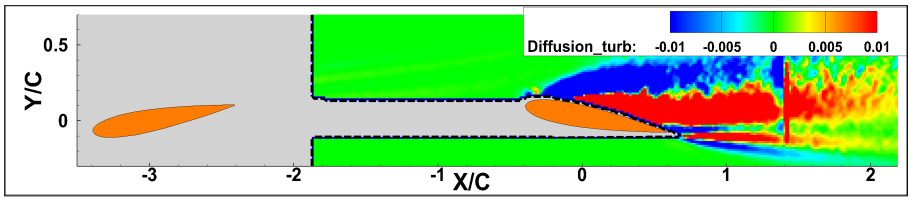

(b) Double airfoil wake.

Figure 8.17: Diffusion $\frac{\partial(\overline{0.5q^2u_j})}{\partial x_j}$ of total turbulent kinetic energy by Reynolds stresses in single and double airfoil wake at $z^+ = 3125$. Terms are normalized by U_0^3/D.

Figures 8.18a and 8.18b show the diffusion through pressure stresses in single and double airfoil wakes at $z^+ = 3125$, respectively. In the single airfoil wake, the diffusion pattern appears similar to the advection term and opposite to the diffusion by turbulence. However, in the double airfoil wake, the diffusion through pressure stresses exhibits distinct behavior. For instance, at the exact position of the edges, the diffusion is opposite to the

advection term. In other zones over the airfoil, the pressure diffusion is opposite to the diffusion through Reynolds stresses.

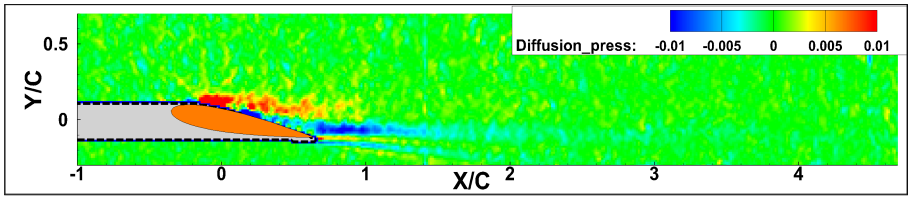

(a) Single airfoil wake.

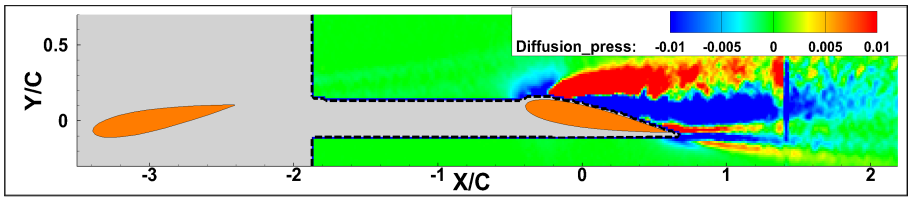

(b) Double airfoil wake.

Figure 8.18: Diffusion $\frac{\partial \overline{pu_j}}{\partial x_j}$ of total turbulent kinetic energy by pressure stresses in single and double airfoil wake at $z^+ = 3125$ (estimated). Terms are normalized by U_0^3/D.

8.4.2 Cross section profiles for total turbulent kinetic energy budget

Single and double airfoil wake

All terms appear to be important over airfoils within the Turbulent Boundary Layer (TBL). This differs from what is observed in wakes without the influence of turbulence, where these terms are significantly downstream and above the airfoils. This suggests that Turbulent Boundary Layer (TBL) enhanced the energy exchange over the airfoil and enhances the aerodynamic stall.

Figures 8.19a and 8.19b provide profiles along the Y direction at position $X/C = 1.6$ for both single and double airfoil wakes, respectively. These profiles are plotted at a location 5 cm behind both the upstream and downstream airfoils, and they correspond to two different heights from the wall, for comparison purpose. In single airfoil wake (Figure 8.19a), it is observed that the advection term is slightly higher close to the wall compared to downstream values, even though the mean velocity is lower. Indeed, close to the wall, the velocity fluctuations are more pronounced, leading to a higher contribution from the advection term. Similarly, other terms such as dissipation and production also exhibit minor differences, with higher values observed near the wall.

In double airfoil wake (Figure 8.19b), it is observed that the production of turbulence becomes slightly higher behind the downstream airfoil, especially further from the wall. Advection and diffusion terms remain significantly high and extend from $Y/C = -0.2$ to beyond $Y/C = 0.3$. These observations can be explained by the presence of higher velocity fluctuations originating from the upstream region, which enhances all the terms in the turbulence transport equation.

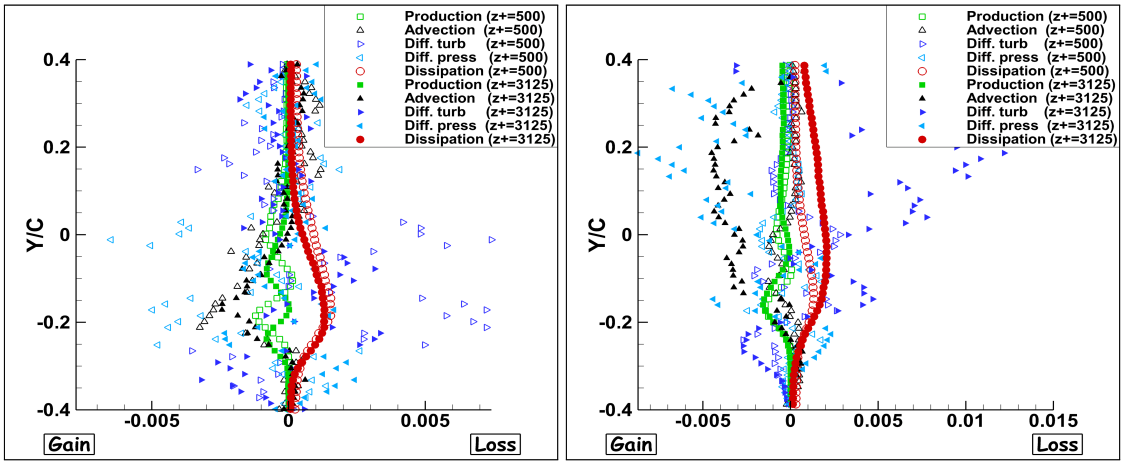

(a) Profiles $5cm$ behind the airfoil ($X/C = 1.6$), in single airfoil configuration.

(b) Profiles $5cm$ behind downstream airfoil ($X/C = 1.6$), in double airfoil configuration.

Figure 8.19: Total TKE terms in single and double airfoil wake at two heights from the wall ($z^+ = 500$ and $z^+ = 3125$). Terms are normalized by U_0^3/D.

Figures 8.19a and 8.19b provide profiles over the airfoil along Y direction with and without upstream airfoil, respectively. These profiles are positioned at $0.6C$ from the leading edge. In Figure 8.19a, it is observed that all the terms reach their maximum values over the airfoil surface and decrease by moving further from the surface, in contrast to the case shown in Figure 6.13a (with no turbulence effect). This phenomenon is due to the early aerodynamic stall of the upstream airfoil caused by the Turbulent Boundary Layer (TBL). In Figure 8.19b, one observe a significant increase in production, advection and both diffusion terms of fluctuations over the airfoil. This increase is attributed to higher incoming fluctuations from the upstream airfoil.

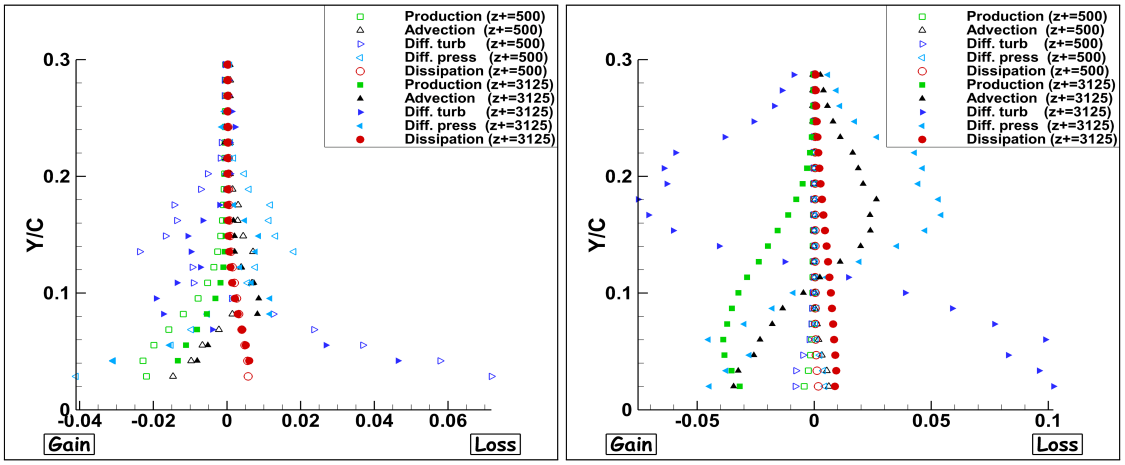

(a) Profiles at $X/C = 0.3$ over the airfoil, in single airfoil configuration.

(b) Profiles at $X/C = 0.3$ over downstream airfoil, in double airfoil configuration.

Figure 8.20: Total TKE terms in single and double airfoil wake at two heights from the wall ($z^+ = 500$ and $z^+ = 3125$). Terms are normalised by U_0^3/D.

Single and double cylinder wake

Figures 8.21a and 8.21b provide profiles along Y direction at $X/D = 5$ behind cylinders in single and double cylinder wakes, respectively (see Sections A.1.2 B.2.2 for more details). These profiles are plotted at a location 5 cm behind both the upstream and downstream cylinders, and they correspond to two different heights from the wall. In Figure 8.21a, it is observed that the advection and diffusion terms are similar to what is observed in Figure 6.14a (with no turbulence effect), i.e. close magnitudes with opposite signs. All terms in single cylinder wake becomes lower in magnitude within the Turbulent boundary layer (TBL) compared to Figure 6.14a. Low production of total turbulence by mean flow within TBL is due to lower ratio v^2/u^2. Knowing that Turbulent Boundary Layer (TBL) involves high values of u^2 that contributes in reducing the production rate (low v^2/u^2) in the wake. Low production of turbulence decreases then the transport terms (advection and diffusion) compared to Figure 6.14a. In Figure 8.21b, it is observed that the production of turbulence is slightly higher, while diffusion and advection become lower compared to Figure 8.21a. This aligns with the observations discussed in Figure 6.14b.

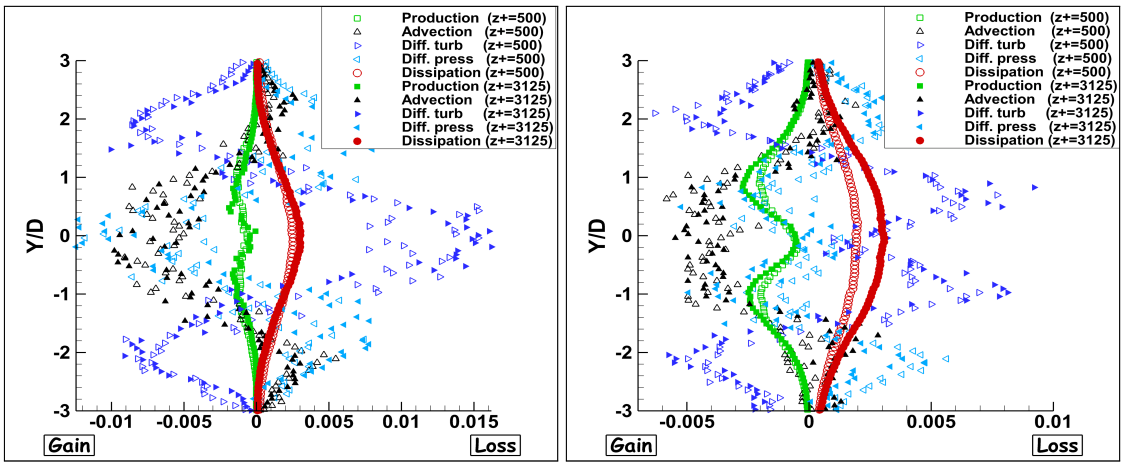

(a) Profiles 5 cm behind the cylinder ($X/D = 5$), in single cylinder configuration.

(b) Profiles 5 cm behind downstream cylinder ($X/D = 15$), in double cylinder configuration.

Figure 8.21: Total TKE terms in single and double cylinder wake at two heights from the wall ($z^+ = 500$ and $z^+ = 3125$). Terms are normalized by U_0^3/D.

Cylinder-airfoil wake

Figure 8.22 presents profiles along Y direction at position 5 cm downstream an airfoil placed in cylinder wake. In this configuration, all energy terms exhibit significant reductions when compared to double cylinder (Figure 8.21b) and airfoil (Figure 8.19b) wakes. Figure 8.22b shows profiles along Y direction over the airfoil surface, specifically at a distance $0.6C$ ($3D$) from the leading edge in cylinder-airfoil configuration. In Figure 8.22b, significant reductions in the production and advection terms are observed compared to Figure 8.20b, particularly further away from the wall ($z^+ = 3125$). This reduction can be attributed to the more energetic coherent structures from the cylinder, which prevents additional production from the downstream airfoil.

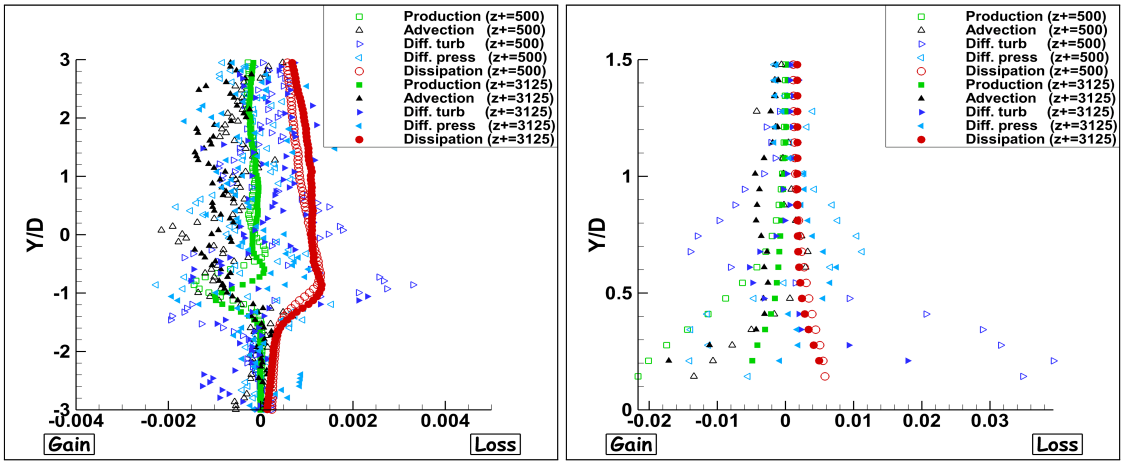

(a) Profiles 5 *cm* downstream the airfoil ($X/C = 1.6$), in cylinder-airfoil configuration.

(b) Profiles at $X/C = 0.3$ over downstream airfoil, in cylinder-airfoil configuration.

Figure 8.22: Total TKE terms in cylinder-airfoil wake at two heights from the wall ($z^+ = 500$ and $z^+ = 3125$). Terms are normalised by U_0^3/D.

8.5 Non organized coherent motion in airfoil wake

In Chapter 4, detection of coherent motion (CM) generated by an airfoil using an "aposteriori" approach are done with no turbulence effect. Based on this decomposition, total and coherent motion energy exchange in Sections 6.2.4 and 6.3 are then studied. Thus, the approach (shown in Chapter 4) is then applied to airfoil wakes within Turbulent Boundary Layer (TBL). However, several challenges appeared to prevent the decomposition of coherent motion (CM):

- The presence of the Turbulent Boundary Layer (TBL) forces coherent motions of the airfoil to goes down by moving downstream.
- Turbulent Boundary Layer (TBL) weakens the production of coherent motion from the airfoil due to early detachment.
- Turbulent Boundary Layer (TBL) affect the spatial period of coherent motions by destroying weaker coherent motions (CM).

Given these challenges, the phase decomposition of airfoil coherent motion (CM) becomes more complex in the presence of TBL. Figure 8.23 provides a comparison between an airfoil wake with and without the Turbulent Boundary Layer (TBL). This Figure includes videos of spanwise (Y) instantaneous velocity fields, illustrating the changes in spatial periods of coherent motion within the Turbulent Boundary Layer.

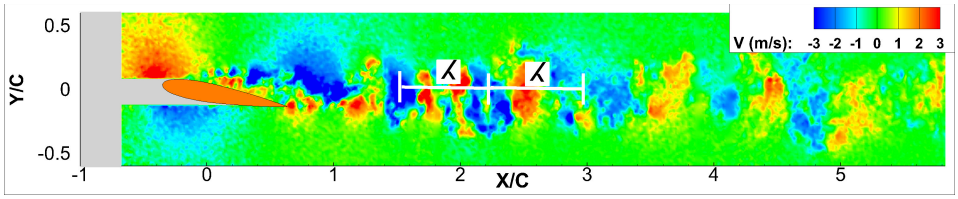

(a) Airfoil wake with no Turbulent Boundary Layer at $Re = 8000$.

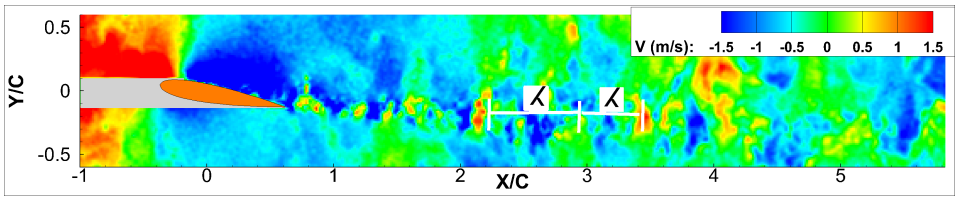

(b) Airfoil wake within Turbulent Boundary Layer at $z^+ = 125$.

Figure 8.23: Comparison in spanwise (Y) instantaneous velocity fields.

In summary, coherent motions (CM) generated by an airfoil within the Turbulent Boundary Layer (TBL) loose their organized characteristics, making the study of coherent motion (CM) and random motion (RM) interactions in airfoil wake challenging. However, the "aposteriori" approach can still be applied to other configurations such as single cylinder, double cylinder, and cylinder-airfoil wakes. This is primarily due to the following reasons:

- The circular shape of cylinders leads to a more horizontally oriented wake.
- Coherent motions (CM) generated by cylinders are more energetic and persistent downstream compared to the airfoil case.

As a result, configurations with an upstream cylinder are studied within the TBL, as demonstrated in previous sections (Sections 6.3.3 and 6.3.6).

8.6 CM and RM interaction TKE

In wakes, coherent motion coexists with random motion leading to significant interactions. These interactions leads to enhancements in turbulent energy cascade. The presence of coherent structures can increase the production of turbulent fluctuations, leading to an increased energy transfer and dissipation at specific locations. This emphasizes the importance of phase averaging methods, as previously discussed in Chapter 4, which is used in this section.

8.6.1 Cross section profiles of coherent motion (CM) energy budget

Since the coherent motion in the airfoil wake cannot be decomposed into phases, the studies are limited to cross-sectional profiles of cylinder configurations.

$$\frac{1}{2}\frac{\overline{\partial \tilde{q}^2}}{\partial t} + \frac{1}{2}\overline{U_j}\frac{\partial \overline{\tilde{q}^2}}{\partial x_j} + \overline{\tilde{u}_i\tilde{u}_j}\frac{\partial \overline{U_i}}{\partial x_j} + \frac{\partial}{\partial x_j}\left(\overline{\tilde{p}\tilde{u}_j} + \overline{\tilde{u}_i\langle u_i'u_j'\rangle} + \frac{1}{2}\overline{\tilde{q}^2\tilde{u}_j}\right) + \left(-\overline{\langle u_i'u_j'\rangle\frac{\partial \tilde{u}_i}{\partial x_j}}\right) + \overline{\tilde{\epsilon}} = 0. \tag{8.15}$$

In the context of coherent motion (CM) phase decomposition, number of samples per phase changes with respect to the configuration, see Table 8.5

Configuration	No. of phases	Couple images per phase	Couple images (total)
Single cylinder	18	556	10000
Double cylinder	18	1667	30000
Cylinder-airfoil	18	1667	30000

Table 8.5: Number of samples per phase

Single and double cylinder wake

Cross-sectional profiles are examined at one position within single and double cylinder wakes to compare energy exchange associated with coherent motion for both cases. Figures 8.24a and 8.24b present profiles along the Y direction, specifically at a distance of 5 cm downstream from the first and second cylinder for both single and double cylinder wakes, respectively. In Figure 8.24a, one can observe a significant reduction in all terms compared to the case without turbulence effect (Figure 6.29a). This reduction is particularly remarked in coherent motion production, which leads to a decrease in other terms, such as diffusion terms and advection. This indicates that the Turbulent Boundary Layer (TBL) has a significant influence on the production process of coherent motion from the cylinder. In the case of the double cylinder wake (Figure 8.24b), the profiles show an important reduction in all terms compared to the single cylinder wake (Figure 8.24a). This reduction can be attributed to the very limited presence of coherent motion after the second cylinder. In this case, two main factors, precisely TBL and the existence of the second obstacle, are responsible for preventing the persistence of coherent motion.

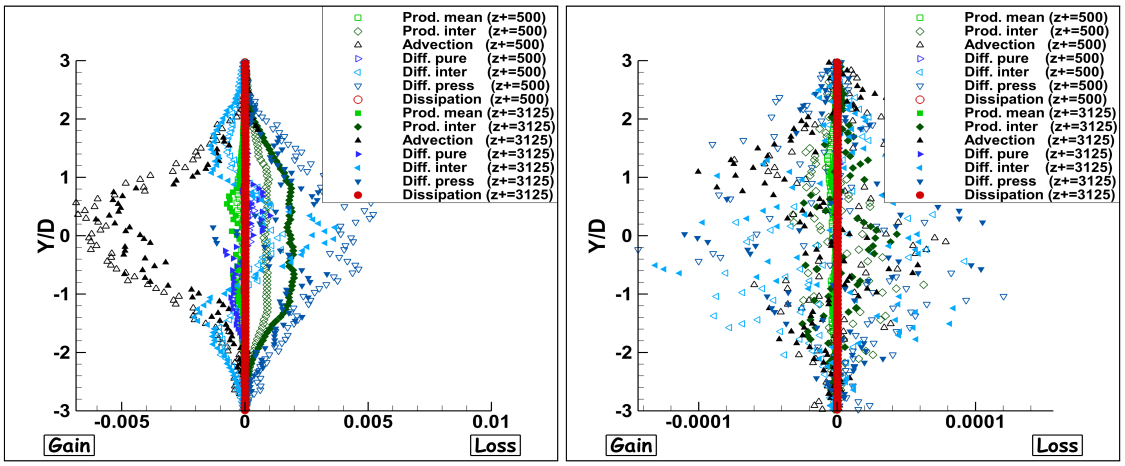

(a) Profiles 5 cm behind the cylinder ($X/D = 5$), in single cylinder configuration.

(b) Profiles 5 cm behind downstream cylinder ($X/D = 5$), in double cylinder configuration.

Figure 8.24: Coherent motion (CM) energy budget terms in single and double cylinder wake at two heights from the wall ($z^+ = 500$ and $z^+ = 3125$), phase decomposition based on upstream cylinder. Terms are normalized by U_0^3/D

Cylinder-airfoil wake

The profiles of coherent motion energy exchange in a cylinder-airfoil configuration provide similar insights to double cylinder wake. Figure 8.25a shows profiles at a position 5 *cm* downstream from the second obstacle (airfoil), in a cylinder-airfoil wake. Significantly, the magnitude of coherent motion energy exchange in this configuration is slightly lower than what is observed in Figure 8.24b, representing a double cylinder wake. In Figure 8.25a, the maximum peaks of advection and diffusion have shifted to $Y/D = 2$, due to the leading edge of the airfoil. This suggests that the presence of the airfoil can influence coherent motions causing deviations in their direction.

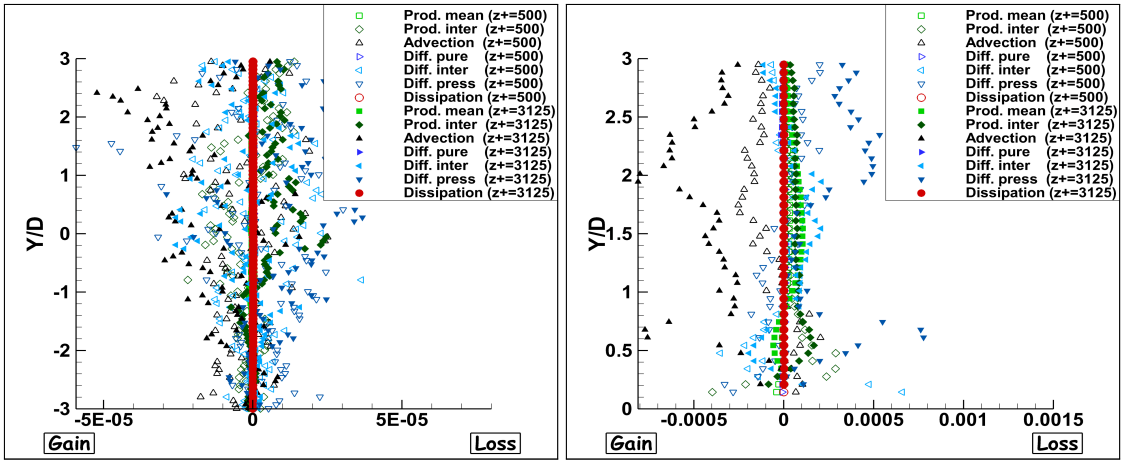

(a) Profiles 5 *cm* downstream the airfoil ($X/C = 1.6$), in cylinder-airfoil configuration.

(b) Profiles at $X/C = 0.3$ over downstream airfoil, in cylinder-airfoil configuration.

Figure 8.25: Coherent motion (CM) energy budget terms in cylinder-airfoil wake at two heights from the wall ($z^+ = 500$ and $z^+ = 3125$), phase decomposition based on upstream cylinder. Terms are normalized by U_0^3/D

In Figure 8.25b, the profiles are obtained over the airfoil, specifically at a distance of $0.6C$ (from leading edge) over the airfoil in the cylinder-airfoil wake. Over the airfoil, one can observe a higher magnitude in advection and diffusion (through pressure) terms of coherent motion (CM) compared to the downstream position (Figure 8.25a). Advection and diffusion at $z^+ = 3125$ are significantly higher compared to the height closer to the wall ($z^+ = 500$). This difference is due to the higher mean velocity and the presence of more energetic coherent motion (CM).

8.6.2 Cross section profiles of random motion (RM) energy budget

The examination of random motion energy exchange at a position downstream using cross-sectional profiles provides insights into the energy transfer of the flow. However, the lack of statistics in the Z direction (w) poses computational challenges in Equation 8.16 within Turbulent Boundary Layer (TBL). Thus, the terms are then calculated in the same way as in Section 6.3.6, leading to less precision in the computation of each term, particularly close to the wall. To simplify, as one moves farther from the wall, the computation precision increases, approaching the conditions discussed in Section 6.3.6 where turbulence effects are not considered. The pressure diffusion is determined by balancing Equation 8.16 through the difference.

$$\frac{1}{2}\frac{\overline{\partial q'^2}}{\partial t} + \frac{1}{2}\overline{U_j}\frac{\partial \overline{q'^2}}{\partial x_j} + \overline{u'_i u'_j}\frac{\partial \overline{U_i}}{\partial x_j} + \frac{\partial}{\partial x_j}\left(\overline{p'u'_j} + \frac{1}{2}\overline{\widetilde{u_j}\langle q'^2\rangle} + \frac{1}{2}\overline{q'^2 u'_j}\right) + \overline{\langle u'_i u'_j\rangle \frac{\partial \widetilde{u}_i}{\partial x_j}} + \overline{\epsilon'} = 0. \tag{8.16}$$

Single and double cylinder wake

The energy exchange of random motion in single and double cylinder wake is reported. Figures 8.26a and 8.26b show cross-sectional profiles along the Y direction at a distance of 5 cm downstream from the first and second cylinder for both single and double cylinder wakes, respectively. In single cylinder wake, Figure 8.26a, one observes that production terms are significantly lower compared to the case with no turbulence effect (Figure 6.44a). Low production of random motion (RM) by mean flow within the Turbulent Boundary Layer (TBL) is attributed to low shear gradient ($\partial U/\partial Y$). Production of random motion (RM) by coherent motion (CM) is lower within TBL, indicating lower energy contained by coherent motion (CM) in the presence of the boundary layer. The low production of random motion (RM) results in decreased transport terms (advection and diffusion) compared to the ones without TBL.

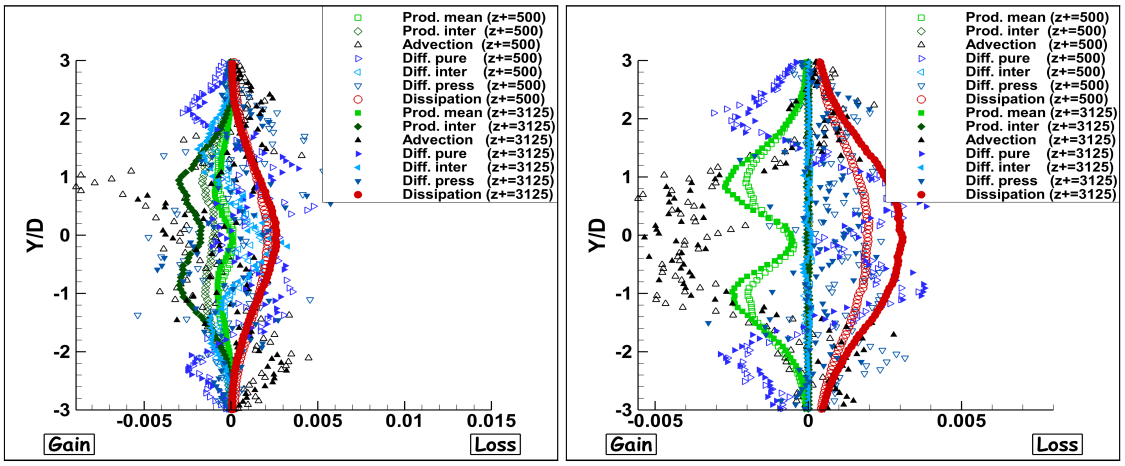

(a) Profiles 5 cm behind the cylinder ($X/D = 5$), in single cylinder configuration.

(b) Profiles 5 cm behind downstream cylinder ($X/D = 5$), in double cylinder configuration.

Figure 8.26: Random motion (RM) energy budget terms in single and double cylinder wake configurations at two heights from the wall ($z^+ = 500$ and $z^+ = 3125$). Phase decomposition is based on upstream cylinder. Terms are normalized by U_0^3/D.

In double cylinder wake (Figure 8.26b), production term is increased due to extended zones of significant Reynolds stresses, see Section B.2.1. However, the presence of the Turbulent Boundary Layer (TBL) prevents the production term from being very close to the advection term, as observed in the case with no turbulence effect (Figure 6.44b). The advection term is decreased due to the lower mean velocity at the center of the wake.

Cylinder-airfoil wake

The energy exchange of random motion in cylinder-airfoil wake is reported. Figure 8.27a shows profiles at a distance of 5 cm downstream from the second obstacle (airfoil) in a cylinder-airfoil wake. In this figure, one observes that the energy exchange between the

terms remains close to what was shown in Figure 6.47a. In Figure 8.27b, the profiles are obtained over the airfoil, at a distance which is $0.6C$ from the leading edge, in the cylinder-airfoil configuration. In this Figure, all terms reach their maximum peaks at the surface of the airfoil and converge to zero as one moves in the transverse direction. However, the maximum peaks are reduced compared to configurations with no Turbulent Boundary Layer (TBL). This reduction is attributed to a lower transversal gradients (i.e $\partial U/\partial Y$ or $\partial q'^2/\partial Y$) over the airfoil resulting from the presence of the Turbulent Boundary Layer.

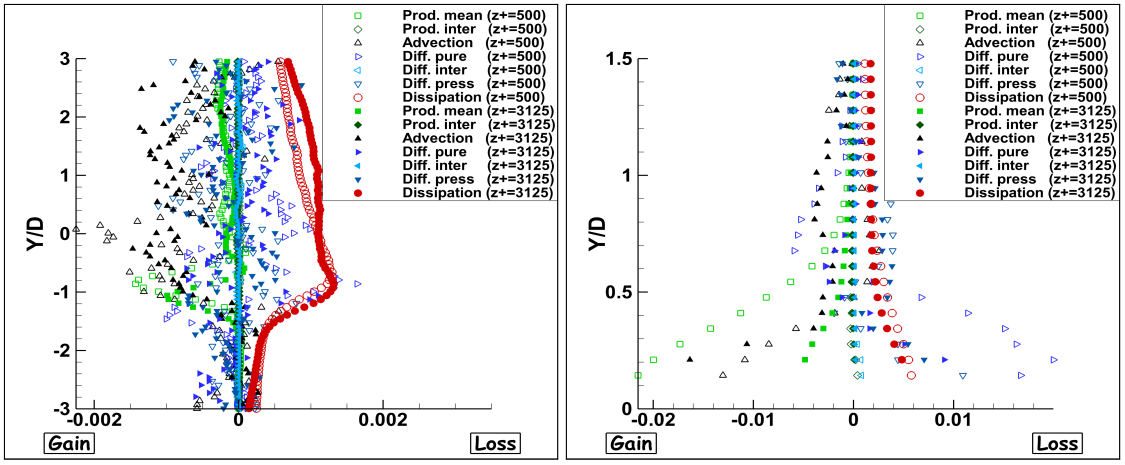

(a) Profiles 5 *cm* downstream the airfoil ($X/C = 1.6$), in cylinder-airfoil configuration.

(b) Profiles at $X/C = 0.3$ over downstream airfoil, in cylinder-airfoil configuration.

Figure 8.27: Random motion (RM) energy budget terms in cylinder-airfoil wake at two heights from the wall ($z^+ = 500$ and $z^+ = 3125$), phase decomposition based on upstream cylinder. Terms are normalized by U_0^3/D

8.7 Observations, reviews and conclusions

This chapter studied the energy exchange within different wakes configurations in the presence of a turbulent boundary layer (TBL). The Turbulent Boundary Layer (TBL) reduces the exchange of coherent motion (CM) kinetic energy for single, double cylinder, and cylinder-airfoil wake configurations compared to cases with no turbulence effect (Chapter 6). CM energy exchange in single and double airfoil wake configurations is not studied due to CM phase decomposition challenges of airfoil wake within TBL. The reduction of CM energy leads to a lower production of random motion, further resulting in a slight reduction in transport terms of random motion (RM). However, the values are still very close to those shown in the absence of the turbulent boundary layer. The Turbulent Boundary Layer (TBL) has the following effects:

- **Reduction of coherent motion (CM) energy exchange.**
- **Reduction of total energy exchange within the wake:**
  - In single obstacle wake, whether the obstacle is an airfoil or a cylinder.
  - In double obstacle wake. However, in the case of an upstream airfoil wake, Turbulent Boundary Layer (TBL) seems to preserve the inclination of the airfoil wake. Consequently, this conservation effect results in increased magnitudes of energy exchange behind an airfoil placed downstream at peculiar positions.

- **Impact on total energy exchange over an airfoil:**
  - Enhancement of total energy exchange over an airfoil with no upstream wake due to aerodynamic stall acceleration.
  - Reduction in total energy exchange over an airfoil with the presence of an upstream wake due to transversal gradients reduction of velocity and fluctuations. However, the upstream airfoil wake at $z^+ = 3125$ remains inclined towards the downstream leading edge of the airfoil due to high transversal fluctuation from TBL. This leads to higher Reynolds stresses $\overline{uv}$ over the downstream airfoil, resulting in higher energy exchange of all terms.

CHAPTER 9

General conclusions and perspectives

9.1 General conclusions

This study is concluded by the following points:

- The opening chapter (preface) initiates with a comprehensive overview of renewable energy, particularly focusing on the essential role played by wind turbines. This section provide the historical timeline, showing past and ongoing wind turbine projects (currently in progress). Within this context, it shows the details of the project's objectives and its purposes.

- In Chapter 2, a literature review is presented showing comprehensive analyses and references focused on turbulent and shear flows (wakes). Within the context of shear flows, this chapter deepen into the detailed process of vortices detaching from the boundary layer above an obstacle surface. The investigation extends to the study of both periodic coherent motion (CM) and non-periodic random motion (RM) structures within wake flows, shedding light on their distinct characteristics. Furthermore, the chapter presents an overview of the Richardson and Kolmogorov viewpoints on the transfer of energy within these flow structures. A comprehensive derivation of equations pertaining to the total turbulent kinetic energy, alongside the kinetic energy associated with various structures, including CM and RM within the wakes are presented.
  Additionally, this chapter provides a discussion of wake interactions, particularly in the context of flow dynamics behind two cylinders configured in tandem. This configuration is one of the focused configuration during this research study, however with larger separation distances between cylinders. This helps in studying the energy exchange behind downstream obstacle without the phenomenon of coupling. This exploration offers valuable insights into the complexities of flow patterns and interactions within this specific arrangement, contributing to a deeper understanding of shear flow dynamics and its associated turbulence.

- In our investigation, experiments are carried out in a low subsonic wind tunnel, as shown in Chapter 3. This chapter provides a comprehensive overview of the

experimental setup, showing details about the wind tunnel's dimensions, the range of airflow velocity, turbulence intensity, and characteristics of the test section. Our study aims to reveal the impact of an upstream wake (formed behind the first obstacle) on a subsequent obstacle positioned downstream. To facilitate this study, High Speed Particle Image Velocimetry (HS-PIV) technique is selected as the most suitable method for our research objectives.
HS-PIV offers advantages over single-point probe techniques, such as Hot Wire Anemometry (HW) or Laser Doppler Anemometry (LDA), as it allows for the investigation of large field views and multiple configurations, a complexity that would be challenging to achieve with single-point probes. Though HS-PIV may have lower spatial resolution, it offers the necessary advantages for our research. To simplify, studying large field of views with multiple configurations is complicated to be studied by one point probe techniques, such as Hot Wire Anemometer (HW) or Laser Doppler Anemometer (LDA). Therefore, this shortcoming is solved by PIV regardless of its lower spatial resolution.
The measurements are done based on three different Reynolds numbers ($Re = 2000$, 4000 and 8000). The study is presented for configurations, involving two fundamental obstacles: a 1 cm cylinder and a NACA 0015 airfoil. Moreover, improvements in the anemometry acquisitions are illustrated within the experimental setup chapter. The improvements are done to expand the range of velocity fluctuations measured. The data measurements resulted in large datasets, each consisting of up to 190,000 images for each Reynolds number and configuration. This extensive dataset ensures the robustness of our statistical analysis. Then, post processing of PIV data (images) are also presented, using an in house code.

- The wake formed behind the upstream obstacle comprises both coherent and random structures. Coherent structures, known for their periodicity and repetitive events, are a focal point of this investigation. Phases decomposition of coherent motion (CM) will help to better understand the downstream flow (over and behind the second obstacle). Within Chapter 4, two distinct methodologies are shown for the phase decomposition of coherent structures that exist obstacle wakes. This decomposition is an essential step for the project's aims, as it aids in the separation of coherent and random structures within the wake flows.
  The methodologies for phase decomposition outlined in this chapter include both experimental and a posteriori perspectives. An evaluation of these methodologies are shown using statistical analyses. The method demonstrating superior reliability and precision is the "aposteriori" method. Therefore, it is chosen for the phases decomposition analyses of our study. Coherent structures detection techniques for both methods are shown in Chapter 4. These phase decomposition methodologies are necessary for achieving a comprehensive understanding of the interactions between coherent and random flow structures in the wakes. Therefore this constitute a fundamental part of the project's research study.

- The advantage of time-resolved Particle Image Velocimetry (PIV), as detailed in Chapter 3, is its capacity to analyze temporal periods and the frequency of coherent motion within the wakes of obstacles. This capability leads to a deep investigation of time periods, power spectra (frequencies), and spatial periods associated with coherent motion within obstacle wakes. The findings and analyses related to these investigations are presented in Chapter 5. Temporal and spatial autocorrelation techniques play a central role in these studies. Development of coherent motion

within a defined field is also studied. The analysis illustrates whether coherent motion maintains its integrity or undergoes deformations as it propagates between two distinct positions in the field. This is shown by temporal cross-correlation techniques.
The investigation of temporal autocorrelation at a position in the wake shows that temporal periods at $Re = 8000$ are lower compared to $Re = 2000$. Then, shedding frequencies of single cylinder and airfoil wake are compared to theoretical values of Table 3.2 and show good agreement. Spatial periods remains approximately constant as a function of Reynolds number for the shown configurations. However, a small shift of spatial period occurred in cylinder wake between two Reynolds numbers. This shift can be attributed to the small changes in Strouhal number (St) at higher Reynolds number ($Re = 8000$). Single and double airfoil wakes have a close and a smallest spatial periods compared to other wakes configurations. In double cylinder wake, the spatial period of coherent motion (CM) are the largest compared to other wake configurations. This is due to the decrease in coherent motion (CM) frequency behind the second cylinder, as discussed Chapter 5.

- The mechanisms of energy exchange is studied in details with the presence and the absence of Turbulent Boundary Layer (TBL). It offers a comprehensive exploration of the processes governing each component, namely Coherent Motion (CM) and Random Motion (RM) within the wake. This research investigated gain and lost of energy for each fluctuation component (CM and RM) in zones within wakes of multiple configurations. This is discussed and shown in Chapters 6 and 8. This study explores the process of energy transfer for coherent motion (CM) within the wake, which is considered as new in research for such configurations.

  In the absense of TBL, enhanced energy exchange is observed over the surface of a downstream airfoil when influenced by upstream wakes, whether generated by a cylinder or an airfoil. This enhancement is evident in all terms related to coherent motion (CM) and random motion (RM) interactions. The presence of upstream wakes results in a noticeable shift in the separation point over the downstream airfoil. Indeed, the energy exchange is more pronounced when the upstream wake is generated by a cylinder compared to an airfoil. Conversely, the energy exchange behind a downstream obstacle is reduced when influenced by upstream wakes, regardless of whether they originate from a cylinder or an airfoil. Coherent motion (CM) experiences a decrease in energy exchange behind a downstream obstacle, and the energy exchange of random motion (RM) is generally slightly reduced. However, in specific cases, such as the production term, there may be a slight increase at the measurement point, attributed to the extension of the shear zone downstream. The persistence of coherent motion energy is observed when it is generated by a cylinder or an airfoil, allowing it to persist over a downstream airfoil. In contrast, coherent motion loses most of its energy behind a downstream cylinder. Furthermore, the generation of coherent motion is observed from a downstream cylinder placed in an upstream wake, while this phenomenon is not observed for an airfoil. The generation of coherent motion from a downstream obstacle is lower than the generation of random motion. Downstream, there is a reduction in the energy exchange of both coherent motion (CM) and random motion (RM). This reduction is attributed to the cascade process, indicating that the energy exchange decreases as a function of the downstream distance.
  The presence of the Turbulent Boundary Layer (TBL) significantly reduces the

energy exchange associated with coherent motion (CM). This leads to lower levels of coherent motion (CM) energy exchange within wakes when TBL is present. In airfoil wakes, the decomposition of coherent motion (CM) phases is challenging due to the relatively lower energy contained in the vortices compared to cylinder wakes. The Turbulent Boundary Layer (TBL) further diminishes the energy associated with airfoil vortices, making phase decomposition of coherent motion in airfoil wakes more challenging. To better understand these effects, the study examines single cylinder, double cylinder, and cylinder-airfoil wake configurations in the presence of TBL with respect to both coherent motion (CM) and random motion (RM) fluctuations. This analysis reveals significant differences in the energy exchange of turbulence when TBL is present compared to when it is absent.

- A comprehensive analysis of second, third, and fourth-order structure functions are presented for various configurations in Chapter 7. These structure functions offer crucial insights into the dynamics of turbulent cascades. They provide valuable information about the distribution of energy at different scales (second-order), the direction of energy transfer across scales (third-order), and details regarding intermittency within the turbulent flow at each scale (fourth-order). These structure functions are studied as a function of coherent motion (CM) phase. For instance, it is observed that large-scale vortices contain the maximum energy at phases of 0° and 180° within single cylinder wake configurations. This finding is crucial for understanding the flow dynamics and identifying the phases with the highest energy in coherent motion. This energy distribution is shown to be linked to the detachment of large vortices from obstacles. Just before vortices detach, they exhibit higher energy at these phases, which decreases once they detach. A universal finding is that larger scales follow a direct cascade to smaller scales. However, it's demonstrated at some cases that a direct cascade occurs at small scales, evolves into an indirect cascade at a certain scale, and then returns to a direct cascade. This phenomenon is shown in cylinder-airfoil configuration, for example. Moreover, it's revealed that intermittency is not limited to small scales but also occurs at larger scales, as observed in cylinder and cylinder-airfoil wake configurations. Intermittency at small scales can be linked to dissipation, while intermittency at large scales is associated with interactions with other scales. This detailed analysis sheds light on the complex dynamics of turbulent flows.

9.2 Perspectives

- **Experimental point of view**
  - Adding up a pressure sensor that is able to detect aerodynamic forces (lift and drag) experienced by cylinders and airfoils when subjected to an upstream flow. Analysing aerodynamic forces is important to gain insights into how these two distinct flow elements (CM and RM) influence the aerodynamic performance of these objects. Finally, this helps engineering to improve their design in wind turbine blades and aircrafts.
  - Research and explore the impact of isotropic turbulence on the mechanism of turbulent kinetic energy of coherent motion (CM) and random motion (RM) within wakes. The isotropic turbulence is created by classic or active grid. This investigation can be studied in single and double obstacles wakes as shown in this

study. This can shed light on the contribution of a three-dimensional turbulent flow with uniform fluctuations, which differs from the findings presented in this study. This investigation is expected to be different from what is shown in wakes within turbulent boundary layer (TBL).

- A research examining of how the aspect ratio of an upstream obstacle, such as a cylinder, influences the dynamics of the downstream flow around a subsequent obstacle, like an airfoil. Specifically, the aspect ratio of the upstream obstacle can play a critical role in affecting the energy carried by coherent motions (CM). As a consequence, this can definitely influence the mechanisms of energy exchange within the proximity of the downstream obstacle.
- An experimental setup involves the installation of high-resolution cameras, such those with high zoom capabilities. This strategic approach enables the examination of zones near obstacles, allowing for the resolution of the smallest-scale flow structures. By gaining access to these fine-scale structures, the computation of dissipation becomes more accurate and reliable compared to the estimation methods used in this study. This method not only enhances the precision of dissipation calculations but also provide more detailed understanding of flow dynamics near obstacles.
- Direct investigation of coherent motion (CM) present in each instantaneous vector field and using their characteristics (circulation, structure size or separation distance between structures) as a condition. This condition serves then to enable different analyses in statistical turbulence computations. For example, one can perform total kinetic energy computations in a particular zone within a wake based on the categorization of circulation rates instead of phase categorization.
- An experimental setup involves an installation leading to 3D velocity components measurements within Turbulent Boundary Layer (TBL). It is shown in this study that the effect of 3D velocity fluctuations are significant and can influence the mechanism of energy exchange compared to case with no turbulence effect. The measurement of 3D velocity fluctuations can lead to better precision to the computation of turbulent kinetic energy.
- Measuring pressure fields using 3D High-Speed Particle Image Velocimetry (HS-PIV) for both wind tunnels studies, one with a Turbulent Boundary Layer (TBL) and the other without. This approach eliminates the need for calculating pressure terms through differences.

- **Turbulence processing point of view**

  - Examination of two-point structure functions for coherent motion (CM) and random motion (RM) in the context of both single and double wake obstacle configurations. The objective is to provide a perspective distinct from the findings concerning total fluctuations in a previous study. This investigation will address an unexplored aspect in wake studies, aiming to reveal more details about the energy distribution of CM and RM at various scales within the wake structures.

References

[1] R. Nicholls-Lee and S. Turnock. "Tidal energy extraction: renewable, sustainable and predictable". In: *Science Progress* (2008).

[2] António F. de O. Falcão. "Wave energy utilization: A review of the technologies". In: *Renewable and Sustainable Energy Reviews* (2009).

[3] Y. Emamia and S. Mehrangiza. "A Brief Review about Salinity Gradient Energy". In: *International Journal of Smart Grid and Clean Energy* (2013).

[4] M. Dolores Esteban and J. Javier Diez. "Why offshore wind energy ?" In: *Renewable energy* (2010).

[5] P. Gipe and E. Mollerstrom. "An overview of the history of wind turbine developement: Part1- The early wind turbines until the 1960s". In: *Wind energy* 46 (2022), pp. 1973–2004.

[6] S. Pope. *Turbulent flows*. The Edinburgh Building, Cambridge CB2 8RU, UK: Cambridge University Press, 2000.

[7] O. Reynolds. "On the Dynamical Theory of Incompressible Viscous Fluids and the Determination of Criterion". In: (1885).

[8] H. Tennekes and J. Lumley. *A first course in Turbulence*. Cambridge, Massachusetts and London, England: Massachusetts Institute of Technology Press, 1972.

[9] A. Townsend. *The structure of turbulent shear flow*. The pitt building, trumpington street Cambridge CB2 1RP: University of Cambridge, 1976.

[10] P. Davidson. *Turbulence*. New york - Great Clarendon Street - Oxford ox 2 6op: Oxford University Press, 2004.

[11] J. Hinze. *Mcgraw-hill classic textbook reissue*. United states of America: Library of congress cataloging in publicating data, 1975.

[12] J. Mathieu and J. Scott. *An introduction to turbulent flow*. The Edinburgh Building, Cambridge CB2 8RU, UK: Cambridge University Press, 2000.

[13] B. sumer and J. Fredsoe. *Hydrodynamics around cylindrical structures*. UK office: 57 Shelton Street, Covent Garden, London WC2H 9HE: World Scientific Publishing Co. Pte. Ltd., 2006.

[14] Roshko. “On the developement of turbulent wakes from vortex street”. In: *National Advisory committee for aeronautics* (1954).

[15] Bloor and Gerrard. “Measurements on turbulent vortices in a cylinder wake”. In: *Journal of Fluid Mechanics* (1966).

[16] S. Yarusevych, P. Sullivan, and J. Kawall. “On vortex shedding from an airfoil in low-Reynolds-number flows”. In: *Journal Fluid Mechanics* 632 (2009), pp. 245–271.

[17] Abernathy and Kronauer. “The formation of vortex streets”. In: *Journal Fluid Mechanics* (1961).

[18] M. Zdravkovich. “Smoke observation of the formation of a Kàrmàn vortex street”. In: *Journal of Fluid Mechanics* 37 (1968), pp. 491–496.

[19] Triantafyllou and Chryssostomidis. “On the formation of vortex streets behind stationary cylinders”. In: *Journal Fluid Mechanics* 170 (1986).

[20] Shapiro and Bergman. “Experiments performed under the direction of L.Prandtl”. In: *Fm-11 Film loop. National Committe for Fluid Mechanics* (1962).

[21] A. Perry and M. Chong. “The vortex-shedding process behind two-dimensional bluff bodies”. In: *Journal fluid mechanics* 116 (1982), pp. 77–90.

[22] A. Kolmogrov. “The local structure of turbulence in incompressible viscous fluid for very large Reynolds numbers”. In: *Mathematical and Physical Sciences* 434 (1941), pp. 9–13.

[23] A. Townsend. “Entrainment and the structure of turbulent flow”. In: *Journal Fluid Mechanics* 41 (1969), pp. 13–46.

[24] A. Townsend. “The mechanism of entrainment in free turbulent flows”. In: *Journal Fluid Mechanics* 26 (1966).

[25] W. Reynolds and A. Hussain. “The mechanics of an organized wave in turbulent shear flow”. In: *Journal Fluid Mechanics* (1972).

[26] A. Hussain and W. Reynolds. “The mechanics of an organized wave in turbulent shear flow. Part 2. Experimental results”. In: *Journal Fluid Mechanics* (1971).

[27] A. Hussain and W. Reynolds. “The mechanics of an organized wave in turbulent shear flow. Part 3. Theoretical models and comparison with experiments”. In: *Journal Fluid Mechanics* (1971).

[28] O. Phillips. *The Dynamics of Upper Ocean*. Cambridge University Press, 1967.

[29] U. Frisch. *Turbulence*. Cambridge University Press, 1940.

[30] A. Kolmogorov. “The local structure of turbulence in incompressible viscous fluid for very large Reynolds numbers”. In: *Dokl. Akad. Nauk SSSR* (1941 b).

[31] A. Kolmogorov. “Dissipation of energy in locally isotropic turbulence”. In: *Dokl. Akad. Nauk SSSR* (1941 a).

[32] E. Kreyszig. *Advanced Engineering Mathematics*. 111 River Street, Hoboken-USA: John Wiley and Sons, Inc, 2011.

[33] F. Benford. *Notes on vector calculus*. 2007.

[34] M. Zdravkovich. *Flow around Circular Cylinders - Fundamentals*. Oxford, UK: Oxford University Press, 1997.

[35] M. Zdravkovich. *Flow Around Circular Cylinders - Application*. Oxford, UK: Oxford University Press, 2003.

[36] M. Zdravkovich. “Flow induced oscillations of two interfering circular cylinders in cross flow”. In: *Journal of Sound and Vibration* 101 (1985), pp. 511–521.

[37] M. Zdravkovich. “The effects of interference between circular cylinders in cross flow”. In: *Journal of Fluids and Structures* 1 (1987), pp. 239–261.

[38] M. Zdravkovich. “Review of flow interference between two circular cylinders in various arrangements”. In: *ASME Journal of Fluids Engineering* 99 (1977), pp. 618–633.

[39] S. Kang. “Characteristics of flow over two circular cylinders in a side-by-side arrangement at low Reynolds numbers”. In: *Physics of Fluids* 15 (2003), pp. 2486–2498.

[40] I. Peshard and P. Le Gal. “Coupled wakes of cylinders”. In: *Phys.Rev.Lett* 77 (1996), p. 3122.

[41] C. Williamson. “Evolution of a single wake behind a pair of bluff bodies”. In: *Journal of Fluid Mechanics* 159 (1985), pp. 1–18.

[42] D. Sumner. “Two circular cylinders in cross-flow: A review”. In: *Journal of Fluids and Structures* 26 (2010), pp. 849–899.

[43] H. Li and D. Sumner. “Vortex shedding from two finite circular cylinders in a staggered configuration”. In: *Journal of Fluids and Structures* 25 (2008), pp. 479–505.

[44] T. Igarashi. “Characteristics of the flow around two circular cylinders arranged in tandem (1st report)”. In: *Bulletin of the JSME* 24 (1981), pp. 323–331.

[45] T. Igarashi. “Characteristics of a flow around two circular cylinders of different diameters arranged in tandem”. In: *Bulletin of the JSME* 25 (1982), pp. 349–357.

[46] T. Igarashi. “Characteristics of the flow around two circular cylinders arranged in tandem (second report, unique flow phenomenon at small spacing)”. In: *Bulletin of the JSME* 27 (1984), pp. 2380–2387.

[47] X. Hu, X. Zhang, and Y. You. “On the flow around two circular cylinders in tandem arrangement at high Reynolds numbers”. In: *Ocean engineering* 189 (2019).

[48] T. Igarashi. “Characteristics of the flow around three circular cylinders arranged in-line”. In: *Bulletin of the JSME* 27 (1984), pp. 2397–2404.

[49] T. Igarashi. “Characteristics of the flow around four circular cylinders arranged in-line”. In: *Bulletin of the JSME* 29 (249) (1986), pp. 751–757.

[50] D. Sumner. *Circular Cylinders in Cross-Flow*. National Library of canada, 1999.

[51] D. Medici and P. Alfredsson. “Measurements on a Wind Turbine Wake: 3D Effects and Bluff Body Vortex Shedding”. In: *wind energy, newyork* (2005).

[52] C. Tropea, A. Yarin, and J. Foss. *Springer Handbook of Experimental Fluid Mechanics*. Verlag Berlin Heidelberg, Germany: Springer, 2007.

[53] M. Raffel et al. *Particle Image Velocimetry*. Verlag Berlin Heidelberg, Germany: Springer, 2007.

[54] R. Rubel and K.Uddin. “Comparison of Aerodynamics Characteristics of NACA 0015 and NACA 4415”. In: *Preprints* (2016). DOI: https://doi.org/10.20944.

[55] M. Hamdi et al. “Comparison of different tracers for PIV measurements in EHD airflow”. In: *Experiments in Fluids* (2014).

[56] Y. Jeon, L. Chatellier, and L. David. “Fluid trajectory evaluation based on an ensemble-averaged cross-correlation in time-resolved PIV”. English. In: *Experiments in Fluids* 55.7 (2014). ISSN: 0723-4864. DOI: https://doi.org/10.1007/s00348-014-1766-9. URL: http://dx.doi.org/10.1007/s00348-014-1766-9.

[57] B. Lecordier and M. Trinite. “Advanced PIV algorithms with image distortion validation and comparison using synthetic images of turbulent flow”. In: (2004), pp. 115–132.

[58] B. Lecordier and M. Trinité. “Accuracy assessment of image interpolation schemes for PIV from real images of particle”. In: (2006).

[59] J. Chang et al. “Shedding vortex characteristics analysis of NACA 0012 airflow at low Reynolds number”. In: *International conference on new eenrgy and power engineering, November 19 to 21, China* 8 (2022), pp. 156–174.

[60] P. Ausoni et al. “Kàrmàn vortex shedding in the wake of a 2D hydrofoil: Measurement and numerical simulation”. In: *IAHR meeting of WG on cavitation and dynamics problems in hydraulic machinery and systems* (2006).

[61] J. Hu et al. “Numerical simulation on vortex shedding from a hydrofoil in steady flow”. In: *Journal of Marine Science and Engineering* 8 (3) (2020), pp. 195–115. DOI: https://doi.org/10.3390/jmse8030195.

[62] P. Drazin and W. Reid. *Hydrodynamic Stability*. Cambridge University Press., 2004.

[63] B. Cantwell. “Introduction to symposium on turbulence in shear flows”. In: *Journal Fluid Mechanics* 221 (1990), pp. 1–4.

[64] M. Landahl. “A note on an instability of inviscid shear flows of parallel flows of incompressible perfect fluids”. In: *Journal Fluid Mechanics* 98(02) (1980), pp. 243–251.

[65] G. Batchelor. *An introduction of fluid dynamics*. Cambridge University Press., 2012.

[66] H. Schlichting and K. Gersten. *Boundary Layer Theory*. Springer Science and Business Media, 2000.

[67] H. Schlichting and D. Tritton. *Boundary layer theory, McGraw-Hill*. Cambridge University Press., 1978.

[68] C. Williamson. “Vortex dynamics in the cylinder wake”. In: *Journal of Fluid Mechanics* 28 (1996), pp. 477–529.

[69] L.O.Valery and V.N.Igor. “A regular Strouhal number for large-scale instability in the far wake of a rotor”. In: *Journal of Fluid Mechanics* (2014).

[70] F. Thiesset. “Exploration analytique et expérimentale des interactions cohérence-turbulence au sein d’un écoulement de sillage”. In: *Université de Rouen* (2011). URL: HAL%20Id%20:%20tel-00880987%20https%20://tel.archivesouvertes.fr/tel-00880987.

[71] M. Armaly et al. “Dynamics and phase decomposition in a cylinder wake”. In: *25eme Congrés Francais Mécanique, Nantes, France* (2022).

[72] F. Thiesset. “Scale-by-scale turbulent energy budget in the intermediate wake of two-dimensional generators”. In: *Physics Of Fluids* 749 (2013), pp. 201–226. DOI: https://doi.org/10.1063/1.4829763.

[73] L. Danaila. “Turbulent energy scale-budget equations for nearly homogeneous sheared turbulence”. In: *Flow, Turbulence and combustion* (2004).

[74] H. Djeridi and M. Braza. "Near-Wake Turbulence Properties around a circular cylinder at high Reynolds number". In: *Flow, Turbulence and combustion* (2003).

[75] M. Armaly et al. "Temporal development of NACA airfoil wake affected by an upstream wake". In: *15th International Symposium on Particle Image Velocimetry – ISPIV 2023, San Diego, USA* (2022).

[76] R. Beauvais et al. "Vortex interactions between two cylinders in a turbulent boundary layer". In: *International Symposium on Particle Image Velocimetry-ISPIV2023* (2023).

[77] R. Vitkovicova. "Identification of structures and mechanisms in a flow field by POD analysis for input data obtained from visualization and PIV". In: *Experiments in Fluid* (2020).

[78] J. Kostas, J. Soria, and M. Chong. "A comparison between snapshot POD analysis of PIV velocity and vorticity data". In: *Experiments in Fluid* 38 (2015), pp. 146–160. DOI: https://doi.org/10.1007/s00348-004-0873-4.

[79] M. Armaly et al. "Turbulent Kinetic Energy Budget and Dynamics of Composed Wakes in TBL". In: *23rd Australian Fluid mechanics Conference, Sydney, Australia* (2022).

[80] M. Armaly et al. "Decomposition en phase du sillage derriere un cylindre". In: *Congrès Francophone de Techniques Laser, CFTL 2022, Leuven, 12 – 16 septembre 2022* (2022).

[81] Acheson. *Elementary Fluid Dynamics*. Oxford University Press, 1990.

[82] R. Decher. *The Vortex and the Jet*. Springer nature Press, 2022.

[83] P. Ouro, V. Muhawenimana, and C. Wilson. "Asymmetric wake of 1 a horizontal cylinder in close proximity to a solid boundary for 2 Reynolds numbers in the sub-critical turbulence regime". In: *Hydro-environmental Research Centre, School of Engineering, Cardiff University-UK* (2019).

[84] I. Tani. "Low speed flows involving bubble separations". In: *Aeronautical Research Institute, University of Tokyo* 5 (1964), pp. 70–103.

[85] S. Yarusevych, P. Sullivan, and J. Kawal. "On vortex shedding from an airfoil in low-Reynolds-number flows". In: *Journal of Fluid Mechanics* 632 (2009), pp. 245–271.

[86] U. Vàclav and P. Pavel. "POD Spectrum of the Wake behind a Circular Cylinder". In: *International Scientific Conference – The Application of Experimental and Numerical Methods in Fluid Mechanics and Energy*. Vol. 328. 2020.

[87] C. Lin et al. "Characteristics of recirculation zone structure behind an impulsivively started circular cylinder". In: *Journal of engineering mechanics* 138 (2012), pp. 184–198.

[88] R. Shanmughan. "Contribution to the analysis of turbulent wakes of bluff bodies : impact on the aerodynamic drag". In: *Université d'Orléans* (2022). URL: HAL%20Id:%20tel-04116885%20https://theses.hal.science/tel-04116885.

[89] J. Chen and T. Zhou. "Characteristics of the turbulent energy dissipation rate in a cylinder wake". In: *Journal of Fluid Mechanics* 835 (2018), pp. 271–300.

[90] S. Obi and N. Tokai. "The pressure-velocity correlation in oscillatory turbulent flow between a pair of bluff bodies". In: *International Journal of Heat and Fluid flow* 27 (2006), pp. 768–776.

[91] G. Tsai and J. Yang. "Pressure fluctuation in correlation with velocity fluctuations in turbulent wake flow". In: *Departement of power mechanical engineering - National Tsing Hua University* (1993), pp. 462–464.

[92] J.L. Lumley. *Computational modeling of turbulent flows. In: Advances in applied Mechanics 18*. Academic press, 1978.

[93] Z. Warhaft. "Passive Scalars in Turbulent Flows". In: *Annual Review of Fluid Mechanics* 32 (2000), pp. 203–240.

[94] M. Gauding et al. "On the combined effect of internal and external intermittency in turbulent non-premixed jet flames". In: *Proceeding of the combustion institute* 38 (2020), pp. 2767–2774.

[95] M. Armaly et al. "Interaction of turbulent kinetic energy and coherent motion in the near field of the cylinder wake". In: *Mechanics and Industry* (2023).

[96] G. Hagen. "Ueber die bewegung des wassers in engen cylindrischen rohren". In: *Annalen der Physik* 122(3) (1839), pp. 423–442.

[97] O. Reynolds. "Xxix. an experimental investigation of the circumstances which determine whether the motion of water shall be direct or sinuou and of the law of resistance in parallel channels." In: *Philosophical Transactions of the Royal society of London* 186 (1883), pp. 123–164.

[98] R. Tiomajou. "Large scale organization of wall turbulence". In: (2016). URL: HAL%20Id:%20tel-01485740%20https://theses.hal.science/tel-01485740.

[99] E. Zanoun and F. Durst. "Evaluating the law of the wall in two-dimentional fully developed turbulent channel flows". In: *Physics of Fluids* 15 (2003), pp. 3079–3089.

[100] URL: https://www.cfdsupport.com/openfoam-training-by-cfd-support/node342.html.

[101] M. Stanislas, L. Perret, and J. Foucaut. "Vortical structures in the turbulent boundary layer: a possible route to a universal representation". In: *Journal of Fluid Mechanics* 602 (2003), pp. 327–382.

[102] M. Stanislas, J. Javier, and M. Ivan. *Proceedings of the WALLTURB International Workshop held in Lille, France*. Springer, 2009.

[103] J. Carlier and M. Stanislas. "Experimental study of eddy structures in a turbulent boundary layer using particle image velocimetry". In: *Journal of Fluid Mechanics* 535 (2005), pp. 143–188.

[104] J. Soria J. Foucaut C. Cuvier and C. Willert. "Characterization of a high Reynolds number turbulent boundary layer by means of PIV". In: *5th International Conference on Experimental Fluid Mechanics-ICEFM* (2018).

[105] J. Soria J. Foucaut C. Cuvier and C. Willert. "Characterization of near-wall structures in the log-region of a turbulent boundary layer by means of conditional statistics of tomographic PIV data". In: *Experimental Thermal and Fluid Science* 105 (2019), pp. 191–205.

[106] F. Scarano and M. Riethmuller. "Advances in iterative multigrid PIV image processing". In: *Experiments in Fluids* 29 (2005), pp. 51–60. DOI: https://doi.org/10.1007/s003480070007.

[107] J. Westerweel and F. Scarano. "Universal Outlier Detection for PIV Data". In: *Experiments in Fluids* 39 (2005), pp. 1096–1100. DOI: https://doi.org/10.1007/s00348-005-0016-6.

Appendices

APPENDIX A

Extensions on energy exchange with no turbulence effect

A.1 Single cylinder configuration

A.1.1 First order statistics

The computation and validation of first-order statistics are initially applied to the single cylinder wake. This configuration is considered the simplest among the various configurations and is readily available in the existing literature. Figure A.1 presents the mean velocity in the streamwise direction for single cylinder wake at two Reynolds numbers.

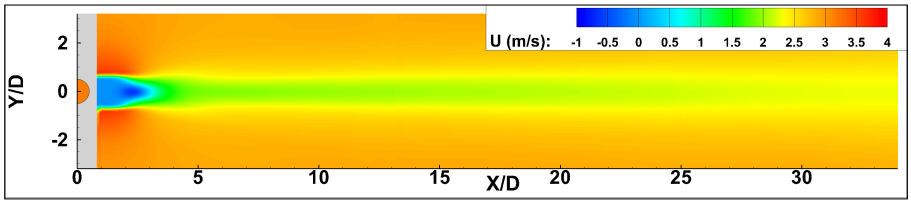

(a) $Re = 2000$

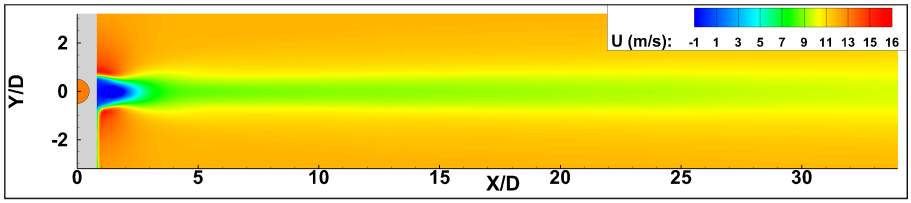

(b) $Re = 8000$

Figure A.1: Streamwise (X direction) mean velocities in cylinder wake

Figure A.2 presents the mean velocity in the spanwise direction for single cylinder wake at two Reynolds numbers.

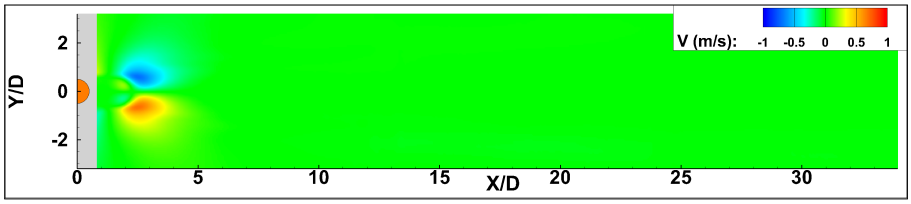

(a) $Re = 2000$

(b) $Re = 8000$

Figure A.2: Spanwise (Y direction) mean velocities in cylinder wake

Figure A.3 presents the RMS in the streamwise direction for single cylinder wake at two Reynolds numbers.

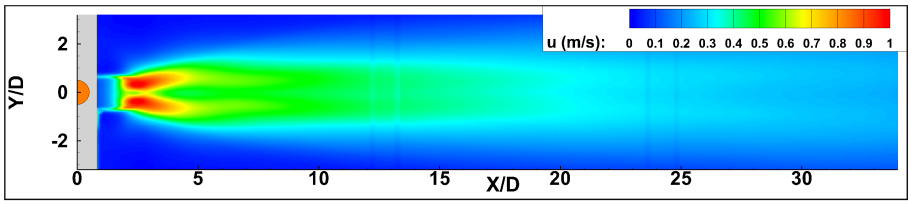

(a) $Re = 2000$

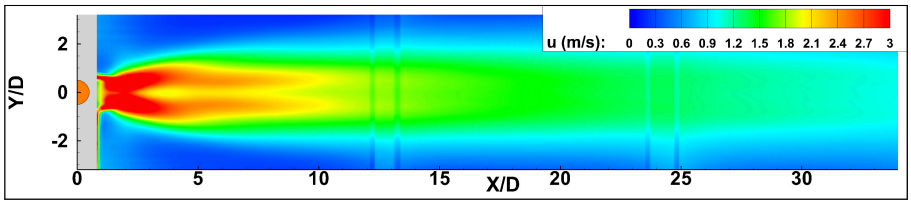

(b) $Re = 8000$

Figure A.3: RMS of streamwise velocities (X direction) in cylinder wake

Figure A.4 presents the RMS in the spanwise direction for single cylinder wake at two Reynolds numbers.

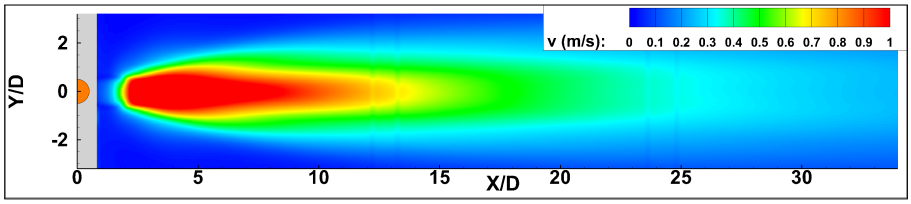

(a) $Re = 2000$

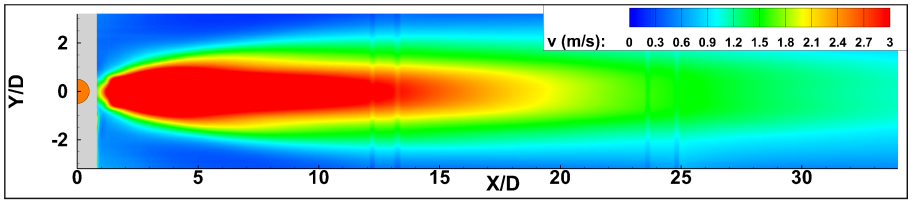

(b) $Re = 8000$

Figure A.4: RMS of spanwise velocities (Y direction) in cylinder wake

Mean and RMS statistics show higher magnitudes for higher Reynolds number and disappearance of recirculation zone behind the cylinder.

A.1.2 Total fluctuations energy exchange

In this section, kinetic energy of the turbulence is shown in cylinder wake for two Reynolds number. Each term of one point turbulent kinetic energy equation is computed showing gain and loss of energy between the mean flow and the turbulence. Figures A.5a and A.5b show the production term maps in single cylinder wake for both Reynolds number $Re = 2000$ and $Re = 8000$, respectively.

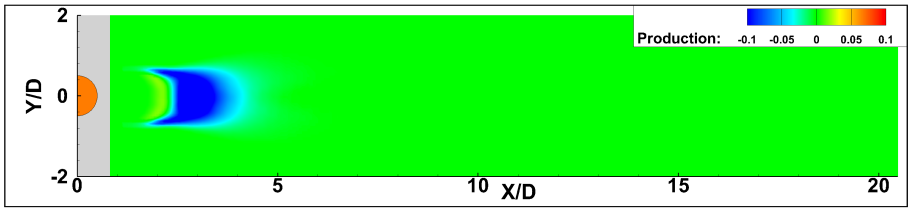

(a) $Re = 2000$

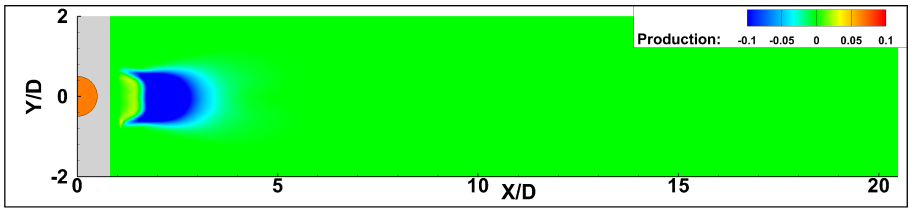

(b) $Re = 8000$

Figure A.5: Production of total turbulent kinetic energy by mean velocity in cylinder wake

Figures A.6a and A.6b show the advection term in single cylinder wake for both Reynolds number $Re = 2000$ and $Re = 8000$, respectively.

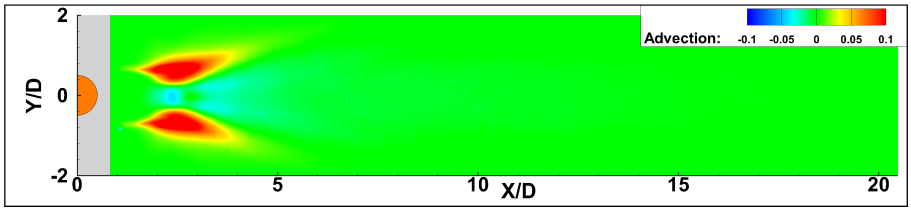

(a) $Re = 2000$

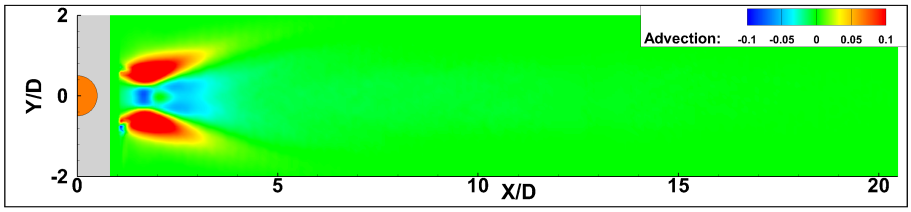

(b) $Re = 8000$

Figure A.6: Advection of total kinetic energy by mean velocity in cylinder wake

Figures A.7a and A.7b show the diffusion through turbulence term in single cylinder wake for both Reynolds number $Re = 2000$ and $Re = 8000$, respectively.

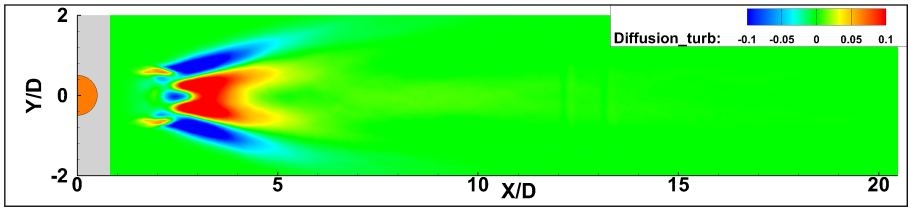

(a) $Re = 2000$

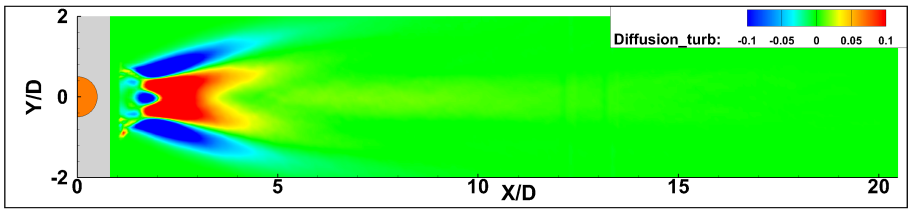

(b) $Re = 8000$

Figure A.7: Diffusion of total turbulent kinetic energy by turbulence in cylinder wake

Figures A.8a and A.8b show the diffusion through pressure term in single cylinder wake for both Reynolds number $Re = 2000$ and $Re = 8000$, respectively.

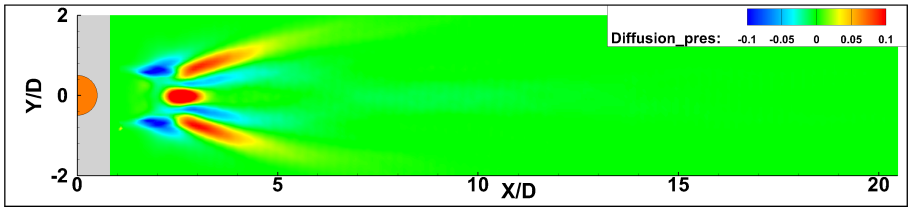

(a) $Re = 2000$

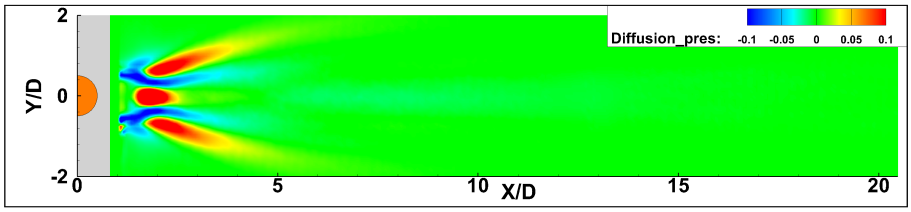

(b) $Re = 8000$

Figure A.8: Diffusion of total turbulent kinetic energy by pressure in cylinder wake

Figures A.9a and A.9b show the dissipation term in single cylinder wake for both Reynolds number $Re = 2000$ and $Re = 8000$, respectively.

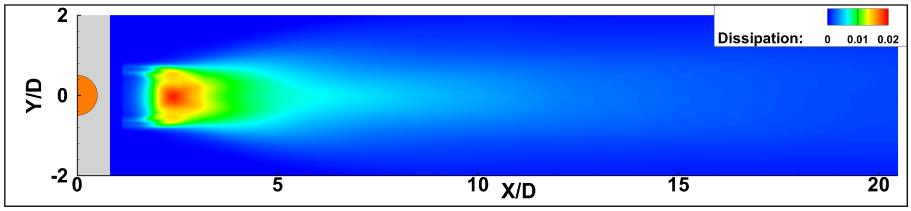

(a) $Re = 2000$

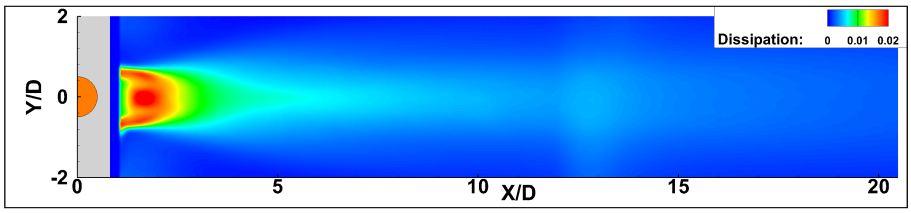

(b) $Re = 8000$

Figure A.9: Dissipation of total turbulent kinetic energy in cylinder wake

All the terms exhibit symmetry with respect to the center of the cylinder wake. These terms are particularly significant in the near region of the cylinder and gradually decrease as one moves downstream.

A.1.3 Decomposed first order statistics

Figures A.10a and A.10b presents the mean velocity in the streamwise direction for single cylinder wake at two Reynolds numbers, respectively. These terms are presented for one particular phase showing good phase decomposition in cylinder wake.

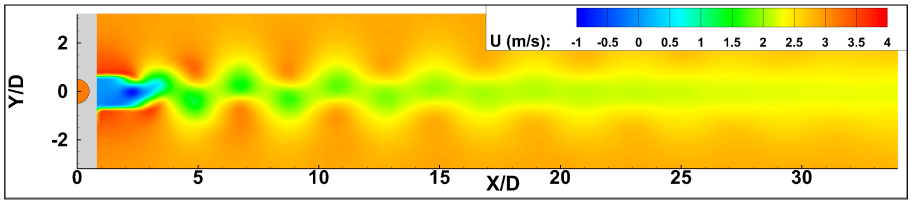

(a) $Re = 2000$

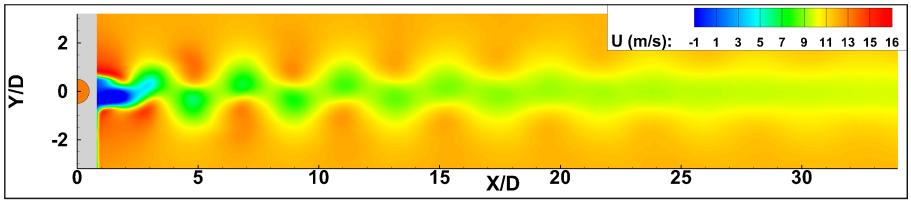

(b) $Re = 8000$

Figure A.10: Mean of streamwise direction (X) for one particular phase (phases decomposed) in cylinder wake

Figures A.11a and A.11b presents the mean velocity in the spanwise direction for single cylinder wake at two Reynolds numbers, respectively.

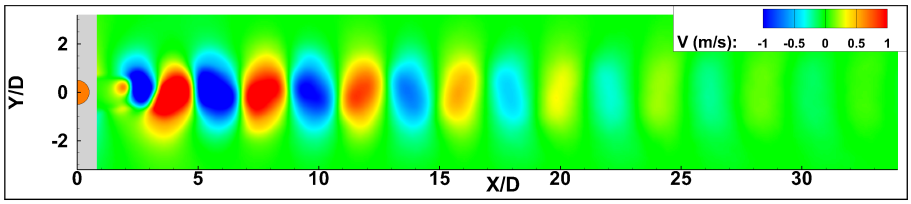

(a) $Re = 2000$

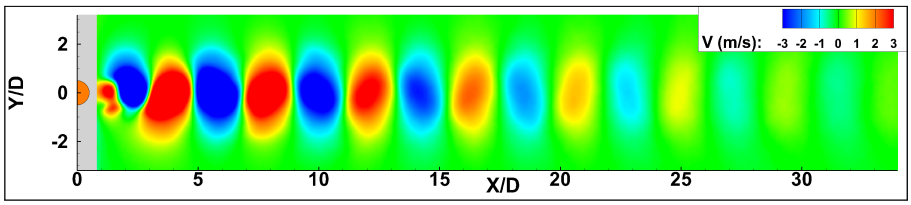

(b) $Re = 8000$

Figure A.11: Mean of spanwise direction (Y) for one particular phase (phases decomposed) in cylinder wake

Figures A.12a and A.12b presents the RMS of velocities in the streamwise direction for single cylinder wake at two Reynolds numbers, respectively.

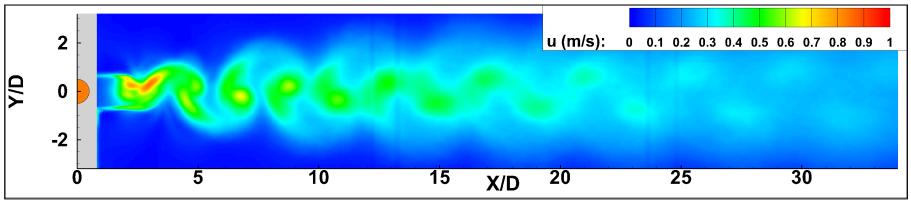

(a) $Re = 2000$

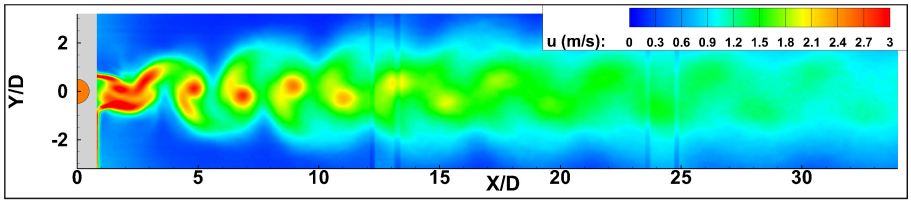

(b) $Re = 8000$

Figure A.12: RMS of streamwise direction (X) for one particular phase (phases decomposed) in cylinder wake

Figures A.13a and A.13b presents the RMS of velocities in the spanwise direction for single cylinder wake at two Reynolds numbers, respectively.

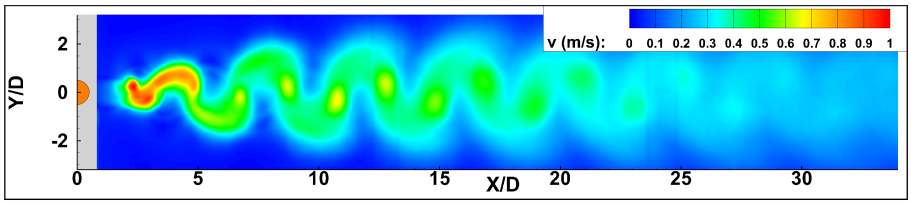

(a) $Re = 2000$

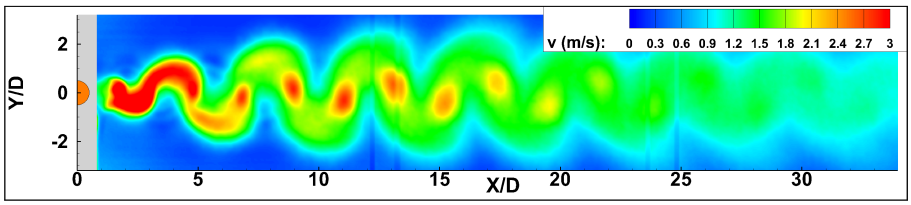

(b) $Re = 8000$

Figure A.13: RMS of spanwise direction (Y) for one particular phase (phase decomposed) in cylinder wake

A.1.4 Decomposed total kinetic energy in phases

It is essential to address the question regarding the total kinetic energy at a specific phase. This analysis helps us to understand the contribution of random motion at that particular phase constructing one phase of coherent motion. This is referred to total energy exchange as the fluctuations contain both random motion and coherent motion (one phase). Figure A.14 show the production term at low Reynolds number ($Re = 2000$) for four distinct phases ($\phi = 0°$, $100°$, $180°$ and $280°$).

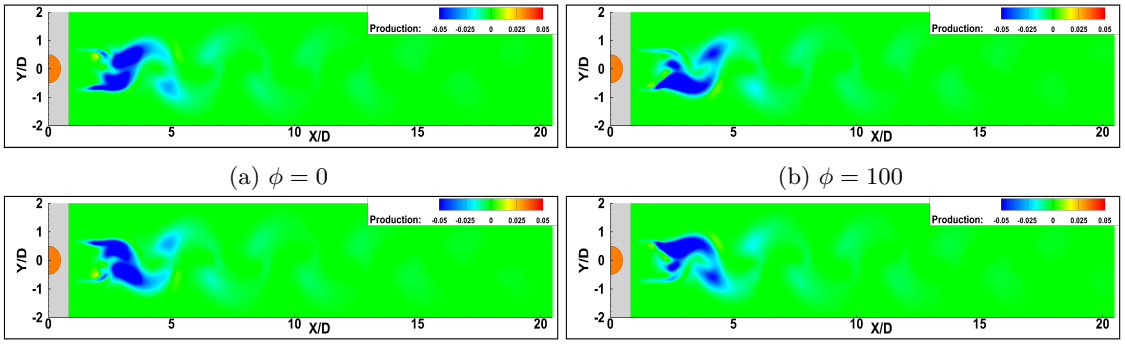

(a) $\phi = 0$ (b) $\phi = 100$

(c) $\phi = 180$ (d) $\phi = 280$

Figure A.14: Decomposed production by mean at $Re = 2000$ in cylinder wake

Figure A.15 show the advection term at low Reynolds number ($Re = 2000$) for four distinct phases ($\phi = 0°$, $100°$, $180°$ and $280°$).

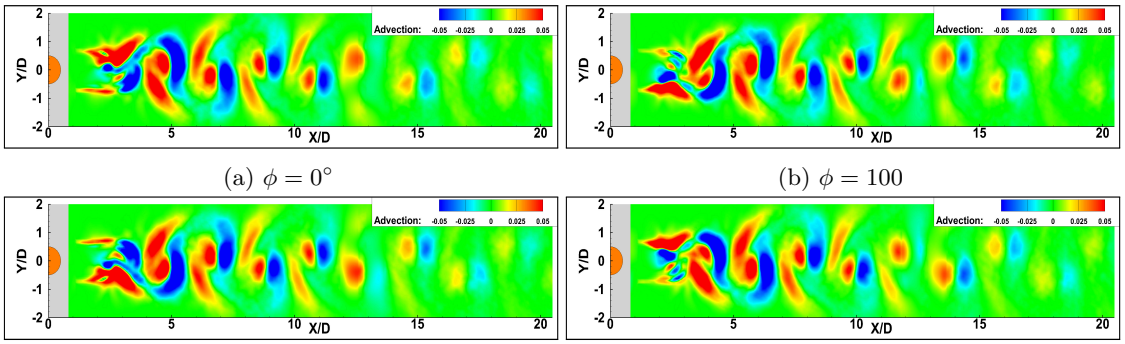

(a) $\phi = 0°$ (b) $\phi = 100$

(c) $\phi = 180$ (d) Coherent structures at $\phi = 280$

Figure A.15: Decomposed advection term at $Re = 2000$ in cylinder wake

Figure A.16 show diffusion through turbulence terms at low Reynolds number ($Re = 2000$) for four distinct phases ($\phi = 0°$, $100°$, $180°$ and $280°$).

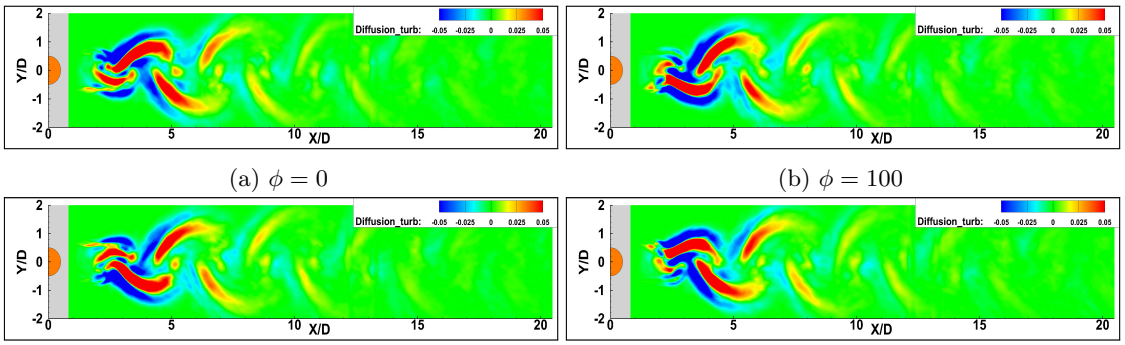

(a) $\phi = 0$ (b) $\phi = 100$

(c) $\phi = 180$ (d) $\phi = 280$

Figure A.16: Decomposed diffusion by turbulence at $Re = 2000$ in cylinder wake

Figure A.17 show diffusion through pressure terms at low Reynolds number ($Re = 2000$) for four distinct phases ($\phi = 0°$, $100°$, $180°$ and $280°$).

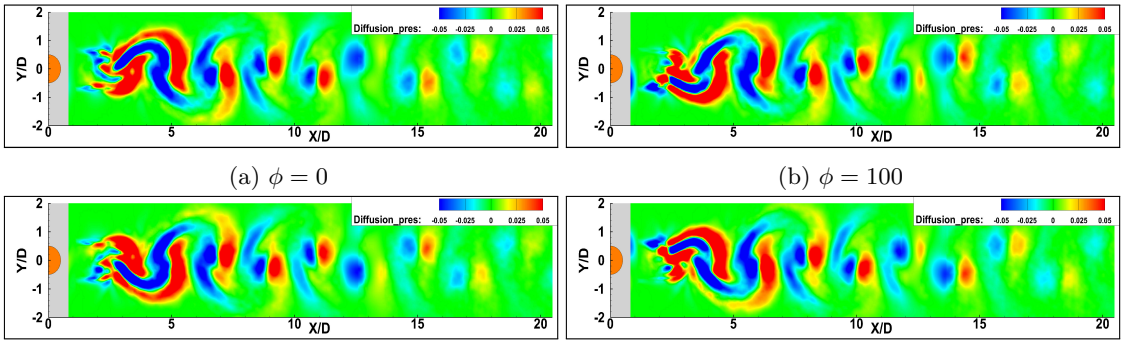

(a) $\phi = 0$ (b) $\phi = 100$

(c) $\phi = 180$ (d) $\phi = 280$

Figure A.17: Decomposed diffusion by pressure at $Re = 2000$ in cylinder wake

Figure A.17 show dissipation terms at low Reynolds number ($Re = 2000$) for four distinct phases ($\phi = 0°$, $100°$, $180°$ and $280°$).

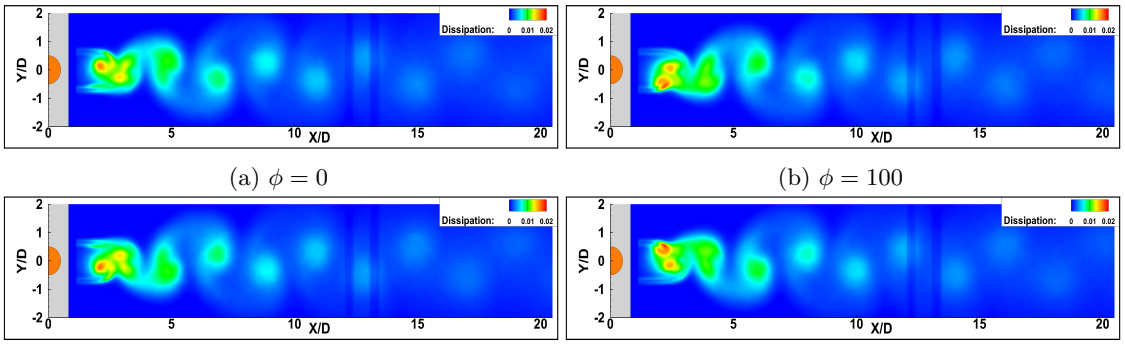

(a) $\phi = 0$ (b) $\phi = 100$

(c) $\phi = 180$ (d) $\phi = 280$

Figure A.18: Decomposed dissipation at $Re = 2000$ in cylinder wake

All the terms exhibit asymmetry with respect to the center of the cylinder wake at one particular phase. Transport and dissipation terms becomes persistent in further region of the cylinder wake and gradually decrease as one moves downstream. These figures show the mechanism of random motion over one phase of coherent motion.

A.1.5 CM energy exchange and interaction with RM

What has been presented so far is valuable, but it still lacks information regarding coherent motion. The 18 decomposed phases, previously discussed is necessary in addressing this gap. In this section, energy exchange between coherent motion, mean flow, and random motion resulting from their interactions are presented. This analysis is important for gaining insights into how coherent motion contributes to the overall flow dynamics.

Low Reynolds number

Figures A.19a and A.19b show the production and dissipation of coherent motion for single cylinder wake at $Re = 2000$, respectively. Production shows continous gain of energy to the coherent motion, while the dissipation shows continous loss.

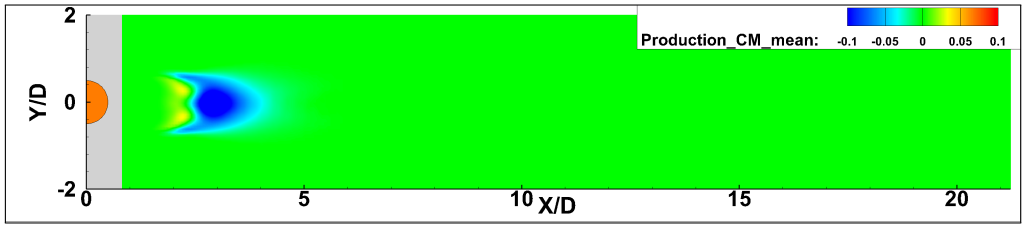

(a) CM production by mean

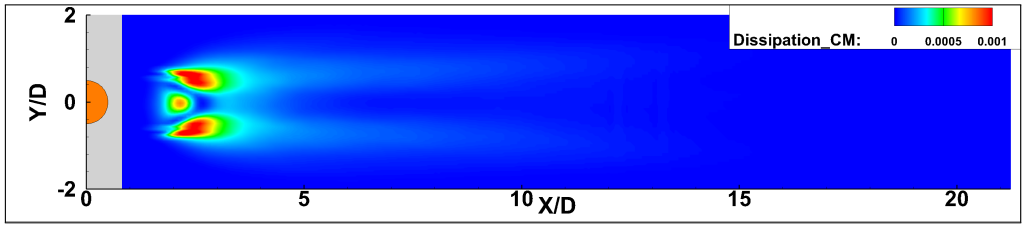

(b) CM dissipation

Figure A.19: Coherent motion (CM) production and dissipation $Re = 2000$

Figure A.20 shows the transport and RM-interaction terms of coherent motion in single cylinder wake at $Re = 2000$. The transport terms is decomposed to transport by mean flow (advection) and transport by fluctuations (diffusion).

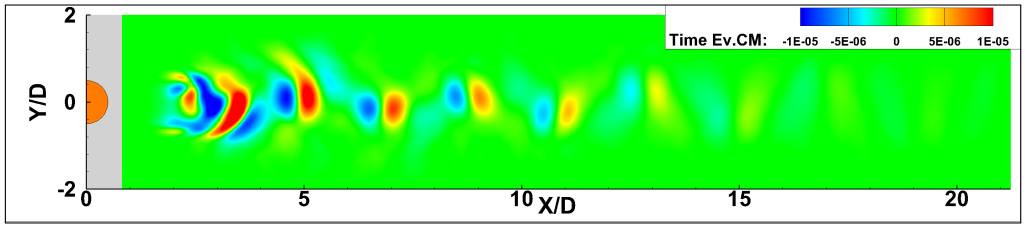

(a) CM time evolution in time

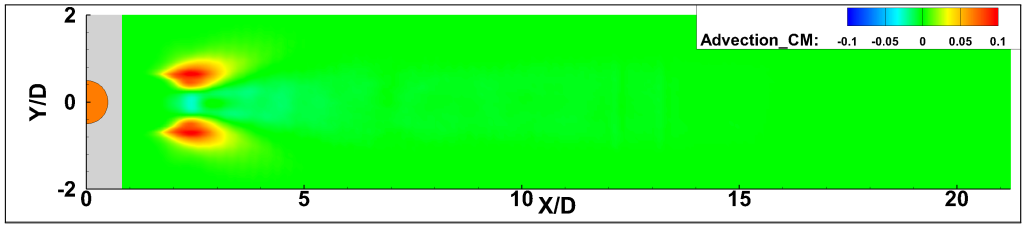

(b) CM advection by mean velocity)

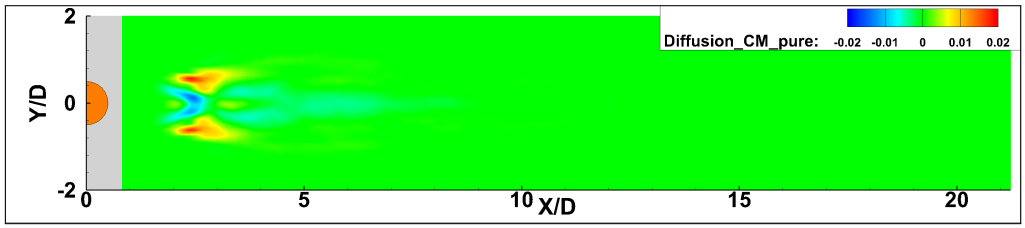

(c) CM pure diffusion

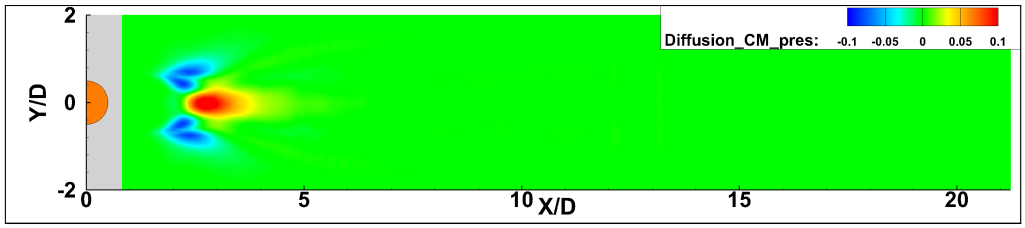

(d) CM diffusion by pressure

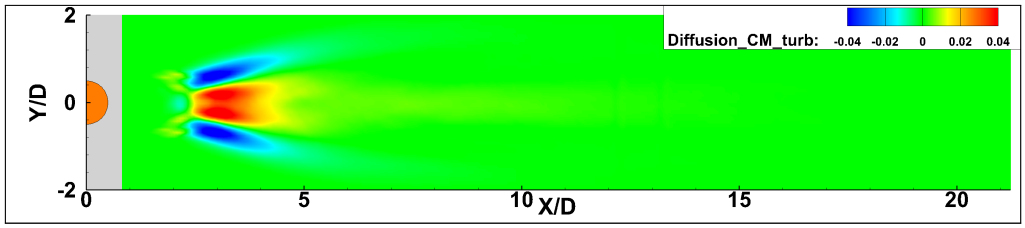

(e) CM diffusion by turbulence

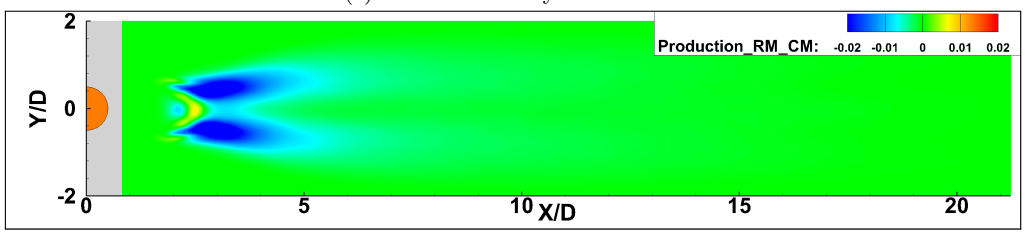

(f) RM production bt CM

Figure A.20: Coherent motion (CM) transport and RM-interaction terms at $Re = 2000$

High Reynolds number

Figures A.21a and A.21b show the production and dissipation of coherent motion for single cylinder wake at $Re = 8000$, respectively.

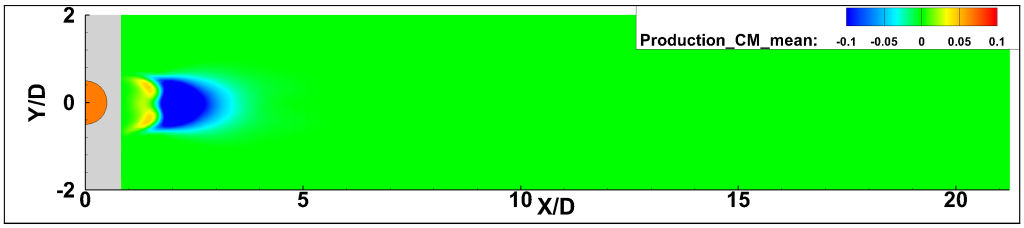

(a) CM production by mean

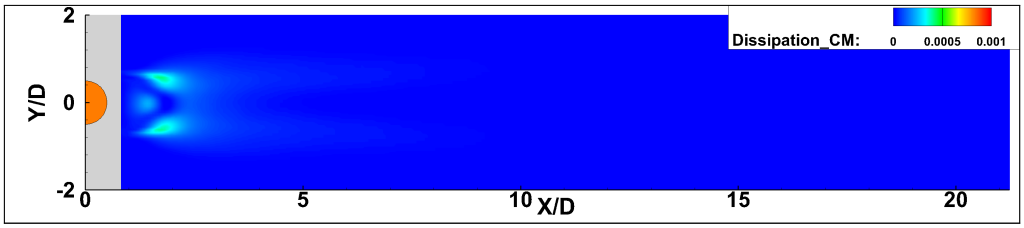

(b) CM dissipation

Figure A.21: Coherent motion (CM) production and dissipation at $Re = 8000$

Figure A.22 shows the transport and RM-interaction terms of coherent motion in single cylinder wake at $Re = 8000$.

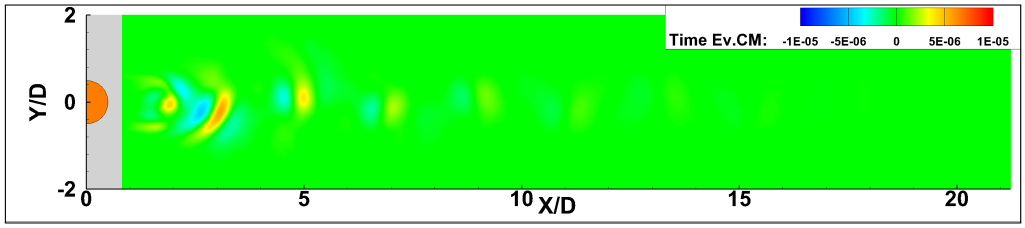

(a) CM time evolution in time

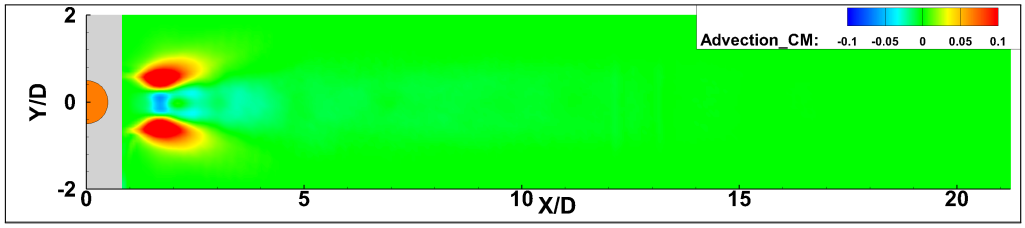

(b) CM advection by mean velocity

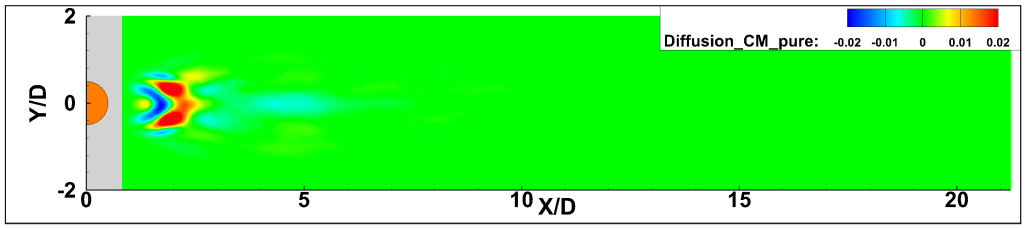

(c) CM pure diffusion

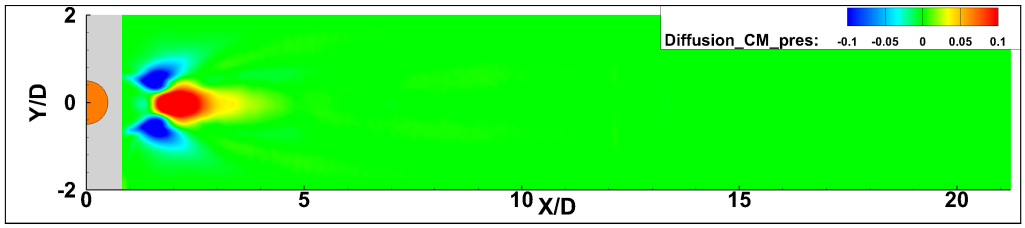

(d) CM diffusion by pressure

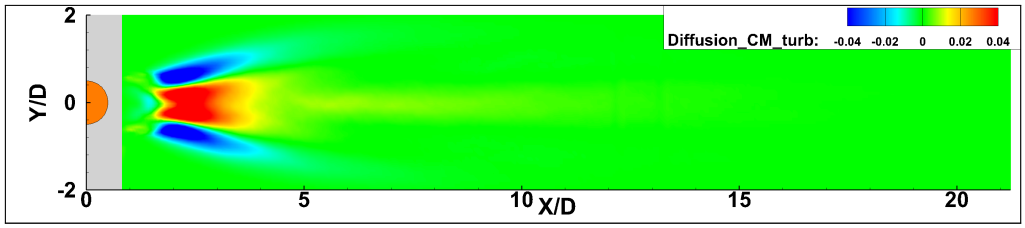

(e) CM diffusion by turbulence

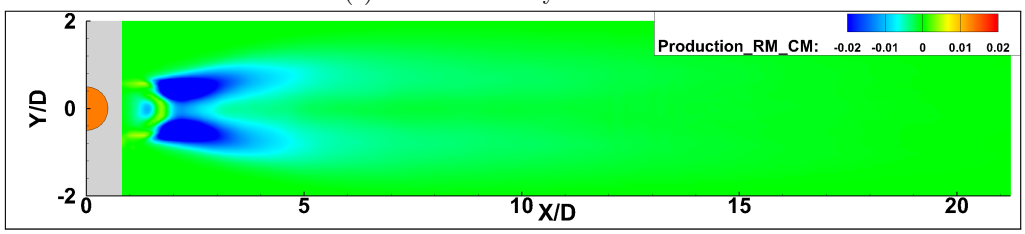

(f) RM production bt CM

Figure A.22: Coherent motion (CM) transport and RM-interaction terms at $Re = 8000$

A.1.6 RM energy exchange and interaction with CM

In this section, energy exchange between random motion, mean flow, and coherent motion resulting from their interactions are presented. This analysis is important for gaining insights into how random motion contributes to the overall flow dynamics.

Low Reynolds number

Figures A.23a and A.23b show the production and dissipation of random motion for single cylinder wake at $Re = 2000$, respectively.

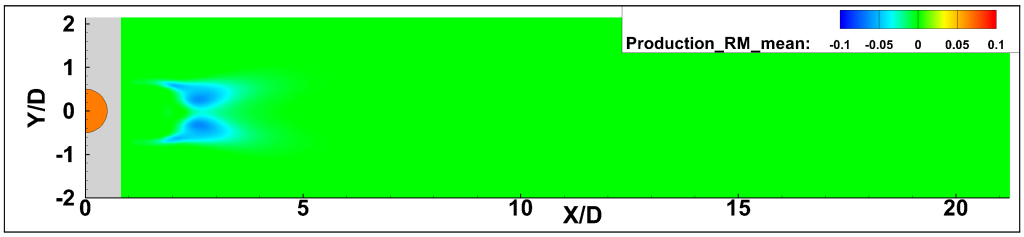

(a) RM production by mean

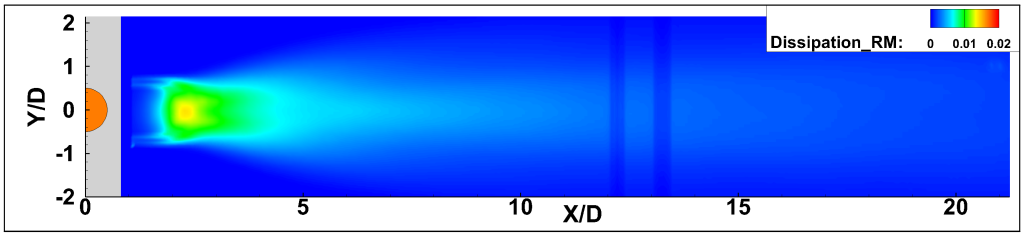

(b) RM dissipation

Figure A.23: Random motion (RM) production and dissipation $Re = 2000$

Figure A.24 shows the transport terms of random motion in single cylinder wake at $Re = 2000$.

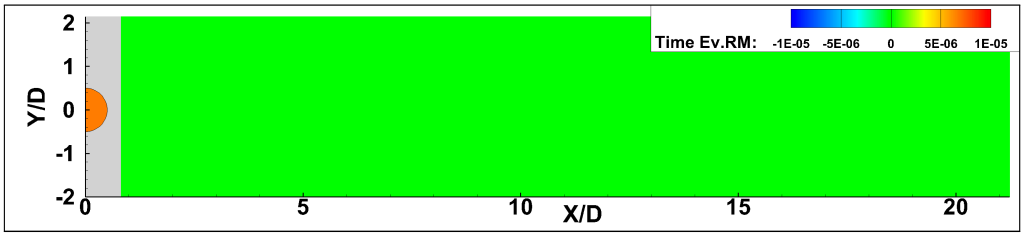

(a) RM time evolution

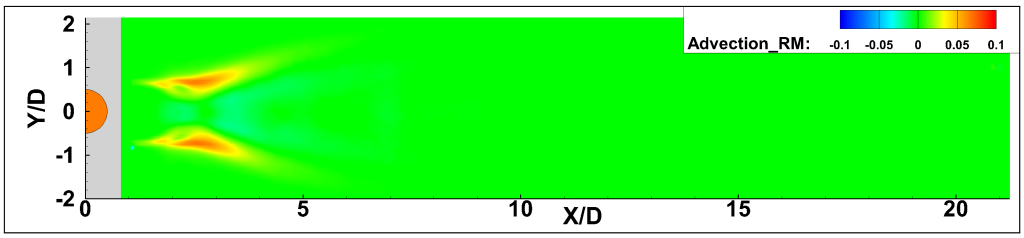

(b) RM advection by mean velocity

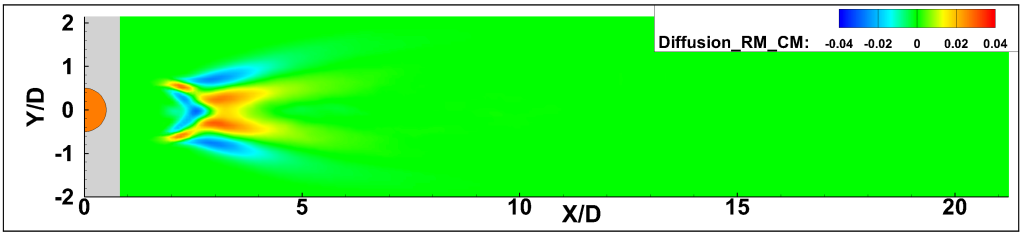

(c) RM diffusion by CM interaction

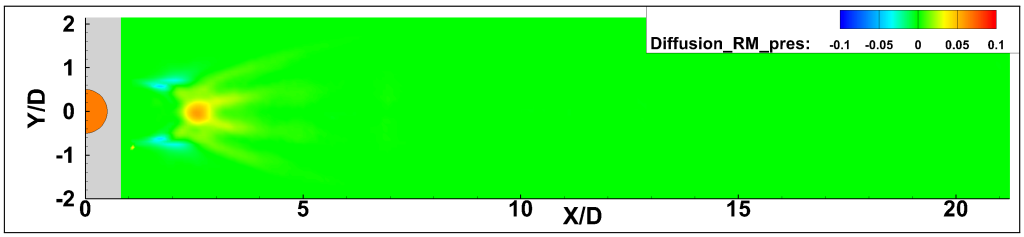

(d) RM diffusion by pressure

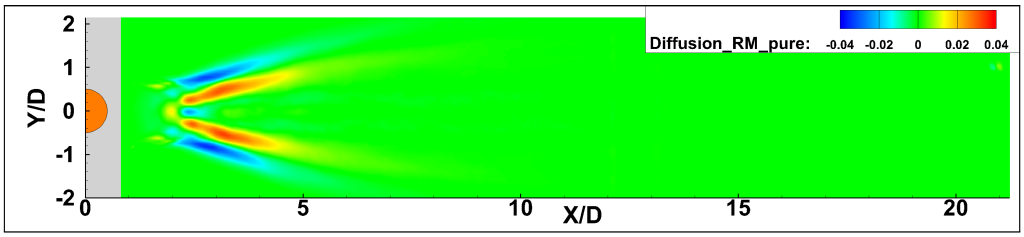

(e) RM pure diffusion

Figure A.24: Random motion (RM) transport terms in cylinder wake at $Re = 2000$

High Reynolds number

Figures A.25a and A.25b show the production and dissipation of random motion for single cylinder wake at $Re = 8000$, respectively.

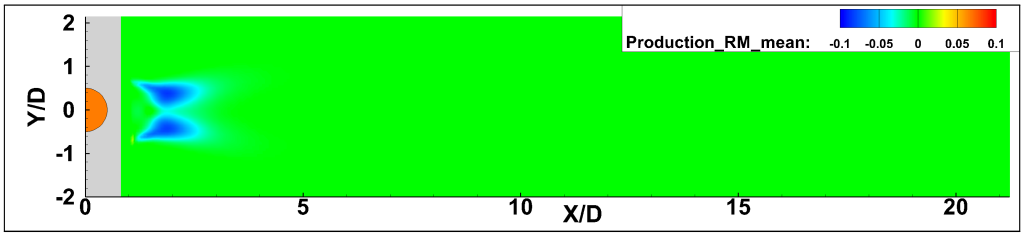

(a) RM production by mean

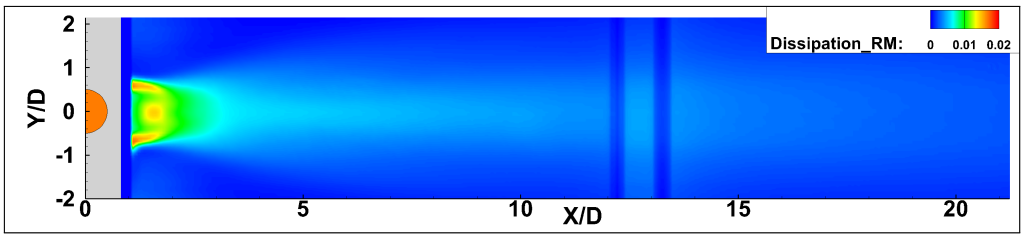

(b) RM dissipation

Figure A.25: Random motion (RM) production and dissipation $Re = 8000$

Figure A.26 shows the transport terms of random motion in single cylinder wake at $Re = 8000$.

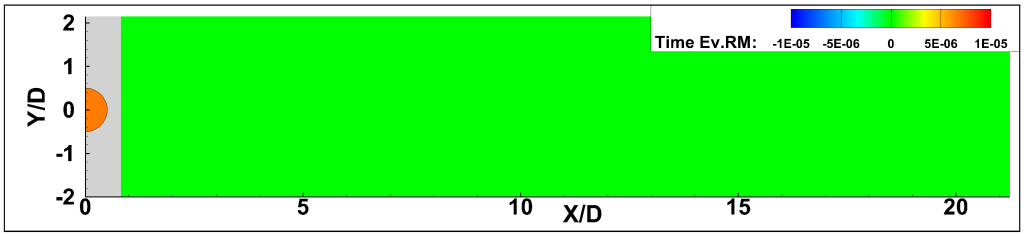

(a) RM time evolution

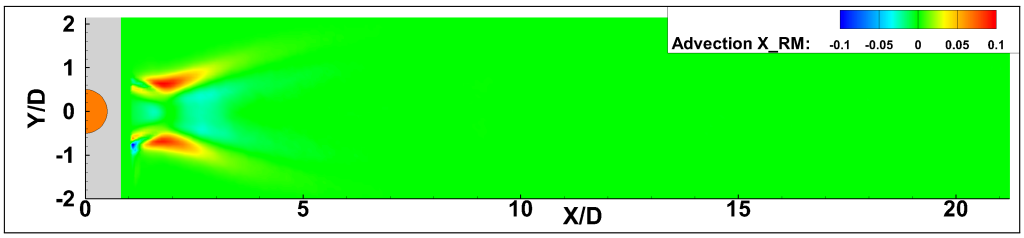

(b) RM advection by mean velocity

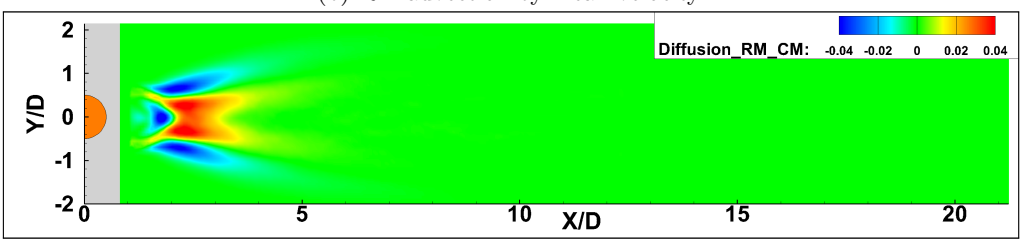

(c) RM diffusion by CM interaction

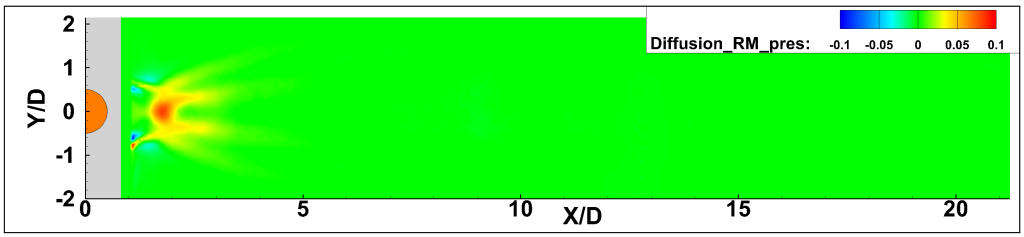

(d) RM diffusion by pressure

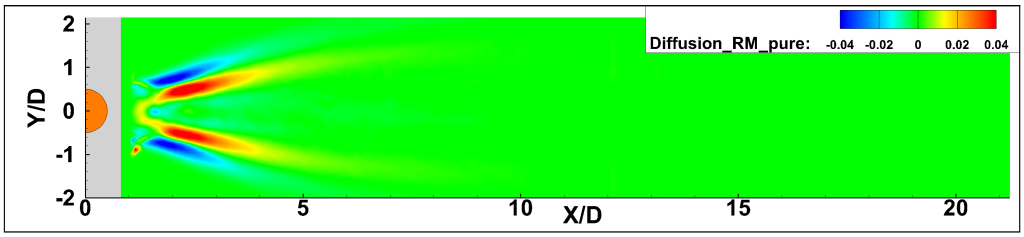

(e) RM pure diffusion

Figure A.26: Random motion (RM) transport terms in cylinder wake at $Re = 8000$

B.2 Double cylinder configuration

The computations of first-order statistics, total fluctuations and coherent-random motions energy exchange are then applied to the double cylinder wake.

B.2.1 First order statistics

Figure A.27 presents the mean velocity in the streamwise (X) direction for double cylinder wake at two Reynolds numbers.

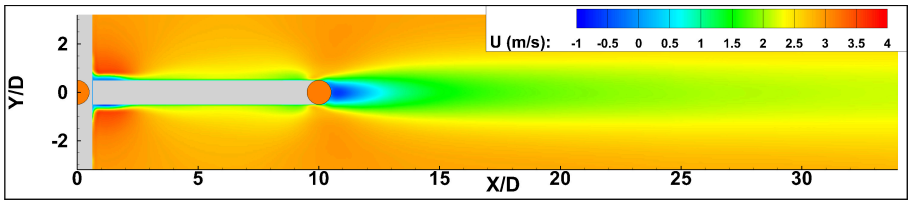

(a) $Re = 2000$

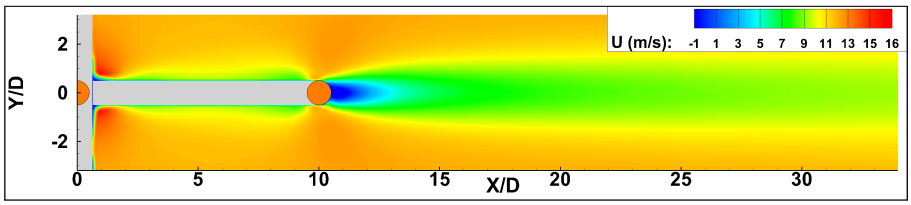

(b) $Re = 8000$

Figure A.27: Streamwise (X direction) mean velocities in double cylinder wake

Figure A.28 presents the mean velocity in the spanwise (Y) direction for double cylinder wake at two Reynolds numbers.

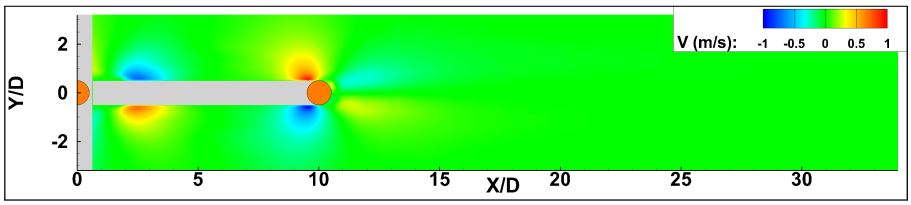

(a) $Re = 2000$

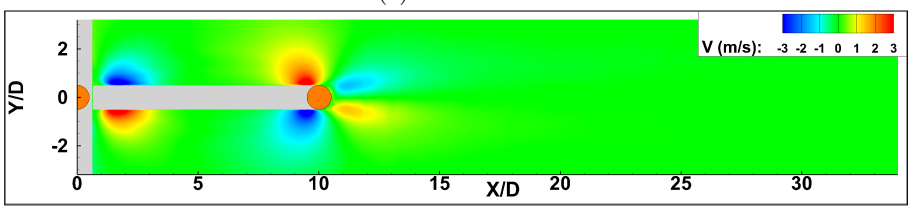

(b) $Re = 8000$

Figure A.28: Spanwise (Y direction) mean velocities in double cylinder wake

Figure A.29 presents the RMS of velocity in the streamwise (X) direction for double cylinder wake at two Reynolds numbers.

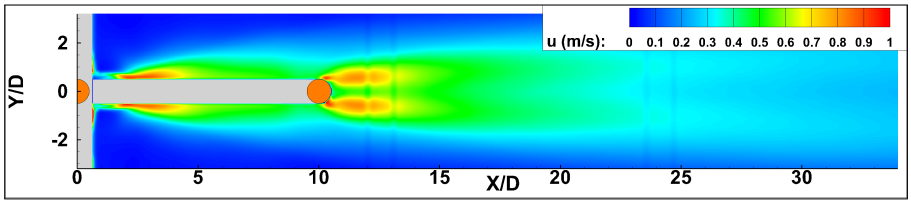

(a) $Re = 2000$

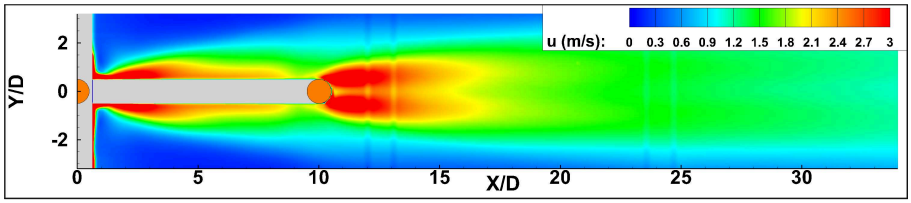

(b) $Re = 8000$

Figure A.29: RMS of streamwise velocities (X direction) in double cylinder wake

Figure A.30 presents the RMS of velocity in the spanwise (Y) direction for double cylinder wake at two Reynolds numbers.

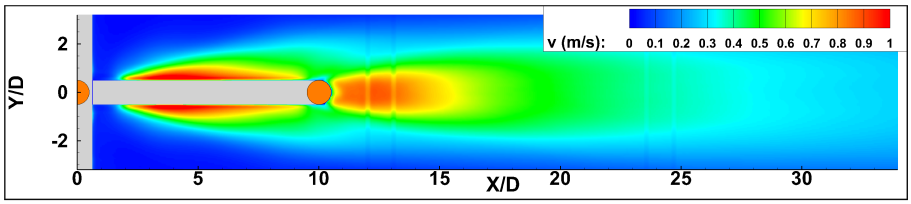

(a) $Re = 2000$

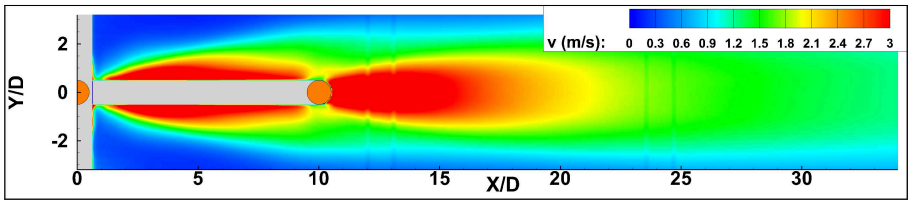

(b) $Re = 8000$

Figure A.30: RMS of spanwise velocities (Y direction) in double cylinder wake

B.2.2 Total fluctuations energy exchange

In this section, kinetic energy of the turbulence is shown in double cylinder wake for two Reynolds number. Each term of one point turbulent kinetic energy equation is computed showing gain and loss of energy between the mean flow and the turbulence. Figures A.31a and A.31b show the production term maps in double cylinder wake for both Reynolds number $Re = 2000$ and $Re = 8000$, respectively.

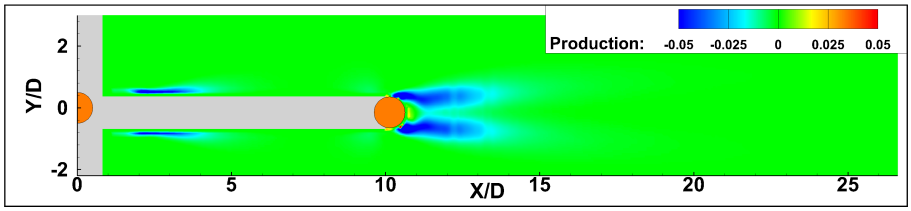

(a) $Re = 2000$

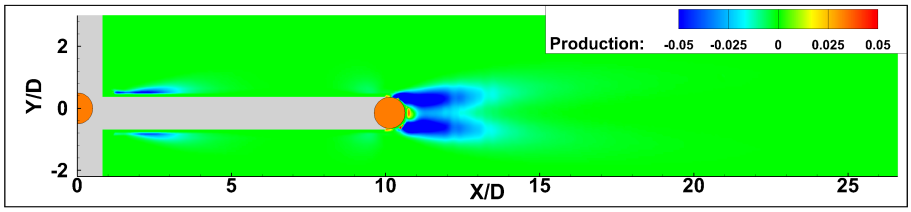

(b) $Re = 8000$

Figure A.31: Production of total turbulent kinetic energy by mean velocity in double cylinder wake

Figures A.32a and A.32b show the advection term in double cylinder wake for both Reynolds number $Re = 2000$ and $Re = 8000$, respectively.

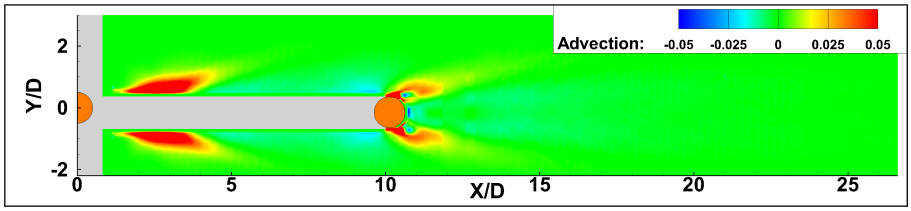

(a) $Re = 2000$

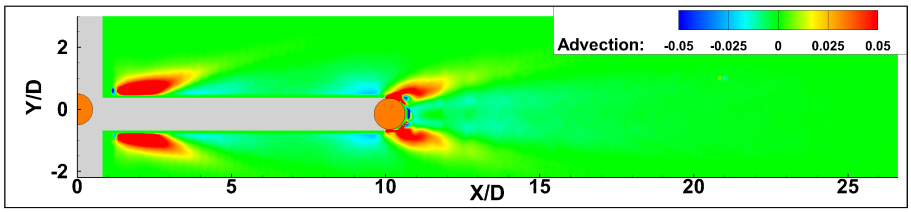

(b) $Re = 8000$

Figure A.32: Advection of total kinetic energy by mean velocity in double cylinder wake

Figures A.33a and A.33b show the diffusion through turbulence term in double cylinder wake for both Reynolds number $Re = 2000$ and $Re = 8000$, respectively.

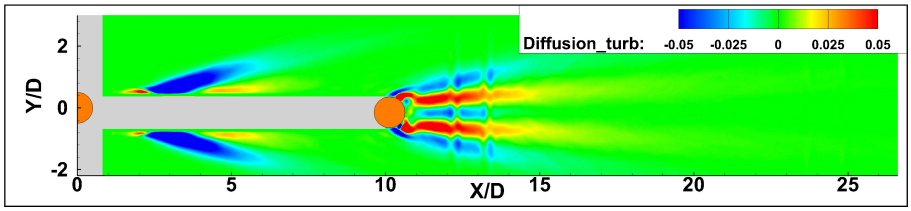

(a) $Re = 2000$

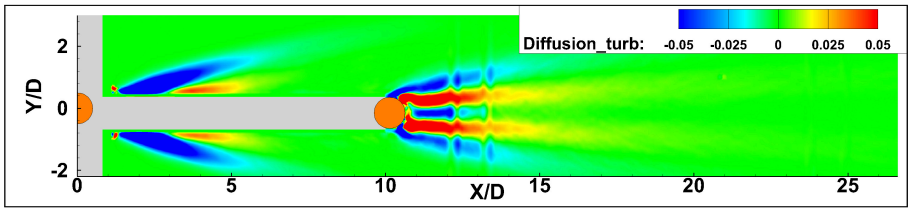

(b) $Re = 8000$

Figure A.33: Diffusion of total turbulent kinetic energy by turbulence in double cylinder wake

Figures A.34a and A.34b show the diffusion through pressure term in double cylinder wake for both Reynolds number $Re = 2000$ and $Re = 8000$, respectively.

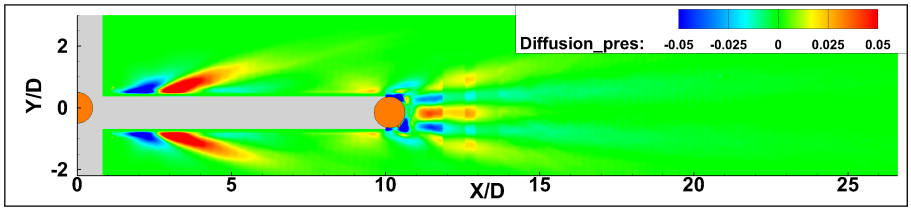

(a) $Re = 2000$

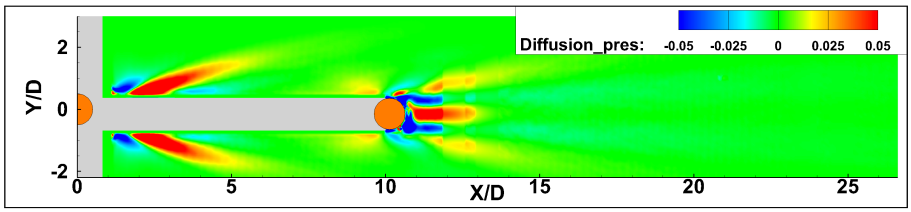

(b) $Re = 8000$

Figure A.34: Diffusion of total turbulent kinetic energy by pressure in double cylinder wake

Figures A.35a and A.35b show the dissipation term in double cylinder wake for both Reynolds number $Re = 2000$ and $Re = 8000$, respectively.

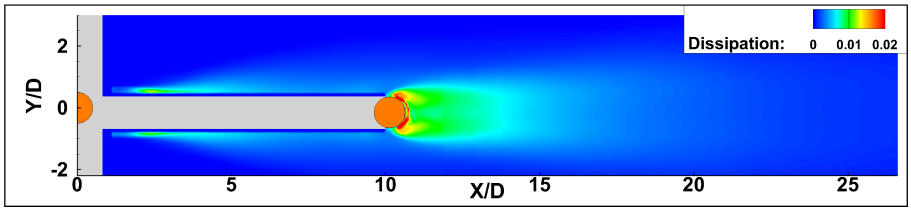

(a) $Re = 2000$

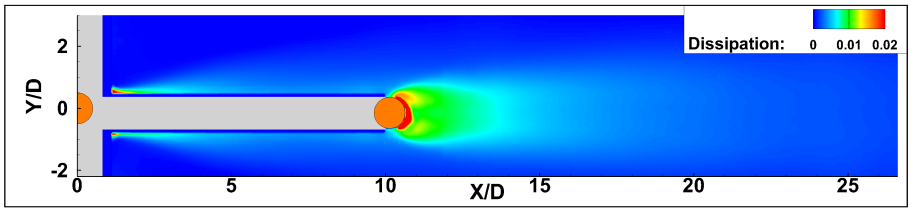

(b) $Re = 8000$

Figure A.35: Dissipation of total turbulent kinetic energy in double cylinder wake

All the terms exhibit symmetry with respect to the center of the cylinders wake. These terms are particularly significant in the near regions of the cylinders and gradually decrease as one moves downstream. Transport terms (advection and diffusion) show significant increase upstream the second cylinder.

B.2.3 Decomposed first order statistics

Figures A.36a and A.36b present the mean velocity in the streamwise direction for double cylinder wake at two Reynolds numbers, respectively. These terms are presented for one particular phase showing good phase decomposition based on upstream cylinder wake.

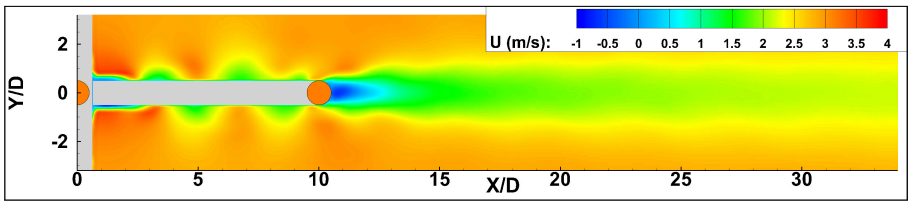

(a) $Re = 2000$

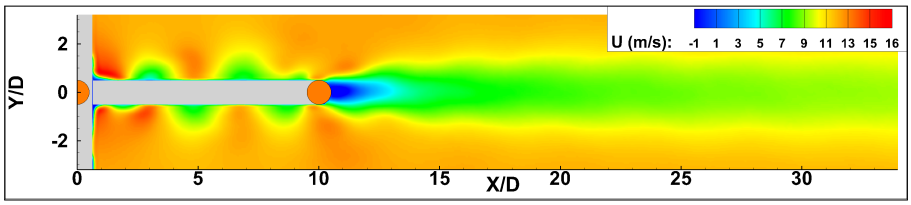

(b) $Re = 8000$

Figure A.36: RMS of streamwise direction (X) for one particular phase (phases decomposed) in double cylinder wake

Figures A.37a and A.37b present the mean velocity in the spanwise direction for double cylinder wake at two Reynolds numbers, respectively.

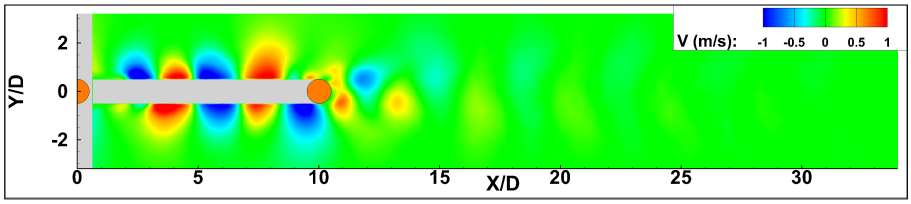

(a) $Re = 2000$

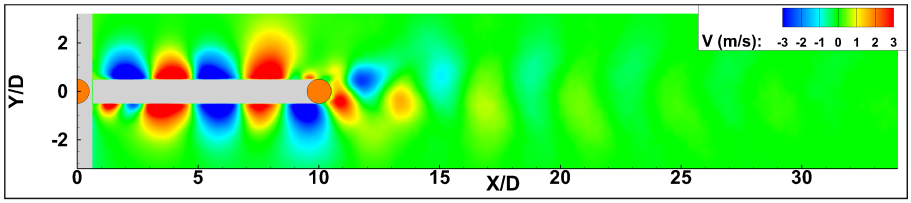

(b) $Re = 8000$

Figure A.37: Mean velocity of spanwise direction (Y) for one particular phase (phases decomposed) in double cylinder wake

Figures A.38a and A.38b present the RMS of velocity in the streamwise direction for double cylinder wake at two Reynolds numbers, respectively.

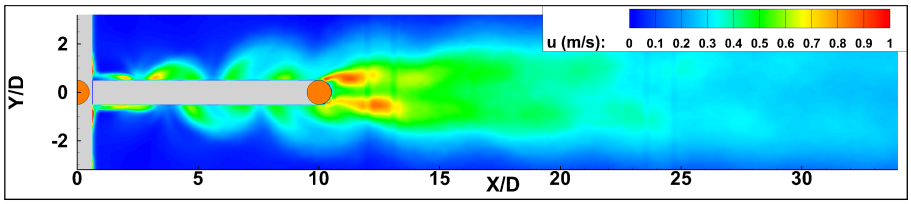

(a) $Re = 2000$

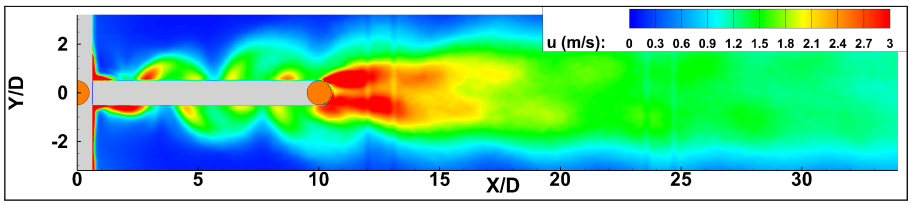

(b) $Re = 8000$

Figure A.38: RMS of streamwise direction (X) for one particular phase (phases decomposed) in double cylinder wake

Figures A.39a and A.39b present the RMS of velocity in the spanwise direction for double cylinder wake at two Reynolds numbers, respectively.

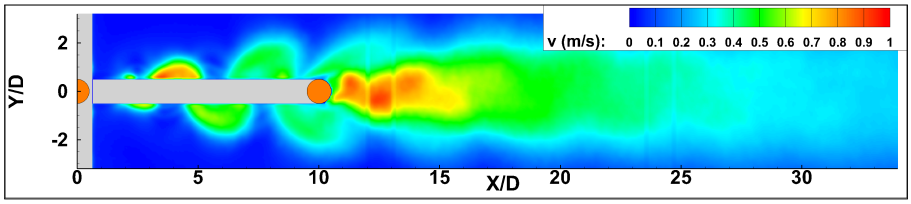

(a) $Re = 2000$

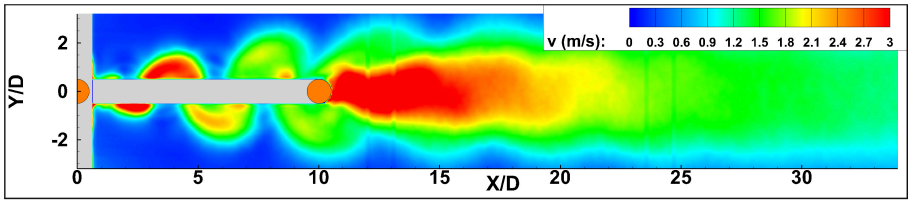

(b) $Re = 8000$

Figure A.39: RMS of spanwise direction (Y) for one particular phase (phase decomposed) in double cylinder wake

B.2.4 Decomposed total kinetic energy in phases

Figure A.40 shows the production term at low Reynolds number ($Re = 2000$) for four distinct phases ($\phi = 0°$, $100°$, $180°$ and $280°$) in double cylinder wake.

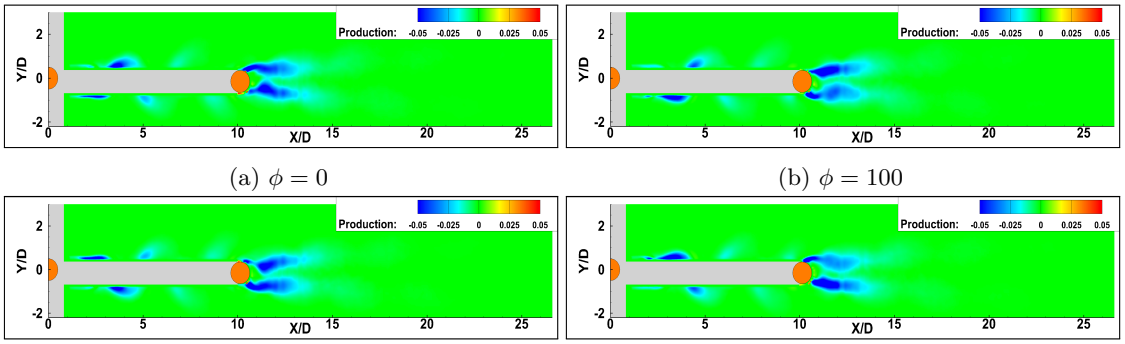

(a) $\phi = 0$ (b) $\phi = 100$

(c) $\phi = 180$ (d) $\phi = 280$

Figure A.40: Decomposed production by mean at $Re = 2000$ in double cylinder wake

Figure A.41 shows the advection term at low Reynolds number ($Re = 2000$) for four distinct phases ($\phi = 0°$, $100°$, $180°$ and $280°$) in double cylinder wake.

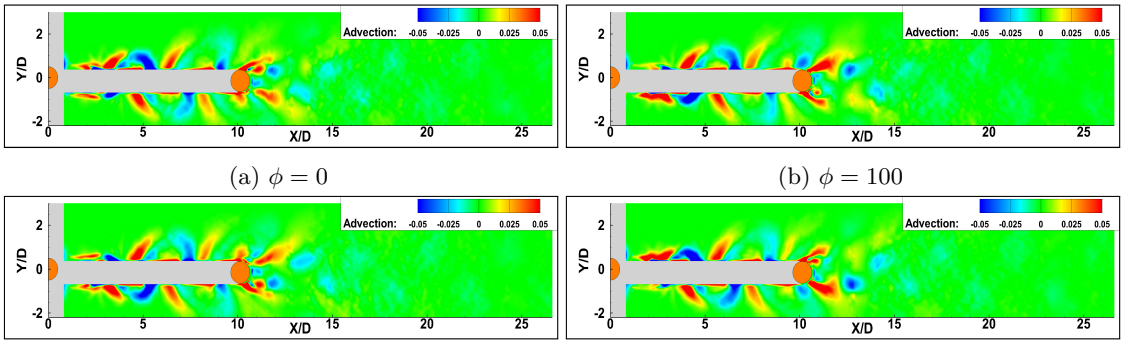

(a) $\phi = 0$ (b) $\phi = 100$

(c) $\phi = 180$ (d) Coherent structures at $\phi = 280$

Figure A.41: Decomposed advection at $Re = 2000$ in double cylinder wake

Figure A.42 shows the diffusion through turbulence at low Reynolds number ($Re = 2000$) for four distinct phases ($\phi = 0°$, $100°$, $180°$ and $280°$) in double cylinder wake.

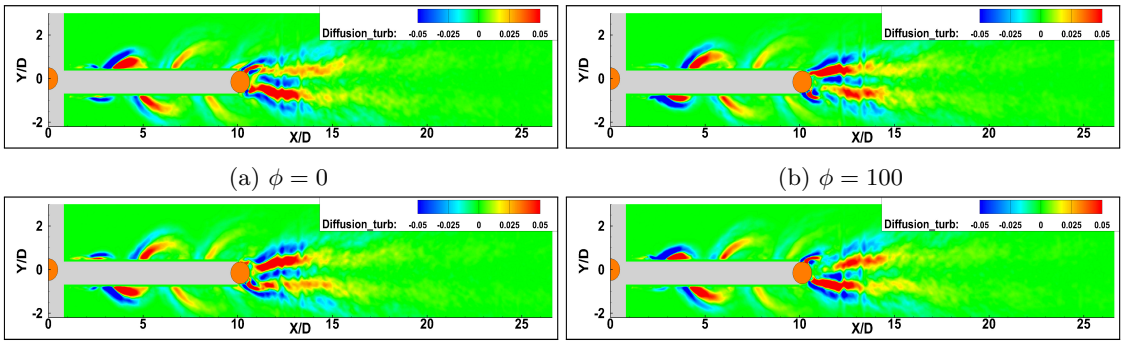

(a) $\phi = 0$ (b) $\phi = 100$

(c) $\phi = 180$ (d) $\phi = 280$

Figure A.42: Decomposed diffusion by turbulence at $Re = 2000$ in double cylinder wake

Figure A.43 shows the diffusion through pressure at low Reynolds number ($Re = 2000$) for four distinct phases ($\phi = 0°$, $100°$, $180°$ and $280°$) in double cylinder wake.

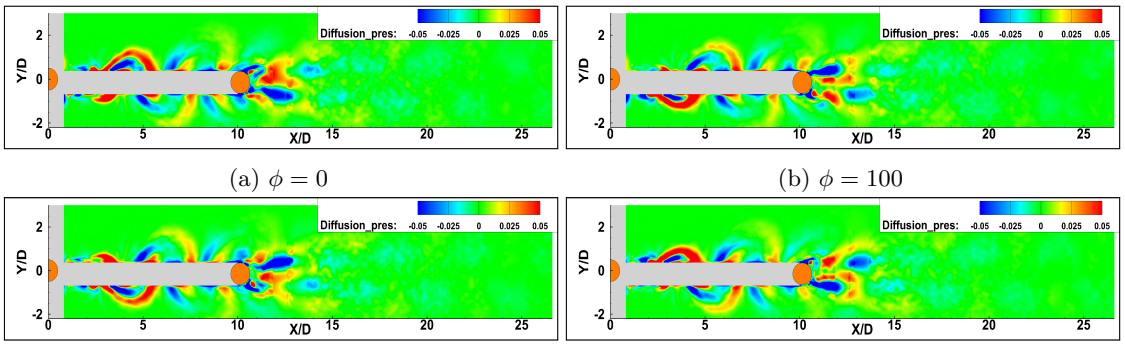

(a) $\phi = 0$ (b) $\phi = 100$

(c) $\phi = 180$ (d) $\phi = 280$

Figure A.43: Decomposed diffusion by pressure at $Re = 2000$ in double cylinder wake

Figure A.43 shows the dissipation at low Reynolds number ($Re = 2000$) for four distinct phases ($\phi = 0°$, $100°$, $180°$ and $280°$) in double cylinder wake.

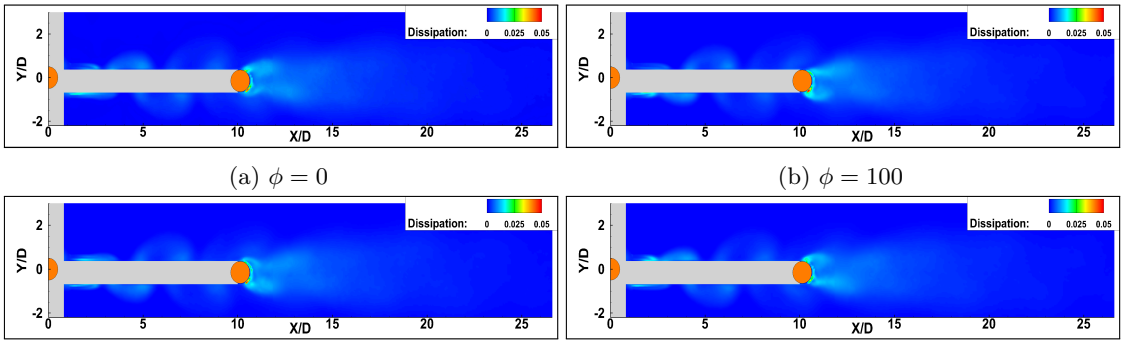

(a) $\phi = 0$ (b) $\phi = 100$

(c) $\phi = 180$ (d) $\phi = 280$

Figure A.44: Decomposed dissipation at $Re = 2000$ in double cylinder wake

In this section of decomposed total kinetic energy, all the terms shows wavy shapes downstream second obstacle. This ensures the influence of the upstream cylinder wake on the downstream one.

B.2.5 CM energy exchange and interaction with RM (based on upstream wake phase decomposition)

In this section, energy exchange between coherent motion, mean flow, and random motion resulting from their interactions are presented. Phases decomposition are based on coherent structures generated by upstream cylinder.

Low Reynolds number

Figures A.45a and A.45b show the production and dissipation of coherent motion for double cylinder wake at $Re = 2000$, respectively. In this configuration, production of coherent motion by downstream cylinder shown to be very low compared to what is seen in Figure A.19a. Dissipation of coherent motion is negligible.
Figure A.46 shows the transport and RM-interaction terms of coherent motion in double cylinder wake at $Re = 2000$. The transport (advection and diffusion) of coherent motion (CM) that is generated by the upstream cylinder significantly diminishes behind the second cylinder. Additionally, the production of random motion resulting from the coherent motion is reduced behind the second cylinder. This can be attributed to the attenuation or destruction of coherent structures, created by the upstream cylinder, as they pass behind the downstream cylinder.

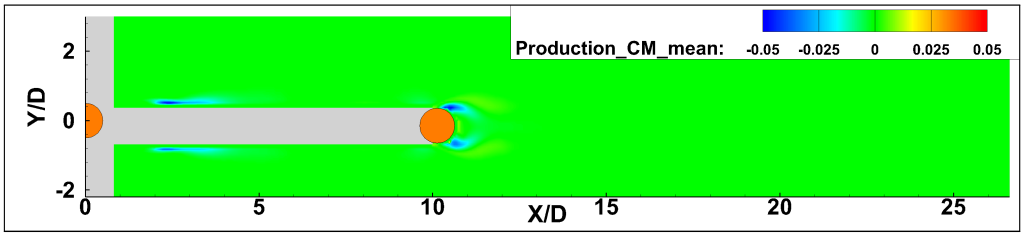

(a) CM production by mean

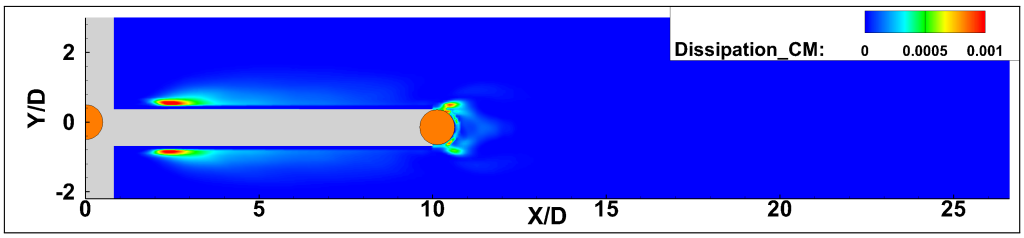

(b) CM dissipation

Figure A.45: Coherent motion (CM) production and dissipation $Re = 2000$ in double cylinder wake

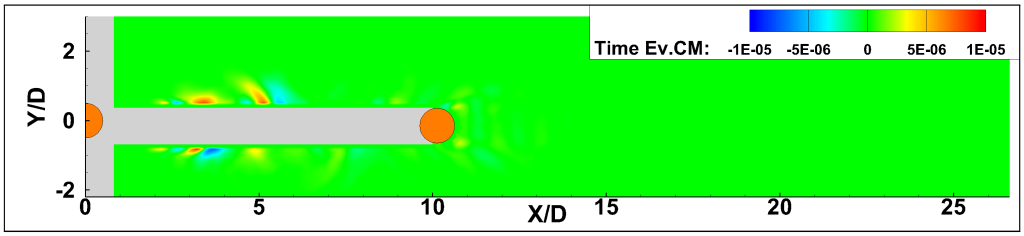

(a) CM time evolution in time

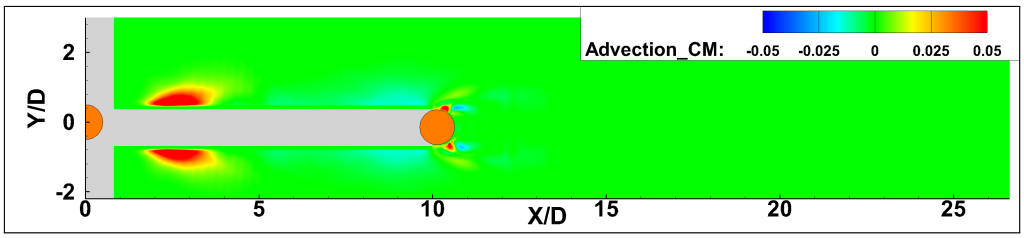

(b) CM advection by mean velocity

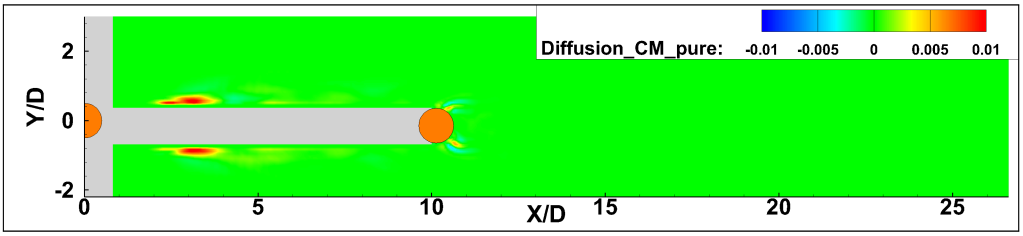

(c) CM pure diffusion

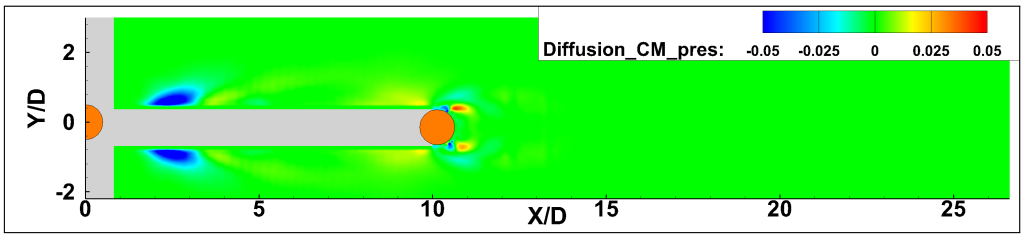

(d) CM diffusion by pressure

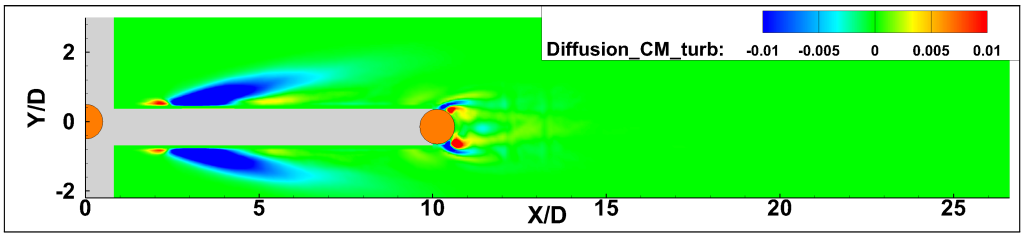

(e) CM diffusion by turbulence

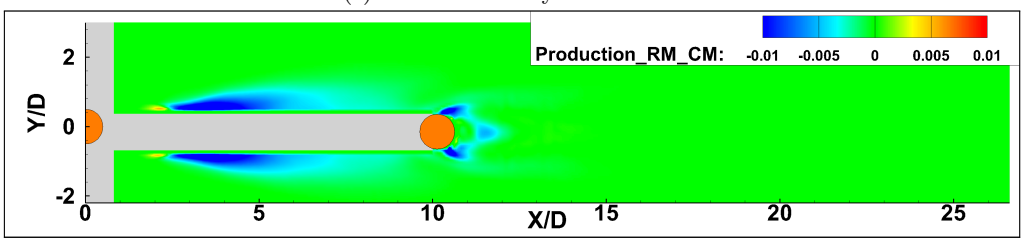

(f) RM production bt CM

Figure A.46: Coherent motion (CM) transport and RM-interaction terms at $Re = 2000$ in double cylinder wake

High Reynolds number

Figures A.47a and A.47b show the production and dissipation of coherent motion for double cylinder wake at $Re = 8000$, respectively.

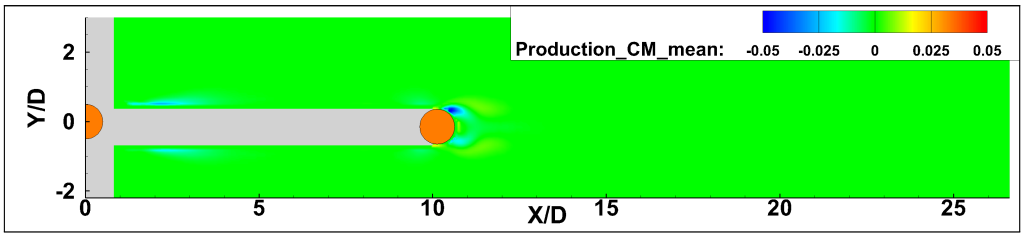

(a) CM production by mean

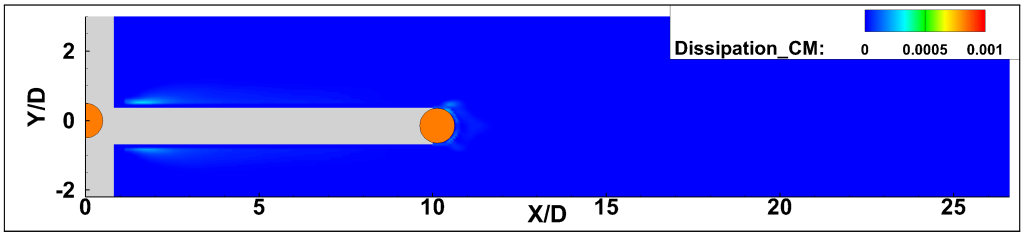

(b) CM dissipation

Figure A.47: Coherent motion (CM) production and dissipation at $Re = 8000$ in double cylinder wake

Figure A.48 shows the transport and RM-interaction terms of coherent motion in double cylinder wake at $Re = 8000$.

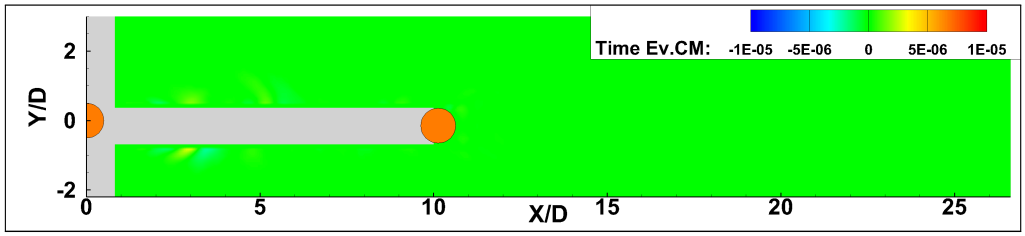

(a) CM time evolution in time

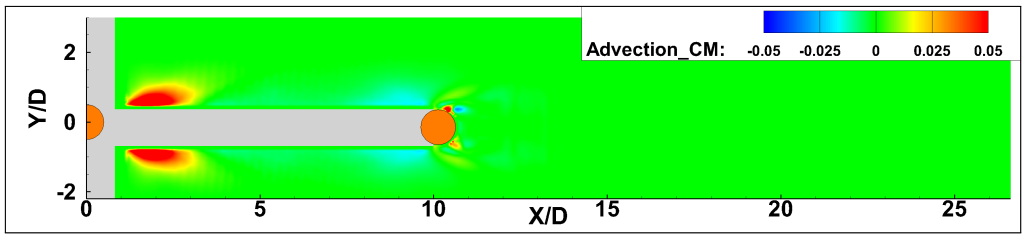

(b) CM advection by mean velocity

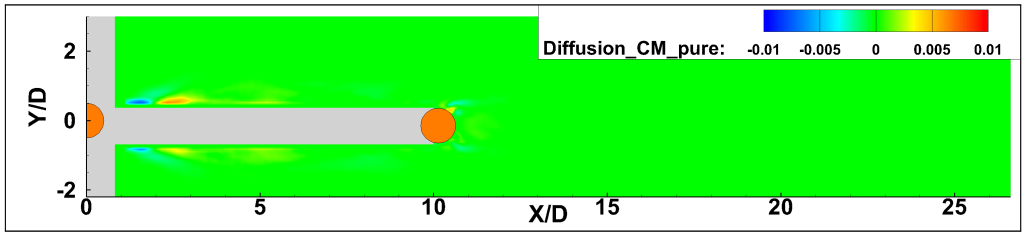

(c) CM pure diffusion

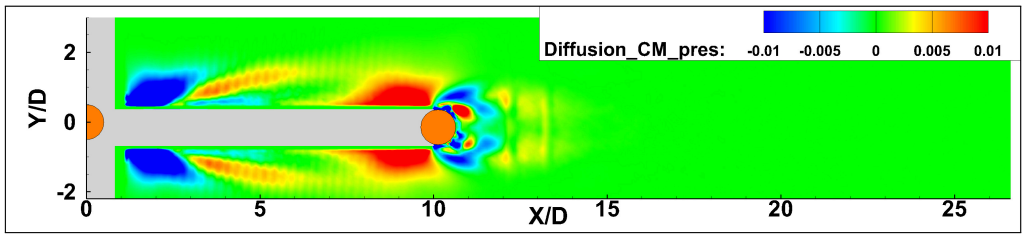

(d) CM diffusion by pressure

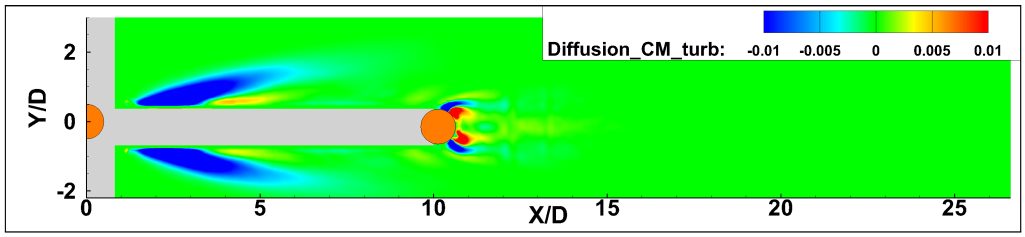

(e) CM diffusion by turbulence

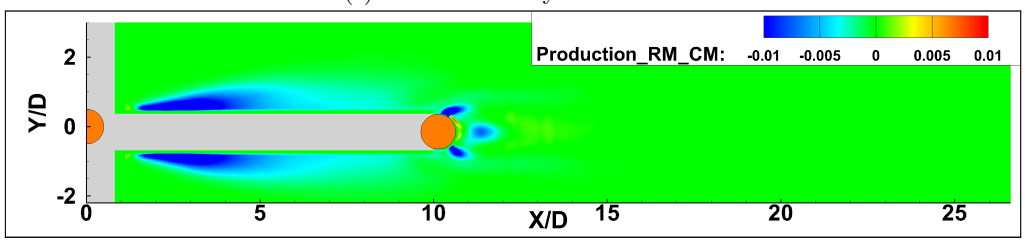

(f) RM production bt CM

Figure A.48: Coherent motion (CM) transport and RM-interaction terms at $Re = 8000$ in double cylinder wake

B.2.6 RM energy exchange and interaction with CM (based on upstream wake phase decomposition)

In this section, energy exchange between random motion, mean flow, and coherent motion resulting from their interactions in double cylinder wake are presented. This analysis is important for gaining insights into how random motion contributes to the overall flow dynamics.

Low Reynolds number

Figures A.49a and A.49b show the production and dissipation of random motion for double cylinder wake at $Re = 2000$, respectively. Production of random motion behind downstream cylinder is slightly extended comparing single cylinder wake in Figure A.23a. Dissipation of random motion reaches its maximum peak directly behind the downstream cylinder and gradually decreases downstream. These observations can be explained by the upstream shift of the separation point on the downstream cylinder due to the high incoming turbulence. This upstream shift of the separation point on the downstream cylinder surface leads to early boundary layer separation and more extended downstream.

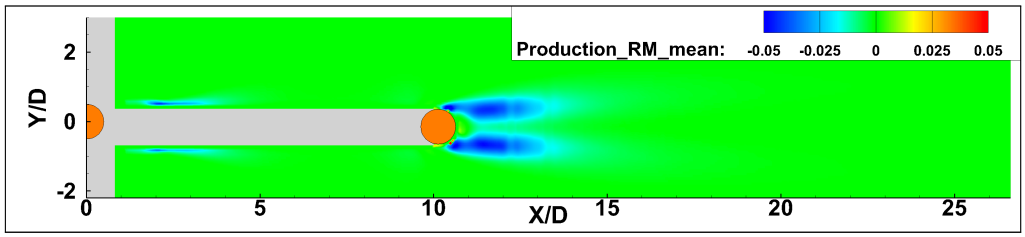

(a) RM production by mean

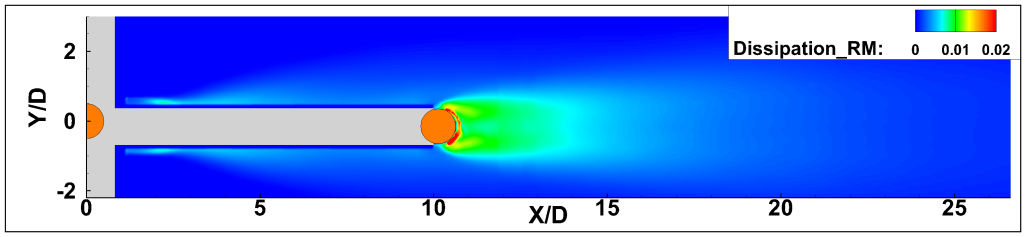

(b) RM dissipation

Figure A.49: Random motion (RM) production and dissipation terms in double cylinder wake at $Re = 2000$

Figure A.50 shows the transport terms of random motion in double cylinder wake at $Re = 2000$. The transport of random motion behind the downstream cylinder is lower when compared to the single cylinder wake. However, it's important to note that the transport of random motion becomes higher when compared to coherent motion, as shown in Figure A.46.

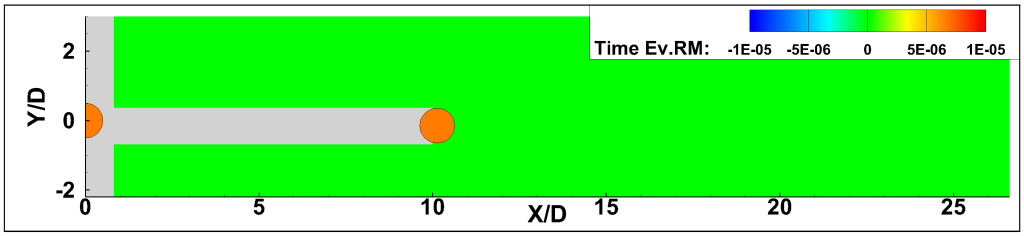

(a) RM time evolution

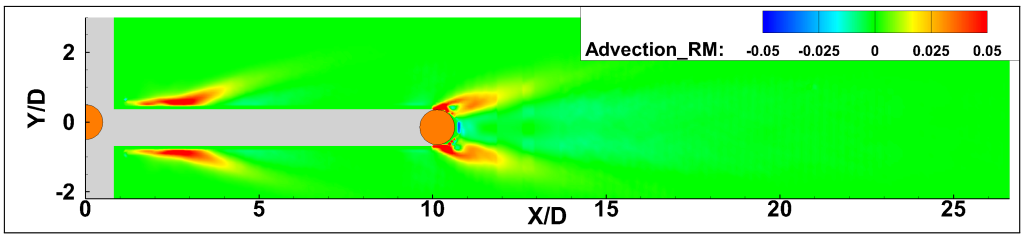

(b) RM advection by mean velocity

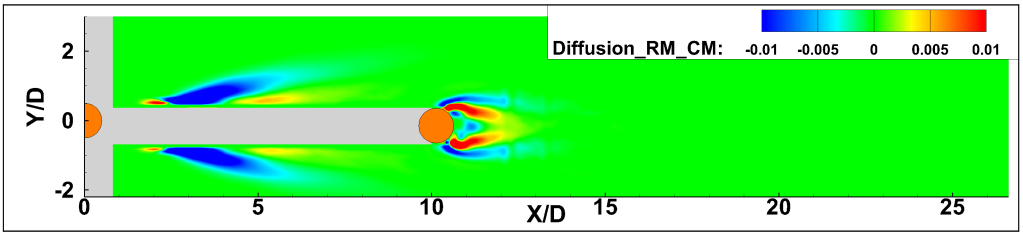

(c) RM diffusion by CM interaction

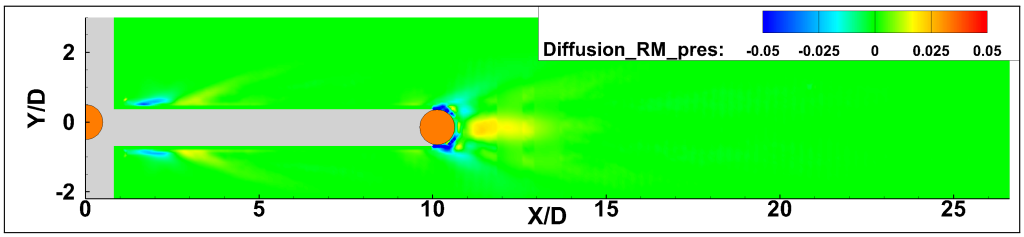

(d) RM diffusion by pressure

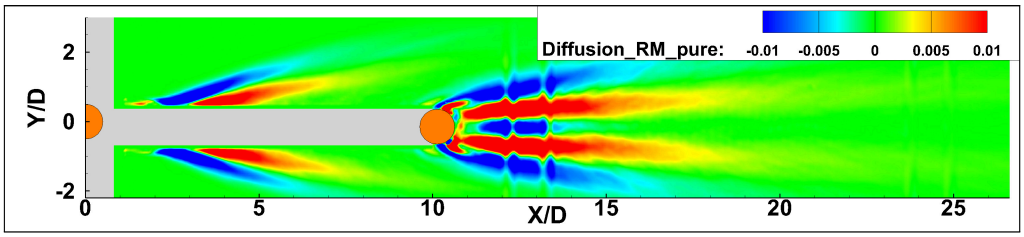

(e) RM pure diffusion

Figure A.50: Random motion (RM) transport terms in double cylinder wake at $Re = 2000$

High Reynolds number

Figures A.51a and A.51b show the production and dissipation of random motion for double cylinder wake at $Re = 2000$, respectively.

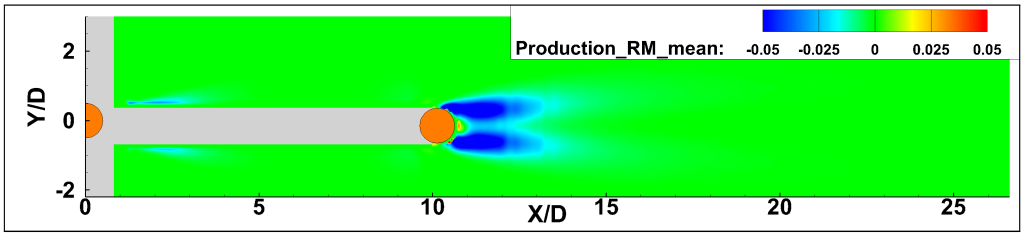

(a) RM production by mean

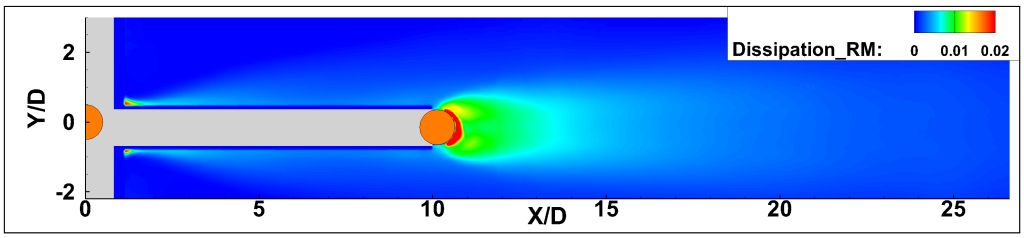

(b) RM dissipation

Figure A.51: Random motion (RM) production and dissipation in double cylinder wake at $Re = 8000$

Figure A.52 shows the transport terms of random motion in double cylinder wake at $Re = 8000$.

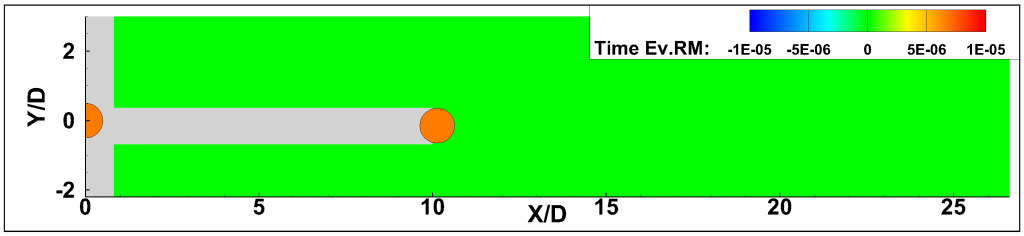

(a) RM time evolution

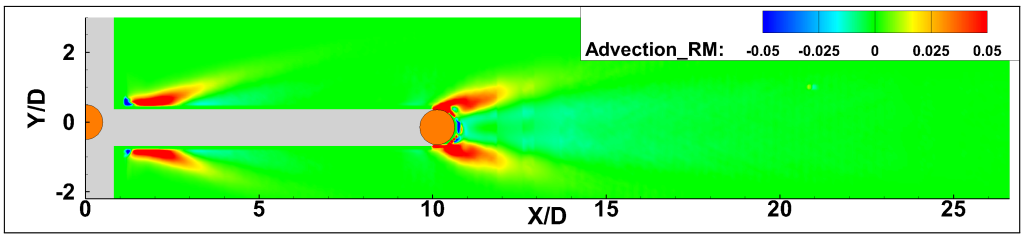

(b) RM advection by mean velocity

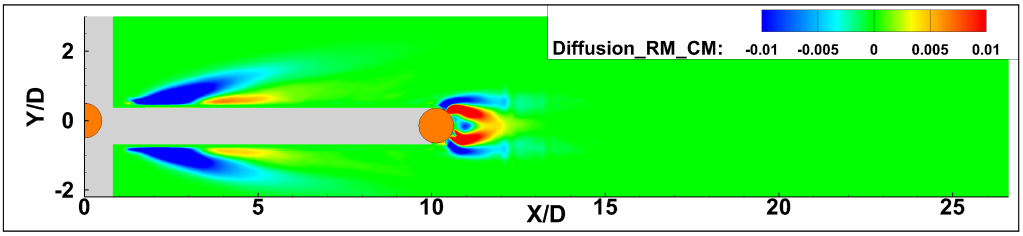

(c) RM diffusion by CM interaction

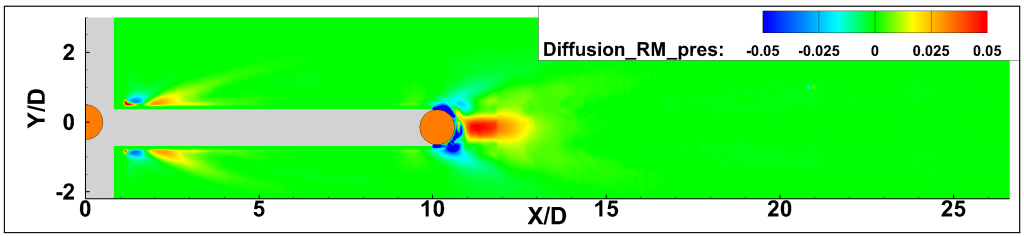

(d) RM diffusion by pressure

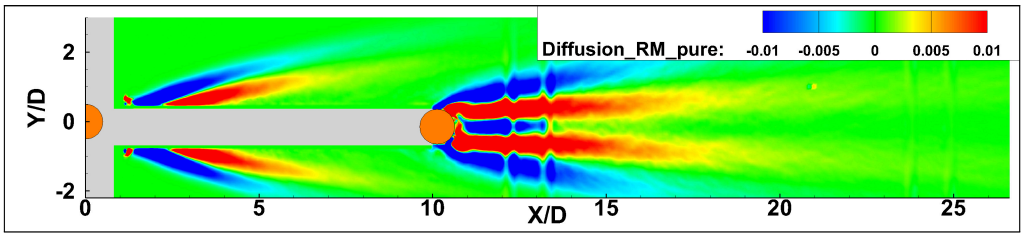

(e) RM pure diffusion

Figure A.52: Random motion (RM) transport terms in double cylinder wake at $Re = 8000$

B.2.7 CM energy exchange and interaction with RM (based on downstream wake phase decomposition)

In this section, energy exchange between coherent motion, mean flow, and random motion interaction are based on downstream cylinder (phases decomposition are based on coherent structures generated by downstream cylinder).

Low Reynolds number

Figures A.53a and A.53b show the production and dissipation of coherent motion for double cylinder wake at $Re = 2000$, respectively. The production of coherent motion generated by the downstream cylinder, which is within the upstream wake, is lower when compared to the upstream cylinder that doesn't have an upstream wake. This difference can be attributed to lower shear of mean velocity on the downstream cylinder, resulting in lower production of coherent motion. Dissipation of coherent motion generated by downstream cylinder remains negligible, however map change is occurred.

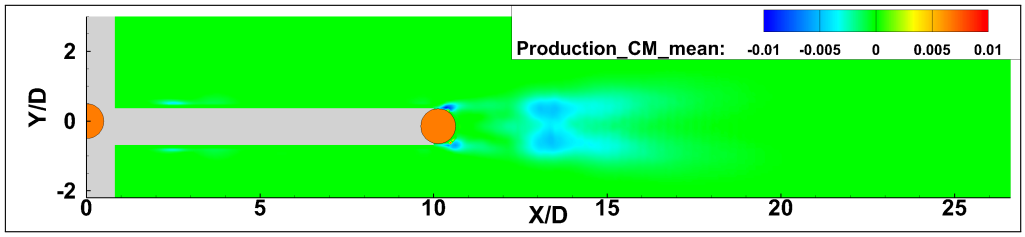

(a) CM production by mean

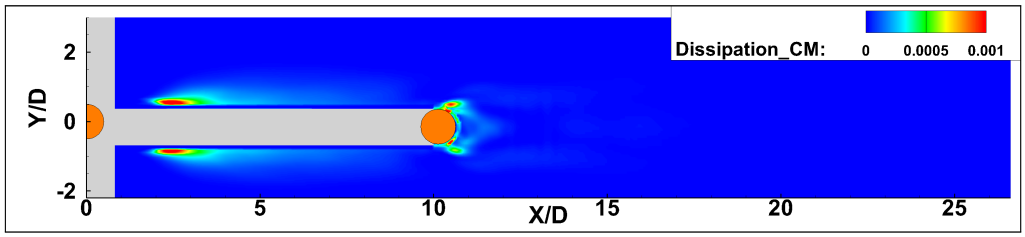

(b) CM dissipation

Figure A.53: Coherent motion (CM) production and dissipation at $Re = 2000$ in double cylinder wake based on second obstacle phase decomposition

Figure A.54 shows the transport and RM-interaction terms of coherent motion in double cylinder wake at $Re = 2000$. The transport of coherent motion generated by the downstream cylinder is lower when compared to the coherent motion produced by the upstream cylinder, as shown in Figure A.20. This observation can be explained by the lower production of coherent motion by the downstream cylinder, resulting in a lower amount of contained energy in the coherent motion field.

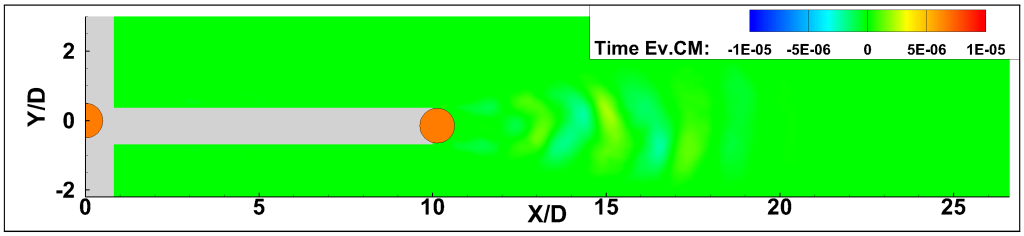

(a) CM time evolution in time

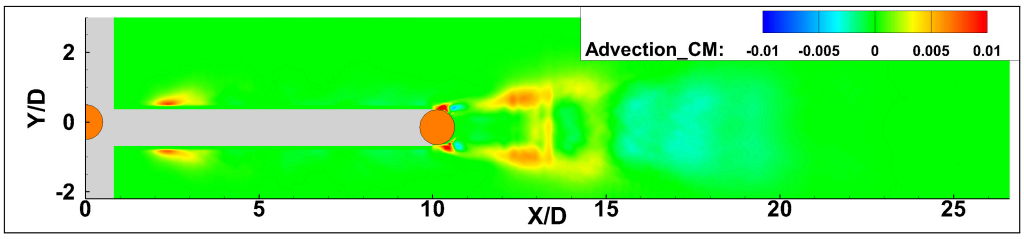

(b) CM advection by mean velocity

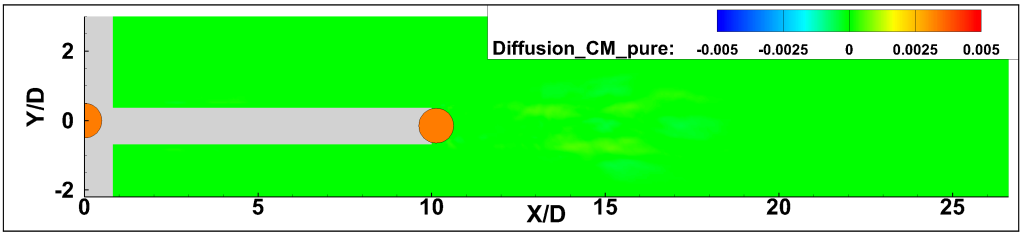

(c) CM pure diffusion

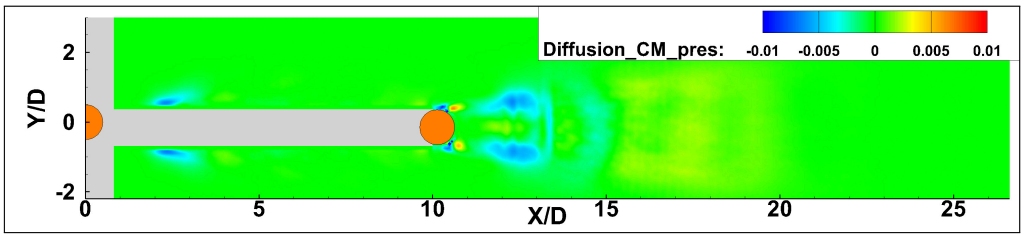

(d) CM diffusion by pressure

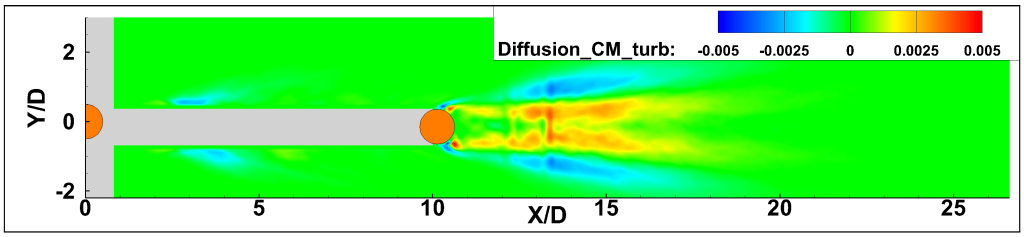

(e) CM diffusion by turbulence

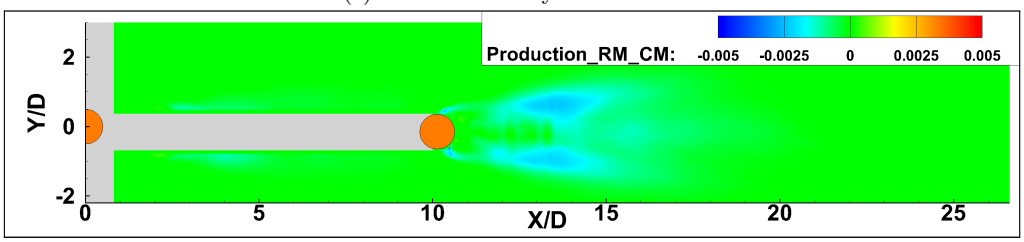

(f) RM production bt CM

Figure A.54: Coherent motion (CM) transport and RM-interaction terms at $Re = 2000$ in double cylinder wake on second obstacle phase decomposition

High Reynolds number

Figures A.55a and A.55b show the production and dissipation of coherent motion for double cylinder wake at $Re = 8000$, respectively.

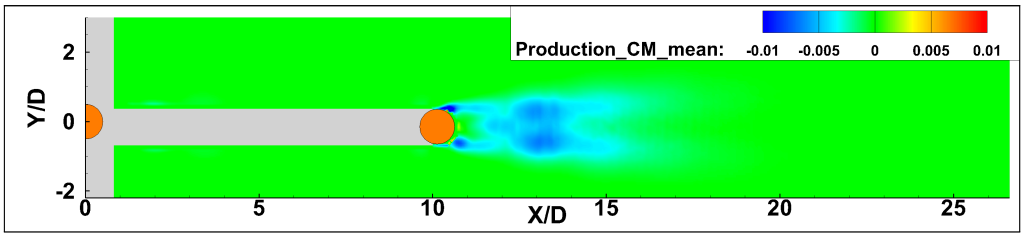

(a) CM production by mean

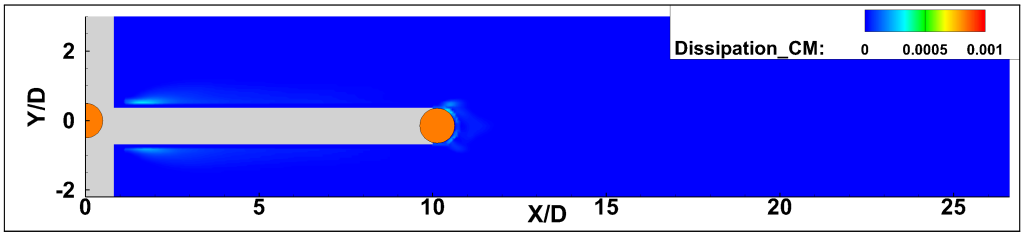

(b) CM dissipation

Figure A.55: Coherent motion (CM) production and dissipation at $Re = 8000$ in 2 cylinders wake based on second obstacle phase decomposition

Figure A.56 shows the transport and RM-interaction terms of coherent motion in double cylinder wake at $Re = 8000$.

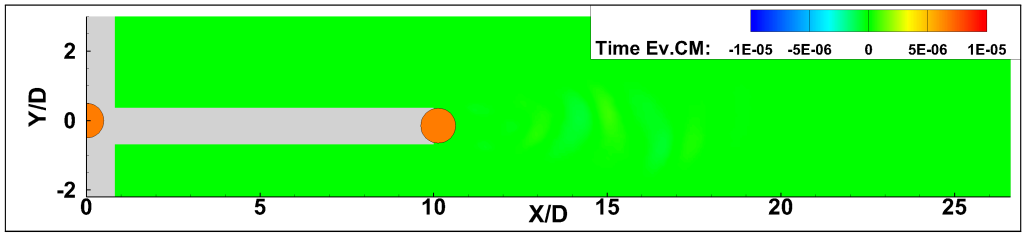

(a) CM time evolution in time

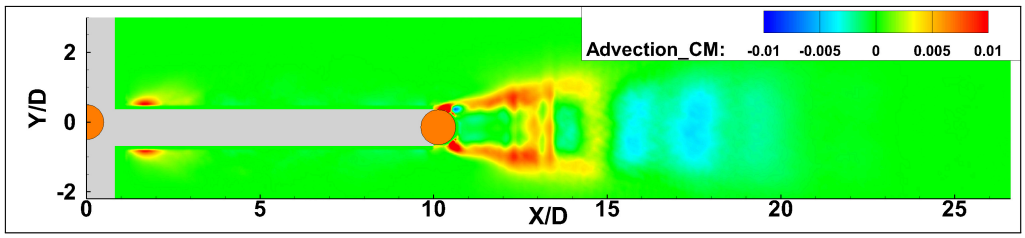

(b) CM advection by mean velocity

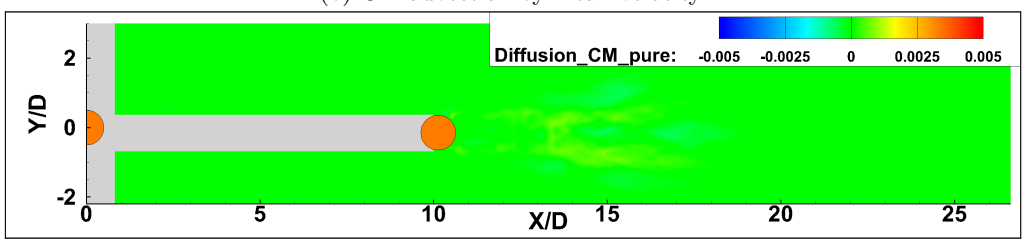

(c) CM pure diffusion

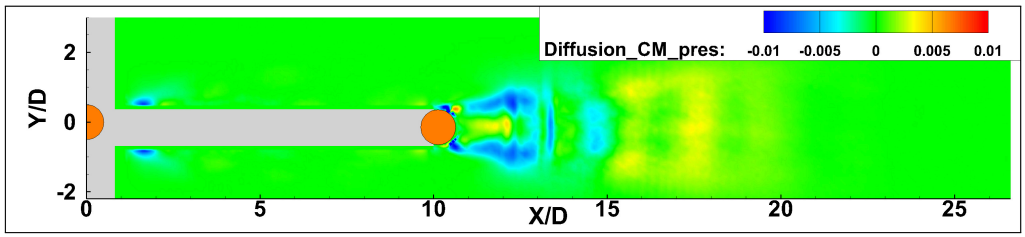

(d) CM diffusion by pressure

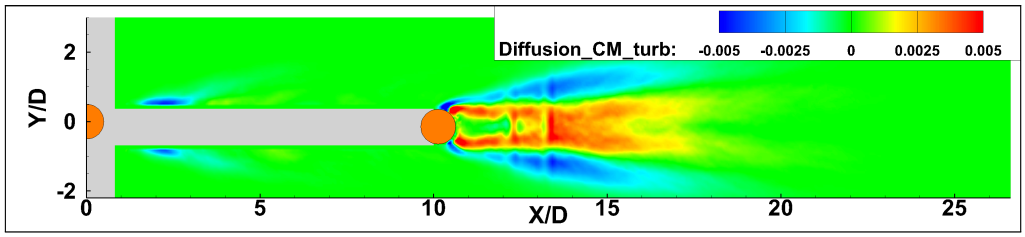

(e) CM diffusion by turbulence

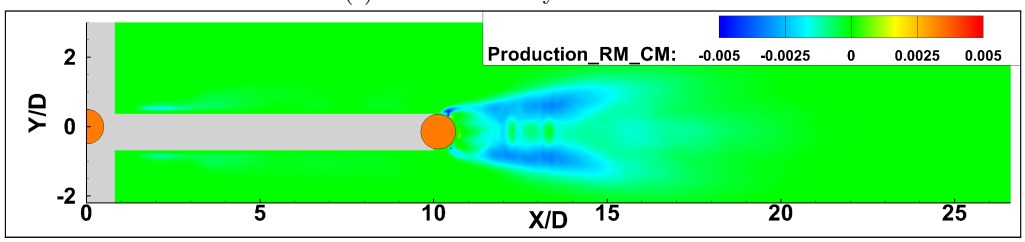

(f) RM production bt CM

Figure A.56: Coherent motion (CM) transport and RM-interaction terms at $Re = 8000$ in double cylinder wake

B.2.8 RM energy exchange and interaction with CM (based on downstream wake phase decomposition)

The only terms that changed in the equation of random motion when decomposed with respect to the downstream obstacle is the production and the diffusion of random motion due to its interaction with coherent motion. All other terms remain constant.

Figures A.57a and A.57b illustrate the production of random motion caused by its interaction with coherent motion in the double cylinder wake at both Reynolds numbers ($Re = 2000$ and $Re = 8000$), respectively.

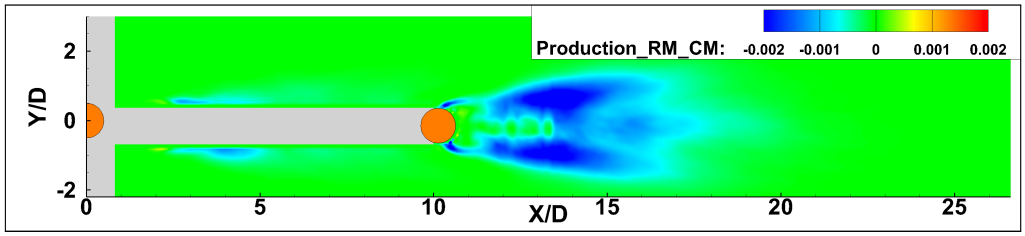

(a) $Re = 2000$

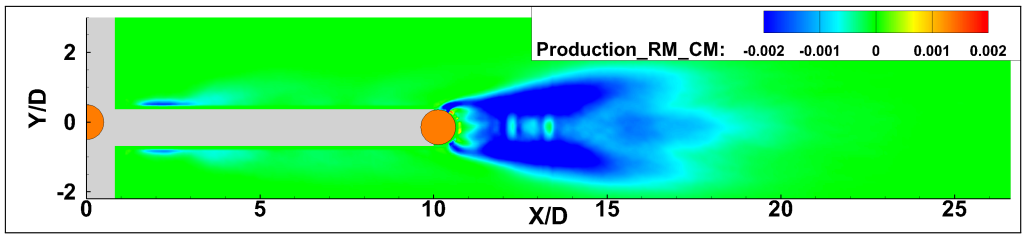

(b) $Re = 8000$

Figure A.57: Production of RM by CM interaction (created by downstream cylinder)

Figures A.58a and A.58b illustrate the diffusion of random motion caused by its interaction with coherent motion in the double cylinder wake at both Reynolds numbers ($Re = 2000$ and $Re = 8000$), respectively. These figures reveal a high transport of random motion by coherent motion at the periphery of the wake, where higher entrainment occurs.

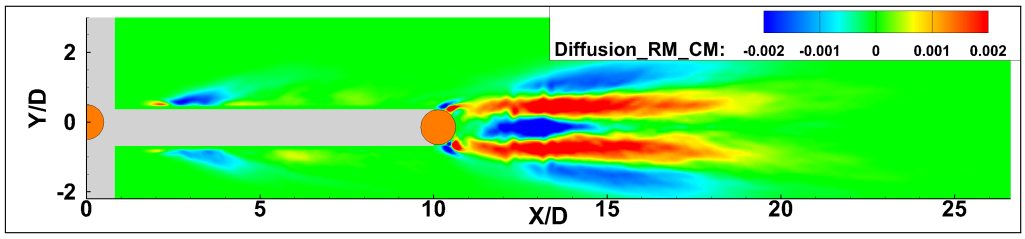

(a) $Re = 2000$

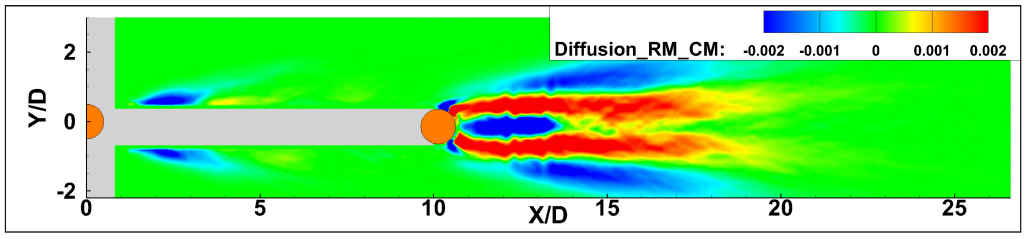

(b) $Re = 8000$

Figure A.58: Diffusion of RM by CM interaction (created by downstream cylinder)

C.3 Cylinder-airfoil configuration

C.3.1 First order statistics

Figure A.59 presents the mean velocity in the streamwise (X) direction for cylinder-airfoil wake at two Reynolds numbers. Figure A.59 shows that the mean velocity is increased over the leading edge of the airfoil, leading further to high shear stress at this position.

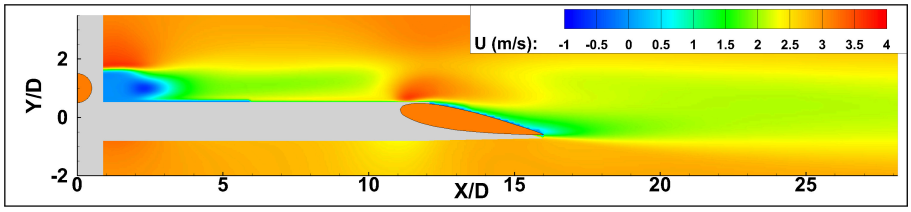

(a) $Re = 2000$

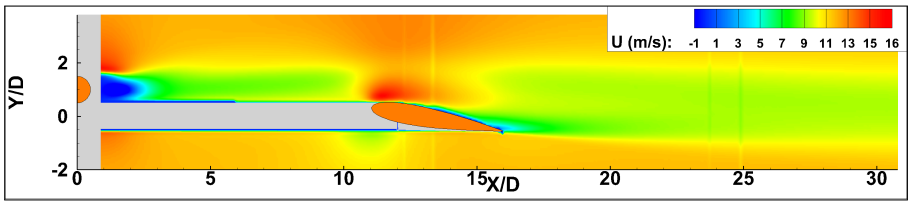

(b) $Re = 8000$

Figure A.59: Streamwise (X direction) mean velocities in cylinder wake

Figure A.60 presents the mean velocity in the spanwise (Y) direction for cylinder-airfoil wake at two Reynolds numbers.

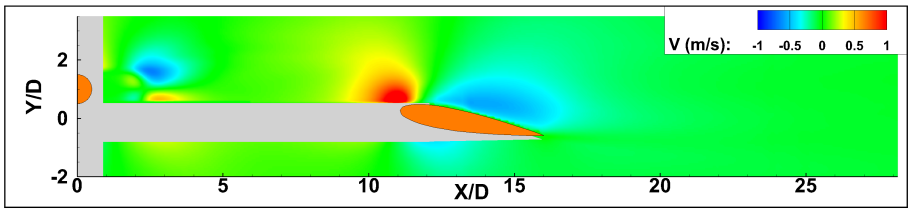

(a) $Re = 2000$

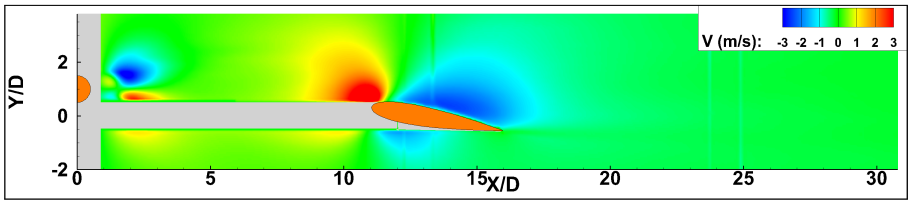

(b) $Re = 8000$

Figure A.60: Spanwise (Y direction) mean velocities in cylinder-airfoil wake

Figure A.61 presents the RMS of velocity in the streamwise (X) direction for cylinder-airfoil wake at two Reynolds numbers. In this figure, it is evident that the total velocity fluctuations are deflected upwards, which is attributed to the presence of the airfoil. Furthermore, the RMS exhibits its highest peak in close proximity to the obstacles, such as behind the cylinder and over the airfoil.

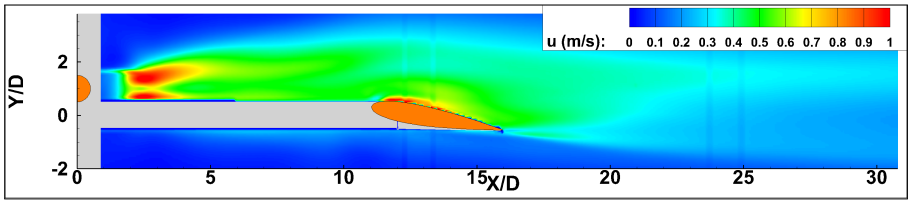

(a) $Re = 2000$

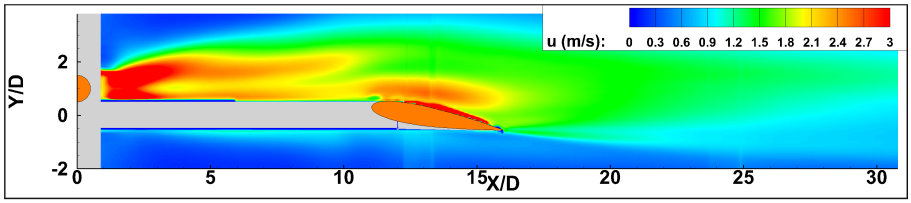

(b) $Re = 8000$

Figure A.61: RMS of streamwise velocities (x direction) in cylinder-airfoil wake

Figure A.62 presents the RMS of velocity in the spanwise (Y) direction for cylinder-airfoil wake at two Reynolds numbers. Figure A.62 reveals that there are higher spanwise fluctuations observed over the airfoil when compared to the streamwise fluctuations shown in Figure A.61.

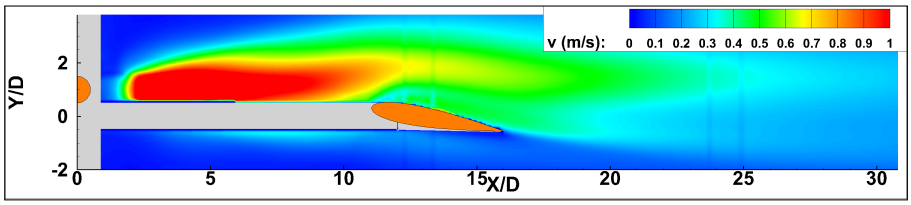

(a) $Re = 2000$

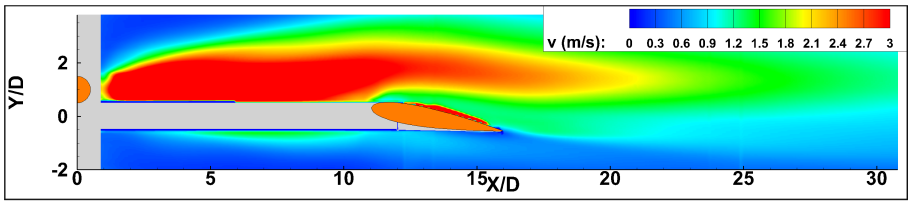

(b) $Re = 8000$

Figure A.62: RMS of spanwise velocities (y direction) in cylinder-airfoil wake

C.3.2 Total fluctuations energy exchange

Figures A.63a and A.63b show the production term in cylinder-airfoil wake for both Reynolds number $Re = 2000$ and $Re = 8000$, respectively. It can be observed that the production of turbulence originating from the airfoil is higher at lower Reynolds numbers (Figure A.63a) compared to higher Reynolds numbers (Figure A.63b). This phenomenon can be explained by the thicker boundary layer present over the airfoil at lower Reynolds numbers, which provides more opportunities for turbulence production.

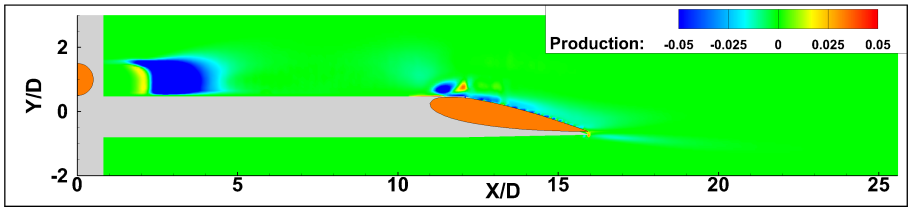

(a) $Re = 2000$

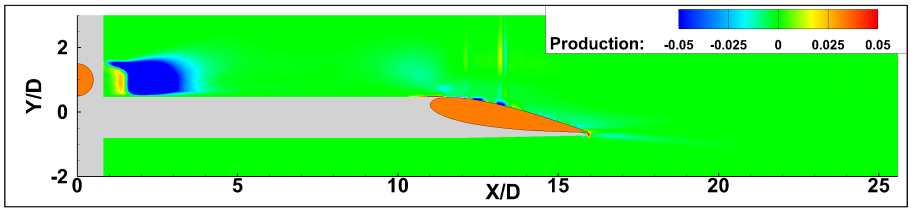

(b) $Re = 8000$

Figure A.63: Production of total turbulent kinetic energy by mean velocity in cylinder-airfoil wake

Figures A.64a and A.64b show the advection term in cylinder-airfoil wake for both Reynolds number $Re = 2000$ and $Re = 8000$, respectively. It is observed that positive advection peaks occured over the leading edge due to high mean velocity. Conversely, negative advection peaks occur over the airfoil itself, which is attributed to the presence of the airfoil boundary layer. Significantly, the thickness of the airfoil boundary layer decreases as the Reynolds number increases, as demonstrated in Figure A.64b.

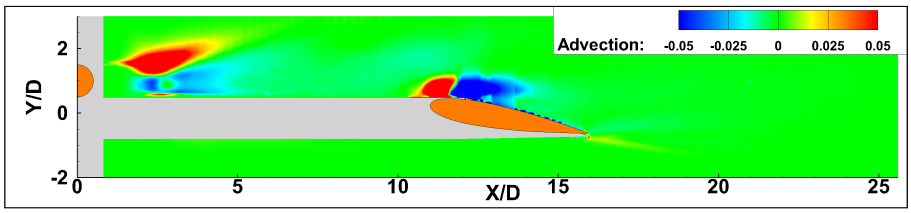

(a) $Re = 2000$

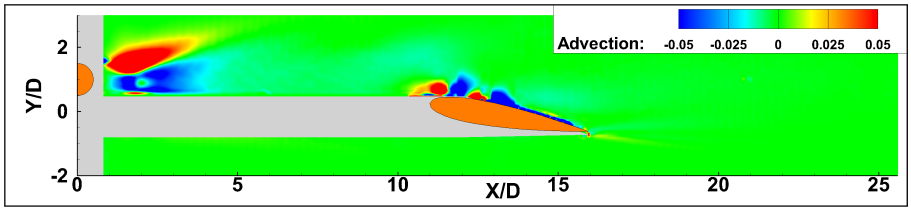

(b) $Re = 8000$

Figure A.64: Advection of total kinetic energy by mean velocity

Figures A.65a and A.65b show the diffusion through turbulence term in cylinder-airfoil wake for both Reynolds number $Re = 2000$ and $Re = 8000$, respectively. In Figure A.65a, one observes that there are positive and negative peaks in the airfoil boundary layer for low Reynolds number ($Re = 2000$). However, for high Reynolds number ($Re = 8000$) shown in Figure A.65b, the diffusion through turbulence term changes to a thin negative layer of diffusion, reflecting the thinner boundary layer at the higher Reynolds number.

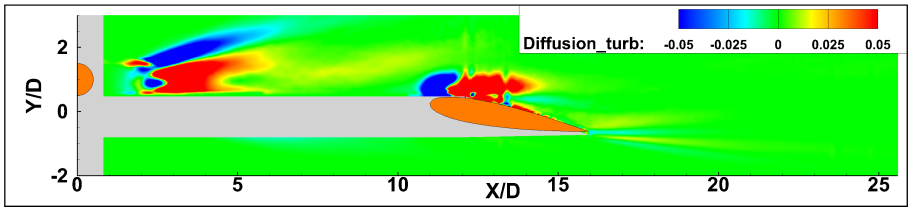

(a) $Re = 2000$

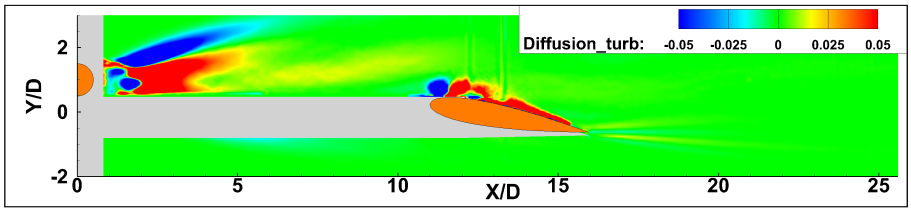

(b) $Re = 8000$

Figure A.65: Diffusion of total turbulent kinetic energy by turbulence in cylinder-airfoil wake

Figures A.66a and A.66b show the diffusion through pressure term in cylinder-airfoil wake for both Reynolds number $Re = 2000$ and $Re = 8000$, respectively. In both cases, a negative peak in the diffusion through pressure is observed over the body of the airfoil. Conversely, positive peaks are observed over the leading edge airfoil. Negative fluctuations in pressure and velocity contribute to positive diffusion.

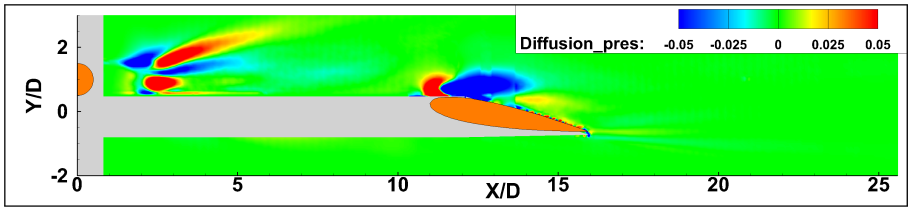

(a) $Re = 2000$

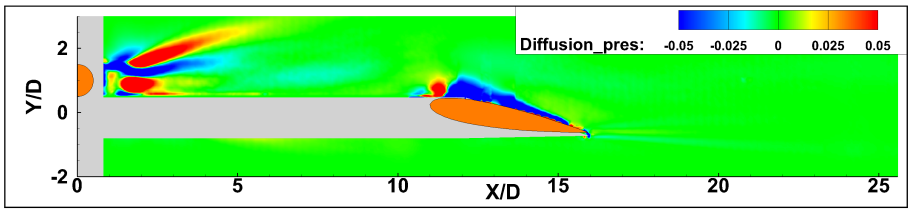

(b) $Re = 8000$

Figure A.66: Diffusion of total turbulent kinetic energy by pressure in cylinder-airfoil wake

Figures A.67a and A.67b show the dissipation term in cylinder-airfoil wake for both Reynolds number $Re = 2000$ and $Re = 8000$, respectively. It can be observed that at lower Reynolds numbers, as shown in Figure A.67a, the dissipation zone is larger over the airfoil compared to higher Reynolds numbers, as seen in Figure A.67b. This difference in the extent of the dissipation zone is attributed to the thicker boundary layer over the airfoil present at lower Reynolds numbers, which leads to increased dissipation.

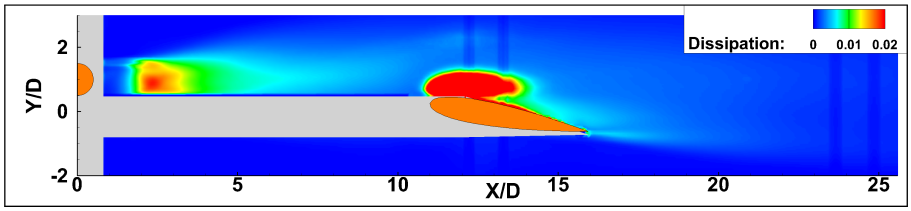

(a) $Re = 2000$

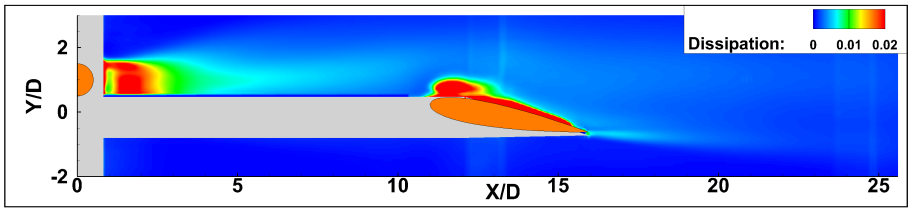

(b) $Re = 8000$

Figure A.67: Dissipation of total turbulent kinetic energy in cylinder-airfoil wake

C.3.3 Decomposed first order statistics

Figures A.68a and A.68b present the mean velocity in the streamwise direction for cylinder-airfoil wake at two Reynolds numbers, respectively. These terms are presented for one particular phase showing good phase decomposition based on upstream cylinder wake.

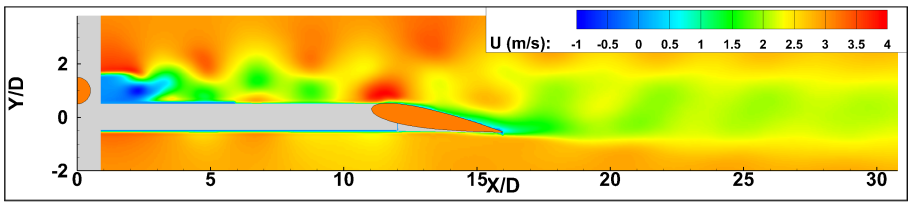

(a) $Re = 2000$

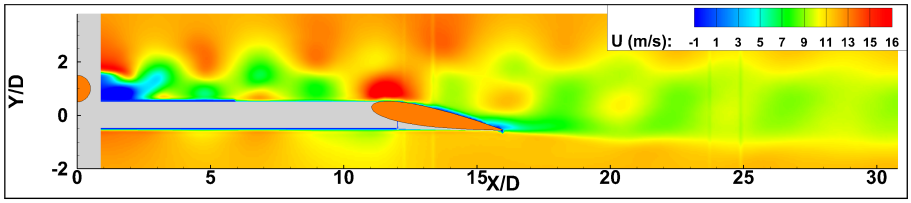

(b) $Re = 8000$

Figure A.68: Mean velocity of streamwise direction (X) for one particular phase (phases decomposed) in cylinder-airfoil wake

Figures A.69a and A.37b present the mean velocity in the spanwise direction for cylinder-airfoil wake at two Reynolds numbers, respectively.

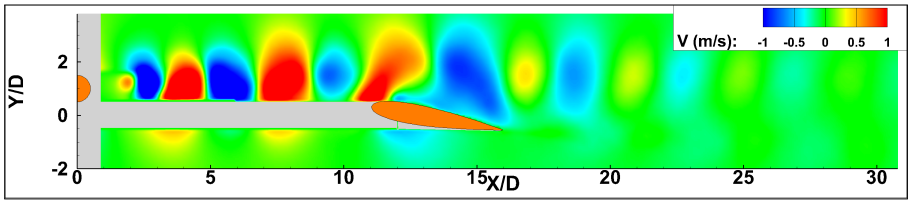

(a) $Re = 2000$

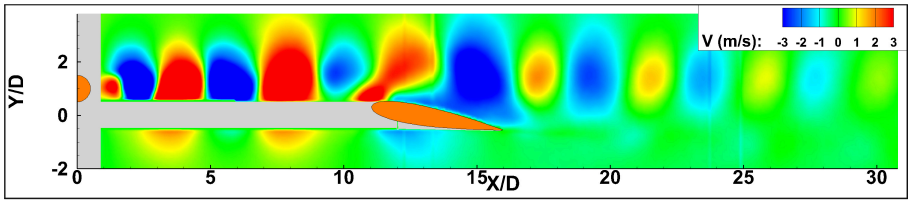

(b) $Re = 8000$

Figure A.69: Mean velocity of spanwise direction (Y) for one particular phase (phases decomposed) in cylinder-airfoil wake

Figures A.70a and A.70b present the RMS of velocity in the streamwise direction for cylinder-airfoil wake at two Reynolds numbers, respectively.

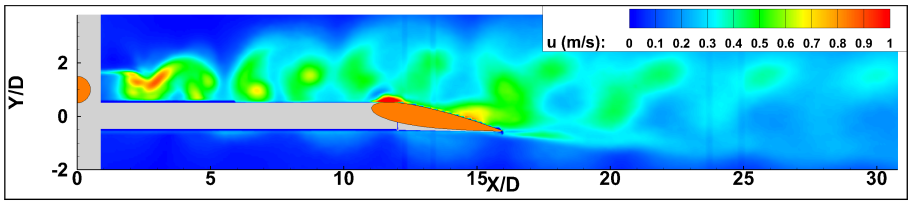

(a) $Re = 2000$

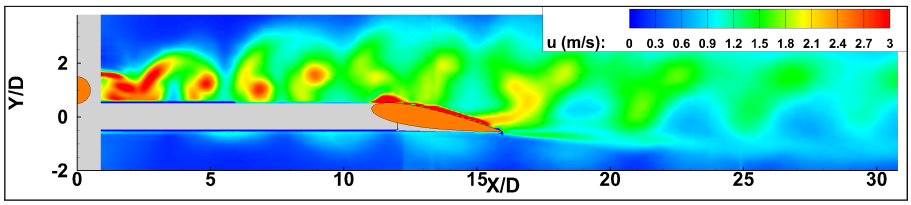

(b) $Re = 8000$

Figure A.70: RMS of streamwise direction (X) for one particular phase (phases decomposed) in cylinder-airfoil wake

Figures A.39a and A.39b present the RMS of velocity in the spanwise direction for cylinder-airfoil wake at two Reynolds numbers, respectively.

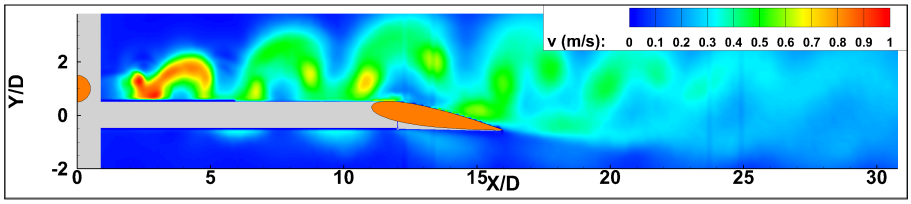

(a) $Re = 2000$

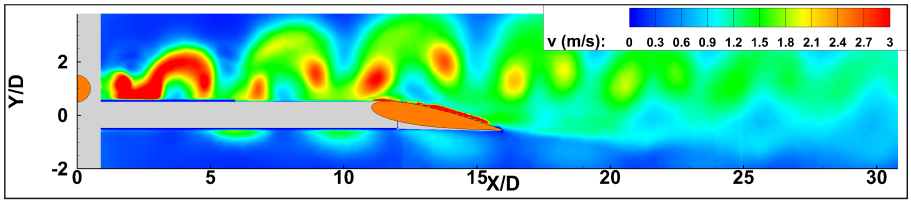

(b) $Re = 8000$

Figure A.71: RMS of spanwise direction (Y) for one particular phase (phase decomposed) in cylinder-airfoil wake

C.3.4 Decomposed total kinetic energy in phases

Figure A.72 shows the production term at low Reynolds number ($Re = 2000$) for four distinct phases ($\phi = 0°$, $100°$, $180°$ and $280°$) in cylinder-airfoil wake.

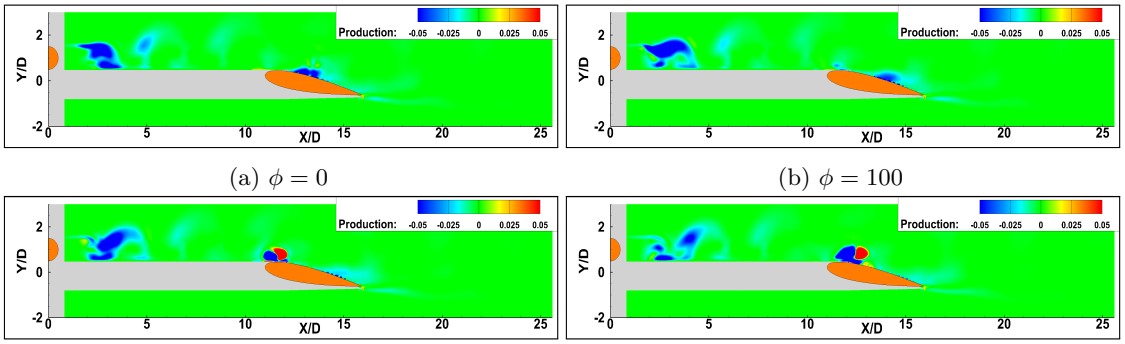

(a) $\phi = 0$ (b) $\phi = 100$

(c) $\phi = 180$ (d) $\phi = 280$

Figure A.72: Decomposed production by mean at $Re = 2000$ in cylinder wake

Figure A.73 shows the advection term at low Reynolds number ($Re = 2000$) for four distinct phases ($\phi = 0°$, $100°$, $180°$ and $280°$) in cylinder-airfoil wake.

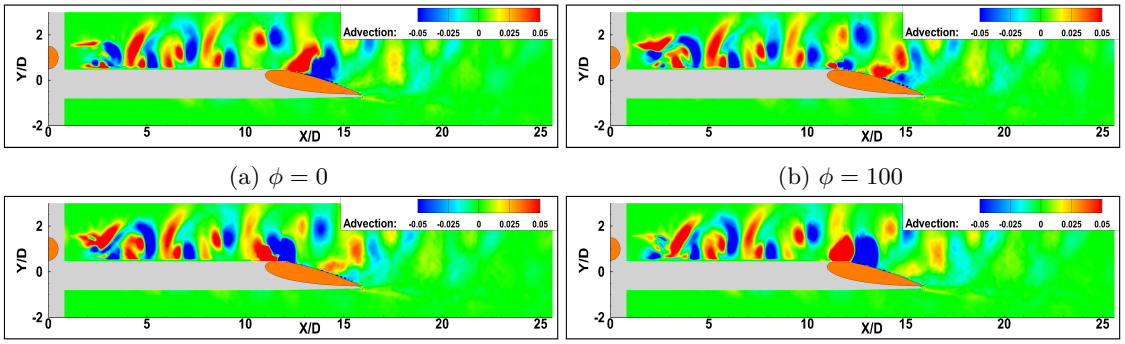

(a) $\phi = 0$ (b) $\phi = 100$

(c) $\phi = 180$ (d) Coherent structures at $\phi = 280$

Figure A.73: Decomposed advection at $Re = 2000$ in cylinder-airfoil wake

Figure A.74 shows the diffusion through turbulence term at low Reynolds number ($Re = 2000$) for four distinct phases ($\phi = 0°$, $100°$, $180°$ and $280°$) in cylinder-airfoil wake.

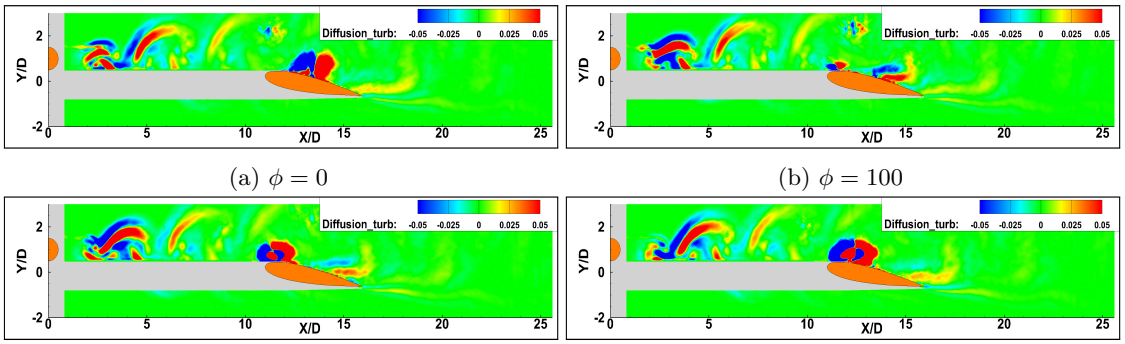

(a) $\phi = 0$ (b) $\phi = 100$

(c) $\phi = 180$ (d) $\phi = 280$

Figure A.74: Decomposed diffusion by turbulence at $Re = 2000$ in cylinder-airfoil wake

Figure A.75 shows the diffusion through pressure term at low Reynolds number ($Re = 2000$) for four distinct phases ($\phi = 0°$, $100°$, $180°$ and $280°$) in cylinder-airfoil wake.

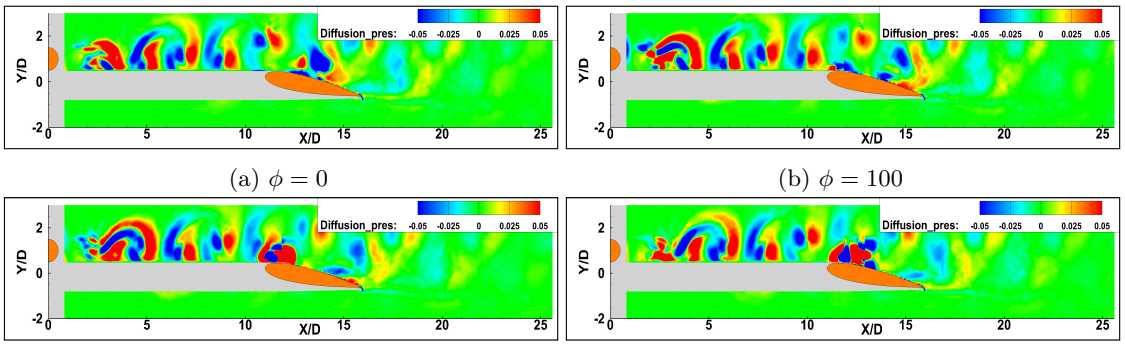

(a) $\phi = 0$ (b) $\phi = 100$

(c) $\phi = 180$ (d) $\phi = 280$

Figure A.75: Decomposed diffusion by pressure at $Re = 2000$ in cylinder-airfoil wake

Figure A.76 shows the dissipation term at low Reynolds number ($Re = 2000$) for four distinct phases ($\phi = 0°$, $100°$, $180°$ and $280°$) in cylinder-airfoil wake.

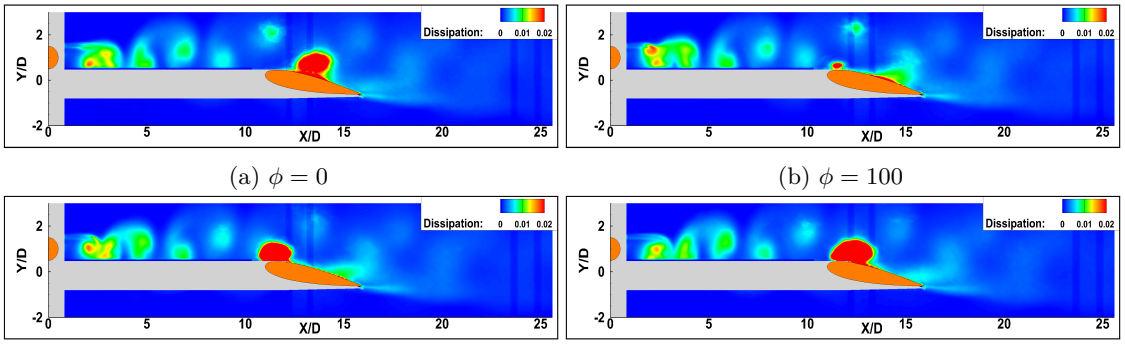

(a) $\phi = 0$ (b) $\phi = 100$

(c) $\phi = 180$ (d) $\phi = 280$

Figure A.76: Decomposed dissipation at $Re = 2000$ in cylinder-airfoil wake

C.3.5 CM energy exchange and interaction with RM

In this section, energy exchange between coherent motion, mean flow, and random motion resulting from their interactions are presented in cylinder-airfoil wake. Phases decomposition are based on coherent structures generated by upstream cylinder.

Low Reynolds number

Figures A.77a and A.77b show the production and dissipation of coherent motion for cylinder-airfoil wake at $Re = 2000$, respectively. In Figure A.77a, it can be observed that there is no production of coherent motion from the airfoil. This is due to the fact that phases decomposition is based on the upstream cylinder, and as such, coherent motion originating from the airfoil is not considered in this specific analysis. However, in Figure A.77b, the dissipation of coherent motion is observed to be maximum at the leading edge of the airfoil, although the magnitudes of this dissipation are relatively negligible.

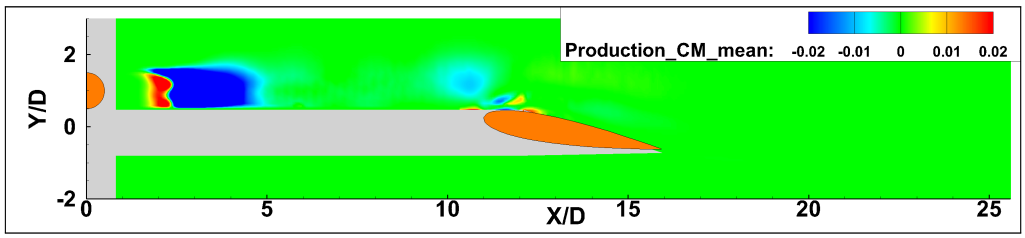

(a) CM production by mean

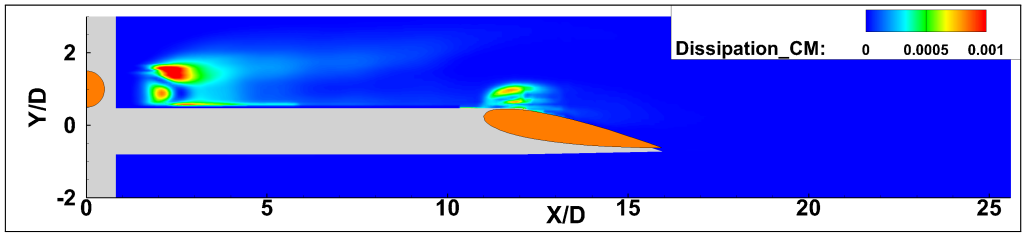

(b) CM dissipation

Figure A.77: Coherent motion (CM) production and dissipation $Re = 2000$ in cylinder-airfoil wake

Figure A.78 shows the transport and RM-interaction terms of coherent motion in cylinder-airfoil wake at $Re = 2000$. The transport (advection and diffusion) of coherent

motion (CM) originating from the upstream cylinder significantly decreases behind the downstream airfoil. However, some transport of coherent motion over the airfoil is still apparent, transported either by the mean flow or by diffusion.

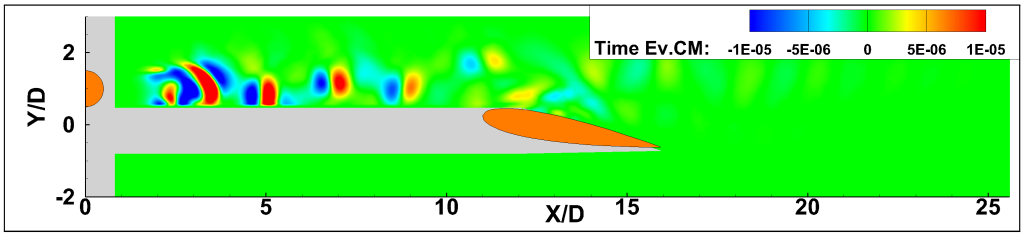

(a) CM time evolution in time

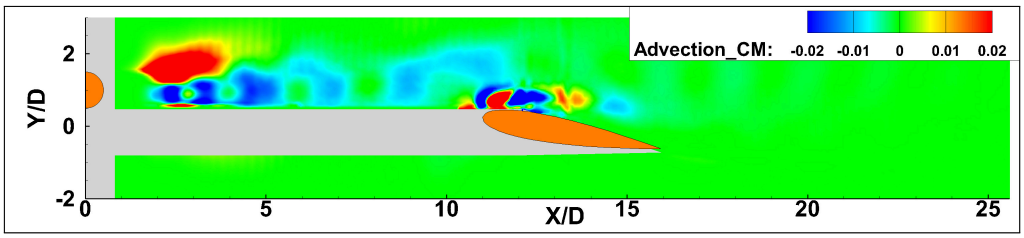

(b) CM advection by mean velocity

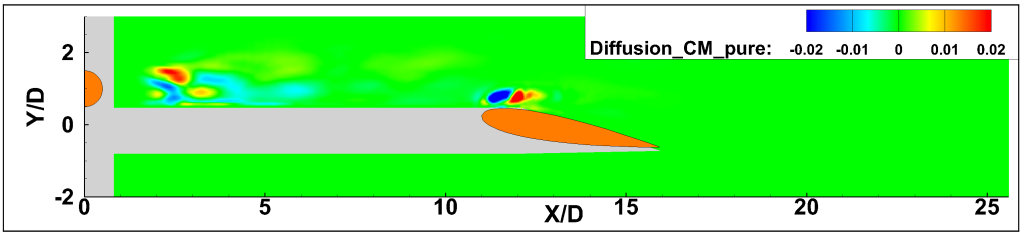

(c) CM pure diffusion

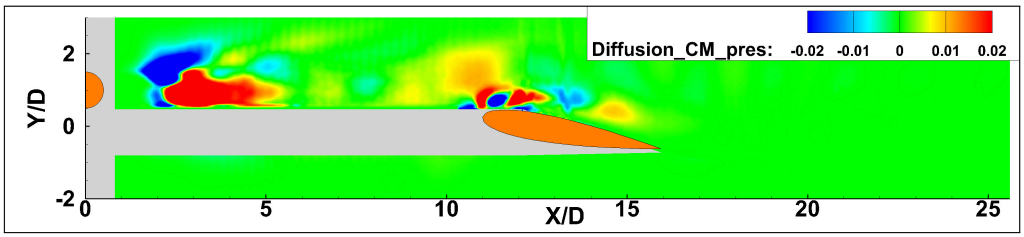

(d) CM diffusion by pressure

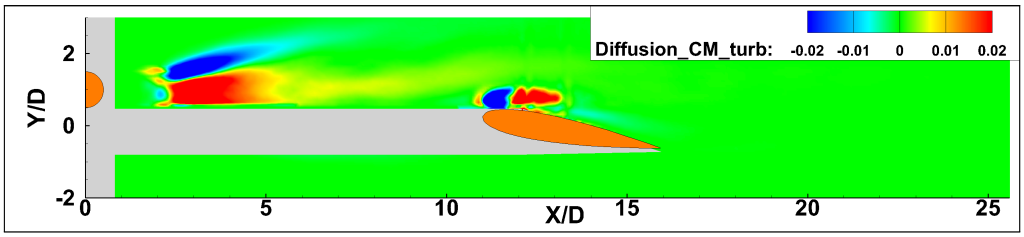

(e) CM diffusion by turbulence

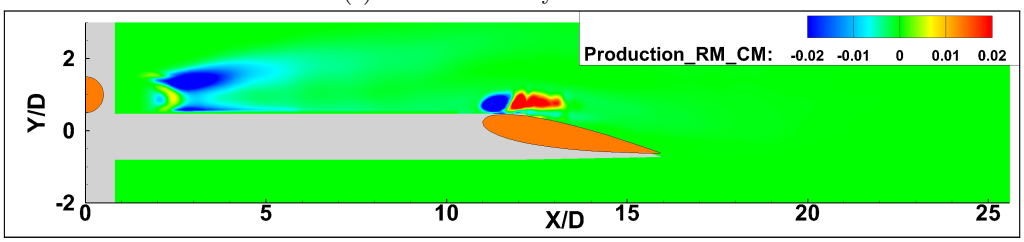

(f) RM production by CM

Figure A.78: Coherent motion (CM) transport and RM-interaction terms at $Re = 2000$ in cylindre-airfoil wake

High Reynolds number

Figures A.79a and A.79b show the production and dissipation of coherent motion for cylinder-airfoil wake at $Re = 8000$, respectively.

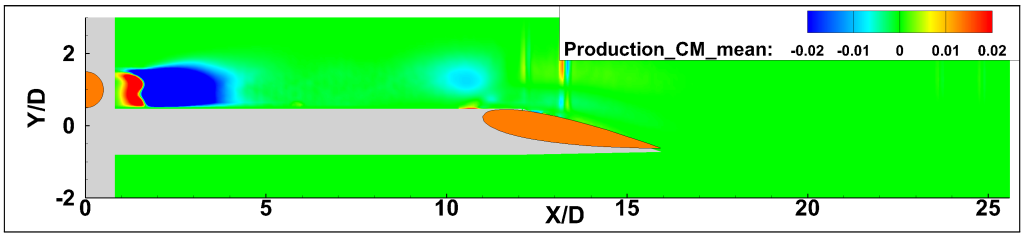

(a) CM production by mean

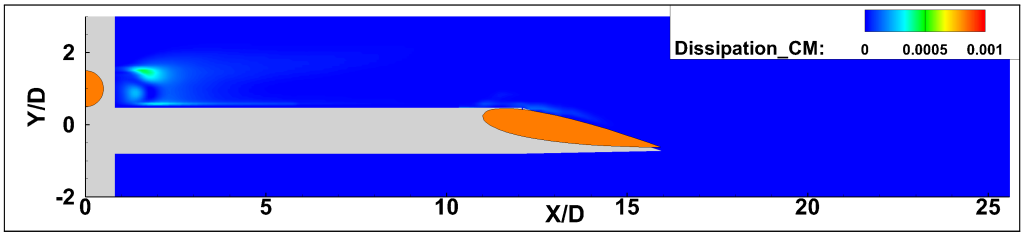

(b) CM dissipation

Figure A.79: Coherent motion (CM) production and dissipation at $Re = 8000$ in cylinder-airfoil wake

Figure A.80 shows the transport and RM-interaction terms of coherent motion in cylinder-airfoil wake at $Re = 8000$.

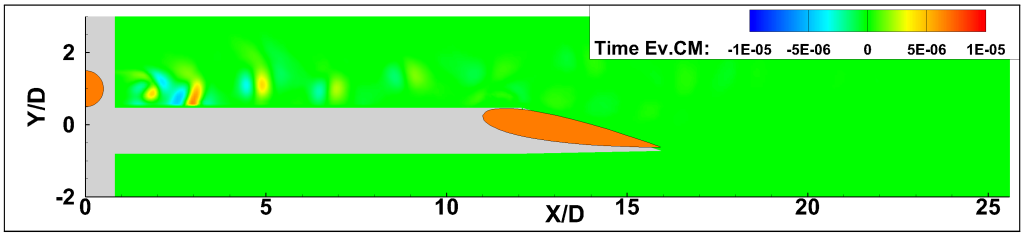

(a) CM time evolution in time

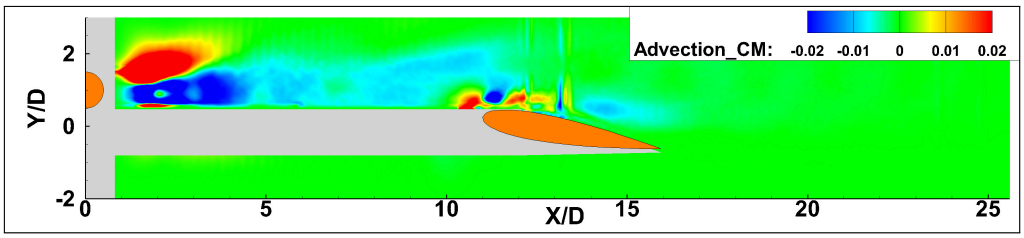

(b) CM advection by mean velocity

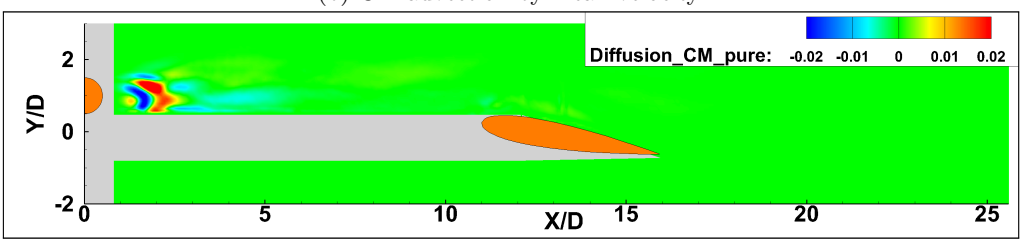

(c) CM pure diffusion

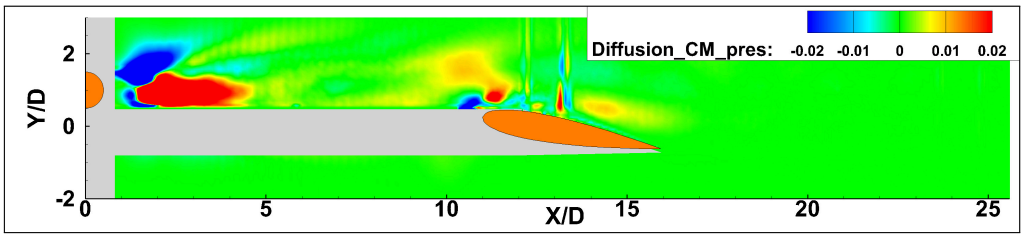

(d) CM diffusion by pressure

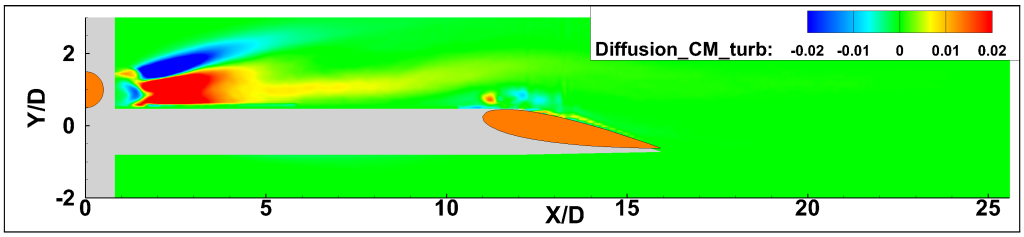

(e) CM diffusion by turbulence

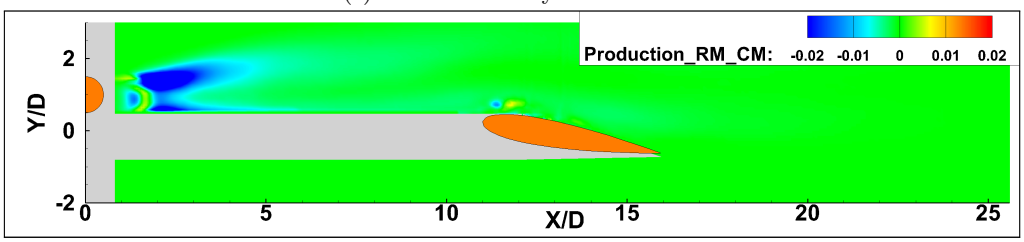

(f) RM production by CM

Figure A.80: Coherent motion (CM) transport and RM-interaction terms at $Re = 8000$ in cylinder-airfoil wake

C.3.6 RM energy exchange and interaction with CM

In this section, energy exchange between random motion, mean flow, and coherent motion resulting from their interactions in cylinder-airfoil wake are presented.

Low Reynolds number

Figures A.81a and A.81b show the production and dissipation of random motion for cylinder-airfoil wake at $Re = 2000$, respectively. One can observe in Figure A.81a significant production of random motion from the airfoil compared to what is seen in Figure A.77a. Furthermore, the dissipation displayed in Figure A.81b can not be ignored or neglected (same order of magnitude with other terms) when compared to the case of coherent motion, as seen in Figure A.77b.

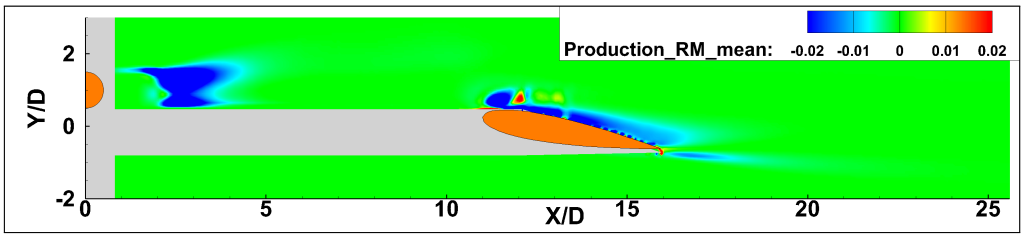

(a) RM production by mean

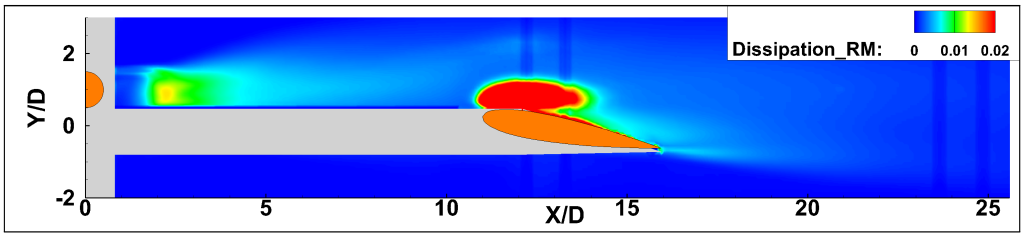

(b) RM dissipation

Figure A.81: Random motion (RM) production and dissipation at $Re = 2000$ in cylinder-airfoil wake

Figure A.82 shows the transport terms of random motion in cylinder-airfoil wake at $Re = 2000$.

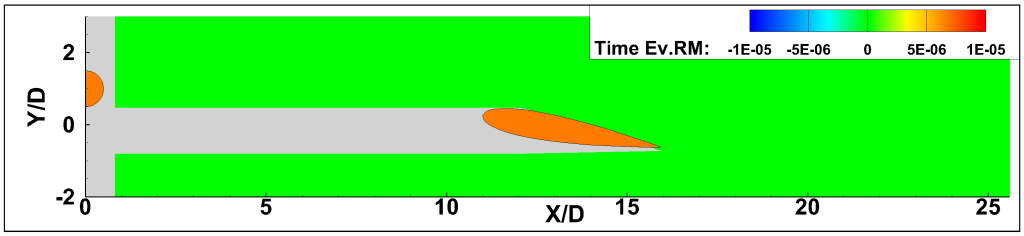

(a) RM time evolution

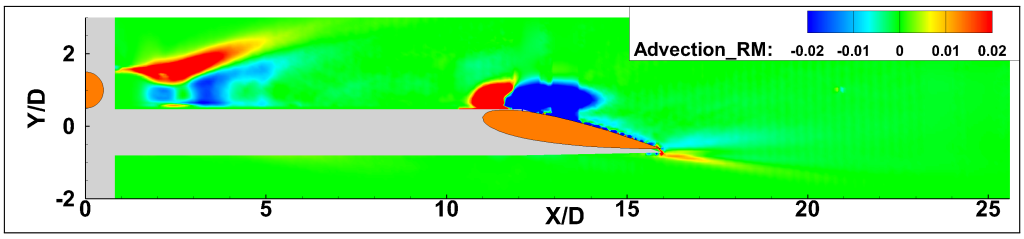

(b) RM advection by mean velocity

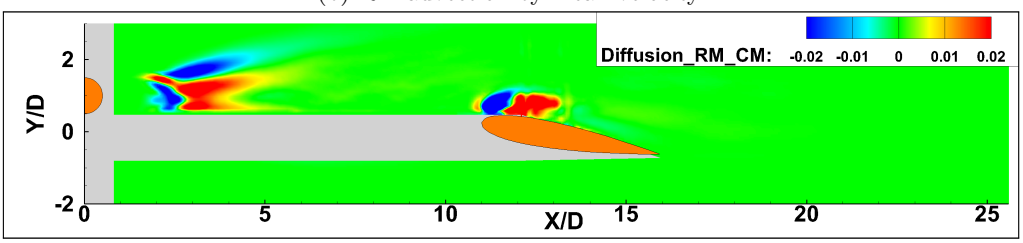

(c) RM diffusion by CM interaction

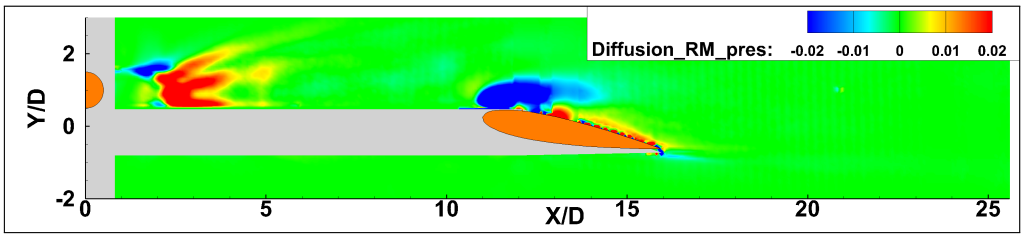

(d) RM diffusion by pressure

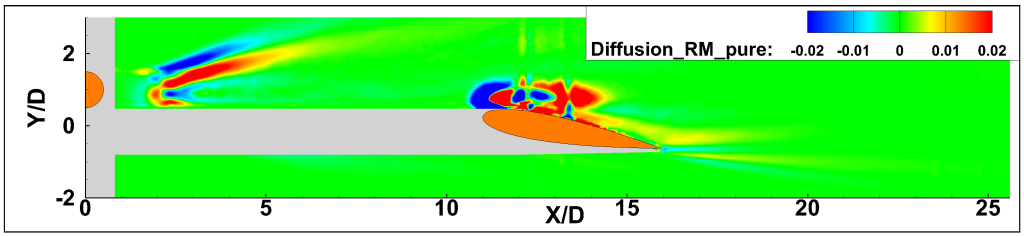

(e) RM pure diffusion

Figure A.82: Random motion (RM) transport terms in cylinder wake at $Re = 2000$ in cylinder-airfoil wake

High Reynolds number

Figures A.84a and A.84b show the production and dissipation of random motion for cylinder-airfoil wake at $Re = 8000$, respectively.

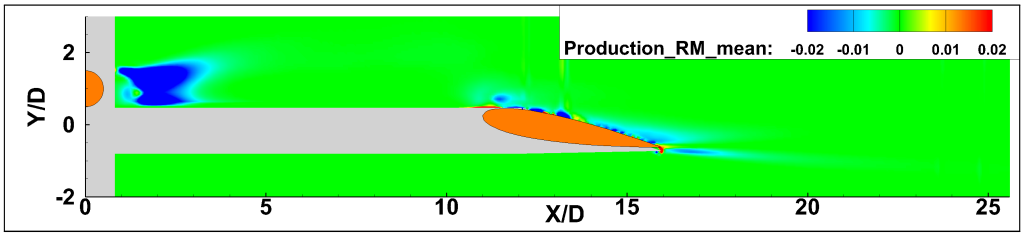

(a) RM production by mean

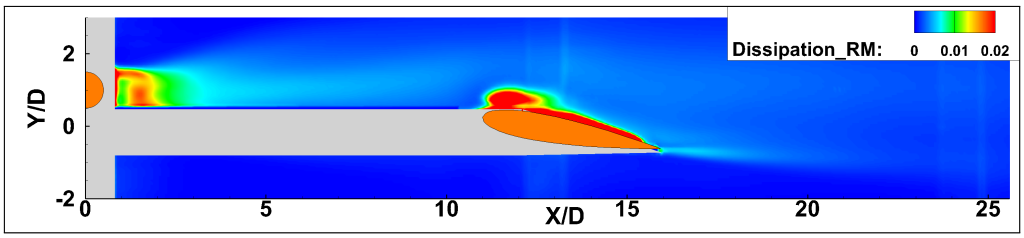

(b) RM dissipation

Figure A.83: Random motion (RM) production and dissipation terms in cylinder-airfoil wake at $Re = 8000$

Figure A.84 shows the transport terms of random motion in cylinder-airfoil wake at $Re = 8000$.

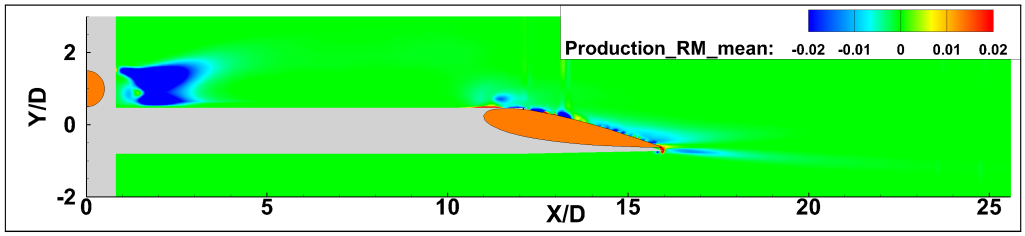

(a) RM production by mean

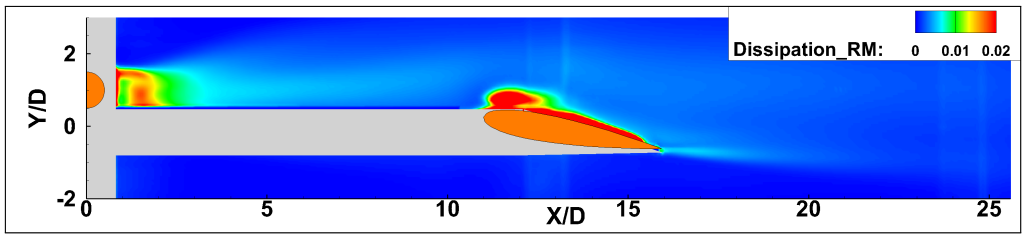

(b) RM dissipation

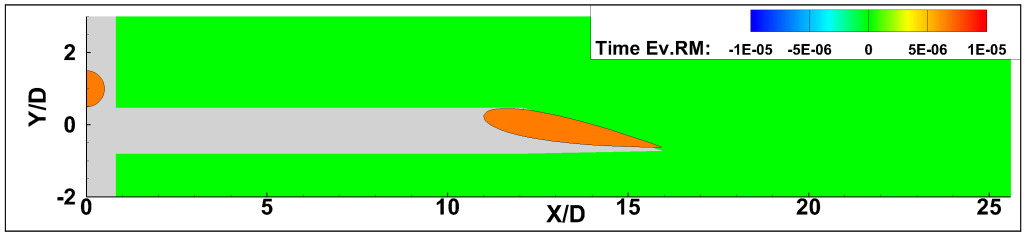

(c) RM time evolution

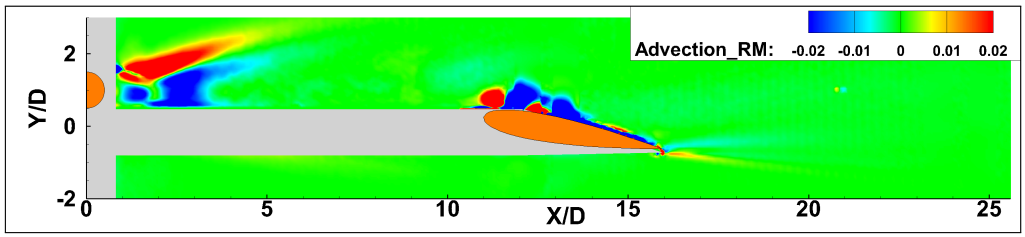

(d) RM advection by mean velocity

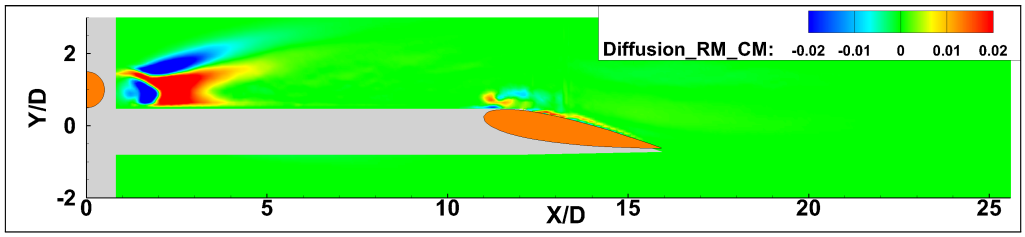

(e) RM diffusion by CM interaction

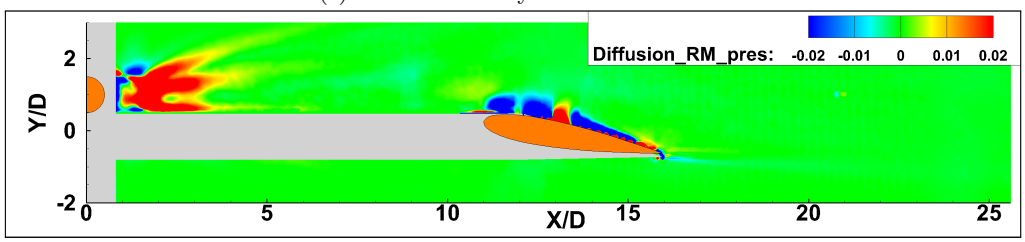

(f) RM diffusion by pressure

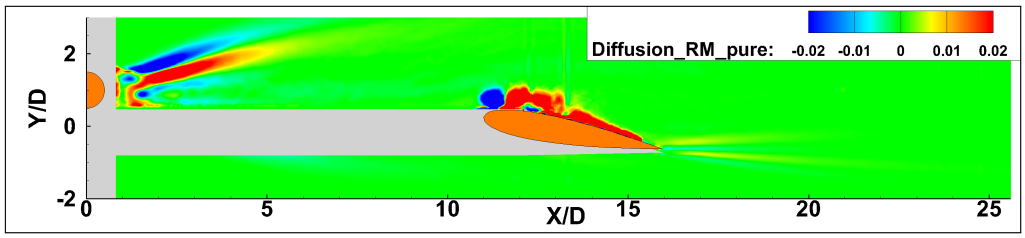

(g) RM pure diffusion

Figure A.84: Random motion (RM) transport terms in cylinder-airfoil wake at $Re = 8000$

D.4 Single airfoil configuration

D.4.1 First order statistics

Figures A.85a and A.85b present the mean velocity in streamwise (X) and spanwise (Y) directions in single airfoil wake at two Reynolds numbers.

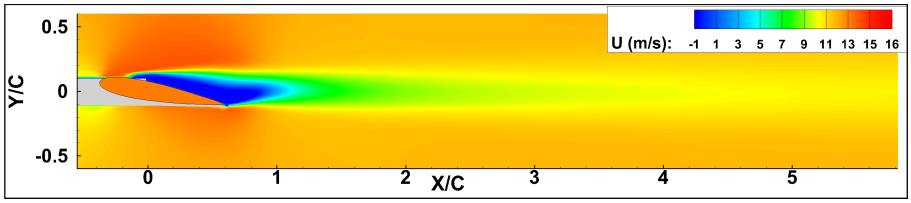

(a) Streamwise (X direction) mean velocities in airfoil wake

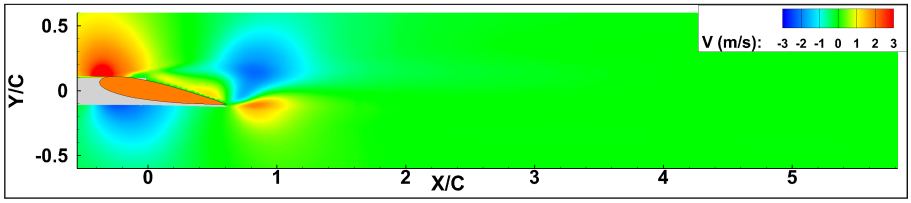

(b) Spanwisewise (Y direction) mean velocities in airfoil wake

Figure A.85: Mean velocities in airfoil wake at high Reynolds number $Re = 8000$

Figures A.86a and A.86b present the RMS of velocity in streamwise (X) and spanwise (Y) directions in single airfoil wake at two Reynolds numbers.

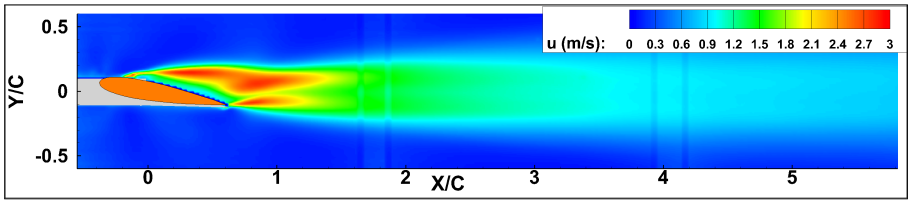

(a) Streamwise (X direction) RMS in airfoil wake

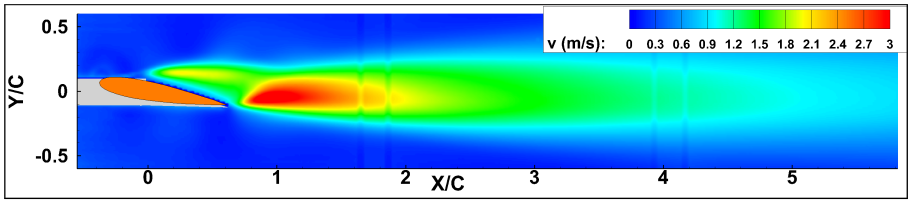

(b) Spanwise (y direction) RMS in airfoil wake

Figure A.86: RMS of velocities (Y direction) in airfoil wake at high Reynolds number $Re = 8000$

D.4.2 Total fluctuations energy exchange

Figure A.87 shows production, transport and dissipation terms of total fluctuations single airfoil wake at $Re = 8000$.

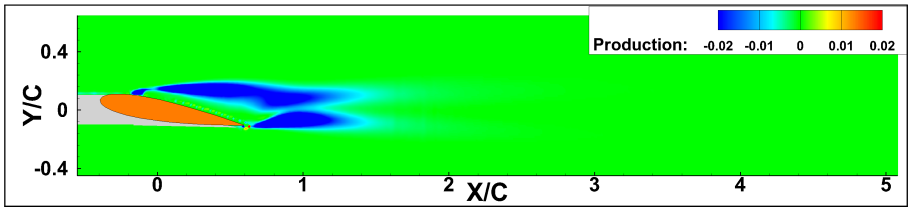

(a) Production of total turbulent kinetic energy by mean velocity in airfoil wake.

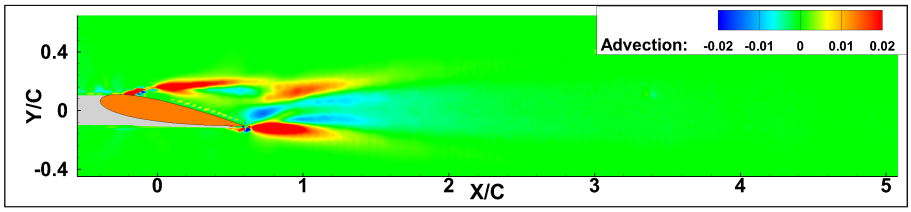

(b) Advection of total turbulent turbulent kinetic energy by streamwise velocity (X direction) in airfoil wake.

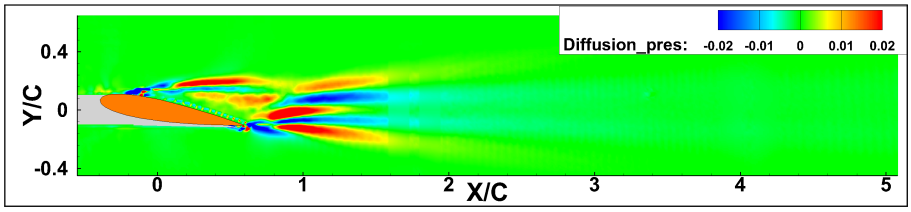

(c) Diffusion of total turbulent kinetic energy by pressure in airfoil wake.

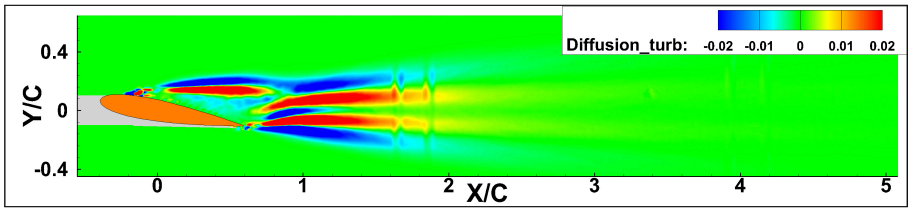

(d) Diffusion of total turbulent kinetic energy by turbulence in airfoil wake.

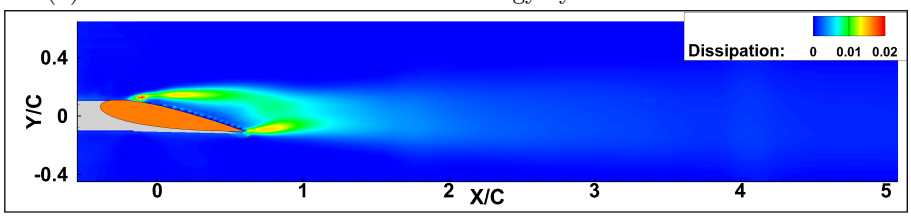

(e) Dissipation of total turbulent kinetic energy in airfoil wake.

Figure A.87: Total kinetic energy of turbulence in airfoil wake at $Re = 8000$. Terms are normalised by D/U_0^3

D.4.3 Decomposed first order statistics

Figures A.88a and A.88b present the RMS of velocity in streamwise (X) direction in single airfoil wake at two Reynolds numbers.

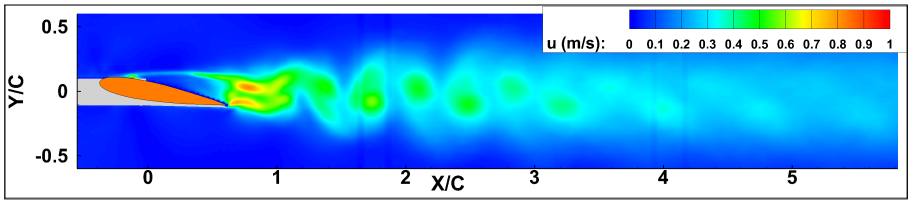

(a) $Re = 2000$

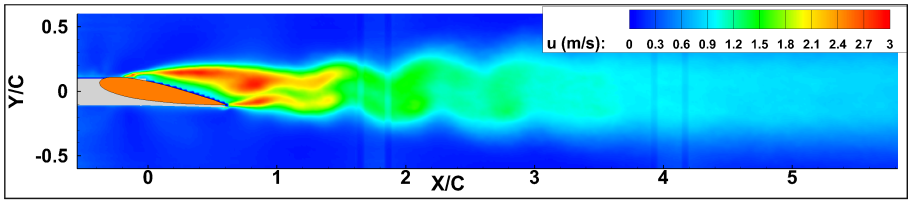

(b) $Re = 8000$

Figure A.88: RMS of streamwise direction (X) for one particular phase (phases decomposed) in single airfoil wake

Figures A.89a and A.89b present the RMS of velocity in spanwise (Y) direction in airfoil wake at two Reynolds numbers.

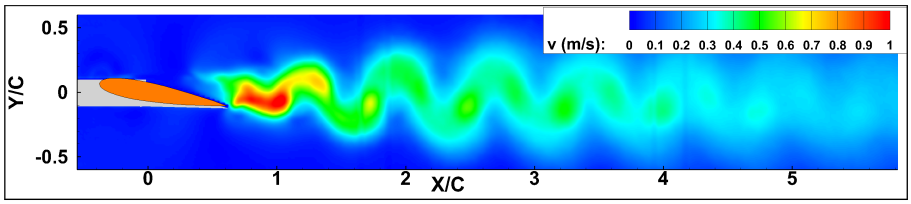

(a) $Re = 2000$

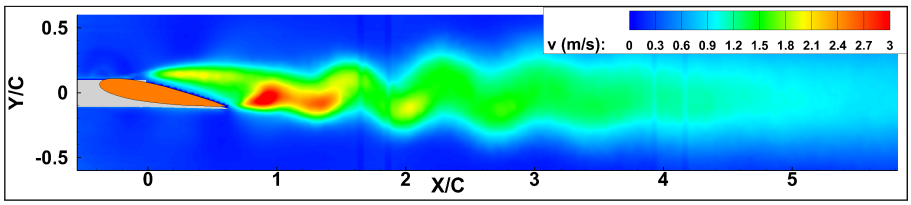

(b) $Re = 8000$

Figure A.89: RMS of spanwise direction (Y) for one particular phase (phase decomposed) in airfoil wake

D.4.4 Decomposed total kinetic energy in phases

Figure A.90 shows the production term at low Reynolds number ($Re = 2000$) for four distinct phases ($\phi = 0°$, $100°$, $180°$ and $280°$) in single airfoil wake.

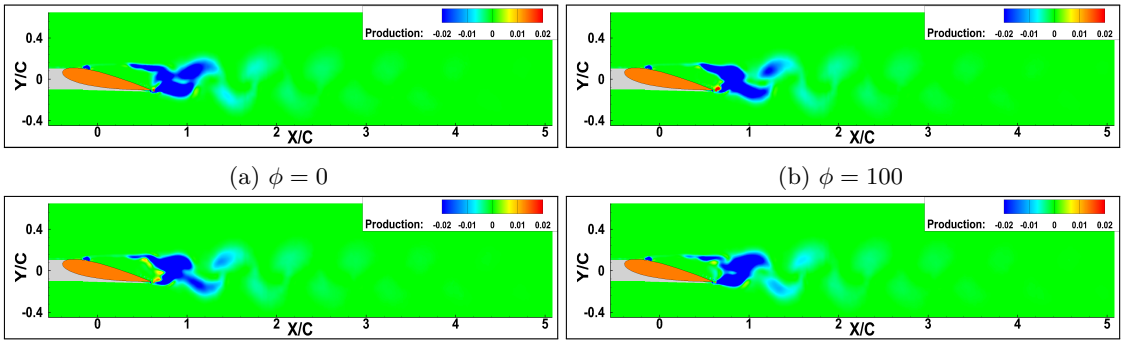

(a) $\phi = 0$ (b) $\phi = 100$

(c) $\phi = 180$ (d) $\phi = 280$

Figure A.90: Decomposed production by mean at $Re = 2000$ in airfoil wake

Figure A.91 shows the advection term at low Reynolds number ($Re = 2000$) for four distinct phases ($\phi = 0°$, $100°$, $180°$ and $280°$) in single airfoil wake.

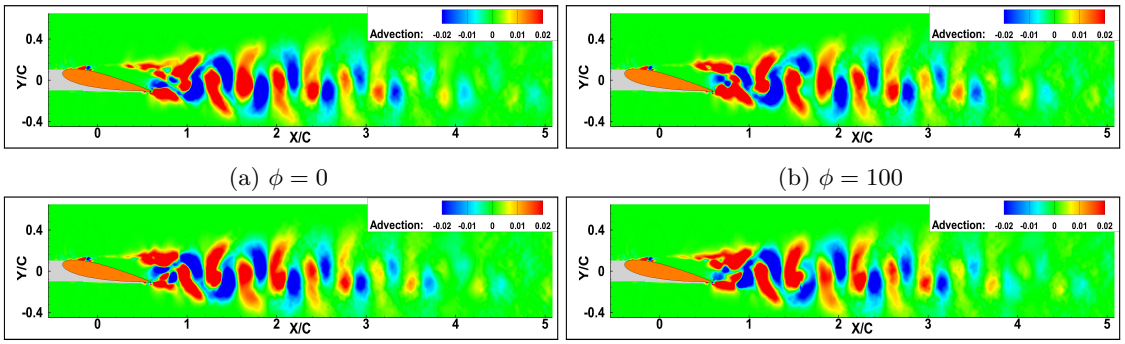

(a) $\phi = 0$ (b) $\phi = 100$

(c) $\phi = 180$ (d) Coherent structures at $\phi = 280$

Figure A.91: Decomposed advection at $Re = 2000$ in airfoil wake

Figure A.92 shows the diffusion through turbulence term at low Reynolds number ($Re = 2000$) for four distinct phases ($\phi = 0°$, $100°$, $180°$ and $280°$) in single airfoil wake.

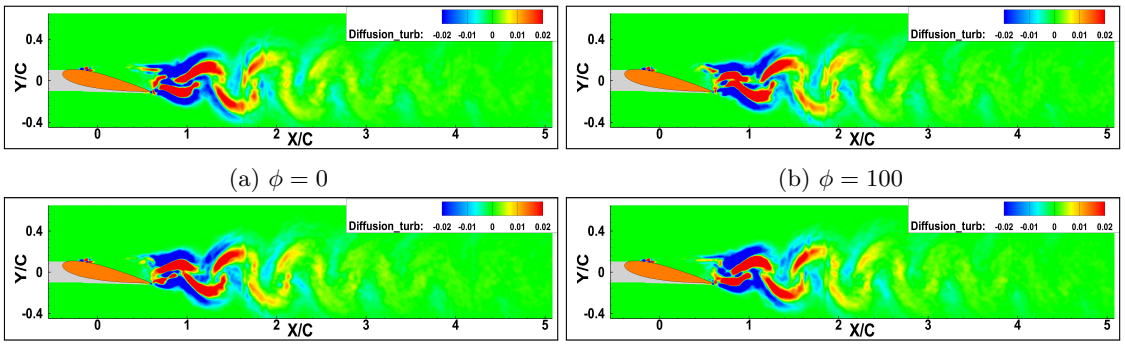

(a) $\phi = 0$ (b) $\phi = 100$

(c) $\phi = 180$ (d) $\phi = 280$

Figure A.92: Decomposed diffusion by turbulence at $Re = 2000$ in airfoil wake

Figure A.93 shows the diffusion through pressure term at low Reynolds number ($Re = 2000$) for four distinct phases ($\phi = 0°$, $100°$, $180°$ and $280°$) in single airfoil wake.

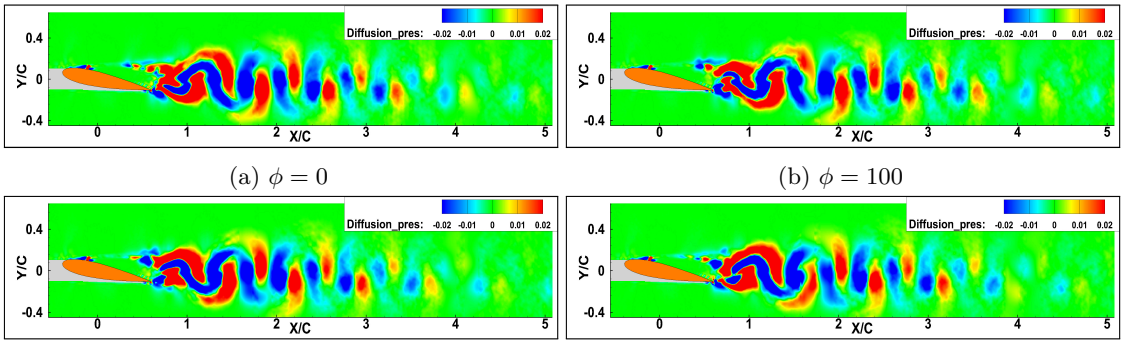

(a) $\phi = 0$ (b) $\phi = 100$

(c) $\phi = 180$ (d) $\phi = 280$

Figure A.93: Decomposed diffusion by pressure at $Re = 2000$ in airfoil wake

Figure A.94 shows the dissipation term at low Reynolds number ($Re = 2000$) for four distinct phases ($\phi = 0°$, $100°$, $180°$ and $280°$) in single airfoil wake.

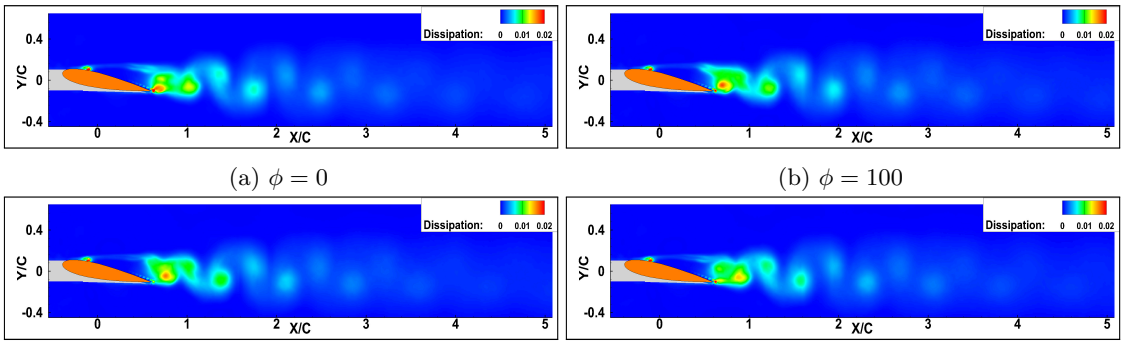

(a) $\phi = 0$ (b) $\phi = 100$

(c) $\phi = 180$ (d) $\phi = 280$

Figure A.94: Decomposed dissipation at $Re = 2000$ in airfoil wake

D.4.5 CM energy exchange and interaction with RM

In this section, energy exchange between coherent motion, mean flow, and random motion resulting from their interactions are presented in single airfoil wake. Results are reported for high Reynolds number, low Reynolds number are shown in chapter 5.

High Reynolds number

Figures A.95a and A.95b show the production and dissipation of coherent motion for single airfoil wake at $Re = 8000$, respectively.

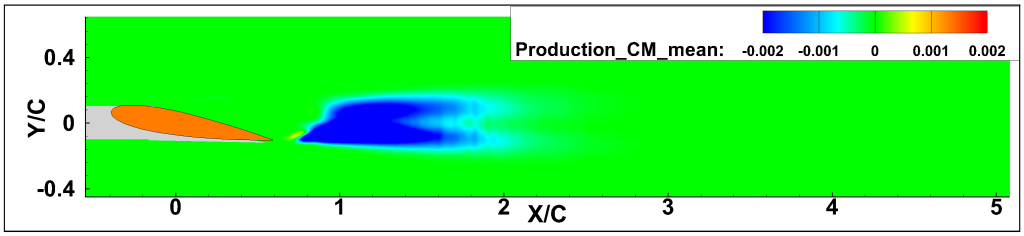

(a) CM production by mean

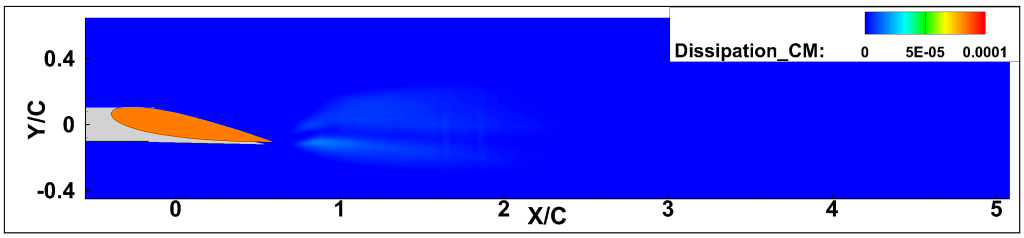

(b) CM dissipation

Figure A.95: Coherent motion (CM) production and dissipation at $Re = 8000$ in airfoil wake

Figure A.96 shows the transport and RM-interaction terms of coherent motion in single airfoil wake at $Re = 8000$.

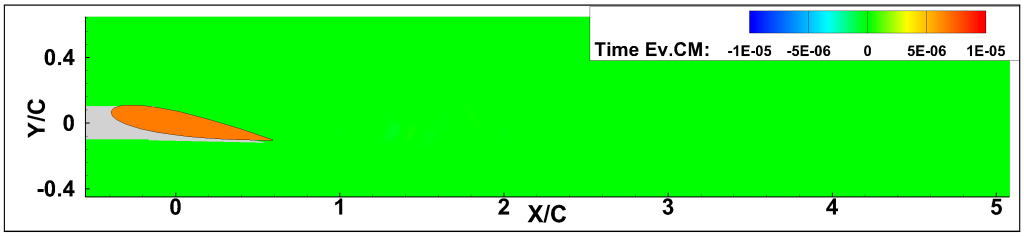

(a) CM time evolution in time

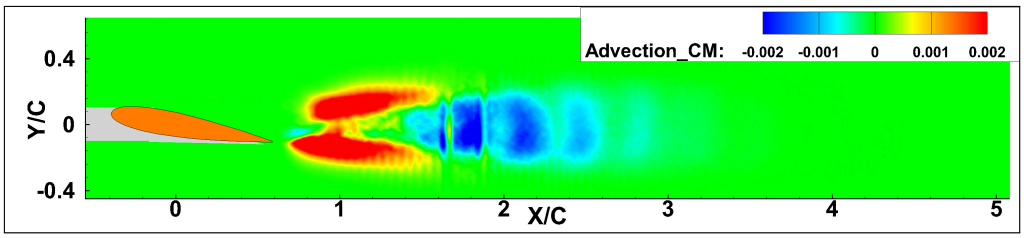

(b) CM advection by mean velocity

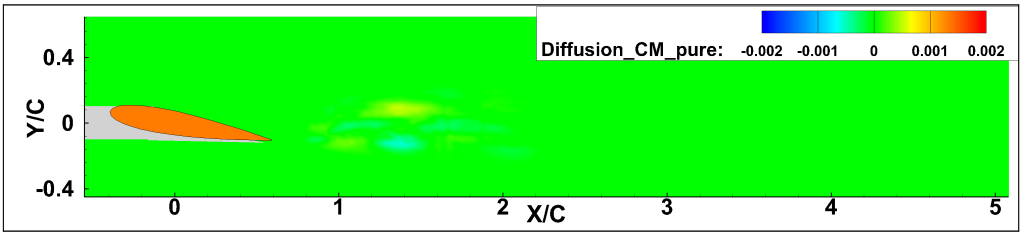

(c) CM pure diffusion

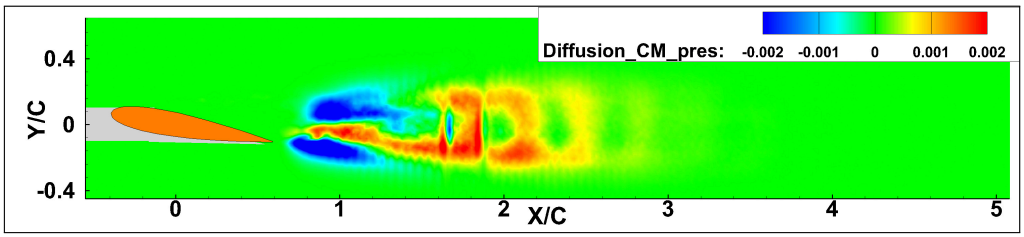

(d) CM diffusion by pressure

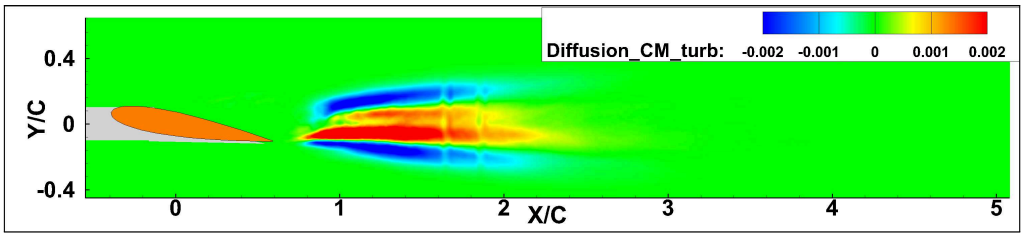

(e) CM diffusion by turbulence

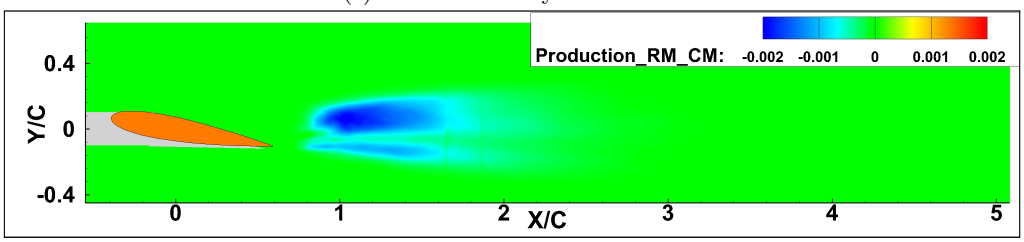

(f) RM production by CM

Figure A.96: Coherent motion (CM) transports at $Re = 8000$ in airfoil wake

D.4.6 RM energy exchange and interaction with CM

In this section, energy exchange between random motion, mean flow, and coherent motion resulting from their interactions in airfoil wake are presented.

High Reynolds number

Figures A.95a and A.95b show the production and dissipation of random motion for single airfoil wake at $Re = 8000$, respectively.

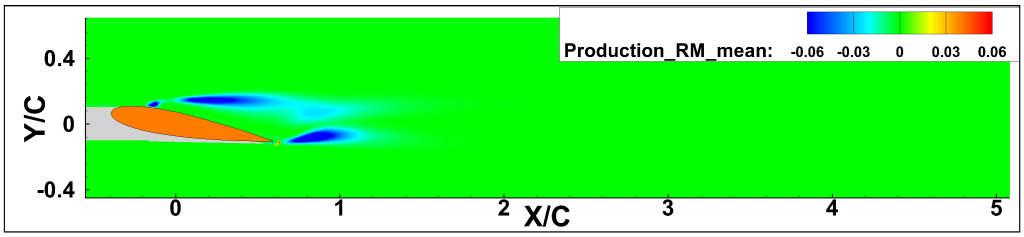

(a) RM production by mean

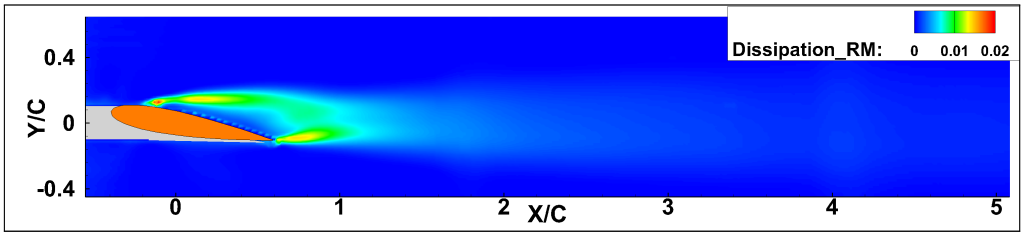

(b) RM dissipation

Figure A.97: Random motion (RM) production and dissipation terms in airfoil wake at $Re = 8000$

Figure A.98 shows the transport terms of random motion in single airfoil wake at $Re = 8000$.

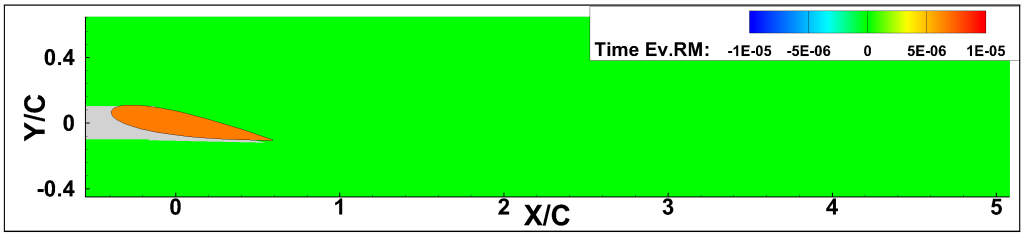

(a) RM time evolution

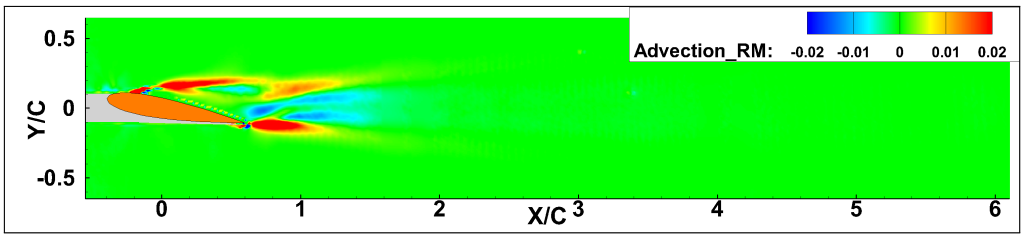

(b) RM advection by mean velocity

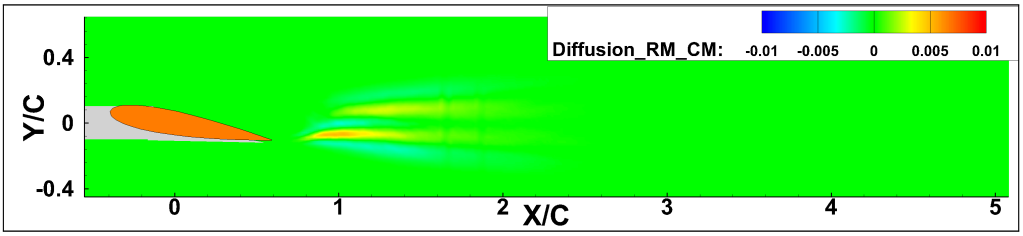

(c) RM diffusion by CM interaction

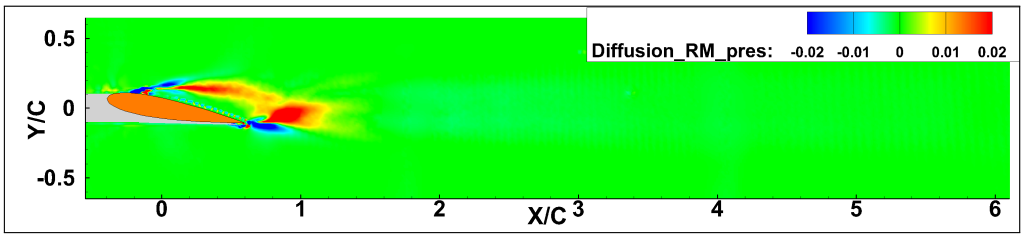

(d) RM diffusion by pressure

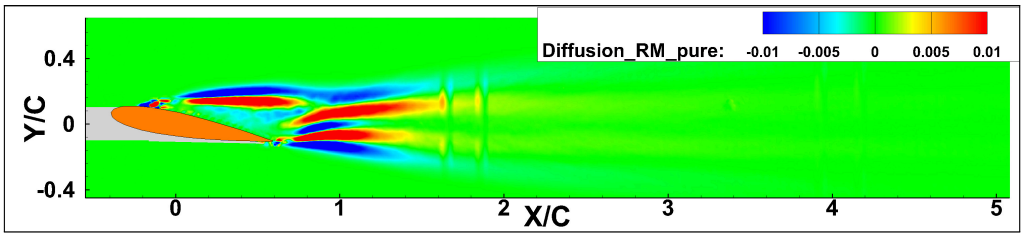

(e) RM pure diffusion

Figure A.98: Random motion (RM) transport terms in airfoil wake at $Re = 8000$

E.5 Double airfoil configuration

E.5.1 First order statistics

Figures A.99a and A.99b present the mean velocity in streamwise (X) and spanwise (Y) directions for double airfoil wake at two Reynolds numbers.

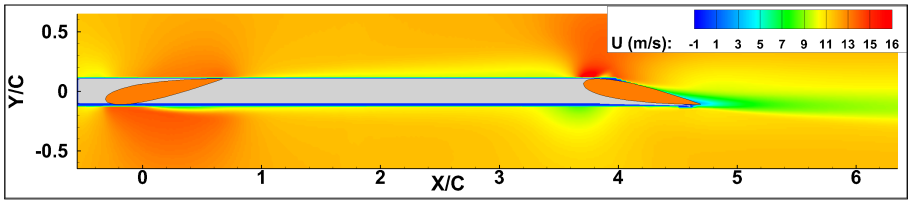

(a) Streamwise (X direction) mean velocities in double airfoil wake

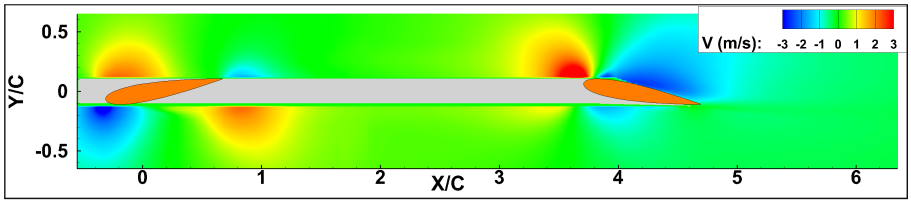

(b) Spanwisewise (Y direction) mean velocities in double airfoil wake

Figure A.99: Mean velocities in double airfoil wake at high Reynolds number $Re = 8000$

Figures A.100a and A.100b present the RMS of velocity in streamwise (X) and spanwise (Y) directions for double airfoil wake at two Reynolds numbers.

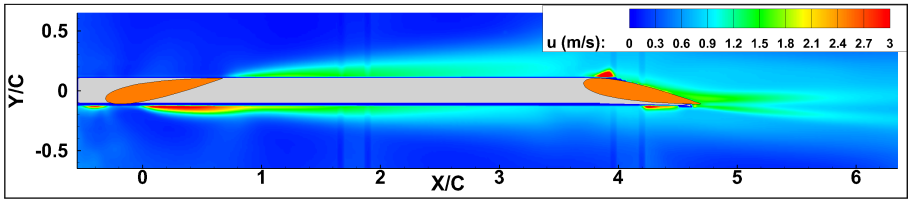

(a) Streamwise (X direction) RMS in double airfoil wake

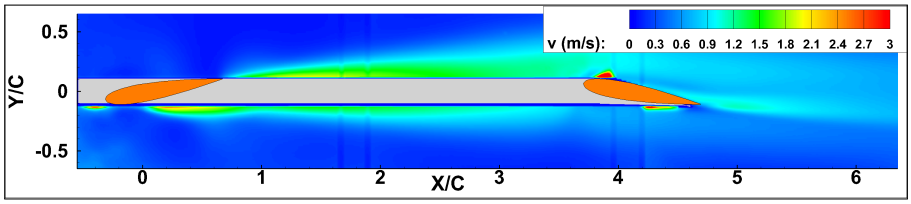

(b) Spanwise (Y direction) RMS in double airfoil wake

Figure A.100: RMS of velocities (y direction) in double airfoil wake at high Reynolds number $Re = 8000$

E.5.2 Total fluctuations energy exchange

Figure A.101 shows production, transport and dissipation terms of total fluctuations double airfoil wake at $Re = 8000$.

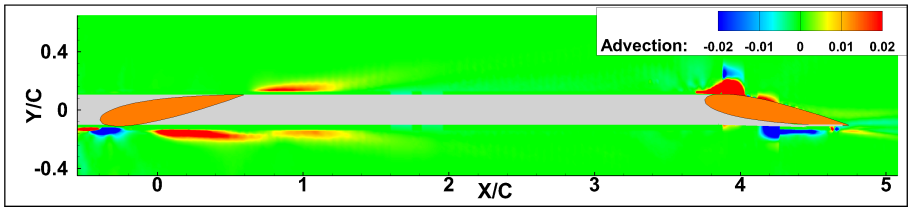

(a) Advection of total turbulent turbulent kinetic energy by mean velocity in double airfoil wake.

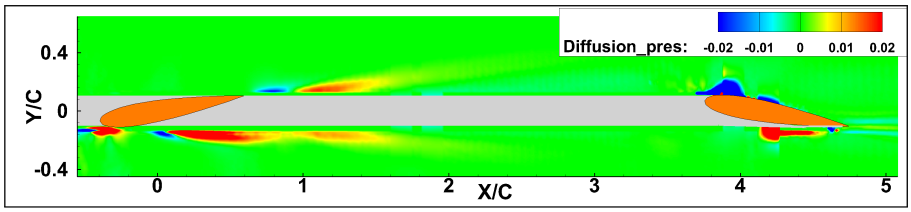

(b) Diffusion of total turbulent kinetic energy by pressure in double airfoil wake.

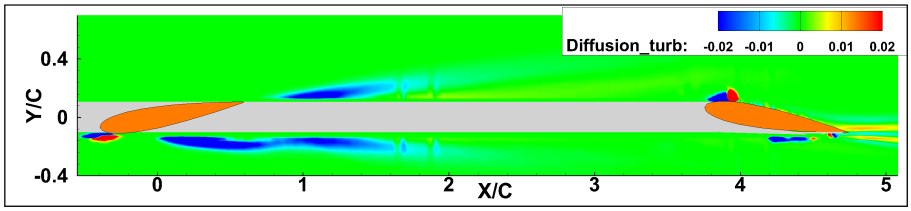

(c) Diffusion of total turbulent kinetic energy by turbulence in double airfoil wake.

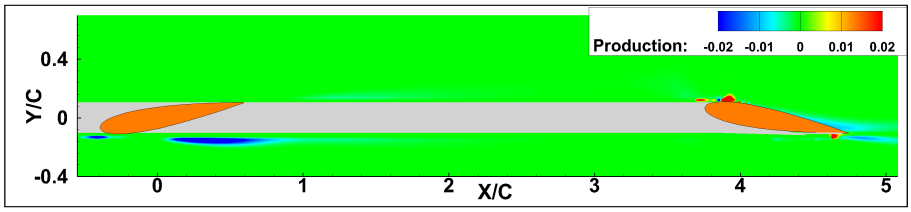

(d) Production of total turbulent kinetic energy by mean velocity in double airfoil wake.

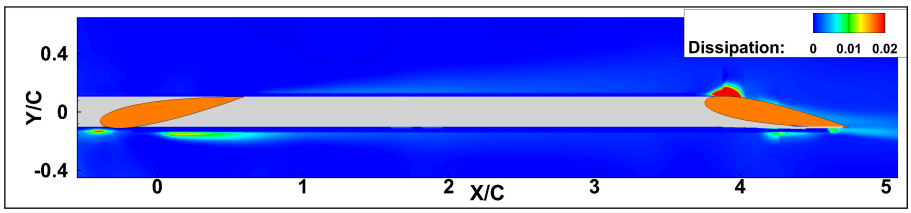

(e) Dissipation of total turbulent kinetic energy in double airfoil wake.

Figure A.101: Total kinetic energy of turbulence in double airfoil wake at $Re = 8000$. Terms are normalised by D/U_0^3

E.5.3 Decomposed first order statistics

Figures A.102a and A.102b present the RMS of velocity in streamwise (x) direction in double airfoil wake at two Reynolds numbers.

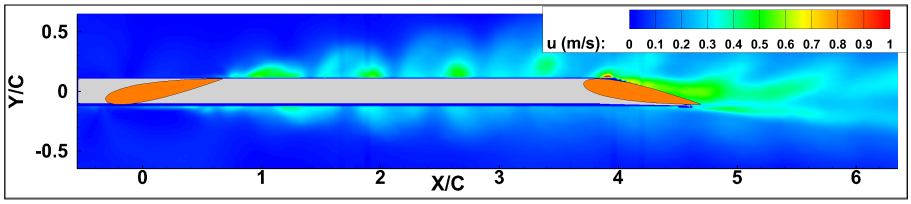

(a) $Re = 2000$

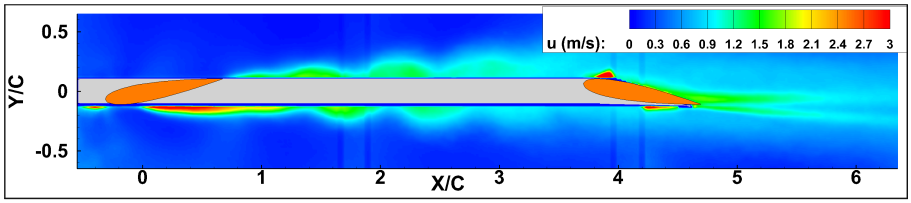

(b) $Re = 8000$

Figure A.102: RMS of streamwise direction (X) for one particular phase (phases decomposed) in double airfoil wake

Figures A.103a and A.103b present the RMS of velocity in spanwise (Y) direction in double airfoil wake at two Reynolds numbers.

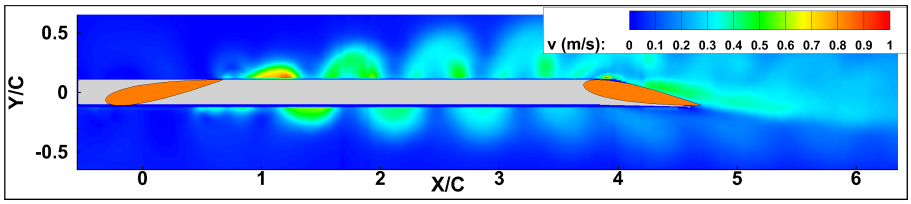

(a) $Re = 2000$

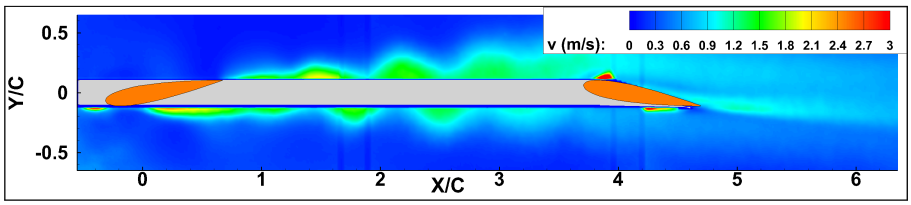

(b) $Re = 8000$

Figure A.103: RMS of spanwise direction (Y) for one particular phase (phase decomposed) in double airfoil wake

E.5.4 Decomposed total fluctuations

Figure A.104 shows the production term at low Reynolds number ($Re = 2000$) for four distinct phases ($\phi = 0°$, $100°$, $180°$ and $280°$) in double airfoil wake.

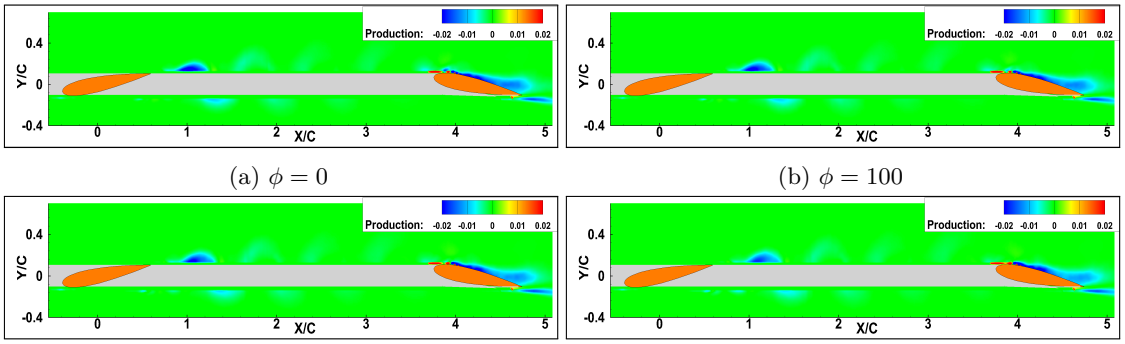

(a) $\phi = 0$ (b) $\phi = 100$

(c) $\phi = 180$ (d) $\phi = 280$

Figure A.104: Decomposed production by mean at $Re = 2000$ in double airfoil wake

Figure A.105 shows the advection term at low Reynolds number ($Re = 2000$) for four distinct phases ($\phi = 0°$, $100°$, $180°$ and $280°$) in double airfoil wake.

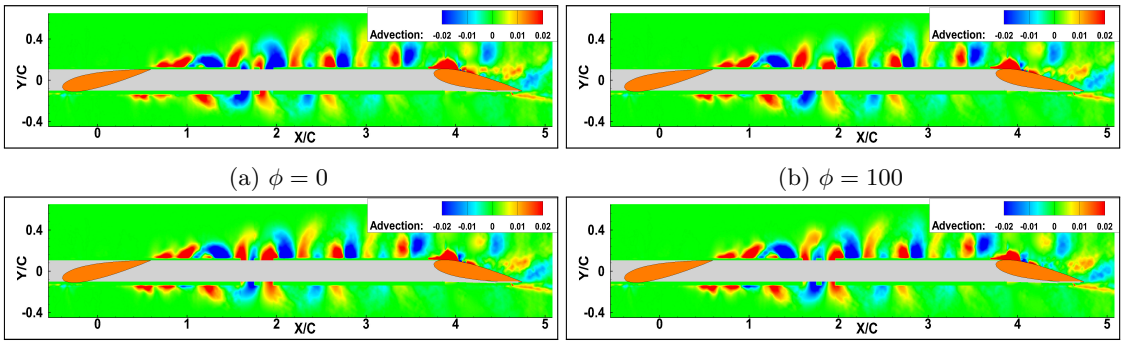

(a) $\phi = 0$ (b) $\phi = 100$

(c) $\phi = 180$ (d) Coherent structures at $\phi = 280$

Figure A.105: Decomposed advection at $Re = 2000$ in double airfoil wake

Figure A.106 shows the diffusion through turbulence term at low Reynolds number ($Re = 2000$) for four distinct phases ($\phi = 0°$, $100°$, $180°$ and $280°$) in double airfoil wake.

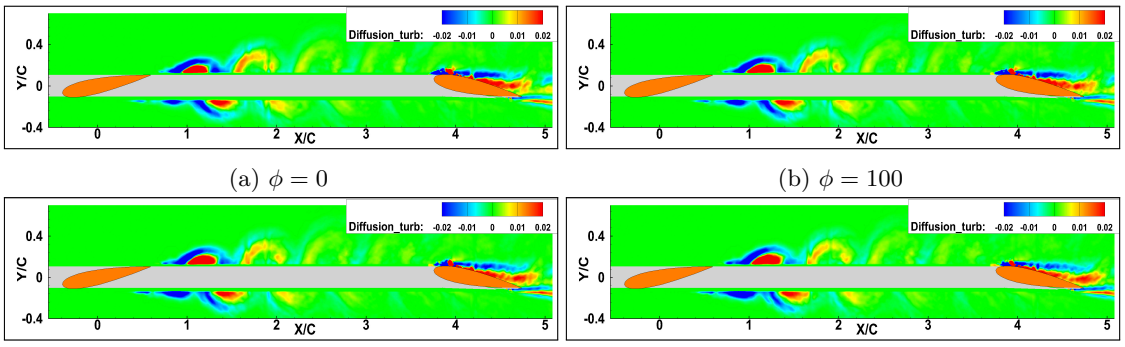

(a) $\phi = 0$ (b) $\phi = 100$

(c) $\phi = 180$ (d) $\phi = 280$

Figure A.106: Decomposed diffusion by turbulence at $Re = 2000$ in double airfoil wake

Figure A.107 shows the diffusion through pressure term at low Reynolds number ($Re = 2000$) for four distinct phases ($\phi = 0°$, $100°$, $180°$ and $280°$) in double airfoil wake.

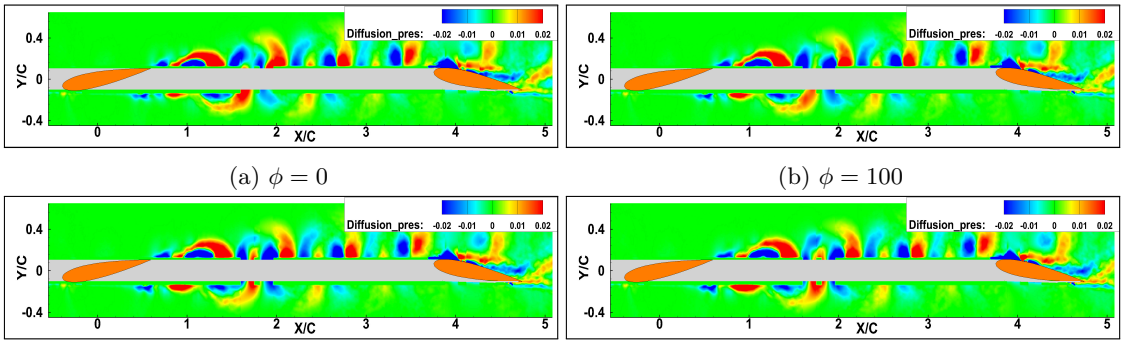

(a) $\phi = 0$ (b) $\phi = 100$

(c) $\phi = 180$ (d) $\phi = 280$

Figure A.107: Decomposed diffusion by pressure at $Re = 2000$ in double airfoil wake

Figure A.108 shows the dissipation term at low Reynolds number ($Re = 2000$) for four distinct phases ($\phi = 0°$, $100°$, $180°$ and $280°$) in double airfoil wake.

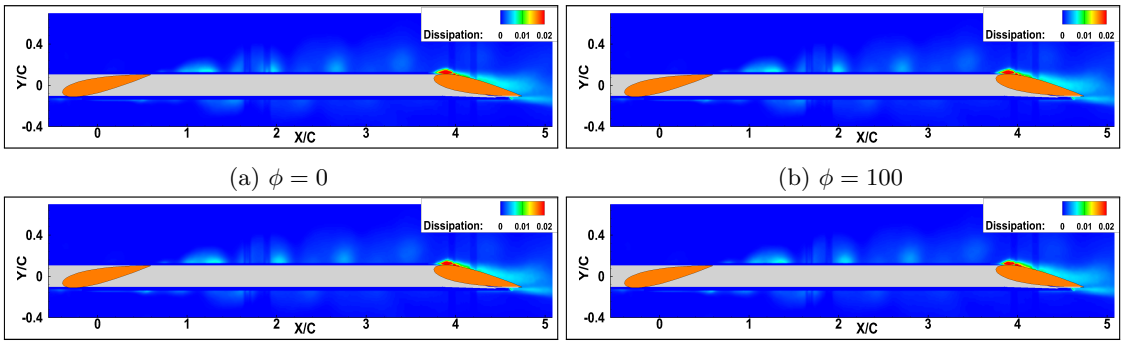

(a) $\phi = 0$ (b) $\phi = 100$

(c) $\phi = 180$ (d) $\phi = 280$

Figure A.108: Decomposed dissipation at $Re = 2000$ in double airfoil wake

E.5.5 CM energy exchange and interaction with RM

In this section, energy exchange between coherent motion, mean flow, and random motion resulting from their interactions are presented in double airfoil wake. Results are reported for high Reynolds number, low Reynolds number are shown in chapter 5. Phases decomposition of coherent structures are based on upstream airfoil.

High Reynolds number

Figures A.109a and A.109b show the production and dissipation of coherent motion for double airfoil wake at $Re = 8000$, respectively.

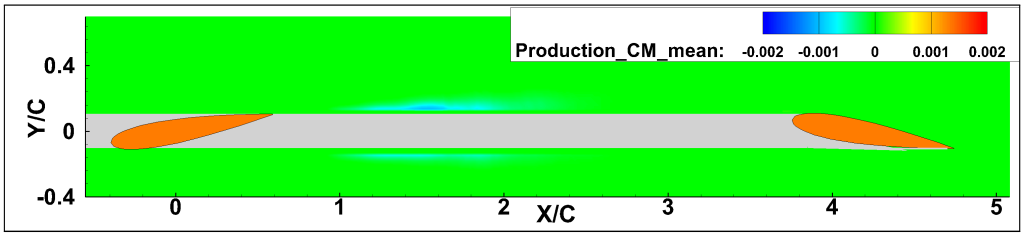

(a) CM production by mean

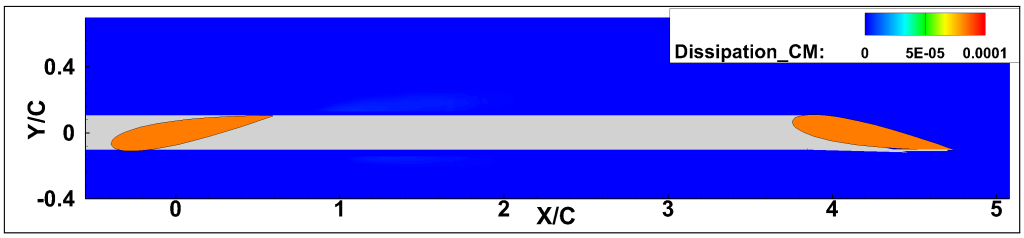

(b) CM dissipation

Figure A.109: Coherent motion (CM) production and dissipation at $Re = 8000$ in 2 airfoils wake

Figure A.110 shows the transport and RM-interaction terms of coherent motion in double airfoil wake at $Re = 8000$.

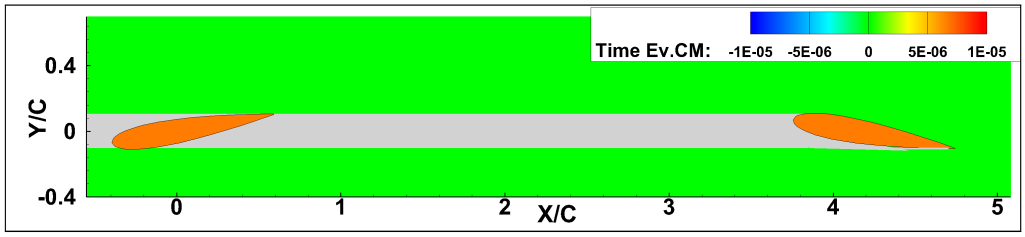

(a) CM time evolution in time

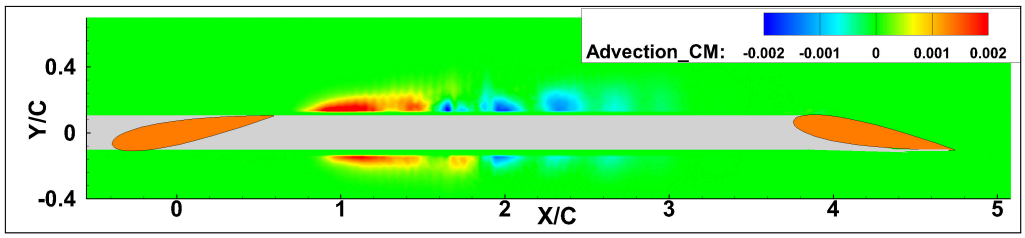

(b) CM advection by mean velocity

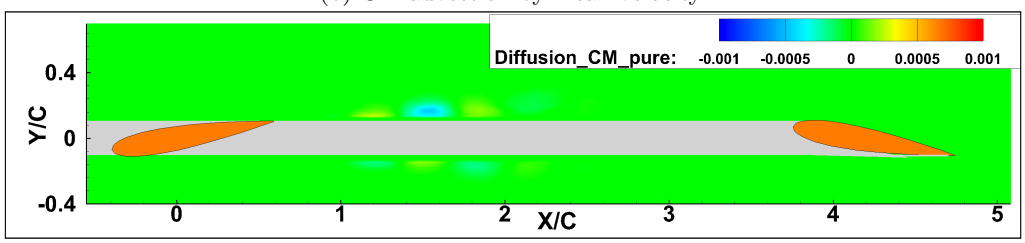

(c) CM pure diffusion

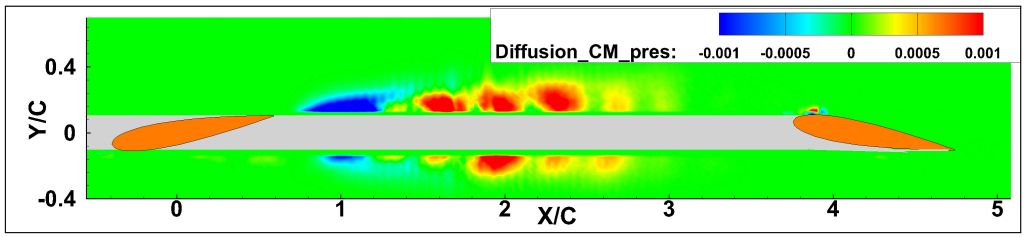

(d) CM diffusion by pressure

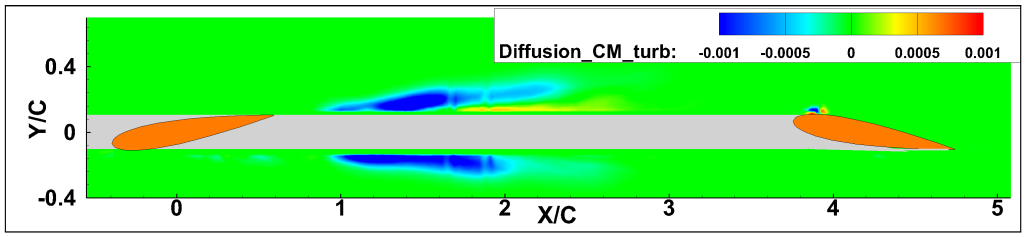

(e) CM diffusion by turbulence

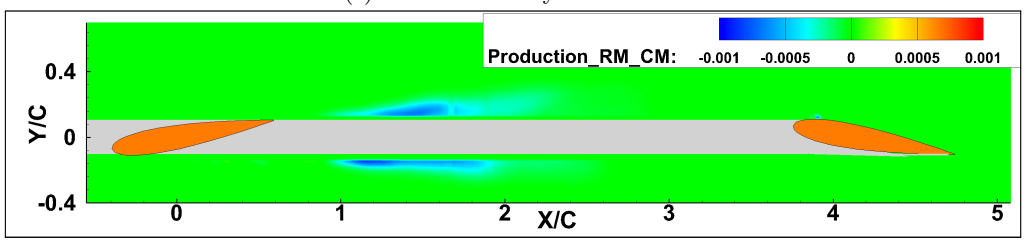

(f) RM production by CM

Figure A.110: Coherent motion (CM) transport and RM-interaction at $Re = 8000$ in double airfoil wake

E.5.6 RM energy exchange and interaction with CM

In this section, energy exchange between random motion, mean flow, and coherent motion resulting from their interactions in airfoil wake are presented.

High Reynolds number

Figures A.111a and A.111b show the production and dissipation of random motion for double airfoil wake at $Re = 8000$, respectively.

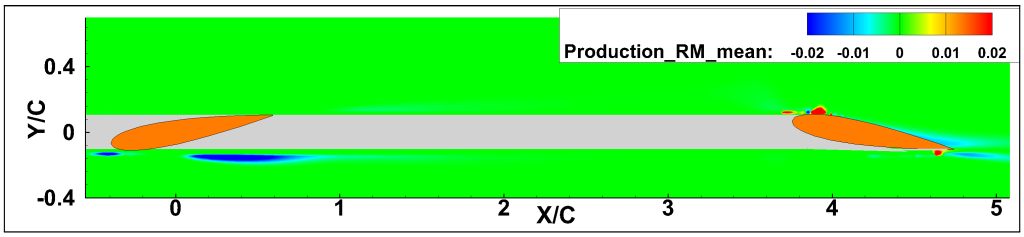

(a) RM production by mean

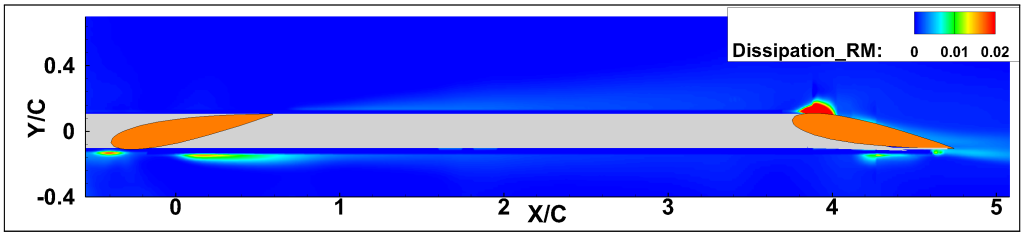

(b) RM dissipation

Figure A.111: Random motion (RM) production and dissipation terms in double airfoil wake at $Re = 8000$

Figure A.112 shows the transport terms of random motion in double airfoil wake at $Re = 8000$.

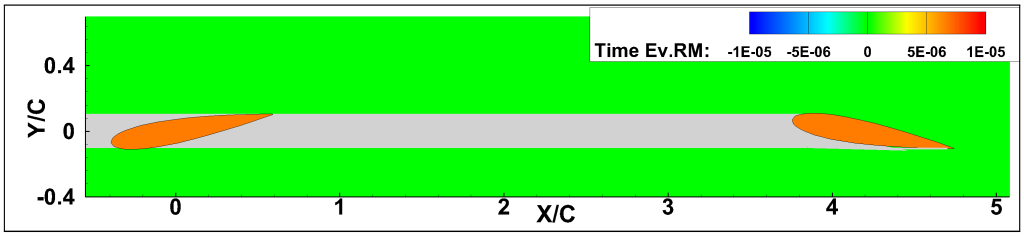

(a) RM time evolution

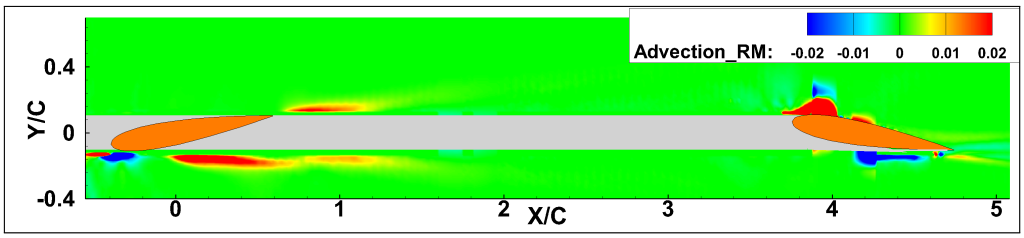

(b) RM advection by mean velocity

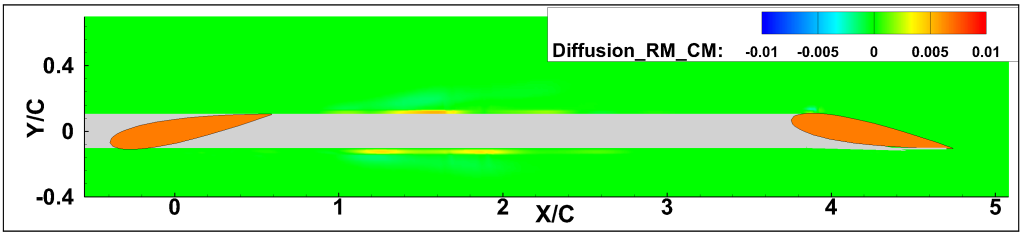

(c) RM diffusion by CM interaction

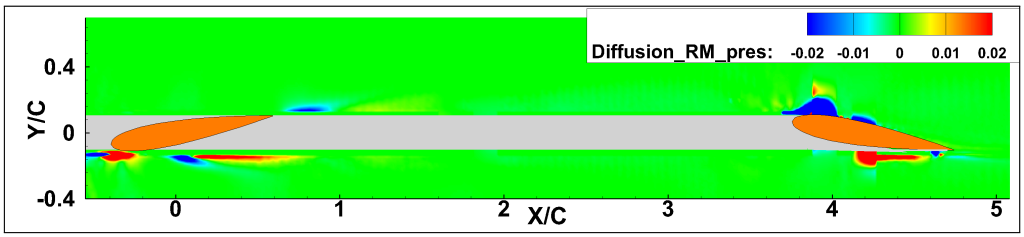

(d) RM diffusion by pressure

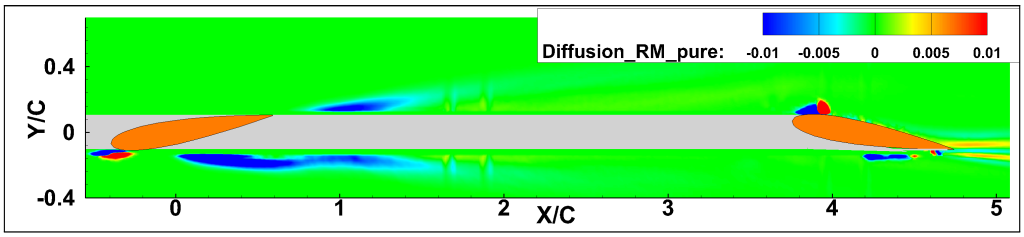

(e) RM pure diffusion

Figure A.112: Random motion (RM) energy budget in double airfoil wake at $Re = 8000$

APPENDIX B

Extensions on energy exchange with turbulence effect

A.1 Single cylinder configuration

A.1.1 First order statistics

The computation and validation of first-order statistics are initially applied to the single cylinder wake. This configuration is considered the simplest among the various configurations and is readily available in the existing literature. Figure B.1 presents the mean velocity in the streamwise direction for single cylinder wake at two heights from the wall ($z^+ = 500$ and $z^+ = 3125$).

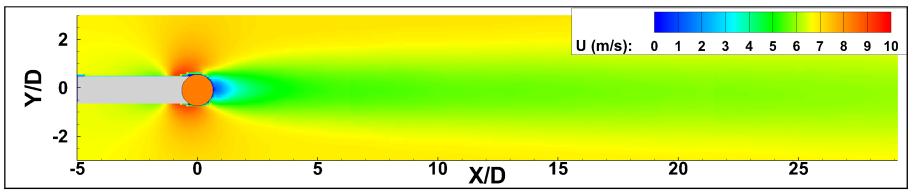

(a) $z^+ = 500$

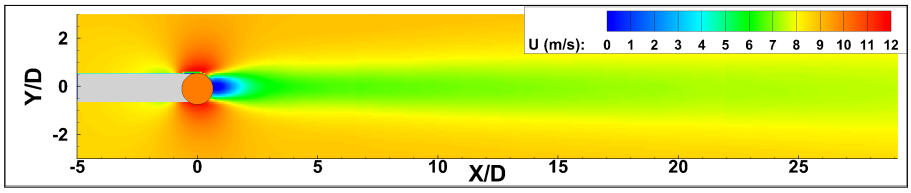

(b) $z^+ = 3125$

Figure B.1: Streamwise (X direction) mean velocities in cylinder wake

Figure B.2 presents the mean velocity in the spanwise direction for single cylinder wake at two heights from the wall ($z^+ = 500$ and $z^+ = 3125$).

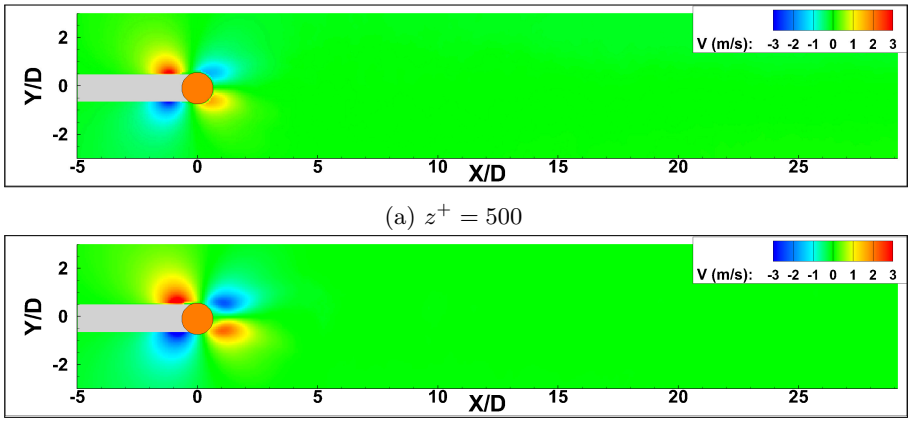

(a) $z^+ = 500$

(b) $z^+ = 3125$

Figure B.2: Spanwise (Y direction) mean velocities in cylinder wake

Figure B.3 presents the RMS in the streamwise direction for single cylinder wake at two heights from the wall ($z^+ = 500$ and $z^+ = 3125$).

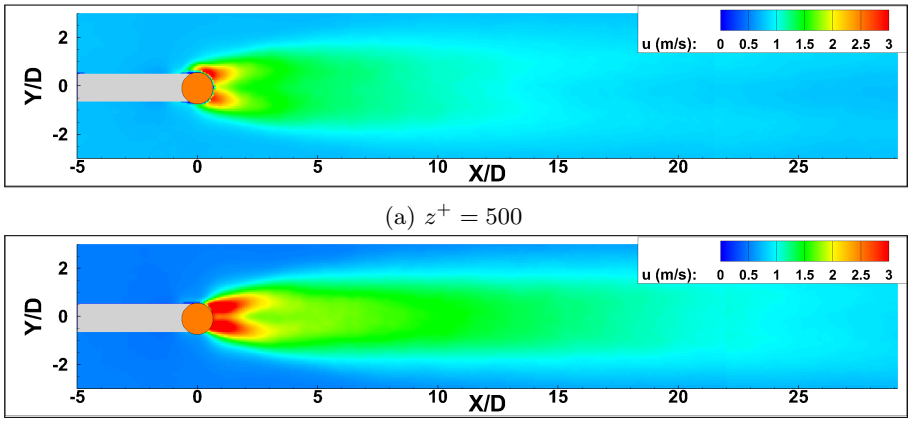

(a) $z^+ = 500$

(b) $z^+ = 3125$

Figure B.3: RMS of streamwise velocities (X direction) in cylinder wake

Figure B.4 presents the RMS in the spanwise direction for single cylinder wake at two heights from the wall ($z^+ = 500$ and $z^+ = 3125$).

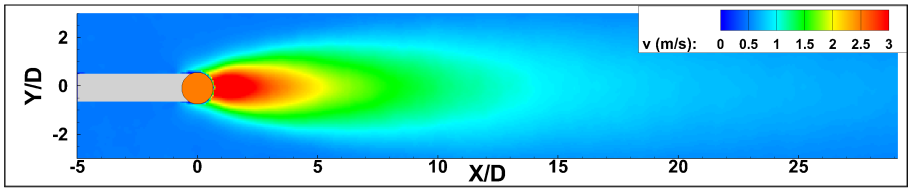

(a) $z^+ = 500$

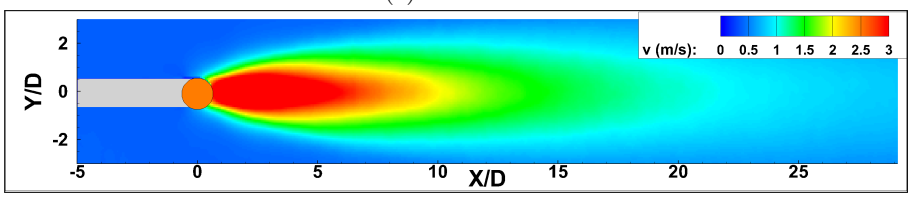

(b) $z^+ = 3125$

Figure B.4: RMS of spanwise velocities (Y direction) in cylinder wake

A.1.2 Total fluctuations energy exchange

In this section, kinetic energy of the turbulence is shown in cylinder wake for two heights from the wall. Each term of one point turbulent kinetic energy equation is computed showing gain and loss of energy between the mean flow and the turbulence. Figures B.5a and B.5b show the production term maps in single cylinder wake for both heights from the wall $z^+ = 500$ and $z^+ = 3125$, respectively.

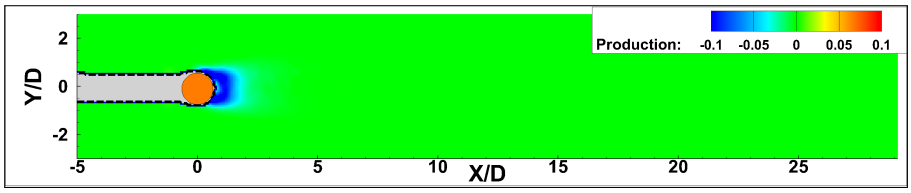

(a) $z^+ = 500$

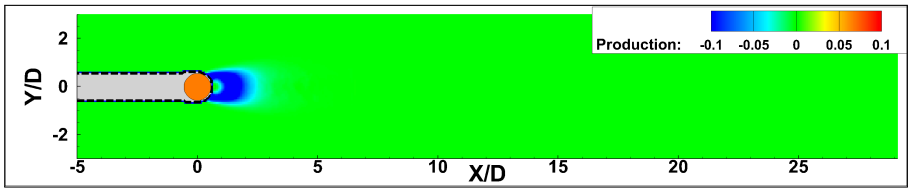

(b) $z^+ = 3125$

Figure B.5: Production of total turbulent kinetic energy by mean velocity in cylinder wake. Term is normalized by U_0^3/D.

Figures B.6a and B.6b show the advection term maps in single cylinder wake for both heights from the wall $z^+ = 500$ and $z^+ = 3125$, respectively.

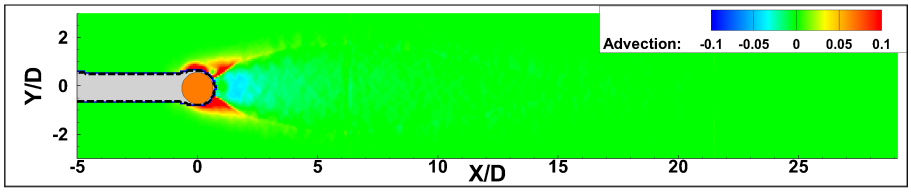

(a) $z^+ = 500$

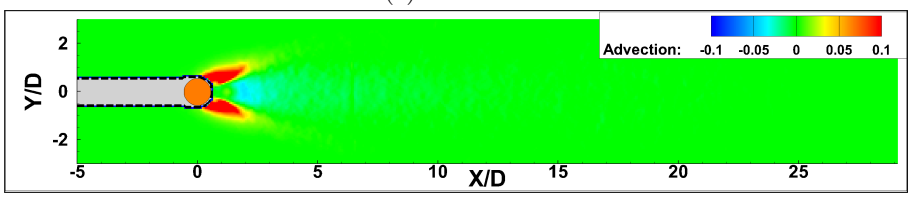

(b) $z^+ = 3125$

Figure B.6: Advection of total kinetic energy by mean velocity in cylinder wake. Terms is normalized by U_0^3/D.

Figures B.7a and B.7b show the diffusion term maps in single cylinder wake for both heights from the wall $z^+ = 500$ and $z^+ = 3125$, respectively.

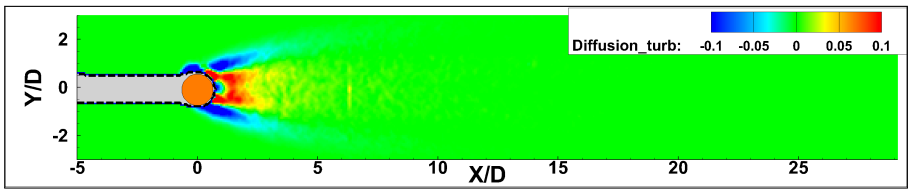

(a) $z^+ = 500$

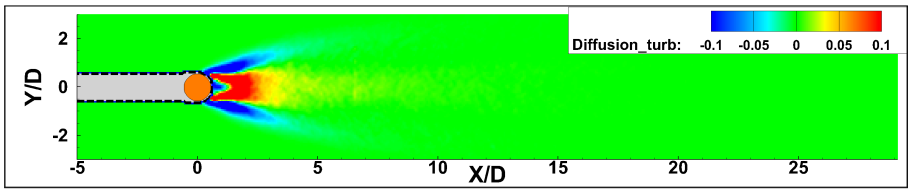

(b) $z^+ = 3125$

Figure B.7: Diffusion of total turbulent kinetic energy by Reynolds stresses in cylinder wake. Term is normalized by U_0^3/D.

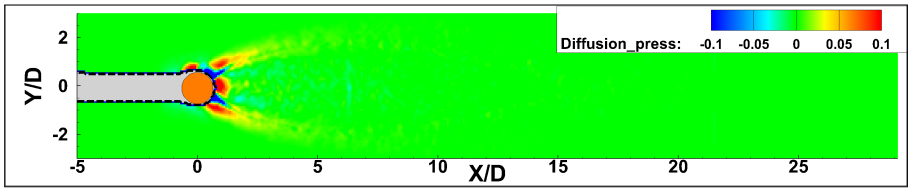

(a) $z^+ = 500$

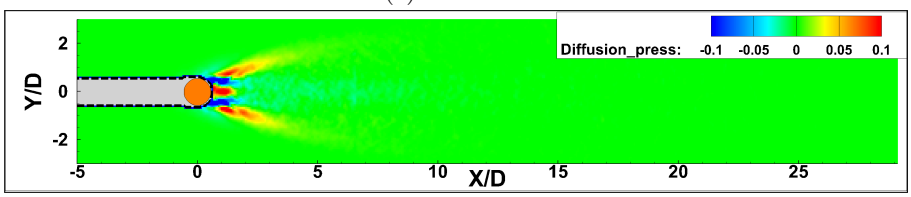

(b) $z^+ = 3125$

Figure B.8: Diffusion of total turbulent kinetic energy by pressure stresses in cylinder wake. Term is normalized by U_0^3/D.

Figures B.9a and B.9b show the dissipation term maps in single cylinder wake for both heights from the wall $z^+ = 500$ and $z^+ = 3125$, respectively.

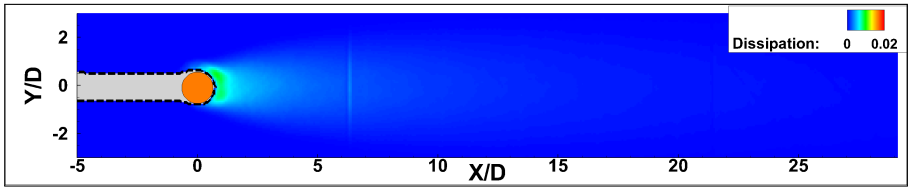

(a) $z^+ = 500$

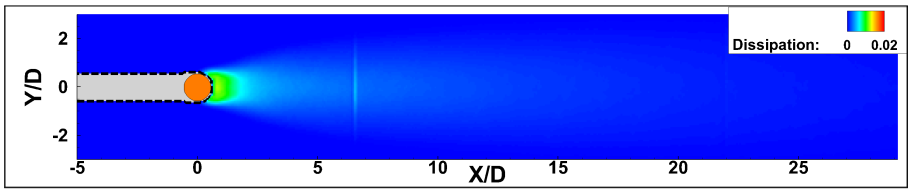

(b) $z^+ = 3125$

Figure B.9: Dissipation of total turbulent kinetic energy in cylinder wake. Term is normalized by U_0^3/D.

A.1.3 Decomposed total kinetic energy in phases

Figure B.10 show the production term close to the wall ($z^+ = 500$) for four distinct phases ($\phi = 0°$, $100°$, $180°$ and $280°$).

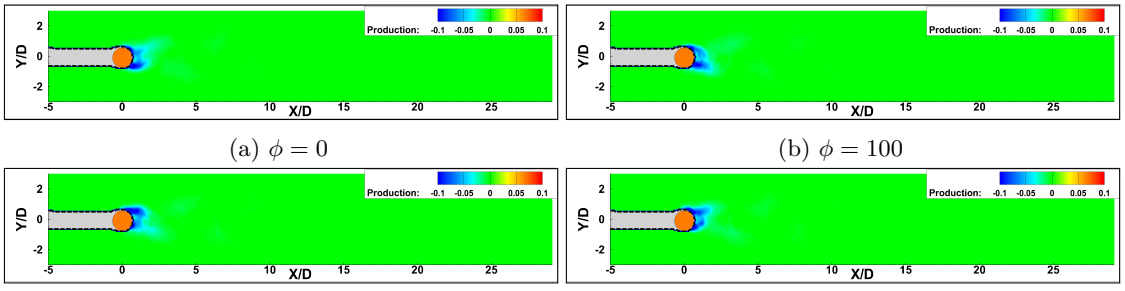

(a) $\phi = 0$ (b) $\phi = 100$

(c) $\phi = 180$ (d) $\phi = 280$

Figure B.10: Decomposed production by mean at $z^+ = 500$ in cylinder wake.Term is normalized by U_0^3/D.

Figure B.11 show the advection term close to the wall ($z^+ = 500$) for four distinct phases ($\phi = 0°$, $100°$, $180°$ and $280°$).

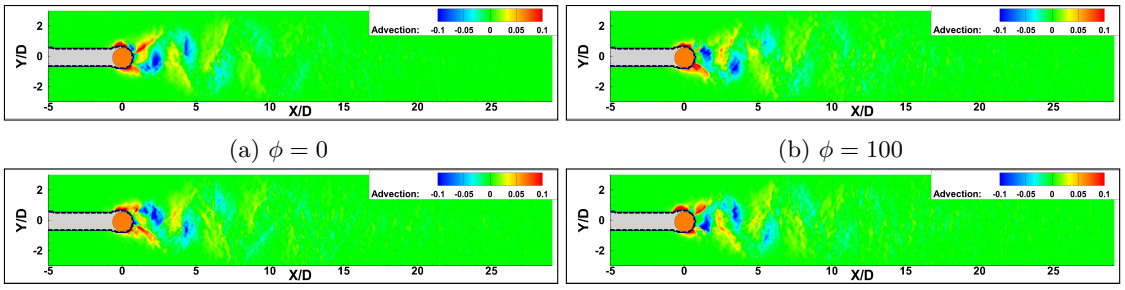

(a) $\phi = 0$ (b) $\phi = 100$

(c) $\phi = 180$ (d) Coherent structures at $\phi = 280$

Figure B.11: Decomposed advection at $z^+ = 500$ in cylinder wake. Term is normalized by U_0^3/D.

Figure B.12 show the diffusion through Reynolds stress term close to the wall ($z^+ = 500$) for four distinct phases ($\phi = 0°$, $100°$, $180°$ and $280°$).

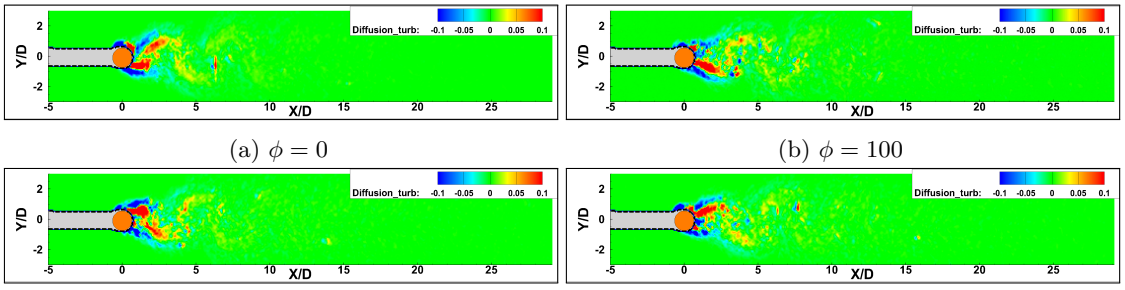

(a) $\phi = 0$ (b) $\phi = 100$

(c) $\phi = 180$ (d) $\phi = 280$

Figure B.12: Decomposed diffusion by turbulence at $z^+ = 500$ in cylinder wake.Term is normalized by U_0^3/D.

Figure B.13 show the diffusion through pressure stress term close to the wall ($z^+ = 500$) for four distinct phases ($\phi = 0°$, $100°$, $180°$ and $280°$).

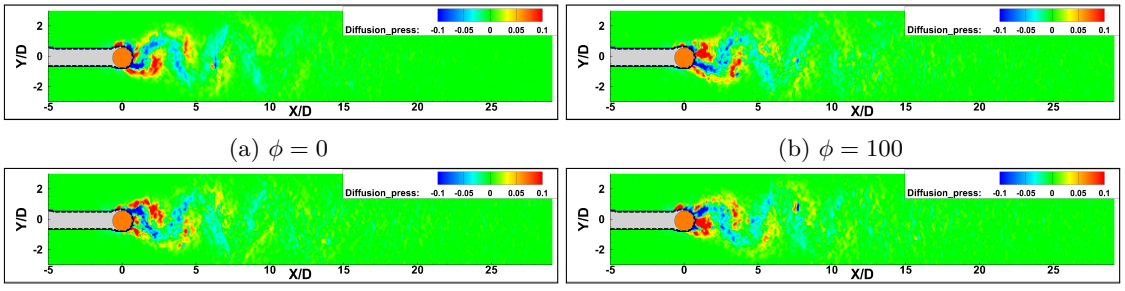

(a) $\phi = 0$ (b) $\phi = 100$

(c) $\phi = 180$ (d) $\phi = 280$

Figure B.13: Decomposed diffusion by pressure at $z^+ = 500$ in cylinder wake.Term is normalized by U_0^3/D.

Figure B.14 show the dissipation term close to the wall ($z^+ = 500$) for four distinct phases ($\phi = 0°$, $100°$, $180°$ and $280°$).

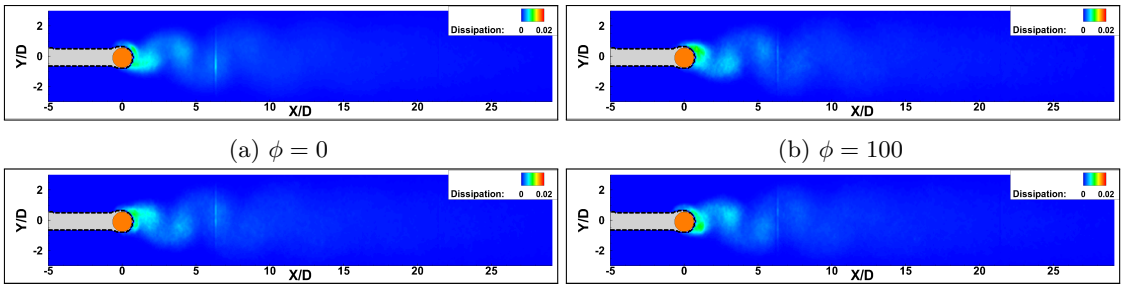

(a) $\phi = 0$ (b) $\phi = 100$

(c) $\phi = 180$ (d) $\phi = 280$

Figure B.14: Decomposed dissipation at $z^+ = 500$ in cylinder wake. Term is normalized by U_0^3/D.

A.1.4 CM energy exchange and interaction with RM

Close to wall

Figures B.15a and B.15b show the production and dissipation of coherent motion for single cylinder wake at $z^+ = 500$, respectively.

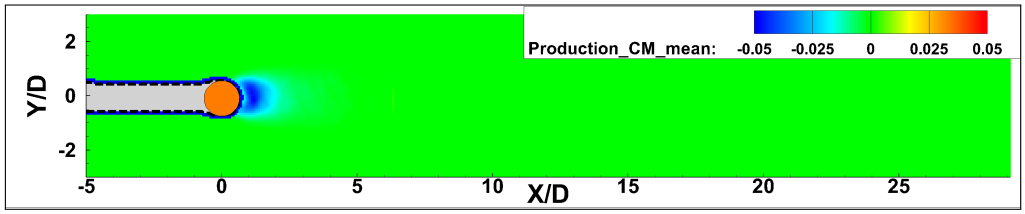

(a) CM production by mean

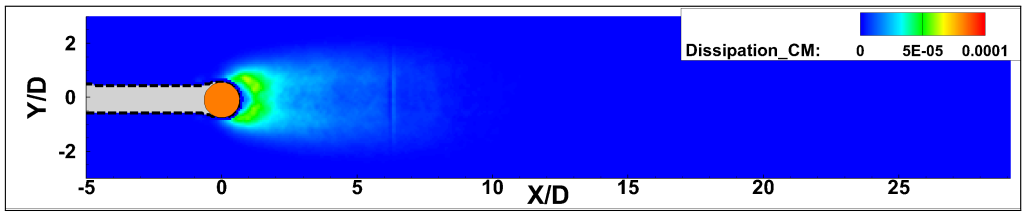

(b) CM dissipation

Figure B.15: Coherent motion (CM) production and dissipation $z^+ = 500$. Terms are normalized by U_0^3/D.

Figure B.16 shows the transport and RM-interaction terms of coherent motion in single cylinder wake at $z^+ = 500$. The transport terms is decomposed to transport by mean flow (advection) and transport by fluctuations (diffusion).

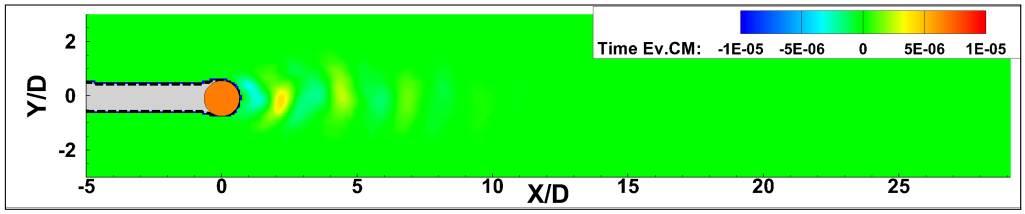

(a) CM time evolution in time

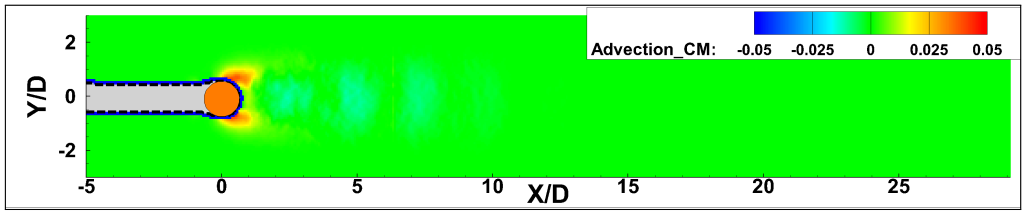

(b) CM advection by mean velocity

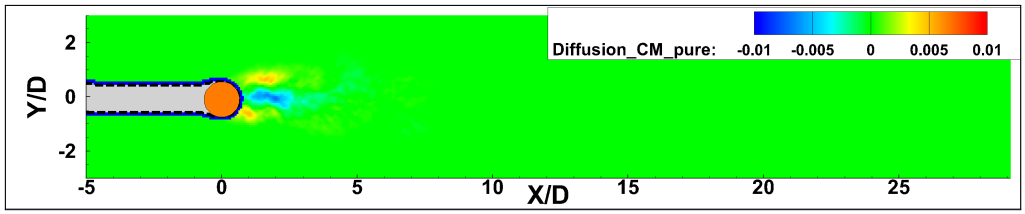

(c) CM pure diffusion

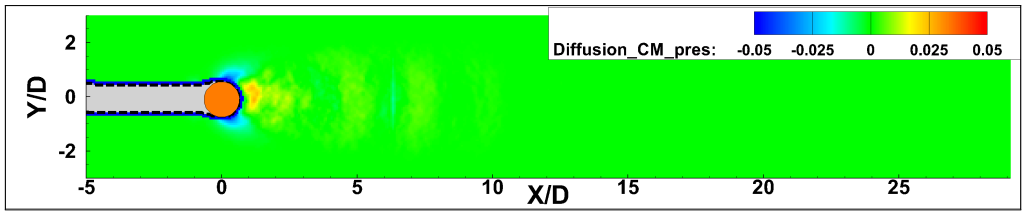

(d) CM diffusion by pressure

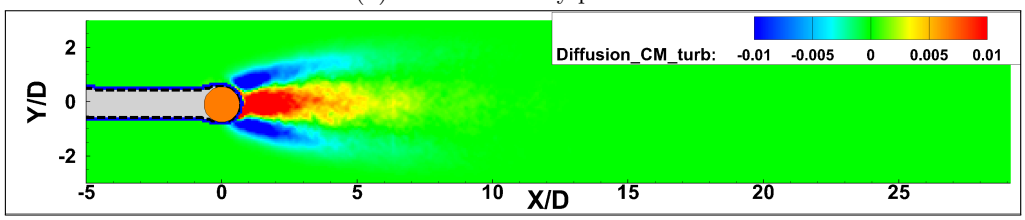

(e) CM diffusion by turbulence

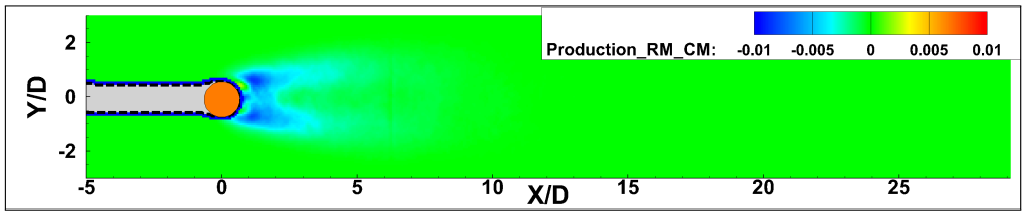

(f) RM production bt CM

Figure B.16: Coherent motion (CM) transports at $z^+ = 500$. Terms are normalized by U_0^3/D.

Far from wall

Figures B.17a and B.17b show the production and dissipation of coherent motion for single cylinder wake at $z^+ = 3125$, respectively.

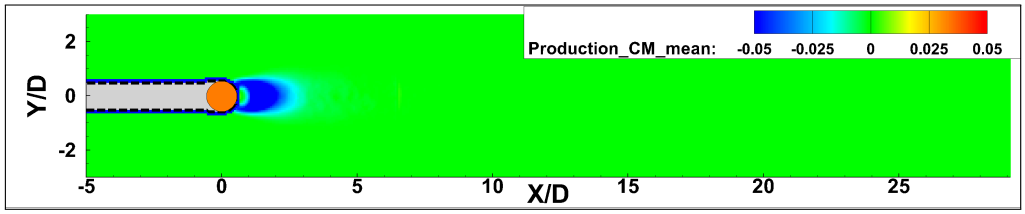

(a) CM production by mean

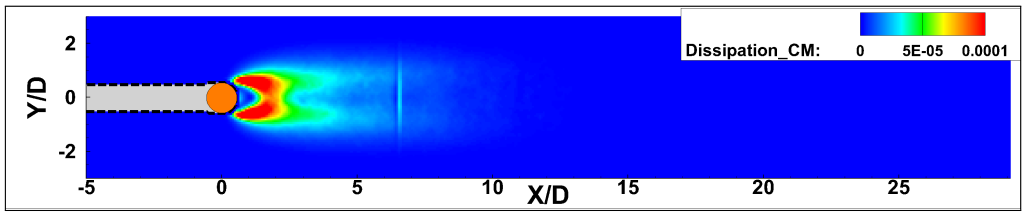

(b) CM dissipation

Figure B.17: Coherent motion (CM) production and dissipation at $z^+ = 3125$. Terms are normalised by U_0^3/D.

Figure B.18 shows the transport and RM-interaction terms of coherent motion in single cylinder wake at $z^+ = 3125$. The transport terms is decomposed to transport by mean flow (advection) and transport by fluctuations (diffusion).

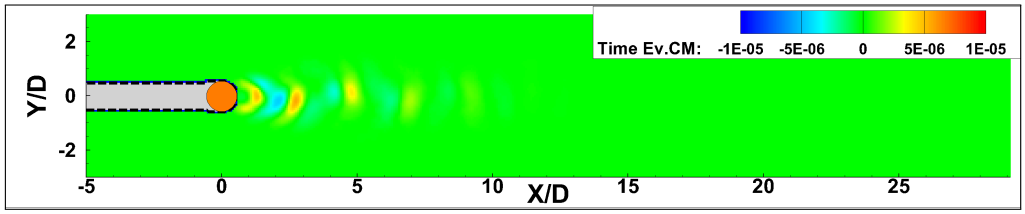

(a) CM time evolution in time

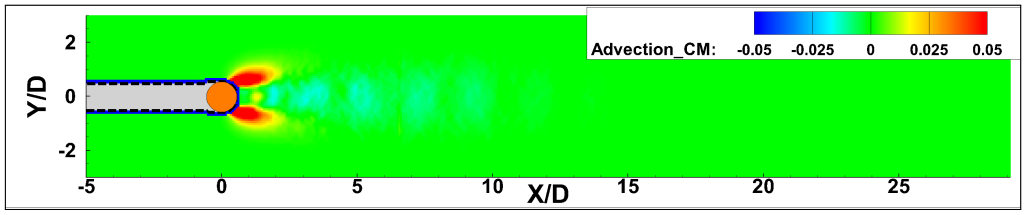

(b) CM advection by mean velocity

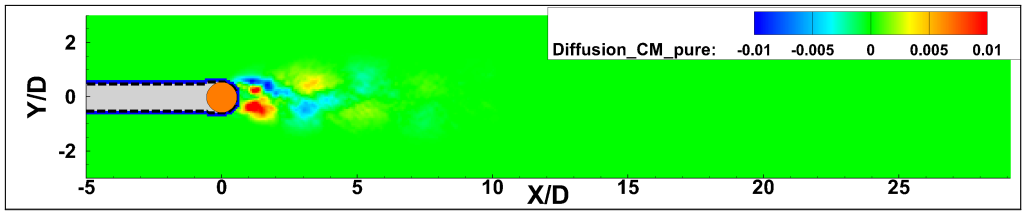

(c) CM pure diffusion

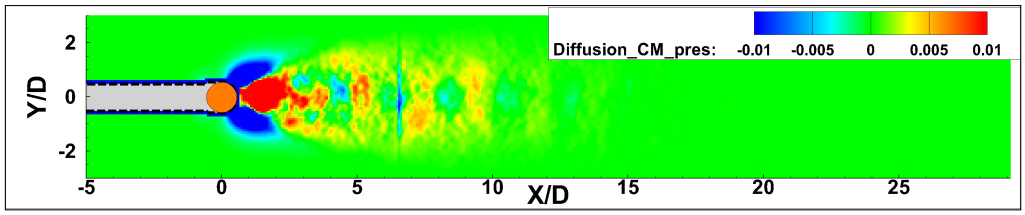

(d) CM diffusion by pressure

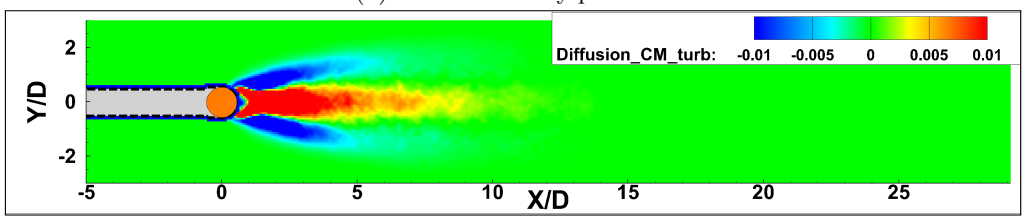

(e) CM diffusion by turbulence

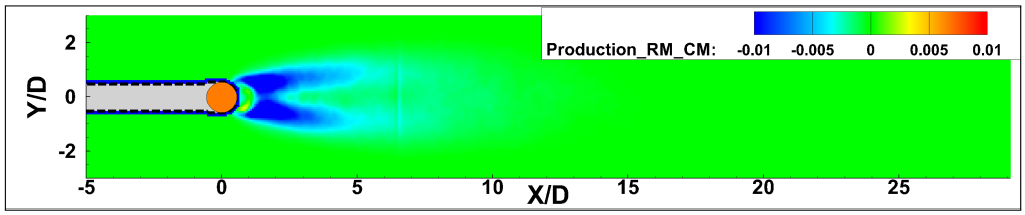

(f) RM production bt CM

Figure B.18: Coherent motion (CM) transports at $z^+ = 3125$. Terms are normalised by U_0^3/D.

A.1.5 RM energy exchange and interaction with CM

Close to wall

Figure B.19 shows the energy exchange terms of random motion equation for single cylinder wake at $z^+ = 500$.

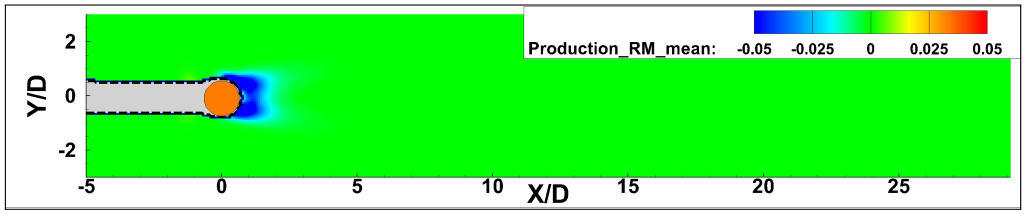

(a) RM production by mean

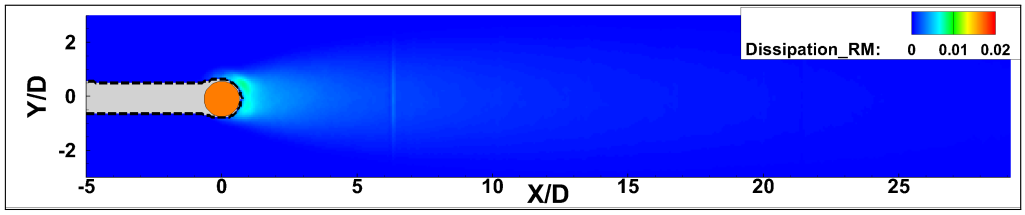

(b) RM dissipation

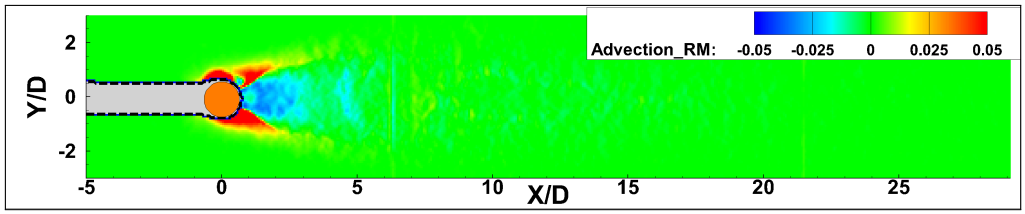

(c) RM advection by mean velocity

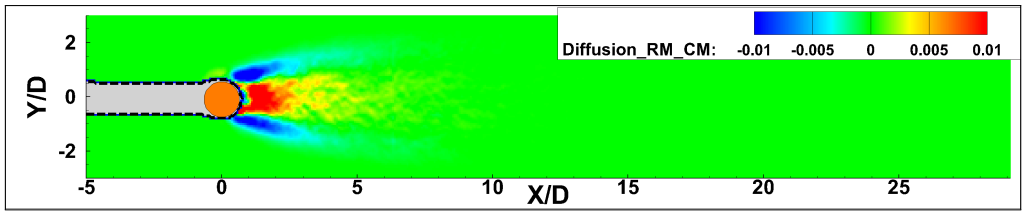

(d) RM diffusion by CM interaction

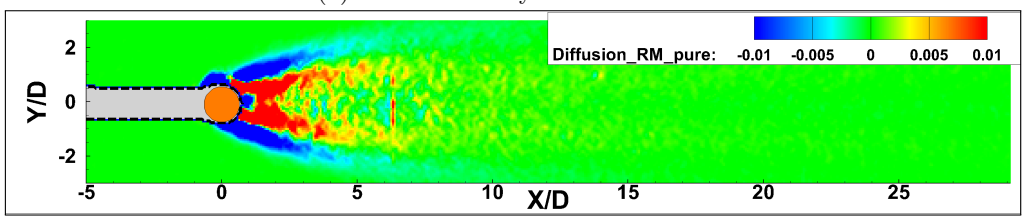

(e) RM pure diffusion

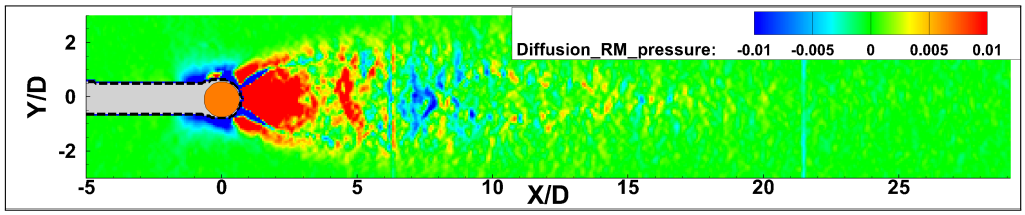

(f) RM pressure diffusion

Figure B.19: Random motion (RM) energy budget in cylinder wake at $z^+ = 500$. Terms are normalised by U_0^3/D.

Far from wall

Figure B.20 shows the energy exchange terms of random motion equation for single cylinder wake at $z^+ = 3125$.

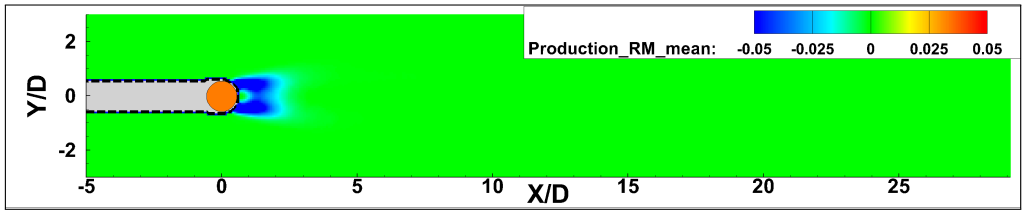

(a) RM production by mean

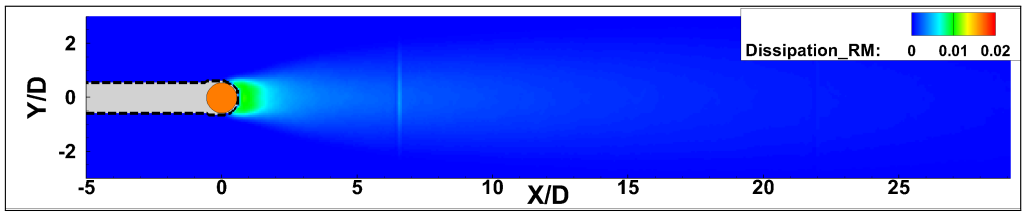

(b) RM dissipation

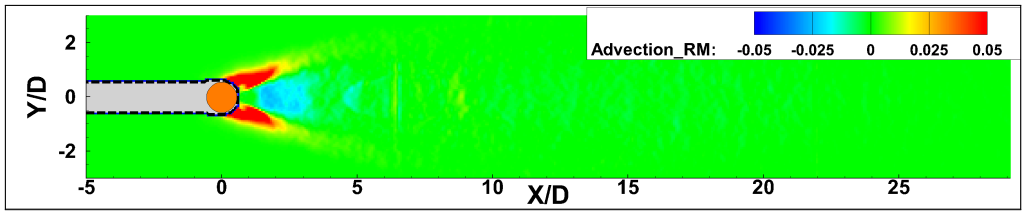

(c) RM advection by mean velocity

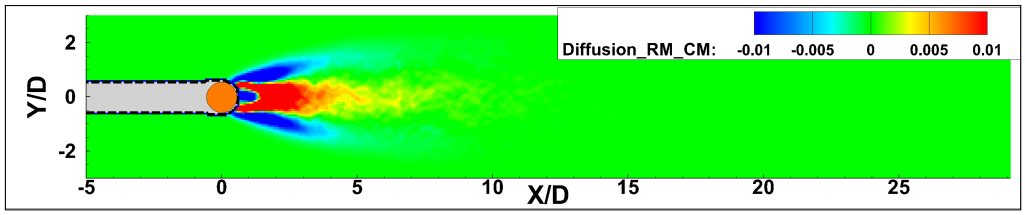

(d) RM diffusion by CM interaction

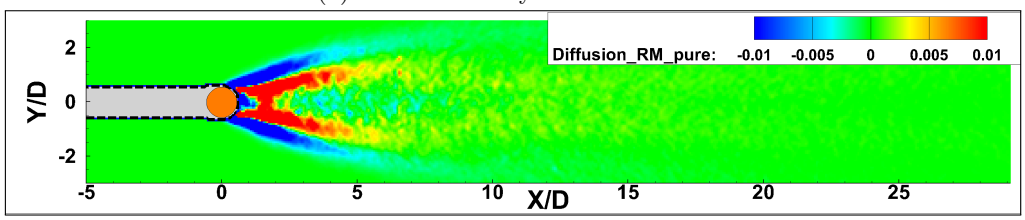

(e) RM pure diffusion

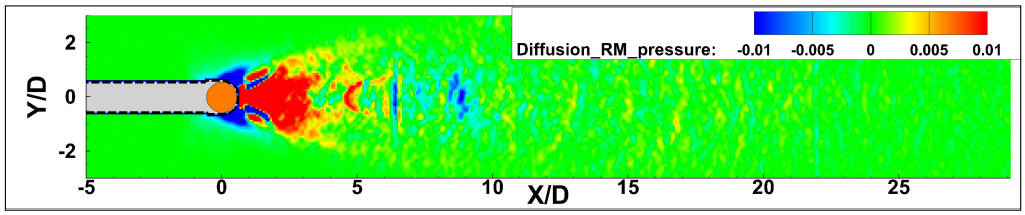

(f) RM pressure diffusion

Figure B.20: Random motion (RM) energy budget in cylinder wake at $z^+ = 3125$. Terms are normalised by U_0^3/D.

B.2 Double cylinder configuration

B.2.1 First order statistics

Figure B.21 presents the mean velocity in the streamwise direction for double cylinder wake configuration at two heights from the wall ($z^+ = 500$ and $z^+ = 3125$).

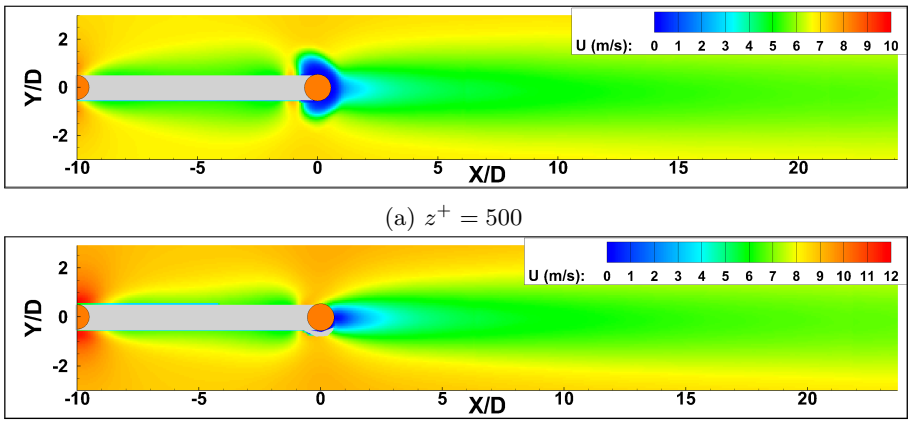

(a) $z^+ = 500$

(b) $z^+ = 3125$

Figure B.21: Streamwise (X direction) mean velocities in double cylinder wake

Figure B.22 presents the mean velocity in the spanwise direction for double cylinder wake configuration at two heights from the wall ($z^+ = 500$ and $z^+ = 3125$).

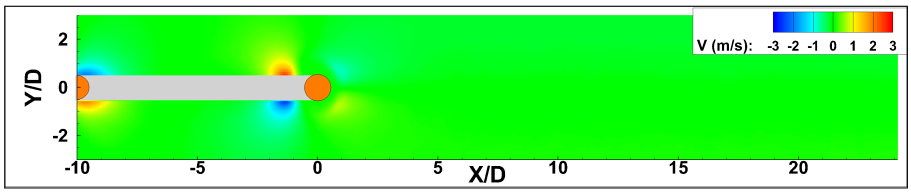

(a) $z^+ = 500$

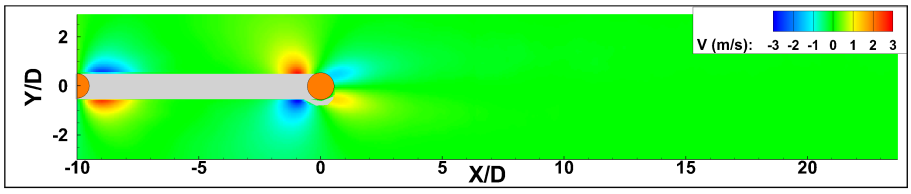

(b) $z^+ = 3125$

Figure B.22: Spanwise (Y direction) mean velocities in double cylinder wake

Figure B.23 presents the RMS in the streamwise direction for double cylinder wake configuration at two heights from the wall ($z^+ = 500$ and $z^+ = 3125$).

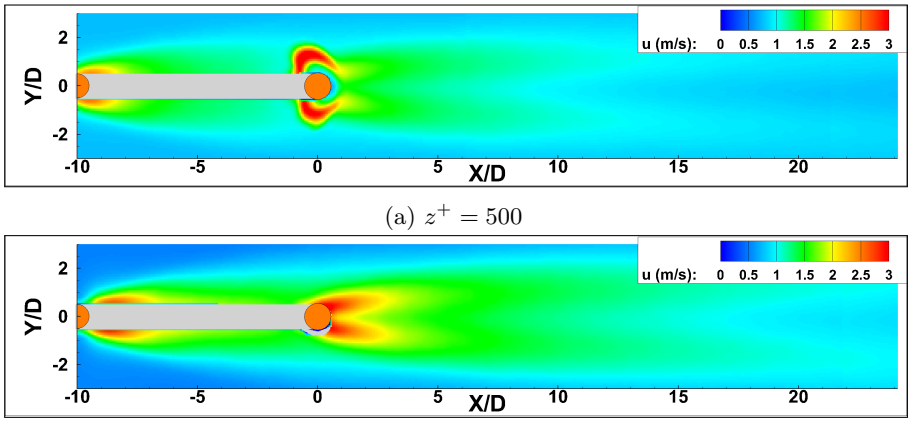

(a) $z^+ = 500$

(b) $z^+ = 3125$

Figure B.23: RMS of streamwise velocities (X direction) in double cylinder wake.

Figure B.24 presents the RMS in the spanwise direction for double cylinder wake configuration at two heights from the wall ($z^+ = 500$ and $z^+ = 3125$).

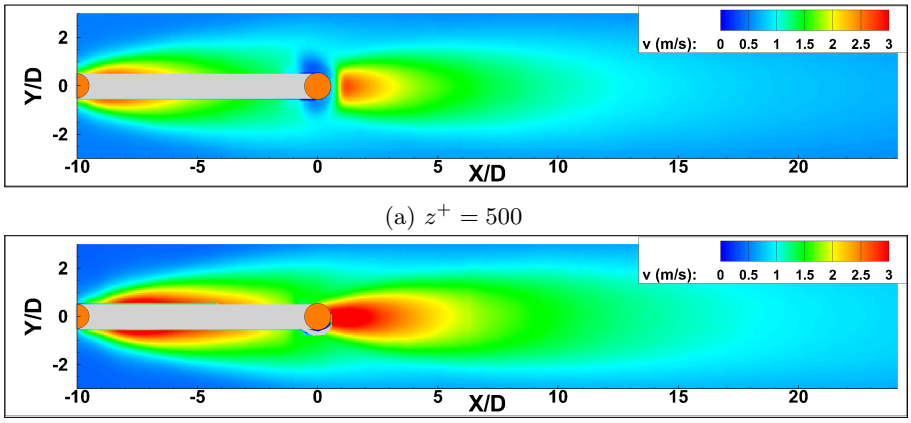

(a) $z^+ = 500$

(b) $z^+ = 3125$

Figure B.24: RMS of spanwise velocities (Y direction) in double cylinder wake.

B.2.2 Total fluctuations energy exchange

Figures B.25a and B.25b show the production term maps in double cylinder wake configuration for both heights from the wall $z^+ = 500$ and $z^+ = 3125$, respectively.

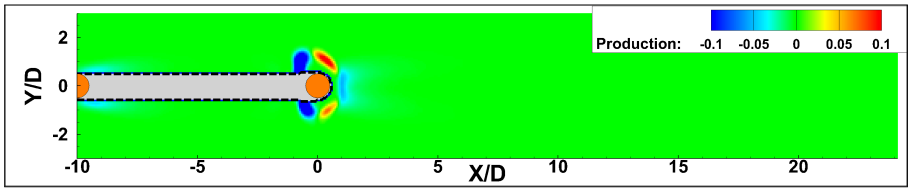

(a) $z^+ = 500$

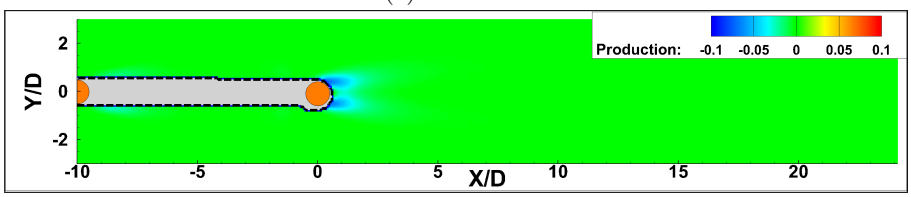

(b) $z^+ = 3125$

Figure B.25: Production of total turbulent kinetic energy by mean velocity in double cylinder wake. Term is normalized by U_0^3/D.

Figures B.26a and B.26b show the advection term maps in double cylinder wake configuration for both heights from the wall $z^+ = 500$ and $z^+ = 3125$, respectively.

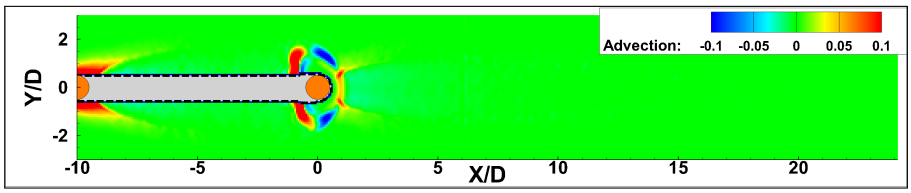

(a) $z^+ = 500$

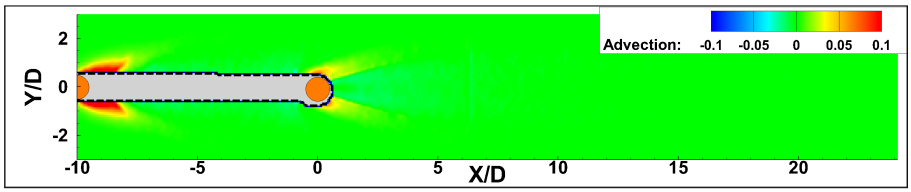

(b) $z^+ = 3125$

Figure B.26: Advection of total kinetic energy by mean velocity in double cylinder wake. Term is normalized by U_0^3/D.

Figures B.27a and B.27b show the diffusion through Reynolds stresses term maps in double cylinder wake configuration for both heights from the wall $z^+ = 500$ and $z^+ = 3125$, respectively.

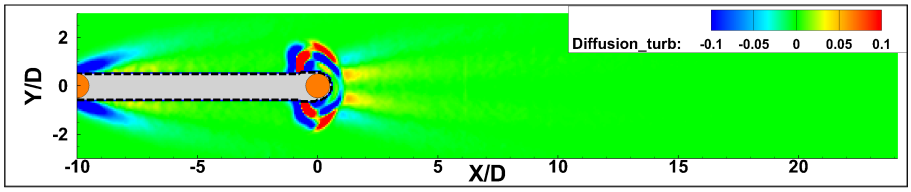

(a) $z^+ = 500$

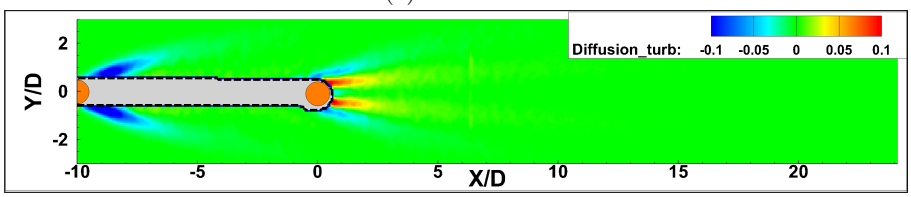

(b) $z^+ = 3125$

Figure B.27: Diffusion of total turbulent kinetic energy by turbulence in double cylinder wake. Term is normalized by U_0^3/D.

Figures B.28a and B.28b show the diffusion term through pressure maps in double cylinder wake configuration for both heights from the wall $z^+ = 500$ and $z^+ = 3125$, respectively.

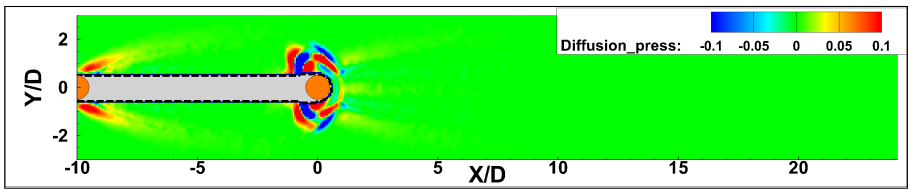

(a) $z^+ = 500$

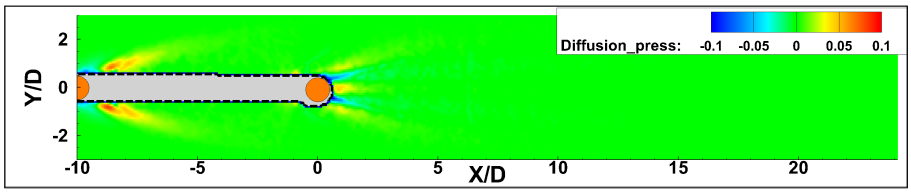

(b) $z^+ = 3125$

Figure B.28: Diffusion of total turbulent kinetic energy by turbulence in double cylinder wake. Term is normalized by U_0^3/D.

Figures B.29a and B.29b show the dissipation term maps in double cylinder wake configuration for both heights from the wall $z^+ = 500$ and $z^+ = 3125$, respectively.

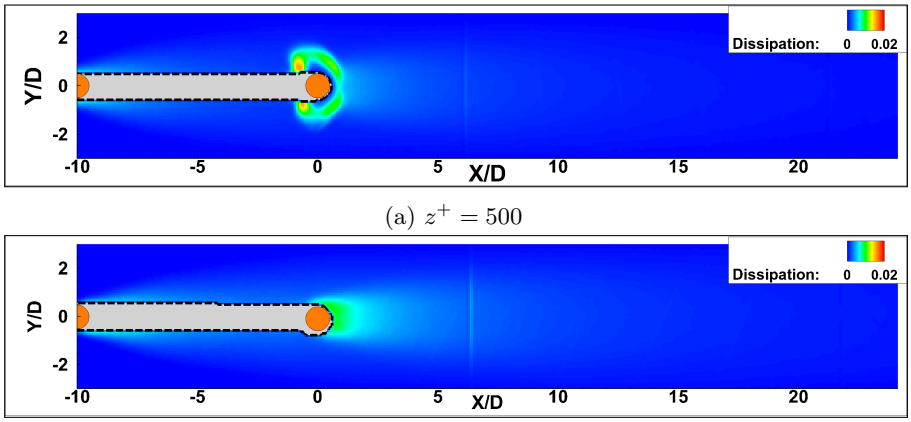

(a) $z^+ = 500$

(b) $z^+ = 3125$

Figure B.29: Dissipation of total turbulent kinetic energy in double cylinder wake. Term is normalised by U_0^3/D.

B.2.3 Decomposed total kinetic energy in phases

Figure B.30 show the production term close to the wall ($z^+ = 500$) for four distinct phases ($\phi = 0°$, $100°$, $180°$ and $280°$).

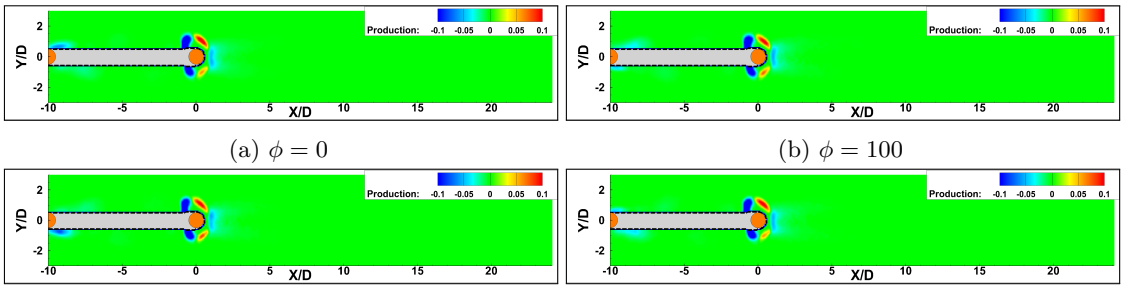

(a) $\phi = 0$

(b) $\phi = 100$

(c) $\phi = 180$

(d) $\phi = 280$

Figure B.30: Decomposed production by mean at $Re = 4667$ in double cylinder wake. Term is normalized by U_0^3/D.

Figure B.31 show the advection close to the wall ($z^+ = 500$) for four distinct phases ($\phi = 0°$, $100°$, $180°$ and $280°$).

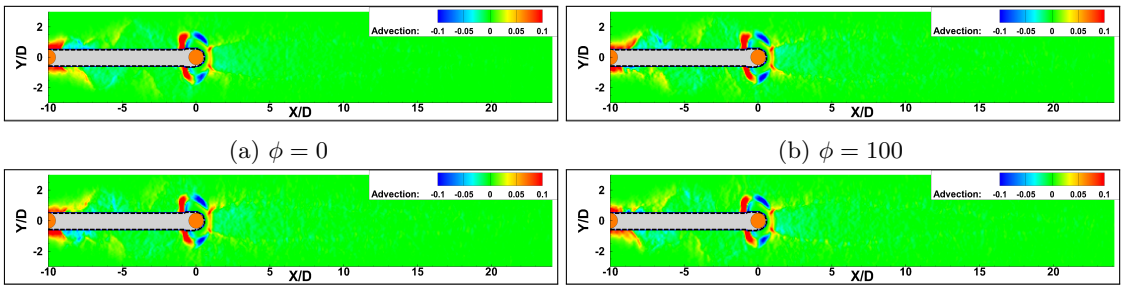

(a) $\phi = 0$

(b) $\phi = 100$

(c) $\phi = 180$

(d) Coherent structures at $\phi = 280$

Figure B.31: Decomposed advection at $z^+ = 500$ in double cylinder wake. Term is normalized by U_0^3/D.

Figure B.32 show the diffusion close to the wall ($z^+ = 500$) for four distinct phases ($\phi = 0°$, $100°$, $180°$ and $280°$).

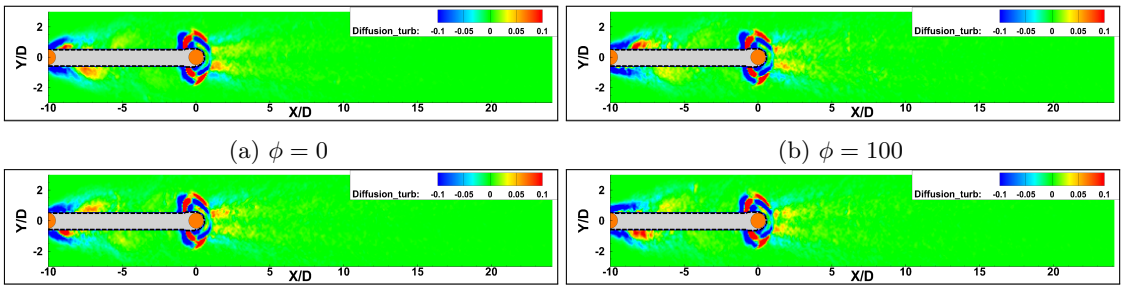

(a) $\phi = 0$ (b) $\phi = 100$

(c) $\phi = 180$ (d) $\phi = 280$

Figure B.32: Decomposed diffusion by pressure at $z^+ = 500$ in double cylinder wake. Term is normalised by U_0^3/D.

Figure B.33 show the diffusion through pressure close to the wall ($z^+ = 500$) for four distinct phases ($\phi = 0°$, $100°$, $180°$ and $280°$).

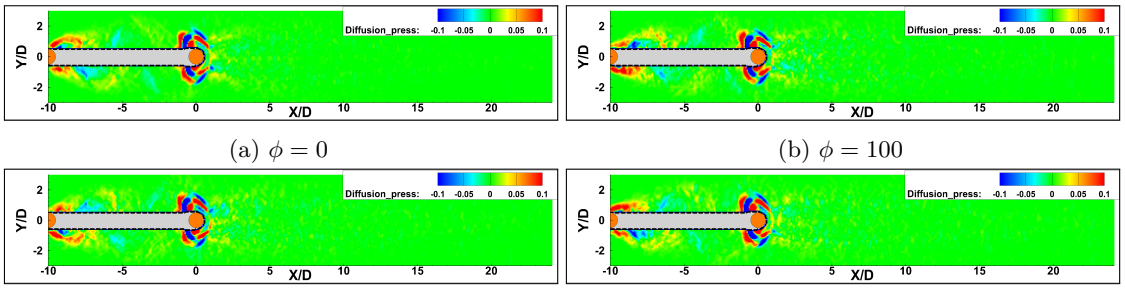

(a) $\phi = 0$ (b) $\phi = 100$

(c) $\phi = 180$ (d) $\phi = 280$

Figure B.33: Decomposed diffusion by pressure at $z^+ = 500$ in double cylinder wake. Term is normalised by U_0^3/D.

Figure B.33 show the dissipation close to the wall ($z^+ = 500$) for four distinct phases ($\phi = 0°$, $100°$, $180°$ and $280°$).

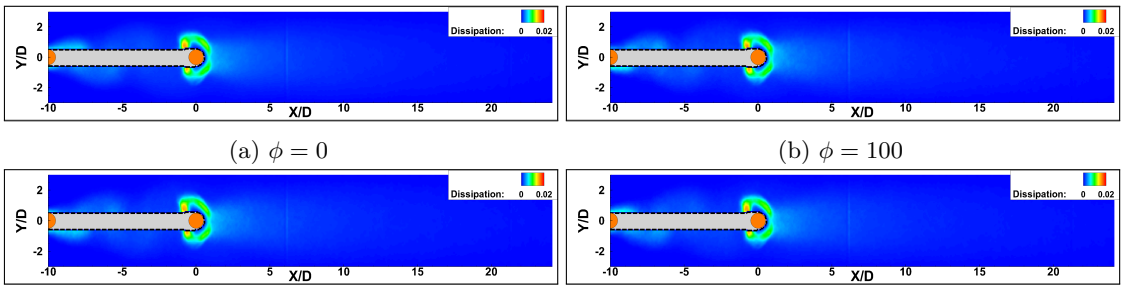

(a) $\phi = 0$ (b) $\phi = 100$

(c) $\phi = 180$ (d) $\phi = 280$

Figure B.34: Decomposed dissipation at $z^+ = 500$ in double cylinder wake. Term is normalised by U_0^3/D.

B.2.4 CM energy exchange and interaction with RM

Close to wall

Figures B.35a and B.35b show the production and dissipation of coherent motion for double cylinder wake configuration at $z^+ = 500$, respectively.

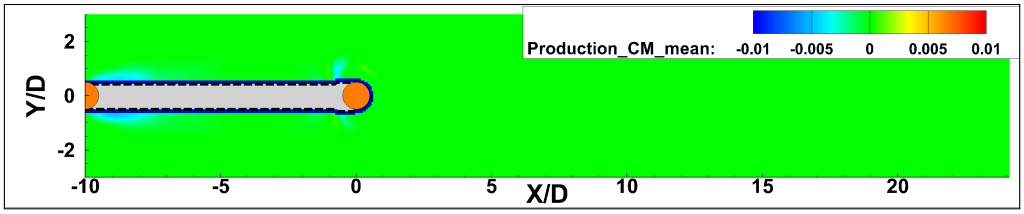

(a) CM production by mean

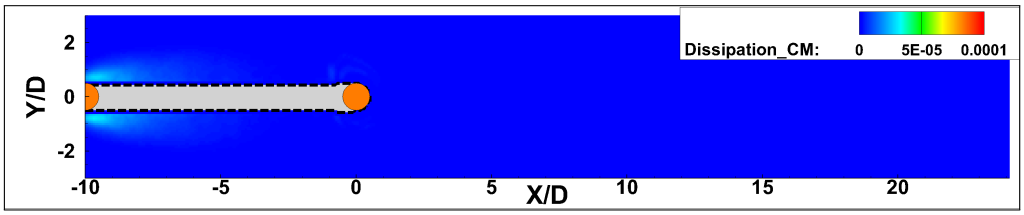

(b) CM dissipation

Figure B.35: Coherent motion (CM) production and dissipation at $z^+ = 500$. Terms are normalised by U_0^3/D.

Figure B.36 shows the transport and RM-interaction terms of coherent motion in double cylinder wake configuration at $z^+ = 500$. The transport terms is decomposed to transport by mean flow (advection) and transport by fluctuations (diffusion).

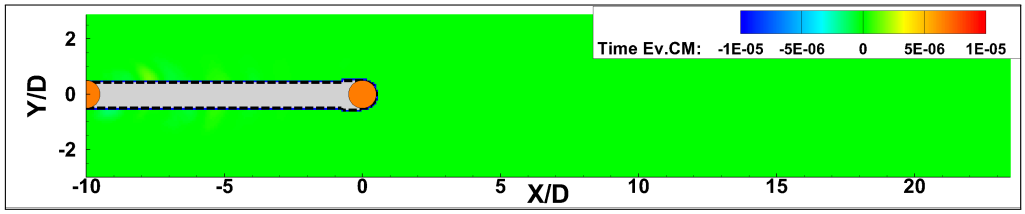

(a) CM time evolution in time

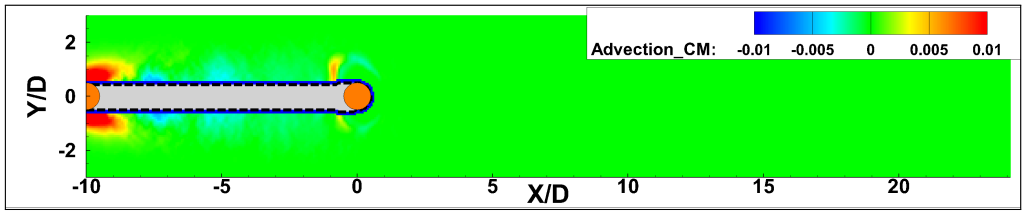

(b) CM advection by mean velocity

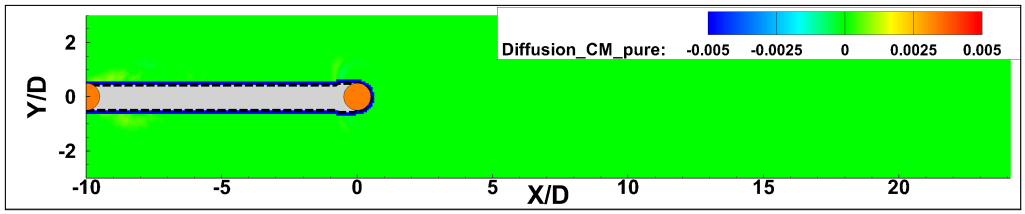

(c) CM pure diffusion

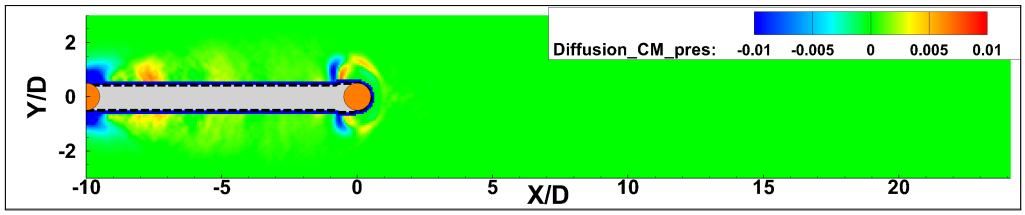

(d) CM diffusion by pressure

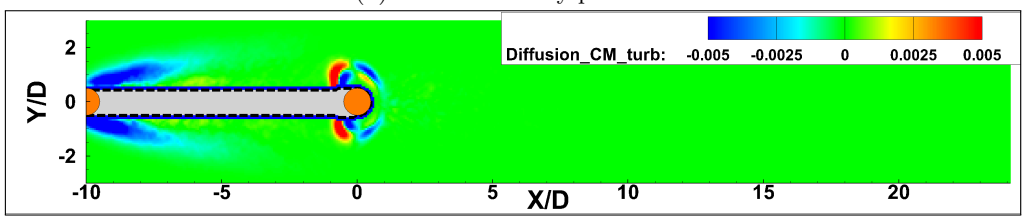

(e) CM diffusion by turbulence

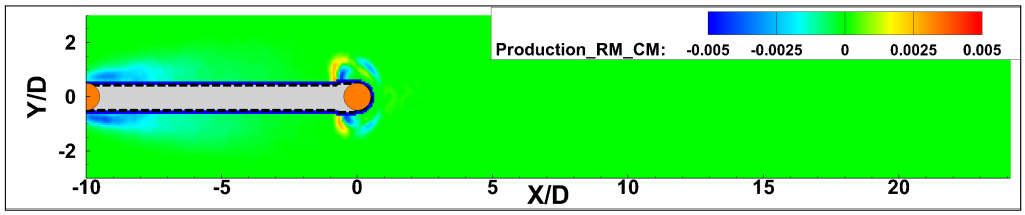

(f) RM production bt CM

Figure B.36: Coherent motion (CM) transports at $z^+ = 500$. Terms are normalised by U_0^3/D.

Far from wall

Figures B.37a and B.37b show the production and dissipation of coherent motion for double cylinder wake configuration at $z^+ = 3125$, respectively.

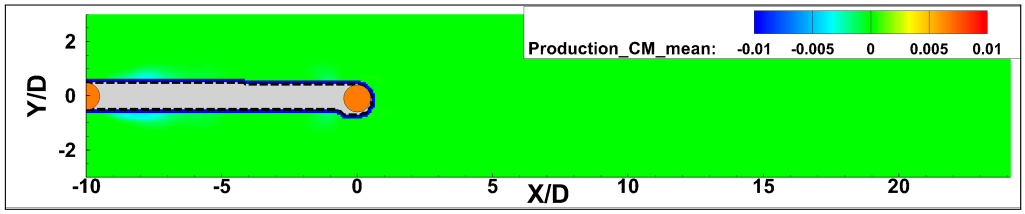

(a) CM production by mean

(b) CM dissipation

Figure B.37: Coherent motion (CM) production and dissipation at $z^+ = 3125$. Terms are normalised by U_0^3/D.

Figure B.38 shows the transport and RM-interaction terms of coherent motion in double cylinder wake configuration at $z^+ = 3125$. The transport terms is decomposed to transport by mean flow (advection) and transport by fluctuations (diffusion).

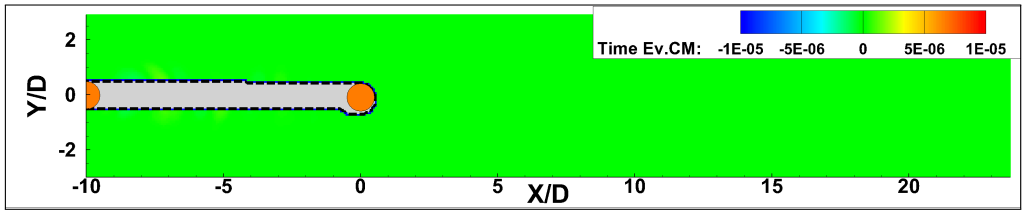

(a) CM time evolution in time

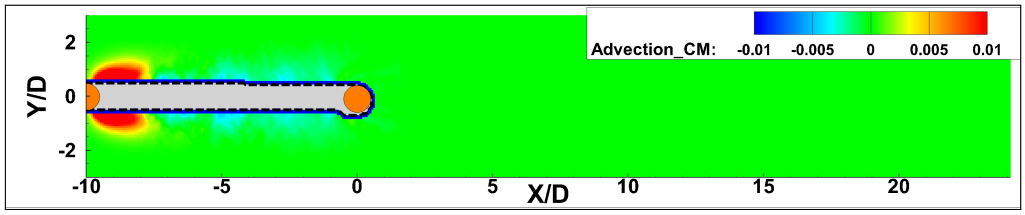

(b) CM advection by mean velocity

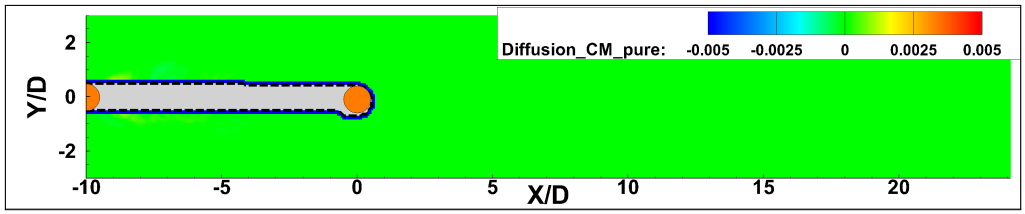

(c) CM pure diffusion

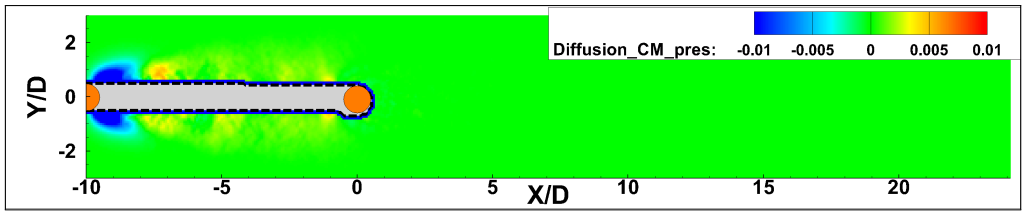

(d) CM diffusion by pressure

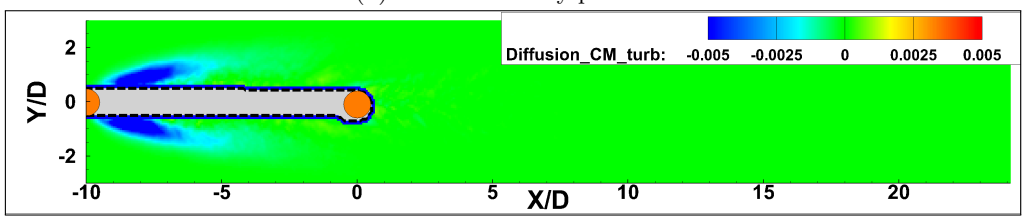

(e) CM diffusion by turbulence

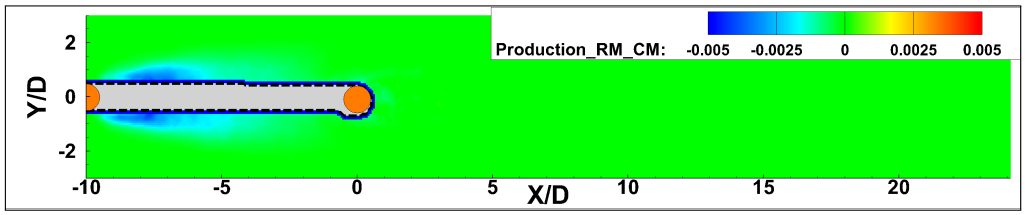

(f) RM production bt CM

Figure B.38: Coherent motion (CM) transports at $z^+ = 3125$. Terms are normalised by U_0^3/D.

B.2.5 RM energy exchange and interaction with CM

Close to wall

Figure B.39 shows the energy exchange terms of random motion equation for double cylinder wake at $z^+ = 500$.

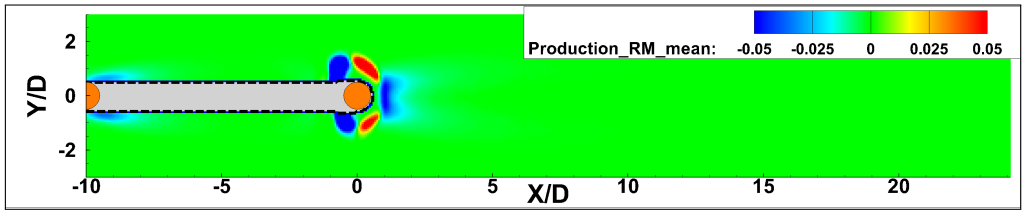

(a) RM production by mean

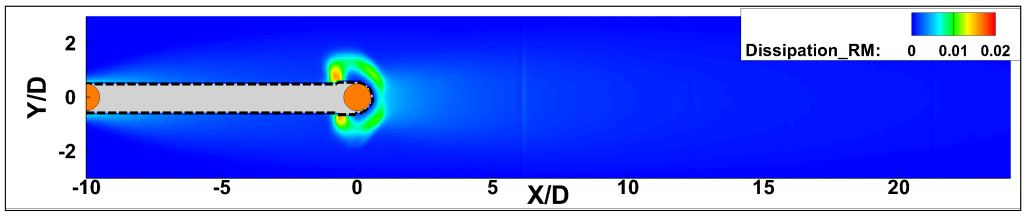

(b) RM dissipation

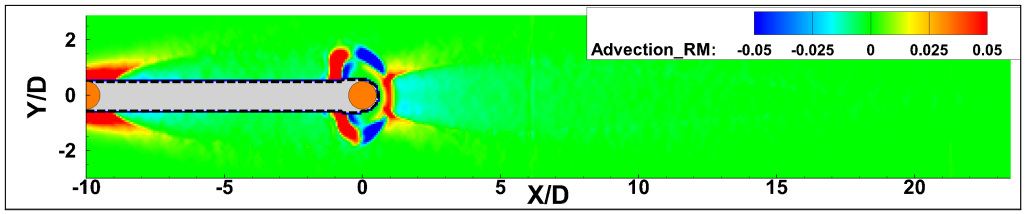

(c) RM advection by mean velocity

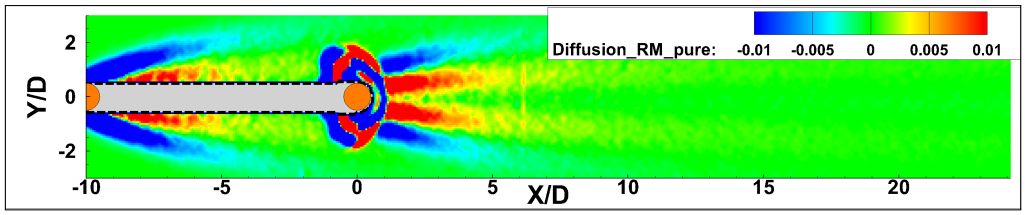

(d) RM diffusion by CM interaction

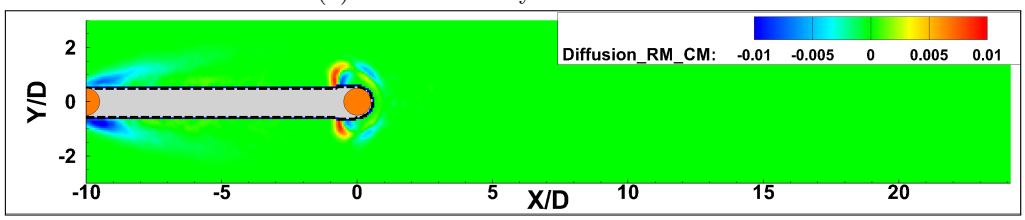

(e) RM diffusion by CM interaction

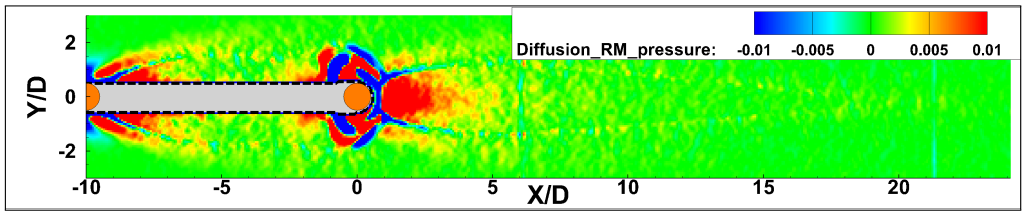

(f) RM pure diffusion

Figure B.39: Random motion (RM) energy budget in double cylinder wake at $z^+ = 500$. Terms are normalised by U_0^3/D.

Far from wall

Figure B.40 shows the energy exchange terms of random motion equation for double cylinder wake at $z^+ = 3125$.

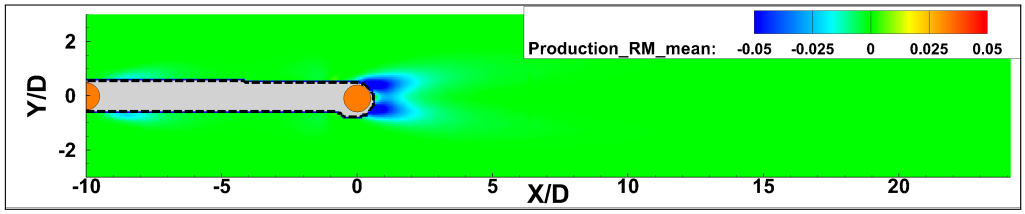

(a) RM production by mean

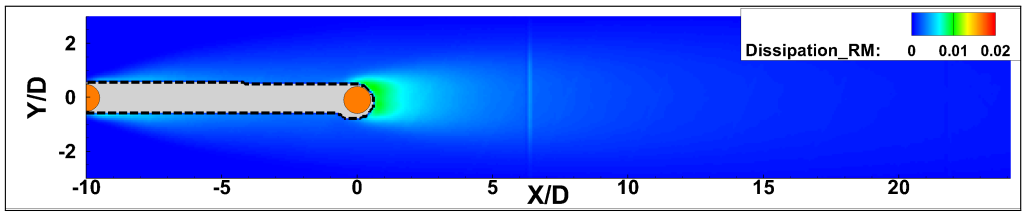

(b) RM dissipation

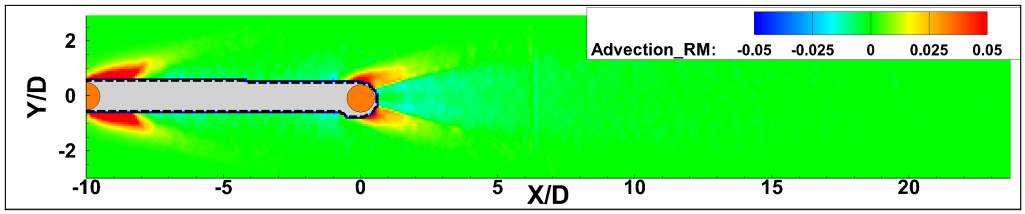

(c) RM advection by mean velocity

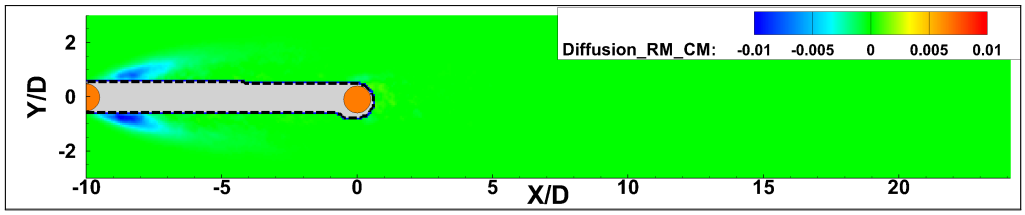

(d) RM diffusion by CM interaction

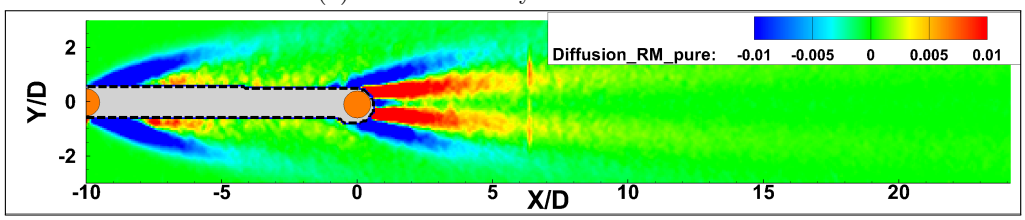

(e) RM pure diffusion

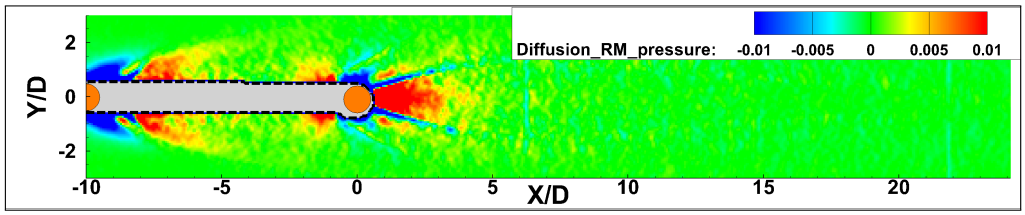

(f) RM pressure diffusion

Figure B.40: Random motion (RM) energy budget in double cylinder wake at $z^+ = 3125$. Terms are normalised by U_0^3/D.

C.3 Cylinder-airfoil configuration

C.3.1 First order statistics

Figure B.41 presents the mean velocity in the streamwise direction for cylinder-airfoil wake configuration at two heights from the wall ($z^+ = 500$ and $z^+ = 3125$).

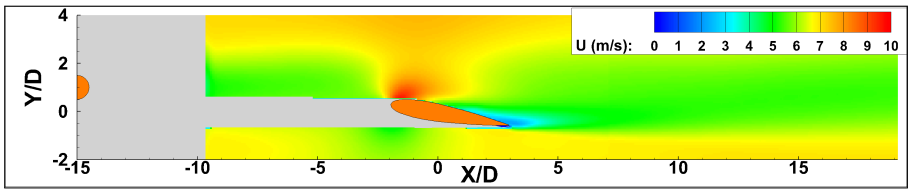

(a) $z^+ = 500$

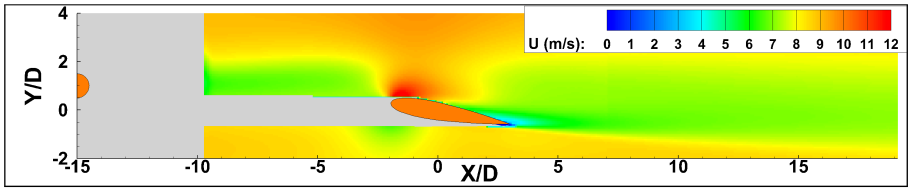

(b) $z^+ = 3125$

Figure B.41: Streamwise (X direction) mean velocities in cylinder-airfoil wake

Figure B.42 presents the mean velocity in the spanwise direction for cylinder-airfoil wake configuration at two heights from the wall ($z^+ = 500$ and $z^+ = 3125$).

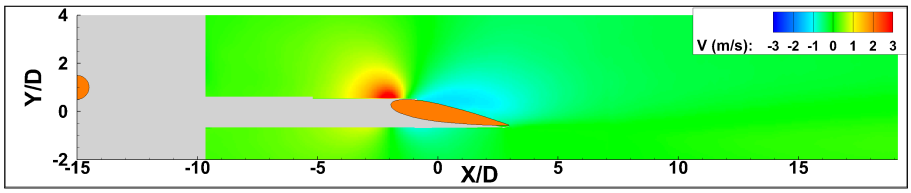

(a) $z^+ = 500$

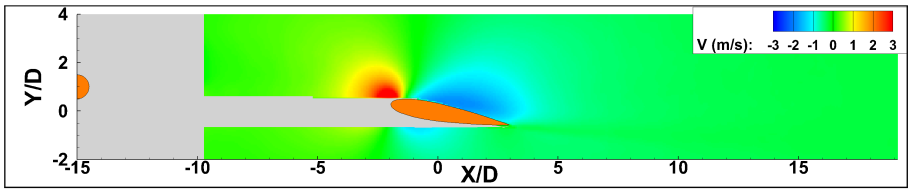

(b) $z^+ = 3125$

Figure B.42: Spanwise (Y direction) mean velocities in cylinder-airfoil wake

Figure B.43 presents the RMS in the streamwise direction for cylinder-airfoil wake configuration at two heights from the wall ($z^+ = 500$ and $z^+ = 3125$).

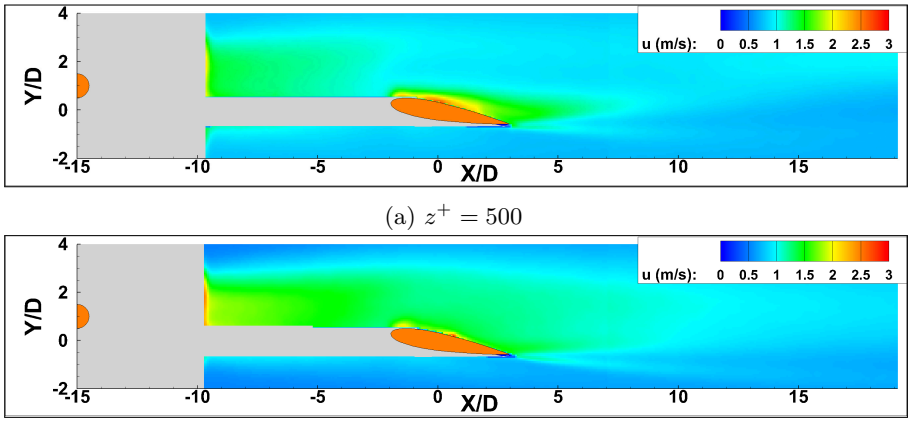

(a) $z^+ = 500$

(b) $z^+ = 3125$

Figure B.43: RMS of streamwise velocities (X direction) in cylinder-airfoil wake

Figure B.44 presents the RMS in the spanwise direction for cylinder-airfoil wake configuration at two heights from the wall ($z^+ = 500$ and $z^+ = 3125$).

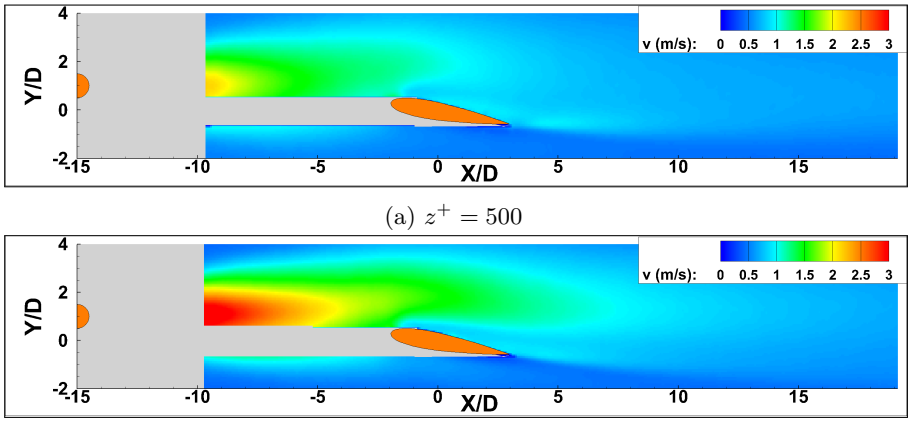

(a) $z^+ = 500$

(b) $z^+ = 3125$

Figure B.44: RMS of spanwise velocities (Y direction) in cylinder-airfoil wake

C.3.2 Total fluctuations energy exchange

Figures B.45a and B.45b show the production term maps in cylinder-airfoil wake configuration for both heights from the wall $z^+ = 500$ and $z^+ = 3125$, respectively.

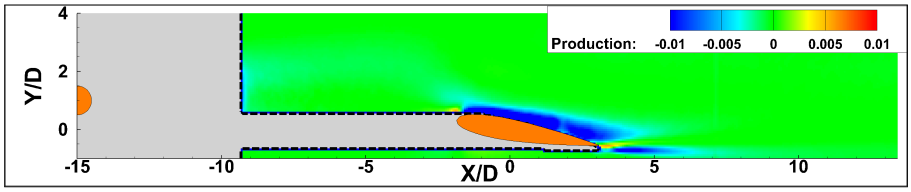

(a) $z^+ = 500$

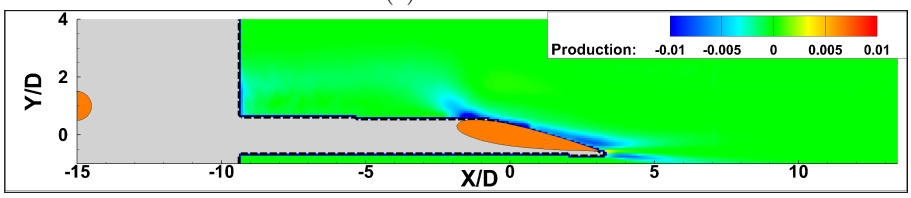

(b) $z^+ = 3125$

Figure B.45: Production of total turbulent kinetic energy by mean velocity in cylinder-airfoil wake. Term is normalized by U_0^3/D.

Figures B.46a and B.46b show the advection term maps in cylinder-airfoil wake configuration for both heights from the wall $z^+ = 500$ and $z^+ = 3125$, respectively.

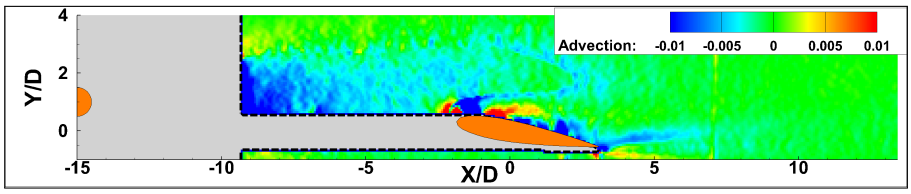

(a) $z^+ = 500$

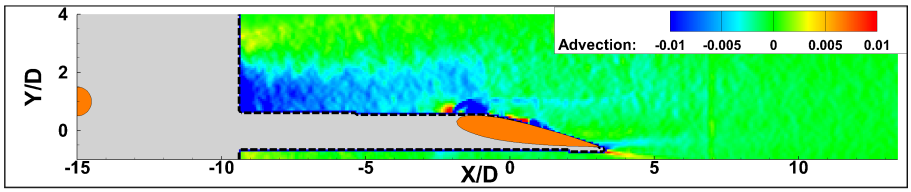

(b) $z^+ = 3125$

Figure B.46: Advection of total kinetic energy by mean velocity in cylinder-airfoil wake. Term is normalized by U_0^3/D.

Figures B.47a and B.47b show the diffusion through Reynolds stresses term maps in cylinder-airfoil wake configuration for both heights from the wall $z^+ = 500$ and $z^+ = 3125$, respectively.

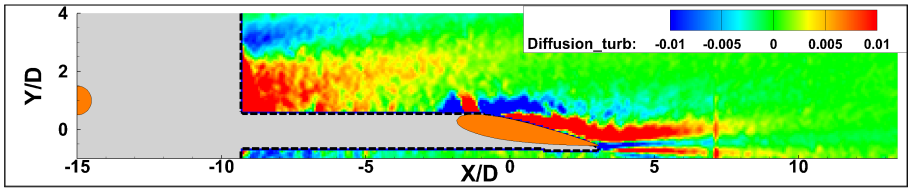

(a) $z^+ = 500$

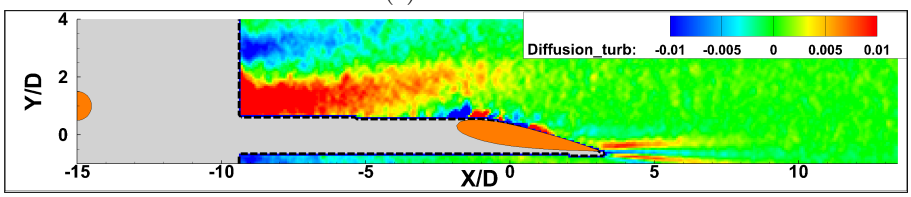

(b) $z^+ = 3125$

Figure B.47: Diffusion of total turbulent kinetic energy by turbulence in cylinder-airfoil wake. Term is normalized by U_0^3/D.

Figures B.48a and B.48b show the diffusion through pressure term maps in cylinder-airfoil wake configuration for both heights from the wall $z^+ = 500$ and $z^+ = 3125$, respectively.

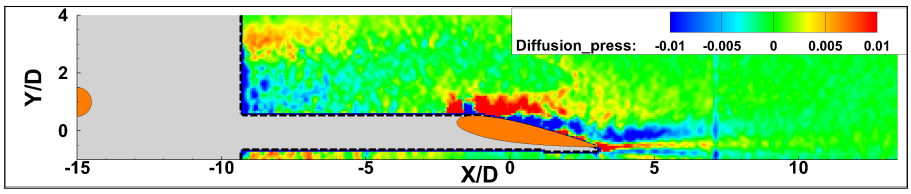

(a) $z^+ = 500$

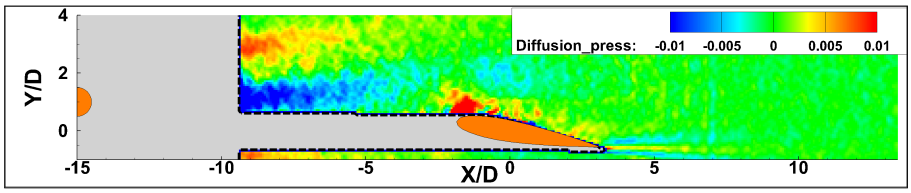

(b) $z^+ = 3125$

Figure B.48: Diffusion of total turbulent kinetic energy by pressure in cylinder-airfoil wake. Term is normalized by U_0^3/D.

Figures B.49a and B.49b show the dissipation term maps in cylinder-airfoil wake configuration for both heights from the wall $z^+ = 500$ and $z^+ = 3125$, respectively.

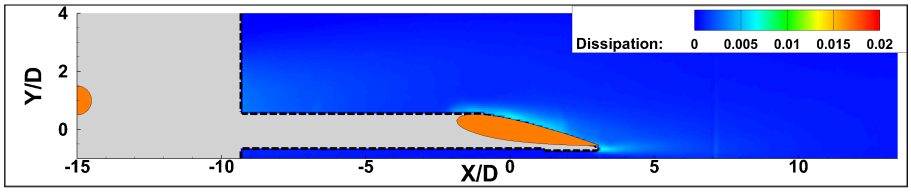

(a) $z^+ = 500$

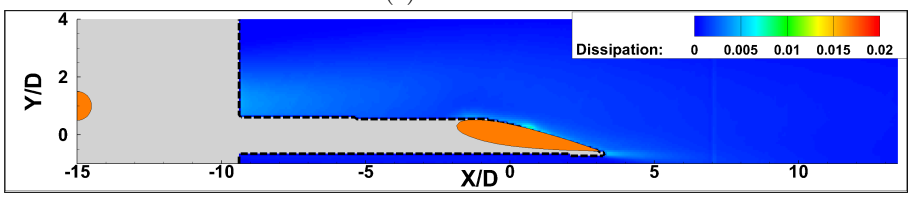

(b) $z^+ = 3125$

Figure B.49: Dissipation of total turbulent kinetic energy in cylinder-airfoil wake. Term is normalized by U_0^3/D.

C.3.3 Decomposed total kinetic energy in phases

Figure B.50 show the production close to the wall ($z^+ = 500$) for four distinct phases ($\phi = 0°$, 100°, 180° and 280°).

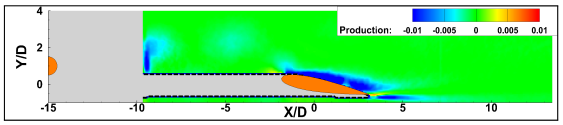

(a) $\phi = 0$

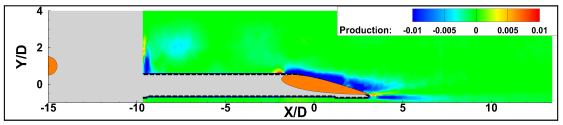

(b) $\phi = 100$

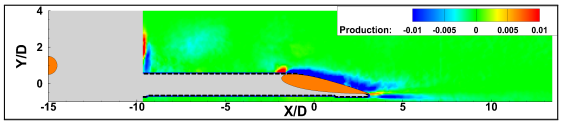

(c) $\phi = 180$

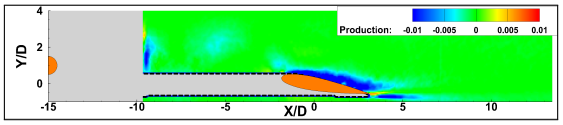

(d) $\phi = 280$

Figure B.50: Decomposed production by mean at $z^+ = 500$ in cylinder-airfoil wake. Term is normalized by U_0^3/D.

Figure B.51 show the advection close to the wall ($z^+ = 500$) for four distinct phases ($\phi = 0°$, 100°, 180° and 280°).

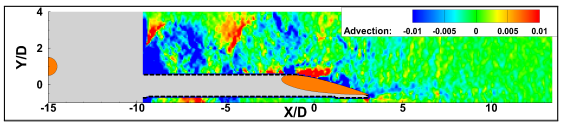

(a) $\phi = 0$

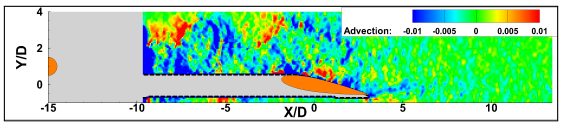

(b) $\phi = 100$

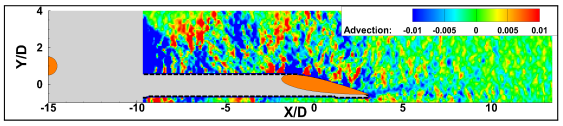

(c) $\phi = 180$

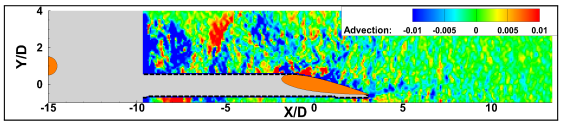

(d) Coherent structures at $\phi = 280$

Figure B.51: Decomposed advection at $z^+ = 500$ in cylinder-airfoil wake. Term is normalized by U_0^3/D.

Figure B.53 show the diffusion close to the wall ($z^+ = 500$) for four distinct phases ($\phi = 0°$, $100°$, $180°$ and $280°$).

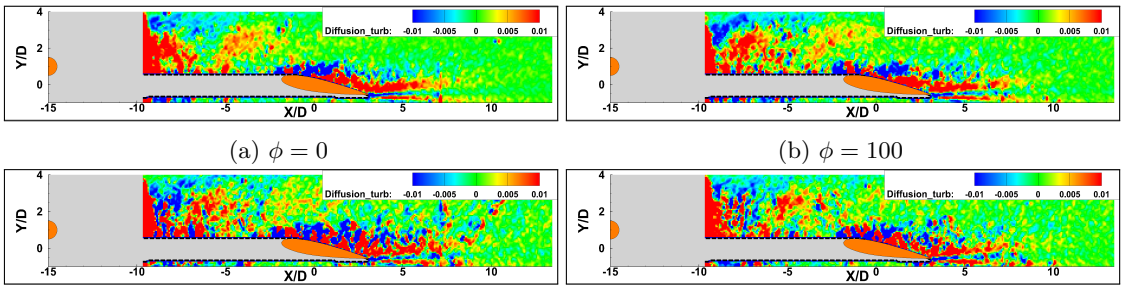

(a) $\phi = 0$ (b) $\phi = 100$

(c) $\phi = 180$ (d) $\phi = 280$

Figure B.52: Decomposed diffusion by turbulence at $z^+ = 500$ in cylinder-airfoil wake. Term is normalized by U_0^3/D.

Figure B.53 show the diffusion through pressure close to the wall ($z^+ = 500$) for four distinct phases ($\phi = 0°$, $100°$, $180°$ and $280°$).

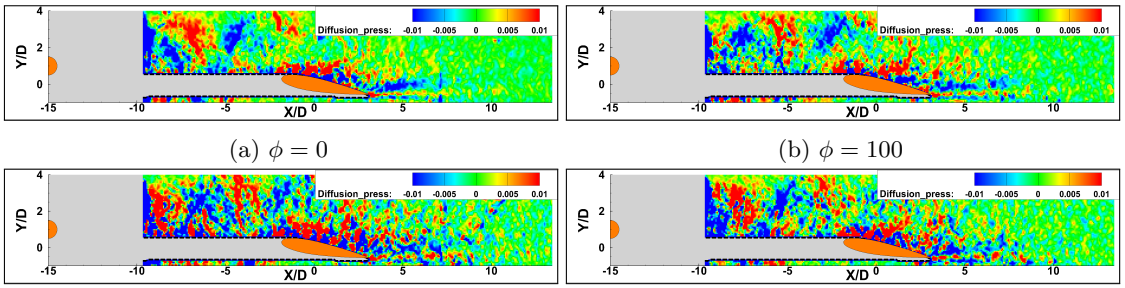

(a) $\phi = 0$ (b) $\phi = 100$

(c) $\phi = 180$ (d) $\phi = 280$

Figure B.53: Decomposed diffusion by pressure at $z^+ = 500$ in cylinder-airfoil wake. Term is normalized by U_0^3/D.

Figure B.54 show the dissipation close to the wall ($z^+ = 500$) for four distinct phases ($\phi = 0°$, $100°$, $180°$ and $280°$).

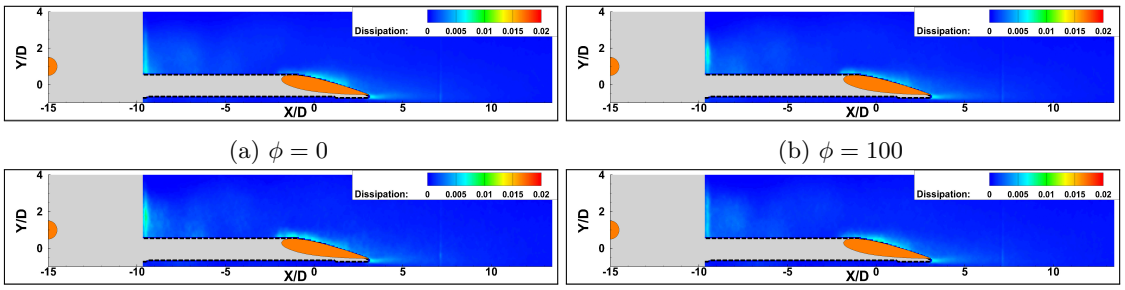

(a) $\phi = 0$ (b) $\phi = 100$

(c) $\phi = 180$ (d) $\phi = 280$

Figure B.54: Decomposed dissipation at $z^+ = 500$ in cylinder-airfoil wake. Term is normalized by U_0^3/D.

C.3.4 CM energy exchange and interaction with RM

Close to wall

Figures B.55a and B.55b show the production and dissipation of coherent motion for cylinder-airfoil wake at $z^+ = 500$, respectively.

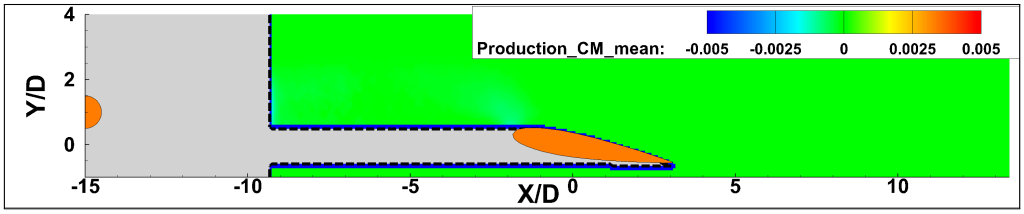

(a) CM production by mean

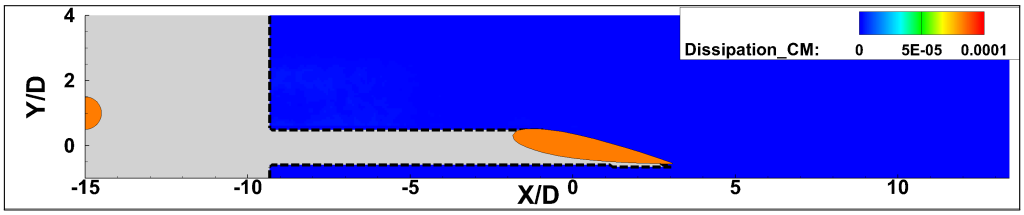

(b) CM dissipation

Figure B.55: Coherent motion (CM) production and dissipation $z^+ = 500$. Terms are normalized by U_0^3/D.

Figure B.56 shows the transport and RM-interaction terms of coherent motion in cylinder-airfoil wake configuration at $z^+ = 500$. The transport terms is decomposed to transport by mean flow (advection) and transport by fluctuations (diffusion).

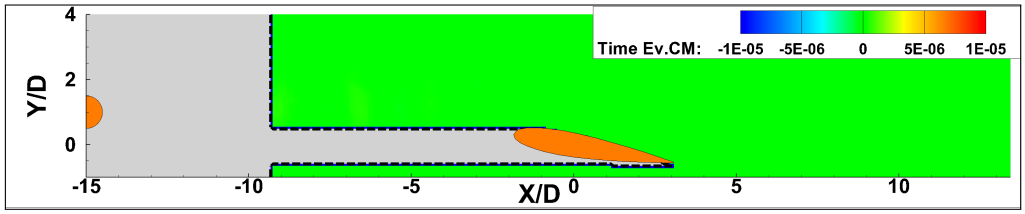

(a) CM time evolution in time

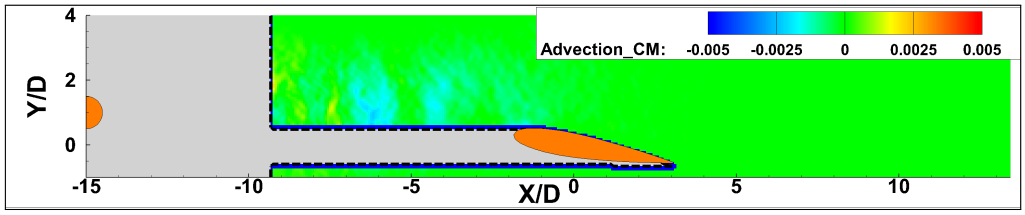

(b) CM advection by mean velocity

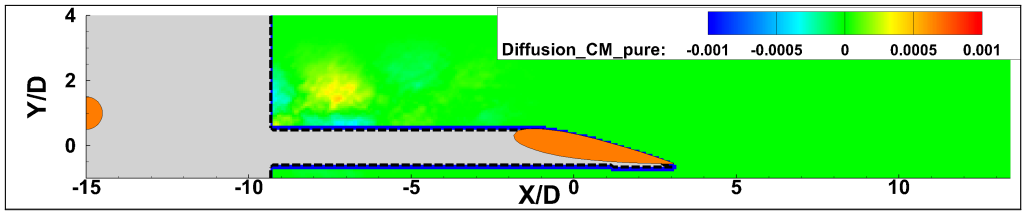

(c) CM pure diffusion

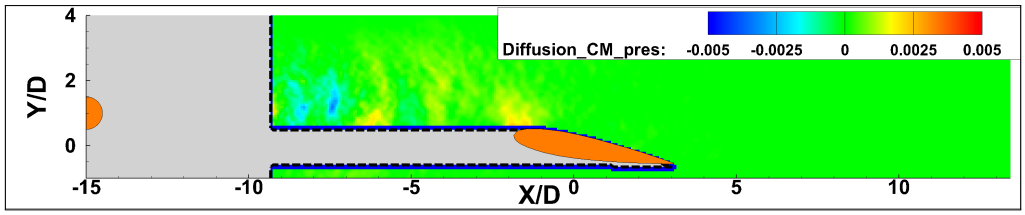

(d) CM diffusion by pressure

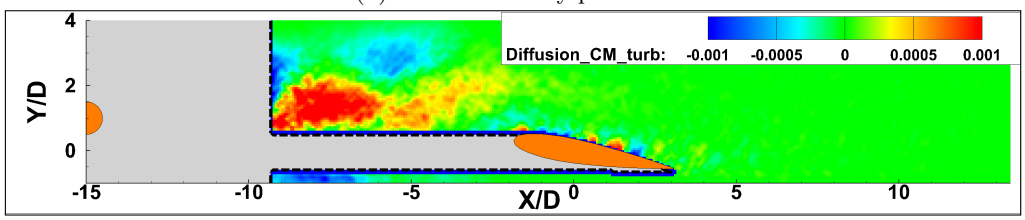

(e) CM diffusion by turbulence

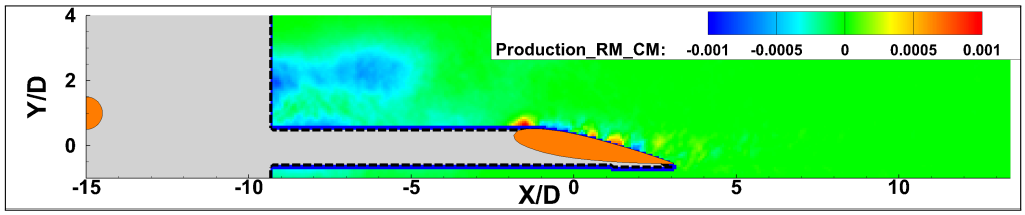

(f) RM production bt CM

Figure B.56: Coherent motion (CM) transports at $z^+ = 500$. Terms are normalized by U_0^3/D.

Far from wall

Figures B.57a and B.57b show the production and dissipation of coherent motion for cylinder-airfoil wake at $z^+ = 3125$, respectively.

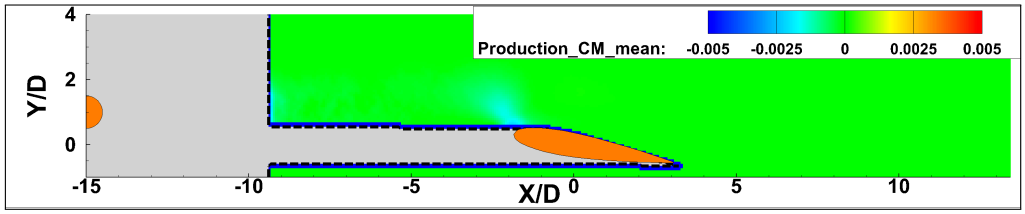

(a) CM production by mean

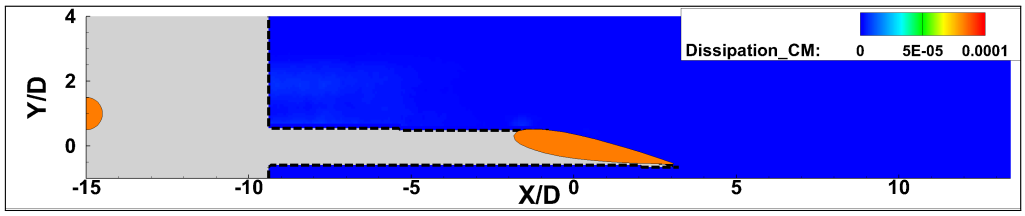

(b) CM dissipation

Figure B.57: Coherent motion (CM) production and dissipation $z^+ = 3125$. Terms are normalised by U_0^3/D.

Figure B.58 shows the transport and RM-interaction terms of coherent motion in cylinder-airfoil wake configuration at $z^+ = 3125$. The transport terms is decomposed to transport by mean flow (advection) and transport by fluctuations (diffusion).

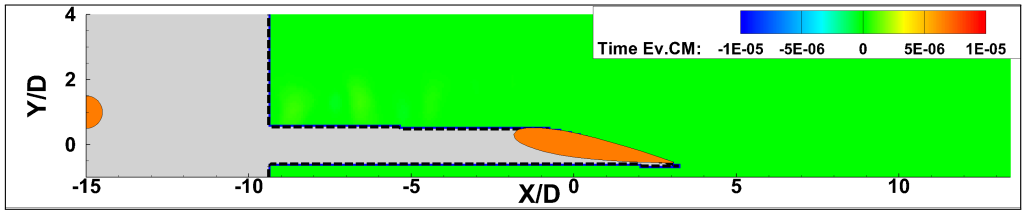

(a) CM time evolution in time

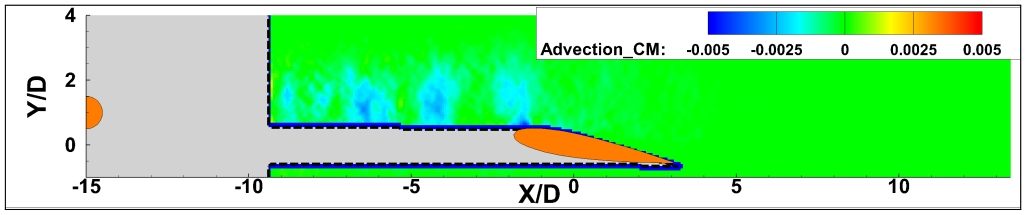

(b) CM advection by mean velocity

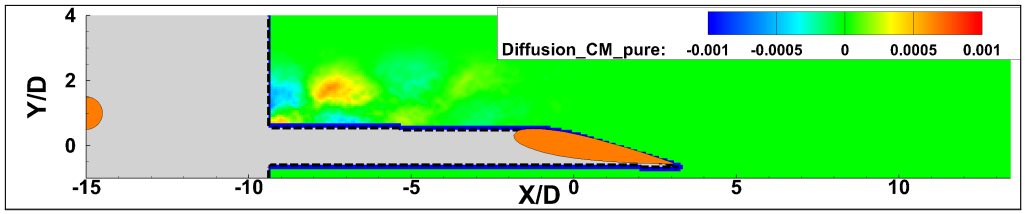

(c) CM pure diffusion

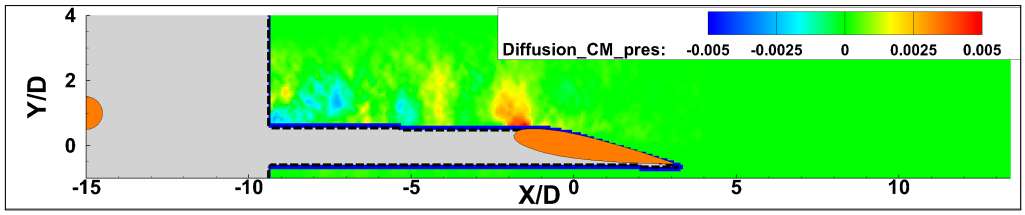

(d) CM diffusion by pressure

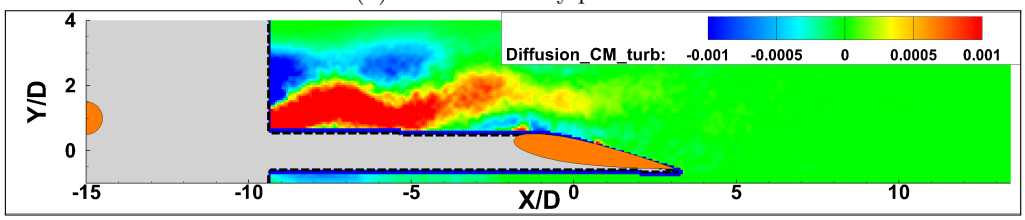

(e) CM diffusion by turbulence

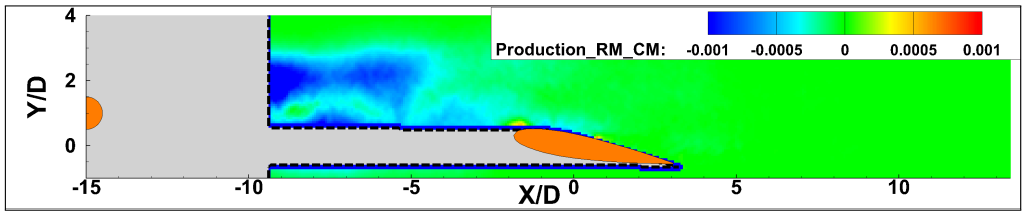

(f) RM production bt CM

Figure B.58: Coherent motion (CM) transports at $z^+ = 3125$. Terms are normalized by U_0^3/D.

C.3.5 RM energy exchange and interaction with CM

Close to wall

Figure B.59 shows the energy exchange terms of random motion equation for cylinder-airfoil wake at $z^+ = 500$.

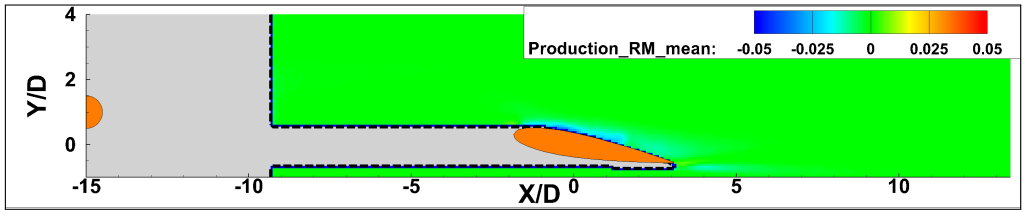

(a) RM production by mean

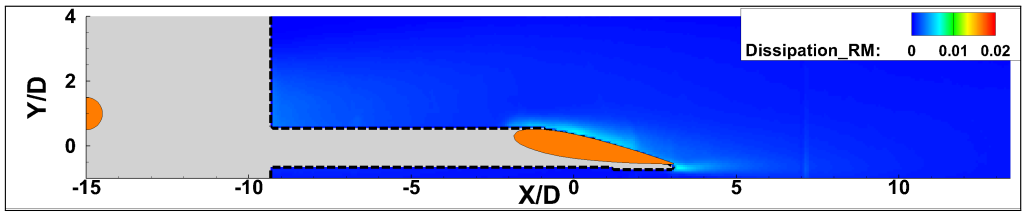

(b) RM dissipation

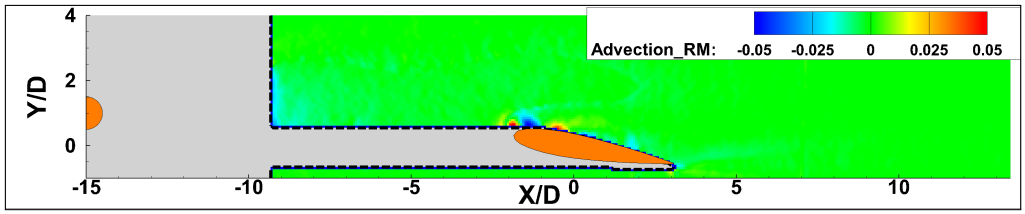

(c) RM advection by mean velocity

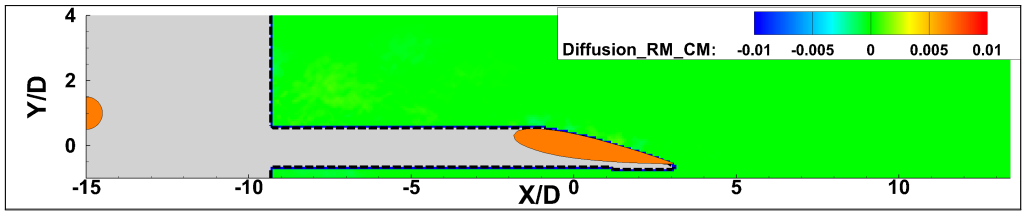

(d) RM diffusion by CM interaction

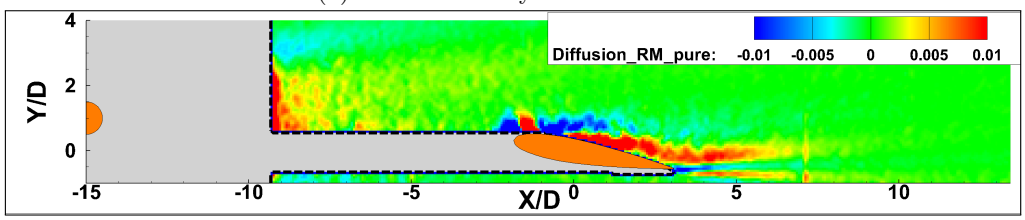

(e) RM pure diffusion

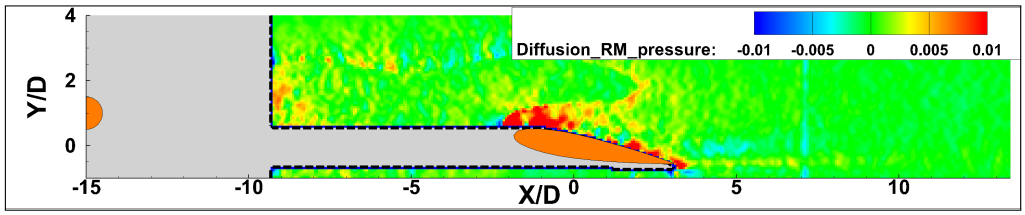

(f) RM pure diffusion

Figure B.59: Random motion (RM) energy budget in cylinder-airfoil wake at $z^+ = 500$.Terms are normalized by U_0^3/D.

Far from wall

Figure B.60 shows the energy exchange terms of random motion equation for cylinder-airfoil wake at $z^+ = 3125$.

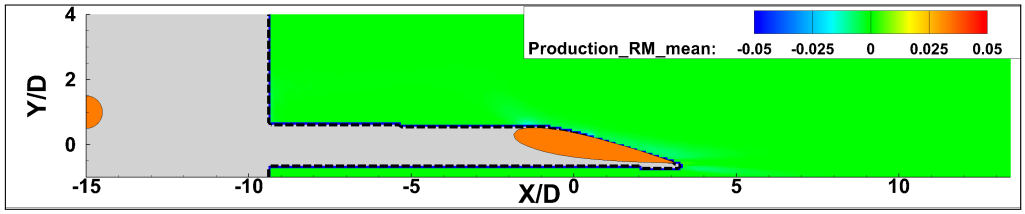

(a) RM production by mean

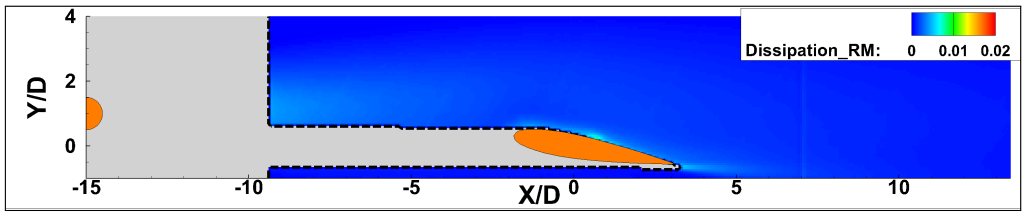

(b) RM dissipation

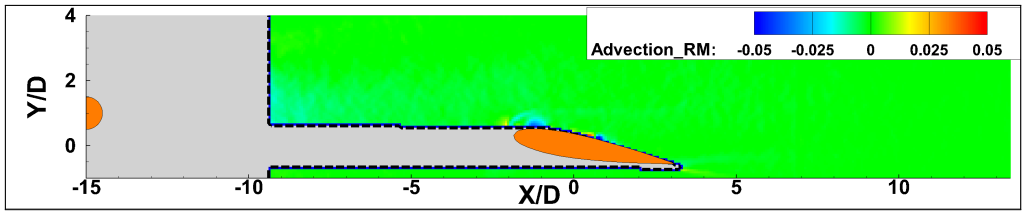

(c) RM advection by mean velocity

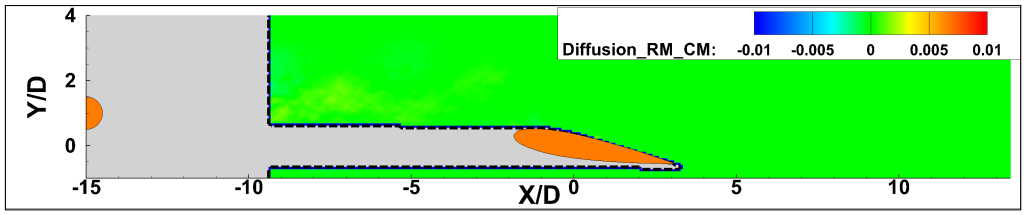

(d) RM diffusion by CM interaction

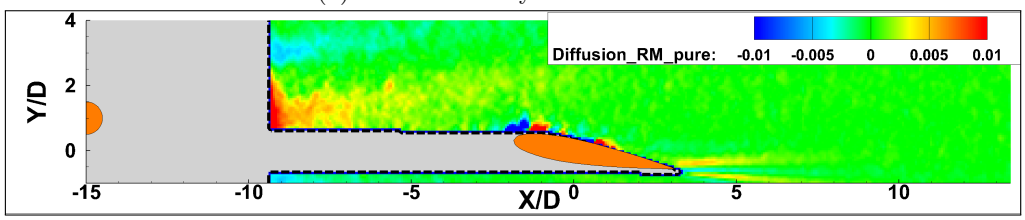

(e) RM pure diffusion

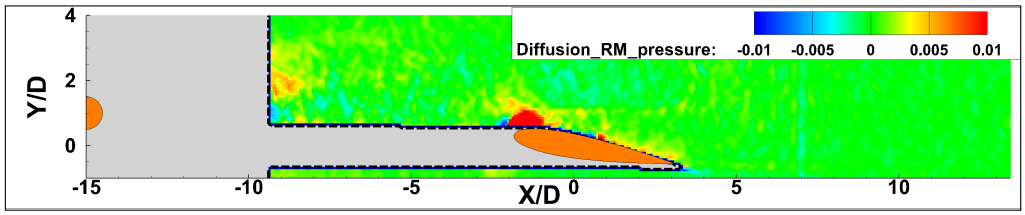

(f) RM pure diffusion

Figure B.60: Random motion (RM) energy budget in cylinder-airfoil wake at $z^+ = 3125$. Terms are normalized by U_0^3/D.

D.4 Airfoil configuration

D.4.1 First order statistics

Figures B.61a and B.61b presents the mean velocity in streamwise and spanwise direction for single airfoil wake configuration at $z^+ = 500$.

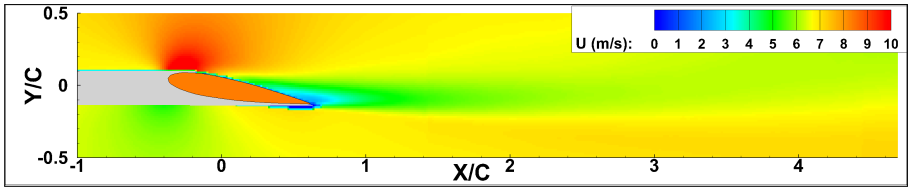

(a) Streamwise (X direction)

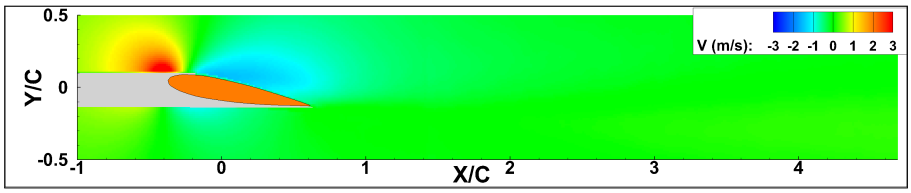

(b) Spanwisewise (Y direction)

Figure B.61: Mean velocities in single airfoil wake at $z^+ = 500$

Figures B.62b and B.62b presents the RMS in streamwise and spanwise direction for single airfoil wake configuration at $z^+ = 500$.

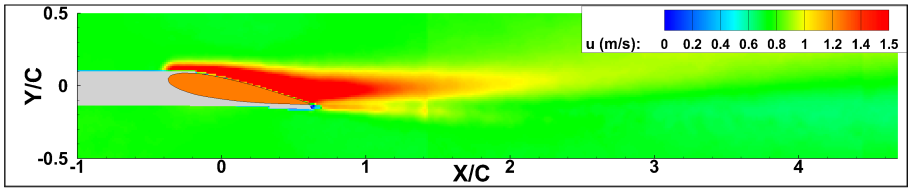

(a) Streamwise (X direction)

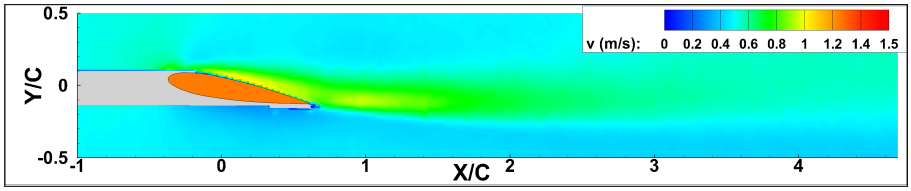

(b) Spanwise (Y direction)

Figure B.62: RMS of velocities in single airfoil wake at $z^+ = 500$

D.4.2 Total fluctuations energy exchange

Figure B.63 presents the total turbulent kinetic energy terms for single airfoil wake configuration at $z^+ = 500$.

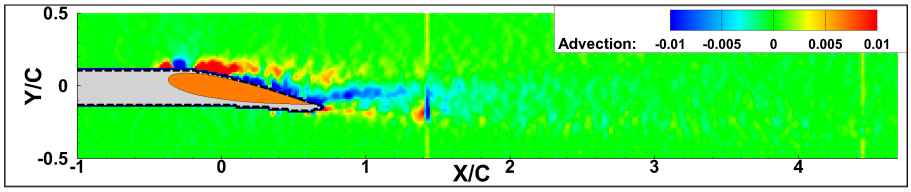

(a) Advection

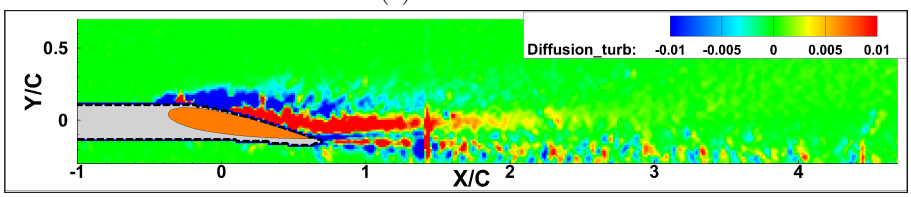

(b) Diffusion by Reynolds stresses

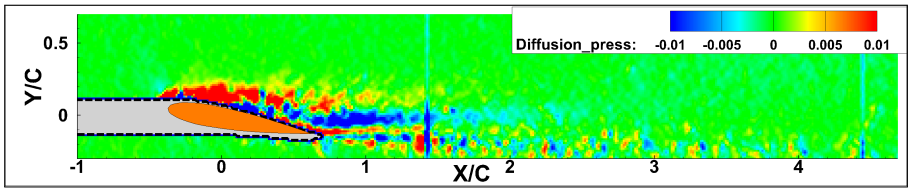

(c) Diffusion by pressure

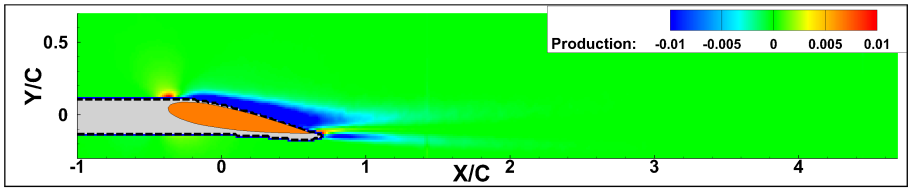

(d) Production by mean velocity

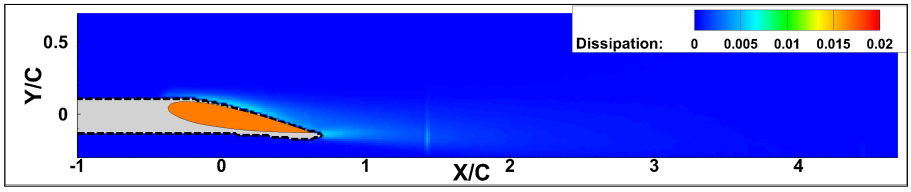

(e) Dissipation

Figure B.63: Total kinetic energy of turbulence in single airfoil wake at $z^+ = 500$. Terms are normalized by U_0^3/D

E.5 Double airfoil configuration

E.5.1 First order statistics

Figures B.64a and B.64b presents the mean velocity in streamwise and spanwise direction for double airfoil wake configuration at $z^+ = 500$.

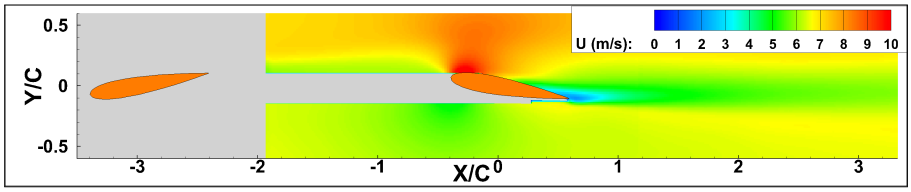

(a) Streamwise (X direction)

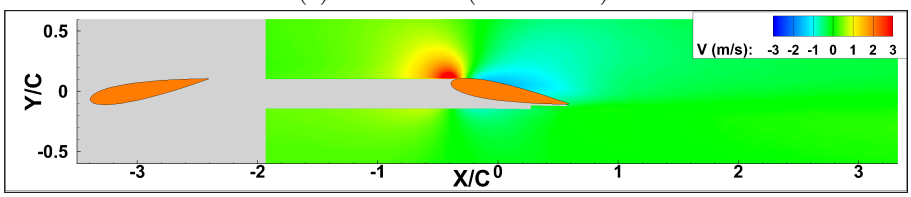

(b) Spanwise (Y direction)

Figure B.64: Mean velocities in double airfoil wake at $z^+ = 500$

Figures B.65b and B.65b presents the RMS in streamwise and spanwise direction for double airfoil wake configuration at $z^+ = 500$.

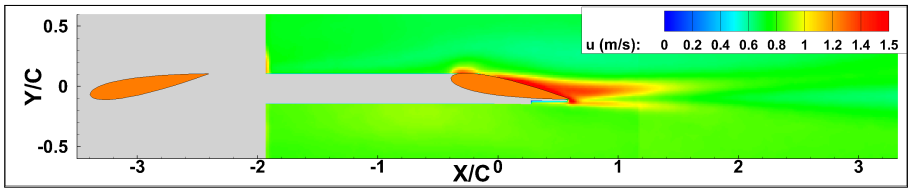

(a) Streamwise (X direction)

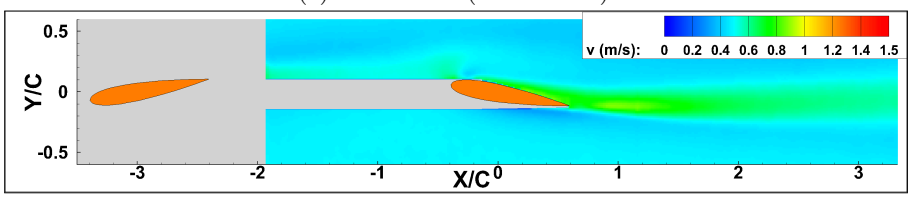

(b) Spanwise (Y direction)

Figure B.65: RMS of velocities in double airfoil wake at $z^+ = 500$

E.5.2 Total fluctuations energy exchange

Figure B.66 presents the total turbulent kinetic energy terms for double airfoil wake configuration at $z^+ = 500$.

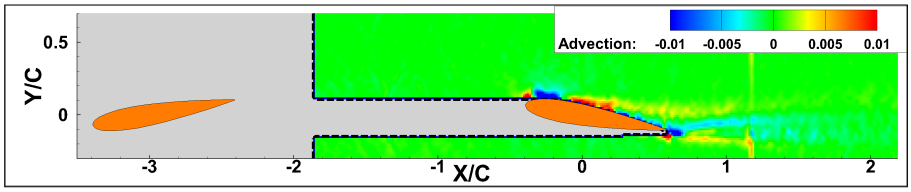

(a) Advection

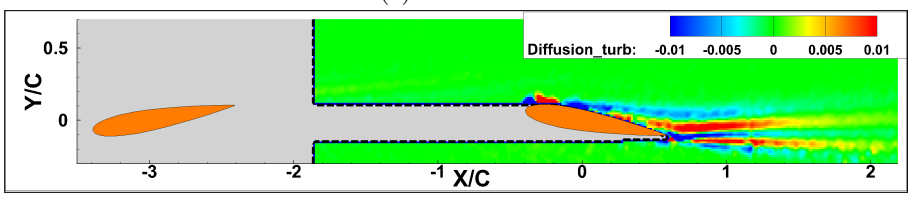

(b) Diffusion by turbulence

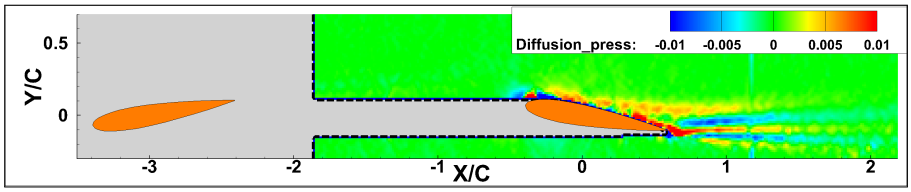

(c) Diffusion by pressure

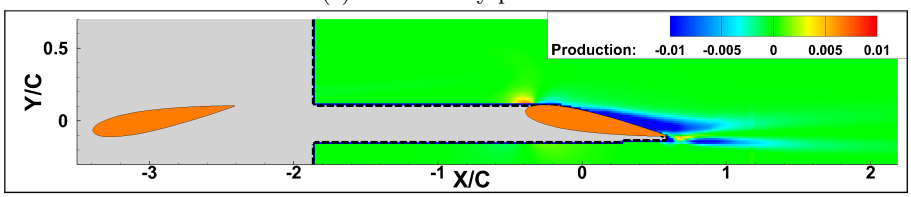

(d) Production by mean velocity.

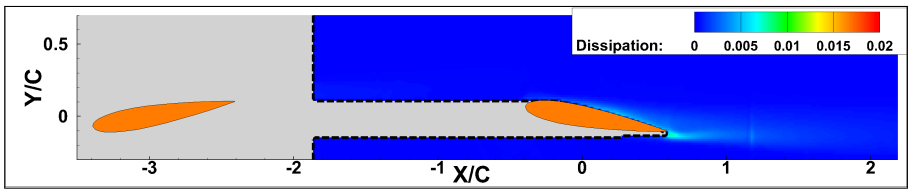

(e) Dissipation

Figure B.66: Total kinetic energy of turbulence in double airfoil wake at $z^+ = 500$. Terms are normalized by U_0^3/D